

Smart Electronic Textile-Based Wearable Supercapacitors

Md Rashedul Islam, Shaila Afroj,* Kostya S. Novoselov, and Nazmul Karim*

Electronic textiles (e-textiles) have drawn significant attention from the scientific and engineering community as lightweight and comfortable next-generation wearable devices due to their ability to interface with the human body, and continuously monitor, collect, and communicate various physiological parameters. However, one of the major challenges for the commercialization and further growth of e-textiles is the lack of compatible power supply units. Thin and flexible supercapacitors (SCs), among various energy storage systems, are gaining consideration due to their salient features including excellent lifetime, lightweight, and high-power density. Textile-based SCs are thus an exciting energy storage solution to power smart gadgets integrated into clothing. Here, materials, fabrications, and characterization strategies for textile-based SCs are reviewed. The recent progress of textile-based SCs is then summarized in terms of their electrochemical performances, followed by the discussion on key parameters for their wearable electronics applications, including washability, flexibility, and scalability. Finally, the perspectives on their research and technological prospects to facilitate an essential step towards moving from laboratory-based flexible and wearable SCs to industrial-scale mass production are presented.

which facilitate the manufacturing of highly innovative and intelligent garments, able to perform as sensors, actuators, power generators, and energy storage devices all at the same time.^[7,8] Combining these electronic fibers/textiles with human skin can potentially build an intelligent system that could be integrated with biological nerves, muscles, and ligaments in the future to endow us with more functions.^[9] E-textiles inherit the advantages of being lightweight, flexible, and air permeable with a certain degree of ductility of traditional fibers/textiles while possessing electronic functions.^[10,11] As a lightweight portable device to monitor vital health parameters (Figure 1), e-textiles have become a focus of research interest due to their prospects in sportswear, military uniforms, safety instruments, environmental monitoring, and health care applications.^[12–14] However, one of the key challenges to integrate such electronic devices into textiles is the requirement of a lightweight, flexible, and high-performance power supply unit.^[15,16]

Conventional energy storage devices (e.g., batteries) can store a large amount of energy that cannot be delivered quickly owing to their higher internal resistance. Capacitors are another type of energy storage device, which can be charged and discharged quickly. However, capacitors have limited storage capacity. Therefore, the development of capacitors with high energy densities (i.e., supercapacitors) has become an exciting area of research for electrochemical energy storage/conversion systems. Supercapacitors (SC), also referred to as ultracapacitors, are promising electrochemical energy storage devices that can be charged and discharged within seconds, and possess high power density, long cycle life, and outstanding cyclic stability.^[17] As a relatively new type of capacitors, they are distinguished by the phenomenon of electrochemical double-layer, diffusion, and large effective area which lead to extremely large capacitance per unit of geometrical area, taking their place in-between batteries and conventional capacitors. Considering energy and power densities, they also possess a wide area between batteries and conventional capacitors (Figure 2). The incorporation of flexible electrodes and/or substrate materials in SCs provides structural flexibility with their inherent high-power density, which are highly attractive for a large number of emerging portable and lightweight consumer devices.^[18] Flexible plastic, elastomeric and textile substrates possess better biocompatibility, stretchability, transparency, and wearability.^[19] In addition to intrinsic wearability and flexibility, a textile-based SC ensures better comfort when worn, better

1. Introduction

Wearable electronic textiles (e-textiles) have been going through significant evolutions in recent years, due to the continuous progress of material science and nanotechnology, miniaturization, and wireless revolution.^[1,2] E-textiles possess functionalities such as sensing, computation, display, and communication,^[3–6]

M. R. Islam, S. Afroj, N. Karim
Centre for Print Research (CFPR)
The University of the West of England
Frenchay Campus, Bristol BS16 1QY, UK
E-mail: shaila.afroj@uwe.ac.uk; nazmul.karim@uwe.ac.uk

K. S. Novoselov
Institute for Functional Intelligent Materials, Department of Materials
Science and Engineering
National University of Singapore
Singapore 117575, Singapore

K. S. Novoselov
Chongqing 2D Materials Institute
Liangjiang New Area, Chongqing 400714, China

 The ORCID identification number(s) for the author(s) of this article can be found under <https://doi.org/10.1002/adv.202203856>

© 2022 The Authors. Advanced Science published by Wiley-VCH GmbH. This is an open access article under the terms of the Creative Commons Attribution License, which permits use, distribution and reproduction in any medium, provided the original work is properly cited.

DOI: 10.1002/adv.202203856



Figure 1. Textile-based flexible supercapacitors for powering up wearable devices to monitor physiological parameters.

integration with the garment, and better wearability of the electronic components in comparison to the conventional rigid and bulky power supply units. It also ensures the enhanced mass loading of active materials, resulting in higher capacitance, energy, and power density. Therefore, textile-based flexible SCs show great potential for wearable electronic applications, due to miniaturized, portable, and flexible consumer electronics in comparison with the current energy storage devices.^[20]

While several flexible substrates can be exploited for SC fabrication, this review focuses on textiles-based flexible and wearable SCs due to their potential for next-generation wearable e-textiles applications. First, we present an overview of electrochemical energy storage technologies and their working principles. We then discuss the basic parameters to evaluate SC performances. Additionally, we summarize suitable textile substrates as well as electroactive materials required for the preparation of conductive textile electrodes and electrolytes for SC fabrications. We then review manufacturing techniques for conductive textile-based electrodes, followed by various forms of textile-based SCs and their integration techniques. We also summarize the energy storage performances of recently developed textile-based SCs in terms of capacitance, energy density, and power density. Furthermore, key properties of textiles-based SCs for wearable e-textiles applications such as flexibility, safety, and washability are discussed. Finally, we conclude our review with recommendations on future research directions for textile-based SCs.

2. Overview of Electrochemical Energy Storage System

Energy storage is defined as the conversion of electrical energy from a power network into a form, that can be stored until con-

verted back to its original electrical form.^[21] The purpose of such a system is to capture produced energy for later use,^[22] offering a number of significant benefits including achieving demand-side energy management, improved stability of power quality, and the reliability of power supply on a long-term basis.^[23] With the intensified energy crisis in recent years, energy storage has become a major research focus in both industry and academia^[24] and is viewed as a promising solution for future highly renewable power systems.^[25] Among the various forms of energy storage, electrochemical energy storage (EES) systems are vital, due to their versatility from assisting very large-scale electrical grids down to tiny portable devices to be used for various purposes.^[26,27] They offer the electrical energy accumulation for longer durability (even over 10^6 cycles) and higher specific power (more than 10 kW kg^{-1}), making them very useful for short-term pulses in hybrid electrical vehicles, digital telecommunications systems, uninterruptible power supply (UPS) for computers, pulse laser techniques, etc.^[28] The electric energy is stored in the chemical bonds of electrode materials of the device, which involves the conversion reaction between chemical and electric energy. Nowadays, EES devices are an integral part of telecommunication systems (cell phones, remote communication, walkie-talkies, etc.), standby power systems, and electric hybrid vehicles in the form of storage components such as batteries, SCs, and fuel cells.^[29]

Two main parameters are important for energy storage: energy density and power density. The energy density is defined as the amount of energy to be stored per unit volume or weight, and the power density is described as the speed at which energy is stored or discharged from the device. An ideal storage device should simultaneously possess both high energy and power densities. Batteries and fuel cells are typical EES devices of small specific power, while conventional capacitors can have higher specific power but exhibit a very low specific energy. The performance parameters of EES such as energy density, power density, and safety mostly depend on the electrode materials, which should have high electro activity, high electron/ion conductivity, and high structure/ electrochemical stability.^[30] Many efforts have been made to develop advanced electrode materials in the last few decades, however, it still requires further development regarding energy density, power density, and lifespan. Additionally, it is desirable to fabricate EES with high electrochemical performance, ultra-flexibility, and lightweight for wearable electronics applications.^[31]

2.1. Structure of EES Devices

EES devices usually consist of electrode material, current collector, separator, and electrolyte.^[32] A thin layer of separator, sandwiched by a pair of electrodes and current collectors, filled with electrolyte make the device, **Figure 3**. Electrodes are composed of electrochemically active materials which store charges. Current collector, made of electrically conductive substrates, connects the electrodes with the external circuitry for the charge transfer. Separators physically and electrically separate electrodes to avoid short circuits. Electrolytes, either in liquid or in gel form, are used to carry and transport charged ions between electrodes. Finally, an encapsulation layer is applied to protect the full integration from any leakage of electrolyte and oxidation of any material, ensuring

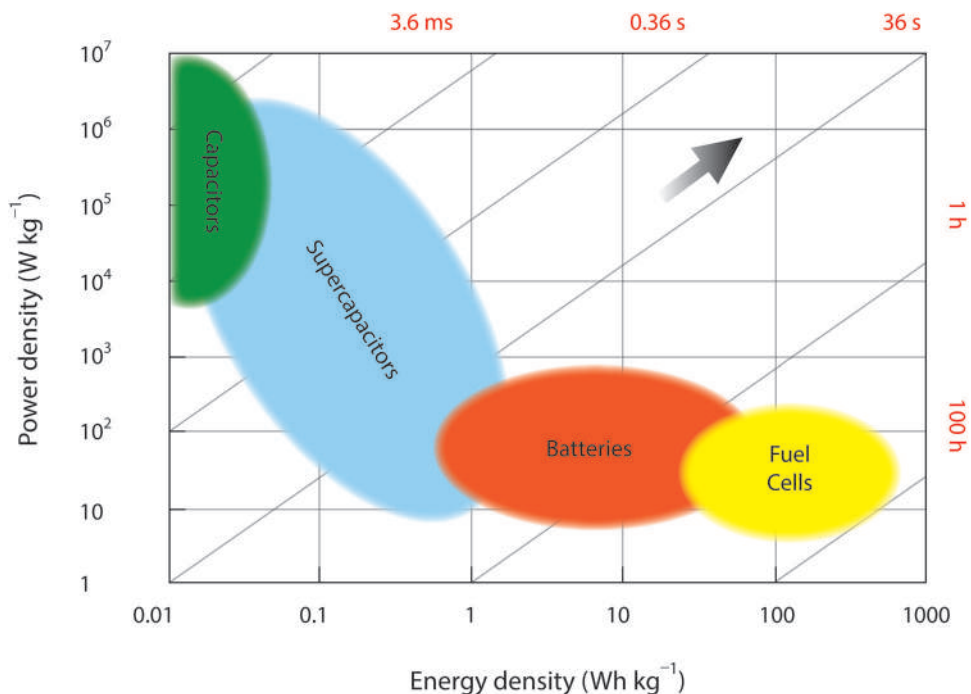


Figure 2. Ragone plot showing comparison of different electrochemical energy storage systems.

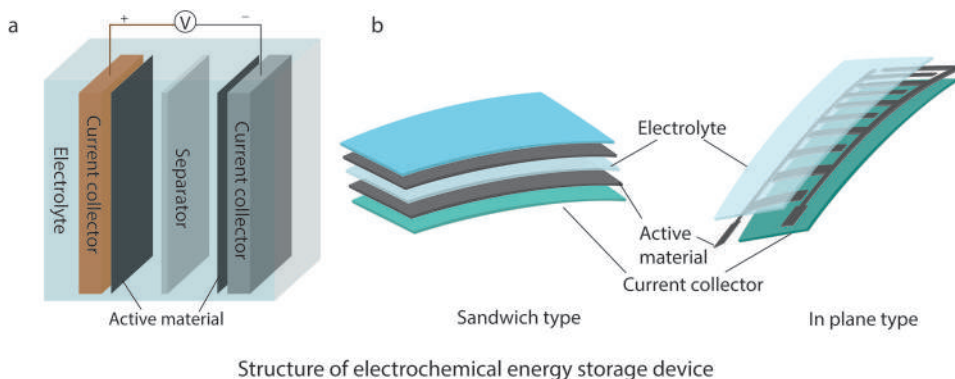


Figure 3. Schematic diagram of the structure of electrochemical energy storage devices. a) Conventional rigid form and b) flexible form.

the stability and safety of the device.^[33] Figure 4(a–c) represents the schematic of the basic structural components of different EES devices.

2.2. Types and Working Principles of EES

EES devices are primarily classified as electrochemical capacitors (Figure 4a), batteries (Figure 4b), and fuel cells (Figure 4c). Due to a comparatively bulk structure, fuel cell is not considered suitable for wearable applications. Therefore, EES devices that are used in wearable systems, may either be electrochemical capacitors or batteries. Electrochemical capacitors, also known as supercapacitors (SCs) or ultracapacitors, can be charged and discharged quickly with nearly 100% efficiency. They possess outstanding power performance, good reversibility, and a very long cycling life (>100 000 cycles). Table 1 compares the char-

acteristics of various EES devices. Depending on the use of electrode materials, SCs are further divided into electrostatic double-layer capacitors (EDLCs), pseudocapacitors, and hybrid capacitors. There are two charge storage mechanisms involved in the operation of SCs: storing the charges electrostatically (at the interface of capacitor electrode as electric double layer capacitance) and storing the charges faradaically (at the electrode surface as pseudocapacitance).^[34] Table 2 compares the properties among various SC types.

2.2.1. Electrical Double-Layer Capacitors (EDLCs)

An electric double layer (EDL) or Helmholtz double-layer (attributed to Helmholtz) involves the formation of two charged layers at the electrode-electrolyte interface. Thus, the ability to store potential-dependent charge is termed as electric double

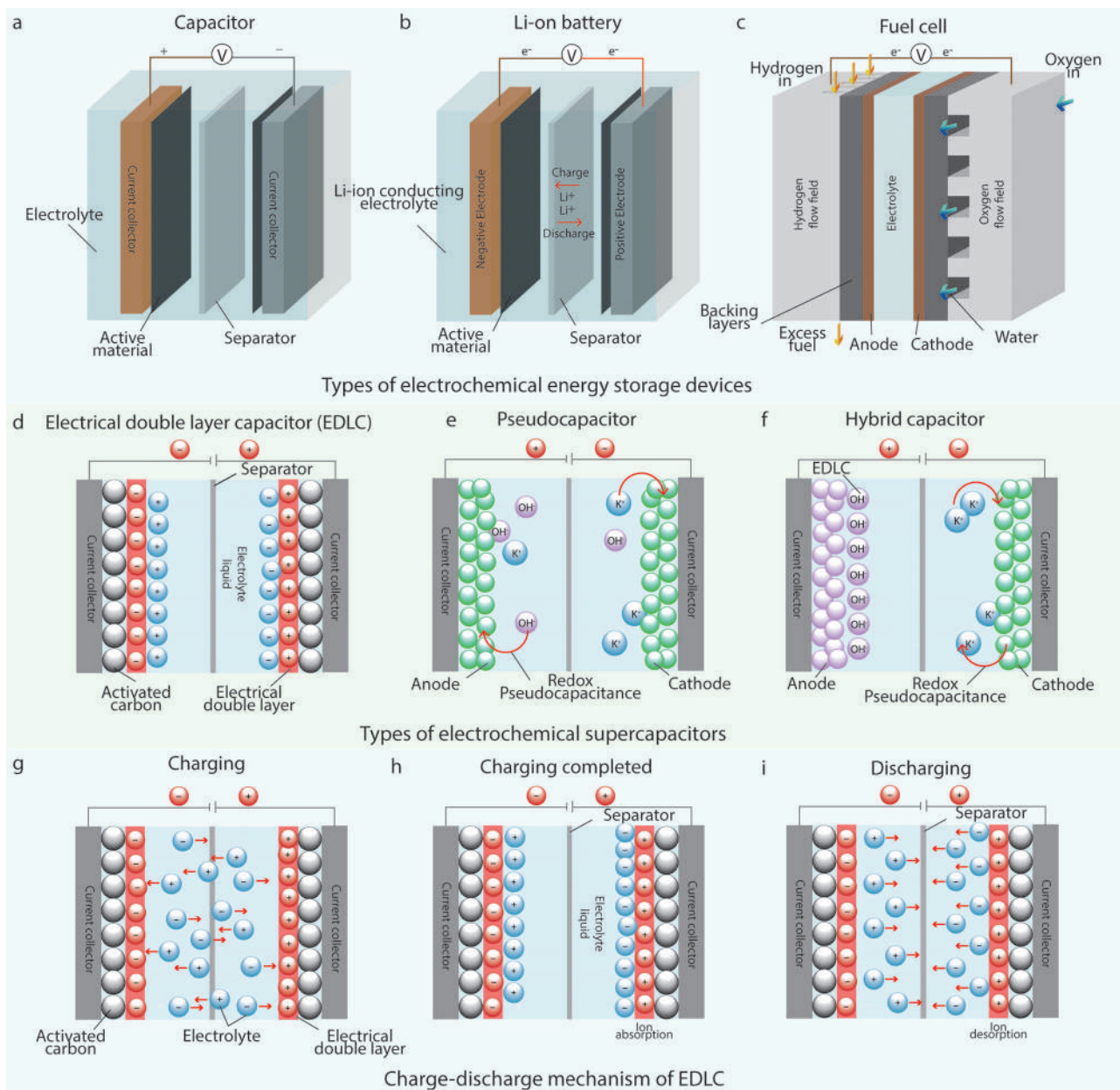


Figure 4. Basic schematic of electrochemical energy storage devices: a) a capacitor, b) a Li-ion battery, and c) a fuel cell. Types of electrochemical supercapacitors: d) EDLC, e) Pseudocapacitor, f) Hybrid capacitor, and g–i) Charge-discharge mechanism of an EDLC.

layer capacitance, and the SCs based on this principle are termed as electric double layer capacitors (EDLCs). From a structural view, they consist of three parts: two active material-loaded electrodes, an electrolyte, and a separator sheet,^[37] Figure 4d. Energy is stored through charge separation and can keep considerably more energy than a classic capacitor. A simple movement of ions migrating to and releasing from electrode surfaces is involved (Figure 4g–i), therefore can respond rapidly.^[38] EDLCs are usually evaluated in terms of Farads (F), instead of picofarads (pF) and microfarads (μ F) for the conventional dielectric and electrolytic capacitors due to their ability to store much more electricity. EDLCs have high power density, good reversibility, and

long cycle life, achieved by the use of high-surface-area activated carbon (AC) as the working medium in the capacitor system.^[34]

2.2.2. Pseudo Capacitors

Pseudo capacitors defeat EDLCs in energy density for the reversible redox reactions between their electrode materials and electrolytes,^[39] Figure 4e. They are also referred to as redox supercapacitors, since they store charges, faradaically, through battery-like redox reactions but at a faster rate than the EDLCs, offering a pathway for achieving both high energy and high-power

Table 1. Comparison among various EESDs.^[35,36]

Characteristics	Li-ion battery	Capacitor	Supercapacitor	Fuel cell
Storage mechanism	Chemical	Physical	Physical and chemical	N/A
Energy storage	High	Limited	Limited	High
Energy density [Wh kg ⁻¹]	8–600	0.01–0.05	1–10	300–3000
Power density [kW kg ⁻¹]	0.005 to 0.4	0.25–10 000	10–120	0.001–0.1
Charge/discharge time	1–10 h	ps-ms	ms-seconds	10–300 h
Operating temperature	–20 to +65 °C	–20 to +100 °C	–40 to +85 °C	+25 to +90 °C
Operating voltage	1.25 to 4.2V	6 to 800V	2.3 to 2.75V	0.6V
Cycle-life	150–1500	>100 000	>50 000+ h, unlimited	1500–10 000 h
Charge-discharge efficiency [%]	70–85	100	85–98	60
Charge stored determinants	Active mass and thermodynamics	Electrode area and dielectric	Electrode microstructure and electrolyte	N/A

Table 2. Comparison among various types of supercapacitors.^[45–47]

Parameters	Electric double layer capacitor (EDLC)	Pseudo-capacitor (PC)	Hybrid capacitor (HC)
Charge storage mechanism	Physical – Non-faradic/electrostatic, electrical charge store at electrode/electrolyte interface	Chemical- faradic, reversible redox reaction	Physical and chemical (both faradic and non-faradic)
Electrode materials	Carbonaceous compounds	Conductive polymers and metal oxides	Combination of EDLC and PC-type materials
Specific capacitance [Fg ⁻¹]	Lower (200–300)	Higher (200–1340)	Higher (50–1893)
Energy density [Wh kg ⁻¹]	Low (6.8–12)	High (167–223)	High (132–231)
Cyclability [cycles]	High (100 000)	Low (5000)	Medium (12 000)
Capacitance retention [%]	60–100	52–96	80–95

densities. Materials that combine these properties are in demand for the realization of fast-charging EES devices capable of delivering high power for a long period of time.^[40] Transition metal oxides such as MnO₂, conductive polymers like Polyaniline (PANI), Polypyrrole (PPy), or derivatives of Polythiophene (PTh) such as Poly (3,4-(ethylenedioxy) thiophene) (PEDOT) are being studied as prominent pseudocapacitive materials nowadays. This faradaic charge transfer process is highly reversible. During charging, the surface region of redox-active electrode materials gets reduced to lower oxidation states coupled with adsorption/insertion of cations from the electrolyte at/near the electrode surfaces. Upon discharge, the process can be almost fully reversed,^[34] similar to the charging and discharging processes that occur in batteries, resulting in faradaic current passing through the SC cell.^[41,42] Pseudo capacitors offer a higher energy density but a lower cycle life than EDLCs.

2.2.3. Hybrid Capacitors

Hybrid SCs offer improved performance in energy density without altering the power density and have been in recent trends. They deliver higher specific capacitance in comparison to the existing EDLC and pseudocapacitors.^[43] They are made by the hybridization of two types of electrodes to form a new capacitor, Figure 4f. This is a unique approach, which is used to enhance the electrochemical properties of a single cell. The exhibition of electrochemical behavior over a wide voltage range will enhance

the overall operating voltage window and increase specific energy density, which is larger than the cells containing a single type of electrode. Among two types of electrodes in hybrid capacitors, one is an energy source electrode (i.e., battery-like electrodes), and the other terminal contains a power source electrode (i.e., either an EDLC or a pseudo capacitor electrode). The selection of the energy source electrode is important to enhance the cell voltage without sacrificing much energy and power densities. Such configuration offers the advantages of both SCs and advanced batteries, resulting in a significant increase in the overall energy density of the system.^[44]

2.2.4. Lithium-Ion Batteries

Batteries store charge through the conversion of electrical energy into chemical energy. In a lithium-ion battery (LIB), lithium ions move from the negative to the positive electrode during discharge, and travel back to the negative electrode when charging, Figure 4b. Unlike lithium primary batteries (which are disposable), LIBs use an intercalated lithium compound as the electrode material, instead of metallic lithium. LIBs are common in consumer electronics as rechargeable batteries for portable electronics, which provide one of the best energy-to-weight ratios, high open circuit voltage, low self-discharge rate, no memory effect, and a slow loss of charge when not in use. Beyond consumer electronics, LIBs are growing in popularity for military, electric vehicle, and aerospace applications due to their

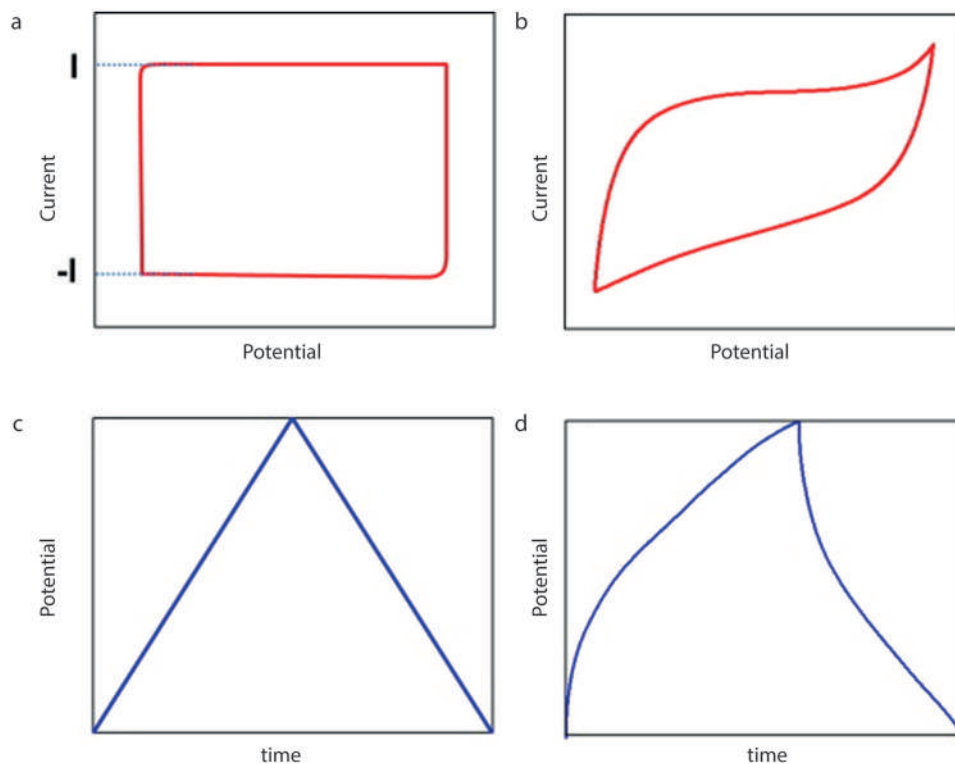


Figure 5. Typical a) CV curves and c) galvanostatic charge-discharge (GCD) curves for ideal supercapacitor; b) CV curve and d) GCD curve distortion due to faradaic reactions.^[55]

high energy density.^[48,49] The diffusion-controlled electrochemical process of lithium-ion insertion/de-insertion in LIBs results in a much lower power density compared to SCs. However, they typically appear in a rigid form which makes them unfavorable for many applications, especially in the field of portable and highly integrated equipment. Several research groups also investigated flexible textile-based batteries for wearable electronics applications.^[50–54] Although this review does not focus on batteries, it is worth noting that in many cases, batteries are used in combination with supercapacitors for achieving high performance.

2.3. Electrochemical Performances of Supercapacitor

A series of key parameters, and various techniques are used for the evaluation of the electrochemical performance of a SC. Among them, widely used techniques are: Cyclic voltammetry (CV), galvanostatic charge/discharge (GCD), and electrochemical impedance spectroscopy (EIS). Three fundamental parameters (voltage, current, and time) for SC can be measured by all these techniques. Additionally, other SC performance metrics including capacitance, equivalent series resistance (ESR), operating voltage, time constant, energy, and power performance can be derived from those parameters.

2.3.1. Cyclic Voltammetry (CV)

CV is a powerful and popular electrochemical technique commonly employed to investigate the reduction and oxidation pro-

cesses of molecular species.^[56] Such technique is used to study the electrochemical properties related to electroactive surfaces, and characterize the electrode materials primarily.^[57,58] In this technique, a linearly changed electric potential is applied against time to measure the current. The graphical analysis of a cyclic voltammogram provides redox peaks (reduction and oxidation peaks of the material) and predicts the capacitive behavior of the electrode. Therefore, the potential at which the material is oxidized and reduced can be found in this technique.^[34,59] A typical cyclic voltammogram for an electrochemically reversible and diffusion-controlled redox process is shown in **Figure 5a**. The curves obtained through CV for both EDLCs and pseudocapacitors are evaluated to measure the capacitance (C) of the material deposited over the electrode by using Equation (1). The shape of the resulting CV curves for an ideal SC is rectangular. However, the variation in the shape and size of the plot can occur when the deposited materials over the electrode are dissolved into the electrolyte. It can also happen due to the detachment of the electrode contacts during cyclic repetition, **Figure 5b**.^[60] The gravimetric capacitance (Equation (4)), lengthwise capacitance (Equation (6)), areal capacitance (Equation (8)), volumetric capacitance (Equation (10)), energy density (Equation (12)) of the electrode or total SC cell can be obtained via integration of CV curves.^[34]

2.3.2. Galvanostatic Charge Discharge (GCD)

Galvanostatic charge-discharge (GCD) test is considered as the most accurate and versatile approach, and the most widely used

Table 3. Technical merits and demerits of the CV, GCD, and EIS techniques.^[60,61]

Techniques	CV	GCD	EIS
Principle	CV is varying the potential against time and measuring the current	GCD is applying a positive or negative current against time and measuring the voltage	Measuring impedance of a power cell as a function of frequency by applying alternating current (AC)
Merits	<ul style="list-style-type: none"> • Degradation process • Specific capacitance • Differentiate between EDLC and PC 	<ul style="list-style-type: none"> • Capacitance calculation • Differentiate between EDL and PC 	<ul style="list-style-type: none"> • Resistance calculation • Specific capacitance calculation • Differentiate between resistive and inductive nature • Nondestructive technique • Relaxation time for recharging • Exhibit Degradation behavior
Demerits	<ul style="list-style-type: none"> • Show only kinetic aspects; thermodynamic aspect is neglected 	<ul style="list-style-type: none"> • Exhibit same triangular shape for all double-layer capacitive materials 	<ul style="list-style-type: none"> • Evaluation at small voltage only • Discrete behavior above 10⁶ Hz

method for capacitance assessment (Equation (2)).^[60] The direct current (DC) at a constant level is imparted in this method for repetitive charging and discharging of the SC device or the working electrode. A potential versus time plot is obtained from this method, Figure 5c. Additionally, the cyclic stability of SC devices can be studied from GCD. The symmetric curves obtained from the charge-discharge through GCD confirm the capacitive behavior of the device, enlightening capacitance as the function of applied voltage. Additionally, gravimetric capacitance (Equation (5)), lengthwise capacitance (Equation (7)), areal capacitance (Equation (9)), and volumetric capacitance (Equation (11)) for SC materials can also be obtained via GCD.^[34]

2.3.3. Electrochemical Impedance Spectroscopy (EIS)

Electrochemical Impedance Spectroscopy (EIS), an electroanalytical method, measures the impedance of a power cell as a function of frequency by applying the alternating current (AC) instead of the DC. The fundamental approach of EIS is the application of a spectrum of small-amplitude sinusoidal AC voltage excitations to the system. The frequency of the AC signal is varied, and the overall impedance of the cell is recorded as a function of frequency. The resulting data are usually expressed graphically in two types of plots: a) the Nyquist plot, which shows imaginary versus real impedance at different frequencies, and b) the Bode plot, which shows absolute impedance versus frequency. For SC materials, EIS testing can be used to study the impedance, charge transfer, mass transport, and charge storage mechanisms as well as to estimate the capacitance (Equation (3)), energy, and power properties.^[34,58] A summary of technical merits and demerits of several characterization techniques is presented in Table 3.

2.4. Key Metrics for Supercapacitor Performances

The key parameters used to evaluate the electrochemical performances of a SC are capacitance, operating voltage, ESR, power density, energy density, and time constant. Capacitance is defined as the ratio of the charge stored (or separated) to the potential difference between the conductors.^[62] The total charge storage ability of a SC device is termed as the capacitance, which is calculated from the formula stated in Table 4 (Equations (1)–(3)). It is noteworthy that, while specifying the capacitance of SC, a more intrinsic specific capacitance is measured in terms of the mass

of the electroactive materials or length, area, and/or volume of the SC device (Equations (4)–(11)). The other two important parameters for evaluating SC performances are: energy density and power density. Energy density, derived from Equation (12), denotes the amount of energy that can be delivered from a SC. The power density denotes how faster the energy can be delivered by a SC and can be calculated from Equation (13), Equation (14), or Equation (15).

Among the performance metrics for all kinds of energy storage and conversion systems, power density and energy density are the most often used parameters for their performance evaluation for all kinds of applications. Compared to batteries, SCs suffer from lower energy density.^[63] The energy density depends on the capacitance and working voltage window (V). Therefore, increasing the capacitance or extending operating voltage window will enhance the energy density of a SC. Power density depends on their working voltage window (V) and internal resistance (R). Therefore, in addition to extending the working voltage window, one of the ways to increase the power density is by the reduction of internal resistances of SC components. Figure 6 summarizes the approaches to improve the energy and power density of SCs.^[64] Additionally, the long cycle life of SC devices is one of the highly desirable characteristics for certain applications. However, the cycle life, when extremely long, is difficult to measure directly. Therefore, the capacitance retention rate is used as an indirect measurement to estimate the cycle life of a SC. By comparing the capacitance after being given thousands of cycles with that of the first cycle in GCD test, the capacitance retention value is obtained.^[34]

3. Components of Textile-Based Supercapacitors

The performance of SC largely depends on the nature of electrode materials, type of electrolyte used, and the range of voltage windows employed. In this section, we will discuss about the basic textile materials used for wearable SC fabrication, as well as the electroactive materials for electrode preparation and electrolyte materials commonly used for textile-based SC fabrication.

3.1. Textiles as the Substrate for Supercapacitor Fabrication

Multifunctional wearable electronics require a conformal platform close to the human body. Textiles or fabrics that are usually embedded with normal clothes and worn on various body

Table 4. Key metrics used for the characterization of a supercapacitor.

Parameters (Unit)	Information obtained	Measurement formula	Equation
Capacitance [F]	Ability to collect and store energy in the form of electrical charge	$C = \frac{\int IdV}{V}$	(1)
		$C = \frac{i \Delta V}{\Delta t}$	(2)
		$2\pi C = \frac{d(-Z'')}{d\left(\frac{1}{f}\right)}$	(3)
Gravimetric capacitance [F g ⁻¹]	Charge storage ability per unit mass	$C_m = \frac{A}{2 s m V}$	(4)
		$C_m = \frac{i \Delta t}{m \Delta V}$	(5)
Lengthwise capacitance [F cm ⁻¹]	Charge storage ability per unit length	$C_l = \frac{A}{2 s l V}$	(6)
		$C_l = \frac{i \Delta t}{l \Delta V}$	(7)
Areal capacitance [F cm ⁻²]	Charge storage ability per unit area	$C_A = \frac{A}{2 s a V}$	(8)
		$C_A = \frac{i \Delta t}{a \Delta V}$	(9)
Volumetric capacitance [F cm ⁻³]	Charge storage ability per unit volume	$C_v = \frac{A}{2 s v V}$	(10)
		$C_v = \frac{i \Delta t}{V \Delta V}$	(11)
Energy density [Wh kg ⁻¹]	Amount of energy able to deliver	$E = \frac{1}{2} CV^2 = \frac{QV}{2}$	(12)
Power density [W kg ⁻¹]	How faster is the energy to deliver	$P = VI$	(13)
		$P = \frac{E}{t}$	(14)
		$P = \frac{V^2}{4R}$	(15)
Coulombic efficiency	Reversible capacity	$\%E = \frac{C_{\text{charging}}}{C_{\text{discharging}}} \times 100$	(16)

[C = capacitance, l = current density, V = voltage window, i = discharging current, Δv = discharge voltage, Δt = discharge time, -Z' = imaginary part of the impedance, A = integrated area of the CV curve, s = scan rate (mV s⁻¹), m = mass of the electroactive material on both electrodes, l = length of the electrode, v = volume of the SC, R = resistance].

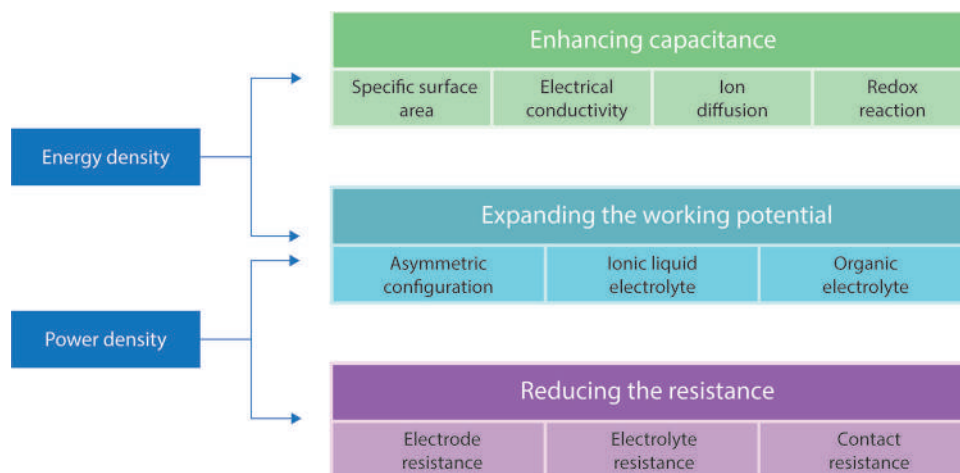


Figure 6. Approaches for enhancing energy and power densities of supercapacitor.^[64]

Table 5. Typical tensile properties of selected fibers.^[71,72]

Fiber	Moisture regain [%]	Density [g cm ⁻³]	Durability	Glass transition temperature [°C]	Tenacity [cN tex ⁻¹]	Yield stress [cN tex ⁻¹]	Yield strain [%]	Strain at break [%]
Cotton	8.0	1.54	Fair	220	40	–	–	7
Wool	16.0	1.32	Fair	160	11	6	5	42
Silk	11.0	1.34	Fair	170	38	16	3	23
Nylon	4.5	1.14	Good	70	47	40	16	26
Polyester	0.4	1.38	Excellent	75	47	30	10	15
Viscose	12.5–13.5	1.46–1.54	Good	120	21	7	2	16
Polypropylene	0.05	0.91	Excellent	–25	–	–	–	–

parts, have emerged as promising substrates and platforms for wearable electronics, due to their unique characteristics including lightweight, soft, flexible, stretchable, air-permeable, low-cost, chemically resistant, scalable production, and integrable with various forms of garments.^[65] In addition to natural fibers (e.g., cotton, silk, wool), other polymeric substrates are commonly used to fabricate e-textiles including poly (ethylene terephthalate) or polyesters (PET), polyamide or nylons (PA), polyimide (PI), viscose, polyethylene naphthalate (PEN) and thermoplastic polyurethane (TPU). Furthermore, some research groups studied papers (specifically for fabricating disposable devices) and polydimethylsiloxane (PDMS) for fabricating such wearable devices.^[66,67] However, these substrates vary in their physical, chemical, thermal and tensile properties,^[68,69] **Table 5.** Therefore, the choice of any specific textile substrate depends on the properties required for the end-products. In addition to being reusable, cheap, and hydrophilic in nature, textile-based substrates have many advantages over plastic- or paper-based substrates, when flexibility and stretchability are concerned. For example, the porous structure of textiles provides abundant support for the loading of active materials and facilitates the rapid absorption of electroactive materials due to their hydrophilic nature, resulting in much higher areal mass loading of active materials and higher areal power and energy density. Therefore, low-cost and highly efficient textile-based SCs have already been integrated into prototype wearable electronics with a great potential to be used for future high-tech sportswear, work wear, portable energy systems, military camouflages and health monitoring systems.^[70]

3.2. Electroactive Materials for Electrode Preparation

As previously discussed in Section 2.2, SCs are classified into two types, according to the charge-storage mechanism, which includes EDLCs based on carbon materials, and pseudocapacitors based on certain transition metal oxides or conductive polymers. The EDLCs usually display perfect cycling stability, but lower specific capacitance. In contrast, pseudocapacitors present high specific capacitance but poor cyclability. These undoubtedly limit their practical application as individual electrode materials for SCs.^[17] Therefore, to enhance the capacitive performance, developing composite materials combining both EDLC materials and pseudocapacitor materials becomes an inevitable trend.^[73]

3.2.1. Carbonaceous Materials

Carbonaceous compounds and their allotropes (**Figure 7a**) are currently of particular interest as key materials for multiple applications including nano- and optoelectronics, photonics, molecular separation and storage, nanomechanics, catalysis, and energy storage.^[74] A unique combination of chemical and physical properties, including exceptionally high Young's modulus and mechanical strength, higher light transmittance, higher conductivity, higher surface-area range (≈ 1 to >2000 m² g⁻¹), good corrosion resistance, higher temperature stability, controlled pore structure, processability and compatibility with composite materials, and relatively lower cost make carbon-based materials attractive material for SC electrodes.^[35,75] Among five forms of carbon allotropes: 3D diamond (Csp³), 2D graphite (Csp²), 1D carbon (Csp¹), 0D fullerene (Csp⁰), and transitional carbons (admixtures of Csp³, Csp², and Csp¹), the first four are crystalline and first two are found naturally. Graphite and fullerene have attracted much attention as electrode materials due to their structures and functionalities.^[76] Additionally, they have faster electron transfer kinetics with lower fabrication costs. However, their specific capacitances were found to be too low for commercial applications.

Carbon nanotubes (CNTs), a 1D allotrope of carbon, are cylindrical large molecules consisting of a hexagonal arrangement of hybridized carbon atoms. Being nano-meter in diameter and several millimeters in length, they are available in the form of single-walled CNTs, SWCNTs (formed by rolling up a single sheet of graphene) or multiwalled CNTs, MWCNTs (by rolling up multiple sheets of graphene).^[77] Chemical vapor deposition (CVD), laser-ablation, and carbon arc-discharge are three common techniques for producing CNTs. Structure, surface area, surface charge, size distribution, surface chemistry, agglomeration state, and purity are the main parameters that affect the reactivity of CNTs.^[78] Their exceptional physical, chemical, and electronic properties offer exciting possibilities for even nano-meter scale electronic applications.^[29] Since its discovery in 1990s, CNTs have been utilized in a variety of applications including actuators, artificial muscles, and lightweight electromagnetic shields.^[79] Additionally, CNTs have been investigated as SC electrodes by several research groups.^[80–83]

Carbon black (CB), a common denomination for particles with a carbonaceous core, is manufactured by thermal decomposition, including detonation, or by incomplete combustion of carbon-hydrogen compounds having a well-defined morphology with a

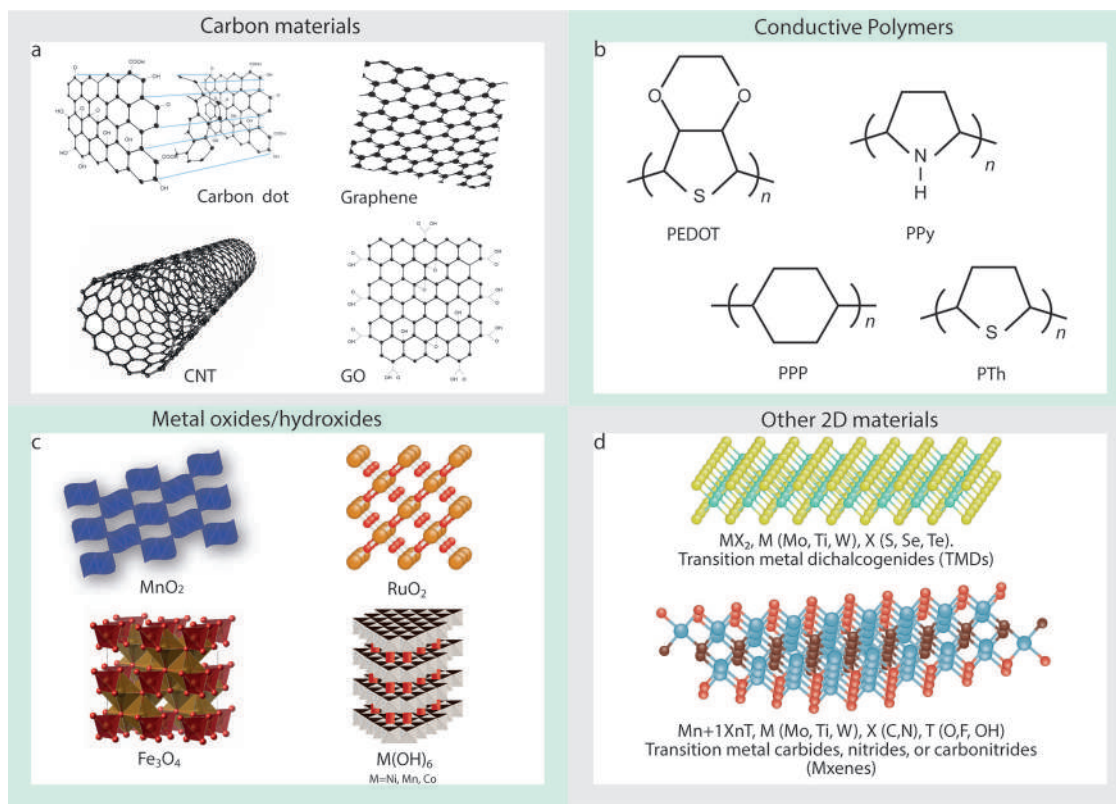


Figure 7. Electrode materials for textile-based supercapacitors: a) carbonaceous materials, b) conductive polymers, c) metal oxides/hydroxides, and d) other 2D materials.

minimum content of tars or other extraneous materials.^[84] In recent years, it has become an interesting modifier of sensors, due to its excellent conductive and electrocatalytic properties, as well as its cost-effectiveness.^[85] Conductive CBs which usually possess electrical conductivity in a range of 10^{-1} to 10^2 (Ωcm)⁻¹ are usually well-structured (i.e., aggregates with a highly branched open structure). They have higher porosity, smaller particle size, and chemically clean (oxygen-free) surfaces.^[35] In addition to using it as electrode material itself,^[86] CB is also used in combination with other materials to enhance the performance of SC.^[87,88]

Activated carbon (AC), in comparison with the other forms of carbonaceous materials, is preferred as electrode materials due to its low cost and environmentally friendly nature.^[89] Carbonization and activation are the main steps for the synthesis of activated carbon. Due to the tunable pore size and higher specific surface area as compared to other carbonaceous material, activated carbon has been widely used as electrode material for SC applications. The high surface area, hierarchical pore structure, and different morphology enable the formation of a bilayer of ions at electrode-electrolyte interfaces.^[90] Activated carbon powder (ACP) is known as an inexpensive yet good electrode material with $1000\text{--}2000$ m^2g^{-1} of specific surface area,^[91] and has widely been studied for SC application.^[92–94]

Graphene, since its isolation in 2004, has unveiled a wide range of other similar 2D materials and received much attention from the research community due to their outstanding mechanical, thermal, electrical, and other properties.^[95–98] It is a 2D allotrope of carbon, which is the basic structural element of car-

bon allotropes including graphite, CNTs, and fullerenes.^[99] It has an isolated single layer of carbon hexagons consisting of sp^2 hybridized C–C bonding with π -electron clouds.^[100] It can be considered the “mother” of all graphitic-based nanostructures, owing to the variety of sizes and morphologies onto which a single graphitic layer can be transformed. It can be wrapped up into the 0D “buckyball” structure, and folded into 1D CNTs. It can also be stacked into multi-layer graphene sheets.^[101] Mechanical, thermal, and liquid phase exfoliation, and chemical vapor deposition (CVD) are the most common techniques to manufacture graphene.^[102,103] Due to its unique physicochemical properties including theoretical specific surface area (2600 m^2g^{-1}), good biocompatibility, strong mechanical strength (130 GPa), excellent thermal conductivity (3000 $\text{Wm}^{-1}\text{K}^{-1}$), high electrical charges mobility ($230\,000$ cm^2 $\text{V}^{-1}\text{s}^{-1}$) and fast electron transportation makes it not only a unique but also a promising material for next-generation energy storage applications, particularly SC devices.^[104–108] Graphene and its derivatives have the capability to form chemical bonds with textiles and therefore, show great potential to be used in smart energy storage textiles SC.^[109–111]

Graphene oxide (GO), a derivative of graphene^[112] can be obtained by treating graphite materials with strong oxidizing agents (potassium chlorate and fuming nitric acid) where tightly stacked graphite layers are loosened by the introduction of oxygen atoms to the carbon,^[113] forming a single-layer sheet of graphite oxide^[114] with strong mechanical, electronic and optical properties, chemical functionalization capability and excellent features such as large surface area, high stability, and layered

structure.^[115–117] Based on the degree of oxidation, GO can be a semiconductor or insulator, enabling it to be used in many fields.^[118] Reduced graphene oxide (rGO), another important derivative of graphene,^[119] consists of few-atom-thick 2D sp^2 hybridized carbon layers with fewer oxygenous functionalities and exhibits properties between graphene and GO.^[120] Though it resembles graphene, containing residual oxygen and other heteroatoms with some structural defects degrade its electric properties.^[121] While graphene derivatives (GO and rGO) can be produced in a huge quantity in their stable dispersions,^[122] the major challenge for such materials is the ability to produce high-quality graphene at a larger scale.^[123] Hybridization of various carbonaceous compounds is also attractive due to their combined electrochemical properties, which provide enhanced capacitive performances of SC devices.^[124–128]

3.2.2. Conductive Polymers

Conductive polymers (CPs) are organic polymers, that are able to conduct electricity through a conjugated bond system along the polymer chain. In the past two decades, they are extensively explored for energy storage applications due to their reversible faradaic redox nature, high charge density, and lower cost as compared to expensive metal oxides. They are considered as promising electrode materials for flexible SCs.^[129] Among CPs, polyaniline, polypyrrole, and derivatives of polythiophene have widely been studied as active electrode materials for energy storage devices, Figure 7b.

PANI, a conductive polymer, has been playing a great role in energy storage and conversion devices due to its high specific capacitance, high flexibility, and low cost. It is said that the era of intrinsically conductive polymers (ICPs) started with the invention of polyacetylene. However, PANI attracted much more attention from researchers due to its cheaper monomer compared to polyacetylene and ease of synthesis.^[130] PANI-based electrodes for SCs provide multi-redox reactions, high conductivity, and excellent flexibility.^[131] However, the inferior stability of PANI limits its application to be used alone in the fabrication of electrodes.^[132] Therefore, the combination of PANI with other active materials (such as carbon materials, metal compounds, or other polymers) is recommended to overcome such intrinsic disadvantages.^[133–135]

Polypyrrole (PPy) is a π -electron conjugated CP, which has been researched widely for energy storage applications due to its good electrical conductivity and environmental stability in ambient conditions. It has shown promise as SC electrodes because of its large theoretical capacitance, good redox properties, superior conductivity, ease of synthesis, nontoxicity, biocompatibility, and high thermal and environmental stability.^[136] However, the brittleness of PPy limits its practical uses. Nevertheless, their processability and mechanical properties can be improved by either blending PPy with some other fiber polymers or forming copolymers of PPy.^[137] Thus, PPy-based composites may provide fibers or fabrics with electrical properties similar to metals or semiconductors.^[138] The water solubility of pyrrole monomers and much less carcinogenic risks associated with its biproducts compared to PANI, makes PPy a proper material as SC electrodes. However, the poor cyclic stability and poor rate be-

havior of pristine PPy-based SCs drastically restrict their practical applications.^[139] Nevertheless, higher electrochemical performance can be achieved by the introduction of a novel design of nanostructured PPy and its nanocomposites, which is currently being explored widely for SC electrode fabrication.^[140–142]

PEDOT is one of the most promising π -conjugated polymers exhibiting some very interesting properties such as excellent conductivity ($\geq 300 \text{ S cm}^{-1}$), electrooptic properties, and processability.^[143,144] PEDOT is highly conductive in its oxidized (doped) state, while in its undoped form is usually nonconductive or shows very little conductivity. Its conductivity can be increased by oxidizing or reducing with a doping agent which introduces positive charges along the backbone structure of PEDOT. These positive charges are later balanced by the anions provided by the doping agent.^[144] The oxidized or doped form of PEDOT shows very high conductivity, flexibility, low-cost, and pseudocapacitance. However, the low stability and limited capacitance have limited its industrial applications. Several approaches have been undertaken to tackle these issues including the addition of conducting nanofillers to increase conductivity, and mixing or depositing metal oxide to enhance capacitance.^[145] Though several studies have reported the electrochemical performance of PEDOT-based SCs,^[146,147] the polymer mixture with polystyrene sulfonate (PEDOT:PSS) possess a high conductivity (up to 4600 S cm^{-1}),^[148] and can be used as an electrode material for SCs.^[149,150] The hybridization of PEDOT:PSS with other active materials has also been studied for SC electrode fabrication.^[150–153]

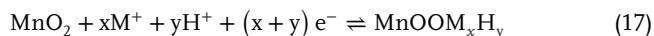
3.2.3. Metal Oxides

Electrodes composed of metal oxides possess exceptional properties, qualifying them as a suitable engineering material with a wide range of applications including sensors, semiconductors, energy storage, lithium-ion batteries, and solar cells.^[154] Metal oxides, due to its wide variety of oxidation states for redox charge transfer, are generally considered as one of the prime candidates for use as electrode materials in SCs,^[155] Figure 7c.

Ruthenium Dioxide (RuO_2): Due to its high theoretical specific capacitance value ($1400\text{--}2000 \text{ F g}^{-1}$), RuO_2 has been extensively recognized as a promising material for SC devices.^[156] Additionally, it demonstrates highly reversible redox reactions, good thermal stability, high electronic conductivity (300 S cm^{-1}), superior cycle lifespan, and high rate capability.^[155] Despite having such outstanding properties, their higher production cost and agglomeration effects limit its practical applications. Therefore, RuO_2 -based nanocomposites have widely been studied to optimize the material cost, with simultaneous improvement in the electrochemical performances.^[156] Several researchers have studied RuO_2 -based nanocomposites for SC fabrication^[157,158] as well as for the improvement of the electrochemical performances for next-generation SCs.^[159–161]

Manganese Dioxide (MnO_2): MnO_2 is considered as one of the most promising electrode materials for electrochemical capacitors, due to its low cost, high theoretical specific capacitance ($\approx 1370 \text{ F g}^{-1}$), natural abundance, environmental friendliness, and nontoxicity.^[162] MnO_2 is a very common material in the battery field, which has long been used as active material for the positive electrode.^[163] The charge storage mechanism is based on the

surface adsorption of electrolyte cations M^+ (e.g., K^+ , Na^+ , Li^+) as well as proton incorporation as follows:^[164]



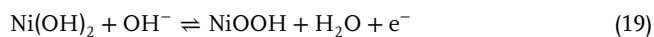
However, the poor conductivity, much lower actual specific capacitance than the theoretical specific capacitance, poor structural stability, and easy dissolving nature in the electrolyte results in poor cycling ability.^[165] Therefore, the combination of MnO_2 with other active components is much preferred by researchers for SC electrode application.^[166–168]

Nickel Oxide (NiO): NiO is another attractive conversion reaction-based anode material in the field of SCs due to its low cost, ease of preparation, nontoxicity, environment friendliness, and high theoretical capacity ($\approx 3750 \text{ F g}^{-1}$).^[169] The pseudocapacitance of NiO is obtained from the following redox reaction:



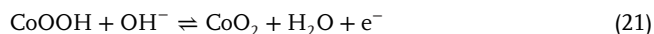
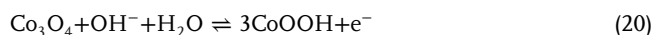
Though theoretically advantageous enormously, the relatively poor electrical conductivity and lower specific surface area hinder their practical applications. One possible solution to these problems is to synthesize nanostructures of NiO with large surface areas, which are associated with more faradaic active sites and higher pseudo capacitance. Therefore, various nanostructured forms of nickel oxides such as nanowires, nanoflakes, nanocolumns, nanosheets, porous nanoflowers, and hollow nanospheres were successfully fabricated in the past few years by various methods^[155] and investigated for SC fabrication.^[170–172]

Nickel Hydroxide [Ni(OH)₂]: Ni(OH)₂ is also an attractive electrode material because of its high theoretical capacity, superior redox behavior, and potential applications in alkaline batteries and SCs. Its main reaction mechanism as positive electrode material for SCs is shown as follows:



However, Ni(OH)₂ usually suffers from poor stability, lower conductivity, and large volume changes during the charge/discharge processes. Thus, composites with high surface-area conductive materials such as CNTs, activated carbon, graphene, show remarkably enhanced electrochemical performance due to improved electrical conductivity of the composites, and the shortening of the electron and ion diffusion pathways.^[173–176]

Cobalt oxide (Co_3O_4) is generally considered one of the best candidates for electrode material in the field of SCs owing to its superior reversible redox behavior, excellent cycle stability, large surface area, and outstanding corrosion stability.^[177–179] The redox reactions in alkaline electrolyte solution can be expressed as follows:

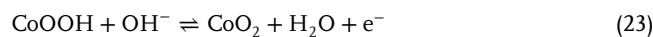
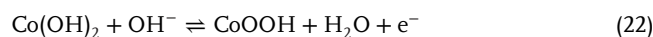


Due to its layered structure with a large interlayer spacing, Cobalt hydroxide [$Co(OH)_2$] provides a large surface area and a high ion insertion/extraction rate and offers a great potential to become a high-performance electrode material^[155] and explored

Table 6. Comparison of various supercapacitor materials.^[129]

Properties	Carbonaceous material	Metal oxides	Conductive polymers
Non-faradic capacitance	Very high	Medium	Medium
Faradic capacitance	Very low	Very high	Very high
Conductivity	Very high	Low	Very high
Energy density	Low	High	Medium
Power density	High	Low	Medium
Cost	Medium	High	Medium
Chemical stability	Very high	Low	High
Cycle life	Very high	Medium	Medium
Ease of fabrication	Medium	Low	High
Flexibility	Medium	Very low	High

for SC studies.^[110,111] The pseudofaradaic reaction at a low potential of $Co(OH)_2$ and the faradaic reaction at a higher potential can be expressed as follows:



Among iron oxides, Fe_3O_4 is one of the main and naturally abundant pseudocapacitive materials with a reasonable metallic electrical conductivity ($\approx 10^2\text{--}10^3 \text{ S cm}^{-1}$). However, the low specific capacitance limits its practical applications. TiO_2 is also considered a very important material for energy storage systems because of its good intercalation/ deintercalation behavior of metal ions (such as Li^+ and Na^+) without the formation of solid electrolyte interface by-products and electrode collapse caused by volume changes. These characteristics contribute to its high-power capacity and long lifespan. Non-toxicity, chemical stability, photocatalytic activity, and low cost make it a promising semiconductor.^[180] In terms of properties, TiO_2 is suitable for use as negative electrode material in organic electrolytes for hybrid SCs. SnO_2 is another alternative electrode material to be used in SCs. But compared to other metal oxides, it has a much lower specific capacitance. The several oxidation states of vanadium in V_2O_5 result in both surface and bulk redox reactions. Therefore, it has been studied for its potential application in energy storage devices. V_2O_5 has a higher capacitance in KCl electrolyte than in any other electrolyte solutions. **Table 6** compares the basic types of electrode materials for the fabrication of SCs.

3.2.4. 2D Materials

Since the discovery of graphene, 2D materials (Figure 7d) such as hexagonal boron nitride (h-BN), transition metal chalcogenides (TMDs)- Molybdenum disulfide (MoS_2), Tungsten selenide (WSe_2), transition metal carbides/nitrides (i.e., MXenes- Ti_2C) and 2D metal-organic frameworks (MOFs) also attracted tremendous research attention due to their extraordinary properties including large surface area, good electronic conductivity, excellent electrochemical properties, and good chemical, electrochemical, and thermal stability, since these properties are

promising for batteries and SCs.^[181–183] 2D materials are generally defined as materials with infinite crystalline extensions along two dimensions and one crystalline dimension with few or single atomic layers thickness. Such materials are derived from most classes of known layered materials and possess strong in-plane bonds within the layers and only weak interactions between neighboring layers.^[184] However poor cyclic stability, large structural changes during metal-ion insertion/extraction, as well as higher manufacturing cost are the major challenges for 2D materials which require further improvements to find their applications in commercial batteries and SCs.^[185]

2D hexagonal boron nitride (2D-hBN), an isomorph of graphene with a very similar layered structure,^[186] is uniquely featured by its exotic opto-electrical properties together with mechanical robustness, thermal stability, and chemical inertness. 2D-hBN is an insulator itself but can well be tuned by several strategies in terms of properties and functionalities, such as doping, substitution, functionalization, and hybridization, making 2D-hBN a truly versatile type of functional material for a wide range of applications. More importantly, both theoretical and experimental results show that the BN–noble metal interface can also improve electrocatalytic activity. Recent studies have also shown that it has the ability to adsorb polysulfides and Li ions, which is a greatly desired property for improving the performance of Li–S and solid-state batteries. Thus, BN-based nanomaterials have huge potential in the field of electrochemical energy storage and conversion.^[187] Additionally, it is considered as one of the most promising materials, which is able to integrate with other 2D materials, including graphene and TMDCs for the next generation microelectronic and other technologies,^[188] as well as SC electrodes.^[189–192]

MoS₂, another exciting 2D material, has been investigated to a lesser extent but is gaining increased interest recently for integration into electronic devices due to their grapheme-like properties. Exfoliated MoS₂ possesses high catalytic activity which makes it an efficient hydrogen evolution catalyst as well as a useful energy storage material for the use in lithium and sodium-ion batteries. In addition to conventional synthesizing processes such as micromechanical peeling or chemical vapor deposition, currently, MoS₂ is being synthesized by ultrasonic treatment similar to graphene. It creates large volumes of monolayer and few-layer flakes that can then be deposited onto a substrate or formed into films.^[193] The favorable electrochemical properties are mainly a result of the hydrophilicity and high electrical conductivity, as well as the ability of the exfoliated layers to dynamically expand and intercalate various ions.^[194] Similar to h-BN, MoS₂ has been explored alone^[195,196] or with other functional materials^[197–200] for SC electrode fabrication.

MXene, a new family of 2D metal carbides, nitrides, and carbonitrides have gained much attention due to their attractive electrical and electrochemical properties such as hydrophilicity, conductivity, surface area, topological structure, rich surface chemistry, tunable terminations, excellent processability, etc.^[201–203] The term MXenes with a formula of M_{n+1}X_n, are named after other 2D analog materials silicene, graphene, phosphorene, and so on, synthesized by extracting an atomic layer from ternary MAX (M_{n+1}AX_n) ceramics, where M = early transition metal elements (Ti, Zr, Mo, Nb, V, Mn, Sc, Hf, W, and so on), A = group 13 or 14 (Si, Al, Ga, and so on), X = C or/and N. Due to their

unique intrinsic physical/chemical properties, 2D MXenes materials have thoroughly been investigated and can be used in various research fields, including ceramics, conductive polymer, energy storage, sensors, water purification, catalysis, thermoelectric conversion, photothermal conversion, solar cell, biomedicine, and microwave absorption and shielding.^[204,205] Moreover, the improved coupling and hybridization of MXene with other materials at the nano-scale make it one of the most intriguing materials for wearable applications.^[206,207]

3.3. Electrolytes for Supercapacitors

Electrolytes are vital constituents of SCs, as their physical and chemical properties play an important role to obtain desired performances in terms of capacitance, power density, rate performance, cyclability, and safety.^[208] For the SC performance, the type, composition, and concentration of the electrolyte are as important as the electrode materials.^[209] An optimized electrolyte concentration is always desired, as the ion transport within the electrode layers becomes easier at high electrolyte concentration, inducing an effective build-up for the double layer. If the concentration becomes too high, the ion activity is reduced due to less water hydration, resulting in decreased ion mobility. A good electrolyte offers a wide voltage window, high electrochemical stability, high ionic concentration and conductivity, low viscosity, and low toxicity. However, a proper cell design should also consider the key electrolyte parameters, such as: i) sufficiently high ion conductivity, ii) electrochemical stability on the anode and cathode surfaces, iii) good wetting in contact with electrode materials, iv) suitable thermal properties, v) adequate cost, and vi) adequate mechanical properties.^[210] Common electrolytes can be classified into three types: aqueous, organic liquid, and ionic liquid (IL).^[211] Due to offering safer and more packageable construction, providing more design freedom, larger operable temperature range, and electrochemical stability, polymer-based electrolytes have also garnered significant attention for SC fabrication.

3.3.1. Aqueous Electrolytes

The aqueous electrolytes can be categorized into three types: acidic solution (such as H₂SO₄ solution), alkaline solution (such as KOH solution), and neutral solution (such as Li₂SO₄, Na₂SO₄, or KCl solution). Due to the high ionic conductivity of acidic aqueous electrolytes, SC electrode materials show better performance in comparison with neutral aqueous electrolytes.^[212] They get dissolved in water, providing high ionic conductivity, and low internal resistance compared with organic electrolytes. Therefore, SCs with an aqueous electrolyte solution may possess a higher capacitance and power than capacitors containing organic electrolytes. The maximum working voltage of aqueous electrolyte is limited to 1.23 V owing to the thermodynamic decomposition of water. In addition, they can be prepared and employed without much tight control of the production process, whereas organic electrolytes require strict preparation procedures to obtain pure electrolytes. Commonly used aqueous electrolytes are inorganic salts (e.g., LiCl, NaCl) (for Li-ion & SCs), alkali (e.g., KOH) and inorganic acid (e.g., H₂SO₄) in water (for SCs).

3.3.2. Organic Electrolytes

Organic electrolytes allow a much wider voltage window of about 3.5 V resulting in a large advantage with respect to higher energy density. Among the organic electrolytes, propylene carbonate (PC) is the most commonly used solvent, because of their environmentally friendly nature and wide voltage window with good conductivity. The complex purification and preparation procedures may cause safety problems due to the flammability and toxicity of some of the organic solvents. Furthermore, their low conductivity could lead to lower power and smaller capacitance. Several combinations of organic solvents and lithium salts have been examined as electrolytes for ambient-temperature, rechargeable lithium batteries.^[213] Inorganic or organic salts, for example, Lithium hexafluorophosphate (LiPF₆); Tetraethylammonium tetrafluoroborate (TEABF₄) in organic solvents (carbonates, ethers, sulfones, etc., some of which may be fluorinated) are the common examples of organic electrolytes for SCs.

3.3.3. Ionic Liquids

ILs are salts having uncommonly low melting points, below 100 °C, which are usually liquid at room temperature.^[214] They are inherent and competitive electrolytes due to their ability to overcome many disadvantages of the conventional aqueous and organic electrolytes,^[215] for instance volatility, high thermal and chemical stability, extensive electrochemical stability window between 2 and 6 V, low flammability, nontoxicity and the wide variety of cation and anion combinations. They are composed entirely of ions, solvent-free, and liquids at room temperature, making them attractive “green electrolytes”. They are usually highly viscous liquids with low ionic conductivity at ambient temperatures, seriously influencing their electrochemical performance. Salts in ILs (for Li-ion batteries) or pure ILs (for SCs); organic cations (e.g., imidazolium, pyridinium, pyrrolidinium, etc.) with inorganic or organic anions (e.g., H₂SO₄) in water (for SCs) are commonly used ILs.

3.3.4. Polymer Electrolytes

In order to meet the safety (for instance the leakage, flammability, and toxicity of organic electrolytes), flexibility, and multifunctionality requirements for advanced energy-storage devices (ESDs), polymer electrolytes are considered to be the best candidate to replace liquid electrolytes due to their wide electrochemical window, good thermal stability and less risk with electrolyte solution leakage.^[216]

Dry Solid Polymer Electrolytes (Polymer-Salt Complex Electrolytes): A solid polymer electrolyte is prepared by dissolving inorganic salts into a polar functional polymer, which forms a solid electrolyte with ion-conducting after drying. With interactions between metal ions and polar groups inside the polymers, electrostatic forces are generated due to the formation of coordinating bonds. Since the coordination of cations to align along the polymer chain is weak, after applying an electric field the cations in the electrolyte may migrate from one coordinated site to another. Various polymers are used to form dry

and solid polymer electrolytes including polycarbonate (PC), poly (methyl methacrylate) (PMMA), poly (ethylene oxide) (PEO), and poly(vinyl alcohol) (PVA). For metal ions, various soluble compounds, such as salts containing lithium (Li), sodium (Na), and potassium (K) can be used. Nevertheless, the room ionic conductivities of SPEs ($\approx 10^{-8}$ – 10^{-5} S cm⁻¹) are lower than the required conductivity of 10⁻³ S cm⁻¹ in actual application, limiting their wide practical applications.^[216]

Gel Polymer Electrolytes: The gel polymer electrolytes possess a higher ionic conductivity at room temperature. It has attracted research attention because of the combination of the advantages of high ionic conductivity of liquid-based electrolytes, and the high stability of solid-based electrolytes. This combination superiority is embodied in high ionic conductivity and good interfacial properties from the liquid phase as well as good mechanical properties from the solid component. They are safer to use compared to liquid-based electrolytes. The majority of GPEs exhibit outstanding ionic conductivity in the order of 10⁻³ S cm⁻¹ at ambient temperature, which can boost the electrochemical performance of the cells involving GPEs. Consequently, GPEs have become one of the most desirable alternatives for the fabrication of advanced ESDs with enhanced safety and flexibility.^[38,217]

Plasticized Polymer Electrolytes: A host polymer with lower molecular weight like poly(ethylene glycol) (PEG), PC, and ethylene carbonate is used to produce plasticized polymer electrolytes. The rigidity of the polymer structure is decreased with a change in their mechanical and thermomechanical properties. The glass transition temperature of the particular polymer electrolyte system is also decreased. The increase of salt dissociation capability and the reduction of crystallinity results in the enhancement of charge carrier transportation.^[38] Polymer electrolytes are found to exhibit higher ionic conductivity at higher plasticizer concentration at the cost of their mechanical stability.^[218]

Composite Polymer Electrolytes: The addition of inorganic fillers in polymer electrolytes increases the mechanical strength and interfacial stability of the resulting electrolytes, providing a new branch of polymer electrolytes (Pes) which are known as composite polymer electrolytes (CPEs).^[219] By doping different types and amounts of high dielectric constant fillers, especially inorganic inert fillers into the polymer matrix, the electrical properties of polymer electrolytes can be improved. Ceramic materials are one of the most used inorganic dopants. They are fragile and have low dielectric strength. By combining such inorganic dopants with polymers, the new composite electrolytic material can be produced for higher relative permittivity. Since these composite electrolytes consist of ceramic particles, they can be regarded as heterogeneously disordered systems, with electrical properties highly dependent on the relative permittivity and conductivity of the dopants. Moreover, electrical performances of these composite electrolytic materials are affected by the size, shape, and volume fraction of the dopants.^[38] **Figure 8** summarizes some of the key features of major electrolyte families to compare their advantages and disadvantages.

4. Manufacturing of Conductive Electrodes

Several technologies can be utilized for the manufacturing of conductive electrodes. Spinning, coating, and printing of active



Figure 8. Comparison of the performance of several electrolyte types.

materials with/on textiles are the key manufacturing techniques for such electrodes. In situ growth of active materials on/ in the substrate is another way of such manufacturing.

4.1. Coating of Active Materials on Substrate

The conventional textile materials such as cotton, polyester, and nylon are electrically nonconductive. Therefore, electrical conductivity must be introduced to such textiles to prepare a textile-based energy storage device. The coating of a layer of electrically conducting material onto non-conductive textiles can impart electronic capabilities in a facile manner. Materials such as ICPs, conductive polymer composites, metals, and carbon based materials (e.g., CNTs, carbon nano powders, graphene, etc.) have been used to achieve this.^[220] The commonly used coating techniques that have been used to deposit such materials on textiles are dip coating, doctor-blade coating, wrapping, physical vapor deposition (VPD), and chemical vapor deposition (CVD).^[32,38]

Dip Coating, also termed as impregnation or saturation coating, is the simplest process of creating a uniform thin layer of conductive materials on a substrate. In such a technique, textile substrates are dipped into a bath containing coating materials in liquid form, **Figure 9a**. The viscosity of the coating liquid is usually very low to enable it to run off while the substrate leaves the coating liquid. A pair of nip rollers are often placed to remove the excessive liquor from coated surface, providing a homogeneous liquid film on the substrate.^[221] After drying, the volatile solvents are eliminated, followed by possible chemical reactions, resulting in a thin coated film.^[222] Dip coating offers a simple, low-cost, reliable, and reproducible method, which is extensively effective for research purposes. However, the inconsistent quality of such coatings makes them unsuitable for industrial-

scale application.^[139] Hu et al. reported a simple dipping and drying of SWNTs ink on textiles to produce highly conductive textiles with electrical conductivity of 125 S cm^{-1} and sheet resistance $< 1 \Omega \text{ sq}^{-1}$. SCs made from such conductive textiles showed high areal capacitance, up to 0.48 F cm^{-2} , and specific energy as high as 20 Wh kg^{-1} at a specific power of 10 kW kg^{-1} , **Figure 9(b-d)**.^[223] The same research group later demonstrated the coating of polyester fabric with solution-exfoliated graphene nanosheets and further electrodeposition of MnO_2 nanomaterials, yielding high specific capacitance up to 315 F g^{-1} . They also successfully fabricated asymmetric electrochemical capacitors with graphene/ MnO_2 -textile as the positive electrode and SWNTs-textile as the negative electrode with aqueous Na_2SO_4 electrolyte, exhibiting promising characteristics with a maximum power density of 110 kW kg^{-1} , an energy density of 12.5 Wh kg^{-1} , and excellent cycling performance with $\approx 95\%$ capacitance retention over 5000 cycles, **Figure 9(e,f)**.^[224] Dip coating is a simple and scalable process, however, the loading of active materials depends on the surface properties as well as the deposition position of the textile substrate. The repeated dipping-drying cycles are usually employed to achieve sufficient material loading which lowers the efficiency of fabrication process. Padding is a modified version of dip coating, used for continuous treatment of textiles for various chemical treatments and finishes. Textile substrate after being impregnated with the solution is squeezed through nip rollers.^[8] In a previous study,^[225] we obtained the lowest sheet resistances ($\approx 11.9 \Omega \text{ sq}^{-1}$) reported on graphene e-textiles, through a simple and scalable pad-dry-cure method with subsequent roller compression and a fine encapsulation of graphene flakes. The graphene-coated textiles were highly conductive even after 10 home laundry washing cycles with extremely high flexibility, bendability, and compressibility as it shows the repeatable response in both forward and backward directions before and after home laundry washing cycles. The potential applications of

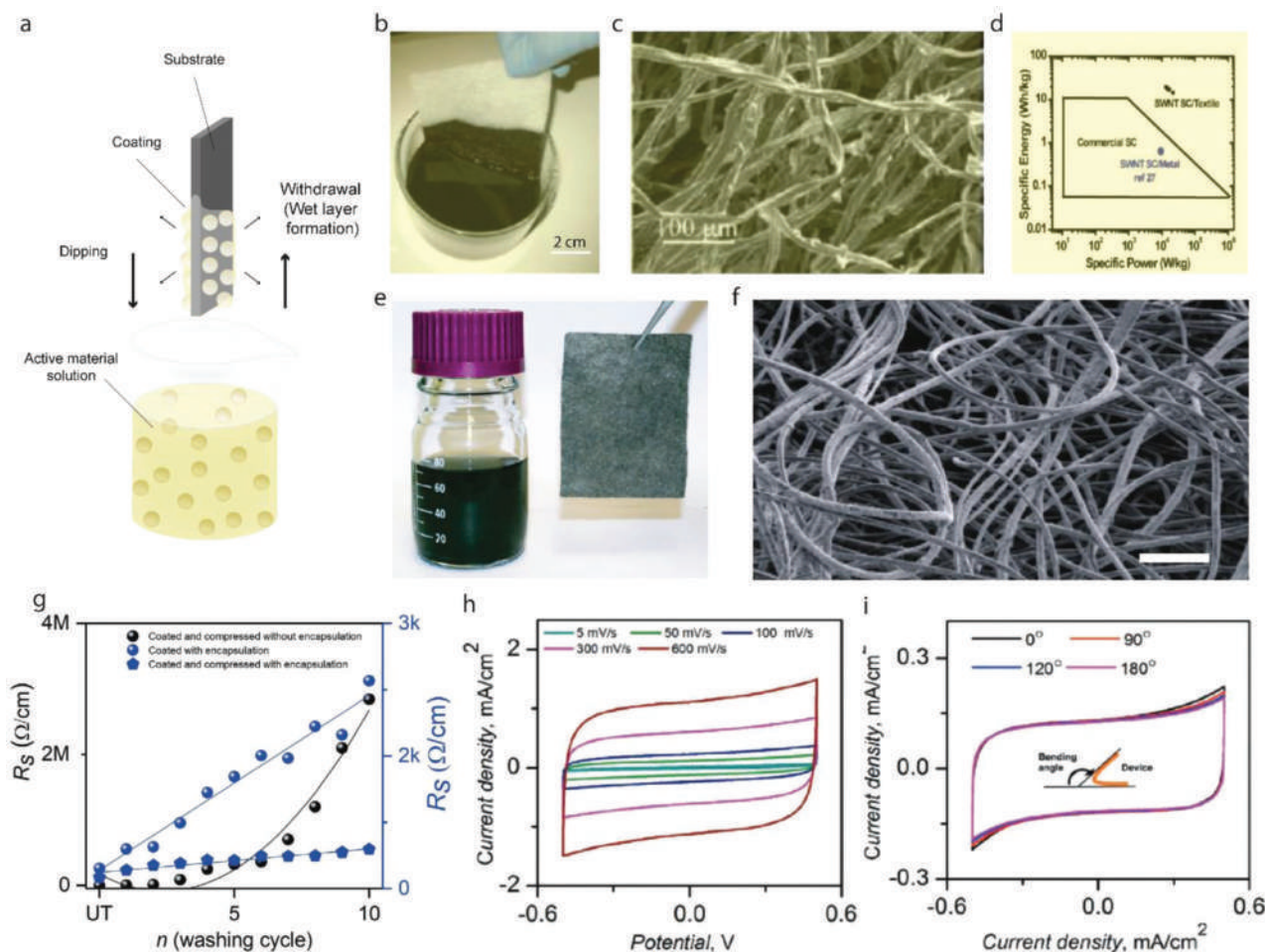


Figure 9. a) Schematic diagram of dip coating technique. b) Conductive textiles fabricated by dipping textile into an aqueous SWNT ink followed by drying in oven at 120 °C for 10 min. c) SEM image of coated cotton reveals the macroporous structure of the cotton sheet coated with SWNTs on the cotton fiber surface. d) Ragone plot of commercial SCs, SWNT SC on metal substrates, and SWNT SC on porous conductors including all the weight. Reproduced with permission.^[223] Copyright 2010, American Chemical Society. e) Photograph of a stable, solution-exfoliated graphene ink suspension prepared by ultrasonication of the graphite powder in a water sodium cholate solution, and a 6 cm X 8 cm graphene-coated conductive textile sheet (polyester fabrics). f) SEM image of a sheet of graphene-coated textile after 60 min MnO₂ electrodeposition showing large-scale, uniform deposition of MnO₂ nanomaterials achieved on almost entire fabric fiber surfaces, Scale bar: 200 μm. Reproduced with permission.^[224] Copyright 2011, American Chemical Society. g) The change in resistance with the number of washing cycles of G-coated compressed (with encapsulation) poly-cotton fabric, G-coated only (with encapsulation) poly-cotton fabric, and G-coated compressed (without encapsulation) poly-cotton fabric. h) Cyclic voltammograms (CV) recorded for the supercapacitor device at different scan rates i) CV curves for the ASC device at different bending angles. Reproduced with permission.^[225] Copyright 2020, Wiley-VCH.

such conductive textiles were demonstrated as ultra-flexible SC and skin-mounted strain sensors, Figure 9(g,i).

Doctor blade coating, also called knife coating or blade coating or tape casting, is another widely used technique for producing thin films on surfaces with large areas. The process involves a constant relative movement between a blade over the substrate or a substrate underneath the blade, resulting in a spread of the coating material on the substrate to form a thin film on the substrate upon drying. The operating speed of such a technique can reach up to several meters per minute, and coat substrate with a very wide range of wet film thicknesses ranging from 20 to several hundred microns.^[226] This process can create thin uniform films over large surface areas quickly and efficiently, though cannot offer nanoscale uniformity or extreme thin film. Nevertheless,

the scalability, versatility, and simplicity of this technique make it perfect for industrial applications. In comparison to dip coating, doctor blade technique allows much more precise and uniform control over the coating amount of active materials in a continuous process.^[33] Though few literatures are available on fabric or thin-film-based lithium-ion batteries fabricated using doctor blade coating,^[227] the fabrication of SCs using such technique is rare.

Conductive materials (fibers, yarns, or fabrics) are integrated with textile fabrics by various methods such as weaving, knitting, braiding, or embroidery process. To protect the conductive material from being rubbed away from the textiles during a washing cycle or to avoid fraying or short circuits between neighboring materials while used underwater, wrapping might be an effective

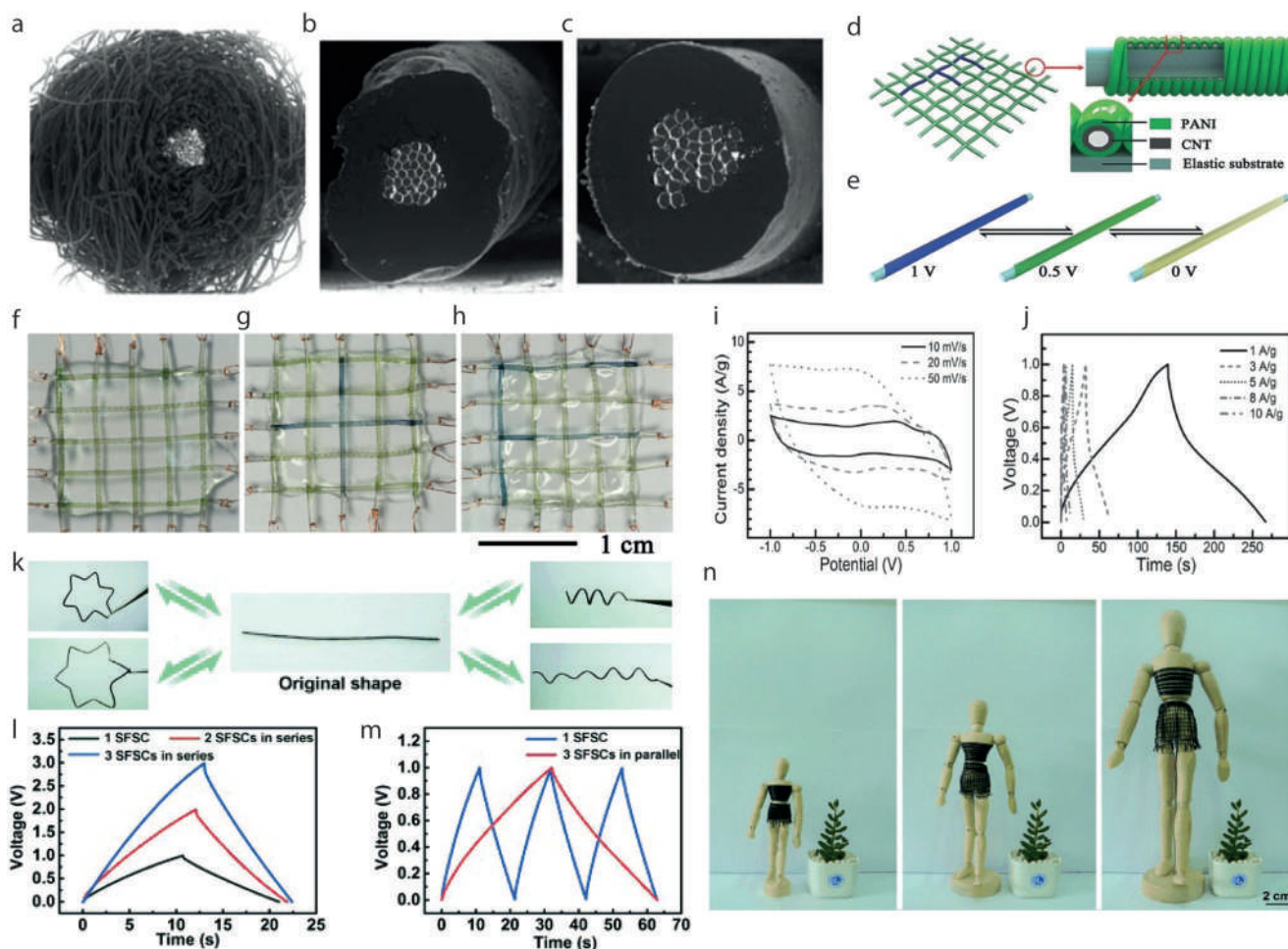


Figure 10. SEM pictures of a) shieldex conductive yarn wrapped with PP staple fiber, b) Melt coated single yarn, and c) Melt coated plied yarn. Reproduced with permission.^[228] Copyright 2012, Taylor & Francis. d) Schematic illustration of the structure of the electrochromic, wearable fiber-shaped supercapacitor. e) Positive electrode demonstrates rapid and reversible chromatic transitions between blue, green, and light yellow under different working states. f) An energy storage textile woven from electrochromic fiber-shaped supercapacitors during the charge–discharge process. g,h) Electrochromic fiber-shaped supercapacitors that have been designed and woven to display the signs “+” and “F”, respectively. i) Cyclic voltammograms at various scan rates. j) Galvanostatic charge–discharge profiles at different current densities. Reproduced with permission.^[229] Copyright 2014, Wiley-VCH. k) Photographs of an SFSC transformed into different shapes and sizes. l,m) Galvanostatic charging and discharging curves of SFSCs arranged in series and parallel, respectively. The galvanostatic charging and discharging tests were performed at a current density of 0.5 A g^{-1} . n) Photographs of the same smart clothes woven from SFSCs that were “frozen” into different shapes and sizes. Reproduced with permission.^[230] Copyright 2015, Wiley-VCH.

solution.^[228] Alagirusamy et al.^[228] reported their attempt to protect single and plied silver-coated polyamide yarns by wrapping polypropylene (PP) staple fibers around the silver-coated polyamide yarns through friction spinning and melting of PP sheath fibers in an oven, **Figure 10(a–c)**.

Chen et al.^[231] fabricated a stretchable wire-shaped SC by twisting two CNTs thin film wrapped elastic wires, pre-coated with poly(vinyl alcohol)/ H_3PO_4 hydrogel, as the electrolyte and separator. It exhibited an extremely high elasticity of up to 350% strain and a high device capacitance of up to 30.7 F g^{-1} . This wire-shaped structure facilitated the integration of multiple SCs into a single wire device to meet specific energy and power needs for various potential applications.^[231] An electrochromic fiber-shaped SC was developed by Chen et al.,^[229] by winding aligned CNT/polyaniline composite sheets on an elastic rubber fiber. It exhibited rapid and reversible chromatic transitions under differ-

ent working states, which can be directly observed by the naked eye, **Figure 10(d–j)**. At 70% wt.-% of PANI, the specific capacitance was 255.5 F g^{-1} and the power density was 1494 W kg^{-1} at 10 A g^{-1} .^[229] A shape-memory fiber-shaped SC was also developed by Deng et al.,^[230] via winding aligned CNT sheets on a shape-memory polyurethane (PU) substrate. The length and volumetric specific capacitances were 0.269 mF cm^{-1} and 42.3 mF cm^{-3} , respectively, which were well-maintained during deformation, both at the deformed state and after the recovery, **Figure 10(k–n)**. A solid-state SC was prepared by Choi et al.^[232] via imparting twist to coil a nylon sewing thread helically wrapped with a CNT sheet and then electrochemically depositing pseudocapacitive MnO_2 nanofibers. The maximum linear and areal capacitances, areal energy storage, and power densities were found as high as 5.4 mF cm^{-1} , 40.9 mF cm^{-2} , $2.6 \mu\text{Wh cm}^{-2}$, and $66.9 \mu\text{W cm}^{-2}$ respectively.

4.2. Printing of Active Material on Substrate

The process described as printing involves the controlled deposition of a material, either for decorative or functional purposes, onto a substrate in such a manner that a pre-defined pattern is produced. Other deposition processes, such as painting or spraying, have much in common, but printing is further defined because the process can rapidly produce identical multiples of the original. There are three basic methods of printing: positive contact, negative contact, and non-contact printing. The first two methods are described as contact printing since the substrate is touched by the print master. The positive contact type resembles the principle of stamping, examples include printing presses and woodcuts. Gravure or screen printing are examples of negative contact type printing. In non-contact printing, the printer does not contact the substrate. The most common example of non-contact printing is inkjet printing (IJP), where ink droplets are ejected from a nozzle, and deposited on a substrate.^[233]

Screen printing is a stencil process, in which the printing ink is transferred to the substrate through a stencil supported by a fine fabric mesh of either silk, synthetic fibers, or metal threads stretched tightly on a frame.^[234] The squeegee or the blade press the ink, which is most often a viscous paste, through the open parts of the mesh. When the print paste is moved over the mesh from one side to the other, it creates the final printed design on the substrate.^[235] Basically, this is a selective transfer process of ink through the open areas of the unmasked portions of a screen. The masking of the screen is accomplished by the transfer of a photographically produced image from its temporary film base support to the screen.^[236] The versatility of print substrates is one of the biggest advantages of screen printing, including paper, paperboard, polymer materials, textiles, wood, metal, ceramics, glass, and leather. The wide variety of polymer substrates requires different types of inks. Printing inks must be selected accordingly to the type and surface characteristics of printing substrates. A sharp edge of printed images requires inks with higher viscosity for screen printing than other printing techniques.^[237]

Jost et al.,^[238] investigated traditional screen printing of porous carbon materials on woven cotton and polyester fabric for fabricating flexible and lightweight SC electrodes as a possible energy source for smart garments. A high gravimetric capacitance (85 Fg⁻¹) and areal capacitance (≈0.43 Fcm⁻²) on both cotton lawn and polyester microfiber were obtained. In another study, Abdelkader et al.^[239] reported a solid-state flexible textiles SC device, produced via screen printing of GO ink on textiles. After the in situ reduction of GO, the printed electrodes exhibited excellent mechanical stability and flexibility, as well as outstanding cyclic stability over 10 000 cycles, which are necessary for wearable applications, **Figure 11(a–c)**. Lu et al.^[240] synthesized FeOOH/MnO₂ composites which were screen-printed as SC electrodes on different substrates, including PET, paper, and textiles. The all-printed solid-state flexible SC device exhibited high area-specific capacitance of 5.7 mF cm⁻² with 80% retention up to 2000 charge-discharge cycles, and high mechanical flexibility. Additionally, they demonstrated printed SCs on different substrates, which are capable of lighting up a 1.9 V yellow light emitting diode (LED), even after bending and stretching, **Figure 11(d–g)**.

IJP is a digital technique, which can be used for printing functional materials with specific electrical, chemical, biological, op-

tical, or structural functionalities. IJP has gained significant research interest due to its wide range of applications for different processes and purposes, from the batch coding of soft drink cans to smart e-textiles.^[241,242] The main advantages of IJP technology include digital and additive patterning, reduction in material waste, and compatibility with a variety of substrates with different degrees of mechanical flexibility and form factor.^[243] IJP forms nano to micron scale film through a one-step printing process that benefits from downsizing the device thickness and increasing the uniformity of the coated area in an economical way. High-performance devices can be produced by printing and stacking the functional inks in desired locations,^[244] **Figure 12a**. IJP allows the deposition of tiny droplets onto the substrate without depending on the high-speed operation of mechanical printing elements. The nozzle size for such printers is typically ≈20–30 μm and ink droplets can be as small as 1.0 pL to achieve high print resolution (dots per inch).^[245,246] In addition to 2D prints, IJP can print layers of “structural” fluids that harden to form 3D structures. In spite of all these benefits, print speed, higher cost, printed film uniformity, and fluids’ jet-ability as ink, are still points of concern for inkjet printers.^[247]

There are two distinct modes of IJP: Continuous inkjet (CIJ), suitable for industrial scale and mass-production, and Drop-on-demand (DOD), used for small-volume and prototype sample production.^[248] The high accuracy and small droplet size of DOD inkjet printers are the key advantages for the direct patterning of functional materials.^[249,250] There are several parameters of ink such as viscosity, surface tension, density and size are important for successful IJP of a fluid. The spreading behavior of the ink is determined by the Ohnesorge number (Oh). The inverse of the Ohnesorge number is used to determine the printability of DOD inkjet inks. This is known as the Z number.^[251] The printability,

$$Z = \frac{1}{\text{Oh}} = \frac{\sqrt{\gamma \rho a}}{\eta} \quad (24)$$

Where, η represents dynamic viscosity, γ is surface tension, ρ is density, and a is the characteristic length (usually the diameter of the print head’s nozzle). Several research groups studied the printability of inkjet inks.^[251,252] Moon et al.^[253] summarized Z values for inkjet ink to be in between 4 and 14 to be ideally printable. Considering the drop generation, drop flight and drop impact, the optimal value of the physical conditions for a robust DOD IJP are typically with surface tension lying in the range of 20–50 mN m⁻¹ and viscosity within the range of 2–20 mPa s. to achieve high-resolution print on the desired trajectory, where narrower and specified range would be more applicable for specific print heads.^[110]

For e-textile fabrication, IJP offers a number of advantages over conventional manufacturing techniques including the ability to deposit controlled quantities of materials at precise locations of the fabric, combined with a reduction in both material waste and water utilization.^[256] However, the key challenge with IJP of e-textiles is the ability to achieve a uniform and continuous highly conductive electrical tracks on a rough and porous textile substrate using low viscosity inkjet inks. To solve this, we developed a novel surface pre-treatment that was inkjet-printed onto rough and porous textiles before IJP of electrically conductive graphene-based inks for wearable e-textiles applications.^[14]

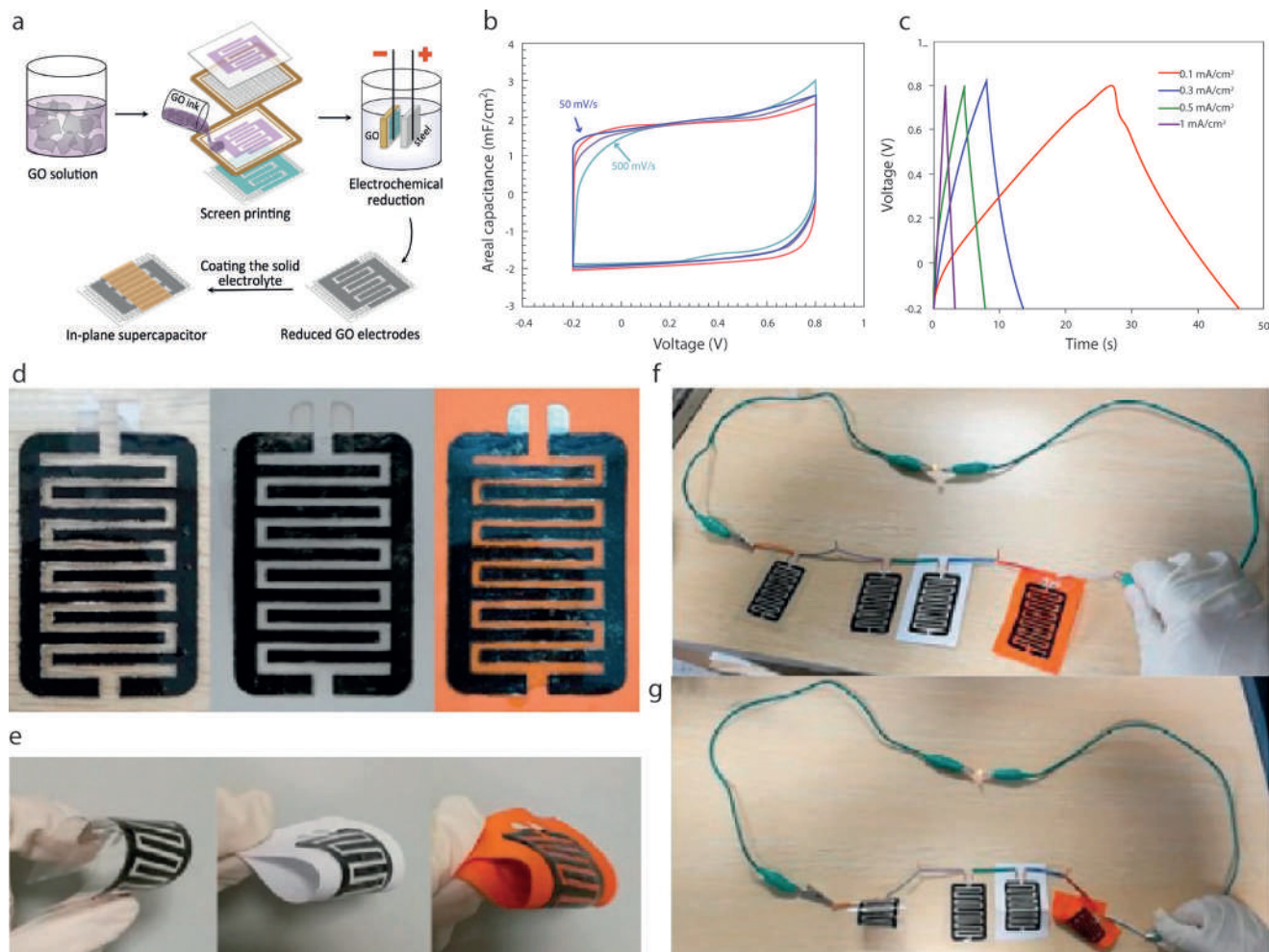


Figure 11. a) Schematic representation of the printed in-plane supercapacitor fabrication process. Electrochemical characterization of printed graphene on textile. b) CV at different scan rates and c) charge/discharge curves at different current densities. Reproduced with Permission.^[239] Copyright 2017, IOP Publishing Ltd. d) Images of all printed solid-state flexible SC devices on PET, paper, and textile substrates, e) images of these SCs after bending, f) image of these SCs in series lighting up a yellow LED, and g) images of the same after bending these SCs. Reproduced with permission.^[240] Copyright 2017, Elsevier B.V.

Later, we formulated graphene-Ag composite inks for IJP onto surface pre-treated cotton fabrics, to enable all-inkjet-printed highly conductive e-textiles with a sheet resistance in the range of $\approx 0.08\text{--}4.74\ \Omega\ \text{sq}^{-1}$.^[256] Stempien et al.^[254] propose an IJP method to prepare PPy layers on textile fabrics using direct freezing of inks under varying temperatures up to $-16\ ^\circ\text{C}$. The as-coated PPy layers on PP textile substrates were further assembled as the electrodes in a symmetric all-solid-state SC device, Figure 12b. The electrochemical results demonstrate that the symmetric SC device made with the PPy prepared at $-12\ ^\circ\text{C}$, showed the highest specific capacitance of $72.3\ \text{F}\ \text{g}^{-1}$ at a current density of $0.6\ \text{A}\ \text{g}^{-1}$, and delivers an energy density of $6.12\ \text{Wh}\ \text{kg}^{-1}$ with a corresponding power density of $139\ \text{W}\ \text{kg}^{-1}$. Sundriyal et al.^[257] reported an inkjet-printed, solid-state, planar, and asymmetric micro-supercapacitor (PA μ SC) deskjet printed on cellulose paper substrate. They digitally designed interdigitated electrode patterns and printed them on paper with rGO ink to construct a conducting matrix. The negative electrode was printed using activated carbon-Bi₂O₃ ink and the positive electrode was printed

with rGO-MnO₂ ink. After that, they demonstrated bamboo fabric as a sustainable substrate for developing SC devices with a replicable IJP process.^[255] Different metal oxide inks such as MnO₂-NiCo₂O₄ were used as a positive and rGO as a negative electrode. With LiCl/PVA gel electrolyte, the textile-based MnO₂-NiCo₂O₄/rGO asymmetric SC displayed excellent electrochemical performance with an overall high areal capacitance of $2.12\ \text{F}\ \text{cm}^{-2}$ ($1766\ \text{F}\ \text{g}^{-1}$) at a current density of $2\ \text{mA}\ \text{cm}^{-2}$, excellent energy density of $37.8\ \text{mWh}\ \text{cm}^{-2}$, a maximum power density of $2678.4\ \text{mW}\ \text{cm}^{-2}$ and good cycle life, Figure 12(c–e).

4.3. Spinning Technology

Spinning of polymer fibers, is an interdisciplinary field applying the principles of engineering and material science toward the development of textile substitutes. Electrically conducting textile materials can be spun in the form of staple fiber or filament yarn based on intrinsic conductive polymers (ICPs). An extruded liq-

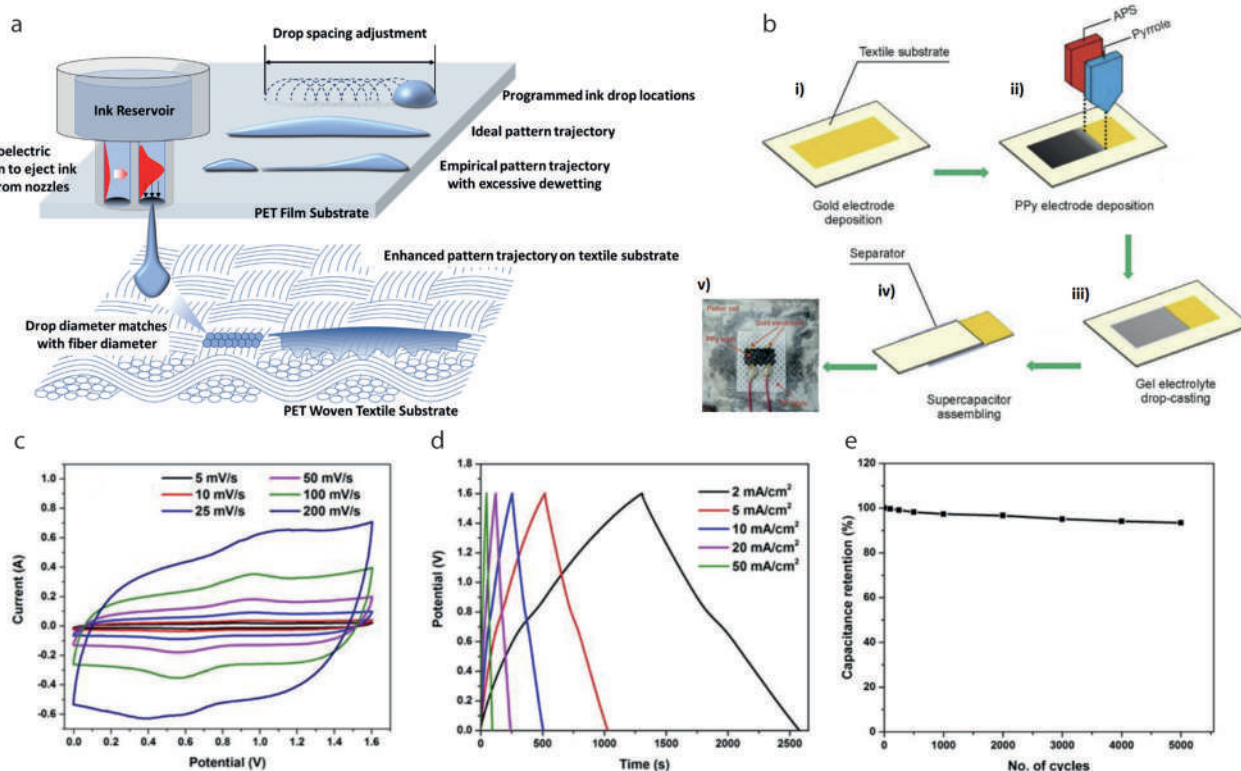


Figure 12. a) Schematic drawing of the inkjet process and ink spreading behavior on the film and textile substrates. Reproduced with permission.^[244] Copyright 2021, American Chemical Society. b) Detailed steps of fabrication of inkjet-printed textile supercapacitor and printed samples. Reproduced with permission.^[254] Copyright 2021, The Authors. c) CV curves of MnO₂-NiCo₂O₄//rGO asymmetric device at different scan rates. d) GCD profiles of the MnO₂-NiCo₂O₄//rGO asymmetric device at various current densities and e) Capacitance retention of the device with the different number of charge-discharge cycles. Reproduced with permission.^[255] Copyright 2020, The Authors.

uid polymer filament is continuously drawn and simultaneously solidified to form a continuous synthetic fiber in this process.^[258] This is based on a special extrusion process that uses spinneret (a nozzle-type device) to form multiple continuous filaments or monofilaments. Available spinning technologies such as dry, wet, melt, or electrospinning can be exploited for this purpose. The polymer, needed to form fiber, is first converted into a spinnable solution. The solidification of the ejected solution is carried out by the removal of heat and/or solvent by contacting the liquid with a suitable moving fluid, either with a gas or a liquid.^[259,260]

The basic dry spinning process involves dissolving the polymer in organic solvents followed by blending with additives and filtering to produce a low viscosity polymer solution, called as “dope.” The dope is filtered, de-aired and pre-heated, and pumped through filters to achieve the right consistency. The dope is then extruded into a spinning tube where the solution is forced through the fine orifices of spinneret (or jet). The exiting jets of the polymer solution, when coming in contact with a stream of hot gas, vaporizes the solvent in the gas stream, increasing the polymer concentration in the filament and thus solidifying it without the need for further drying.^[261] This complex process makes dry spun fibers very expensive. Additionally, the poor solubility of most conductive polymers in organic solvents, makes them unsuitable for the production of conductive polymer filaments using such a technique. Wet spinning is another technique, which requires pumping of the polymer solution through

the fine orifices of a spinneret into a coagulating bath and drawing off as continuous filaments by means of take-up rollers. The bath removes the solvent from the as-spun filaments so that they become solidified. They are collected together to form a continuous tow or rope.^[262] Wet spinning is slower than other spinning processes due to the mass transfer of the solvent and non-solvent for fiber solidification. Zhang et al.,^[263] exploited the solubility properties of polyaniline (PANI) to blend with poly- ω -aminoundecanoyl (PA11) in concentrated sulfuric acid (c-H₂SO₄) to form a spinning dope solution to spin conductive PANI / PA11 fibers by wet-spinning technology. Kou et al.,^[264] proposed a coaxial wet-spinning assembly to spin polyelectrolyte-wrapped graphene/CNT core-sheath fibers continuously, which were used directly as safe electrodes to assemble two-ply yarn SCs, **Figure 13(a-d)**. The yarn SCs using liquid and solid electrolytes exhibited ultra-high capacitances of 269 and 177 mF cm⁻² and energy densities of 5.91 and 3.84 mWh cm⁻², respectively.

Melt spinning is one of the most popular methods for manufacturing synthetic fiber filaments. It requires no solvents, thus a simple and economical process. In melt-spinning process, the polymer pellets or granules are fed into an extruder for melting by heating, and then the polymer melt is pumped through a spinneret under pressure. After extrusion, it is quenched with cold air which solidifies the molten mass to form filaments. Spinning is followed by a mechanical drawing to improve the degree of crystallinity, which contributes to improving physical, mechanical,

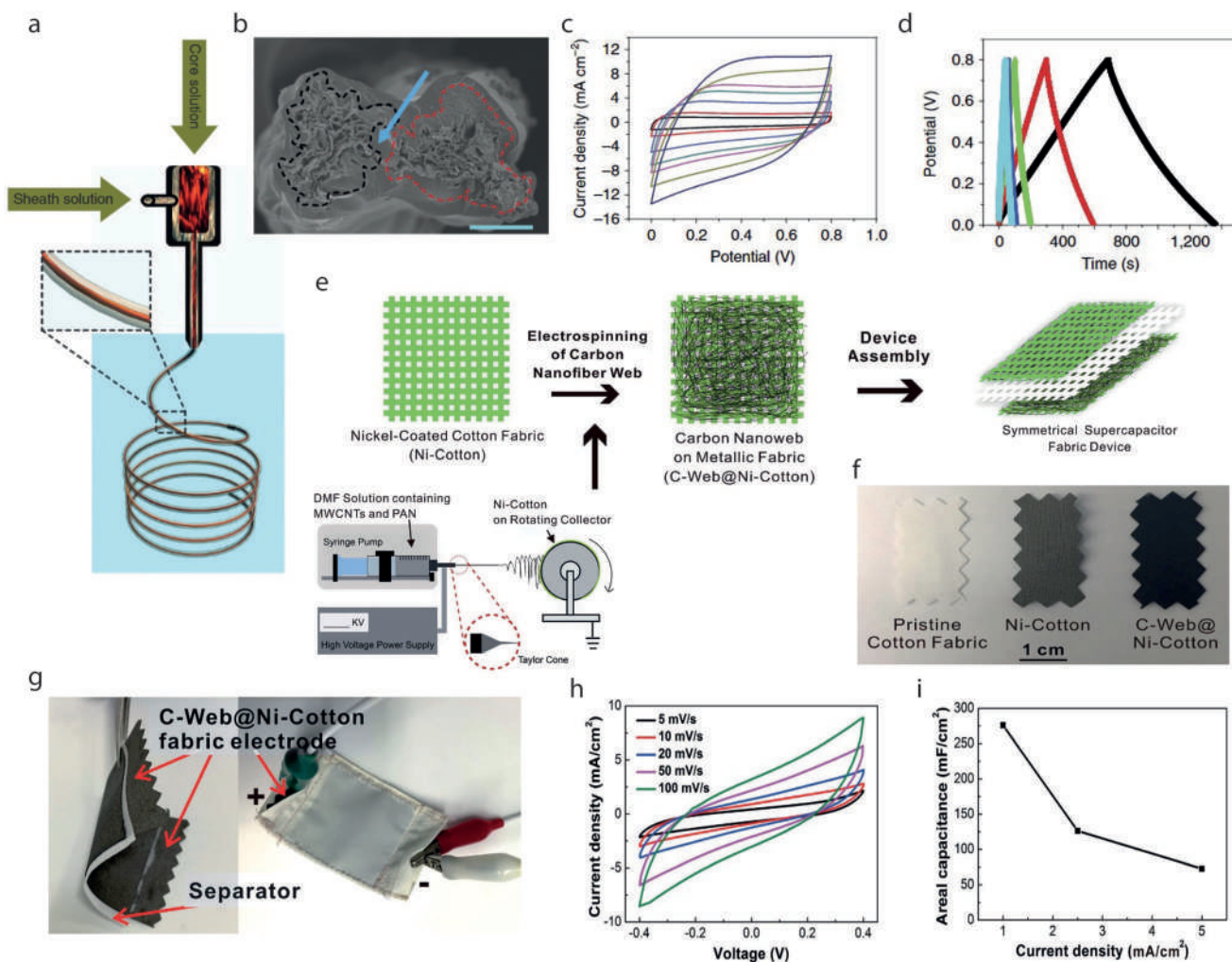


Figure 13. a) Schematic illustration showing the coaxial spinning process. Two-ply YSCs and their electrochemical properties. b) SEM images of cross-sectional view of a two-ply YSC. The arrow area is PVA/H₃PO₄ electrolyte (scale bar: 50 μm). c) CV curves of RGO+CNT@CMC. d) GCD curves of RGO+CNT@CMC. Reproduced with permission.^[264] Copyright 2014, The Authors. e) Schematic illustration of the textile based SC fabrication process. The inset shows details of one-step electrospinning setup. f) Photographs of the pristine cotton fabric, Ni-coated cotton fabric (Ni-cotton), and CNF web-coated Ni-cotton fabric (C-web@Ni-cotton). g) Photographs of a large supercapacitor fabric (active area: 4 cm × 4 cm) enclosed with commercial nonconductive fabrics. h) CV curves of solid-state C-web@Ni-cotton supercapacitor fabric. i) Summary of the areal capacitance of the supercapacitor at different current densities. Reproduced with permission.^[267] Copyright 2016, The Royal Society of Chemistry.

and chemical properties.^[265] Kim et al.,^[266] melt-mixed polyaniline emeraldine salt (PANI-ES), PPy, and graphite with PP and low-density polyethylene (LDPE) using a co-rotating twin screw extruder. However, the electrical conductivity of conductive materials/PP monofilament obtained by melt spinning process was not found satisfactory, due to the problems of structural homogeneity and the aggregation of conductive materials.

Electrospinning is another fiber spinning process, which is used to produce ultrafine fibers by charging and ejecting a polymer melt or solution through a spinneret under a high-voltage electric field and to solidify or coagulate to form filaments.^[268] This is a relatively simpler and cheaper spinning process, as well as a versatile method to produce continuous, long, and fine (in the range of nano to sub-micron size range) fibers. These fibers possess a high surface-to-volume ratio, high aspect ratio, controlled pore size, and superior mechanical prop-

erties than conventional fibers. Electrospinning can be used to produce novel fibers with diameters between 100 nm and 10 μm. Electro-spun fibers have been investigated as sensor, LEDs, rechargeable batteries, electroactive actuators, nano-electronic devices, and electromagnetic shielding for wearable electronics applications.^[269,270] Wei et al.,^[271] prepared core-sheath nanofibers with conductive polyaniline as the core and an insulating polymer as the sheath by electrospinning of blends of polyaniline with polystyrene and polycarbonate. These unique core-sheath structures offer potential in a number of applications including nanoelectronics. Huang et al., reported the development of high-performance wearable SC fabrics based on flexible metallic fabrics (Ni-cotton), in which multi-walled CNTs (MWCNTs)-based nanofiber webs were directly electro-spun, showing a high areal capacitance of 973.5 mF cm⁻² (2.5 mA cm⁻²), Figure 13(e-i). The SC fabrics were also integrated into

commercial textiles with desirable forms, demonstrating its potential for wearable electronics applications.^[267] Table 7 provides an overview of chronological research of several spinning techniques to produce conductive textiles.

4.4. In Situ Growth of Active Material on Substrate

Electrodeposition is a well-known method of producing in situ metallic coatings or thin films of oxides and/or hydroxides by applying an electric current to a conductive material immersed in a solution containing a metal salt. By controlling several experimental parameters including solution potential, current density, deposition time, and plating solution composition, the morphology and texture of the film can be modified.^[293] The process may either be anodic or cathodic. In an anodic process, a metal anode is electrochemically oxidized in the solution, and then deposited on anode. In a cathodic process, components (ions, clusters, or NPs) are deposited onto cathode from solution precursors. The increase in the reaction time causes more source materials deposition resulting in larger film thickness. The deposition rate can be maintained by the variation of current with time.^[294] E. Gasana et al.^[295] reported an electroconductive polyaramide woven textile structure produced via electroless deposition of PPy and copper at a deposition time of 240 s, providing a resistance of $5 \pm 1 \Omega$ with a surface coverage of $100 \pm 1\%$. Zhao et al.^[296] deposited copper galvanostatically in the copper citrate complex anions on poly (ethylene terephthalate) (PET) fabric treated with polyaniline (PANI) to produce flexible Cu–PANI/PET conducting textiles.

Hydrothermal reaction is a synthesis mechanism, which involves chemical reactions of substances in a sealed and heated aqueous solution or organic solvent at an appropriate temperature (100–1000 °C) and pressure (1–100 MPa). Many compounds or materials with special structures and properties, which cannot be prepared from solid-state synthesis, can be obtained via hydrothermal reactions. In some cases, it offers an alternative and mild synthetic method for solid-state reactions by lowering the reaction temperature. Hydrothermal synthesis has been successful in the preparation of important solids such as zeolites, open-framework compounds, organic-inorganic hybrid materials, MOF materials, superionic conductors, chemical sensors, electronically conducting solids, complex oxide ceramics and fluorides, magnetic materials, and luminescence phosphors. It is also a route to unique condensed materials including nanometer particles, gels, thin films, equilibrium defect solids, distinguished helical and chiral structures, and particularly stacking-sequence materials.^[297] Hydrothermal synthesis relies on the forced hydrolysis of the reactants in order to produce the oxide ceramics. This is achieved at moderate temperatures (<200 °C) and high pressures by placing the reagents in a sealed container and heating the system to the reaction temperatures. The solvent is usually water; a metal hydroxide (e.g., NaOH) is added as a mineralizer while metal alkoxides or metal salts serve as the source of metal ions. As in precipitation systems, the nucleation is followed by particle growth to yield a powder with a certain particle-size distribution.^[298] Huang et al.^[299] demonstrated the synthesis of Fe_3O_4 through hydrothermal reaction, wrapped on stainless steel fiber (SSF) which assisted the self-healing of a yarn-based SC to

enhance the reliability and lifetime of a SC in practical usage, Figure 14(a–f). The specific capacitance was restored up to 71.8% even after four breaking/healing cycles with great maintenance of the whole device's mechanical properties. Li et al.^[300] reported the fabrication of hierarchical graphene fiber fabrics (GFFs) with significantly enlarged specific surface area using a hydrothermal activation strategy. The achieved areal capacitance was 1060 mF cm^{-2} with a very thin thickness (150 μm) and further magnified up to 7398 mF cm^{-2} by overlaying several layers of HAGFFs.

In situ polymerization is another fabrication technique for conductive electrodes. This is typically a chemical encapsulation process similar to interfacial polymerization except there are no reactive monomers in the organic phase. All polymerization occurs in the continuous phase rather than in the interface as in interfacial polymerization. The most common example of this method is the condensation polymerization of urea or melamine with formaldehyde to form cross-linked urea-formaldehyde or melamine-formaldehyde capsule shells. In this method, an oil-phase is emulsified in water using water-soluble polymers and high-shear mixers, yielding a stable emulsion at the required droplet size. A water-soluble melamine resin is added and dispersed. The pH of the system is then lowered, initiating the polycondensation which yields crosslinked resins that deposit at the interface between the oil droplets and the water phase. During the hardening of the wall material, the microcapsules are formed and the aqueous dispersion of polymer-encapsulated oil droplets is produced.^[301,302] Lee et al.^[303] reported 1D metal oxide nanostructure-based SC of multiscale architecture. In their work, MnO_2 -micronodules were deposited on carbon cloth, followed by coating with partially carbonized polypyrrole (CPPy) through vapor deposition polymerization (VDP). Then, the PPy-coated MnO_2 -based multiscale micronodules were assembled within a PVA–KOH polymer electrolyte as the positive-electrodes of solid-state asymmetric SCs (ASCs) which demonstrated ultrahigh performance (59.5 F cm^{-3} of capacitance, 27.0 mWhcm^{-3} of energy and 1.31 Wcm^{-3} power density).

Carbon fiber, though exhibit high conductivity, suffer from agglomeration problem which creates obstacle during application in several fields. Additionally, the small surface area and low specific capacitance limit the wide-scale use as conductive material, therefore surface functionalization offers scopes to overcome the limitations and exploit the fiber properties fully. Oxidation (wet and dry), amidation, silanization, silylation, polymer grafting, polymer wrapping, surfactant adsorption, thermal annealing, and encapsulation are some of the functionalization techniques.^[304] Cotton, the most popular fiber ever, can be considered as an innovative platform for wearable, smart and interactive electronic devices, like batteries, SCs, and various sensors if their electrochemical performances are ensured. It is a natural polymer of cellulose, burns readily, but in low oxygen concentration, it chars leaving a carbon skeleton, which improves the conductivity.^[305] Carbonization/Pyrolysis of cotton fibers can be an alternative option to produce conductive electrodes. Zhang et al.^[306] simply annealed pristine woven cotton fabric in an inert atmosphere, producing flexible and highly conductive fabric, which was used as a strain sensor to demonstrate its superior performance in the detection of both large and subtle human body motions, Figure 14(g–k). However, the release of toxic substances during carbonization process limits the viability of the process.

Table 7. Comparison of several spinning techniques.

Fiber /yarn	Spinning method	Polymer/doped with	Conductivity (σ in S cm ⁻¹)	Refs.
Polyaniline (PANI) (1999)	Air-gap/ dry-jet spinning	PANI/poly(p-phenylene terephthalamide), PPD-T, sulfuric acid solutions.	0.1	[272]
PANI/poly- ω -aminoundecanoyle (PA11) (2002)	Wet spinning	concentrated sulfuric acid (c-H ₂ SO ₄)	10 ⁻⁵ (5wt% PANI) to 10 ⁻¹ (20% PANI)	[263]
PANI/polyamide-11 (2001)	Wet Spinning	concentrated sulfuric acid (c-H ₂ SO ₄)	10 ⁻⁶ to 10 ⁻¹ (3–16 wt.% PANI)	[273]
Microfibers of poly(3,4-ethylenedioxythiophene) (PEDOT) (2003)	Wet spinning	Poly (4-styrene sulfonate) PSS	10 ⁻¹	[274]
PANI/PP (2004)	Melt spinning	PANI/PP/DBSA	10 ⁻⁹	[266]
Core-sheath nanofibers with a conductive polymer, PANI with PSS/PMMA/PC/PEO (2005)	Electrospinning	PANI/PS	4.1 × 10 ⁻¹⁴	[271]
		PANI/PMMA	4.3 × 10 ⁻¹⁴	
		PANI/PC	5.5 × 10 ⁻¹⁴	
		PANI/PEO	2.4 × 10 ⁻¹³	
PANI (2005)	Wet Spinning	dodecylbenzene sulfonic acid (PANI-DBSA) and polyacrylonitrile containing methylacrylate (Co-PAN)	10 ⁻³	[275]
PANI (2008)	Electrospinning	H ₂ SO ₄ or HCl	52.9	[276]
PPy (2009)	Wet Spinning	di(2-ethylhexyl) sulfosuccinate (DEHS)	30	[277]
PEDOT/PSS (2009)	Wet Spinning	dip-treatment for 3 min EG (P grade) EG (PH grade)	195	[278]
			467	
PPy (2010)	Electrospinning	PPy-MWCNTs composite	10 ⁻¹	[279]
Poly(3,4-ethylenedioxythiophene) poly(styrenesulfonate)–Polyvinyl Alcohol (PEDOT:PSS–PVA) nanofibers (2011)	Electrospinning	(0%, 3%, 5%, and 8%) of DMSO	4.8 × 10 ⁻⁸ to	[280]
			1.7 × 10 ⁻⁵	
PANI/PP (2011)	Melt Spinning	Polyaniline/PP/dodecylbenzene sulfonic acid (DBSA)	10 ⁻⁹	[281]
poly(3-hexylthiophene) (P3HT) (2012)	Wet Spinning	FeCl ₃	160	[282]
poly(3-hexylthiophene) (P3HT) (2012)	Melt Spinning	FeCl ₃ in nitromethane	350	[282]
PANI (2012)	Electrospinning	(+)-camphor-10-sulfonic acid (HCSA) and blended with poly(methyl methacrylate) (PMMA) or poly-(ethylene oxide)	50 ± 30 (100% doped PANI)	[283]
Ternary blend of PP/PA6/PANI (20% wt.)-complex polypropylene / polyamide-6 / polyaniline-complex (2012)	Melt Spinning		4 × 10 ⁻³	[284]
Binary blend fibers of PP / PANI (20% wt.)-complex (2012)	Melt Spinning		5 × 10 ⁻³	[284]
poly(3-hexylthiophene) (P3HT) nanofiber (2012)	Electrospinning	Iodine	122 ± 9	[285]
PEDOT-PSS/PAN (2014)	Wet spinning	PAN	5	[286]
PEDOT:PSS/PEO fiber mats (2014)	Electrospinning	PEDOT:PSS	35.5	[287]
Graphene (1% wt.) / polyamide-6 yarn (2017)	Melt Spinning		14 ± 2 × 10 ⁻⁴ (fiber draw ration 2.0)	[288]
Conductive filaments made of silk fibroin (SF) and PANI (2018)	Wet Spinning	SF–FA–shell solution	1.42 × 10 ⁻⁴ (0.28 wt. % PANI)	[289]
PANI/PEO side-by-side bi-component fiber (2019)	Electrospinning	PAni doped with Camphoric acid CSA. Insulating PEO (3/4/5 w/v% to solvent) & conductive PANI-CSA (1.5/2.5/3.5 w/v% to solvent)	10 ⁻⁶ to 10 ⁻⁴	[290]
PANI/PVP (polyvinylpyrrolidone) (2020)	Electrospinning	N,N-dimethylformamide (DMF)	Membranes 1.7 × 10 ⁻² and yarns 4.1 × 10 ⁻⁴	[291]
PANI–poly(ethylene oxide) (PEO) fibers (2020)	Electrospinning	(+)-camphor-10-sulfonic acid (CSA), m-cresol, and chloroform	1.73	[292]

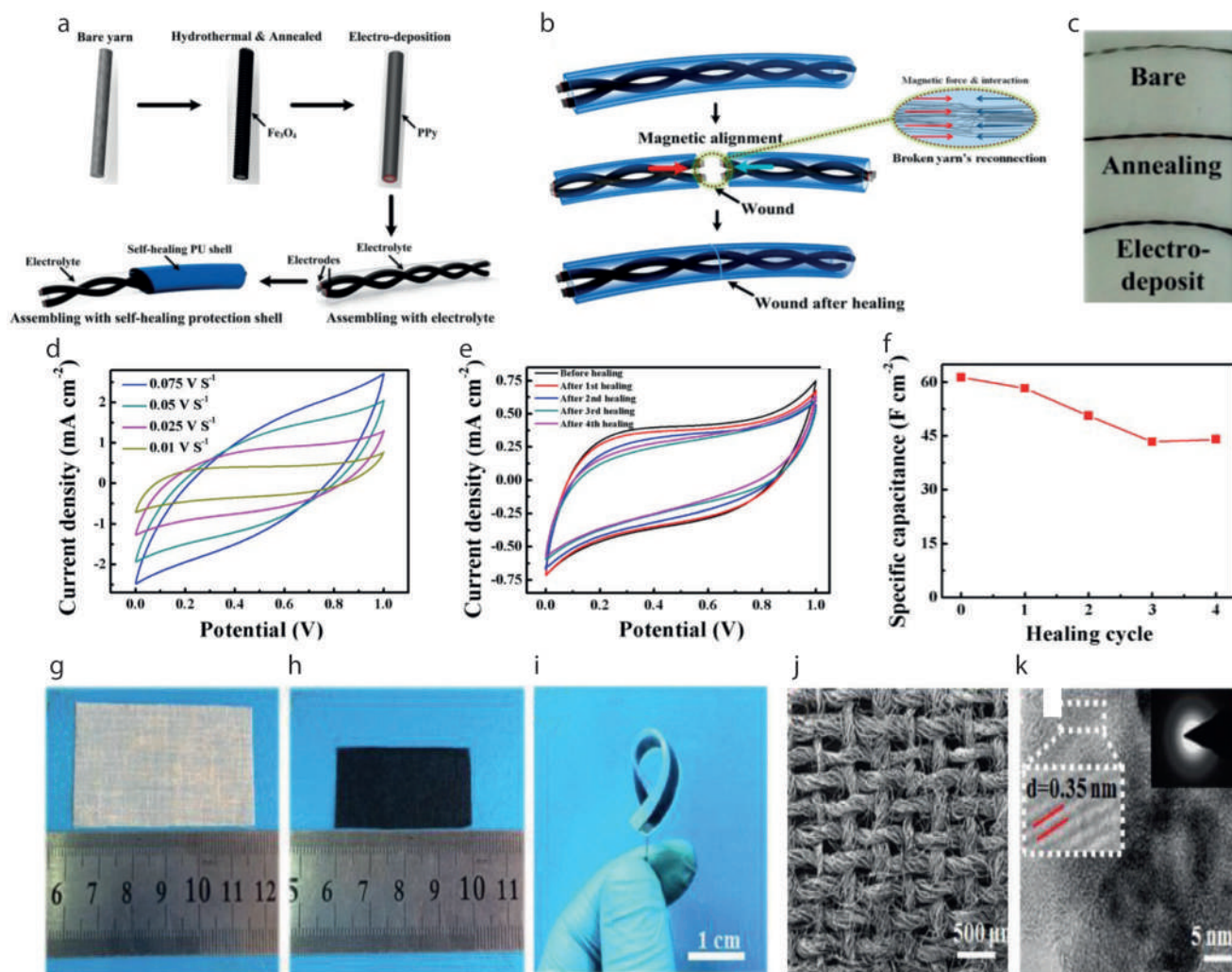


Figure 14. a) Design and manufacturing process flow of magnetic-assisted self-healable supercapacitor. Fe_3O_4 nanoparticles anchor on the surface of yarn by a microwave-assisted hydrothermal method. The processed yarn is annealed to ensure the magnetic particles anchor on the yarn tightly. To achieve a better electrochemical performance, a layer of PPy is electrodeposited on the annealed yarn. Finally, two yarns as a set of electrodes are assembled with a solid electrolyte and a self-healing shell to form a self-healing supercapacitor. b) Schematic illustration of supercapacitor's self-healing process. The magnetic alignment could assist the reconnection of fibers in broken yarn electrodes when they are brought together, as shown in inset image. c) From top to bottom, pristine yarn, hydrothermal and annealing-treated yarn, and PPy-electrodeposited yarn. Electrochemical measurements for as-prepared capacitor. d) CVs obtained at various scan rates. e) CVs after healing for different cycles. f) Specific capacitance of the original device and after healing for different cycles. Reproduced with permission.^[299] Copyright 2015, American Chemical Society. g) Fabrication process and characterization of carbonized plain weave cotton fabric (CPCF)- Photograph of a pristine cotton fabric h) Photograph of the CPCF made from (g). i) A flexible CPCF-based strain sensor. j,k) SEM image and TEM image of the CPCF. Reproduced with permission.^[306] Copyright 2016, Wiley-VCH.

5. Fabrication of Textiles Supercapacitors

5.1. Device Configurations

Textile-based flexible energy storage devices that are used for wearable applications can be categorized into: 1D fiber/yarn shaped device and 2D fabric shaped device. Additionally, there are very few 3D-shaped energy storage devices that have been reported in the literatures.^[307] **Figure 15** represents the schematic diagram of textile substrates that have been exploited as 1D and 2D-shaped storage devices.

5.1.1. 1D Fiber/Yarn Shaped Supercapacitors

In this type, energy storage device or SC components (i.e., the current collector, electrode, separator, and electrolyte) are all integrated into 1D system, possibly in fiber or wire or cable-shaped SCs. Several forms of 1D-shaped textiles are: filament or staple fibers converted into two -or multi-ply yarn, split film, core-sheath yarn, multi- or mono- filament, and staple yarn, **Figure 15(a–i)**. They are generally small in size, light in weight, and possess dimensions typically ranging from tens to hundreds of micrometers in diameter, and several millimeters to meters in

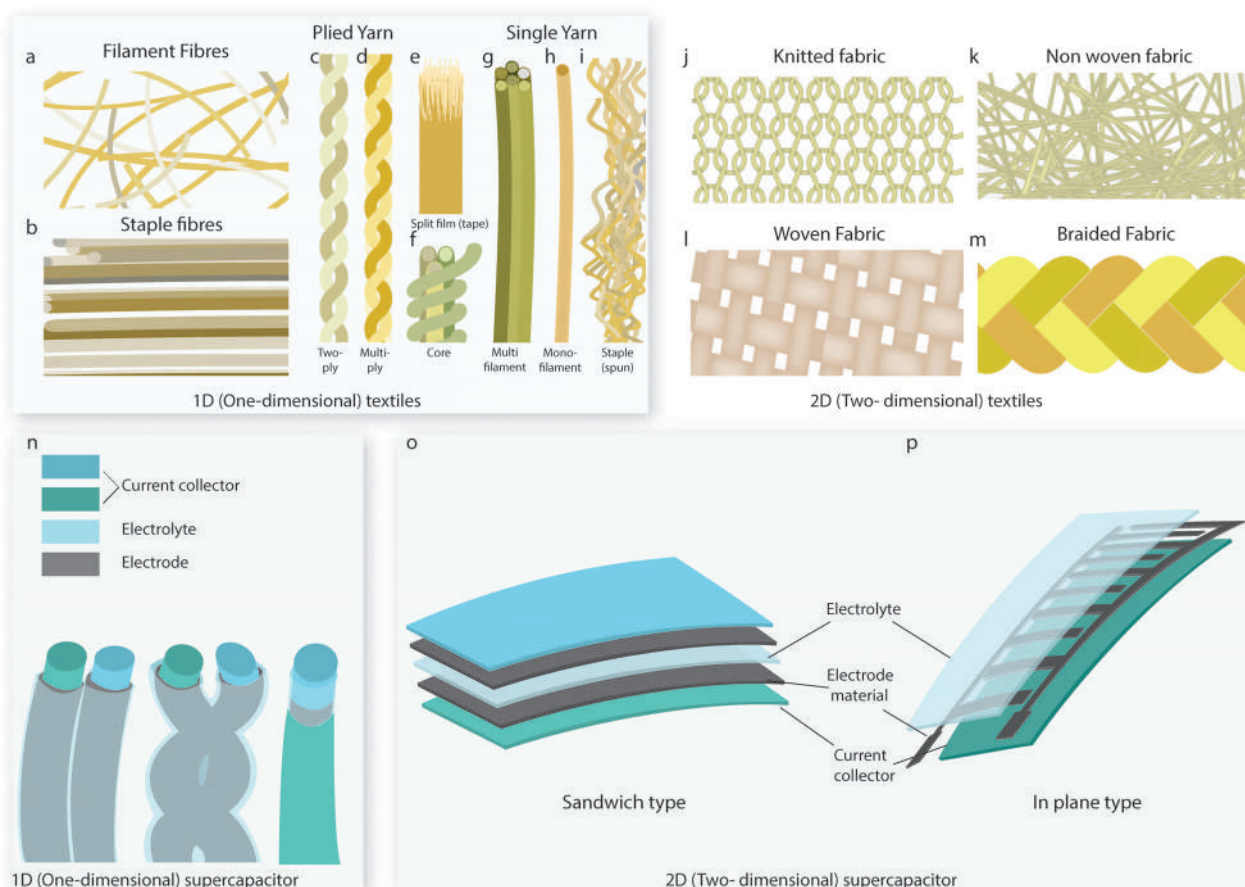


Figure 15. Textile-based energy storage device configuration. 1D substrate forms a) filament fibers, b) staple fibres, c) two plied, d) multiplied, e) split film, and f) core-sheath yarn, g) multifilament, h) monofilament, and i) staple yarn. 2D substrate forms j) knitted, k) non-woven, l) woven, and m) braided fabric. Textile supercapacitor forms n) 1D fiber or yarn shaped o) Sandwich type and p) in plane type 2D supercapacitor.

length.^[64,308] For instance, the electrode materials with separator are twisted to form ply yarn or all the electrodes and electrolyte are wrapped together to form a single yarn of core-sheath configuration, Figure 15n. 1D electrochemical energy storage devices offer several potential advantages over other conventional SCs including mechanical flexibility and deformability under various bending and twisting conditions, enabling better wearability and integrability into flexible textiles. The ease of integration via weaving, knitting, stitching, or embroidery provides scopes to get assembled into various shapes at different desirable locations in several wearable devices. It enables a greater design versatility and scope of integration with 1D energy harvesting (EH) or other devices such as displays and sensors, to create multifunctional wearable systems.^[309] However, the increased electrical resistance along the device length is a major challenge that affects the electrochemical performance of such devices.^[210]

5.1.2. 2D Fabric Shaped Supercapacitors

2D planar SC devices are particularly suitable for use in thin or layered products, such as smart cards, packaging and labels, magazines, books, skin patches and healthcare devices, jewelries, and

a broad range of other products comprising flexible electronic components.^[210] Different substrates are usually used to fabricate 2D SCs including plastic films, sponge, metal sheets, papers, and textiles.^[310] Among them, textile fabrics offer excellent flexibility due to their intrinsic mechanical properties and ability to be integrated directly with any other textile fabrics or garments for wearable applications via any simple methods of joining (e.g., sewing technology).^[1] Any form of fabric including woven, knit, non-woven, or braided can be used for 2D SCs, Figure 15(j–m). In such a 2D configuration, a pair of fabric electrodes are usually separated by an electrolyte and a separator in a sandwich or planar structure, Figure 15(o,p). However, it is challenging to maintain the appropriate dimension/thickness of such configurations in order to achieve high areal device performance, flexibility, and comfort.^[33]

5.1.3. 3D Energy Storage Device

The existing fabrication techniques of electrochemical energy storage devices have limitations in controlling the geometry and architecture of electrodes and solid-state electrolytes, which limits the charge storage performance for most electrodes.^[311] The

potential solution to improve the areal capacitance and energy density of EES devices is to build thicker electrodes, ensuring the increase of active materials loading without sacrificing the fast ion diffusion. In the case of 2D structures, the ion transport distance and overall electrical resistance of the thicker electrodes increase inevitably, causing a decrease in rate capability and power density.^[312] In contrast, a 3D structure provides shorter diffusion pathways and smaller resistance during the ion transport process.^[313] It also effectively enhances the energy density by creating porous structure and efficiently utilizing the available limited space.^[314] 3D structured devices with high energy and power density, lightweight, and well-controlled geometry within an architecture (all in a miniaturized package) are being experimented nowadays, to enhance electrochemical performance and safety.^[312] Additionally, 3D flexible conductors are mechanically durable and more promising in comparison to their 2D counterparts in maintaining their functionalities when subject to various mechanical deformation, such as bending, stretching, shearing, compressing, and twisting.^[315] 3D printing, also known as “Additive Manufacturing” (AM), has gained much attention as a powerful manufacturing technique for the fabrication of 3D-structured EES devices. Such technique provides freedom for designing complex 3D prototypes and devices from the macroscale to nanoscale range in a programmable, facile, rapid, cheap, and flexible manner.^[316] Successive layers of selected materials are deposited together by following a digital 3D model guidance using computer-aided design (CAD) and computer-aided manufacturing (CAM). 3D printed electrochemical devices for energy storage, conversion, and/or sensor have the potential to be used in various sectors including healthcare, biomedicine, pharmaceutical, engineering, etc.^[317–319] It also provides great opportunities to accurately control device spatial geometries and architectures, offers greater control over electrode thickness with simplified and low-cost process enhancing both the energy density and power densities.^[312,320] Additionally, it allows the manufacturing of complex-shaped SCs, as well as offers flexibility in packaging due to a wide range of 3D shapes.^[321]

5.2. Integration of the EES Device

After the formation of the electrode materials, there comes the final but critical stage of the integration of the components to complete the full SC. LIB cells are typically parallel assembled in modules (with internal electrical circuits), which are then integrated within a battery management system. Cable-shaped 1D devices (e.g., for smart textiles) can be embedded into textiles by weaving, knitting, or embroidery.^[210] Conductive electrodes and separators along with electrolytes are all integrated on a simple wire/cable shape, **Figure 16j**. 2D planar or thicker 3D devices may be integrated on a chip or a soft substrate into planar flexible objects. Electrodes with separators and/or electrolytes can be sandwiched by compression and/or encapsulation to form the integrated device, **Figure 16(k,l)**. However, there exist requirements for simpler and low-cost assemblies for flexible and wearable device architectures. Additionally, the encapsulation of the integrated device is crucial to improve the washability and durability of wearable e-textiles devices. Several methods have been used, either as surface pre-treatments (e.g., Bovine Serum Albumin (BSA) treat-

ment) or post-treatments (e.g., PDMS, PU coatings), to seal conductive track and encapsulate integrated devices, protecting them from the exposure to harsh treatments during daily usages.^[225]

5.3. Combined Energy Harvesting and Storage

The EH devices harvest energy that dissipates around us, in the form of electromagnetic waves, heat, and vibration, and then convert them into easy-to-use electric energy with relatively small levels of power in nW-mW range.^[322,323] The principle is similar to large-scale renewable energy generations such as wind turbines, but with a smaller amount of energy produced from such devices. EH is a promising technique for solving the global energy challenge without depleting natural resources and as an everlasting source of power supply.^[324] It can reduce greenhouse gas emissions generated with traditional energy sources.^[325] Though cheap, conventional batteries limit the amount of energy, and therefore require periodic replacement or recharging. In addition to that, rigid bulky structure limits their usage in smart fabrics applications.^[326] Flexible EH devices thus have the potential to replace conventional power sources for wearable electronics. EH sources are classified into two groups according to the characteristics of their source, i) Natural sources are those available readily from the environment such as sunlight, wind, and geothermal heat and ii) artificial sources are those generated from human or system activities including human motion, pressure on floors/shoe inserts when walking or running, and system vibration when operating.^[327] Biomechanical EH from human motion has attracted attention in the past decade for potential applications in charging portable electronic device, batteries, and self-powered sensor systems.^[328,329] Satharasinghe et al.^[330] presented an innovative solar EH fabric and demonstrated its suitability for powering wearable and mobile devices. A large solar EH fabric containing 200 miniature solar cells was demonstrated which can charge a 110 mF textile SC bank within 37s. Lv et al.^[331] demonstrated the first example of a stretchable and wearable textile-based hybrid supercapacitor–biofuel cell (SC–BFC) system, screen-printed on both sides of the fabric, designed to scavenge biochemical energy from the wearer’s sweat and store it in the SC module for subsequent uses, **Figure 17(a–g)**. Yong et al.^[332] presented a textile-based power module for the first time that combines a ferroelectric biomechanical energy harvester and solid-state SC-based energy storage device, fabricated in a single woven cotton textile layer, **Figure 17(h,i)**. The textile power module was highly flexible, and the fluorinated ethylene propylene (FEP) based ferroelectret was able to generate electric energy with an instantaneous output voltage of ≈ 10 V and power density of $\approx 2.5 \mu\text{W cm}^{-2}$, with a solid-state SC having a capacitance of 5.55 mF cm^{-2} .

6. Electrochemical Performance of Textile-Based Supercapacitor Devices

Capacitance/capacity per unit length (F cm^{-1}), area (F cm^{-2}), or volume (F cm^{-3}) are usually reported to evaluate the performance of a textile-based SC. However, the gravimetric capacitance of electrode materials does not necessarily represent the full device

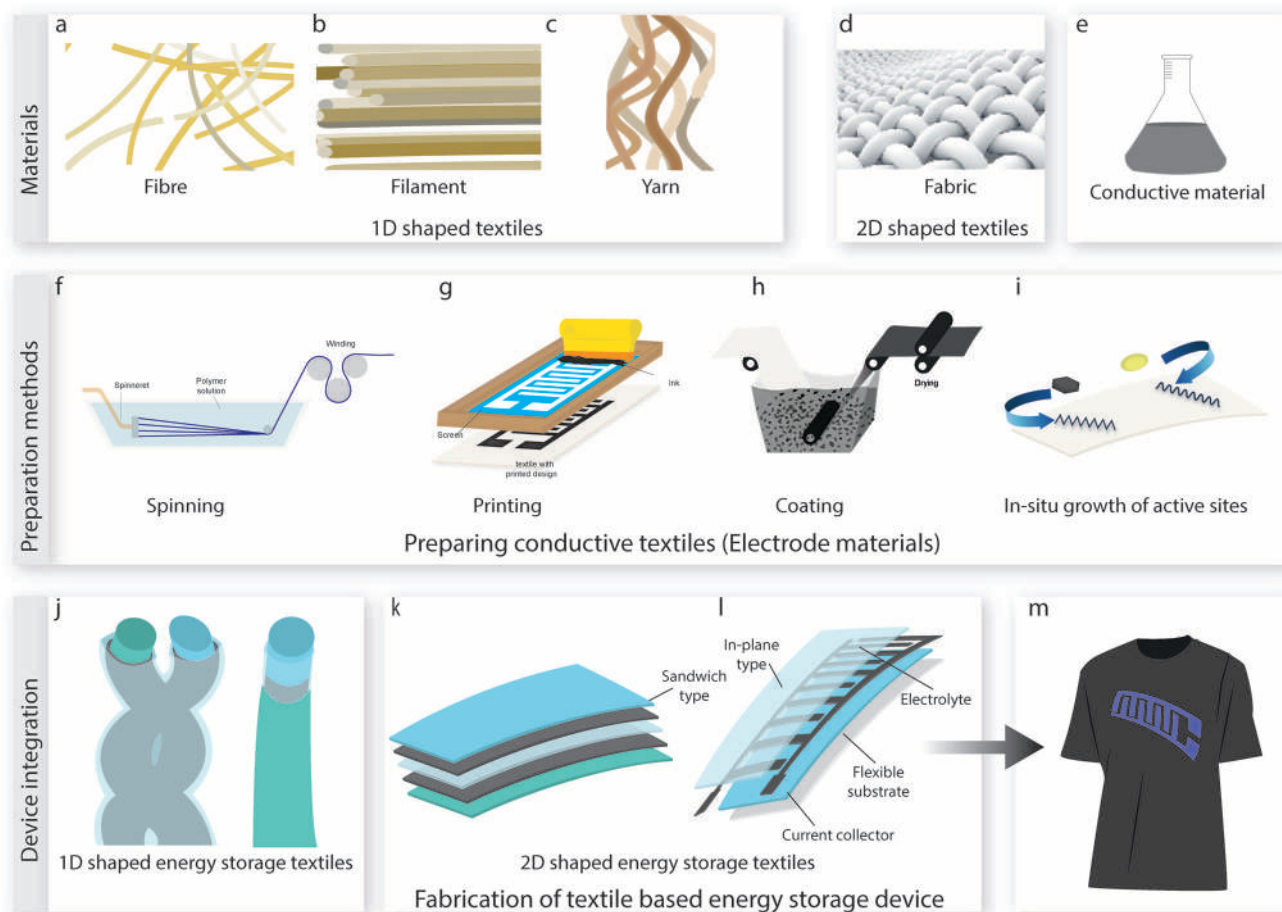


Figure 16. Fabrication of textile-based supercapacitor devices. 1D shaped textiles, a) fiber, b) filament, c) yarn, and 2D shaped fabric and c) conductive materials. Preparation of conductive textiles by f) spinning, g) printing, h) coating, and i) in situ growth of active sites on textiles to produce. j) 1D shaped energy storage textiles, 2D shaped k) sandwich type and l) in-plane type supercapacitor, and m) the final e-textiles.

capacitive performance. In addition to capacitance, the other two key parameters for evaluating SC performance are energy density and power density. Maintaining higher energy and power density is still a major challenge for such energy storage devices. SCs, in comparison with lithium-ion batteries, usually exhibit relatively lower energy density but higher power density. Whereas for LIBs, it is desirable to improve the power density while keeping the high energy density. The major challenge in achieving high-performance SC textiles is to enhance the energy density while maintaining the high-power density.^[333]

The capacitance retention of textile-based energy storage devices is another important property for wearable applications, since the replacement of such devices would be difficult during the product lifetime. In most cases, 10 000 cycles of charge-discharge are employed for the capacitance retention assessment. For 1D-shaped energy storage devices, several configurations were reported with full capacitance retention up to 10 000 cycles.^[333,334] Additionally, Fu et al.^[335] reported a fiber-shaped SC, developed by pen ink, which retains full capacitance even after 15 000 of charge-discharge cycles. For 2D-shaped energy storage devices, full capacitance retentions were reported even after longer (20 000–25 000) charge-discharge cycles.^[336,337] Wang

et al.^[338] developed a fabric type asymmetric SC using electrochemically activated carbon cloth as anode, TiN@MnO₂ on carbon cloth as cathode, and LiCl solution as electrolyte, which significantly boosted the energy storage capability. The device showed no capacitive decay even at 70 000 cycles of charge-discharge. In another study, Hu et al.^[223] reported a fabric-based SC device made of Cotton/SWNTs, exhibiting extremely good cycling stability of 98% capacitance retention over a remarkably large cycle number of 130 000 charge-discharge cycles. As we previously classified the active materials into four categories, in this section we will discuss active materials of textile-based SCs. Each subsection focuses on both 1D and 2D shaped textile SCs. Combining any of the two or more types are also summarized under hybrid materials section. In addition, we throw light on SCs based on fiber types, particularly focusing on most widely used natural cotton, manmade polyester and carbon fibers.

6.1. Carbon-Based Textiles Supercapacitors

Among all the active materials, carbonaceous compounds, that is, CNTs, graphene and its derivatives have mostly been studied

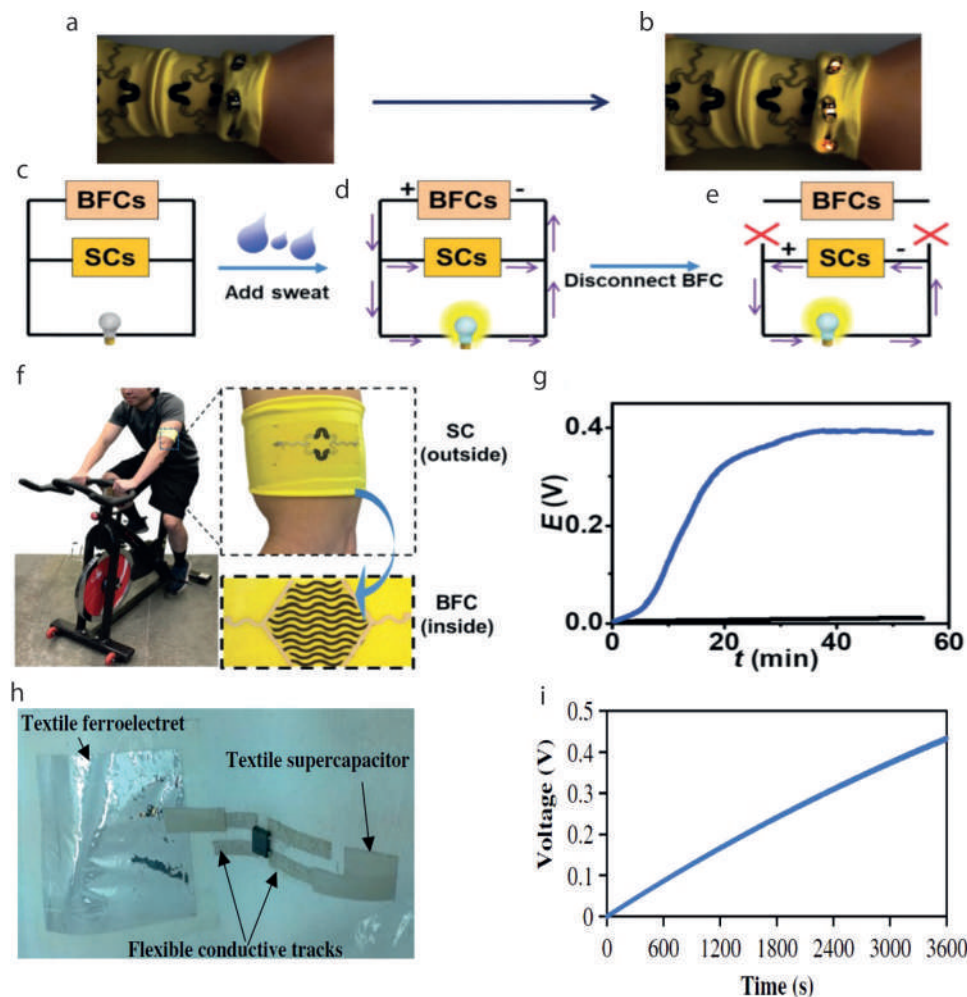


Figure 17. a,b) Demonstration of the hybrid SC–BFC device, Photographs showing the application of three SCs charged by five BFCs to light LEDs using the following procedure: c) without lactate, no power; d) with lactate, LEDs were turned on; e) upon disconnecting BFCs and SCs, LEDs could still be turned on. f) The integrated chemical self-powered system on one piece of textile was applied to the arm of a volunteer. The SC and BFC were printed outside and inside the textile band, respectively. g) The real-time voltage of the printed SC charged from the on-body BFC during a constant cycling exercise for 56 min. The SC charged by lactate BFC immobilized with LOx (blue plot) and without LOx as a control (black plot). Reproduced with permission.^[331] Copyright 2018, The Royal Society of Chemistry. h) Assembled textile power module and i) FEP-textile ferroelectret charging the 2 mF textile capacitor. Reproduced with permission.^[332] Copyright 2019, Wiley-VCH.

for the fabrication of textile-based SC devices. **Table 8** summarizes the electrochemical performances of carbon-based 1D fiber/yarn-shaped and 2D fabric-shaped SCs. Several research groups reported graphene fiber,^[339] GO fiber,^[340] rGO fiber,^[341] and modified rGO^[342] fiber as SC electrodes. Kou et al.^[264] twisted two coaxial fibers composed of polyelectrolyte-wrapped carbon nanomaterial core-sheath fiber, rGO@CMC, CNT@CMC, rGO+CNT@CMC, together to form a two-ply SC electrode, and then coated with PVA electrolyte. In presence of 1 M H₂SO₄ liquid electrolyte, the device exhibited length, areal, and volumetric capacitance of 8.0 mF cm⁻¹, 269 mF cm⁻², 239 F cm⁻³, respectively. Zhai et al.^[343] drop-casted activated carbon on carbon fiber yarn to prepare SC electrode. For the fabrication of yarn-shaped SC, two coated strands were twisted together and finally dipped in PVA-H₃PO₄ electrolyte. The resultant device exhibited a specific length capacitance of 45.2 mF cm⁻¹ at a scan rate of 2 mV s⁻¹.

For 2D fabric-shaped SC conventional cotton, polyester, poly-cotton, PP, and carbon fiber textiles (CFTs) were investigated. Several research groups^[223,344] coated cotton fabric with single or MWCNT, however, better performances were obtained while using graphene or its derivatives. For example, Hu et al.^[223] coated cotton fabric with SWNT ink by simple dipping and drying method to obtain SC electrode. In the presence of LiPF₆ electrolyte, the device exhibited specific capacitance of 140 Fg⁻¹ at 20 μA cm⁻² and an areal capacitance of 0.48 F cm⁻². The energy density was as high as 20 Wh kg⁻¹ at 10 kW kg⁻¹ with an outstanding cyclic stability of 98% after 130 000 charge-discharge cycles. In another study by Li et al.,^[344] the gravimetric capacitance was enhanced by coating cotton fabric with reduced GO and using coated fabrics as SC electrode. The sandwiched-shaped SC device combined with raw cotton fabric separator and H₃PO₄/PVA gel electrolyte exhibited a gravimetric capacitance of 464 F g⁻¹ at 0.25 A g⁻¹ and a higher energy density of 27.05 W h kg⁻¹.

Table 8. Summary of Carbon-based supercapacitors or supercapacitor electrodes.

1D shaped	Substrate (Reporting year)	Device Configuration	Device capacitance	Energy density	Power density	Capacitance retention	Flexibility	Refs.
Carbon fiber and Gold coated plastic fiber (2012)	Commercial graphite pen ink used as active material and deposited on fiber surface. Spacer wire evenly twisted onto the surface of one fiber electrode. Two fiber electrodes placed parallelly in a flexible plastic tube filled with PVA-H ₂ SO ₄ electrolyte	11.9–19.5 mF cm ⁻²	1.76×10 ⁻⁶ –2.70×10 ⁻⁶ Wh cm ⁻²	Up to 9.07 mW cm ⁻²	Remains similar after 15 000 cycles	Only slight drop at 180°, 360° bending	[335]	
Carbon microfiber bundle (2013)	A carbon microfiber bundle coated with MWCNs as a core electrode in the center of the coaxial SC and a carbon nanofiber (CNF) film prepared by electrospinning as an outer electrode	6.3 mF cm ⁻¹ (86.8 mF cm ⁻²)	0.7 μWh cm ⁻¹ (9.8 μWh cm ⁻²)	583 μW cm ⁻¹	94% after 1000 cycles	Negligible change at 180° bending	[349]	
Carbon fiber (2013)	Electrochemically reduced GO(ERGO) coated carbon fiber followed by acid treatment (ERGO@CF-H) with PVA-H ₃ PO ₄ gel electrolyte	13.5 mF cm ⁻¹ (307 mF cm ⁻²) at 0.05 mA cm ⁻¹	1.9 mW h cm ⁻¹ (21.4 mW h cm ⁻²)	0.74 mW cm ⁻¹ (8.5 mW cm ⁻²)	85% after 5000 cycles	No decay at bending 0°–180°	[350]	
rGO fiber yarns (2014)	rGO fiber yarns deposited on a titanium current collector and separated by a PVDF membrane	409 Fg ⁻¹	14 Wh kg ⁻¹	25 kW g ⁻¹	No decay after 5000 cycles		[341]	
Carbon nanotube and rGO composite yarn (2014)	Two SWNTs/rGO electrode mounted on a polyester (PET) substrate using PVA-H ₃ PO ₄ electrolyte	116.3 mFcm ⁻² , 45 Fcm ⁻³ at 26.7 mA cm ⁻³	6.3 mWh cm ⁻³	1085 mW cm ⁻³	93% after 10 000 cycles	>97% after 1000 bending cycles at 90°	[351]	
GO, carbon nanotube (CNT) and their mixture wet spun filament (2014)	Polyelectrolyte-wrapped graphene/carbon nanotube core-sheath fibers, Polyelectrolyte-wrapped carbon nanomaterial (graphene, CNTs, and their mixture) core-sheath fiber, RGO@CMC, CNT@CMC, RGO+CNT@CMC. Two coaxial fibers twisted together to form two-ply SC electrodes, then coated with PVA electrolyte	269 mF cm ⁻² , 239 F cm ⁻³ , 8.0 mF cm ⁻¹ (liquid electrolyte 1 M H ₂ SO ₄), 177 mF cm ⁻² , 158 F cm ⁻³ , 5.3 mF cm ⁻¹ @ current density of 0.1 mA cm ⁻² (solid electrolyte H ₃ PO ₄ /PVA)	5.91 mWh cm ⁻² (liquid) 3.84 mWh cm ⁻² , 3.5 mWh cm ⁻³ (solid)		No decay within 2000 times	Dropped 2% at 200 times of bending and rose persistently up to 111% at 1000 times of bending	[264]	
GO fiber (2014)	Region-specific reduction of GO fiber by laser irradiation, to prepare rGO/GO/rGO single fiber SC with ionic liquid electrolyte of 1-butyl-3-methylimidazolium tetrafluoroborate.	1.2mF cm ⁻² at 80 μA cm ⁻² , 0.45 mF cm ⁻² at 200 μA cm ⁻²	2–5.4×10 ⁻⁴ Wh cm ⁻²	3.6–9×10 ⁻² W cm ⁻²	No obvious degradation after 1000 cycles	No decrease after 160 bending cycle	[340]	
Carbon fiber yarn (2015)	Two hybrid activated carbon drop casted carbon fiber yarn electrodes, twisted together, dipped in PVA/H ₃ PO ₄ gel electrolyte, dried	Specific length capacitance 45.2 mF cm ⁻¹ at 2 mV s ⁻¹	Specific length energy 6.5 μWh cm ⁻¹	27 μWcm ⁻¹	86.6% after 10 000 cycle	98% after 1000 bending cycles	[343]	
CNT fiber (2015)	GO sheets coated on CNT fiber, reduced to RGO, forming a core-sheath-structured CNT/RGO composite fiber. Two composite fibers drawn into a gel electrolyte consisting of poly(vinyl alcohol) (PVA), phosphoric acid, and water, followed by twisting into fiber-shaped SC	68.4 F cm ⁻³ (126.7 F g ⁻¹) at 31 mA cm ⁻³	2.4 mW h cm ⁻³ , 3.8 μW h cm ⁻²	0.016 W cm ⁻³ , 0.025 mW cm ⁻²	No decay after 10 000	No decrease at bending 180°	[334]	

(Continued)

Table 8. (Continued).

1D shaped	Substrate (Reporting year)	Device Configuration	Device capacitance	Energy density	Power density	Capacitance retention	Flexibility	Refs.
Graphene fiber (2015)	Spun-rGO/rGO Coaxial all graphene fiber SC with a continuous liquid crystal wet-spun core fiber electrode followed by reduction, PVA gel coating as separator, a clip-coated cylinder sheath fiber as the other electrode followed by reduction, coating of H ₂ SO ₄ /PVA gel electrolyte.	205 mF cm ⁻² (182 F g ⁻¹)	17.5 μWh cm ⁻² (15.5 Wh kg ⁻¹), increased to 104 μWh cm ⁻² with organic ionic electrolyte	700 mW cm ⁻³	No decay at 10 000th cycle	92% after 100 times of bending	[339]	
Graphene fiber (2015)	Two MWCNTs-rGO fiber electrodes with PVA-H ₃ PO ₄ electrolyte	0.35 mF cm ⁻¹ , 38.8 F cm ⁻³ at 50 mA cm ⁻³	3.4 mWh cm ⁻³		93% after 10 000 cycle	No decrease after knotting	[352]	
Porous graphene ribbon (PGRs) (2015)	The PGRs freeze-dried for 24 h to obtain the dried porous graphene ribbons (DGRs) followed by immersion in H ₃ PO ₄ /PVA electrolyte solution. Two pairs of electrodes pressed together under slight pressure to fabricate the PGR and DGR SC.	208.7 F g ⁻¹ (78.3 mF cm ⁻²) or 3.12 mF cm ⁻¹			99% after 5000 cycles	No decrease at bending 45°, 90°, 135°, 180°, 95% after 100 cycle bending when woven to glove	[353]	
GO fiber (2015)	Region-specific reduction of wet spun GO fiber by laser irradiation to prepare alternate rGO-GO electrolyte-free fiber SCs	14.3 mF cm ⁻² at 50 mA cm ⁻³			93% after 1000 cycles	No decrease after 1000 cycles	[354]	
PVA/RGO hybrid fibers (2016)	Incorporating hydrophilic PVA into a non-liquid-crystalline GO dispersion before wet spinning and chemical reduction, two bundles of PVA/RGO fibers with PVA/ H ₂ SO ₄ / H ₂ O gel electrolyte	Fiber 241 F cm ⁻³	5.97 mW h cm ⁻³ (5.32 mW h g ⁻¹)	At 26.9 mW cm ⁻³ (23.9 mW g ⁻¹)	85% after 1000 cycles	97% retention after cyclic bending between 0 and 180 for 1000 times	[342]	
Graphene and few-walled carbon nanotubes composite yarn (2018)	Hybrid fiber based on graphene and few-walled carbon nanotubes (G ₁₀ /CNTs) electrode with 6 M KOH aqueous electrolyte	312.6 F g ⁻¹ at 200 mA g ⁻¹	Varied from 23.46 to 9.66 Whkg ⁻¹ at 84.68 to 1134.56 Wkg ⁻¹		89.6% after 10 000 cycles		[355]	
2D shaped								
Cotton fabric (2010)	Dipping and drying of cotton with single-walled carbon nanotube (SWNT) ink electrodes with LiPF ₆ electrolyte to form fabric SC	140 Fg ⁻¹ at 20 μA cm ⁻² , 0.48 F cm ⁻²	20 Wh kg ⁻¹ at 10 kW kg ⁻¹		98% after 130 000 cycles	No decrease @ 100th 120% strain	[223]	
Cotton Stretchable fabric (2010)	Dipping and drying of cotton with single-walled carbon nanotube (SWNT) ink electrodes with LiPF ₆ electrolyte to form fabric SC	62 Fg ⁻¹ at 1 mA cm ⁻²			<6% decrease after 8000 cycles	Almost similar after stretching 120% strain 100 times.	[223]	

(Continued)

Table 8. (Continued).

Substrate (Reporting year)	Device Configuration	Device capacitance	Energy density	Power density	Capacitance retention	Flexibility	Refs.
2D shaped							
Cotton fabric (2010)	Conformal coating of single-walled carbon nanotubes (SWNTs) ink with $2 \text{ mol L}^{-1} \text{ Li}_2\text{SO}_4$ electrolyte	$70\text{--}80 \text{ Fg}^{-1}$ at 0.1 mA cm^{-2}			Coulombic efficiency >99% after 35 000 cycles		[356]
Cotton cloth (2012)	Brush-coating of cotton cloth with GO suspension ink as electrode, nickel foam current collector, pure cotton cloth as separator, and 6 M KOH electrolyte	81.7 Fg^{-1}	7.13 Wh kg^{-1}	1.5 kW kg^{-1}	93.8% after 1500 cycles		[357]
Cotton woven (2017)	Screen printing of GO, followed by electrochemical reduction to produce rGO-cotton electrode, with PVA- H_2SO_4 gel electrolyte	2.5 mF cm^{-2} , 257 F g^{-1}			97% after 10 000 cycles	95.6% after folding 180° for 2000 cycles	[239]
Cotton fabric (2019)	Dry-coated and subsequently two-step reduced GO coated cotton fabric as electrode, raw cotton fabric separator, H_3PO_4 /PVA gel electrolyte sandwich to form flexible SC	464 F g^{-1} at 0.25 A g^{-1}	27.05 Wh kg^{-1}		91.6% after 1000 cycles	No apparent performance degradation after 0° and 180° bending	[344]
Cotton fabric (2022)	Graphene ink screen printed on cotton textiles with PVA/ H_2SO_4 gel electrolyte	3.2 mF cm^{-2}	0.28 mWh cm^{-2} at 3 mW cm^{-2}		95% after 10 000 cycles		[358]
Polyester fabric (2014)	CNT dip-coated onto PET fabrics electrode	$1.4 \times 10^{-4} \text{ F cm}^{-2}$					[359]
Polyester fabric (2019)	By sandwiching 2 dip-dried graphene nanoparticle/ polyester electrodes and 1 h-boron nitride/polyester dielectric layer in between to form flexible textile-based capacitor (FTC)	26 pF cm^{-2}				Sustains 100 cycles of repeated bending	[360]
Poly-cotton (65/35) 2/1 twill fabric (2020)	Graphene-coated textile electrodes with PVA- H_2SO_4 gel electrolyte	2.7 mF cm^{-2} (electrode)			$\approx 98\%$ after 15 000 cycles	98% after bending 150 cycles at 180°	[225]
Cotton and polyester fabric (2011)	Cotton and polyester screen printed with activated carbon as SC electrode, polyester separator, and Li_2SO_4 and Na_2SO_4 electrolyte	Electrode 0.43 F cm^{-2} at 5 mA cm^{-2} (Na_2SO_4), $85\text{--}95 \text{ Fg}^{-1}$ at $1\text{--}10 \text{ mVs}^{-1}$			92% after 10 000 cycles		[345]

(Continued)

Table 8. (Continued).

Substrate (Reporting year)	Device Configuration	Device capacitance	Energy density	Power density	Capacitance retention	Flexibility	Refs.
Polypropylene fabric (2019)	Reactive inkjet printing of rGO layers on PP fabric as electrode with PVA/H ₃ PO ₄ gel electrolyte to form flexible solid-state SC	13.3 mF cm ⁻² (79.9 F g ⁻¹) at 0.1 mA cm ⁻²	1.18 mWh cm ⁻²	4.6 mW cm ⁻²	Almost 100% after 5000 cycles		[361]
Carbon fabric (2012)	Entangled carbon nanofibers (CNFs) were synthesized on a flexible carbon fabric (CF) via water-assisted chemical vapor deposition to form CNF/CF electrode with 0.5 M Na ₂ SO ₄ aqueous neutral solution	140 F g ⁻¹ at 5 mV s ⁻¹			≈95% after 2000 cycle		[362]
Carbon fiber knit and woven fabric (2013)	Carbon fabric screen printed with activated carbon with solid polymer electrolyte	88 Fg ⁻¹ , 0.51 F cm ⁻² (Knitted), 66 Fg ⁻¹ , 0.19 F cm ⁻² (Woven)				80% after bending at 90°, 135°, and 180°	[346]
Carbon cloth (2014)	Electrochemically activated carbon cloth electrode with PVA-H ₂ SO ₄ electrolyte	Electrode 88 mF cm ⁻² (8.8 mFg ⁻¹) at 10 mVs ⁻¹ , SC 15.3 mF cm ⁻² (0.765 mFg ⁻¹)			95% after 20 000 cycles		[336]
Activated Carbon fiber felt (2015)	Carbon nanotube (CNTs) and graphene (GN) modified composite ACFF textile electrodes, non-woven fabric separator, with KOH aqueous electrolyte	3350 mF cm ⁻² , device 2700 mFcm ⁻²	112 μW h cm ⁻²	490 μW cm ⁻²	No decay at 1000 cycles		[347]
Stainless steel fabric (2016)	Two chemically converted graphene (CCG) on Stainless steel fabrics (SSF) electrode with 1 M H ₂ SO ₄ to form flexible solid-state symmetrical SC	730.8 mF cm ⁻² at 2 mA cm ⁻² , 180.4 mF cm ⁻² at 1 mA cm ⁻²	19.2 W h cm ⁻² at 386.2 W cm ⁻²		96.8% after 7500 cycles	96.4% after 800 stretching-bending cycles	[348]
Silver fiber fabric (2017)	Electrophoretic deposition of graphene on silver fiber fabric (rGO/SFF) electrode with KOH (3 M) as electrolyte	172 mF cm ⁻² at 4 mA cm ⁻²			97% after 5000 cycles		[363]

The highest areal capacitance for conventional textiles SC prepared by carbonaceous compounds was reported by Jost et al.^[345] They screen printed activated carbon on both cotton and polyester fabric. The fabric SC achieved a high areal capacitance of 430 mFcm⁻² at 5 mAcm⁻² and a gravimetric capacitance of 85–95 Fg⁻¹ at 10 mV s⁻¹. The device also exhibited very good cyclic stability of 92% after 10 000 charge-discharge cycles. Additionally, they screen printed activated carbon on carbon fiber fabric and achieved even higher areal capacitance.^[346] They achieved gravimetric capacitance of 88 Fg⁻¹ and areal capacitance of 510 mF cm⁻² for knitted carbon fiber fabric, and that of 66 Fg⁻¹ and 190 mFcm⁻² for the woven carbon fiber fabric. The highest areal capacitance for both electrode (3350 mFcm⁻²) and SC device (2700 mF cm⁻²) was obtained through composite electroactive materials, as reported by Dong et al.^[347] CNTs and graphene (GN) were coated on activated carbon fiber felt (ACFF) to prepare electrodes. The asymmetric SC was fabricated by as-prepared CNT/ACFF and GN/ACFF composite textile electrodes with a non-woven fabric separator, and KOH aqueous electrolyte. The energy and power densities were reported as 112 μW h cm⁻² and 490 μW cm⁻², respectively. Furthermore, several research groups have investigated stainless steel fabric (SSF) and silver fiber fabric for fabric-based SCs. Yu et al.^[348] prepared two chemically converted graphene (CCG) on SSF electrode with 1 M H₂SO₄ to form flexible solid-state symmetrical SC. The areal capacitance was reported as high as 730.8 mF cm⁻² at 2 mA cm⁻² and 180.4 mF cm⁻² at 1 mA cm⁻². The energy density was reported as 19.2 W h cm⁻² at 386.2 W cm⁻². The device was able to retain the capacitance up to 96.8% after 7500 charge-discharge cycles and 96.4% after 800 stretching-bending cycles.

6.2. Conductive Polymer-Based Textiles Supercapacitors

CPs are pseudo-capacitive materials, the bulk of the material undergoes a fast redox reaction to provide the capacitive response exhibiting superior specific energies to the carbon-based double-layer SCs.^[364] Table 9 summarizes the conductive polymer-based 1D fiber or yarn-shaped and 2D fabric-shaped SCs. Only a few works have been reported for fiber or yarn-shaped textile SCs. For example, Wei et al.^[365] directly coated cotton yarns by PPy nanotubes via in situ polymerization of pyrrole in presence of methyl orange. The electrode thus obtained was used to fabricate an all-solid-state yarn SC, which provided a high areal-specific capacitance of 74.0 mF cm⁻² and an energy density of 7.5 μWh cm⁻².

However, several works^[366–368] have been reported on 2D fabric-shaped SCs. For instance, Wang et al.^[366] prepared flexible and stretchable electrodes via in situ polymerization of conducting PPy polymers on knitted cotton fabrics. The areal capacitances of symmetric all-solid-state SC based on those electrodes were found to be 101 and 450 mF cm⁻² at 5 mV s⁻¹ and 1 mA cm⁻², respectively. The capacitance retention of such devices was reported at 53% after 5000 charge-discharge cycles. In another study by Lv et al.,^[367] the electrochemical performances of several woven and knitted fabrics-based electrodes of cotton, wool, silk, and polyester fibers were enhanced via an improved in situ polymerization method. The conjugate length of the PPy molecule and doping levels were improved to provide a thin and

dense conductive polymer coating on the fabric surface with a sheet resistance <10 Ω sq⁻¹. The highest specific capacitance of 4848 mF cm⁻² at 1 mA cm⁻² was reported for PPy-coated knitted electrodes of cotton fibers, with a capacitance retention of 88% after 5000 cycles, which is 35% higher than the previously reported work. The electrical conductivity of electrodes was also found to be almost unchanged even after washing in dichloromethane up to 20 laundering cycles.^[367] The same research group further improved the capacitive performance of knitted electrodes of cotton fibers using an improved chemical polymerization technique.^[368] The PPy-coated fabric electrode showed a superior specific areal capacitance of 5073 mF cm⁻², and the fabric-based symmetric all-solid-state SC exhibited an enhanced specific areal capacitance of 1167.9 mF cm⁻² at 1 mA cm⁻² which are highest among conductive polymer-based textile SCs of cotton fibers. Additionally, the same device provided a very high energy density of 102.4 μWh cm⁻² at a power density of 0.39 mW cm⁻² which maintained ≈90% capacitance after 2000 cycles.

Few researchers also investigated polyester fabric-based electrodes for fabricating textiles SCs. Cárdenas-Martínez et al.^[369] deposited electro-spun PEDOT: PSS nanofibers on flexible polyester textiles. The all solid-state SC exhibited an areal capacitance of 1.8 mF cm⁻² and gravimetric capacitances of 3.6 Fg⁻¹ at a discharge current of 5 μA cm⁻². However, like cotton textiles, in situ polymerization of PPy resulted in better capacitive performances for polyester fabrics. Such PPy coating on polyester fabrics exhibited an areal capacitance of 1213 mF cm⁻² at 1 mA cm⁻².^[367] Additionally, an in situ polymerization of aniline and pyrrole on polyester (PET) was reported by Xie et al.^[370] to produce SC electrodes. The electrode exhibited an areal capacitance of 1046 mF cm⁻² at 2 mA cm⁻² when the monomer ratio of aniline to pyrrole was 0.75:0.25. The SC device showed areal capacitance of 537 mF cm⁻², volumetric capacitance of 1.13 F cm⁻³ at 2 mA cm⁻² with energy and power densities of 0.043 mWhcm⁻³ and 0.005 Wcm⁻³, respectively. In addition to cotton and polyester, Lv et al.^[367] also used protein fibers as SC substrate. The in situ polymerization of PPy exhibited an areal capacitance of 1349 mFcm⁻² in case of silk and 1007 mFcm⁻² in case of wool gauze fabric at 1 mA cm⁻². Few other research groups also investigated carbon fabric as SC substrates. The highest gravimetric capacitance on carbon cloth was reported by Wang et al.^[371] They drop casted polyaniline on functionalized carbon cloth, the SC showed a gravimetric capacitance of 319.5 Fg⁻¹ at 0.2 A g⁻¹ with cyclic stability up to 82% after 1000 charge-discharge cycle.

6.3. Metal-Based Textiles Supercapacitors

Distinguished by particular physical and chemical properties, metal and metal oxide materials have been a focus of research and exploitation for applications in SCs,^[382] Table 10. CNTs were studied mostly as substrate for the fabrication of metal-based 1D fiber or yarn-shaped SCs. Su et al.^[383] produced high-performance asymmetric two-ply yarn SC from spun CNT yarn (as negative electrode) and CNT@MnO₂ composite yarn (as positive electrode) in aqueous electrolyte. This asymmetric architecture resulted in areal capacitance of 12.5 Fg⁻¹ with higher energy and power densities compared to the reference symmetric two-ply

Table 9. Summary of CP-based supercapacitors or supercapacitor electrodes.

1D shaped	Substrate (Reporting year)	Device Configuration	Device capacitance	Energy density	Power density	Capacitance retention	Flexibility	Refs.
	Cotton yarn (2017)	Cotton yarns coated with PPy nanotubes	74.0 mF cm ⁻²	7.5 μWhcm ⁻²			97% after 200 cycles	[365]
	Carbon fiber thread (2015)	carbon fiber thread (CFT) @polyaniline (PANI) as positive and functionalized carbon fiber thread (FCFT) as negative electrode, coated with PVA-H3PO4 gel electrolyte and twisted together	High operating voltage (1.6 V).	2 mWh cm ⁻³	11 W cm ⁻³		Almost unchanged at a strain of 100%	[372]
2D shaped	Substrate (Reporting year)	Device Configuration	Device capacitance	Energy density	Power density	Capacitance retention	Flexibility	Refs.
	Cotton fabric (2013)	Poly(pyrrole)-coated cotton fabrics electrode, prepared in mixed surfactants: cetyltrimethylammonium bromide (CTAB) and sodium dodecyl benzene sulfonate (SDBS), with NaCl solution	51.7 mAh g ⁻¹			Negligible decay after 100 cycles		[373]
	Cotton fabric (2013)	In situ oxidation polymerization of pyrrole in the presence of lignosulfonate as both template and dopant to prepare PPy/ lignosulfonate (PPy/LGS) coated cotton fabric electrode	304 F g ⁻¹ at 0.1 A g ⁻¹					[374]
	Cotton fabric (2015)	PPy nanorods deposited on cotton fabrics via in situ polymerization	325 F g ⁻¹	24.7 Wh kg ⁻¹ at 0.6 mA cm ⁻²		200 F g ⁻¹ after 500 cycles		[375]
	Cotton fabric (2016)	Polyppyrole, PPy coated cotton as working, Pt sheet as counter, Ag/AgCl as reference electrode with 1 M H ₂ SO ₄ as electrolyte	Knitted 4117, woven 2191, and nonwoven fabrics 2905 mF cm ⁻²	5.94 Wh kg ⁻¹	259.55 W kg ⁻¹	Stable within 5000 cycles		[376]
	Cotton woven and knit (2019)	In situ polymerization coating of PPy on fabric	Woven 1748, Knitted 4848 mF cm ⁻² at 1 mA cm ⁻²			88% after 5000 cycles		[367]

(Continued)

Table 9. (Continued).

Substrate (Reporting year)	Device Configuration	Device capacitance	Energy density	Power density	Capacitance retention	Flexibility	Refs.
2D shaped							
Cotton knit fabric (2019)	In situ chemical polymerization of Polypyrrole on fabric with PVA-H ₂ SO ₄ gel electrolyte	Electrode 481 and 1433 mFcm ⁻² at 5 mVs ⁻¹ and 1 mAcm ⁻² respectively, device 101 and 450 mFcm ⁻² at 5 mVs ⁻¹ and 1 mAcm ⁻² respectively	0.4 Whm ⁻² (2.3 Wh kg ⁻¹ based on total mass of 2 electrodes)	10 W m ⁻² (57.5 W kg ⁻¹)	30% after 500 cycles (gel electrolyte), above 53% at 5000th cycle (aqueous electrolyte)	Electrode ≈78%–91% after stretched 1000 times, device capacitance enhanced to 160% at 5 mA cm ⁻²	[366]
Cotton knit fabric (2019)	PPy-coated fabric electrodes via chemical polymerization technique with 1 M sulfuric acid aqueous electrolyte	Electrode 5073 mF cm ⁻² at 1 mA cm ⁻² , device 1167.9 mF cm ⁻² at 1 mA cm ⁻² and 904.2 mF cm ⁻² at 20 mA cm ⁻²	102.4 μWh cm ⁻² at 0.39 mW cm ⁻²		90% capacitance after 2000 cycles		[368]
Nylon/lycra (80/20) knitted fabric (2012)	Synthesis of PPy by chemical polymerization on the fabric with 1.0 M NaCl electrolyte	123.3 F g ⁻¹ at a scan rate of 10 mV s ⁻¹	6.7 Wh kg ⁻¹	753.4 W kg ⁻¹		90% after being stretched to 100% for 1000 times	[377]
Polyester fabric (2018)	Repeated spray-coating of PEDOT:PSS solutions containing 5 wt-% dimethyl sulfoxide (DMSO)	75.30 F g ⁻¹ at the scan rate of 20 mVs ⁻¹					[378]
Polyester knitted fabric (2019)	In situ polymerization coating of PPy on fabric	1213 mF cm ⁻² at 1 mA cm ⁻²					[367]
Polyester fabric (2020)	Electrospun poly(3,4-ethylene dioxathiophene) polystyrene sulfonate (PEDOT: PSS) nanofibers were deposited onto flexible polyethylene terephthalate (PET) substrates to obtain electrodes with PVA/H ₃ PO ₄ gel polyelectrolyte	1.8 mF cm ⁻² and 3.6 F g ⁻¹ at 5 μA cm ⁻²	0.32 Whkg ⁻¹ at 5 μA cm ⁻²	11.8 Wkg ⁻¹	92% after 1000 cycles		[369]
Polyester fabric (2021)	Conductive polyester (PET) fabric electrode is prepared by in situ polymerizations of aniline and pyrrole.	Electrode 1046 mF cm ⁻² at 2 mA cm ⁻² (aniline to pyrrole is 0.75:0.25), Device 537 mFcm ⁻² , 1.13 F cm ⁻³ at 2 mA cm ⁻²	0.043 mWh cm ⁻³	0.005 Wcm ⁻³	54.2% after 1000 cycles.		[370]

(Continued)

Table 9. (Continued).

Substrate (Reporting year)	Device Configuration	Device capacitance	Energy density	Power density	Capacitance retention	Flexibility	Refs.
2D shaped Cotton/polyester (55/45) fabric (2020)	Dimethyl sulfoxide (DMSO)-doped PEDOT:PSS-coated cloth as an active electrode and sweat as an electrolyte	Artificial sweat (7.64 F g ⁻¹ in terms of weight and 8.45 mF cm ⁻² in terms of area at the low current density, 0.07 A g ⁻¹) and real human sweat (3.88 F g ⁻¹)	Artificial sweat 1.36 Wh kg ⁻¹ (1.63 μWh cm ⁻²). With real human sweat 0.25 Wh kg ⁻¹	Artificial sweat 329.70 W kg ⁻¹ (0.40 mW cm ⁻²). With real human sweat 30.62 W kg ⁻¹	75% after 4000 cycles, 45% after 5000 cycles		[149]
Polypropylene (PP) non-woven textile (2021)	Reactive inkjet printing to fabricate PPy layers on textile substrates with direct freezing of inks	72.3 F g ⁻¹ at 0.6 A g ⁻¹ at -12 °C	6.12 Wh kg ⁻¹	139 W kg ⁻¹	55.4% after 2000 cycles		[254]
Silk woven fabric (2019)	In situ polymerization coating of PPy on fabric	1349 mF cm ⁻² at 1 mA cm ⁻²					[367]
Wool gauze fabric (2019)	In situ polymerization coating of PPy on fabric	1007 mF cm ⁻² at 1 mA cm ⁻²					[367]
Fiberglass cloth (2020)	Conductive fiberglass cloth (CFC) derived from gas-phase polymerization of pyrrole, followed by electrochemical polymerization of a layer of PPy attached to the surface of the conductive fiberglass cloth. SC formed by sandwiching two PPy/CFC composites and a layer of PVA-H ₂ SO ₄ gel electrolyte	549.6 mF cm ⁻²	48.85 μWh cm ⁻²		92.4% after 10,000 cycles	96.08% after 1000 bending cycles	[379]
Carbon fabric (2010)	PEDOT nanofiber electrode, carbon cloths as the current collectors, and electrospun PAN nanofibrous membranes as the separator with ionic liquid electrolyte	20 Fg ⁻¹			90% after 10,000 cycles		[380]
CNT fiber woven textiles (2014)	Two PANI deposited CNT fiber textile stacked with PVA-H ₃ PO ₄ gel electrolyte	272.7 Fg ⁻¹ at 1 Ag ⁻¹			No decay after 2000 cycles	96.4% after 200 cycles bending at 150°	[381]

Table 10. Summary of Metal-based supercapacitors or supercapacitor electrodes.

Substrate (Reporting year)	Device Configuration	Device capacitance	Energy density	Power density	Capacitance retention	Flexibility	Refs.
1D shaped							
Kevlar fiber (2011)	Kevlar fibers and flexible plastic wire substrates for ZnO NW arrays, Plastic wire/ZnO, Kevlar/ZnO/Au electrodes with KNO ₃ and PVA-H ₃ PO ₄ electrolyte	0.21 mF cm ⁻² at 100 mV s ⁻¹ (aqueous) and 2.4 mF cm ⁻² and 0.2 mF cm ⁻¹ (gel electrolyte)	2.7 × 10 ⁻⁸ Wh cm ⁻² (gel)	1.4 × 10 ⁻⁵ Wcm ⁻² (gel)			[389]
Carbon nanotube (CNT) yarn (2014)	CNT CNT, CNT@MnO ₂ CNT, CNT@MnO ₂ CNT@MnO ₂ with aqueous electrolyte	Asymmetric SC CNT@MnO ₂ (positive) and CNT (negative) possess a capacitance of 12.5 F g ⁻¹ at a current density of 0.14 A g ⁻¹	1 to 2.12 Wh kg ⁻¹ (CNT CNT), For CNT@MnO ₂ CNT, up to 42.0 Wh kg ⁻¹ (low power density), and 28.02 Wh kg ⁻¹ (at high power density)	241.8 to 10 000 W kg ⁻¹ (CNT CNT), for CNT@MnO ₂ CNT, low power density of 483.7 W kg ⁻¹ , high power density of 19 250 W kg ⁻¹	For CNT@MnO ₂ CNT, 98% of its original capacitance after 500 cycles, in comparison with 99% for CNT CNT	For CNT@MnO ₂ CNT, specific capacitance suffered only 0.5% reduction after 200 cycles of folding and unfolding actions	[383]
Carbon nanotube (CNT) yarn (2015)	NiO and Co ₃ O ₄ deposited on spun CNT yarn, Two PVA-H ₂ SO ₄ coated CNT, CNT@NiO, and CNT@Co ₃ O ₄ yarns placed together and coated with electrolyte again	CNT@Co ₃ O ₄ yarn based SC 52.6 mF cm ⁻² at 0.053 mA cm ⁻² , 87.6 Ag ⁻¹ , CNT based SC 7.4 mF cm ⁻² , 13.4 Ag ⁻¹ , CNT@NiO based SC 15.2 mF cm ⁻² , 25.9 Ag ⁻¹	CNT@Co ₃ O ₄ yarn based SC 1.1 μWh cm ⁻²	CNT@Co ₃ O ₄ yarn based SC 0.01 mW cm ⁻²	Pure CNT, CNT@NiO, and CNT@Co ₃ O ₄ maintain 96%, 94%, and 91%, respectively, of original capacitance after 1000 cycles	No decrease after 100 cycles bending at 90° and 180°	[385]
Carbon nanofiber (CNF) (2015)	CNFs containing Co ₃ O ₄ nanoparticles electrodes with 6 M KOH	586 Fg ⁻¹ at 1 Ag ⁻¹					[384]
2D shaped							
Substrate (Reporting year)	Device Configuration	Device capacitance	Energy density	Power density	Capacitance retention	Flexibility	Refs.
Polyester (2020)	Ni nanoparticle in situ synthesized, two Ni-plated polyester electrodes with PVA/KOH gel electrolyte	450 mF cm ⁻² at 7.5 mA cm ⁻²					[386]
Silk fabric (2021)	Graphite coated Berlin (silver coated silk) as the negative electrode and Nora Dell (Ni/Cu/Ag coated) fabric as the positive electrode with biocompatible PVA-KCl gel electrolyte	32 mF cm ⁻² at 25 mV s ⁻¹ , 41 mF cm ⁻² at 0.75 mA cm ⁻²	2.8 μWh cm ⁻² at 25 mV s ⁻¹ , 3.6 μWh cm ⁻² at 0.75 mA cm ⁻²		45% retention after 1000 cycles		[390]
Carbon cloth (2013)	Hydrogenated single-crystal ZnO @ amorphous ZnO-doped MnO ₂ core-shell nanocables (HZM) on carbon cloth as SC electrodes using PVA/LiCl electrolyte	26 mFcm ⁻² (325 mF cm ⁻³) at a current density of 0.5 mA cm ⁻²	0.04 mWh cm ⁻³	2.44 mW cm ⁻³	87.5% after 10 000 charge/discharge cycles		[391]

(Continued)

Table 10. (Continued).

Substrate (Reporting year)	Device Configuration	Device capacitance	Energy density	Power density	Capacitance retention	Flexibility	Refs.
Carbon cloth (2015)	Electrochemically activated carbon cloth (EACC) as anode and TiN@MnO ₂ on CC as cathode with LiCl solution as electrolyte.	2.69 F cm ⁻³ at 6 mA cm ⁻²	1.5 mWh cm ⁻³	1.71 W cm ⁻³	No decay at 70 000 cycles		[338]
Carbon fabric (2016)	uniform large-area manganese oxide (MnO ₂) nanosheets on carbon fabric which oxidized using O ₂ plasma treatment (MnO ₂ /O ₂ -carbon fabric) via electrodeposition process with 1 M sodium sulfate (Na ₂ SO ₄) electrolyte	275 Fg ⁻¹ at a scan rate of 5 mVs ⁻¹			80% after 10 000 cycles.		[392]
Carbon cloth (2016)	In situ electrodeposition of MnO ₂ on carbon cloth with 1 M Na ₂ SO ₄ aqueous electrolyte	275 F g ⁻¹ at 0.2 A g ⁻¹					[393]
Carbon textile (2016)	Zinc sulfide (ZnS) nanospheres hydrothermally grown on flexible carbon textile (CT)	540 F g ⁻¹ (56.25 F cm ⁻²) at 5 mV s ⁻¹	51 W h kg ⁻¹ at a power density of 205 W kg ⁻¹		94.6% after 5000 cycles		[387]
Carbon fiber fabric (2017)	KOH activation of commercial CF threads followed by coated with PVA/ H ₃ PO ₄ electrolyte and woven to SC fabric	18.6 F g ⁻¹ at 2 mV s ⁻¹ , 300 mF cm ⁻² , 26 F cm ⁻³	2.58 mWh g ⁻¹ or 3.6 mWh cm ⁻³ , 42 μWh cm ⁻² , 3.6 mWh cm ⁻³		Over 80% after 10 000 at 20 mV s ⁻¹		[394]
Carbon fabric (2017)	Fabrication of Co ₃ O ₄ nanowires on a flexible carbon fabric electrode (CoNW/CF) with PVA-KOH gel electrolyte	Electrode 3290 F g ⁻¹ at a scan rate of 5 mV s ⁻¹	6.7 Wh kg ⁻¹	5 kW kg ⁻¹	95.3% after 5000 cycles		[388]
Carbon cloth (2018)	Anodic deposition of MnOx on Pd coated carbon cloth electrode with 0.5 M Na ₂ SO ₄	186 F g ⁻¹ at 1 mA cm ⁻²					[395]
Carbon fiber fabric (2020)	Viscose fiber woven fabrics carbonized and activated (ACVF), CeO ₂ , ZnO hydrothermally deposited, CeO ₂ -ACVF & ZnO-ACVF electrode, polyester separator, carbon cloth current collector with PVA/H ₃ PO ₄ electrolyte	13.24 mF cm ⁻² at 0.2 mVs ⁻¹	4.6×10 ⁻⁷ Whcm ⁻² at 3.3 1×10 ⁻⁶ Wcm ⁻²		87.6% at 5000 cycles	Increases by 13.4% after 200 bending cycles	[396]
Carbon fiber textile (2021)	Crystalline nano-flowers structured zinc oxide (ZnO) was directly grown on carbon fiber textile (CFT) substrate via hydrothermal process and fabricated with a binder-free electrode (denoted as ZnO@CFT) for SC	201 Fg ⁻¹ at 1 Ag ⁻¹			90.32% after 3000 cycles at 10 Ag ⁻¹		[397]

yarn SCs, 42.0 Whkg⁻¹ at a lower power density of 483.7 Wkg⁻¹, and 28.02 Whkg⁻¹ at a higher power density of 19,250 W kg⁻¹. Co₃O₄ was also studied by several research groups for enhancing capacitive performance. Abouali et al.^[384] employed a facile electrospinning method with subsequent heat treatments to prepare carbon nanofibers (CNFs) electrodes for SCs. The electrodes possessed a remarkable capacitance of 586 F g⁻¹ at a current density of 1 Ag⁻¹ with excellent cyclic stability of 74% upto 2000 cycles at 2 A g⁻¹. Su et al.^[385] in another study, further compared the electrochemical performance of CNT yarn electrodeposited with NiO along with Co₃O₄. The two-ply SCs formed from CNT@Co₃O₄ composite yarns displayed excellent electrochemical properties with high capacitance of 52.6 mF cm⁻² and energy density of 1.10 μWh cm⁻².

Among conventional textiles, polyester and silk were studied for 2D fabric-shaped SC. Shahidi et al.^[386] deposited Ni nanoparticles on polyester to prepare flexible electrodes for SC application. The device achieved a high areal capacitance of 450 mF cm⁻² at 7.5 mA cm⁻². Similar to 1D type, carbon fabrics were investigated mostly for the 2D fabric-shaped textile SC. Javed et al.^[387] hydrothermally grew zinc sulfide (ZnS) nanospheres on a flexible carbon textile. The flexible and lightweight electrode exhibited a higher capacitance of 747 F g⁻¹ at a scan rate of 5 mV s⁻¹ in the LiCl aqueous electrolyte. The SC device demonstrated specific capacitance of 540 F g⁻¹ and areal capacitance of 56.25 F cm⁻² with excellent cycling stability of 94.6% after 5000 cycles. The energy density was reported as high as 51 W h kg⁻¹ at a power density of 205 W kg⁻¹. However, the highest capacitance for the metal-based textile SC was achieved utilizing Co₃O₄. Howli et al.^[388] hydrothermally fabricated Co₃O₄ nanowires on carbon fabric substrate to form SC electrode. With PVA-KOH electrolyte the electrode exhibited gravimetric capacitance of 3290 F g⁻¹ at a scan rate of 5 mV s⁻¹ with high energy and power densities of 6.7 Wh kg⁻¹ and 5000 W kg⁻¹, respectively, and capacitance retention of 95.3% after 5000 cycles.

6.4. Other 2D Material-Based Textile Supercapacitor

Very recently several 2D materials are explored for the fabrication of SC electrodes. It is evident from the literature that carbon, and cotton textiles were mainly studied for 2D fabric-shaped SCs, **Table 11**. Uzun et al.^[398] coated cellulose yarns with Ti₃C₂T_x to produce conductive yarns. The yarn electrode exhibited linear, areal, and volumetric capacitance of ≈759.5 mF cm⁻¹, ≈3965.0 mF cm⁻², and ≈260.0 mF cm⁻³ respectively at 2 mV s⁻¹. With PVA-H₂SO₄ gel electrolyte, the SC device showed linear, areal, and volumetric capacitance of ≈306.9 mF cm⁻¹, ≈1865.3 mF cm⁻², and ≈142.4 mF cm⁻³ respectively. Levitt et al.^[307] coated cotton yarn with Ti₃C₂T_x (referred to as MXene), knitted the yarn 3D, and used 1 M H₃PO₄-PVA gel electrolyte for analyzing the structure performance as SC. The areal capacitance was reported at 519 mF cm⁻² at 2 mV s⁻¹. They further replaced the electrolyte with 1 M H₃PO₄ electrolyte and the capacitance increased up to 707 mF cm⁻² at 2 mV s⁻¹. The device showed >100% capacitance over 10 000 charge-discharge cycles and coulombic efficiency of ≈100%.

6.5. Hybrid Materials

The hybridization of the active materials from one or more subgroups (e.g., carbonaceous compounds, conductive polymers, metal-based, and other 2D materials) is one of the attractive routes to fabricate high-performance energy storage textiles, **Table 12**. Several research groups have focused on hybridizing carbonaceous compounds with conductive polymers or metal oxides to prepare 1D fiber or yarn-shaped SC. For example, several articles reported cotton fiber or yarn-based SC devices as hybrid active compounds. Liu et al.^[403] reported a fully cable-type SC composed of two PPy-MnO₂-CNT-cotton thread (CT) electrodes, separated by cotton textiles wrapped with 0.5 M Na₂SO₄ electrolyte in a transparent silicone pipeline package shell. The CTs were coated with SWCNT, followed by electrochemical deposition of MnO₂ nanostructures and PPy film. The resulting electrodes achieved a high areal capacitance of 1490 mF cm⁻² at a scan rate of 1 mVs⁻¹, which is one of the highest among cotton fiber-based SC electrodes. The device prepared from such electrode achieved an energy density of 33 μWh cm⁻² at a power density of 0.67 mWcm⁻². In another study,^[404] almost similar capacitive performances were obtained by Wang et al. with considerably higher energy and power densities. They modified cotton yarns with 2D metallic Ni conductive network and pseudocapacitive Co-Ni layered double hydroxide nanosheet array. The flexible yarn electrodes achieved a areal capacitance of 1260 mF cm⁻² (121 571.1 C cm⁻²) at a scan rate of 5 mV s⁻¹. The SC device was prepared by twisting two as-made yarn together, and then painted with PVA/KOH gel electrolyte, which provided an areal capacitance of 221 mFcm⁻² (21 323.2 C cm⁻²) at 0.04 mA cm⁻². The energy and power densities were reported as 9.3 mWh cm⁻² and 43.99 mW cm⁻², respectively.

The pseudocapacitive properties of PEDOT:PSS in combination with PPy were utilized to obtain a cotton fiber-based 1D SC device. Ma et al.^[405] blended short-staple length SSFs with cotton fibers to spin SSF/cotton blended yarn. PPy was deposited on PEDOT:PSS coated composite yarn, followed by a coating with PVA/H₃PO₄ electrolyte. Two pieces of yarns were placed in parallel and twisted together to produce a solid-state two-ply nanocomposite yarn SC. The cotton-based SC device exhibited maximum areal capacitance of 1360 mF cm⁻² at 0.16 mWh cm⁻² energy density. In another study, Yang et al.^[406] reported one of the highest gravimetric capacitances (≈506.6 F g⁻¹ at 1 A g⁻¹) on cotton-based 1D SC electrode, where PPy and MXene composite was grown on cotton fiber to prepare fiber-based electrodes. Li et al.^[407] obtained the highest volumetric capacitance of 221.9 F cm⁻³ at a current of 50 mA, by modifying GO nanosheets (NSs) with ultrathin and large area MoS₂ NSs followed by reduction and using PVA-H₃PO₄ electrolyte to produce all-solid-state hybrid fiber shaped SC. Such composite devices also retained 100% capacitance even after bending at 30 and 60 degrees.

Unlike cotton fiber or yarn-based SCs, only a very few reports are available on hybridizing carbonaceous compounds with conductive polymers or metal oxides for producing 1D fiber or yarn-shaped SCs based on synthetic textiles including polyester,^[408] polyaniline,^[409] nylon,^[232] and some elastic^[229,230,410] fibers. For example, Zhang et al.^[411] reported a high specific capacitance of 278.6 mF cm⁻² for stretchable textiles (CNTF). The process

Table 11. Summary of other 2d material-based supercapacitors or supercapacitor electrodes.

1D shaped	Substrate (Reporting year)	Device Configuration	Device capacitance	Energy density	Power density	Capacitance retention	Flexibility	Refs.
	Cotton yarn (2019)	Coating cellulose yarns with $Ti_3C_2T_x$ MXene with 1 M H ₂ SO ₄ electrolyte	Electrode $\approx 759.5 \text{ mF cm}^{-1}$, $\approx 3965.0 \text{ mF cm}^{-2}$ and $\approx 260.0 \text{ mF cm}^{-3}$ at 2 mV s^{-1} . Device $\approx 306.9 \text{ mF cm}^{-1}$, $\approx 1865.3 \text{ mF cm}^{-2}$, $\approx 142.4 \text{ mF cm}^{-3}$ at 2 mV s^{-1})			$\approx 100\%$ after 10 000 cycles		[398]
2D shaped	Substrate (Reporting year)	Device Configuration	Device capacitance	Energy density	Power density	Capacitance retention	Flexibility	Refs.
	Cotton fabric (2018)	Dipping and drying of cotton into MXene ($Ti_3C_2T_x$) nanosheets	182.70 F g ⁻¹					[399]
	Cotton fabric (2020)	3D knitted cotton yarn coated with $Ti_3C_2T_x$ (referred as MXene) and 1 M H ₃ PO ₄ /PVA gel electrolyte	519 mF cm ⁻² at 2 mV s ⁻¹ , (707 mF cm ⁻² at 2 mV s ⁻¹ with 1 M H ₃ PO ₄ electrolyte)	25.4 $\mu\text{Wh cm}^{-2}$	0.47 mWcm ⁻²	> 100% over 10 000 cycles		[307]
	Carbon cloth (2018)	Hydrothermal growth of molybdenum disulfide (MoS ₂) nanosheets on carbon fabrics, with Lithium metal counter electrode, and a 1.0 M LiPF ₆ solution with mixture of ethylene carbonate and dimethyl carbonate (EC/DMC, 1:1 in volume) electrolyte	159.38 mF cm ⁻² at 0.5 mA cm ⁻²			80.6% after 15 000 cycles		[400]
	Carbon fabric (2018)	Stacking the RuO ₂ coated carbon fabric (CF) as positive and $Ti_3C_2T_x$ coated CF as negative electrode with 1 M H ₂ SO ₄ electrolyte	Electrode 416 mF cm ⁻² , 200 F g ⁻¹	Device 37 $\mu\text{Wh cm}^{-2}$ at a power density of 40 mW cm ⁻²		86% after 20 000 cycles		[401]
	Carbon cloth (2021)	Hierarchical flower-like Mn ₃ O ₄ @N, P-doped carbon (NPC) composite cathode with an electrochemically reduced porous carbon (PC) anode and a PVA-Na ₂ SO ₄ hydrogel electrolyte	81.97 Fg ⁻¹ at 1 A g ⁻¹	76.96 Wh kg ⁻¹	26.02 kW kg ⁻¹ at 32.65 Wh kg ⁻¹	92.71% after 10 000 cycles		[402]
	Carbon cloth (2021)	MoS ₂ drop cast on functionalized carbon cloth; MoS ₂ /FCC electrodes soaked with 1 M H ₂ SO ₄ electrolyte	56.525 F g ⁻¹ at 0.2 A g ⁻¹			29% after 1000 cycles		[371]

Table 12. Summary of Hybrid material-based supercapacitors or supercapacitor electrodes.

Substrate (Reporting year)	Device Configuration	Device capacitance	Energy density	Power density	Capacitance retention	Flexibility	Refs.
1D shaped							
Cotton thread (2013)	Two PPy-MnO ₂ -CNT-cotton thread electrodes, separated with cotton textile wrapping with 0.5 M Na ₂ SO ₄ electrolyte, transparent silicone pipeline as a package shell, and a fully cable-type SC	1.49 Fcm ⁻² at scan rate 1 mVs ⁻¹ (electrode)	33 μWhcm ⁻² at power density 0.67 mWcm ⁻²	13 mWcm ⁻² at an energy density of 14.7 μWhcm ⁻²	87% after 2000 cycles		[403]
Cellulose yarns (cotton, linen, bamboo, viscose) (2015)	Yarns welded with activated carbon and twisting with stainless steel yarn	120 F g ⁻¹ , 37 mF cm ⁻¹ at 2 mV s ⁻¹			77% after 3000 cycles	Some decay at 180° bent, curled, and crumpled	[428]
Cotton yarn (2015)	Electroless deposition of Ni and electrochemical deposition of graphene on commercial cotton yarns (RGO/Ni cotton composite electrodes) with PVA/LiCl gel, as electrolyte and separator	0.11 F cm ⁻¹	6.1 mWh cm ⁻³	1400 mW cm ⁻³	82% after 10 000 cycles	No decrease at 45°, 90°, and 180° bending, 95% after 4000 cycles at 180°	[429]
Cotton thread (2016)	Twisting 2 strands of PVA-H ₃ PO ₄ gel electrolyte coated carbon nanoparticles /rGO-cotton thread (CNPs/rGO-CT) together	3.79 mF cm ⁻³ at 50 mVs ⁻¹	0.084 μWhcm ⁻³ (with 35.3 μWcm ⁻³), Varies from 0.084 μWhcm ⁻³ to 0.047 μWhcm ⁻³ (in the power density range of 35.3 μWcm ⁻³ to 56.4 μWcm ⁻³)		95.23% after 10 000 cycles	92.30% after 2000 bending cycles	[430]
Cotton thread (2016)	Twisting 2 strands of PVA-H ₃ PO ₄ gel electrolyte coated graphene hydrogels/multi-walled carbon nanotubes-cotton thread (GHs/MWCNTs-CT)	9.7.73 μFcm ⁻¹ at a scan rate of 2 mV s ⁻¹	4.79 × 10 ⁻³ mWh cm ⁻¹ (with power density 0.75 mWcm ⁻¹)	1.25 mWcm ⁻¹ (with energy density 3.06 × 10 ⁻³ mWh cm ⁻¹)	95.51% after 8000 cycles	90.75% after 500 continuous bending cycles	[430]
Cotton thread (2018)	Two cotton/Ni/Co-Ni layered double hydroxide (CT/Ni/Co-Ni LDH) hybrid yarn electrodes twisted together and painted with PVA/KOH gel electrolyte	Electrode material 1.26 Fcm ⁻² (121 571.1 C cm ⁻²) at a scan rate of 5 mV s ⁻¹ , SC 221 mFcm ⁻² (21 323.2 C cm ⁻²) at 0.04 mA cm ⁻²	9.3 mWh cm ⁻²	43.99 mW cm ⁻²	79% after 2000 cycles		[404]
Cotton yarn (2018)	Cotton electrode by dip-dried in MWCNT followed by interfacial polymerization of PPy, two parallel electrodes embedded in a thin layer of PVA/H ₃ PO ₄ layer	30 F g ⁻¹	2.63 mWh g ⁻¹	11.33 mW g ⁻¹			[431]

(Continued)

Table 12. (Continued).

1D shaped	Substrate (Reporting year)	Device Configuration	Device capacitance	Energy density	Power density	Capacitance retention	Flexibility	Refs.
	Cotton fibers (2018)	Short-staple length stainless steel fibers (SSFs) blended with cotton fibers to spin SSF/cotton blended yarn, PPy deposited on PEDOT:PSS coated composite yarn, followed by coating with PVA/H ₃ PO ₄ electrolyte, placed in parallel and twisted together, followed by coating again to produce a solid-state two-ply nanocomposite yarn SC.	1.36 F cm ⁻²	0.16 mWh cm ⁻²		80% over 5000 cycles		[405]
	Cotton (2019)	GO nanosheets (NSs) are modified with ultrathin and large area MoS ₂ NSs followed by reduction with PVA-H ₃ PO ₄ electrolyte to produce all-solid-state hybrid fiber shaped SC (ASFS). 3 symmetrically assembled tandem and parallel ASFS groups in cotton textile (ASFSs-T) fabricated	134.38 F g ⁻¹ , 332.85 mF cm ⁻² , and 221.9 F cm ⁻³ at a current of 50 mA				100% when bent by 30 and 60 degrees	[407]
	Cotton fiber (2021)	In situ growth of PPy and MXene composite, on cotton fiber to prepare fiber electrode	506.6 F g ⁻¹ , at 1 A g ⁻¹ and 455.9 mF cm ⁻² at 0.9 mA cm ⁻²			83.3% after 2000 cycles		[406]
	Polyester fiber (2018)	PPy electrochemically deposited on rGO painted SnCl ₂ modified polyester yarn electrode with PVA/H ₂ SO ₄ gel electrolyte for SC	Electrode 175.7 mF cm ⁻¹ , 699.6 mF cm ⁻² , 239.6 F g ⁻¹ , 35.0 Fcm ⁻³ at 0.13 mA cm ⁻¹ , Device 85.3 mFcm ⁻¹ , 339.7 mF cm ⁻² , 116.4 Fg ⁻¹ , 17.0 F cm ⁻³	0.0472 mWhcm ⁻²	26.5 mWcm ⁻²		Almost original electrochemical performance after 1000 bending cycles	[408]
	Polyaniline fiber (2013)	Two polyaniline composite fibers incorporated with aligned multi-walled carbon nanotubes (MWCNTs/PANI) twisted	274 Fg ⁻¹ , 263 mF cm ⁻¹ at 2 A g ⁻¹			99% after 1000 cycles	>97% after 50 bending cycles	[409]
	Nylon fiber (2015)	Carbon multiwalled nanotube (MWNT) helically wrapped around nylon fibers, followed by electrochemical deposition of MnO ₂ . Two coiled MnO ₂ /CNT/nylon fiber electrodes placed parallel and coated with PVA-LiCl gel electrolyte	5.4 mF cm ⁻¹ , 40.9 mF cm ⁻² , 3.8 Fcm ⁻³ at 10 mVs ⁻¹	2.6 μWh cm ⁻²	66.9 μW cm ⁻²		90.8% at 12% strain, 50% during large strain	[232]
	Elastic fiber (2014)	Elastic fiber/CNTs/PANI	255.5 Fg ⁻¹ , 0.19 mF cm ⁻¹ at 1 A g ⁻¹	12.75 Wh kg ⁻¹	1494 W kg ⁻¹	69% after 10 000 cycles	93.8% after 1000 cycles bending at 180°	[229]

(Continued)

Table 12. (Continued).

1D shaped	Substrate (Reporting year)	Device Configuration	Device capacitance	Energy density	Power density	Capacitance retention	Flexibility	Refs.
Shape-memory polyurethane (SMP) substrate (2015)	By wrapping aligned carbon nanotube (CNT) sheets onto a shape-memory polyurethane (SMP) substrate as electrode, coated with PVA gel electrolyte followed by winding another layer of aligned CNTs as the outer electrode	24 Fg ⁻¹ , 0.269 mF cm ⁻¹ and 42.3 mFcm ⁻³				No loss after 12 000 cycles	No obvious decrease after 500 cycles of deformation	[230]
Urethane stretchable yarn (2016)	CNTs dipping and PPy electrodeposition on urethane elastic fiber core spun yarns (UY)	69 mF cm ⁻²					Nearly unchanged at a strain of 80%.	[410]
Stretchable substrate (2017)	Electrochemical activation of pristine carbon nanotube fibers (CNTF), coating of PEDOT:PSS followed by electrochemical deposition of MnO ₂ to form MnO ₂ @PEDOT:PSS@OCNTF positive electrode and hydrothermal synthesis of MoS ₂ to form MoS ₂ @CNTF negative electrode with LiCl-PVA gel electrolyte placed on a stretchable substrate	278.6 mF cm ⁻²	125.37 μWh cm ⁻² at 540 μWcm ⁻²				92% after stretching at a strain of 100% for 3000 cycles.	[411]
Carbon nanotube (CNT) yarn (2013)	PANI nanowire arrays in situ deposited on CNT yarn, PVA gel coated on CNT yarn, or CNT/PANI yarn. Two CNT yarns or composite yarns twisted together	At 0.01 mA cm ⁻² CNT/PANI yarn based SC 38 mFcm ⁻² , pure CNT yarn-based SC 2.3 mFcm ⁻² . CNT/PANI yarn 12 mFcm ⁻² at 1 mAcm ⁻²				91% after 800 cycles	No decrease at 45°, 90°, 135°, 180° bending	[432]
Carbon nanotube (CNT) yarn (2014)	Electrochemical deposition of MnO ₂ onto CNT yarn, Two PVA-KOH coated CNT/MnO ₂ composite yarns placed on top of each other, and finally coated by PVA-KOH again.	25.4 F cm ⁻³ at 10 mV s ⁻¹	3.52 mWh cm ⁻³	127 mW cm ⁻³			No decrease after 1000 bending at 90°	[433]
Carbon nanotube CNT fiber (2017)	MnO nanosheets in situ grown on CNT fiber (positive), polyimide deposited on CNT fiber (negative electrode)		36.4 μWh cm ⁻² (At 0.78 mW cm ⁻²)	15.6 mW cm ⁻² at 30.2 μWh cm ⁻²		Well upto 2000 cycles	Specific capacitances remained almost unchanged at bending to various degrees (0–180)	[434]
Carbon nanotube (CNT) yarn (2017)	Twisting a number of CNT yarns (n) with Pt filament as current collector, PANI nanowires further deposited in situ to form the final Pt/n-CNT @ PANI with alkaline electrolyte	Pt/5-CNT@PANI FSSC 217.7 Fg ⁻¹ , 48.27 mFcm ⁻³ at current density 0.2 Ag ⁻¹	30.22 Wh kg ⁻¹ at 91.88 W kg ⁻¹ , 19.31 Wh kg ⁻¹ at 9072.88 W kg ⁻¹			Negligible changes after 5000 cycles	Capacitance retention was 98.17% after 3000 cycles and 95.91% after 5000 flexing cycles	[435]

(Continued)

Table 12. (Continued).

Substrate (Reporting year)	Device Configuration	Device capacitance	Energy density	Power density	Capacitance retention	Flexibility	Refs.
1D shaped Carbon nanotube (CNT) fiber (2021)	Coating electroactive molybdenum disulfide (MoS ₂) nanoflakes on a CNT fiber backbone with rGO as the adhesion layer.	190.4 F g ⁻¹ , 93.2 mFcm ⁻²	26.4 Wh Kg ⁻¹	4000 Wkg ⁻¹	85% after 5000 cycles	No performance decay observed after 1000 cyclic bending	[436]
Carbon nanotube (CNT) and Polyaniiline Nanowire (PANINW) composite yarn (2014)	Spun yarn composed of SWCNTs and PANINWs, coated with PVA/H ₂ SO ₄ gel electrolyte and twisted together	2.67 mF cm ⁻² at 0.6 A g ⁻¹	0.8 μWh cm ⁻²	150 μW cm ⁻²	86% after 800 cycles	No decrease at 45°, 90°, 135°, 180° bending	[437]
Carbon nanotube (CNT) /MXene yarn (2018)	Yarn electrodes by bisrolling MXene with CNTs, freestanding asymmetric yarn SC prototypes by pairing with bisrolled RuO ₂ yarns with 3.0 M H ₂ SO ₄ electrolyte	3 188 mF cm ⁻² , 1083 F cm ⁻³ , 523 F g ⁻¹ at a current density of 2 mA cm ⁻²	61.6 mWh cm ⁻³ (168 μWh cm ⁻² and 8.4 μWh cm ⁻¹)	5428 mW cm ⁻³ (14.8 mW cm ⁻² and 741 μW cm ⁻¹)	≈90% @10 000th cycle		[412]
Graphene fiber (2013)	2 intertwined hierarchical hybrid core-sheath fiber electrode [a core of graphene fiber (GF) covered with a sheath of 3D porous network-like graphene framework, denoted as GF@3D-G], solidified in the H ₂ SO ₄ -PVA gel electrolyte.	1.7 mF cm ⁻² , 25–40 F g ⁻¹ , 20 μF cm ⁻¹ at 17 μA cm ⁻²	0.4–1.7 × 10 ⁻⁷ Wh cm ⁻²	6–100 × 10 ⁻⁶ W cm ⁻²	Almost similar after 500 cycles	No decrease after bending 500 cycles	[438]
Graphene/PPy composite fiber (2014)	Intertwining two C/PPy electrodes pre-coated with H ₂ SO ₄ -PVA gel polyelectrolyte	107 mF cm ⁻² at 0.24 mA cm ⁻²	9.7 μWh cm ⁻²			No decrease after 1000 bending cycles	[439]
GO/MXene (≈88 wt.%) fiber (2017)	Wet spinning of GO liquid crystal-assisted MXene fiber with 1 M H ₂ SO ₄ electrolyte	233 mF cm ⁻² , 257 F g ⁻¹ , 34.1 F cm ⁻³					[440]
rGO/MXene hybrid fiber (2020)	Electrolyte Mediated hybrid fiber made of rGO and MXene, assembled into fibers via wet spinning with PVA/H ₂ SO ₄ electrolyte	550.96 mF cm ⁻² and 110.89 F g ⁻¹ at 20 mV s ⁻¹ ,	12 μWh cm ⁻² and 9.85 mWh cm ⁻³ at 8.8 mW cm ⁻² and 7.1 W cm ⁻³		85% @ 10 000 cycle		[413]
rGO/10 wt.% MoS ₂ composite fiber (2021)	Wet spun rGO/10 wt.% MoS ₂ composite fiber with PVA- H ₂ SO ₄ electrolyte	185.3 mF cm ⁻²	3.38 mW h cm ⁻³ and 0.0936 W cm ⁻³				[441]
rGO/20 wt.% MoS ₂ composite fiber (2021)	Wet spun rGO/20 wt.% MoS ₂ composite fiber with PVA- H ₂ SO ₄ electrolyte	282.6 mF cm ⁻²	4.92 mW h cm ⁻³ and 0.051 W cm ⁻³				[441]

(Continued)

Table 12. (Continued).

1D shaped	Substrate (Reporting year)	Device Configuration	Device capacitance	Energy density	Power density	Capacitance retention	Flexibility	Refs.
	MXene (70%) /PEDOT:PSS hybrid fiber (2019)	Wet spun fibers using hybrid formulations of $\text{Ti}_3\text{C}_2\text{T}_x$ MXene nanosheets and PEDOT:PSS with $\text{PVA}/\text{H}_2\text{SO}_4$ electrolyte	Electrode 676 mF cm^{-2} , 258 F g^{-1} , 615 F cm^{-3}	$\approx 7.13 \text{ Wh cm}^{-3}$	$\approx 8249 \text{ mW cm}^{-3}$	$\approx 95\%$ after 10 000 cycle	96% when cyclically stretched to 100% strain	[414]
	Carbon fiber tow (CFT) (2015)	Activation of pristine CFTs by oxidative exfoliation by $\text{KMnO}_4/\text{H}_2\text{SO}_4$, annealing in air, and reduction by a mixture of hydrogen iodide (HI) and acetic acid (AcOH). Twisting two activated electrodes together after coating with $\text{PVA}/\text{H}_3\text{PO}_4$ gel electrolyte	2.55 F cm^{-3} at 10 mV s^{-1}	0.35 mWh cm^{-3}	3000 mW cm^{-3}	91% after 10 000 cycles	No decrease after 1000 bending at 90° , 135° knotting	[442]
	Carbon fiber (2015)	A manganese oxide nanosheet grown on carbon nanoparticle coated carbon fiber (CF@CNP) and functionalized CF@CNPs are employed as the positive and negative electrodes respectively with LiCl-PVA solid-state electrolyte	5 F cm^{-3} at 2 mA cm^{-3}	2.1 mWh cm^{-3}	10.22 W cm^{-3}	81.2% after 10 000 cycles	No decrease after bending at 180° , 360° .	[443]
	Carbon fiber (2013)	PPy deposition on MnO_2 nanoflakes coated carbon fiber (CF/ MnO_2 /PPy) hybrid structure. Two PPy- MnO_2 -CFs were fixed on a preservative film substrate and assembled into a SC by sandwiching $\text{PVA}/\text{H}_3\text{PO}_4$ membrane as separator and electrolyte between electrodes	69.3 F cm^{-3} at 0.1 A cm^{-3}	6.16 mWh cm^{-3}	0.04 W cm^{-3}	86.7% after 1000 cycles	99.8% after rolling up	[415]
	Carbon fiber (2016)	Carbon fiber bundle @ CNT-NiCo(OH)x (CF@CNC) as positive and carbon fiber bundle @ activated carbon (CF@AC) as negative electrode, both immersed in PVA-KOH gel electrolyte & dried, twisted together	111 mF cm^{-2} (64.0 mF cm^{-1})	$33.0 \mu\text{Wh cm}^{-2}$, 0.84 mWh cm^{-3}	0.75 mW cm^{-2} , 19.1 mW cm^{-3}	103% after 8000 cycles	20% decay after 1000 bending times and 107% retention after 1000 twisting times	[444]
	Carbon fiber (2017)	Braided carbon fiber electrodes coated with $\text{MWN}/\text{V}_2\text{O}_5$ nanowires (NWS), a cellulose-based separator, and an ionic-liquid based electrolyte of [EMIM][TFSI]/LiCl/ Al_2O_3 nanoparticles	10.6 mF cm^{-2} at 0.5 mA cm^{-2}			Almost 100% after > 10 000 cycles	98.7% after 1000 bending cycles	[445]

(Continued)

Table 12. (Continued).

1D shaped	Substrate (Reporting year)	Device Configuration	Device capacitance	Energy density	Power density	Capacitance retention	Flexibility	Refs.
Carbon fiber yarn (CFY) (2018)	Sheath-core polyaniline nanowire array grown on aligned carbon nanofibers/ carbon fiber yarn electrode (CFY@CNFs@PANI NWA). Two fiber-shaped electrodes parallelly placed on PET substrate and immersed in PVA/H ₂ SO ₄ gel electrolyte		234 mF cm ⁻² at a current density of 0.1 mA cm ⁻²	21.4 μWh cm ⁻²	at 0.52 mW cm ⁻²	90% after 8000 cycles		[444]
Carbon fiber (2019)	Dip-coating of mixture of ionic liquid 1-ethyl-3-methylimidazolium bis(trifluoromethylsulfonyl) imide ([EMIM][TFSI]), carbon nanotubes, and electro-polymerization of PPy onto Au coated carbon fiber with propylene carbonate-poly(methyl methacrylate)-[EMIM][TFSI] gel electrolyte to form wire-type SC		38.49 mF cm ⁻² at 0.6 mAcm ⁻²	24.7 μWh cm ⁻²	3.52 mW cm ⁻²		99% after 100 bending cycles, 95.6% capacitance retention at 60 min in water	[447]
Carbon fiber (2020)	PEDOT:PSS- rGO drop coating and MnO ₂ electrodeposition on carbon fiber, MnO ₂ /PEDOT:PSS-rGO, and PEDOT:PSS-rGO as positive and negative electrodes with Na ₂ SO ₄ -CMC solid-state electrolyte		Electrode 2.92 F cm ⁻² (194 F cm ⁻³ , 550 mF cm ⁻¹) at 5 mA cm ⁻²	295 μWh cm ⁻² (19 mWh cm ⁻³ , 55 μWh cm ⁻¹)	2900 μWcm ⁻² (190 mW cm ⁻³ , 545 μWcm ⁻¹)	96% after 5000 cycles		[416]
Platinum wire (2013)	PEDOT/MWNT bisrolled yarn with Pt wire with liquid electrolyte (H ₂ SO ₄) or, with 1 M H ₂ SO ₄ /PVA gel electrolyte.		At 0.01 Vs ⁻¹ , ≈167 F cm ⁻³ (liquid electrolyte), ≈180 F cm ⁻³ (solid). At 1 V s ⁻¹ ≈147 F cm ⁻³ (liquid) and ≈145 F cm ⁻³ (solid). At 10 V s ⁻¹ , 13 F cm ⁻³ (liquid) and 10 F cm ⁻³ (solid)	1.4 mWh cm ⁻³ (Solid)	40 W cm ⁻³ (Solid)	98% after 2000 cycles	98% after 2000 bending, 92% after 10 000 winding, 99% after 10 000 cycles woven into gloves	[448]
Platinum yarn (2014)	PANI nanowire solution coated on CNT wrapped Pt yarns (Pt wire/CNTs/PANI) with PVA-H ₃ PO ₄ electrolyte		86.2 Fg ⁻¹ , 0.24 mF cm ⁻¹ , 52.5 mF cm ⁻² at 5 mVs ⁻¹	35.27 Wh kg ⁻¹	10.69 kW kg ⁻¹		No decrease after folding/unfolding 1000 cycles	[80]

(Continued)

Table 12. (Continued).

Substrate (Reporting year)	Device Configuration	Device capacitance	Energy density	Power density	Capacitance retention	Flexibility	Refs.
Au wire (2018)	Two wire electrodes prepared by layer-by-layer (LBL) assembly of multiwalled carbon nanotubes (MWCNTs), vanadium oxide (VO _x), wetted with organic electrolyte of propylene carbonate (PC)–acetonitrile (ACN)–lithium perchlorate (LiClO ₄)–poly(methyl methacrylate) (PMMA) and twisted together	5.23 mF cm ⁻² at 0.2 mA cm ⁻²	1.86 μWhcm ⁻²	8.5 mW cm ⁻²	94% after 10 000 cycles		[417]
Stainless steel yarn (2015)	Two PPy-wrapped Fe ₃ O ₄ deposited SS magnetic electrodes coated with PVA-H ₃ PO ₄ gel electrolyte, dried, twisted, and coated with PU	61.4 mF cm ⁻² at 10 mV s ⁻¹			77% after 1000 cycles	Self-healing 71.8% at 4 breakings & reconnecting	[299]
Stainless steel fiber yarn (2015)	PPy@MnO ₂ @rGO-deposited conductive yarns as both active materials and current collectors, two parallel yarn electrodes were coated with PVA/H ₃ PO ₄ electrolyte	36.6 mF cm ⁻¹ & 486 mF cm ⁻² in aqueous Na ₂ SO ₄ electrolyte (3-electrode cell) or 31 mF cm ⁻¹ and 411 mF cm ⁻² in PVA / H ₃ PO ₄ (2-electrode cell)	SS SC 0.0092 mWh cm ⁻² & 1.1 mWh cm ⁻³	1.33 mW cm ⁻² , 160 mW cm ⁻³	SS SC 92% over 4950 cycles	80% after 1000 cycles at 90 bending, 91% after 1000 cycles knotting, 103% after 1000 cycles twisting	[418]
Stainless steel spring (SSS) (2018)	In situ synthesis of hierarchical carbon tubular nanostructures (hCTNs) and conducting polyamine (PANI) composites onto SSS substrate to form stretchable SC electrode	277.8 F g ⁻¹ at 1 A g ⁻¹ , and 402.8 mF cm ⁻¹ at 1 mA cm ⁻¹			75% over 3000 cycles	100% stretchable	[449]
Stainless steel filament (2020)	Core-sheath single yarn was produced by PVA-H ₂ SO ₄ electrolyte-mediated rGO & MXene fibers twisted around the SS filament core. Two-ply yarns made from plying of two single core-sheath yarns. Two yarn electrodes plied to obtain the ultimate YSCs.	Dual-core YSC 253.01 mF cm ⁻² (43.6 mF cm ⁻¹ at 20 mV s ⁻¹)	27.1 μWh cm ⁻² at a power density of 2502.6 μW cm ⁻²	2502.6 μWcm ⁻² at 27.1 μWh cm ⁻² , 510.9 μWcm ⁻¹ 5.5 μWh cm ⁻¹	18% deterioration after 10 000 cycles	90% after 1000 bending cycles	[450]

(Continued)

Table 12. (Continued).

1D shaped	Substrate (Reporting year)	Device Configuration	Device capacitance	Energy density	Power density	Capacitance retention	Flexibility	Refs.
Stainless steel filament (2020)	Hydrothermal deposition of nickel-cobalt oxide on stainless steel cables, stainless steel cables @nickel-cobalt oxide electrode	113×10^{-3} mAh cm ⁻¹ at 0.3 mA cm ⁻¹ , 449×10^{-3} mAh cm ⁻² at 1.2 mA cm ⁻² , 69 mAh cm ⁻³ at 1.0 A cm ⁻³ and linear density capacitance with 433×10^{-3} mAh N ⁻¹ and 0.22×10^{-3} mAh Tex ⁻¹ at 0.6 mA.						[451]
2D shaped	Substrate (Reporting year)	Device Configuration	Device capacitance	Energy density	Power density	Capacitance retention	Flexibility	Refs.
Cotton fabric (2010)	Deposition of MnO ₂ after dipping and drying of cotton with single-walled carbon nanotube (SWNT) ink electrodes with 2 M aqueous Li ₂ SO ₄ electrolyte to form fabric SC	0.41 F cm ⁻²				Negligible change over 35 000 cycles		[223]
Non-woven cloth (2011)	Dip coating of nonwoven wiper cloth in the SWCNT ink followed by deposition of PANI nanowire arrays to obtain the PANI/SWCNT/ cloth composite electrode,	390 F g ⁻¹ at 1 A g ⁻¹	26.6 Wh kg ⁻¹	7000 W kg ⁻¹	90% after 3000 cycles	No decrease at 90° bending		[452]
Cotton t-shirt (2012)	MnO ₂ / ACT (activated carbon textiles from cotton t-shirt) as positive, ACT as negative electrode, copper foil as current collectors, and Whatman filter paper soaked with 1 M Na ₂ SO ₄ aqueous solution as the separator	120 F g ⁻¹ at 1 mA cm ⁻²	66.7 Wh kg ⁻¹	4.97 kW kg ⁻¹	97.5% after 1000 cycles			[453]
Cotton stretchable knitted fabric (90% cotton/10% Lycra) (2013)	Electrochemical deposition of polypyrrole on pre-strained Au coated cotton fabric with 1.0 M NaCl	255 F g ⁻¹ at 10 mV s ⁻¹					Sustain up to 140% strain without electric failure	[454]
Cotton (2015)	Electrodes prepared by dip coating cotton on GO dispersion, thermal reduction, and polypyrrole deposition. SC device with 2.0 M NaCl aqueous solution electrolyte.	336 F g ⁻¹	21.1 Wh kg ⁻¹ at 0.6 mA cm ⁻²					[455]

(Continued)

Table 12. (Continued).

Substrate (Reporting year)	Device Configuration	Device capacitance	Energy density	Power density	Capacitance retention	Flexibility	Refs.
2D shaped							
Cotton (2015)	PPy-coated cotton fabric electrode through in situ chemical polymerization by using CuO nanoparticles as template, with 2.0 M NaCl aqueous solution	225 F g ⁻¹ at 0.6 mA cm ⁻²			92% after 200 cycles		[456]
Cotton fabric (2015)	PPy-conductive polymer coated on top of MnO ₂ nanoparticles deposited- CNT textile with PEO/Na ₂ SO ₄ -based gel-type electrolyte	461 F g ⁻¹	31.1 Wh kg ⁻¹	22.1 kW kg ⁻¹	93.8% over 10 000 cycles	98.5% upon 2.1% tensile strain, no capacity change upon 13% bending strain. 96.3% after imposing cyclic bending of 750 000 cycles	[457]
Cotton fabric (2015)	Binder-free ternary composites of manganese oxide (MnO ₂) nanoparticles, SWNT, and conductive polymer PANI and (PEDOT:PSS) deposited layer-by-layer by dip coating to prepare cotton electrode with gel electrolyte composed of Acetonitrile (ACN): propylene carbonate (PC): polymethyl methacrylate (PMMA): tetra-butylammonium hexafluorophosphate (TBAPF6) in a ratio of 70:20:7:3 by weight	MnO ₂ /SWNT/PANI: 294 Fg ⁻¹ MnO ₂ /SWNT/PEDOT:PSS ternary composite devices: 246 Fg ⁻¹	MnO ₂ /SWNT/PANI: 66.4 Whkg ⁻¹ MnO ₂ /SWNT/PEDOT:PSS ternary composite devices: 60.2 Whkg ⁻¹	MnO ₂ /SWNT/PANI: 746.5 Whkg ⁻¹ MnO ₂ /SWNT/PEDOT:PSS ternary composite devices: 640.5 Whkg ⁻¹		<3%, down to a bending angle of 180°	[458]
Cotton fabric (2016)	Direct electrospinning of MWCNTs on nickel-coated cotton fabrics (Ni-cotton)	973.5 mF cm ⁻² at 2.5 mA cm ⁻²			No decay after 3000 cycles		[419]
Cotton fabric (2017)	CNT/CO-coated fabric as the negative electrode and PPy-coated fabric as the positive electrode	570 mF cm ⁻² at 1 mA cm ⁻²	0.26 mWh cm ⁻²		91% after 1000 cycles	Excellent stability under bending 100 times with an angle of 180°.	[459]
Cotton fabric (2018)	PPy electrochemically deposited on the surface of dip-dried cotton into MXene (Ti ₃ C ₂ T _x) nanosheets with H ₂ SO ₄ /PVA solid electrolyte	Electrode (with 1 M H ₂ SO ₄ solution) 343.20 F g ⁻¹	Device 1.30 mWh g ⁻¹	Device 41.1 mWh g ⁻¹			[399]
Cotton fabric (2018)	PPy/TiO ₂ -coated cotton fabric electrode prepared via sol-gel and in situ chemical oxidation method with 2.0 M NaCl aqueous was used as the electrolyte.	Electrode 733 F g ⁻¹ at 0.6 A cm ⁻²	44.4 Wh kg ⁻¹ at a power density of 555 W kg ⁻¹				[460]

(Continued)

Table 12. (Continued).

Substrate (Reporting year)	Device Configuration	Device capacitance	Energy density	Power density	Capacitance retention	Flexibility	Refs.
Cotton fabric (2020)	GO deposited by "dip and dry" method, chemically reduced into rGO/cotton fabric. MnO ₂ nanoparticles accumulated on rGO/cotton fabric by in situ chemical deposition, PANI layer coated on rGO/MnO ₂ /cotton fabric by in situ oxidative polymerization technique with 1 M H ₂ SO ₄ electrolyte solution	888 and 252 F g ⁻¹ at 1 and 25 A g ⁻¹ , 444 F cm ⁻²			70% after 3000 cycles at 15 A g ⁻¹		[420]
Cotton fabric (2021)	PPy/rGO nanocomposite cotton fabric (NCF) by chemical polymerization,	PPy/0.5/rGO NCF electrode 9300 mF cm ⁻² at 1 mA cm ⁻²	Device 167 μWh cm ⁻²	Device 1.20 mW cm ⁻²	Electrode retention 94.47% after 10 000 cycles.		[461]
Cotton fabric (2022)	GO nanosheets fixed on the cotton fabric (CF) by vacuum filtration, pyrrole monomers and silver ions (Ag ⁺) adsorbed on the surface of GO/CF by π-π and electrostatic interactions, respectively to form flexible PPy/Ag/GO/CF electrodes with PVA/H ₂ SO ₄ gel electrolyte	Electrode 1664.0 mF cm ⁻² , 27.0 F cm ⁻³ , SC 286.6 mF cm ⁻² (4.7 F cm ⁻³)	SC 25.5 μWh cm ⁻²	SC 1149.5 μW cm ⁻²	89.7% after 10 000 bending cycles		[462]
Bamboo fabric (2020)	MnO ₂ -NiCo ₂ O ₄ printed bamboo fabric as positive electrode, and rGO printed bamboo fabric as negative electrode with LiCl/PVA gel as solid-state electrolyte	2.12 F cm ⁻² (1766 F g ⁻¹) at 2 mA cm ⁻²	37.8 mW cm ⁻³	2678.4 mW cm ⁻³	92% of after 5000 cycles		[255]
Polyester fabric (2011)	Graphene/MnO ₂ -textile as positive and SWNTs-textile as negative electrode in aqueous Na ₂ SO ₄ electrolyte	Hybrid graphene /MnO ₂ -based textiles, up to 315 F g ⁻¹	12.5 Wh kg ⁻¹	110 kW kg ⁻¹	95% after 5000 cycles		[224]
Polyester fabric (2011)	MnO ₂ nanoflowers electrodeposited onto carbon nanotube (CNT)-enabled conductive textile fibers,	410 F g ⁻¹ at 5 mVs ⁻¹ and 2.8 F cm ⁻² at 0.05 mV s ⁻¹	≈5–20 Wh kg ⁻¹	≈13 000 W kg ⁻¹	80% after first 200 cycles, 60% after 10 000 and 50% after 50 000 cycles		[463]
Polyester film (2013)	Directly growing CNTs along graphene fibers with Fe ₃ O ₄ nanoparticles for CVD of the nanotubes, PET films coated with Au layer as supporting substrates and current collectors, separator is a filter paper soaked with 1 M Na ₂ SO ₄ aqueous electrolyte.	200.4 F g ⁻¹ , 0.98 mF cm ⁻² at 20 mA cm ⁻²			No decrease after 200 bending cycles		[464]

(Continued)

Table 12. (Continued).

Substrate (Reporting year)	Device Configuration	Device capacitance	Energy density	Power density	Capacitance retention	Flexibility	Refs.
Polyester fabric (2014)	CNT dip-coated onto Cu metalized PET fabrics electrode	$8.5 \times 10^{-3} \text{ F cm}^{-2}$					[359]
Polyester fabric (2014)	PANI film deposited on the CNT/Au/PET; (CNT dip-coated onto Au metalized PET fabrics) to fabricate a solid-state flexible CNT SC with PVA/H ₃ PO ₄ electrolyte	7.1 mF cm ⁻² (electrode) Specific capacitance (CV) 0.51 F cm ⁻² , GCD 0.103 F cm ⁻² at current density of 1 m A cm ⁻²	$2.412 \times 10^{-4} \text{ W h cm}^{-3}$ with 0.011 W cm ⁻³		89% after 2500 cycles	excellent performance under bending at 45°, 90°, 135°	[359]
Polyester fabric (2015)	Strip-shaped electrode prepared by PANI deposited on aligned CNTs, with PVA/H ₃ PO ₄ gel electrolyte	421.7 F cm ⁻³ (343.6 F g ⁻¹ and 47.8 F cm ⁻² at 0.5 A cm ⁻³ (strip-shaped electrode) Device 3.9 F g ⁻¹	9.56 mWh cm ⁻³	2.91 W cm ⁻³	Stable within 10 000 cycles	81% after immersion in water for 48 h	[421]
Polyester fabric (2016)	Two pieces of MnO ₂ deposited conductive graphene/polyester composite fabric with PVA-NaNO ₃ gel electrolyte	265.8 F g ⁻¹ at 2 mV s ⁻¹				87% after 100 times of bending	[465]
Polyester fabric (2018)	PPy electrochemically deposited on rGO painted SnCl ₂ modified polyester textiles with PVA/H ₂ SO ₄ gel electrolyte	Electrode 1117 mF cm ⁻² at 1 mA cm ⁻² , 329.5 F g ⁻¹ at 1 mA cm ⁻¹ , Device 474 mF cm ⁻²	0.0658 mWh cm ⁻² at 1 mA cm ⁻²	25 mW cm ⁻²	100% after 10 000 cycles	98.3% after 1000 bending cycles	[408]
Polyester fabric (2019)	Dipping and drying of PET with GO, followed by chemical reduction of GO and subsequent chemical growth of PPy on PET. Composite electrodes of PET/rGO/PPy sandwiched using PVA-H ₂ SO ₄ gel electrolyte.	230 mF cm ⁻² at 1 mV s ⁻¹ , 5.5 F cm ⁻³ at 1.6 mA cm ⁻³	11 μWh cm ⁻²	0.03 mW cm ⁻²	76% after 6000 cycles		[466]
Polyester fabric (2020)	Pre-treated polyester dip coated in GO, followed by reduction of GO and in situ polymerization of PPy particles on fabric surface with aqueous 1 M H ₂ SO ₄ solution	Electrode 8300 mF g ⁻¹ and 640 mF cm ⁻²					[467]
Polyester fabric (2020)	Silver paste printed on PET, MnHCF-MnOx/GO ink overprinted and reduced to form the electrode, PVA/LiCl electrolyte, and paper separator	16.8 mF cm ⁻²	0.5 mWh cm ⁻²	0.0023 mW cm ⁻²		Stable capacitance even while bending to angles 60°, 90°, and 180° for 100 cycles	[468]

(Continued)

Table 12. (Continued).

2D shaped	Substrate (Reporting year)	Device Configuration	Device capacitance	Energy density	Power density	Capacitance retention	Flexibility	Refs.
	Silk fabric (2016)	Current collector and the active materials layers were screen printed [MnO-coated hollow carbon microspheres, acetylene black, and binder] mixed in a weight ratio of 7:2:1 as printing ink] on a commercial silk fabrics substrate and a PDMS film, respectively. After being pasted with gel electrolyte, the PDMS-based electrode was transferred exactly on top of the silk fabric-based one.	19.23 mF cm ⁻² at 1 mA cm ⁻²			84% after 2000 cycles	98.5% after 100 times bending and 96.8% after 100 times twisting	[422]
	Nylon/PU (67/33) (2021)	Supersonic spraying rGO/SnO ₂ on fabric with 2 M KOH electrolyte	1008 mF cm ⁻² at 1.5 mA cm ⁻²			93% after 10 000 cycles		[423]
	Stretchable textiles (2018)	Fully printed Ag@PPy@MnO ₂ on Ag cathode electrode and activated carbon on Ag anode electrode with PVA/Na ₂ SO ₄ electrolyte	426.3 mF cm ⁻² (cathode)	0.0337 mWh cm ⁻² at 0.38 mW/cm ⁻²		90.8% after 5000 cycles	86.2% after 40% stretching strain	[424]
	Spandex fabric (2019)	Assembling vertical Polypyrrole nanotube (VPPyNT) grown on the carbon nano onions (CNO) @ Polypyrrole granula (PPyG)-textile electrodes with a PVA/H ₃ PO ₄ gel electrolyte into a sandwiched structure	64 Fg ⁻¹	5.7 Wh Kg ⁻¹		85% after 1000 cycles	99% retention after stretching for 500 cycles at a strain of 50%, 88% at a strain of 100%	[469]
	Carbon nanofiber web (2008)	PPy was coated on multi-walled carbon nanotube (CNT)-embedded activated carbon nanofibers (PPy/ACNF/CNT) using Ni foil as the current collector with 6 M KOH aqueous solution electrolyte for fabric SC electrode	333 Fg ⁻¹ at 1 mA cm ⁻² , 275 Fg ⁻¹ at 10 mA cm ⁻²			Negligible change after 500 cycles		[470]
	Graphene fiber fabric (2017)	Hierarchical graphene fiber fabrics (GFFs) with significantly enlarged specific surface area using a hydrothermal activation strategy with (PVA)/H ₂ SO ₄ gel electrolyte	Electrode 244 Fg ⁻¹ , 1060 mF cm ⁻² at thickness of 150 μm, magnified up to 7398 mF cm ⁻² by overlaying 5 layers	23.5 μWh cm ⁻²	26.3 mW cm ⁻²	Good rate capability up to 50 000 cycles	Bendable to 180° without breaking, CV barely changed while bending and releasing 300 cycles	[300]
	Carbon fabric (2012)	Carbon fabric-aligned carbon nanotube/MnO ₂ /conductive polymers (CF-ACNT-MnO ₂ -PEDOT) with 1 M Na ₂ SO ₄ Composite SC electrodes	1.3 F cm ⁻² at 0.1 mV s ⁻¹			5% loss after 1000 cycles		[425]

(Continued)

Table 12. (Continued).

Substrate (Reporting year)	Device Configuration	Device capacitance	Energy density	Power density	Capacitance retention	Flexibility	Refs.
Carbon cloth (2013)	TiO ₂ NWs grown on carbon cloth, Hydrogen-treated TiO ₂ NWs as core, electrochemically active MnO ₂ (H-TiO ₂ @MnO ₂ as positive) and carbon shells (H-TiO ₂ @C as negative) electrodes with separator, PVA/LiCl gel and LiCl aqueous electrolytes	0.68 F cm ⁻³ (PVA/LiCl gel), GCD 0.70 F cm ⁻³ at 0.5 mA cm ⁻² (139.6 Fg ⁻¹ at 1.1 A g ⁻¹ (LiCl electrolyte)	0.3 mWh cm ⁻³ (59 Wh kg ⁻¹)	0.23 W cm ⁻³ (45 kW kg ⁻¹)	91.2% after 5000 cycles	No decay in bending & twisting	[471]
Carbon cloth (2015)	MnO ₂ as cathode, Ti-Fe ₂ O ₃ @PEDOT as anode with NKK separator, and PVA/LiCl gel electrolyte	Anode 1.15 Fcm ⁻² (311.6 F g ⁻¹ and 28.8 Fcm ⁻³ at 1 mAcm ⁻²) SC 365.8 mF cm ⁻² at 10 mV s ⁻¹ , 444.2 mF cm ⁻² at 1 mA cm ⁻² , 2.40 F cm ⁻³ at 1 mA cm ⁻²	0.89 mWh cm ⁻³ at 1 mA cm ⁻²	0.44 W cm ⁻³	85.4% after 6000 cycles		[472]
Carbon cloth (2015)	SnO ₂ @MO _x (SnO ₂ @NiO, SnO ₂ @Co ₃ O ₄ , SnO ₂ @MnO ₂) heterostructures grown on carbon cloth (CC) with 1 M Na ₂ SO ₄ aqueous electrolyte (for SnO ₂ and SnO ₂ @MnO ₂) and 1 M KOH aqueous electrolyte (for SnO ₂ @NiO and SnO ₂ @Co ₃ O ₄)	SnO ₂ @MnO ₂ heterostructure electrode showed the highest discharge areal capacitance (980 mF cm ⁻² at 1 mA cm ⁻²)			After 6000 cycles, SnO ₂ @Co ₃ O ₄ , SnO ₂ @NiO, and SnO ₂ @MnO ₂ electrodes can maintain 58.3%, 63.8%, and 78.1% of its initial SC, respectively at 1 mA cm ⁻²		[473]
Carbon cloth (2015)	Two symmetric freestanding polyaniline-cobalt-based metal-organic framework (MOF) crystals (PANI-ZIF-67) electrodes with H ₂ SO ₄ /PVA as gel electrolyte	Areal capacitances 2146 mF cm ⁻² for PANI-ZIF-67-CC electrode at scan rates of 10 mV s ⁻¹ , For the device 35 mF cm ⁻² at the scan rate of 0.05 mA cm ⁻²	0.0161 mWh cm ⁻³ (0.0044 mWh cm ⁻²)	0.833 Wcm ⁻³ (0.245 Wcm ⁻²)	80% after 2000 cycles		[474]
Carbon cloth (2015)	Assembly of MnO ₂ @Carbonized Polypyrrole (CPPy) as positive and carbon coated Co ₃ O ₄ (Co ₃ O ₄ @C) microsheet as negative electrode with PVA/KOH electrolyte	59.5 F cm ⁻³ at a current density of 20 mA cm ⁻²	27.0 mWh cm ⁻³	1.31 W cm ⁻³	96% after 5000 cycles	97% after 500 bending cycles	[303]

(Continued)

Table 12. (Continued).

Substrate (Reporting year)	Device Configuration	Device capacitance	Energy density	Power density	Capacitance retention	Flexibility	Refs.
Carbon cloth (2015)	Hierarchical structure of ALD Co_3O_4 nanolayer successfully deposited on CVD derived flexible carbon cloth (CNT/CC), (CNTs@ Co_3O_4 /CC) with 2 M KOH is used as electrolyte	Highest 416.7 mF cm^{-2} , 347.2 mF cm^{-2} at 1.25 mA cm^{-2}			No capacity fading is observed even after 50 000 cycles		[82]
Carbon cloth (2016)	In situ electrodeposition of MnO_2 and PPy composite on carbon cloth with 1 M Na_2SO_4 aqueous electrolyte	Electrode 325 F g^{-1} at a current density of 0.2 A g^{-1} , 228 mF cm^{-2} at 0.14 mA cm^{-2}			\approx 96% after over 1000 cycles		[393]
Carbon cloth (2017)	SnO_2 nanoparticles, CNTs, ethyl cellulose, and terpineol composite ink screen-printed onto carbon cloth. Furnace-calcined SnO_2 /CNT electrodes sandwiched with PVA/ H_2SO_4 gel electrolyte	5.61 mF cm^{-2} (flat) and 5.68 mF cm^{-2} (bent)					[475]
Carbon cloth (2018)	Solothermal MoO_3 coating of carbon fibers followed by covered and interconnect by rGO film to form an electrode with 1 mol L^{-1} H_2SO_4 aqueous electrolyte	Electrode 8132 mF cm^{-2} at 2 mVs $^{-1}$	143 μWhcm^{-2} at 10 mA cm^{-2} (corresponding to a power density of 2176 μWhcm^{-2})	15 022 μWhcm^{-2} at 100 mA cm^{-2} (energy density 56.5 μWhcm^{-2})	95% after 30 000 cycles at 120 mA cm^{-2}	77% after 6000 times folding tests	[426]
Carbon cloth (2018)	The MnO_2 /cotton derived carbon cloth (CDCC) as positive, CDCC as negative electrode attached by nickel foams, cotton woven separator sandwiched with 1 M Na_2SO_4 aqueous electrolyte	202 mF cm^{-2} at 0.1 mA cm^{-2}	30.1 mWh cm^{-2} at 0.15 mW cm^{-2}		87.7% after 5000 cycles		[476]

(Continued)

Table 12. (Continued).

Substrate (Reporting year)	Device Configuration	Device capacitance	Energy density	Power density	Capacitance retention	Flexibility	Refs.
Carbon cloth (2019)	Hydrothermal incorporation of Pt into MoS ₂ nanosheets grown on carbon cloth as electrode in 1 M Na ₂ SO ₄ solution, Pt-doped MoS ₂ , and activated carbon electrodes with PVA- H ₃ PO ₄ electrolyte	250 F g ⁻¹ at 0.5 A g ⁻¹ (electrode), 42 F g ⁻¹ at 0.4 A g ⁻¹ (device)			87.96% after 3000 cycles		[477]
Carbon fiber textile (CFT) (2019)	Activated porous CFT (APCFT) electrode as anode and TiN@MnO ₂ on CFT as cathode with PVA-LiCl electrolyte	Anode 1.2 F cm ⁻² at 4 mA cm ⁻²	4.70 mWh cm ⁻³	2.29 W cm ⁻³	No capacitance decay after 25 000 cycles		[337]
Carbon fabric (2019)	Two, rGO enfolded cobalt (II, III) oxide nanowires on flexible carbon fabric substrate (CONW-RGO) electrodes with PVA/KOH gel electrolyte and filter paper as a separator	Electrode 1110 Fg ⁻¹ at 1 Ag ⁻¹ , SC 111.35 Fg ⁻¹ , 33.4 mF cm ⁻² and 685 mF cm ⁻³	34.78 Wh kg ⁻¹ or 0.0104 mWh cm ⁻² or 0.214 mWh cm ⁻³ at power density 750 W kg ⁻¹ or 0.225 mW cm ⁻² or 4.6 mW cm ⁻³	3.6 kW kg ⁻¹ or 1.2 mW cm ⁻² or 23 mWcm ⁻³ at 24.68 Wh kg ⁻¹ or 0.007 mWh cm ⁻² or 0.16 mWh cm ⁻³	Electrode 94.2% after 2000 cycles		[478]
Carbon cloth (2020)	One-step hydrothermal method to prepare NiMnO ₃ nanosheets on a carbon cloth (CC) with 6 M KOH was the electrolyte	2330 F g ⁻¹ at 1 A g ⁻¹			67.8% after 1000 cycles at 10 A g ⁻¹		[427]
Carbon cloth (2021)	MoS ₂ /PANI composite material drop cast on functionalized carbon cloth; MoS ₂ /PANI/FCC electrodes soaked with 1 M H ₂ SO ₄ electrolyte	452.25 F g ⁻¹ at 0.2 A g ⁻¹ (electrode), 72.8 F g ⁻¹ at 0.2 A g ⁻¹ (device)			87% after 1000 cycles at 10 A g ⁻¹ (electrode)		[371]
Carbon fabric (2022)	Cobalt doped MoS ₂ (Co-MoS ₂) nanoflower electrode with 1 M KOH electrolyte	86 F g ⁻¹	4.30 Wh kg ⁻¹	0.6 KW kg ⁻¹	98.5% after 10 000 cycles		[479]
Multidimensional hierarchical fabric (2019)	Graphene nanosheets (GNS) and PEDOT: PSS deposited on the hierarchical fabric via spraying method to fabricate flexible SCs with PVA/H ₂ SO ₄ gel electrolyte	245.5 mFcm ⁻² at 1 mVcm ⁻²	21.82 μWhcm ⁻² at 0.4 mWcm ⁻²		83.9% after 10 000 cycles	mere capacitance loss under different bending states	[480]

involved electrochemical activation of pristine CNT fibers (OCNTF) and coating of PEDOT:PSS, followed by electrochemical deposition of MnO_2 to form MnO_2 @PEDOT:PSS@OCNTF positive electrode and hydrothermal synthesis of MoS_2 on CNTF to form MoS_2 @CNTF negative electrode, with LiCl-PVA gel electrolyte placed on a stretchable substrate.

Among carbon-based materials, CNT and graphene alone and/or in combination with other active materials were studied for 1D fiber or yarn-shaped SCs. Wang et al.^[412] reported bis-rolled MXene with CNTs, which was used to prepare a free-standing asymmetric yarn SC prototype via pairing bis-rolled RuO_2 yarns with 3 M H_2SO_4 electrolyte. The areal, volumetric, and gravimetric capacitance of the yarn electrode were reported as high as 3188 mF cm^{-2} , 1083 F cm^{-3} and 523 F g^{-1} , respectively, at a current density of 2 mA cm^{-2} . The SC device also exhibited high energy and power densities of 61.6 mWh cm^{-3} (168 $\mu\text{Wh cm}^{-2}$ and 8.4 $\mu\text{Wh cm}^{-1}$) and 5428 mW cm^{-3} (14.8 mW cm^{-2} and 741 $\mu\text{W cm}^{-1}$), respectively, with outstanding cycle stability of $\approx 90\%$ up to 10 000 charge-discharge cycle. Similarly, He et al.^[413] reported electrolyte mediation of hybrid fiber made of rGO and MXene, which were assembled into fibers via wet spinning with PVA- H_2SO_4 electrolyte. Such hybrid fiber provided an areal and gravimetric capacitance of 550.96 mF cm^{-2} and 110.89 F g^{-1} , respectively at 20 mV s^{-1} . The device also exhibited energy and power densities of 12 $\mu\text{Wh cm}^{-2}$ and 9.85 mWh cm^{-3} at power densities of 8.8 mW cm^{-2} and 7.1 W cm^{-3} , respectively. Additionally, Zhang et al.^[414] reported $\text{Ti}_3\text{C}_2\text{T}_x$ in combination with PEDOT:PSS to form wet-spun hybrid fiber electrodes for SC applications. Such electrodes provided areal, gravimetric, and volumetric capacitance of 676 mF cm^{-2} , 258 F g^{-1} , and 615 F cm^{-3} , respectively. The device fabricated with PVA/ H_2SO_4 electrolyte achieved an energy density of ≈ 7.13 Wh cm^{-3} and ≈ 8249 mW cm^{-3} with excellent stability of $\approx 95\%$ after 10 000 charge-discharge cycles. The device showed outstanding flexibility of 96% when stretched to 100% strain. Furthermore, Tao et al.^[415] reported carbon fibers or yarns-based 1D SC with a volumetric capacitance of 69.3 F cm^{-3} at 0.1 A cm^{-3} . A hybrid structure was prepared by depositing PPy on MnO_2 nanoflakes coated carbon fiber (CF/ MnO_2 /PPy). Two PPy- MnO_2 -CFs were fixed on a preservative film substrate and assembled into a SC by sandwiching with PVA/ H_3PO_4 membrane as a separator and electrolyte between electrodes. Naderi et al.^[416] drop coated PEDOT:PSS- rGO and deposited MnO_2 on carbon fiber to form yarn-shaped SC. MnO_2 /PEDOT:PSS-rGO and PEDOT:PSS-rGO were used as positive and negative electrodes, respectively, with Na_2SO_4 -CMC as a solid-state electrolyte. The electrodes exhibited capacitance of 2.92 F cm^{-2} (194 F cm^{-3} , 550 mF cm^{-1}) at 5 mA cm^{-2} , which is the highest among such SCs. The energy and power densities were reported as 295 $\mu\text{Wh cm}^{-2}$ (19 mWh cm^{-3} , 55 $\mu\text{Wh cm}^{-1}$) and 2900 μWcm^{-2} (190 mW cm^{-3} , 545 μWcm^{-1}), respectively. The device was also able to retain 96% of its initial capacitance after 5000 cycles.

Platinum,^[80] gold,^[417] and stainless-steel fiber yarns^[299] were also studied as wearable SC substrates. For example, Huang et al.^[418] deposited rGO hydrothermally, and MnO_2 and PPy electrically on spun stainless steel yarn. The PPy@ MnO_2 @rGO-conductive yarns worked as both active materials and current collectors. The length and areal capacitances made from this yarn were reported as 36.6 mF cm^{-1} and 486 mF cm^{-2} in aqueous

Na_2SO_4 electrolyte or 31 mF cm^{-1} and 411 mF cm^{-2} in all solid-state PVA/ H_3PO_4 electrolyte. The capacitance retained up to 92% over 4950 charge-discharge cycles, and even 80% after 1000 cycles at 90 bending, 91% after 1000 cycles knotting, and 103% after 1000 cycles twisting.

For 2D fabric-shaped SCs, conventional textiles such as cotton, polyester, polycotton, and carbon textiles have widely been studied. In such SC devices, carbonaceous compounds are used in combination with conductive polymers and/or metal oxides for SC fabrication via various fabrication techniques. Huang et al.^[419] electro-spun carbon nanoweb on nickel-coated cotton fabrics (Niccotton). The as-prepared fabric SC device achieved an areal capacitance of 973.5 mF cm^{-2} at 2.5 mA cm^{-2} . A simple dip-drying method was reported by Etana et al.^[420] for fabricating cotton textiles-based SC, where GO was deposited by a “dip and dry” method and chemically reduced to form rGO/cotton fabric. MnO_2 nanoparticles were accumulated on rGO/cotton fabric by in situ chemical deposition, and then PANI layer was coated. With 1 M H_2SO_4 electrolyte solution, the SC provided high gravimetric capacitance of 888 F g^{-1} and high areal capacitance of 444 F cm^{-2} , the highest reported for such SC configuration. In another study by Li et al.^[408] PPy was electrochemically deposited on rGO painted and SnCl_2 -modified polyester textiles, which provided areal capacitance of 1117 mF cm^{-2} at a current density of 1 mA cm^{-2} with 100% retention after 10 000 cycles. The SC device fabricated from such fabric electrodes and PVA/ H_2SO_4 gel electrolyte exhibited an aerial capacitance of 474 mF cm^{-2} . Cheng et al.^[421] developed strip-shaped composite electrodes, which were prepared via depositing PANI on aligned CNTs, exhibiting a high volumetric capacitance of 421.7 F cm^{-3} .

In addition to polyester fabrics, silk,^[422] nylon,^[423] and stretchable^[424] textiles have also been studied for the fabrication of 2D fabric-shaped SCs. However, carbon fiber fabric has widely been used as SC substrate by several research groups.^[425–427] For instance, Lv et al.^[425] reported a composite SC electrode prepared by depositing aligned CNT/ MnO_2 /conductive polymers on carbon fabric (CF-ACNT- MnO_2 -PEDOT). With 1 M Na_2SO_4 electrolyte, the composite electrodes achieved a high areal capacitance of 1300 mF cm^{-2} at 0.1 mV s^{-1} . Though several attempts were reported for the enhancement of the capacitive performance, the highest areal capacitance for carbon fabric-based SC was reported by Zhu et al.^[426] They coated carbon fibers MoO_2 by solvothermal method; covered and interconnected with rGO film to form SC electrode. The areal capacitance of the electrode was reported as high as 8132 mF cm^{-2} at 2 mV s^{-1} . The electrode also retained 95% capacitance after 30 000 charge-discharge cycles at 120 mA cm^{-2} and 77% after 6000 times folding tests. However, the highest gravimetric capacitance was reported by Mu et al.^[427] who hydrothermally prepared NiMnO_3 nanosheets on a carbon cloth. With 6 M KOH electrolyte, the electrodes reached 2330 F g^{-1} at the current density of 1 Ag⁻¹.

7. Other Key Properties of SCs for Wearable Applications

7.1. Flexibility

To be considered as wearable, a SC device must be flexible and durable under the physical movement of the body. The

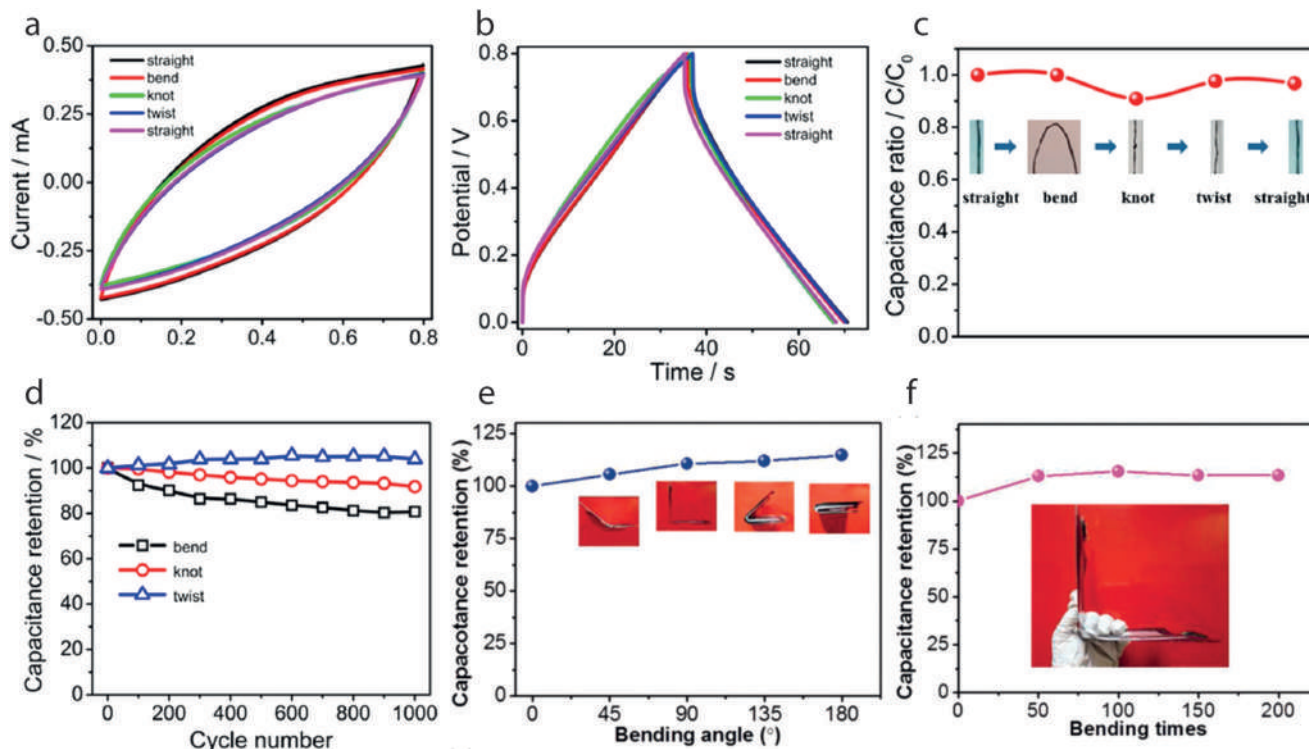


Figure 18. Flexibility tests of PPy@MnO₂@rGO-deposited conductive yarns measured in the two-electrode cell. a) CV curves of the all-solid-state yarn supercapacitor undergoing consecutive deformations at a scan rate of 100 mV s⁻¹. b) GCD curves of the all-solid-state yarn supercapacitor undergoing consecutive deformations at a current density of 80 mA cm⁻³. c) Capacitance ratio under various deformations. d) Capacitance retention of the all-solid-state yarn supercapacitor after each deformation. Reproduced with permission.^[418] Copyright 2015, American Chemical Society. Influence of bending deformation on CeO₂-ACVF capacitive performance; specific capacitance e) under various bending angles; and f) after different bending cycles. ACVF: activated viscose fabric. Reproduced with permission.^[396] Copyright 2020, SAGE Publications.

bending of SC devices for hundred to several hundred cycles is performed at various angles to evaluate the flexibility of a SC device. Additionally, twisting, winding, and other deformations are also assessed. Yu et al.,^[351] reported more than 97% capacitance retention after 1000 bending cycles at a 90° angle of hierarchically structured CNT-graphene fiber-based micro SCs. Chen et al.^[229] reported an electrochromic fiber-shaped SC composed of elastic fiber/CNTs/PANI retaining capacitance of 93.8% after 1000 bending cycles at 180°. Choi et al.^[433] reported a flexible SC made of CNT yarn with MnO₂ exhibiting no decrease of capacitance even after 1000 bending at 90°. Ding et al.^[439] fabricated a graphene/PPy composite fibers for all-solid-state, flexible fiber form SC that exhibited similar performance.

In addition to bending, the flexibility of SCs for other mechanical deformations was reported by some research groups. For example, a yarn-based SC was developed by Lee et al.,^[448] composed of Pt/MWCNTs/PEDOT retained 98% of its initial capacitance after 2000 bending, 92% after 10 000 winding, and 99% after 10 000 cycles when woven into a glove. Huang et al.^[418] reported yarn-based SC of rGO/MnO₂/PPy that retained 80% capacitance after 1000 cycles at 90° bending, 91% after 1000 cycles of knotting, and 103% after 1000 cycles of twisting, revealing the enhancement of the capacitive performance, **Figure 18(a–d)**. Similarly, the capacitance was increased (107% retention) after 1000 cycles of twisting for an asymmetric fiber-shaped solid-state SC based on carbon fiber bundle.^[444] Additionally, several other articles have reported

higher bending cycles. For example, Ye et al.^[430] reported a fiber-shaped SC by introducing rGO and carbon nanoparticles (CNPs) on commercial CTs using dip-coating technique combined with low-temperature vapor reduction, which resulted in 92.30% capacitance retention after 2000 bending cycles. Liu et al.^[429] examined their 1D-shaped flexible yarn SC composed of rGO/Ni cotton composite electrodes with PVA/LiCl gel as electrolyte and separator for 4000 cycles, and found 95% of retention after at 180° bending angle. Furthermore, Wu et al.^[435] reported a flexible fiber-shaped SCs (FSSCs) by twisting a number of CNT yarns (n) with a Pt filament as current collector and PANI nanowires. They obtained a capacitance retention of 98.17% after 3000 cycles and 95.91% after 5000 flexing cycles.

For 2D-shaped SC devices, shorter bending cycles were used for testing capacitance retention of textile SCs. Zhang et al.^[422] reported a silk fabric-based SC which retained 98.5% after 100 bending cycles and 96.8% after 100 twisting cycles. Lee et al.^[303] developed an asymmetric SC by assembling MnO₂@CPPy and carbon coated Co₃O₄ microsheet (Co₃O₄@C)-decorated carbon cloths with a solid-state PVA/KOH electrolyte, which retained 97% capacitance after 500 bending cycles. Luo et al.^[396] reported an increase of 13.4% capacitance after 200 bending cycles for an all-fabric solid-state flexible SC, made of activated carbon fiber fabric, **Figure 18(e,f)**. The capacitance of a solid-state stretchable SC, prepared by assembling VPPyNTs/CNOs@PPyG-textile electrodes with a PVA/H₃PO₄ gel electrolyte into a sandwiched

structure, was nearly unchanged after stretching for 500 cycles at a strain of 50%. However, the capacitance retention ratio decreased slightly to 88% as the strain% was increased to 100%.^[469]

7.2. Safety Issue

To be wearable, the flexible SC device components must be non-toxic to avoid any health concerns as well as for the environment when disposed of. The concerns with wearable SCs are raised due to the toxic nanoparticles or metal particles of all sizes entering or generated during manufacturing stages as well as during usage. In addition, the effect of electromagnetic fields, accidental electric shock, and the inability to activate the emergency shut-off in case of malfunctioning are also matters of concern.^[481] In addition, wearable SCs and other wearable electronic devices have limited lifetimes. Therefore, it is also critical to ensure that the waste generated by the SCs does not create new hazards for health and the environment.

A report was published revealing that more than 8 billion batteries enter the US and European markets annually. Also, 3 billion alkaline units get discarded each year in North America alone.^[333] Another report projected a generation of more than 130 g of battery waste per person each year.^[482] Besides battery, increasing usage of mobile, computing, and other autonomous electrical devices increases the production and disposal of SC devices exponentially.^[333] An estimated 20 000 tonnes of old household batteries end up in landfill every year.^[483] The challenges of such disposal to the environment are due to the presence of a large number of toxic metals (e.g., Cd, Ni, Pb), F-containing electrolytes and device components, corrosive fluids (e.g., H₂SO₄ and H₃PO₄), and fire hazards from organic electrolytes, which may have negative environmental impacts and may induce numerous health problems such as acute or long-term exposure. The principal issue of the release of metals into landfills is the potential to contaminate the groundwater. Incineration of them may also pose two major potential environmental concerns; the release of metals (mostly mercury, cadmium, and lead) into the ambient air and the concentration of metals in the ashes which must be landfilled. The F-containing electrolyte salts (tetraethylammonium tetrafluoroborate, Net₄BF₄), carbon particle binder (such as PTFE or PVDF), and electrode separator (often PTFE) are likely to generate volatile fluorocarbons during traditional incineration, which are highly toxic to organisms and are likely to damage incinerators and nearby structures. Acetonitrile solvents, commonly implemented in high-performance devices, are flammable, carcinogenic, and may decompose into highly toxic cyanides upon heating. Some ions commonly used in promising ILs, such as bis(trifluoromethanesulfonyl)imide (TFSI), have been shown to inhibit cellular respiration. Although some aqueous electrolytes that implement Li₂SO₄ or Na₂SO₄ are expected to be benign to the environment, they still emit SO₂, contributing to acid rain when released during incineration. Although SCs, unlike fuel cells and batteries, contain no noble or heavy metals that are particularly difficult to dispose of, conventional collectors and packaging materials, such as steel and Al, are incombustible and cannot be fully burned without leaving ash residue. Thus, the disposal of SCs not only generates harmful substances but

also incombustible waste materials that need to be stored in a landfill.^[482]

7.3. Washability

Washability is a product's ability to withstand a predetermined number of cycles of a specified washing process, able to adequately clean the product without loss of functionality and/or serviceability, and without resulting security risks for the user.^[484] Most e-textiles still suffer from poor wash ability, reducing the reliability of e-textiles to be ready for the market. Many experimental wearable e-textiles are not suitable for real-life applications because of this problem. The hydrophobic textile substrate, due to the capillary effect, can still absorb water in the textile bulk making the device fail. Also, the mechanical stresses incorporated by the washing cycles may destroy the electrical contacts between the conductive thread and the electronic wearable device. Thus, the electric impedance becomes uncontrollable after several washing cycles, making the wearable device unstable and often stops functioning.^[485] Therefore, there remains a need for technology that can provide better wash stability for conductive textiles.

Wash ability is usually reported by the retention of performance after several washing cycles. We encapsulated screen-printed graphene-based conductive patterns on textiles to protect them from being washed away, **Figure 19b**.^[358] The sheet resistance before and after encapsulation of the printed pattern was evaluated. It was found that the bare pattern had an increase of 10 times resistance, whereas the encapsulated pattern exhibited only a 3.5 times increase in the sheet resistance after 10 wash cycle, **Figure 19c**. Cao et al.^[487] also reported a screen-printed washable e-textile electrodes, which were tested after being immersed in water for different times, showed very negligible variation, after soaking in water repeatedly and for a longer duration, **Figure 19(d,e)**. A KAIST research team, fabricated a self-powered washable textile-based wearable display module on real textiles that integrate polymer solar cells (PSCs) with organic light emitting diodes (OLEDs), exhibiting little change in characteristics after 10 min-long 20 washings cycles.^[486] Qiang et al.^[360] demonstrated a super-hydrophobic conducting fabric with graphene and hexagonal boron nitride inks. The different fabrics were then integrated to engineer an all-textile-based capacitive heterostructure that sustained 20 cycles of repeated washing. Barazekhi et al.^[467] also reported a negligible decrease in conductivity after 20 laundry cycles for rGO – PPy based polyester textile SC.

8. Future Research Directions and Conclusion

8.1. Towards High-Performance Energy Storage Textiles

The continuous development of various wearable and portable electronic devices integrated with textiles has increased the demand for commercially available textile-based flexible energy storage devices. According to research by Fact.MR,^[488] the e-textiles demand is expected to grow due to the growing demand for equipment that can track body movements. From 2021–2031,

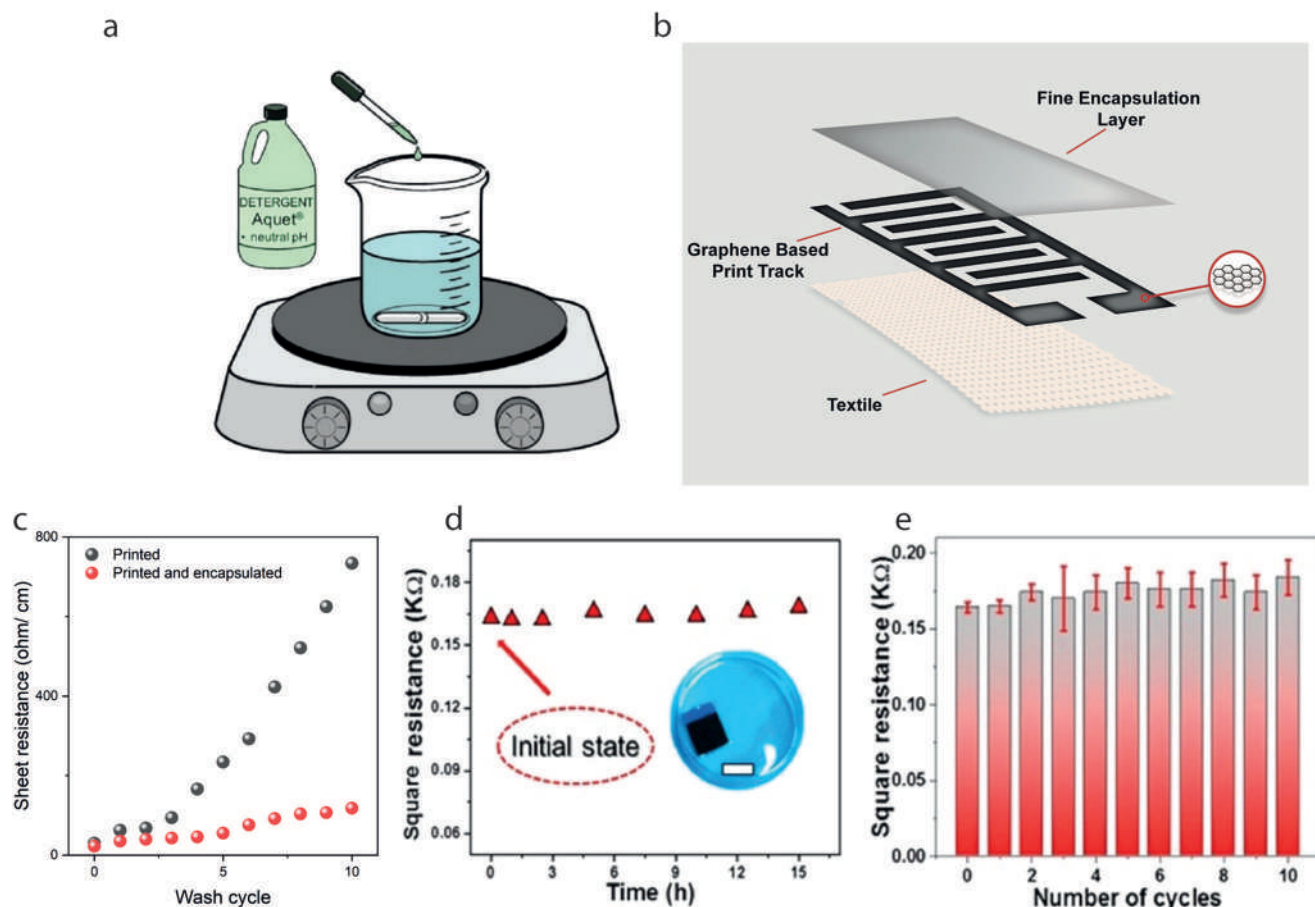


Figure 19. a) Schematic diagram of washing test. Reproduced with permission.^[486] Copyright 2019, The Royal Society of Chemistry. b) Illustration of graphene-based ink pattern and encapsulation layer on textile substrate. c) The change in electrical resistance with number of washing cycles of graphene-based ink printed (without encapsulation) and graphene-based ink-printed (with encapsulation) cotton fabric. Reproduced with permission.^[358] Copyright 2022, Elsevier. d) Resistances of electrode after being immersed in water for different times. The inset is the photograph of electrode immersed in water for 1 week (scale bar, 20 mm). e) Resistances of same electrode on nylon substrate after being immersed in water for different times and 2 h for each time. Reproduced with permission.^[487] Copyright 2018, American Chemical Society.

the market is expected a rapid growth owing to its expanding applications in health monitoring, sports training, hazardous materials monitoring, military monitoring, etc. The IDTechEx Research forecasts that the market for wearables will reach \$138 bn by 2025.^[489] The Acumen Research and Consulting says e-textiles and smart clothing market surpass \$15 018.9 Mn by 2028 with a CAGR of 32.3%.^[490] In this review, we have discussed a brief overview of the textile-based energy storage SCs, from materials to device fabrication. Though various laboratory-scale devices have already been reported, there remain many challenges for the wide-scale commercial adaptation of such energy storage textiles. Since the principal function of energy storage textiles is to power up various wearable electronics, the most important challenge is the improvement of energy storage capacity comparable to the existing rigid conventional batteries. Energy densities of SCs are not very high, and there still remains a clear gap between SCs ($<20 \text{ Wh kg}^{-1}$) and batteries ($30\text{--}200 \text{ Wh kg}^{-1}$) in terms of energy densities.^[491] The SC with lower energy density will result in bulkier devices that are not compact. An effective way to improve the storage capacity of SCs could be the

improvement of manufacturing processes and technology. But in the long run, it is essential and difficult to find new electrolyte and electrode active materials with higher electrochemical performance. Considering the energy formula, $[0.5CV^2]$, the three main approaches usually taken into consideration to increase the energy density are: improving the capacitance of the system by fine-tuning the electrode materials' surface properties, improving the voltage of the device by selecting electrodes, and electrolytes providing wide electrochemically stable potential windows and increasing the capacitance and the voltage at the same time by assembling a faradaic electrode with a non-Faradaic one, such as a hybrid system.^[492] The rated voltage of a SC is very low (less than 2.7 V), which requires a lot of series connections for practical applications. Because of the need for high current charging/discharging in applications, and damage of capacitors due to overcharging, it is very important whether the voltages on individual capacitors (in series) are consistent or not.^[491] However, the increased loading of active material to improve the energy storage capacity always makes the textiles stiff and inappropriate for wearable applications. Therefore, energy storage

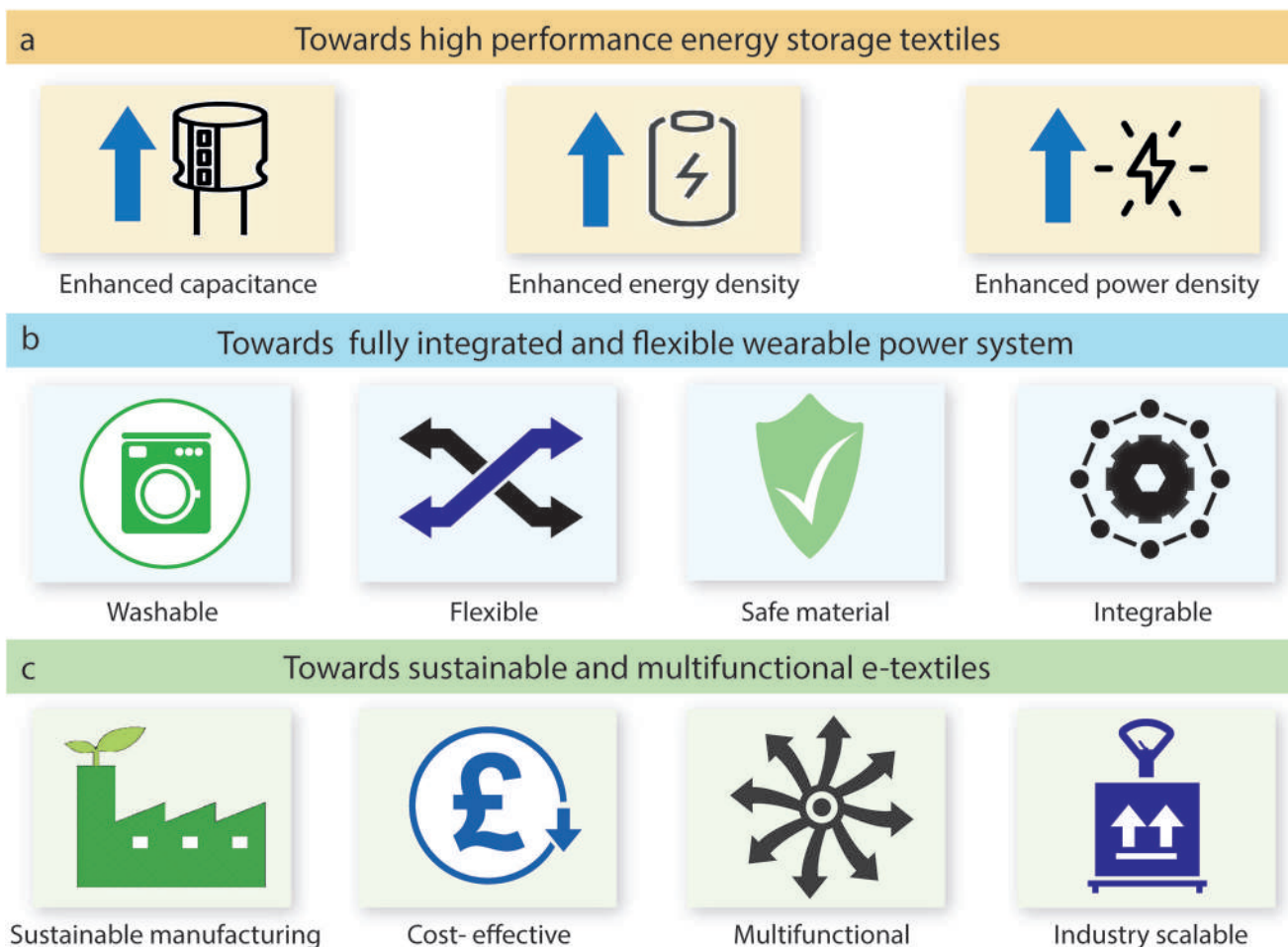


Figure 20. Future research direction of flexible supercapacitors.

nanomaterials with a high specific area, high conductivity, and good mechanical properties are attractive for further research and improvement. An energy storage system based on a battery electrode and a SC electrode, called battery-SC hybrid (BSH), offers a promising way to construct a device with merits of both secondary batteries and SCs.^[493] Such hybrid battery-SCs inherit the high power ($\approx 0.1\text{--}30\text{ kW kg}^{-1}$) of SCs and the high energy density ($\approx 5\text{--}200\text{ Wh kg}^{-1}$) of secondary batteries, with the advantages of stable long cycle performance and low cost. By addressing all these issues appropriately, energy densities of SCs can become comparable to batteries (Figure 20a).^[491]

8.2. Towards Fully-Integrated and Flexible Wearable Power System

8.2.1. Washability

E-textiles, like other everyday textiles, often need to withstand washing procedures to ensure its general usability, Figure 20b.^[494] However, washability is seen as one of the main obstacles to reach a wider market of e-textile products. To assess, improve, and evaluate the extent of an e-textile's in terms of washing, re-

peated test cycles are executed. So far, there are no standardized methods for testing the wash fastness of e-textiles and no protocols to comparably assess the washability of tested products.^[495] Washing e-textiles is challenging. The effect of washing on the e-textile performance relies not only on the type of conductive materials or fabrication process but also on the specific textile substrate used (i.e., materials and constructions) along with their interdependency. Therefore, no global conclusion can be drawn on how a washing program for smart e-textiles should be configured. Considering textile substrates, the applicability and suitability of different textiles depend on the type of conductive track used while looking to achieve the best washability results. On the other hand, if the choice of textile for a smart textile application is fixed due to specific requirements (such as sufficient elasticity for sports clothing, etc.), the type of conductive track used needed to be adapted accordingly for best reliability results.^[484]

8.2.2. Flexibility

With the rapid advancement of portable electronic products and the concept of wearable electronics, flexible energy storage devices have become popular with researchers. The traditional SCs,

however, are greatly restricted to the shape of the device due to the rigid nature of the electrode. Flexible and small SCs with high electrochemical performance compatible with portable electronics can be the direction for next-generation flexible SCs, Figure 20b. The textile substrate is naturally flexible, however, the flexibility of the electrode material is the prime concern for SC flexibility. Enhancing the electrochemical performance often requires the deposition of additional electroactive material which in return makes the structure rigid. Therefore, there remains still a need for further exploration of suitable electrode materials which could possess ultra-flexibility while keeping ultra-high electrochemical performances.

8.2.3. Safety

One of the important considerations of fabricating textile-based SCs is the utilization of safe electroactive materials. Since such textile-based devices are aimed at powering other e-textiles for human health management, the final device must be safe for human body as well for the environment when disposed, Figure 20b. Till now, most used materials for SCs electrodes are generally toxic, environmentally unfriendly, and not biocompatible, and thus need a safer and environmentally friendly substitute.

8.2.4. Integration

Integration of sandwiched battery or SC device in textiles is a challenge due to the accumulation of device components (current collector, electrodes, separator, etc.) onto thin textiles substrate, Figure 20b. This is faced by most single-layer fabrics, however multi-layer fabrics such as jackets and winter coats may suffer less from this issue. Only a few reports were published demonstrating the successful weaving or knitting of SC yarns to produce energy storage fabrics. Meeting the strict quality requirements of industrially-used weaving and knitting machines is one of the main challenges here. Therefore, coating or printing of conductive materials on existing textiles or conductive fibers/yarns to be used directly into full fabrics could be possible solutions to such problems. For fabric-shaped devices, the traditional cut-and-sew method is the simplest method to encapsulate and integrate fabric-based energy storage devices into final textile products together with other electronic components. Adhesive bonding, ultrasonic welding, and laser welding are other joining methods able to eliminate bulky stitched seams and bring less damage to the electronic components within the devices.^[33] However, fabrication complexity and cost gradually decrease from a single fiber/yarn to a whole piece of textile. In the meantime, the output performance could be improved by introducing materials with larger electron affinity differences, enlarging the contact area by expanding the dimension, and increasing the distance gap.^[65]

8.3. Towards Sustainable Materials and Electronics

8.3.1. Sustainable Manufacturing

The rapid development of the electronic industry has accelerated the demand for high-performance portable power supply units.

In addition, to meet social needs and promote industrial development, the application aspects of SCs have also gained importance. People all over the world, nowadays, have been paying more and more attention to energy consumption and environmental protection, towards the use of more and more clean energy. As a result, the consumer culture around the world has also raised the need for all products to be more sustainable and recyclable to reduce the environmental impact.^[496] This the SC industries too. Therefore, the need to explore safe and sustainable manufacturing of energy storage devices is an imperative concern of the world today. New eco-friendly, as well as cost-efficient energy storage systems, should be developed, in view of the requirements of emerging ecological concerns and modern society, Figure 20c.^[497]

8.3.2. Improving the Cost Performance

The most important consideration for any industry to endure is the improvement of product performance along with the reduction of production costs. Similarly, in SC technology, in addition to improving the manufacturing process and technology, finding stable and effective electrode and electrolyte materials along with reducing the cost is the future research focus. Several approaches could be considered for the cost reduction of any technology. Replacing an existing material with a new low-cost raw material, such as natural mineral resources is an attractive option. The combination of a low-price raw materials with high price raw materials without compromising the performance could be another approach to reduce the overall cost. In brief, the development of SCs is inseparable from the progress of science and technology and the demand for application. We believe the development of SCs will also be more rapid and far-reaching with the popularity of new and smart wearable devices, Figure 20c.^[491]

8.3.3. Multifunctionality

Textile-based wearable electronics have attracted immense attention during the past few years due to their softness, breathability, and biocompatibility, making them durable and wearable for long-term application.^[498,499] The rapid progress of intelligent electronic devices has put people in need of intelligent and controllable multifunctional devices which allow manufacturers and users to program themselves to ease performing different functions to be utilized in fulfillment of different requirements in real life. Several research groups have already reported multifunctionalities in textiles,^[500-502] however, a textile that can monitor several health parameters is of special interest for personalized health care applications.^[503,504] Tian et al.^[505] prepared multifunctional e-textiles with high conductivity by a simple screen-printing method, which not only exhibit excellent sensing performance, but also have outstanding joule heating performance. As a proof of concept, we reported a flexible and washable screen printed graphene-based e-textiles platform that can work as activity sensor, can monitor the brain activity, and can store energy in the form of SC.^[358] Future development of modern electronics inspires the use of flexible devices for both energy conversion and storage.^[506,507] An effective solution to the ever-increasing energy crisis could be the use of solar energy. Excitonic solar cells

such as polymer and dye-sensitized solar cells could convert the solar energy into electric energy which is transferred to electrochemical devices, such as lithium-ion batteries and supercapacitors, for storage.^[508] E-textiles are a promising technology that could soon become part of our everyday lives. However, e-textiles with a single functionality cannot meet the requirements of electronics. Increasing attention is thus being paid to realizing the functional integration among the generation, storage, and utilization of electricity and the introduction of other functionalities into e-textiles.^[509] In the future, the integration of SCs with sensors, actuators, electrochromic, shape memory, and even self-repair functions will be very attractive for multifunctional and self-powering personal health management textiles, Figure 20c.

8.3.4. Industrial Scalability

Large-scale manufacturing ability is an important criterion to be considered for the development of e-textiles, Figure 20c. The electrode materials to be integrated into the full garment must be scalable for industrial manufacture. Many experimental designs lack this criterion hindering the scope of the device to be used commercially. The major challenge for constructing conductive fiber/yarn is their length-related resistance. Since the resistance is directly proportional to its length and inversely proportional to its cross-sectional area, it shows that shorter lengths and larger cross-sectional areas of such fiber/yarn give lower resistance.^[510] Therefore, many devices showing low ESR per length may become too resistive beyond a certain working length to act as an energy storage device. Another challenge may arise with the fabrication techniques to form the electrode materials. Many sophisticated fabrication techniques such as ink-jet printing of conductive materials, and coating by physical or chemical vapor deposition methods may appear feasible for lab-based experiments but are too expensive for large-scale production.

Acknowledgements

Authors gratefully acknowledge funding from UWE-Augtex partnership Ph.D. award, and UKRI Research England The Expanding Excellence in England (E3) grant. K.S.N. was supported by the Ministry of Education, Singapore, under its Research Centre of Excellence award to the Institute for Functional Intelligent Materials (I-FIMs, project No. EDUNC-33-18-279-V12) and by the Royal Society (UK, grant number RSRP\R-190000). The authors also thank Laura Wescott for the professional support with the graphics for this paper.

Conflict of Interest

The authors declare no conflict of interest.

Keywords

electronic textiles, energy storage devices, smart textiles, supercapacitors, wearable electronics

Received: July 5, 2022
Revised: September 5, 2022
Published online:

- [1] I. Wicaksono, C. I. Tucker, T. Sun, C. A. Guerrero, C. Liu, W. M. Woo, E. J. Pence, C. Dagdeviren, *npj Flexible Electron.* **2020**, *4*, 5.
- [2] E. Ismar, S. Kurşun Bahadır, F. Kalaoglu, V. Koncar, *Global Challenges* **2020**, *4*, 1900092.
- [3] H. Peng, X. Sun, F. Cai, X. Chen, Y. Zhu, G. Liao, D. Chen, Q. Li, Y. Lu, Y. Zhu, Q. Jia, *Nat. Nanotechnol.* **2009**, *4*, 738.
- [4] X. Shi, Y. Zuo, P. Zhai, J. Shen, Y. Yang, Z. Gao, M. Liao, J. Wu, J. Wang, X. Xu, Q. Tong, B. Zhang, B. Wang, X. Sun, L. Zhang, Q. Pei, D. Jin, P. Chen, H. Peng, *Nature* **2021**, *591*, 240.
- [5] L. Wang, S. Xie, Z. Wang, F. Liu, Y. Yang, C. Tang, X. Wu, P. Liu, Y. Li, H. Saiyin, S. Zheng, X. Sun, F. Xu, H. Yu, H. Peng, *Nat. Biomed. Eng.* **2020**, *4*, 159.
- [6] Z. Zhang, K. Guo, Y. Li, X. Li, G. Guan, H. Li, Y. Luo, F. Zhao, Q. Zhang, B. Wei, Q. Pei, H. Peng, *Nat. Photonics* **2015**, *9*, 233.
- [7] R. Lin, H.-J. Kim, S. Achavananthadith, Z. Xiong, J. K. W. Lee, Y. L. Kong, J. S. Ho, *Nat. Commun.* **2022**, *13*, 2190.
- [8] N. Karim, S. Afroj, K. Lloyd, L. C. Oaten, D. V. Andreeva, C. Carr, A. D. Farmer, I.-D. Kim, K. S. Novoselov, *ACS Nano* **2020**, *14*, 12313.
- [9] J. S. Heo, J. Eom, Y. H. Kim, S. K. Park, *Small* **2018**, *14*, 1703034.
- [10] Y. Zhang, H. Wang, H. Lu, S. Li, Y. Zhang, *iScience* **2021**, *24*, 102716.
- [11] J. Zhao, Y. Fu, Y. Xiao, Y. Dong, X. Wang, L. Lin, *Adv. Mater. Technol.* **2020**, *5*, 1900781.
- [12] V. Kaushik, J. Lee, J. Hong, S. Lee, S. Lee, J. Seo, C. Mahata, T. Lee, *Nanomaterials* **2015**, *5*, 1493.
- [13] A. Hatamie, S. Angizi, S. Kumar, C. M. Pandey, A. Simchi, M. Willander, B. D. Malhotra, *J. Electrochem. Soc.* **2020**, *167*, 037546.
- [14] N. Karim, S. Afroj, A. Malandraki, S. Butterworth, C. Beach, M. Rigout, K. S. Novoselov, A. J. Casson, S. G. Yeates, *J. Mater. Chem. C* **2017**, *5*, 11640.
- [15] J. Chen, Y. Huang, N. Zhang, H. Zou, R. Liu, C. Tao, X. Fan, Z. L. Wang, *Nat. Energy* **2016**, *1*, 16138.
- [16] Y. Yang, Q. Huang, L. Niu, D. Wang, C. Yan, Y. She, Z. Zheng, *Adv. Mater.* **2017**, *29*, 1606679.
- [17] S. Ahmed, A. Ahmed, M. Rafat, *J. Saudi Chem. Soc.* **2018**, *22*, 993.
- [18] S. Palchoudhury, K. Ramasamy, R. K. Gupta, A. Gupta, *Front. Mater.* **2019**, *5*, 83.
- [19] Y. Gu, T. Zhang, H. Chen, F. Wang, Y. Pu, C. Gao, S. Li, *Nanoscale Res. Lett.* **2019**, *14*, 263.
- [20] S. Shi, C. Xu, C. Yang, J. Li, H. Du, B. Li, F. Kang, *Particuology* **2013**, *11*, 371.
- [21] A. Price, in *Small and Micro Combined Heat and Power (CHP) Systems* (Ed: R. Beith), Woodhead Publishing, Sawston, Cambridge **2011**.
- [22] G. Liu, L. Qu, R. Zeng, F. Gao, in *The Energy Internet* (Eds: W. Su, A. Q. Huang), Woodhead Publishing, Sawston, Cambridge **2019**.
- [23] S. Kalaiselvam, R. Parameshwaran, in *Thermal Energy Storage Technologies for Sustainability* (Eds: S. Kalaiselvam, R. Parameshwaran), Academic Press, Boston **2014**.
- [24] F. Hussain, M. Z. Rahman, A. N. Sivasengaran, M. Hasanuzzaman, in *Energy for Sustainable Development* (Eds: M. D. Hasanuzzaman, N. A. Rahim), Academic Press, Cambridge, Massachusetts **2020**.
- [25] Y. Wang, Y. Xu, J. Qiu, in *Distributed Control Methods and Cyber Security Issues in Microgrids* (Eds: W. Meng, X. Wang, S. Liu), Academic Press, Cambridge, Massachusetts **2020**.
- [26] B. G. Pollet, I. Staffell, J. L. Shang, V. Molokov, in *Alternative Fuels and Advanced Vehicle Technologies for Improved Environmental Performance* (Ed: R. Folkson), Woodhead Publishing, Sawston, Cambridge **2014**.
- [27] R. A. Huggins, in *Energy Storage: Fundamentals, Materials and Applications* (Ed: R. Huggins), Springer International Publishing, Cham **2016**.
- [28] C. Vix-Guterl, E. Frackowiak, K. Jurewicz, M. Friebe, J. Parmentier, F. Béguin, *Carbon* **2005**, *43*, 1293.

- [29] R. B. Rakhi, in *Nanocarbon and its Composites* (Eds: A. Khan, M. Jawaid, Inamuddin, A. M. Asiri), Woodhead Publishing, Sawston, Cambridge **2019**.
- [30] K. Chen, D. Xue, *J. Mater. Chem. A* **2016**, *4*, 7522.
- [31] W. Lv, Z. Li, Y. Deng, Q.-H. Yang, F. Kang, *Energy Storage Mater.* **2016**, *2*, 107.
- [32] K. Jost, G. Dion, Y. Gogotsi, *J. Mater. Chem. A* **2014**, *2*, 10776.
- [33] Q. Huang, D. Wang, Z. Zheng, *Adv. Energy Mater.* **2016**, *6*, 1600783.
- [34] S. Zhang, N. Pan, *Adv. Energy Mater.* **2015**, *5*, 1401401.
- [35] A. G. Pandolfo, A. F. Hollenkamp, *J. Power Sources* **2006**, *157*, 11.
- [36] D. A., G. Hegde, *RSC Adv.* **2015**, *5*, 88339.
- [37] X. You, M. Misra, S. Gregori, A. K. Mohanty, *ACS Sustainable Chem. Eng.* **2018**, *6*, 318.
- [38] C.-y. Hui, C.-w. Kan, C.-l. Mak, K.-h. Chau, *Processes* **2019**, *7*, 922.
- [39] Y.-E. Miao, T. Liu, in *Electrospinning: Nanofabrication and Applications* (Eds: B. Ding, X. Wang, J. Yu), William Andrew Publishing, Norwich, NY **2019**.
- [40] C. Choi, D. S. Ashby, D. M. Butts, R. H. DeBlock, Q. Wei, J. Lau, B. Dunn, *Nat. Rev. Mater.* **2020**, *5*, 5.
- [41] B. Viswanathan, in *Energy Sources* (Ed: B. Viswanathan), Elsevier, Amsterdam **2017**.
- [42] U. Gazal, I. Khan, M. A. Usmani, A. H. Bhat, in *Polymer-based Nanocomposites for Energy and Environmental Applications* (Eds: M. Jawaid, M. M. Khan), Woodhead Publishing, Sawston, Cambridge **2018**.
- [43] A. Muzaffar, M. B. Ahamed, K. Deshmukh, J. Thirumalai, *Renewable Sustainable Energy Rev.* **2019**, *101*, 123.
- [44] K. Karthikeyan, S. Amaresh, K. J. Kim, S. H. Kim, K. Y. Chung, B. W. Cho, Y. S. Lee, *Nanoscale* **2013**, *5*, 5958.
- [45] Q. Abbas, M. Mirzaeian, M. R. C. Hunt, P. Hall, R. Raza, *Energies* **2020**, *13*, 5847.
- [46] P. E. Lokhande, U. S. Chavan, A. Pandey, *Electrochem. Energy Rev.* **2020**, *3*, 155.
- [47] Y. Zhang, H. Feng, X. Wu, L. Wang, A. Zhang, T. Xia, H. Dong, X. Li, L. Zhang, *Int. J. Hydrogen Energy* **2009**, *34*, 4889.
- [48] C. Qian, G. Yongji, *Materials Lab* **2022**, *1*, 220034.
- [49] H. Xiang-Xi, Z. Jia-Hua, L. Wei-Hong, Y. Zhuo, G. Yun, Z. Hang, Q. Yun, L. Li, C. Shu-Lei, *Materials Lab* **2022**, *1*, 210001.
- [50] J. Ren, L. Li, C. Chen, X. Chen, Z. Cai, L. Qiu, Y. Wang, X. Zhu, H. Peng, *Adv. Mater.* **2013**, *25*, 1155.
- [51] J. He, C. Lu, H. Jiang, F. Han, X. Shi, J. Wu, L. Wang, T. Chen, J. Wang, Y. Zhang, H. Yang, G. Zhang, X. Sun, B. Wang, P. Chen, Y. Wang, Y. Xia, H. Peng, *Nature* **2021**, *597*, 57.
- [52] A. Weston, E. G. Castanon, V. Enaldiev, F. Ferreira, S. Bhattacharjee, S. Xu, H. Corte-León, Z. Wu, N. Clark, A. Summerfield, T. Hashimoto, Y. Gao, W. Wang, M. Hamer, H. Read, L. Fumagalli, A. V. Kretinin, S. J. Haigh, O. Kazakova, A. K. Geim, V. I. Fal'ko, R. Gorbachev, *Nat. Nanotechnol.* **2022**, *17*, 390.
- [53] A. E. Ali, V. Jeoti, G. M. Stojanović, *Sci. Technol. Adv. Mater.* **2021**, *22*, 772.
- [54] M. Liao, C. Wang, Y. Hong, Y. Zhang, X. Cheng, H. Sun, X. Huang, L. Ye, J. Wu, X. Shi, X. Kang, X. Zhou, J. Wang, P. Li, X. Sun, P. Chen, B. Wang, Y. Wang, Y. Xia, Y. Cheng, H. Peng, *Nat. Nanotechnol.* **2022**, *17*, 372.
- [55] N. H. N. Azman, M. S. Mamat @ Mat Nazir, L. H. Ngee, Y. Sulaiman, *Int. J. Energy Res.* **2018**, *42*, 2104.
- [56] N. Elgrishi, K. J. Rountree, B. D. McCarthy, E. S. Rountree, T. T. Eisenhart, J. L. Dempsey, *J. Chem. Educ.* **2018**, *95*, 197.
- [57] N. Asthana, K. Pal, in *Nanofabrication for Smart Nanosensor Applications* (Eds: K. Pal, F. Gomes), Elsevier, London, UK **2020**.
- [58] P. S. Nnamchi, C. S. Obayi, in *Characterization of Nanomaterials* (Eds: S. M. Bhagyaraj, O. S. Oluwafemi, N. Kalarikkal, S. Thomas), Woodhead Publishing, Sawston, Cambridge **2018**.
- [59] Y. S. Choudhary, L. Jothi, G. Nageswaran, in *Spectroscopic Methods for Nanomaterials Characterization* (Eds: S. Thomas, R. Thomas, A. K. Zachariah, R. K. Mishra), Elsevier, London, UK **2017**.
- [60] M. Z. Iqbal, M. M. Faisal, S. R. Ali, *Int. J. Energy Res.* **2021**, *45*, 1449.
- [61] W. Raza, F. Ali, N. Raza, Y. Luo, K.-H. Kim, J. Yang, S. Kumar, A. Mehmood, E. E. Kwon, *Nano Energy* **2018**, *52*, 441.
- [62] R. E. Diaz, in *The Electrical Engineering Handbook* (Ed: W.-K. Chen), Academic Press, Burlington **2005**.
- [63] J. Yan, Q. Wang, T. Wei, Z. Fan, *Adv. Energy Mater.* **2014**, *4*, 1300816.
- [64] S. Zhai, H. E. Karahan, C. Wang, Z. Pei, L. Wei, Y. Chen, *Adv. Mater.* **2020**, *32*, 1902387.
- [65] Z. Zhang, X. Guo, F. Wen, Q. Shi, T. He, B. Dong, C. Lee, in *Reference Module in Biomedical Sciences*, Elsevier, London, UK **2021**.
- [66] J. Lessing, A. C. Glavan, S. B. Walker, C. Keplinger, J. A. Lewis, G. M. Whitesides, *Adv. Mater.* **2014**, *26*, 4677.
- [67] D. Maddipatla, B. B. Narakathu, M. M. Ali, A. A. Chlahawi, M. Z. Atashbar, in *2017 IEEE Sensors Applications Symp. (SAS)*, IEEE, New York, US **2017**.
- [68] D. Maddipatla, B. B. Narakathu, M. Atashbar, *Biosensors* **2020**, *10*, 199.
- [69] S. P. Sreenilayam, I. U. Ahad, V. Nicolosi, V. Acinas Garzon, D. Brabazon, *Mater. Today* **2020**, *32*, 147.
- [70] D. P. Dubal, in *Emerging Materials for Energy Conversion and Storage* (Eds: K. Y. Cheong, G. Impellizzeri, M. A. Fraga), Elsevier, London, UK **2018**.
- [71] A. Lund, N. M. van der Velden, N.-K. Persson, M. M. Hamed, C. Müller, *Mater. Sci. Eng., R* **2018**, *126*, 1.
- [72] i. Zupin, K. Dimitrovski, *Intechopen* **2010**, <https://doi.org/10.5772/10479>
- [73] Y. Zhao, Z. Zhang, Y. Ren, W. Ran, X. Chen, J. Wu, F. Gao, *J. Power Sources* **2015**, *286*, 1.
- [74] T. Lin, Y. Q. Zhang, L. Zhang, F. Klappenberger, in *Encyclopedia of Interfacial Chemistry* (Ed: K. Wandelt), Elsevier, Oxford **2018**.
- [75] C. Liao, Y. Li, S. C. Tjong, *Int. J. Mol. Sci.* **2018**, *19*, 356.
- [76] J. Yuansheng, L. Shenghua, in *Superlubricity* (Eds: A. Erdemir, J.-M. Martin), Elsevier Science BV, Amsterdam **2007**.
- [77] S. Mallakpour, S. Rashidimoghadam, in *Composite Nanoadsorbents* (Eds: G. Z. Kyzas, A. C. Mitropoulos), Elsevier, London, UK **2019**.
- [78] A. Eatemadi, H. Daraee, H. Karimkhanloo, M. Kouhi, N. Zarghami, A. Akbarzadeh, M. Abasi, Y. Hanifehpour, S. W. Joo, *Nanoscale Res. Lett.* **2014**, *9*, 393.
- [79] Z. Lu, R. Raad, F. Safaei, J. Xi, Z. Liu, J. Foroughi, *Front. Mater.* **2019**, *6*, 1.
- [80] D. Zhang, M. Miao, H. Niu, Z. Wei, *ACS Nano* **2014**, *8*, 4571.
- [81] C. Choi, J. W. Park, K. J. Kim, D. W. Lee, M. J. de Andrade, S. H. Kim, S. Gambhir, G. M. Spinks, R. H. Baughman, S. J. Kim, *RSC Adv.* **2018**, *8*, 13112.
- [82] C. Guan, X. Qian, X. Wang, Y. Cao, Q. Zhang, A. Li, J. Wang, *Nanotechnology* **2015**, *26*, 094001.
- [83] T. Lv, Y. Yao, N. Li, T. Chen, *Angew. Chem., Int. Ed.* **2016**, *55*, 9191.
- [84] H. Marsh, F. Rodríguez-Reinoso, in *Activated Carbon* (Eds: H. Marsh, F. Rodríguez-Reinoso), Elsevier Science Ltd, Oxford **2006**.
- [85] D. Talarico, F. Arduini, A. Constantino, M. Del Carlo, D. Compagnone, D. Moscone, G. Palleschi, *Electrochem. Commun.* **2015**, *60*, 78.
- [86] P. Kossyrev, *J. Power Sources* **2012**, *201*, 347.
- [87] K. Yang, K. Cho, S. Kim, *Sci. Rep.* **2018**, *8*, 11989.
- [88] N. Jäckel, D. Weingarth, M. Zeiger, M. Aslan, I. Grobelsek, V. Presser, *J. Power Sources* **2014**, *272*, 1122.
- [89] W. Gu, G. Yushin, *Wiley Interdiscip. Rev.: Energy Environ.* **2014**, *3*, 424.
- [90] P. Sinha, S. Banerjee, K. K. Kar, in *Handbook of Nanocomposite Supercapacitor Materials II: Performance* (Ed: K. K. Kar), Springer International Publishing, Cham **2020**.
- [91] J.-H. Choi, *Sep. Purif. Technol.* **2010**, *70*, 362.

- [92] P. Merin, P. Jimmy Joy, M. N. Muralidharan, E. Veena Gopalan, A. Seema, *Chem. Eng. Technol.* **2021**, *44*, 844.
- [93] J. Phiri, J. Dou, T. Vuorinen, P. A. C. Gane, T. C. Maloney, *ACS Omega* **2019**, *4*, 18108.
- [94] I. Piñeiro-Prado, D. Salinas-Torres, R. Ruiz-Rosas, E. Morallón, D. Cazorla-Amorós, *Front. Mater.* **2016**, *3*, 16.
- [95] S. Afroj, L. Britnell, T. Hasan, D. V. Andreeva, K. S. Novoselov, N. Karim, *Adv. Funct. Mater.* **2021**, *31*, 2107407.
- [96] S. Bhattacharjee, R. Joshi, A. A. Chughtai, C. R. Macintyre, *Adv. Mater. Interfaces* **2019**, *6*, 1900622.
- [97] N. Karim, S. Afroj, S. Tan, P. He, A. Fernando, C. Carr, K. S. Novoselov, *ACS Nano* **2017**, *11*, 12266.
- [98] M. H. Islam, S. Afroj, M. A. Uddin, D. V. Andreeva, K. S. Novoselov, N. Karim, *Adv. Funct. Mater.* **2022**, 2205723.
- [99] M. A. Mutalib, N. M. Rashid, F. Aziz, in *Carbon-Based Polymer Nanocomposites for Environmental and Energy Applications* (Eds: A. F. Ismail, P. S. Goh), Elsevier, London, UK **2018**.
- [100] M. Inagaki, F. Kang, M. Toyoda, H. Konno, in *Advanced Materials Science and Engineering of Carbon* (Eds: M. Inagaki, F. Kang, M. Toyoda, H. Konno), Butterworth-Heinemann, Boston **2014**.
- [101] R. Kumar, S. Sahoo, E. Joanni, R. K. Singh, R. M. Yadav, R. K. Verma, D. P. Singh, W. K. Tan, A. Pérez del Pino, S. A. Moshkalev, A. Matsuda, *Nano Res.* **2019**, *12*, 2655.
- [102] D. G. Papageorgiou, I. A. Kinloch, R. J. Young, *Carbon* **2015**, *95*, 460.
- [103] A. Ciesielski, P. Samori, *Chem. Soc. Rev.* **2014**, *43*, 381.
- [104] N. Karim, M. Zhang, S. Afroj, V. Koncherry, P. Potluri, K. S. Novoselov, *RSC Adv.* **2018**, *8*, 16815.
- [105] A. S. Lemine, M. M. Zagho, T. M. Altahtamouni, N. Bensalah, *Int. J. Energy Res.* **2018**, *42*, 4284.
- [106] M. Chakraborty, M. S. J. Hashmi, *Reference Module Mater. Sci. Mater. Eng.* **2018**, <https://doi.org/10.1016/B978-0-12-803581-8.10319-4>
- [107] S. Banerjee, J. H. Lee, T. Kuila, N. H. Kim, in *Fillers and Reinforcements for Advanced Nanocomposites* (Eds: Y. Dong, R. Umer, A. K.-T. Lau), Woodhead Publishing, Sawston, Cambridge **2015**.
- [108] T. Xu, L. Sun, in *Defects in Advanced Electronic Materials and Novel Low Dimensional Structures* (Eds: J. Stehr, I. Buyanova, W. Chen), Woodhead Publishing, Sawston, Cambridge **2018**.
- [109] S. Bhattacharjee, C. R. Macintyre, P. Bahl, U. Kumar, X. Wen, K.-F. Aguey-Zinsou, A. A. Chughtai, R. Joshi, *Adv. Mater. Interfaces* **2020**, *7*, 2000814.
- [110] N. Karim, S. Afroj, D. Leech, A. M. Abdelkader, in *Oxide Electronics* (Ed: A. Ray), John Wiley & Sons, Ltd, Hoboken, New Jersey, US **2021**, p. 2.
- [111] S. Afroj, N. Karim, Z. Wang, S. Tan, P. He, M. Holwill, D. Ghazaryan, A. Fernando, K. S. Novoselov, *ACS Nano* **2019**, *13*, 3847.
- [112] F. Sarker, P. Potluri, S. Afroj, V. Koncherry, K. S. Novoselov, N. Karim, *ACS Appl. Mater. Interfaces* **2019**, *11*, 21166.
- [113] R. S. Kalash, V. K. Lakshmanan, C.-S. Cho, I.-K. Park, in *Biomaterials Nanoarchitectonics* (Ed: M. Ebara), William Andrew Publishing, Norwich, NY **2016**.
- [114] K. Radhapyari, S. Datta, S. Dutta, N. Jadon, R. Khan, in *Two-Dimensional Nanostructures for Biomedical Technology* (Eds: R. Khan, S. Barua), Elsevier, London, UK **2020**.
- [115] R. Kecili, C. M. Hussain, in *Nanomaterials in Chromatography* (Ed: C. M. Hussain), Elsevier, London, UK **2018**.
- [116] P. Vandezande, in *Pervaporation, Vapour Permeation and Membrane Distillation* (Eds: A. Basile, A. Figoli, M. Khayet), Woodhead Publishing, Oxford **2015**.
- [117] F. Sarker, N. Karim, S. Afroj, V. Koncherry, K. S. Novoselov, P. Potluri, *ACS Appl. Mater. Interfaces* **2018**, *10*, 34502.
- [118] M. Inagaki, F. Kang, in *Materials Science and Engineering of Carbon: Fundamentals (Second Edition)* (Eds: M. Inagaki, F. Kang), Butterworth-Heinemann, Oxford **2014**.
- [119] N. Karim, F. Sarker, S. Afroj, M. Zhang, P. Potluri, K. S. Novoselov, *Adv. Sustainable Syst.* **2021**, *5*, 2000228.
- [120] V. B. Mohan, R. Brown, K. Jayaraman, D. Bhattacharyya, *Mater. Sci. Eng., B* **2015**, *193*, 49.
- [121] R. Bayan, N. Karak, in *Two-Dimensional Nanostructures for Biomedical Technology* (Eds: R. Khan, S. Barua), Elsevier, London, UK **2020**.
- [122] M. H. Islam, M. R. Islam, M. Dulal, S. Afroj, N. Karim, *iScience* **2021**, *25*, 103597.
- [123] J. Phiri, P. Gane, T. C. Maloney, *Mater. Sci. Eng., B* **2017**, *215*, 9.
- [124] L.-N. Jin, F. Shao, C. Jin, J.-N. Zhang, P. Liu, M.-X. Guo, S.-W. Bian, *Electrochim. Acta* **2017**, *249*, 387.
- [125] K. Liu, Y. Yao, T. Lv, H. Li, N. Li, Z. Chen, G. Qian, T. Chen, *J. Power Sources* **2020**, *446*, 227355.
- [126] Y. Li, C. Chen, *J. Mater. Sci.* **2017**, *52*, 12348.
- [127] M. Rapisarda, A. Damasco, G. Abbate, M. Meo, *ACS Omega* **2020**, *5*, 32426.
- [128] I. I. Gürten Inal, *Türk. J. Chem.* **2021**, *45*, 927.
- [129] I. Shown, A. Ganguly, L.-C. Chen, K.-H. Chen, *Energy Sci. Eng.* **2015**, *3*, 2.
- [130] S. Bhandari, in *Polyaniline Blends, Composites, and Nanocomposites* (Eds: P. M. Visakh, C. D. Pina, E. Falletta), Elsevier, London, UK **2018**.
- [131] H. Wang, J. Lin, Z. X. Shen, *J. Sci.: Adv. Mater. Devices* **2016**, *1*, 225.
- [132] G. Konwar, S. C. Sarma, D. Mahanta, S. C. Peter, *ACS Omega* **2020**, *5*, 14494.
- [133] Ruchi, V. Gupta, R. Pal, S. L. Goyal, *AIP Conf. Proc.* **2021**, *2369*, 020051.
- [134] Y.-Y. Horng, Y.-C. Lu, Y.-K. Hsu, C.-C. Chen, L.-C. Chen, K.-H. Chen, *J. Power Sources* **2010**, *195*, 4418.
- [135] M. M. Rahman, P. M. Joy, M. N. Uddin, M. Z. B. Mukhlis, M. M. R. Khan, *Heliyon* **2021**, *7*, e07407.
- [136] J. Parayangattil Jyothibasua, M.-Z. Chen, R.-H. Lee, *ACS Omega* **2020**, *5*, 6441.
- [137] P. Xue, X. M. Tao, K. W. Y. Kwok, M. Y. Leung, T. X. Yu, *Text. Res. J.* **2004**, *74*, 929.
- [138] A. Harlin, M. Ferenets, in *Intelligent Textiles and Clothing* (Ed: H. R. Mattila), Woodhead Publishing, Sawston, Cambridge **2006**.
- [139] K. Kakaei, M. D. Esrafil, A. Ehsani, in *Interface Science and Technology, Vol. 27* (Eds: K. Kakaei, M. D. Esrafil, A. Ehsani), Elsevier, London, UK **2019**.
- [140] Y. Huang, H. Li, Z. Wang, M. Zhu, Z. Pei, Q. Xue, Y. Huang, C. Zhi, *Nano Energy* **2016**, *22*, 422.
- [141] M. Feng, W. Lu, Y. Zhou, R. Zhen, H. He, Y. Wang, C. Li, *Sci. Rep.* **2020**, *10*, 15370.
- [142] Y. He, X. Ning, L. Wan, *Polym. Bull.* **2021**.
- [143] S. Nie, Z. Li, Y. Yao, Y. Jin, *Front. Chem.* **2021**, *9*, 803509.
- [144] V. Koncar, in *Smart Textiles for In Situ Monitoring of Composites* (Ed: V. Koncar), Woodhead Publishing, Sawston, Cambridge **2019**.
- [145] Z. Zhao, G. F. Richardson, Q. Meng, S. Zhu, H.-C. Kuan, J. Ma, *Nanotechnology* **2015**, *27*, 042001.
- [146] B. Li, H. Lopez-Beltran, C. Siu, K. H. Skorenko, H. Zhou, W. E. Bernier, M. S. Whittingham, W. E. Jones, *ACS Appl. Energy Mater.* **2020**, *3*, 1559.
- [147] M. Rajesh, C. J. Raj, R. Manikandan, B. C. Kim, S. Y. Park, K. H. Yu, *Mater. Today Energy* **2017**, *6*, 96.
- [148] B. J. Worfolk, S. C. Andrews, S. Park, J. Reinspach, N. Liu, M. F. Toney, S. C. B. Mannsfeld, Z. Bao, *Proc. Natl. Acad. Sci. USA* **2015**, *112*, 14138.
- [149] L. Manjakkal, A. Pullanchiyodan, N. Yogeswaran, E. S. Hosseini, R. Dahiya, *Adv. Mater.* **2020**, *32*, 1907254.
- [150] Y. Liu, B. Weng, J. M. Razal, Q. Xu, C. Zhao, Y. Hou, S. Seyedin, R. Jalili, G. G. Wallace, J. Chen, *Sci. Rep.* **2015**, *5*, 17045.
- [151] G. Liu, X. Chen, J. Liu, C. Liu, J. Xu, Q. Jiang, Y. Jia, F. Jiang, X. Duan, P. Liu, *Electrochim. Acta* **2021**, *365*, 137363.

- [152] S. Khasim, A. Pasha, N. Badi, M. Lakshmi, Y. K. Mishra, *RSC Adv.* **2020**, *10*, 10526.
- [153] M. Yoonessi, A. Borenstein, M. F. El-Kady, C. L. Turner, H. Wang, A. Z. Stieg, L. Pilon, *ACS Appl. Energy Mater.* **2019**, *2*, 4629.
- [154] C. Chukwuneka, J. O. Madu, F. V. Adams, O. T. Johnson, in *Nanostructured Metal-Oxide Electrode Materials for Water Purification: Fabrication, Electrochemistry and Applications* (Eds: O. M. Ama, S. S. Ray), Springer International Publishing, Cham **2020**.
- [155] L. Zhou, C. Li, X. Liu, Y. Zhu, Y. Wu, T. van Ree, in *Metal Oxides in Energy Technologies* (Ed: Y. Wu), Elsevier, London, UK **2018**.
- [156] D. Majumdar, T. Maiyalagan, Z. Jiang, *ChemElectroChem* **2019**, *6*, 4343.
- [157] H. Xia, Y. Shirley Meng, G. Yuan, C. Cui, L. Lu, *Electrochem. Solid-State Lett.* **2012**, *15*, A60.
- [158] V. Subramanian, S. C. Hall, P. H. Smith, B. Rambabu, *Solid State Ionics* **2004**, *175*, 511.
- [159] S. Jeon, J. H. Jeong, H. Yoo, H. K. Yu, B.-H. Kim, M. H. Kim, *ACS Appl. Nano Mater.* **2020**, *3*, 3847.
- [160] V. K. A. Muniraj, P. K. Dwivedi, P. S. Tamhane, S. Szunerits, R. Boukherroub, M. V. Shelke, *ACS Appl. Mater. Interfaces* **2019**, *11*, 18349.
- [161] Z. J. Han, S. Pineda, A. T. Murdock, D. H. Seo, K. Ostrikov, A. Bendavid, *J. Mater. Chem. A* **2017**, *5*, 17293.
- [162] D. D. L. Chung, in *Carbon Composites (Second Edition)* (Ed: D. D. L. Chung), Butterworth-Heinemann, Oxford, UK **2017**.
- [163] K. Nishio, in *Encyclopedia of Electrochemical Power Sources* (Ed: J. Garche), Elsevier, Amsterdam **2009**.
- [164] K. Kordesch, W. Taucher-Mautner, in *Encyclopedia of Electrochemical Power Sources* (Ed: J. Garche), Elsevier, Amsterdam **2009**.
- [165] M. Zhang, D. Yang, J. Li, *Vacuum* **2020**, *178*, 109455.
- [166] G. Zhu, Z. He, J. Chen, J. Zhao, X. Feng, Y. Ma, Q. Fan, L. Wang, W. Huang, *Nanoscale* **2014**, *6*, 1079.
- [167] D. Wu, X. Xie, Y. Zhang, D. Zhang, W. Du, X. Zhang, B. Wang, *Front. Mater.* **2020**, *7*, 1.
- [168] L. Xu, M. Jia, Y. Li, X. Jin, F. Zhang, *Sci. Rep.* **2017**, *7*, 12857.
- [169] Y. Chen, X. Li, L. Zhou, Y.-W. Mai, H. Huang, in *Multifunctionality of Polymer Composites* (Eds: K. Friedrich, U. Breuer), William Andrew Publishing, Oxford **2015**.
- [170] H. Xiao, S. Yao, H. Liu, F. Qu, X. Zhang, X. Wu, *Prog. Nat. Sci.: Mater. Int.* **2016**, *26*, 271.
- [171] S. D. Dhas, P. S. Maldar, M. D. Patil, A. B. Nagare, M. R. Waikar, R. G. Sonkawade, A. V. Moholkar, *Vacuum* **2020**, *181*, 109646.
- [172] S. Vijayakumar, S. Nagamuthu, G. Muralidharan, *ACS Appl. Mater. Interfaces* **2013**, *5*, 2188.
- [173] S. Ramesh, K. Karuppasamy, H. M. Yadav, J.-J. Lee, H.-S. Kim, H.-S. Kim, J.-H. Kim, *Sci. Rep.* **2019**, *9*, 6034.
- [174] H. Jiang, C. Li, T. Sun, J. Ma, *Chem. Commun.* **2012**, *48*, 2606.
- [175] J. Cai, D. Zhang, W.-P. Ding, Z.-Z. Zhu, G.-Z. Wang, J.-R. He, H.-B. Wang, P. Fei, T.-L. Si, *ACS Omega* **2020**, *5*, 29896.
- [176] A.-L. Brisse, P. Stevens, G. Toussaint, O. Crosnier, T. Brousse, *Materials* **2018**, *11*, 1178.
- [177] S. K. Meher, G. R. Rao, *J. Phys. Chem. C* **2011**, *115*, 15646.
- [178] C. Guo, M. Yin, C. Wu, J. Li, C. Sun, C. Jia, T. Li, L. Hou, Y. Wei, *Front. Chem.* **2018**, *6*, 1.
- [179] I. Rabani, J. Yoo, H.-S. Kim, D. V. Lam, S. Hussain, K. Karuppasamy, Y.-S. Seo, *Nanoscale* **2021**, *13*, 355.
- [180] M. Morozova, P. Kluson, J. Krysa, M. Vesely, P. Dzik, O. Solcova, *Proc. Eng.* **2012**, *42*, 573.
- [181] Q. Yun, L. Li, Z. Hu, Q. Lu, B. Chen, H. Zhang, *Adv. Mater.* **2020**, *32*, 1903826.
- [182] S. Tanwar, A. Arya, A. Gaur, A. L. Sharma, *J. Phys.: Condens. Matter* **2021**, *33*, 303002.
- [183] N. Joseph, P. M. Shafi, A. C. Bose, *Energy Fuels* **2020**, *34*, 6558.
- [184] A. Schneemann, R. Dong, F. Schwotzer, H. Zhong, I. Senkovska, X. Feng, S. Kaskel, *Chem. Sci.* **2021**, *12*, 1600.
- [185] D. M. Soares, S. Mukherjee, G. Singh, *Chem. - Eur. J.* **2020**, *26*, 6320.
- [186] J. Bao, K. Jeppson, M. Edwards, Y. Fu, L. Ye, X. Lu, J. Liu, *Electron. Mater. Lett.* **2016**, *12*, 1.
- [187] J. Pu, K. Zhang, Z. Wang, C. Li, K. Zhu, Y. Yao, G. Hong, *Adv. Funct. Mater.* **2021**, *31*, 2106315.
- [188] K. Zhang, Y. Feng, F. Wang, Z. Yang, J. Wang, *J. Mater. Chem. C* **2017**, *5*, 11992.
- [189] O. Ergen, *AIP Adv.* **2020**, *10*, 045040.
- [190] T. Gao, L.-j. Gong, Z. Wang, Z.-k. Yang, W. Pan, L. He, J. Zhang, E.-c. Ou, Y. Xiong, W. Xu, *Mater. Lett.* **2015**, *159*, 54.
- [191] S. Byun, J. H. Kim, S. H. Song, M. Lee, J.-J. Park, G. Lee, S. H. Hong, D. Lee, *Chem. Mater.* **2016**, *28*, 7750.
- [192] S. T. Gunday, E. Cevik, A. Yusuf, A. Bozkurt, *J. Energy Storage* **2019**, *21*, 672.
- [193] M. A. Bissett, I. A. Kinloch, R. A. W. Dryfe, *ACS Appl. Mater. Interfaces* **2015**, *7*, 17388.
- [194] M. Acerce, D. Voiry, M. Chhowalla, *Nat. Nanotechnol.* **2015**, *10*, 313.
- [195] S. Wei, R. Zhou, G. Wang, *ACS Omega* **2019**, *4*, 15780.
- [196] H. Gupta, S. Chakrabarti, S. Mothkuri, B. Padya, T. N. Rao, P. K. Jain, *Mater. Today: Proc.* **2020**, *26*, 20.
- [197] F. Ghasemi, M. Jalali, A. Abdollahi, S. Mohammadi, Z. Sanaee, S. Mohajerzadeh, *RSC Adv.* **2017**, *7*, 52772.
- [198] F. Wang, J. Ma, K. Zhou, X. Li, *Mater. Chem. Phys.* **2020**, *244*, 122215.
- [199] Q. Chen, F. Xie, G. Wang, K. Ge, H. Ren, M. Yan, Q. Wang, H. Bi, *Ionics* **2021**, *27*, 4083.
- [200] M. M. Baig, E. Pervaiz, M. Yang, I. H. Gul, *Front. Mater.* **2020**, *7*, 580424.
- [201] R. Garg, A. Agarwal, M. Agarwal, *Mater. Res. Express* **2020**, *7*, 022001.
- [202] Y. Sun, D. Chen, Z. Liang, *Mater. Today Energy* **2017**, *5*, 22.
- [203] A. Ahmed, M. M. Hossain, B. Adak, S. Mukhopadhyay, *Chem. Mater.* **2020**, *32*, 10296.
- [204] X. Li, Z. Huang, C. Zhi, *Front. Mater.* **2019**, *6*, 1.
- [205] B. Anasori, M. R. Lukatskaya, Y. Gogotsi, *Nat. Rev. Mater.* **2017**, *2*, 16098.
- [206] A. Ahmed, S. Sharma, B. Adak, M. M. Hossain, A. M. LaChance, S. Mukhopadhyay, L. Sun, *InfoMat* **2022**, *4*, e12295.
- [207] A. Ahmed, S. Sharma, B. Adak, M. M. Hossain, A. M. LaChance, S. Mukhopadhyay, L. Sun, *InfoMat* **2022**, *4*, e12295.
- [208] B. Pal, S. Yang, S. Ramesh, V. Thangadurai, R. Jose, *Nanoscale Adv.* **2019**, *1*, 3807.
- [209] B. Balli, A. Şavk, F. Şen, in *Nanocarbon and its Composites* (Eds: A. Khan, M. Jawaid, Inamuddin, A. M. Asiri), Woodhead Publishing, Sawston, Cambridge **2019**.
- [210] W. Fu, K. Turcheniuk, O. Naumov, R. Mysyk, F. Wang, M. Liu, D. Kim, X. Ren, A. Magasinski, M. Yu, X. Feng, Z. L. Wang, G. Yushin, *Mater. Today* **2021**, *48*, 176.
- [211] Q. Wang, S. Chen, D. Zhang, in *Carbon Nanotube Fibers and Yarns* (Ed: M. Miao), Woodhead Publishing, Sawston, Cambridge **2020**.
- [212] M. Z. Iqbal, S. Zakar, S. S. Haider, *J. Electroanal. Chem.* **2020**, *858*, 113793.
- [213] Y. Matsuda, M. Morita, *J. Power Sources* **1987**, *20*, 273.
- [214] E. Jónsson, *Energy Storage Mater.* **2020**, *25*, 827.
- [215] L. Yu, G. Z. Chen, *Front. Chem.* **2019**, *7*, 7.
- [216] M. Zhu, J. Wu, Y. Wang, M. Song, L. Long, S. H. Siyal, X. Yang, G. Sui, *J. Energy Chem.* **2019**, *37*, 126.
- [217] X. Cheng, J. Pan, Y. Zhao, M. Liao, H. Peng, *Adv. Energy Mater.* **2018**, *8*, 1702184.
- [218] R. Arunkumar, R. S. Babu, M. Usha Rani, S. Rajendran, *Ionics* **2017**, *23*, 3097.
- [219] N. Boaretto, L. Meabe, M. Martinez-Ibañez, M. Armand, H. Zhang, *J. Electrochem. Soc.* **2020**, *167*, 070524.
- [220] K. Chatterjee, J. Tabor, T. K. Ghosh, *Fibers* **2019**, *7*, 51.
- [221] M. Joshi, B. S. Butola, in *Advances in the Dyeing and Finishing of Technical Textiles* (Ed: M. L. Gulrajani), Woodhead Publishing, Sawston, Cambridge **2013**.

- [222] I. A. Neacșu, A. I. Nicoară, O. R. Vasile, B. Ș. Vasile, in *Nanobiomaterials in Hard Tissue Engineering* (Ed: A. M. Grumezescu), William Andrew Publishing, Norwich, NY **2016**.
- [223] L. Hu, M. Pasta, F. La Mantia, L. Cui, S. Jeong, H. D. Deshazer, J. W. Choi, S. M. Han, Y. Cui, *Nano Lett.* **2010**, *10*, 708.
- [224] G. Yu, L. Hu, M. Vosgueritchian, H. Wang, X. Xie, J. R. McDonough, X. Cui, Y. Cui, Z. Bao, *Nano Lett.* **2011**, *11*, 2905.
- [225] S. Afroj, S. Tan, A. M. Abdelkader, K. S. Novoselov, N. Karim, *Adv. Funct. Mater.* **2020**, *30*, 2000293.
- [226] A. Berni, M. Mennig, H. Schmidt, in *Sol-Gel Technologies for Glass Producers and Users* (Eds: M. A. Aegerter, M. Mennig), Springer US, Boston, MA **2004**.
- [227] L. Hu, F. La Mantia, H. Wu, X. Xie, J. McDonough, M. Pasta, Y. Cui, *Adv. Energy Mater.* **2011**, *1*, 1012.
- [228] R. Alagirusamy, J. Eichhoff, T. Gries, S. Jockenhoevel, *J. Text. Inst.* **2013**, *104*, 270.
- [229] X. Chen, H. Lin, J. Deng, Y. Zhang, X. Sun, P. Chen, X. Fang, Z. Zhang, G. Guan, H. Peng, *Adv. Mater.* **2014**, *26*, 8126.
- [230] J. Deng, Y. Zhang, Y. Zhao, P. Chen, X. Cheng, H. Peng, *Angew. Chem., Int. Ed.* **2015**, *54*, 15419.
- [231] T. Chen, R. Hao, H. Peng, L. Dai, *Angew. Chem., Int. Ed.* **2015**, *54*, 618.
- [232] C. Choi, S. H. Kim, H. J. Sim, J. A. Lee, A. Y. Choi, Y. T. Kim, X. Lepró, G. M. Spinks, R. H. Baughman, S. J. Kim, *Sci. Rep.* **2015**, *5*, 9387.
- [233] V. Beedasy, P. J. Smith, *Materials* **2020**, *13*, 704.
- [234] B. W. Blunden, J. W. Birkenshaw, in *The Printing Ink Manual* (Eds: R. H. Leach, C. Armstrong, J. F. Brown, M. J. Mackenzie, L. Randall, H. G. Smith), Springer US, Boston, MA **1988**.
- [235] L. W. C. Miles, *Textile printing*, Society of Dyers and Colourists, Bradford **2003**.
- [236] H. R. Shemilt, *Circuit World* **1975**, *1*, 7.
- [237] D. Novaković, N. Kašiković, G. Vladić, M. Pál, in *Printing on Polymers* (Eds: J. Izdebska, S. Thomas), William Andrew Publishing, Norwich, NY **2016**.
- [238] K. Jost, C. R. Perez, J. K. McDonough, V. Presser, M. Heon, G. Dion, Y. Gogotsi, *Energy Environ. Sci.* **2011**, *4*, 5060.
- [239] A. M. Abdelkader, N. Karim, C. Vallés, S. Afroj, K. S. Novoselov, S. G. Yeates, *2D Mater.* **2017**, *4*, 035016.
- [240] Q. Lu, L. Liu, S. Yang, J. Liu, Q. Tian, W. Yao, Q. Xue, M. Li, W. Wu, *J. Power Sources* **2017**, *361*, 31.
- [241] C. Cie, in *Ink Jet Textile Printing* (Ed: C. Cie), Woodhead Publishing, Sawston, Cambridge **2015**.
- [242] S. H. Ko, in *Micromanufacturing Engineering and Technology (Second Edition)* (Ed: Y. Qin), William Andrew Publishing, Boston **2015**.
- [243] E. B. Secor, P. L. Prabhuramirashi, K. Puntambekar, M. L. Geier, M. C. Hersam, *J. Phys. Chem. Lett.* **2013**, *4*, 1347.
- [244] I. Kim, B. Ju, Y. Zhou, B. M. Li, J. S. Jur, *ACS Appl. Mater. Interfaces* **2021**, *13*, 24081.
- [245] A. Manthiram, X. Zhao, W. Li, in *Functional Materials for Sustainable Energy Applications* (Eds: J. A. Kilner, S. J. Skinner, S. J. C. Irvine, P. P. Edwards), Woodhead Publishing, Sawston, Cambridge **2012**.
- [246] J. Yang, F. Zheng, B. Derby, *Langmuir* **2021**, *37*, 26.
- [247] A. Soleimani-Gorgani, in *Printing on Polymers* (Eds: J. Izdebska, S. Thomas), William Andrew Publishing, Norwich, NY **2016**.
- [248] B. S. Cook, B. Tehrani, J. R. Cooper, S. Kim, M. M. Tentzeris, in *Handbook of Flexible Organic Electronics* (Ed: S. Logothetidis), Woodhead Publishing, Oxford **2015**.
- [249] R. Daly, T. S. Harrington, G. D. Martin, I. M. Hutchings, *Int. J. Pharm.* **2015**, *494*, 554.
- [250] C. Parraman, in *Colour Design (Second Edition)* (Ed: J. Best), Woodhead Publishing, Sawston, Cambridge **2017**.
- [251] Z. Yin, Y. Huang, N. Bu, X. Wang, Y. Xiong, *Chin. Sci. Bull.* **2010**, *55*, 3383.
- [252] Y. Liu, B. Derby, *Phys. Fluids* **2019**, *31*, 032004.
- [253] P. J. Smith, A. Morrin, *J. Mater. Chem.* **2012**, *22*, 10965.
- [254] Z. Stempien, M. Khalid, M. Kozanecki, P. Filipczak, A. Wrzeńska, E. Korzeniewska, E. Szaśiadek, *Materials* **2021**, *14*, 3577.
- [255] P. Sundriyal, S. Bhattacharya, *Sci. Rep.* **2020**, *10*, 13259.
- [256] N. Karim, S. Afroj, S. Tan, K. S. Novoselov, S. G. Yeates, *Sci. Rep.* **2019**, *9*, 8035.
- [257] P. Sundriyal, S. Bhattacharya, *ACS Appl. Energy Mater.* **2019**, *2*, 1876.
- [258] M. M. Denn, in *Computational Analysis of Polymer Processing* (Eds: J. R. A. Pearson, S. M. Richardson), Springer, Netherlands, Dordrecht **1983**.
- [259] A. Mirabedini, J. Foroughi, G. G. Wallace, *RSC Adv.* **2016**, *6*, 44687.
- [260] T. Onggar, I. Kruppke, C. Cherif, *Polymers* **2020**, *12*, 2867.
- [261] Y. Imura, R. M. C. Hogan, M. Jaffe, in *Advances in Filament Yarn Spinning of Textiles and Polymers* (Ed: D. Zhang), Woodhead Publishing, Sawston, Cambridge **2014**.
- [262] B. Ozipek, H. Karakas, in *Advances in Filament Yarn Spinning of Textiles and Polymers* (Ed: D. Zhang), Woodhead Publishing, Sawston, Cambridge **2014**.
- [263] Q. Zhang, X. Wang, D. Chen, X. Jing, *J. Appl. Polym. Sci.* **2002**, *85*, 1458.
- [264] L. Kou, T. Huang, B. Zheng, Y. Han, X. Zhao, K. Gopalsamy, H. Sun, C. Gao, *Nat. Commun.* **2014**, *5*, 3754.
- [265] A. Rawal, S. Mukhopadhyay, in *Advances in Filament Yarn Spinning of Textiles and Polymers* (Ed: D. Zhang), Woodhead Publishing, Sawston, Cambridge **2014**.
- [266] B. Kim, Y. Koncar, E. Devaux, C. Dufour, P. Viallier, *Synth. Met.* **2004**, *146*, 167.
- [267] Q. Huang, L. Liu, D. Wang, J. Liu, Z. Huang, Z. Zheng, *J. Mater. Chem. A* **2016**, *4*, 6802.
- [268] W. Zhong, in *Advances in Smart Medical Textiles* (Ed: L. van Langenhove), Woodhead Publishing, Oxford **2016**.
- [269] Q. Q. Ni, X. D. Jin, H. Xia, F. Liu, in *Advances in Filament Yarn Spinning of Textiles and Polymers* (Ed: D. Zhang), Woodhead Publishing, Sawston, Cambridge **2014**.
- [270] T. A. Arica, T. Isik, T. Guner, N. Horzum, M. M. Demir, *Macromol. Mater. Eng.* **2021**, *306*, 2100143.
- [271] M. Wei, J. Lee, B. Kang, J. Mead, *Macromol. Rapid Commun.* **2005**, *26*, 1127.
- [272] C. H. Hsu, H. Shih, S. Subramoney, A. J. Epstein, *Synth. Met.* **1999**, *101*, 677.
- [273] Q. Zhang, H. Jin, X. Wang, X. Jing, *Synth. Met.* **2001**, *123*, 481.
- [274] H. Okuzaki, M. Ishihara, *Macromol. Rapid Commun.* **2003**, *24*, 261.
- [275] J. Jianming, P. Wei, Y. Shenglin, L. Guang, *Synth. Met.* **2005**, *149*, 181.
- [276] Q.-Z. Yu, M.-M. Shi, M. Deng, M. Wang, H.-Z. Chen, *Mater. Sci. Eng., B* **2008**, *150*, 70.
- [277] J. Foroughi, G. M. Spinks, G. G. Wallace, *Synth. Met.* **2009**, *159*, 1837.
- [278] H. Okuzaki, Y. Harashina, H. Yan, *Eur. Polym. J.* **2009**, *45*, 256.
- [279] K. Ketpang, J. S. Park, *Synth. Met.* **2010**, *160*, 1603.
- [280] N. Liu, G. Fang, J. Wan, H. Zhou, H. Long, X. Zhao, *J. Mater. Chem.* **2011**, *21*, 18962.
- [281] A. Soroudi, M. Skrifvars, H. Liu, *J. Appl. Polym. Sci.* **2011**, *119*, 558.
- [282] J. Fanous, M. Schweizer, D. Schawaller, M. R. Buchmeiser, *Macromol. Mater. Eng.* **2012**, *297*, 123.
- [283] Y. Zhang, G. C. Rutledge, *Macromolecules* **2012**, *45*, 4238.
- [284] A. Soroudi, M. Skrifvars, *Polym. Eng. Sci.* **2012**, *52*, 1606.
- [285] Q. Gao, H. Meguro, S. Okamoto, M. Kimura, *Langmuir* **2012**, *28*, 17593.
- [286] X. Li, Y. Liu, Z. Shi, C. Li, G. Chen, *RSC Adv.* **2014**, *4*, 40385.
- [287] W. Zhao, B. Yalcin, M. Cakmak, *Synth. Met.* **2015**, *203*, 107.
- [288] B. Weise, L. Völkel, G. Köppe, S. Schriever, J. Mroszczok, J. Köhler, P. Scheffler, M. Wegener, G. Seide, *Mater. Today: Proc.* **2017**, *4*, S135.
- [289] X. Li, J. Ming, X. Ning, *J. Appl. Polym. Sci.* **2019**, *136*, 47127.
- [290] W. Liu, J. Zhang, H. Liu, *Polymers* **2019**, *11*, 1.

- [291] P. Perdigão, B. M. Morais Faustino, J. Faria, J. P. Canejo, J. P. Borges, I. Ferreira, A. C. Baptista, *Fibers* **2020**, *8*, 24.
- [292] S. Bhattacharya, I. Roy, A. Tice, C. Chapman, R. Udangawa, V. Chakrapani, J. L. Plawsky, R. J. Linhardt, *ACS Appl. Mater. Interfaces* **2020**, *12*, 19369.
- [293] F. Basile, P. Benito, G. Fornasari, M. Monti, E. Scavetta, D. Tonelli, A. Vaccari, in *Studies in Surface Science and Catalysis*, Vol. 175 (Eds: E. M. Gaigneaux, M. Devillers, S. Hermans, P. A. Jacobs, J. A. Martens, P. Ruiz), Elsevier, London, UK **2010**.
- [294] A. Karatutlu, A. Barhoum, A. Sapelkin, in *Emerging Applications of Nanoparticles and Architecture Nanostructures* (Eds: A. Barhoum, A. S. H. Makhlof), Elsevier, London, UK **2018**.
- [295] E. Gasana, P. Westbroek, J. Hakuzimana, K. De Clerck, G. Prinotakis, P. Kiekens, D. Tseles, *Surf. Coat. Technol.* **2006**, *201*, 3547.
- [296] Y. Zhao, Z. Cai, X. Fu, B. Song, H. Zhu, *Synth. Met.* **2013**, *175*, 1.
- [297] S. H. Feng, G. H. Li, in *Modern Inorganic Synthetic Chemistry (Second Edition)* (Eds: R. Xu, Y. Xu), Elsevier, Amsterdam **2017**.
- [298] R. Dorey, in *Ceramic Thick Films for MEMS and Microdevices* (Ed: R. Dorey), William Andrew Publishing, Oxford **2012**.
- [299] Y. Huang, Y. Huang, M. Zhu, W. Meng, Z. Pei, C. Liu, H. Hu, C. Zhi, *ACS Nano* **2015**, *9*, 6242.
- [300] Z. Li, T. Huang, W. Gao, Z. Xu, D. Chang, C. Zhang, C. Gao, *ACS Nano* **2017**, *11*, 11056.
- [301] G. Nelson, in *Advances in the Dyeing and Finishing of Technical Textiles* (Ed: M. L. Gulrajani), Woodhead Publishing, Sawston, Cambridge **2013**.
- [302] R. Al Shannaq, M. M. Farid, in *Advances in Thermal Energy Storage Systems* (Ed: L. F. Cabeza), Woodhead Publishing, Sawston, Cambridge **2015**.
- [303] J. S. Lee, D. H. Shin, J. Jang, *Energy Environ. Sci.* **2015**, *8*, 3030.
- [304] L. Nayak, M. Rahaman, R. Giri, in *Carbon-Containing Polymer Composites* (Eds: M. Rahaman, D. Khastgir, A. K. Aldalbah), Springer Singapore, Singapore **2019**.
- [305] D. V. Lam, S. Won, H. C. Shim, J.-H. Kim, S.-M. Lee, *Carbon* **2019**, *153*, 257.
- [306] M. Zhang, C. Wang, H. Wang, M. Jian, X. Hao, Y. Zhang, *Adv. Funct. Mater.* **2017**, *27*, 1604795.
- [307] A. Levitt, D. Hegh, P. Phillips, S. Uzun, M. Anayee, J. M. Razal, Y. Gogotsi, G. Dion, *Mater. Today* **2020**, *34*, 17.
- [308] D. Yu, Q. Qian, L. Wei, W. Jiang, K. Goh, J. Wei, J. Zhang, Y. Chen, *Chem. Soc. Rev.* **2015**, *44*, 647.
- [309] S. Zhai, L. Wei, H. E. Karahan, X. Chen, C. Wang, X. Zhang, J. Chen, X. Wang, Y. Chen, *Energy Storage Mater.* **2019**, *19*, 102.
- [310] D. P. Dubal, J. G. Kim, Y. Kim, R. Holze, C. D. Lokhande, W. B. Kim, *Energy Technol.* **2014**, *2*, 325.
- [311] T. Chu, S. Park, K. Fu, *Carbon Energy* **2021**, *3*, 424.
- [312] P. Chang, H. Mei, S. Zhou, K. G. Dassios, L. Cheng, *J. Mater. Chem. A* **2019**, *7*, 4230.
- [313] D.-W. Wang, F. Li, M. Liu, G. Q. Lu, H.-M. Cheng, *Angew. Chem., Int. Ed.* **2008**, *47*, 373.
- [314] M. Wei, F. Zhang, W. Wang, P. Alexandridis, C. Zhou, G. Wu, *J. Power Sources* **2017**, *354*, 134.
- [315] S. Liang, Y. Li, J. Yang, J. Zhang, C. He, Y. Liu, X. Zhou, *Adv. Mater. Technol.* **2016**, *1*, 1600117.
- [316] H. Yuk, B. Lu, S. Lin, K. Qu, J. Xu, J. Luo, X. Zhao, *Nat. Commun.* **2020**, *11*, 1604.
- [317] H. Zhou, S. B. Bhaduri, in *Biomaterials in Translational Medicine* (Eds: L. Yang, S. B. Bhaduri, T. J. Webster), Academic Press, Cambridge, Massachusetts **2019**.
- [318] S. H. Park, G. Goodall, W. S. Kim, *Mater. Des.* **2020**, *193*, 108797.
- [319] R. G. Rocha, R. M. Cardoso, P. J. Zambiasi, S. V. F. Castro, T. V. B. Ferraz, G. d. O. Aparecido, J. A. Bonacin, R. A. A. Munoz, E. M. Richter, *Anal. Chim. Acta* **2020**, *1132*, 1.
- [320] M. Cheng, R. Deivanayagam, R. Shahbazian-Yassar, *Batteries Supercaps* **2020**, *3*, 130.
- [321] M. Areir, Y. Xu, D. Harrison, J. Fyson, *Mater. Sci. Eng., B* **2017**, *226*, 29.
- [322] N. Soin, in *Magnetic Nanostructured Materials* (Eds: A. A. El-Gendy, J. M. Barandiarán, R. L. Hadimani), Elsevier, London, UK **2018**.
- [323] H. Akinaga, *Jpn. J. Appl. Phys.* **2020**, *59*, 110201.
- [324] C. R. Saha, T. O. Donnell, H. Loder, S. Beeby, J. Tudor, *IEEE Trans. Magn.* **2006**, *42*, 3509.
- [325] H. Wang, A. Jasim, in *Eco-Efficient Pavement Construction Materials* (Eds: F. Pacheco-Torgal, S. Amirkhanian, H. Wang, E. Schlangen), Woodhead Publishing, Sawston, Cambridge **2020**.
- [326] S. P. Beeby, Z. Cao, A. Almussallam, in *Multidisciplinary Know-How for Smart-Textiles Developers* (Ed: T. Kirstein), Woodhead Publishing, Sawston, Cambridge **2013**.
- [327] N. Dang, E. Bozorgzadeh, N. Venkatasubramanian, in *Advances in Computers*, Vol. 87 (Eds: A. Hurson, A. Memon), Elsevier, London, UK **2012**.
- [328] Y. Yang, H. Zhang, Z.-H. Lin, Y. S. Zhou, Q. Jing, Y. Su, J. Yang, J. Chen, C. Hu, Z. L. Wang, *ACS Nano* **2013**, *7*, 9213.
- [329] W. Yang, J. Chen, G. Zhu, J. Yang, P. Bai, Y. Su, Q. Jing, X. Cao, Z. L. Wang, *ACS Nano* **2013**, *7*, 11317.
- [330] A. Satharasinghe, T. Hughes-Riley, T. Dias, *Proceedings* **2019**, *32*, 1.
- [331] J. Lv, I. Jeerapan, F. Tehrani, L. Yin, C. A. Silva-Lopez, J.-H. Jang, D. Joshua, R. Shah, Y. Liang, L. Xie, F. Soto, C. Chen, E. Karshalev, C. Kong, Z. Yang, J. Wang, *Energy Environ. Sci.* **2018**, *11*, 3431.
- [332] S. Yong, J. Shi, S. Beeby, *Energy Technol.* **2019**, *7*, 1800938.
- [333] B. Dyatkin, V. Presser, M. Heon, M. R. Lukatskaya, M. Beidaghi, Y. Gogotsi, *ChemSusChem* **2013**, *6*, 2269.
- [334] B. Wang, X. Fang, H. Sun, S. He, J. Ren, Y. Zhang, H. Peng, *Adv. Mater.* **2015**, *27*, 7854.
- [335] Y. Fu, X. Cai, H. Wu, Z. Lv, S. Hou, M. Peng, X. Yu, D. Zou, *Adv. Mater.* **2012**, *24*, 5713.
- [336] G. Wang, H. Wang, X. Lu, Y. Ling, M. Yu, T. Zhai, Y. Tong, Y. Li, *Adv. Mater.* **2014**, *26*, 2676.
- [337] Y. Han, Y. Lu, S. Shen, Y. Zhong, S. Liu, X. Xia, Y. Tong, X. Lu, *Adv. Funct. Mater.* **2019**, *29*, 1806329.
- [338] W. Wang, W. Liu, Y. Zeng, Y. Han, M. Yu, X. Lu, Y. Tong, *Adv. Mater.* **2015**, *27*, 3572.
- [339] X. Zhao, B. Zheng, T. Huang, C. Gao, *Nanoscale* **2015**, *7*, 9399.
- [340] Y. Hu, H. Cheng, F. Zhao, N. Chen, L. Jiang, Z. Feng, L. Qu, *Nanoscale* **2014**, *6*, 6448.
- [341] S. H. Aboutalebi, R. Jalili, D. Esrafilzadeh, M. Salari, Z. Gholamvand, S. Aminoroaya Yamini, K. Konstantinov, R. L. Shepherd, J. Chen, S. E. Moulton, P. C. Innis, A. I. Minett, J. M. Razal, G. G. Wallace, *ACS Nano* **2014**, *8*, 2456.
- [342] S. Chen, W. Ma, H. Xiang, Y. Cheng, S. Yang, W. Weng, M. Zhu, *J. Power Sources* **2016**, *319*, 271.
- [343] S. Zhai, W. Jiang, L. Wei, H. E. Karahan, Y. Yuan, A. K. Ng, Y. Chen, *Mater. Horiz.* **2015**, *2*, 598.
- [344] Y. Li, Y. Zhang, H. Zhang, T.-I. Xing, G.-q. Chen, *RSC Adv.* **2019**, *9*, 4180.
- [345] K. Jost, C. R. Perez, J. K. McDonough, V. Presser, M. Heon, G. Dion, Y. Gogotsi, *Energy Environ. Sci.* **2011**, *4*, 5060.
- [346] K. Jost, D. Stenger, C. R. Perez, J. K. McDonough, K. Lian, Y. Gogotsi, G. Dion, *Energy Environ. Sci.* **2013**, *6*, 2698.
- [347] L. Dong, C. Xu, Q. Yang, J. Fang, Y. Li, F. Kang, *J. Mater. Chem. A* **2015**, *3*, 4729.
- [348] J. Yu, J. Wu, H. Wang, A. Zhou, C. Huang, H. Bai, L. Li, *ACS Appl. Mater. Interfaces* **2016**, *8*, 4724.
- [349] V. T. Le, H. Kim, A. Ghosh, J. Kim, J. Chang, Q. A. Vu, D. T. Pham, J.-H. Lee, S.-W. Kim, Y. H. Lee, *ACS Nano* **2013**, *7*, 5940.
- [350] Y. Cao, M. Zhu, P. Li, R. Zhang, X. Li, Q. Gong, K. Wang, M. Zhong, D. Wu, F. Lin, H. Zhu, *Phys. Chem. Chem. Phys.* **2013**, *15*, 19550.

- [351] D. Yu, K. Goh, H. Wang, L. Wei, W. Jiang, Q. Zhang, L. Dai, Y. Chen, *Nat. Nanotechnol.* **2014**, *9*, 555.
- [352] Y. Ma, P. Li, J. W. Sedloff, X. Zhang, H. Zhang, J. Liu, *ACS Nano* **2015**, *9*, 1352.
- [353] G. Huang, C. Hou, Y. Shao, B. Zhu, B. Jia, H. Wang, Q. Zhang, Y. Li, *Nano Energy* **2015**, *12*, 26.
- [354] Y. Liang, Z. Wang, J. Huang, H. Cheng, F. Zhao, Y. Hu, L. Jiang, L. Qu, *J. Mater. Chem. A* **2015**, *3*, 2547.
- [355] Y. Jia, L. Zhou, J. Shao, *Synth. Met.* **2018**, *246*, 108.
- [356] M. Pasta, F. L. Mantia, L. Hu, H. D. Deshazer, Y. Cui, *Nano Res.* **2010**, *3*, 452.
- [357] W.-w. Liu, X.-b. Yan, J.-w. Lang, C. Peng, Q.-j. Xue, *J. Mater. Chem.* **2012**, *22*, 17245.
- [358] M. R. Islam, S. Afroj, C. Beach, M. H. Islam, C. Parraman, A. Abdelkader, A. J. Casson, K. S. Novoselov, N. Karim, *iScience* **2022**, *25*, 103945.
- [359] W. C. Li, C. L. Mak, C. W. Kan, C. Y. Hui, *RSC Adv.* **2014**, *4*, 64890.
- [360] S. Qiang, T. Carey, A. Arbab, W. Song, C. Wang, F. Torrisi, *Nanoscale* **2019**, *11*, 9912.
- [361] Z. Stempien, M. Khalid, M. Kozicki, M. Kozanecki, H. Varela, P. Filipczak, R. Pawlak, E. Korzeniewska, E. Sasiadek, *Synth. Met.* **2019**, *256*, 116144.
- [362] Y. Gao, G. P. Pandey, J. Turner, C. R. Westgate, B. Sammakia, *Nanoscale Res. Lett.* **2012**, *7*, 651.
- [363] B. Mehrabi-Matin, S. Shahrokhian, A. Iraj-Zad, *Electrochim. Acta* **2017**, *227*, 246.
- [364] G. A. Snook, P. Kao, A. S. Best, *J. Power Sources* **2011**, *196*, 1.
- [365] C. Wei, Q. Xu, Z. Chen, W. Rao, L. Fan, Y. Yuan, Z. Bai, J. Xu, *Carbohydr. Polym.* **2017**, *169*, 50.
- [366] B. Wang, W. Song, P. Gu, L. Fan, Y. Yin, C. Wang, *Electrochim. Acta* **2019**, *297*, 794.
- [367] J. Lv, P. Zhou, L. Zhang, Y. Zhong, X. Sui, B. Wang, Z. Chen, H. Xu, Z. Mao, *Chem. Eng. J.* **2019**, *361*, 897.
- [368] J. Lv, L. Zhang, Y. Zhong, X. Sui, B. Wang, Z. Chen, X. Feng, H. Xu, Z. Mao, *Org. Electron.* **2019**, *74*, 59.
- [369] J. Cárdenas-Martínez, B. L. España-Sánchez, R. Esparza, J. A. Ávila-Niño, *Synth. Met.* **2020**, *267*, 116436.
- [370] X. Xie, B. Xin, Z. Chen, Y. Xu, *J. Text. Inst.* **2021**, *1*, 1.
- [371] Y. Wang, X. Lv, S. Zou, X. Lin, Y. Ni, *RSC Adv.* **2021**, *11*, 10941.
- [372] H. Jin, L. Zhou, C. L. Mak, H. Huang, W. M. Tang, H. L. W. Chan, *Nano Energy* **2015**, *11*, 662.
- [373] G. Liang, L. Zhu, J. Xu, D. Fang, Z. Bai, W. Xu, *Electrochim. Acta* **2013**, *103*, 9.
- [374] L. Zhu, L. Wu, Y. Sun, M. Li, J. Xu, Z. Bai, G. Liang, L. Liu, D. Fang, W. Xu, *RSC Adv.* **2014**, *4*, 6261.
- [375] J. Xu, D. Wang, L. Fan, Y. Yuan, W. Wei, R. Liu, S. Gu, W. Xu, *Org. Electron.* **2015**, *26*, 292.
- [376] L. Liu, W. Weng, J. Zhang, X. Cheng, N. Liu, J. Yang, X. Ding, *J. Mater. Chem. A* **2016**, *4*, 12981.
- [377] B. Yue, C. Wang, X. Ding, G. G. Wallace, *Electrochim. Acta* **2012**, *68*, 18.
- [378] F. Gong, C. Meng, J. He, X. Dong, *Prog. Org. Coat.* **2018**, *121*, 89.
- [379] Q. Liu, J. Qiu, C. Yang, L. Zang, G. Zhang, E. Sakai, *Int. J. Energy Res.* **2020**, *44*, 9166.
- [380] A. Laforgue, *J. Power Sources* **2011**, *196*, 559.
- [381] S. Pan, H. Lin, J. Deng, P. Chen, X. Chen, Z. Yang, H. Peng, *Adv. Energy Mater.* **2015**, *5*, 1401438.
- [382] C. An, Y. Zhang, H. Guo, Y. Wang, *Nanoscale Adv.* **2019**, *1*, 4644.
- [383] F. Su, M. Miao, *Nanotechnology* **2014**, *25*, 135401.
- [384] S. Abouali, M. Akbari Garakani, B. Zhang, Z.-L. Xu, E. Kamali Heidar, J.-q. Huang, J. Huang, J.-K. Kim, *ACS Appl. Mater. Interfaces* **2015**, *7*, 13503.
- [385] F. Su, X. Lv, M. Miao, *Small* **2015**, *11*, 854.
- [386] S. Shahidi, F. Kalaoglu, *J. Ind. Text.* **2020**, *51*, 1528083720944252.
- [387] M. S. Javed, J. Chen, L. Chen, Y. Xi, C. Zhang, B. Wan, C. Hu, *J. Mater. Chem. A* **2016**, *4*, 667.
- [388] P. Howli, S. Das, S. Sarkar, M. Samanta, K. Panigrahi, N. S. Das, K. K. Chattopadhyay, *ACS Omega* **2017**, *2*, 4216.
- [389] J. Bae, M. K. Song, Y. J. Park, J. M. Kim, M. Liu, Z. L. Wang, *Angew. Chem., Int. Ed.* **2011**, *50*, 1683.
- [390] A. Pullanchiyodan, L. Manjakkal, R. Dahiya, *IEEE Sens. J.* **2021**, *21*, 26208.
- [391] P. Yang, X. Xiao, Y. Li, Y. Ding, P. Qiang, X. Tan, W. Mai, Z. Lin, W. Wu, T. Li, H. Jin, P. Liu, J. Zhou, C. P. Wong, Z. L. Wang, *ACS Nano* **2013**, *7*, 2617.
- [392] J. Zhang, M. Chen, Y. Ge, Q. Liu, *J. Nanomater.* **2016**, *2016*, 2870761.
- [393] X. Fan, X. Wang, G. Li, A. Yu, Z. Chen, *J. Power Sources* **2016**, *326*, 357.
- [394] C. Shen, Y. Xie, B. Zhu, M. Sanghadasa, Y. Tang, L. Lin, *Sci. Rep.* **2017**, *7*, 14324.
- [395] T. A. Babkova, H. Fei, N. E. Kazantseva, I. Y. Sapurina, P. Saha, *Electrochim. Acta* **2018**, *272*, 1.
- [396] W. Luo, X. Li, J. Y. Chen, *J. Ind. Text.* **2018**, *49*, 1061.
- [397] Q. Abbas, M. S. Javed, A. Ahmad, S. H. Siyal, I. Asim, R. Luque, M. D. Albaqami, A. M. Tighezza, *Coatings* **2021**, *11*, 1337.
- [398] S. Uzun, S. Seyedin, A. L. Stoltzfus, A. S. Levitt, M. Alhabeab, M. Anayee, C. J. Strobel, J. M. Razal, G. Dion, Y. Gogotsi, *Adv. Funct. Mater.* **2019**, *29*, 1905015.
- [399] J. Yan, Y. Ma, C. Zhang, X. Li, W. Liu, X. Yao, S. Yao, S. Luo, *RSC Adv.* **2018**, *8*, 39742.
- [400] H. Yin, Y. Liu, N. Yu, H.-Q. Qu, Z. Liu, R. Jiang, C. Li, M.-Q. Zhu, *ACS Omega* **2018**, *3*, 17466.
- [401] Q. Jiang, N. Kurra, M. Alhabeab, Y. Gogotsi, H. N. Alshareef, *Adv. Energy Mater.* **2018**, *8*, 1703043.
- [402] Y. Ding, L. Dai, R. Wang, H. Wang, H. Zhang, W. Jiang, J. Tang, S.-Q. Zang, *Chem. Eng. J.* **2021**, *407*, 126874.
- [403] N. Liu, W. Ma, J. Tao, X. Zhang, J. Su, L. Li, C. Yang, Y. Gao, D. Golberg, Y. Bando, *Adv. Mater.* **2013**, *25*, 4925.
- [404] H. T. Wang, C. Jin, Y. N. Liu, X. H. Kang, S. W. Bian, Q. Zhu, *Electrochim. Acta* **2018**, *283*, 1789.
- [405] Y. Ma, Q. Wang, X. Liang, D. Zhang, M. Miao, *J. Mater. Sci.* **2018**, *53*, 14586.
- [406] L. Yang, F. Lin, F. Zabihi, S. Yang, M. Zhu, *Int. J. Biol. Macromol.* **2021**, *181*, 1063.
- [407] J. Li, Y. Shao, P. Jiang, Q. Zhang, C. Hou, Y. Li, H. Wang, *J. Mater. Chem. A* **2019**, *7*, 3143.
- [408] X. Li, R. Liu, C. Xu, Y. Bai, X. Zhou, Y. Wang, G. Yuan, *Adv. Funct. Mater.* **2018**, *28*, 1800064.
- [409] Z. Cai, L. Li, J. Ren, L. Qiu, H. Lin, H. Peng, *J. Mater. Chem. A* **2013**, *1*, 258.
- [410] J. Sun, Y. Huang, C. Fu, Z. Wang, Y. Huang, M. Zhu, C. Zhi, H. Hu, *Nano Energy* **2016**, *27*, 230.
- [411] Q. Zhang, J. Sun, Z. Pan, J. Zhang, J. Zhao, X. Wang, C. Zhang, Y. Yao, W. Lu, Q. Li, Y. Zhang, Z. Zhang, *Nano Energy* **2017**, *39*, 219.
- [412] Z. Wang, S. Qin, S. Seyedin, J. Zhang, J. Wang, A. Levitt, N. Li, C. Haines, R. Ovalle-Robles, W. Lei, Y. Gogotsi, R. H. Baughman, J. M. Razal, *Small* **2018**, *14*, 1802225.
- [413] N. He, S. Patil, J. Qu, J. Liao, F. Zhao, W. Gao, *ACS Appl. Energy Mater.* **2020**, *3*, 2949.
- [414] J. Zhang, S. Seyedin, S. Qin, Z. Wang, S. Moradi, F. Yang, P. A. Lynch, W. Yang, J. Liu, X. Wang, J. M. Razal, *Small* **2019**, *15*, 1804732.
- [415] J. Tao, N. Liu, W. Ma, L. Ding, L. Li, J. Su, Y. Gao, *Sci. Rep.* **2013**, *3*, 2286.
- [416] L. Naderi, S. Shahrokhian, F. Soavi, *J. Mater. Chem. A* **2020**, *8*, 19588.
- [417] K. Keum, G. Lee, H. Lee, J. Yun, H. Park, S. Y. Hong, C. Song, J. W. Kim, J. S. Ha, *ACS Appl. Mater. Interfaces* **2018**, *10*, 26248.
- [418] Y. Huang, H. Hu, Y. Huang, M. Zhu, W. Meng, C. Liu, Z. Pei, C. Hao, Z. Wang, C. Zhi, *ACS Nano* **2015**, *9*, 4766.

- [419] Q. Huang, L. Liu, D. Wang, J. Liu, Z. Huang, Z. Zheng, *J. Mater. Chem. A* **2016**, *4*, 6802.
- [420] B. B. Etana, S. Ramakrishnan, M. Dhakshnamoorthy, S. Saravanan, P. C. Ramamurthy, T. A. Demissie, *Mater. Res. Express* **2020**, *6*, 125708.
- [421] X. Cheng, X. Fang, P. Chen, S. G. Doo, I. H. Son, X. Huang, Y. Zhang, W. Weng, Z. Zhang, J. Deng, X. Sun, H. Peng, *J. Mater. Chem. A* **2015**, *3*, 19304.
- [422] H. Zhang, Y. Qiao, Z. Lu, *ACS Appl. Mater. Interfaces* **2016**, *8*, 32317.
- [423] T. Kim, E. P. Samuel, C. Park, Y.-I. Kim, A. Aldalbahi, F. Alotaibi, S. S. Yoon, *J. Alloys Compd.* **2021**, *856*, 157902.
- [424] L. Liu, Q. Tian, W. Yao, M. Li, Y. Li, W. Wu, *J. Power Sources* **2018**, *397*, 59.
- [425] P. Lv, Y. Y. Feng, Y. Li, W. Feng, *J. Power Sources* **2012**, *220*, 160.
- [426] J. Zhu, S.-X. Zhao, X. Wu, Y.-F. Wang, L. Yu, C.-W. Nan, *Electrochim. Acta* **2018**, *282*, 784.
- [427] F. Mu, J. Zhao, C. Gu, *AIP Adv.* **2020**, *10*, 065002.
- [428] K. Jost, D. P. Durkin, L. M. Haverhals, E. K. Brown, M. Langenstein, H. C. De Long, P. C. Trulove, Y. Gogotsi, G. Dion, *Adv. Energy Mater.* **2015**, *5*, 1401286.
- [429] L. Liu, Y. Yu, C. Yan, K. Li, Z. Zheng, *Nat. Commun.* **2015**, *6*, 7260.
- [430] X. Ye, Q. Zhou, C. Jia, Z. Tang, Z. Wan, X. Wu, *Electrochim. Acta* **2016**, *206*, 155.
- [431] R. Lima, J. J. Alcaraz-Espinoza, F. A. G. da Silva Jr., H. P. de Oliveira, *ACS Appl. Mater. Interfaces* **2018**, *10*, 13783.
- [432] K. Wang, Q. Meng, Y. Zhang, Z. Wei, M. Miao, *Adv. Mater.* **2013**, *25*, 1494.
- [433] C. Choi, J. A. Lee, A. Y. Choi, Y. T. Kim, X. Lepró, M. D. Lima, R. H. Baughman, S. J. Kim, *Adv. Mater.* **2014**, *26*, 2059.
- [434] G. Huang, Y. Zhang, L. Wang, P. Sheng, H. Peng, *Carbon* **2017**, *125*, 595.
- [435] Y. Wu, Q. Wang, T. Li, D. Zhang, M. Miao, *Electrochim. Acta* **2017**, *245*, 69.
- [436] X. Jian, H. Li, H. Li, Y. Li, Y. Shang, *Carbon* **2021**, *172*, 132.
- [437] Q. Meng, K. Wang, W. Guo, J. Fang, Z. Wei, X. She, *Small* **2014**, *10*, 3187.
- [438] Y. Meng, Y. Zhao, C. Hu, H. Cheng, Y. Hu, Z. Zhang, G. Shi, L. Qu, *Adv. Mater.* **2013**, *25*, 2326.
- [439] X. Ding, Y. Zhao, C. Hu, Y. Hu, Z. Dong, N. Chen, Z. Zhang, L. Qu, *J. Mater. Chem. A* **2014**, *2*, 12355.
- [440] S. Seyedin, E. R. S. Yanza, J. M. Razal, *J. Mater. Chem. A* **2017**, *5*, 24076.
- [441] A. K. Roy, S. N. Faisal, A. Spickenheuer, C. Scheffler, J. Wang, A. T. Harris, A. I. Minett, M. S. Islam, *Carbon Trends* **2021**, *5*, 100097.
- [442] D. Yu, S. Zhai, W. Jiang, K. Goh, L. Wei, X. Chen, R. Jiang, Y. Chen, *Adv. Mater.* **2015**, *27*, 4895.
- [443] H. Jin, L. Zhou, C. L. Mak, H. Huang, W. M. Tang, H. L. Wa Chan, *J. Mater. Chem. A* **2015**, *3*, 15633.
- [444] X. Lu, Y. Bai, R. Wang, J. Sun, *J. Mater. Chem. A* **2016**, *4*, 18164.
- [445] D. Kim, K. Keum, G. Lee, D. Kim, S.-S. Lee, J. S. Ha, *Nano Energy* **2017**, *35*, 199.
- [446] N. Mao, W. Chen, J. Meng, Y. Li, K. Zhang, X. Qin, H. Zhang, C. Zhang, Y. Qiu, S. Wang, *J. Power Sources* **2018**, *399*, 406.
- [447] C. Song, J. Yun, K. Keum, Y. R. Jeong, H. Park, H. Lee, G. Lee, S. Y. Oh, J. S. Ha, *Carbon* **2019**, *144*, 639.
- [448] J. A. Lee, M. K. Shin, S. H. Kim, H. U. Cho, G. M. Spinks, G. G. Wallace, M. D. Lima, X. Lepró, M. E. Kozlov, R. H. Baughman, S. J. Kim, *Nat. Commun.* **2013**, *4*, 1970.
- [449] X. Chu, H. Zhang, H. Su, F. Liu, B. Gu, H. Huang, H. Zhang, W. Deng, X. Zheng, W. Yang, *Chem. Eng. J.* **2018**, *349*, 168.
- [450] N. He, J. Liao, F. Zhao, W. Gao, *ACS Appl. Mater. Interfaces* **2020**, *12*, 15211.
- [451] T. Zhang, Z. Wang, A. Zhu, F. Ran, *Electrochim. Acta* **2020**, *348*, 136312.
- [452] K. Wang, P. Zhao, X. Zhou, H. Wu, Z. Wei, *J. Mater. Chem.* **2011**, *21*, 16373.
- [453] L. Bao, X. Li, *Adv. Mater.* **2012**, *24*, 3246.
- [454] B. Yue, C. Wang, X. Ding, G. G. Wallace, *Electrochim. Acta* **2013**, *113*, 17.
- [455] J. Xu, D. Wang, Y. Yuan, W. Wei, L. Duan, L. Wang, H. Bao, W. Xu, *Org. Electron.* **2015**, *24*, 153.
- [456] J. Xu, D. Wang, Y. Yuan, W. Wei, S. Gu, R. Liu, X. Wang, L. Liu, W. Xu, *Cellulose* **2015**, *22*, 1355.
- [457] T. G. Yun, B. i. Hwang, D. Kim, S. Hyun, S. M. Han, *ACS Appl. Mater. Interfaces* **2015**, *7*, 9228.
- [458] R. Yuksel, H. E. Unalan, *Int. J. Energy Res.* **2015**, *39*, 2042.
- [459] Y. Liang, W. Weng, J. Yang, L. Liu, Y. Zhang, L. Yang, X. Luo, Y. Cheng, M. Zhu, *RSC Adv.* **2017**, *7*, 48934.
- [460] Q. Xu, C. Wei, L. Fan, W. Rao, W. Xu, H. Liang, J. Xu, *Appl. Surf. Sci.* **2018**, *460*, 84.
- [461] S. Xu, H. Hao, Y. Chen, W. Li, W. Shen, P. R. Shearing, D. J. L. Brett, G. He, *Nanotechnology* **2021**, *32*, 305401.
- [462] C. Liang, L. Zang, F. Shi, C. Yang, J. Qiu, Q. Liu, Z. Chen, *Cellulose* **2022**, *29*, 2525.
- [463] L. Hu, W. Chen, X. Xie, N. Liu, Y. Yang, H. Wu, Y. Yao, M. Pasta, H. N. Alshareef, Y. Cui, *ACS Nano* **2011**, *5*, 8904.
- [464] H. Cheng, Z. Dong, C. Hu, Y. Zhao, Y. Hu, L. Qu, N. Chen, L. Dai, *Nanoscale* **2013**, *5*, 3428.
- [465] M.-X. Guo, S.-W. Bian, F. Shao, S. Liu, Y.-H. Peng, *Electrochim. Acta* **2016**, *209*, 486.
- [466] M. Barakzahi, M. Montazer, F. Sharif, T. Norby, A. Chatzidakis, *Electrochim. Acta* **2019**, *305*, 187.
- [467] M. Barakzahi, M. Montazer, F. Sharif, *J. Text. Polym.* **2020**, *8*, 15.
- [468] J. Liang, B. Tian, S. Li, C. Jiang, W. Wu, *Adv. Energy Mater.* **2020**, *10*, 2000022.
- [469] L. Wang, C. Zhang, X. Jiao, Z. Yuan, *Nano Res.* **2019**, *12*, 1129.
- [470] Y.-W. Ju, G.-R. Choi, H.-R. Jung, W.-J. Lee, *Electrochim. Acta* **2008**, *53*, 5796.
- [471] X. Lu, M. Yu, G. Wang, T. Zhai, S. Xie, Y. Ling, Y. Tong, Y. Li, *Adv. Mater.* **2013**, *25*, 267.
- [472] Y. Zeng, Y. Han, Y. Zhao, Y. Zeng, M. Yu, Y. Liu, H. Tang, Y. Tong, X. Lu, *Adv. Energy Mater.* **2015**, *5*, 1402176.
- [473] Y. Liu, Y. Jiao, B. Yin, S. Zhang, F. Qu, X. Wu, *J. Mater. Chem. A* **2015**, *3*, 3676.
- [474] L. Wang, X. Feng, L. Ren, Q. Piao, J. Zhong, Y. Wang, H. Li, Y. Chen, B. Wang, *J. Am. Chem. Soc.* **2015**, *137*, 4920.
- [475] F.-H. Kuok, C.-Y. Liao, C.-W. Chen, Y.-C. Hao, I.-S. Yu, J.-Z. Chen, *Mater. Res. Express* **2017**, *4*, 115501.
- [476] C. Wan, Y. Jiao, D. Liang, Y. Wu, J. Li, *Electrochim. Acta* **2018**, *285*, 262.
- [477] J. Shao, Y. Li, M. Zhong, Q. Wang, X. Luo, K. Li, W. Zhao, *Mater. Lett.* **2019**, *252*, 173.
- [478] P. Howli, K. Panigrahi, A. Mitra, N. S. Das, K. K. Chattopadhyay, *Appl. Surf. Sci.* **2019**, *485*, 238.
- [479] R. Rohith, M. Manuraj, R. I. Jafri, R. B. Rakhi, *Mater. Today: Proc.* **2022**, *50*, 1.
- [480] Z. Li, Y. Ma, L. Wang, X. Du, S. Zhu, X. Zhang, L. Qu, M. Tian, *ACS Appl. Mater. Interfaces* **2019**, *11*, 46278.
- [481] P. I. Dolez, J. Decaens, T. Buns, D. Lachapelle, O. Vermeersch, *IOP Conf. Ser.: Mater. Sci. Eng.* **2020**, *827*, 012014.
- [482] A. M. Bernardes, D. C. R. Espinosa, J. A. S. Tenório, *J. Power Sources* **2004**, *130*, 291.
- [483] M. Hall, *businesswaste.co.uk waste management*, **2021**.
- [484] S. Rotzler, C. Kallmayer, C. Dils, M. von Krshiwoblozki, U. Bauer, M. Schneider-Ramelow, *J. Text. Inst.* **2020**, *111*, 1766.
- [485] X. Tao, V. Koncar, T.-H. Huang, C.-L. Shen, Y.-C. Ko, G.-T. Jou, *Sensors* **2017**, *17*, 1.
- [486] E. G. Jeong, Y. Jeon, S. H. Cho, K. C. Choi, *Energy Environ. Sci.* **2019**, *12*, 1878.

- [487] R. Cao, X. Pu, X. Du, W. Yang, J. Wang, H. Guo, S. Zhao, Z. Yuan, C. Zhang, C. Li, Z. L. Wang, *ACS Nano* **2018**, *12*, 5190.
- [488] Fact.MR, E-textile Market, **2021**.
- [489] IDTechEx Wearable Technology Forecasts 2021–2031; IDTechEx, **2021**.
- [490] Acumen Global E-Textiles & Smart Clothing Market Acumen Research and Consulting, **2021**.
- [491] S. Huang, X. Zhu, S. Sarkar, Y. Zhao, *APL Mater.* **2019**, *7*, 100901.
- [492] E. Redondo, L. W. L. Fevre, R. Fields, R. Todd, A. J. Forsyth, R. A. W. Dryfe, *Electrochim. Acta* **2020**, *360*, 136957.
- [493] W. Zuo, R. Li, C. Zhou, Y. Li, J. Xia, J. Liu, *Adv. Sci.* **2017**, *4*, 1600539.
- [494] S. Rotzler, M. Schneider-Ramelow, *Textiles* **2021**, *1*, 37.
- [495] S. Rotzler, M. v. Krshiwoblozki, M. Schneider-Ramelow, *Text. Res. J.* **2021**, *91*, 0040517521996727.
- [496] S. Maiti, M. R. Islam, M. A. Uddin, S. Afroj, S. J. Eichhorn, N. Karim, *Adv. Sustainable Syst.* **2022**, 2200258.
- [497] S. Verma, S. Arya, V. Gupta, S. Mahajan, H. Furukawa, A. Khosla, *J. Mater. Res. Technol.* **2021**, *11*, 564.
- [498] Y. Lian, H. Yu, M. Wang, X. Yang, Z. Li, F. Yang, Y. Wang, H. Tai, Y. Liao, J. Wu, X. Wang, Y. Jiang, G. Tao, *J. Mater. Chem. C* **2020**, *8*, 8399.
- [499] M. Zhang, M. Zhao, M. Jian, C. Wang, A. Yu, Z. Yin, X. Liang, H. Wang, K. Xia, X. Liang, J. Zhai, Y. Zhang, *Matter* **2019**, *1*, 168.
- [500] Z. Mai, Z. Xiong, X. Shu, X. Liu, H. Zhang, X. Yin, Y. Zhou, M. Liu, M. Zhang, W. Xu, D. Chen, *Carbohydr. Polym.* **2018**, *199*, 516.
- [501] J. Huang, Y. Yang, L. Yang, Y. Bu, T. Xia, S. Gu, H. Yang, D. Ye, W. Xu, *Mater. Lett.* **2019**, *237*, 149.
- [502] Y. Yang, Z. Guo, W. Huang, S. Zhang, J. Huang, H. Yang, Y. Zhou, W. Xu, S. Gu, *Appl. Surf. Sci.* **2020**, *503*, 144079.
- [503] S. Yang, C. Li, N. Wen, S. Xu, H. Huang, T. Cong, Y. Zhao, Z. Fan, K. Liu, L. Pan, *J. Mater. Chem. C* **2021**, *9*, 13789.
- [504] S. Afroj, M. H. Islam, N. Karim, *Proceedings* **2021**, *68*, 1.
- [505] B. Tian, Y. Fang, J. Liang, K. Zheng, P. Guo, X. Zhang, Y. Wu, Q. Liu, Z. Huang, C. Cao, W. Wu, *Small* **2022**, *18*, 2107298.
- [506] Z. Zhang, X. Chen, P. Chen, G. Guan, L. Qiu, H. Lin, Z. Yang, W. Bai, Y. Luo, H. Peng, *Adv. Mater.* **2014**, *26*, 466.
- [507] L. Qiu, J. Deng, X. Lu, Z. Yang, H. Peng, *Angew. Chem., Int. Ed.* **2014**, *53*, 10425.
- [508] T. Chen, L. Qiu, Z. Yang, Z. Cai, J. Ren, H. Li, H. Lin, X. Sun, H. Peng, *Angew. Chem., Int. Ed.* **2012**, *51*, 11977.
- [509] W. Weng, P. Chen, S. He, X. Sun, H. Peng, *Angew. Chem., Int. Ed.* **2016**, *55*, 6140.
- [510] L. Li, A. Wai Man, W. Kam Man, W. Sai Ho, C. Wai Yee, W. Kwok Shing, *Text. Res. J.* **2009**, *80*, 935.



Md Rashedul Islam is a Ph.D. student under the supervision of Dr. Nazmul Karim at the Graphene Application Laboratory of the Centre for Print Research (CFPR), UWE Bristol, UK. He has been investigating Graphene and other 2D materials-based energy storage textiles, aimed at developing and powering next-generation multifunctional wearable electronic textiles for personalized healthcare applications. Prior to that, he obtained his BSc and MSc in Textile Engineering, from Bangladesh University of Textiles (BUTex). He has ≈ 9 years of industry and academic experience related to textile chemical processing, advanced materials, and smart electronic textiles.



Shaila Afroj is Senior Research Fellow at the Centre for Print Research (CFPR), UWE Bristol (UK), where she investigates graphene and other 2D materials-based technologies aimed at developing next-generation wearable electronics textiles and sustainable functional clothing. Prior to that, she worked as a Research Associate at National Graphene Institute (NGI), the University of Manchester after completing her Ph.D. from the same university. She has ≈ 14 years of industry (including multi-nationals companies like C&A and Intertek) and academic experiences related to smart textiles, advanced materials, wearable electronics, and fashion clothing.



Kostya S. Novoselov is a condensed matter physicist, specializing in the area of mesoscopic physics and nanotechnology. He is currently Tan Chin Tuan Centennial Professor at National University of Singapore with broad research interests from mesoscopic transport, ferromagnetism, and superconductivity to electronic and optical properties of graphene and 2D materials. He also has got a vast background in nanofabrication and nanotechnology.



Nazmul Karim is Associate Professor at the Centre for Print Research (CFPR), UWE Bristol, UK. He is currently leading a research team to investigate into graphene and other 2D materials-based technologies for developing next-generation wearable electronic textiles, environmentally sustainable functional clothing, and natural fiber-reinforced smart composites. Prior to that, Karim was a Knowledge Exchange Fellow (graphene) at the National Graphene Institute of University of Manchester. He has \approx 14 years of industry and academic experience in new materials and textile-related technologies, and a passion for getting research out of the lab and into real-world applications.

Advances in Printed Electronic Textiles

Md Rashedul Islam, Shaila Afroj,* Junyi Yin, Kostya S. Novoselov, Jun Chen, and Nazmul Karim*

Electronic textiles (e-textiles) have emerged as a revolutionary solution for personalized healthcare, enabling the continuous collection and communication of diverse physiological parameters when seamlessly integrated with the human body. Among various methods employed to create wearable e-textiles, printing offers unparalleled flexibility and comfort, seamlessly integrating wearables into garments. This has spurred growing research interest in printed e-textiles, due to their vast design versatility, material options, fabrication techniques, and wide-ranging applications. Here, a comprehensive overview of the crucial considerations in fabricating printed e-textiles is provided, encompassing the selection of conductive materials and substrates, as well as the essential pre- and post-treatments involved. Furthermore, the diverse printing techniques and the specific requirements are discussed, highlighting the advantages and limitations of each method. Additionally, the multitude of wearable applications made possible by printed e-textiles is explored, such as their integration as various sensors, supercapacitors, and heated garments. Finally, a forward-looking perspective is provided, discussing future prospects and emerging trends in the realm of printed wearable e-textiles. As advancements in materials science, printing technologies, and design innovation continue to unfold, the transformative potential of printed e-textiles in healthcare and beyond is poised to revolutionize the way wearable technology interacts and benefits.

1. Introduction

Fusing electronics into daily textiles, i.e., e-textiles, being sufficiently soft to wear and smart to interact with their surroundings, holds great potential to transform the current healthcare that based on disease management into a personalized model based on disease prevention and healthcare enhancement.^[1–3] By definition, e-textiles refer to electronic devices, that can be attached to the body or clothes^[4,5] comfortably and un-obstructively to deliver intelligent assistance.^[6] With the rapid advancement of the Internet of Things, intelligent hardware, and big data, e-textiles have been growing in momentum since the 2000s,^[7] with great potential in health care, energy, education, social networking, the military, etc.^[8,9] Advantages such as great flexibility, light weight, breathability, and ease of integration with traditional clothes, make e-textiles an ideal candidate platform as wearable bioelectronics.^[10–12] Such electronics can be worn either internally as implantable devices or externally as skin-interfaced devices.^[8,13] Many of these technologies have become popular parts of

people's daily lives as lifestyle and healthcare products, including fitness tracking, rehabilitation, fall detection, and even wound healing.^[14,15] The regular and continuous real-time monitoring of various human health indicators, i.e., heart rate, blood pressure, glucose level, body temperature, etc. noninvasively can alert users and health care providers about abnormal and/or urgent critical indications.^[16–18] It enables cost-effective and affordable personalized healthcare at any time and place and obviates the need for advanced healthcare facilities and skilled healthcare professionals.^[19] Additionally, such soft bioelectronics can detect various signals with high sensitivity, with the potential to be used in artificial electronic skin, motion detection, telemedicine, and in-home healthcare.^[20,21] Considerable efforts have been devoted over the past few years to the development of wearable electronics through advancements in new materials, new processes, and sensing mechanisms.^[20]

The development of electronic textiles essentially requires the fabrication of electro-active materials onto textiles. 1D-shaped conductive textiles are generally prepared by spinning inherently conductive polymer or mixing electroactive material with the spinning dope and/or surface coating of fiber/filament. Padding and/or coating methods are generally used when conductive 2D plane-shaped fabric/textiles are required. A thorough deposition

M. R. Islam, S. Afroj, N. Karim
Centre for Print Research (CFPR)
University of the West of England
Frenchay Campus, Bristol BS16 1QY, UK
E-mail: shaila.afroj@uwe.ac.uk; nazmul.karim@ntu.ac.uk

J. Yin, J. Chen
Department of Bioengineering
University of California
Los Angeles, CA 90095, USA

K. S. Novoselov
Institute for Functional Intelligent Materials
Department of Materials Science and Engineering
National University of Singapore
Singapore 117575, Singapore

N. Karim
Nottingham School of Art and Design
Nottingham Trent University
Shakespeare Street, Nottingham NG1 4GG, UK

 The ORCID identification number(s) for the author(s) of this article can be found under <https://doi.org/10.1002/advs.202304140>

© 2023 The Authors. Advanced Science published by Wiley-VCH GmbH. This is an open access article under the terms of the Creative Commons Attribution License, which permits use, distribution and reproduction in any medium, provided the original work is properly cited.

DOI: 10.1002/advs.202304140

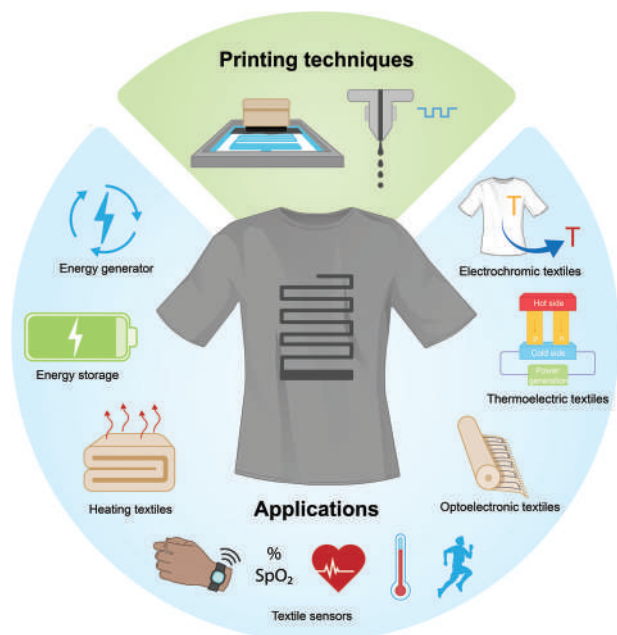


Figure 1. Printing techniques and printed electronic textiles (e-textiles) for energy and healthcare.

of electroactive material occurs in such cases. All these processes require the utilization and disposal of a huge quantity of conductive materials that are often toxic, environmentally harmful, and non-biodegradable. Printing, i.e., localized deposition of active material in the form of printing ink/paste onto textiles, could be a sustainable solution as the material disposal is significantly low compared to yarn/fabric coating process. Additionally, the printing technique offers simple, low-cost, timesaving, versatile, and environmentally friendly manufacturing technologies on various textile substrates. Therefore, the next trend for wearable e-textile fabrication is the printing of all electronic parts onto textiles,^[22] (Figure 1).

There is no doubt that next-generation printed flexible and wearable electronics will lead to a revolution in the human way of life.^[20] Though great progress has been made in the field of e-textiles, most of the reported results are still far from commercial adoption for practical applications. The obstacles mainly come from the aspects namely materials, manufacturing techniques, integration, testing standards, and methods for wearable technology. Currently, there is a lack of comprehensive review on the material, manufacturing, and performance of the printed flexible wearable e-textiles, which is exactly the purpose of this review. In this review (Figure 2), first, we introduced the scope of our review in Section 1. Additionally, conductive materials and suitable textiles for the fabrication of e-textiles are summarized in Section 2. Section 3 introduces the printing techniques and the requirements for various functional printing techniques are discussed in Section 4. Applications of printed e-textiles in terms of various wearable sensors, energy storage devices, and heating textiles are reviewed in Section 5. We finally conclude our review presenting our outlook on various aspects of printed wearables.

2. Materials for Printed E-textiles

2.1. Functional Materials for Printed E-textiles

Development of smart/intelligent and interactive printed e-textiles requires fabrication of flexible and durable conductive components which is an integrated part of the textile. Therefore, the first and an important element in fabricating e-textiles is developing the electrically conductive printing ink/paste,^[23] to ensure the flow of electrons, i.e., electrical current within the printed pattern. SI unit of siemens per meter ($S\ m^{-1}$) is commonly used to measure electrical conductivity (σ).^[24] Alternatively, resistivity (inversely proportional to conductivity) is used to measure the electrical properties of materials. Sheet resistance is used for 2D materials with a consistent thickness (ohms per square meter, $\Omega\ m^{-2}$) and linear resistance is measured for 1D conductive threads (ohms per unit length, $\Omega\ m^{-1}$). Additionally, other characteristics, including thermal and mechanical properties, chemical and thermal resistance, weight and density, heat removal efficiency, interconnections with traditional wires, reliability, and durability, are also considered for textile-based conductor preparation.^[25] Figure 3 summarizes the commonly used functional materials for the fabrication of e-textiles.

2.1.1. Carbonaceous Materials

Carbonaceous compounds and their allotropes (Figure 3) are key materials for applications in nano and optoelectronics, photonics, energy generation and storage, nano-mechanics, and catalysis, and are therefore, topics of particular interest for the researchers.^[26] In addition to high electrical conductivity, they possess a unique combination of other chemical and physical properties, including exceptionally high Young's modulus, mechanical strength, light transmittance, surface-area range (≈ 1 to $2000\ m^2\ g^{-1}$), temperature stability, good corrosion resistance, controlled pore structure, processability and compatibility with various materials, and are relatively cheap.^[27,28]

Carbon nanotube (CNT) is a 1D allotrope of carbon. They are nano-meter in diameter and several millimeters in length and are available in the form of single-walled carbon nanotubes, SWCNTs, or multiwalled carbon nanotubes, MWCNTs (by rolling up single or multiple sheets of graphene respectively).^[29] Since its discovery in the 1990s, CNTs have been utilized in a variety of applications including actuators, artificial muscles, and lightweight electromagnetic shields.^[30] Their exceptional physical, chemical, and electronic properties offer exciting possibilities for nano-scale electronic applications.^[31]

Carbon black (CB), has become an interesting material for sensor fabrication in recent years, due to its excellent conductive and electrocatalytic properties, as well as its cost-effectiveness.^[32] Conductive CBs usually possess electrical conductivity in the range of 10^{-1} to $10^2\ (\Omega\ cm)^{-1}$ with high porosity, small particle size, and a chemically clean (oxygen-free) surface.^[27] CBs are manufactured generally by thermal decomposition, including detonation, or by incomplete combustion of carbon-hydrogen compounds.^[33]

Activated carbon (AC) powder, in comparison with the other forms of carbonaceous materials, is known as a good electrode material with a specific surface area of $1000\text{--}2000\ m^2\ g^{-1}$,^[34]

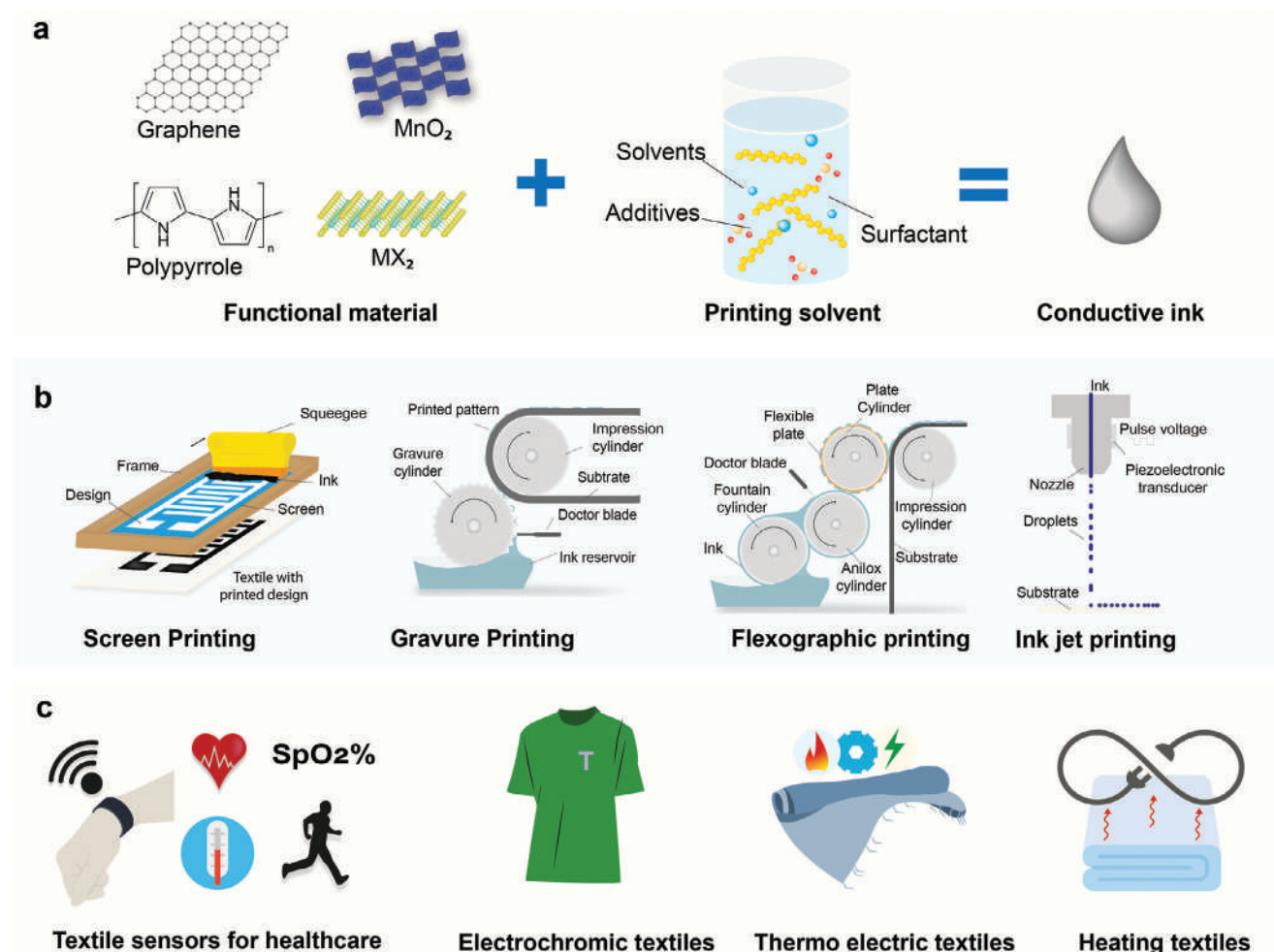


Figure 2. Print ink and printing processes for e-textiles a) Preparation of conductive inks b) Printing techniques for e-textiles fabrication and c) Applications of printed e-textiles.

inexpensive and environmentally friendly alternative.^[35] The tuneable pore size, high specific surface, hierarchical pore structure, and different morphology enable the formation of bilayer of ions at electrode-electrolyte interfaces of AC,^[36] which is beneficial for energy storage applications.

Graphene is a 2D allotrope of carbon, which is the basic structural element of carbon allotropes including graphite, carbon nanotubes, and fullerenes.^[37] Since its isolation in 2004, graphene received much attention from the research community due to its outstanding mechanical, thermal, electrical, and other properties which unveiled a wide range of other similar 2D materials.^[38–41] It is considered as the “mother” of all graphitic-based nanostructures, due to the variety of sizes and morphologies. In addition to a single-layer structure, graphene can also be stacked into multi-layered sheets.^[42] Mechanical, thermal, and liquid phase exfoliation and chemical vapor deposition (CVD) are the common techniques to manufacture graphene.^[43,44] The unique physicochemical properties including theoretical high specific surface area ($2600 \text{ m}^2 \text{ g}^{-1}$), good biocompatibility, strong mechanical strength (130 GPa), excellent thermal conductivity ($3000 \text{ W m}^{-1} \text{ K}^{-1}$), high electrical charges

mobility ($230\,000 \text{ cm}^2 \text{ V}^{-1} \text{ s}^{-1}$) and fast electron transportation makes it not only a unique but also a promising material for next-generation electronics applications.^[45–47] Graphene and its derivatives have the capability to form chemical bonds with textiles and therefore, offer great potential to be used in wearable smart e-textiles.^[48–51] Graphene oxide (GO),^[52] possesses strong mechanical, electronic, and optical properties, chemical functionalization capability, large surface area, high stability, and layered structure.^[53–55] Based on the degree of oxidation, it acts as a semiconductor or insulator, enabling usage in many fields.^[56] It is obtained by treating graphite materials with strong oxidizing agents which loosen the tightly stacked graphite layers by introducing oxygen atoms to the carbon,^[57] and forming single-layer graphite oxide sheets.^[58] Reduced graphene oxide (rGO), is another important derivative of graphene exhibiting properties between graphene and GO.^[59,60] It consists of few-atom-thick 2D sp^2 hybridized carbon layers with fewer oxygenous compounds. Though resembles graphene, residual oxygen, and other heteroatoms with possible structural defects degrade its electric properties.^[61] Graphene derivatives (GO and rGO) can be produced in large quantities in their stable dispersions,^[62] however,

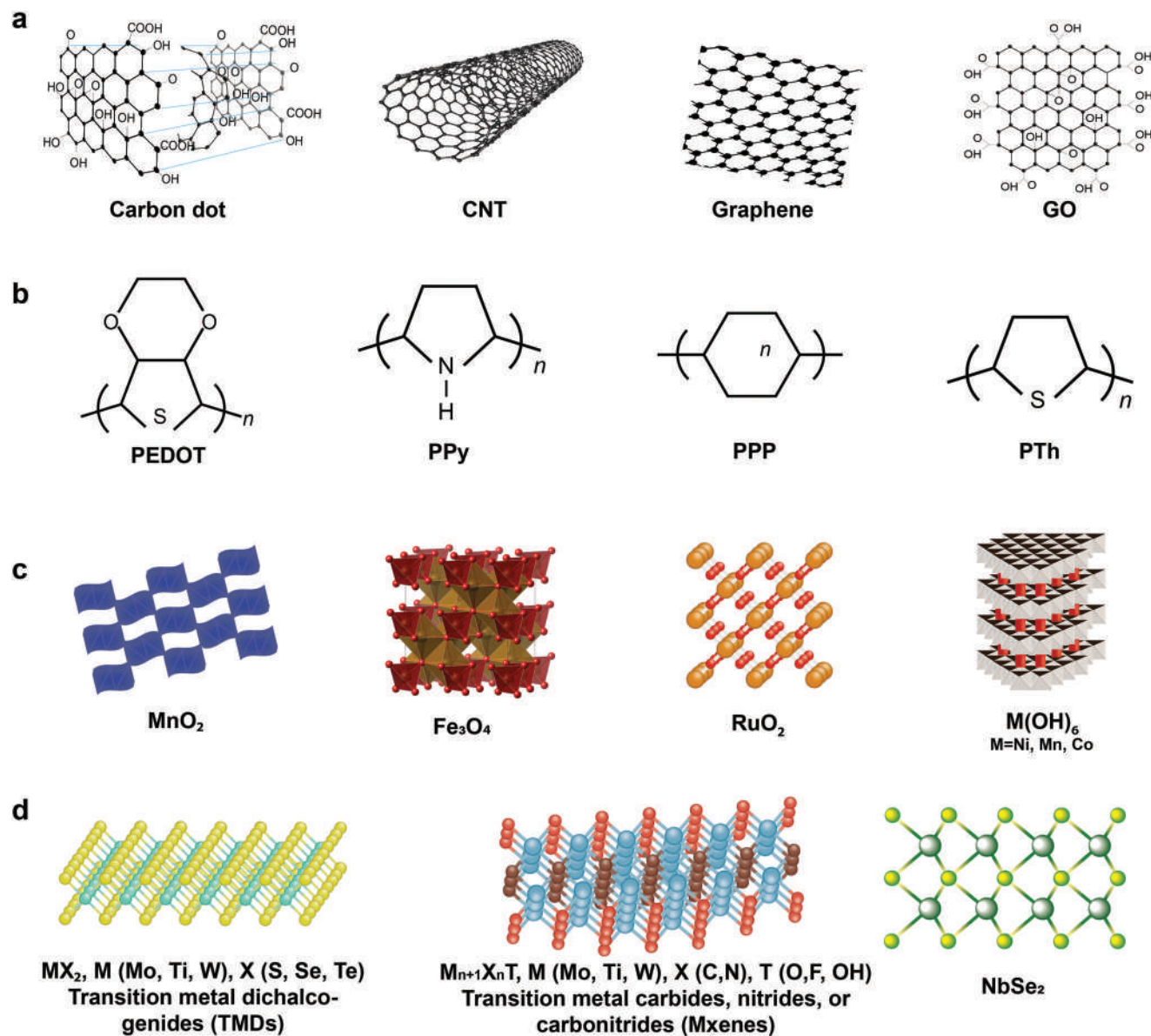


Figure 3. Printable functional materials for e-textiles a) Carbonaceous materials b) Conductive polymers c) Metal oxides/hydroxides and d) 2D materials.

the major challenge is the production of high-quality graphene at a larger scale.^[63] Hybridization of various carbonaceous compounds is also attractive in wearable electronics applications.^[64,65]

2.1.2. Conductive Polymers

Conductive polymers (CPs) are organic polymers that conduct electricity through a conjugated bond system along their polymer chain. Over the past two decades, CPs have been widely studied as a promising active material for wearable electronics owing to their reversible faradaic redox nature, high charge density, and low cost in comparison to metal oxides.^[66] The era of intrinsic CPs started with the invention of polyacetylene; however, Polyaniline (PANI) attracted much more attention due to its cheaper

monomer compared to polyacetylene and ease of synthesis.^[67] PANI offers multi-redox reactions, high conductivity, high specific capacitance, and excellent flexibility,^[68] thus playing a great role in flexible electronics, energy storage, and conversion devices. Sometimes, the use of PANI is recommended with other active materials (carbons, metals, or other polymers) due to its instability issue.^[69,70]

Polypyrrole (PPy) is a π -electron conjugated CP that offers large theoretical capacitance, good redox properties, superior conductivity, ease of synthesis, nontoxicity, biocompatibility, and high thermal and environmental stability.^[71] Similar to PANI, PPy also possesses intrinsic disadvantages, such as brittleness. The processability and mechanical properties can be improved by blending PPy with other fiber polymers or forming copolymers of PPy.^[72] This PPy-based composite material can

demonstrate electrical properties similar to metals or semiconductors while used for wearable applications.^[73] Good water solubility and safety (less carcinogenic than PANI), make PPy a suitable electrode material for wearable electronics.^[74,75]

Poly(3,4-ethylenedioxythiophene), PEDOT is another π -conjugated polymer that exhibits properties such as excellent conductivity ($\geq 300 \text{ S cm}^{-1}$), electro-optic properties, and processability.^[76,77] Though PEDOT is usually nonconductive or shows very little conductivity in its undoped state, it is highly conductive in its oxidized (doped) state. However, the low stability limits its industrial application. Several approaches have been considered to tackle this issue including: the addition of conducting nanofillers to increase conductivity and mixing or depositing metal oxide to enhance capacitance.^[78] For example, the polymer combination with polystyrene sulfonate, i.e., PEDOT:PSS, possesses a high conductivity (up to 4600 S cm^{-1}),^[79] and thus offers promise as an electrode material for wearable electronics.^[80,81] It is known to be a mixed conductor to function as both an ionic and electronic conductor, where PEDOT is responsible for electronic conductivity, and PSS contributes to ionic conductivity.^[82] It is also considered as environmentally stable, and decently biocompatible.^[83] The hybridization of PEDOT:PSS with other active materials (such as carbonaceous compounds) has also been studied for electrode fabrication.^[84,85]

2.1.3. Metals and their Oxides

Production of conductive components is currently based on carbon nanotubes, graphene, organometallic compounds, conductive polymers, and metal nanoparticles. However, the high conductivity values make metal nanoparticles as one of the most effective components for producing conductive tracks. They possess conductivity 2–4 orders of magnitude higher (10^4 – 10^5 S cm^{-1}) than the CPs, carbon, and graphene, (10 – 10^2 S cm^{-1}).^[86] Noble metal particles such as gold (Au), silver (Ag), and copper (Cu) are mostly exploited as potential conductive materials in printed electronics.^[87]

Silver (Ag) has the highest electrical conductivity ($6.3 \times 10^7 \text{ S m}^{-1}$) among the metals, which facilitates direct electronic conduction.^[88] Thus Ag nanoparticles are considered as a suitable choice for the formulation of conductive inks. In addition to high conductivity, it has other advantages including low melting point, high resistance to oxidation, and a feasible processing method.^[86] Therefore, silver is the material of choice for printed electronics^[22,89] and has been used in various substrates via various fabrication techniques; spin coating on PI,^[90] inkjet^[91] or nozzle-jet^[92] printing on PET, inkjet printing on PI,^[93] etc. However, the high cost of Ag limits its commercial use. Copper (Cu), as an alternate material to Ag, has been actively studied due to its lower cost (about only 1% of Ag) and high electrical conductivity (about only 6% less than that of Ag).^[94] However, Cu easily gets oxidized during the synthesis process and post-treatments such as washing, mixing, and storage in ambient conditions.^[95] Due to high intrinsic conductivity ($2.44 \mu\Omega\text{-cm}$), Gold (Au) is considered one of the highly conductive metal inks for wearable electronics.^[96] It also offers good ductility, reliable performance, and easy fabrication.^[97]

Metal oxides, on the other hand, due to their wide variety of oxidation states, are generally considered as prime candidates to use as electrode material in energy storage devices.^[98] Metal oxide electrodes possess exceptional properties, which makes them suitable for a wide range of applications including sensors, semiconductors, energy storage, lithium-ion batteries, solar cells, etc.^[99] Ruthenium dioxide (RuO_2) possesses a high theoretical specific capacitance value (1400 – 2000 F g^{-1}),^[100] demonstrates highly reversible redox reactions, good thermal stability, high electronic conductivity (300 S cm^{-1}), and superior cycle lifespan with high rate capability.^[98] All these properties make RuO_2 as a promising material for supercapacitor (SC) devices.^[101,102] Manganese dioxide (MnO_2) is considered another promising electrode material for electrochemical capacitors,^[103] due to its low cost, high theoretical specific capacitance ($\approx 1370 \text{ F g}^{-1}$), natural abundance, nontoxicity, and environmental friendliness.^[104] Nickel oxide (NiO) is considered another attractive conversion reaction-based anode material in the field of supercapacitors due to its low cost, ease of preparation, environment friendliness, nontoxicity, and high theoretical capacity ($\approx 3750 \text{ F g}^{-1}$).^[105] Additionally, Nickel hydroxide [$\text{Ni}(\text{OH})_2$] is another attractive electrode material for supercapacitors due to its high theoretical capacity and superior redox behavior.^[106,107] Furthermore, Cobalt oxide (Co_3O_4) also possesses superior reversible redox behavior, excellent cycle stability, large surface area, and outstanding corrosion stability,^[108–110] thus another suitable electrode material for supercapacitor electrodes. Due to its layered structure with a large interlayer spacing, Cobalt hydroxide [$\text{Co}(\text{OH})_2$] provides a large surface area with a high ion insertion/extraction rate offering a great potential to become a high-performance electrode material^[98] specifically for energy storage studies.^[110,111] Fe_3O_4 , TiO_2 , SnO_2 , V_2O_5 , etc are also other metal oxides used for electrode fabrication. Despite having such outstanding properties, a few problems still exist that hinder their practical application. Such as the production cost of RuO_2 is higher, and it also suffers from the agglomeration effects.^[100] MnO_2 possesses poor conductivity, considerably lower actual specific capacitance than the theoretical, poor structural stability, and easy dissolving nature in the electrolyte resulting in poor cycling ability.^[111] NiO also has relatively poor electrical conductivity and lower specific surface area. Similarly, $\text{Ni}(\text{OH})_2$ suffers from lower conductivity, and poor stability, with large volume changes during charge–discharge processes. As a consequence, the combination of metal oxides with other active components is much preferred by the researchers for electrode application.^[112–116]

2.1.4. 2D Materials

The discovery of graphene has unveiled a wide range of graphene-like 2D materials (2DM) with outstanding properties.^[38] 2DMs such as transition metal chalcogenides (TMDs)- Molybdenum disulfide (MoS_2), Tungsten selenide (WSe_2), hexagonal boron nitride (h-BN), transition metal carbides/nitrides (i.e., MXenes- Ti_2C) and 2D metal-organic frameworks (MOFs) attracted tremendous research attention due to their extraordinary properties such as large surface area, good electronic conductivity, excellent electrochemical properties, and good chemical, electrochemical, and thermal stability.^[117–119]

2DMs are generally defined as materials with infinite crystalline extensions along two dimensions and one crystalline dimension with few or single atomic layers thickness.^[120] However poor cyclic stability, and large structural changes during metal-ion insertion/extraction, as well as higher manufacturing cost are the major challenges for 2DMs which require further improvements to find their wide applications in wearable electronics.^[121]

MoS₂, an exciting 2D material due to its graphene-like properties has been investigated to a lesser extent but is gaining increased interest nowadays for integration into electronic devices.^[122] In addition to conventional synthesizing processes such as micromechanical peeling or chemical vapor deposition, MoS₂ is currently being synthesized by ultrasonic treatment similar to graphene. Large volumes of monolayer and few-layer flakes can be produced which can further be deposited onto a substrate or formed into films.^[123] Their favorable electrochemical properties are mainly a result of the hydrophilicity and high electrical conductivity, as well as the ability of the exfoliated layers to dynamically expand and intercalate various ions.^[124] Hexagonal boron nitride (2D-hBN), an isomorph of graphene,^[125] is uniquely featured by its exotic optoelectrical properties together with mechanical robustness, thermal stability, and chemical inertness. Though an insulator itself, strategies such as doping, substitution, functionalization, and hybridization can tune its properties and functionalities, making it a truly versatile functional material for a wide range of applications. BN-based nanomaterials alone or in combination with other 2DMs, have huge potential in next-generation microelectronic and other technologies,^[126] especially electrodes, electrochemical energy storage and conversion.^[127]

MXene is a relatively new family of 2D metal carbides, nitrides, and carbonitrides, with unique intrinsic physical/chemical properties, that have thoroughly been investigated and can be used in various research fields, including ceramics, energy storage, sensors, water purification, catalysis, thermoelectric and photothermal conversion, solar cell, biomedicine, and microwave absorption and shielding.^[128,129] 2D MXenes possess attractive electrical and electrochemical properties including hydrophilicity, conductivity, surface area, topological structure, rich surface chemistry, tunable terminations, excellent processability, etc.^[130–132] and thus gained much attention in electrochemistry. The term MXenes (with a formula of M_{n+1}X_n) are named after other 2D analog materials silicene, graphene, phosphorene, and so on, synthesized by extracting an atomic layer from ternary MAX (M_{n+1}AX_n) ceramics, where M = early transition metal elements (Ti, Zr, Mo, Nb, V, Mn, Sc, Hf, W, and so on), A = group 13 or 14 (Si, Al, Ga, and so on), X = C or/and N. In addition to being used as alone, the improved coupling and hybridization of MXene with other materials at the nano-scale makes it one of the most intriguing materials for wearable applications.^[133]

2.2. Textile Substrates for Printed E-textiles

With the development of technology and a variety of requirements, the demand for smart materials and intelligent textiles growing rapidly all over the world. A multifunctional wearable electronic device requires a conformal platform close to the human body, thus textile or fabric that is usually em-

bedded with normal clothes and worn on various body parts has emerged as a promising substrate and platform for wearable electronics. Textiles with basic characteristics of being soft, flexible, air-permeable, low-cost, and integrable with various forms of garments^[134,135] are commonly made of natural cotton, silk, or wool fibers or synthetic poly (ethylene terephthalate) (PET) or polyester, polyamide or nylon, polypropylene, viscose rayon filament.^[136] Additionally, there are polyimide (PI), thermoplastic, polyethylene naphthalate (PEN), and thermoplastic polyurethane (TPU) based textiles in use. These textiles vary in their physical, chemical, thermal, and tensile properties and therefore, the choice of any specific substrate depends on the properties required for the end-product. For example, PET excels in applications requiring a smooth surface of a few nanometres of thickness and optical transparency. PI possesses high glass transition temperatures and relatively higher mechanical as well as chemical strength in comparison to PET and is widely preferred for fabricating flexible printed circuit boards (PCBs). TPU and polydimethylsiloxane (PDMS) are suitable for developing stretchable devices, whereas paper is suitable for cheap and disposable devices. Textile-based substrates offer several advantages over plastic or paper-based substrates when flexibility and stretchability are concerned. For instance, the porous structure of textiles provides abundant support for the loading of active materials, facilitating rapid absorption due to their hydrophilic nature, resulting in much higher areal mass loading. Therefore, low-cost, and highly efficient textile-based wearable electronics have already gained the potential to be used for future high-tech sportswear, work wear, portable energy systems, military camouflages, and health monitoring systems.^[137,138]

The surface wettability of a polymeric material is of great importance when it comes to different applications in material science.^[139] This is a basic feature of printing substrate which is a direct intermolecular interaction occurring when liquid and solid medium are brought together. The study of wettability involves the measurements of contact angle (CA), indicating the degree of wetting when a solid and liquid interact. CA when low (<90°) corresponds to high wettability, meaning that the fluid will spread over a large surface area. A high CA (>90°) represents low wettability, so the fluid will minimize contact with the surface and form a compact liquid droplet. CA>150° indicates minimal contact between the liquid droplet and the surface and it corresponds to a superhydrophobic behavior.

Surface tension, or surface free energy, both similar parameters, corresponds to the residual binding capacity of a material surface, i.e., the binding capacity of atoms or groups of atoms that constitute the border surface of the material of interest.^[140] When talking about solid surfaces only, the term “free surface energy” is usually used. Both terms refer to the same physical quantity and share the same symbol. The unit of the free surface energy is Jm⁻², and the unit of surface tension is Nm⁻¹, which is, once multiplied by m m⁻¹ the same unit.^[141] The values of surface free energy of some non-modifiable polymer films are in **Table 1**.

2.3. Textile Surface Engineering and Post-Treatment

The key motivation behind the development of smart textile technologies is providing additional functionalities to common

Table 1. Specification of various substrates employed for e-textile fabrication.^[142,143]

Flexible textiles/ polymer substrates	Surface energy (mN m ⁻¹)	Transparency (%)	Water absorption (%)	Solvent resistance	Folding endurance (cycles)	Dimensional stability	Thickness (μm)	Surface roughness	Density (g/cc)	Glass transition temperature (Tg)	Young modulus (GPa)
PET	44.0	90	0.6	Good	>800	Good	13–356	Poor	1.38	81–150	2–3.2
Polycarbonate (PC)	34.2	92	0.16–0.35	Poor		Fair		Good		145	2.0–2.6
Polyurethane (PU)	38	-	0.2	Good	2 000 000	Good	25–500		1.32	80	2.41
Polyimide (PI)	43.8	35–60	1.3–3.0	Good	5000–285 000	Fair	25–125	Good	1.42	360–410	2.76
PDMS	20.4	-	>0.1	Poor		Good	125–4775		0.97	145–150	0.57–3.7
Polypropylene (PP)	30.2	84.0–90.0	0.01	Good		Good		Good		0	0.008–8.25
Polyacrylate (Pacr)	-	>90	0.2	Good		Good		Fair		105	2.4–3.4
PEN	-	88	0.3–0.4	Good	>1000	Good	12.5–250	Good	1.33	120–200	2.2–3
Polyethersulphonate (PES)	-	89.0	1.4	Poor		Fair		Good		223	2.2
Polycyclic olefin (PCO) /polynorbornene (PNB)	-	91.6	0.03	Good		Good		Poor		35	1.9

textiles and consequently to a garment.^[144] Functional textiles can be prepared in two ways. One way is to prepare the functional fiber first and then weave or knit it into a textile. This is achieved by blending and composite spinning of the fiber solution with the functional additives of uniform dispersion to achieve fiber functionalization. The other way is to modify ordinary textiles with functional finishes by coating or printing. The main drawback of this technique is the weak bonding force between the finishing agent and textiles. However, its strength is more durable, and functionality can be maintained for a long time.^[145]

Printed electronics often require a uniform and smooth substrate that is also solvent resistant, chemically and thermally stable, stretchable, conformal, flexible, and light weight. One of the key challenges with printed e-textiles is the ability to achieve continuous highly conductive electrical tracks on a rough and porous textile substrate. Due to the orientation of fibers or yarns, textile fabrics demonstrate an intrinsic planar anisotropy of the general properties.^[146] Also, the morphology of the fiber changes constantly due to the exchange of water molecules with surroundings, which makes it extremely difficult to produce uniform and continuous conductive paths using low viscous inkjet inks.^[147] A number of researches have been conducted to introduce an interface layer for reducing such roughness and porosity of textiles. Previous studies have suggested polyurethane acrylate-based interface layers,^[148] however the deposition of such interface layers suffers from a few drawbacks. These usually constrain the potential feature resolution, not suitable for small quantities of material deposition or roll-to-roll manufacturing. In our previous work,^[147] we reported an organic nanoparticle-based inkjet printable textile surface pre-treatment which enables the production of all inkjet-printed graphene-based wearable e-textiles which is breathable, comfortable and environmentally friendly, **Figure 4a**.

Another key challenge of the wide commercial adoption of textile-based wearable electronics is their poor stability on repeated laundry washing.^[149] Good washability is essential for e-textiles to survive intense mechanical deformations and water invasion of washing cycles used during their life cycles.^[150] The delamination of the conductive functional materials due to the mechanical forces experienced during washing cycles, results in a loss the electrical performance.^[151] The wash stability of wear-

able e-textiles can be improved via a number of methods including a textile surface pre-treatment with Bovine Serum Albumin (BSA), or by a post-treatment for instance embedding with PDMS, polyurethane (PU) sealing, a screen-printed PU top layer, and transferred mold or, hot melt encapsulation to seal conductive track on the textile surface.^[152] In our other work,^[151] we used a translucent, thin, and stretchable PU-based encapsulant to protect screen-printed graphene-printed wearable e-textiles, **Figure 4b,c**. Such encapsulation material adheres with textile materials, keeping the printed graphene layer attached to textiles but covered and protected even during repeated wash cycles, **Figure 4d**.

Textiles with other functional properties such as antimicrobial, water resistance or water proofing, soil resistance, self-cleaning, thermoregulations, etc are also of particular interest for various functional applications.^[153] For example, efforts at the development of functional textiles with antibacterial effects have accelerated recently to provide protection against airborne bio-particles and micro-organisms.^[154] Especially in healthcare environments, textiles with antibacterial properties form a significant part of the hygienic regime of surgical procedures, preventing the spread of infectious pathogens to both patients and staff. Antibacterial finishing thus provides the textiles an improved resilience against microorganisms to prevent the destruction of fibers and discoloration and increases the durability of the textiles with longer life by minimizing microbial colonization of textiles and the potential for transfer from fabric surfaces.^[155] Numerous methods have been developed in this context to impart antibacterial properties to textiles namely padding, spraying, coating, printing, or foam finishing.^[156]

3. Printing Techniques for E-textiles

The printing process involves a controlled deposition of material, either for decorative or functional purposes, onto a substrate in such a manner that a pre-defined pattern is produced. Though other deposition processes including painting or spraying are there, printing is further highlighted because it can rapidly produce identical multiples of the original. Three basic methods of printing are there; positive contact, negative contact, and

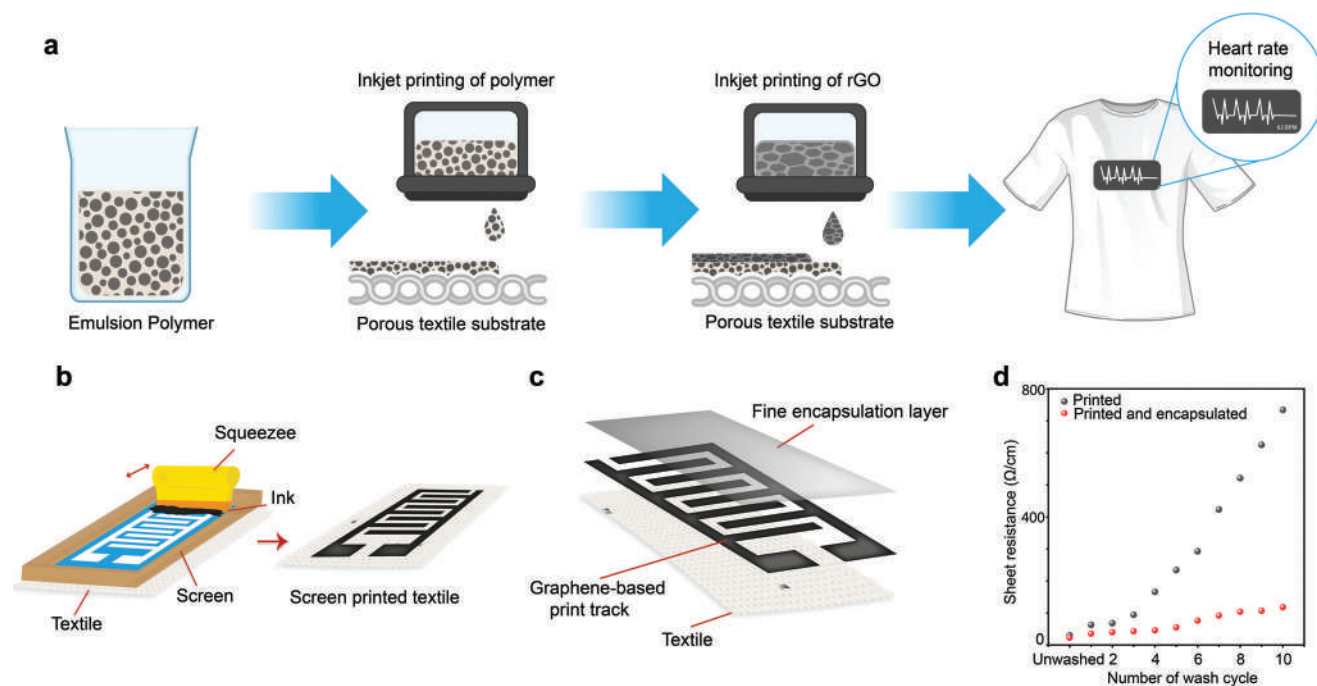


Figure 4. Textile surface pre-treatment and post-treatment for e-textiles. a. Inkjet printing of organic nanoparticle coating followed by inkjet printing of conductive rGO to prepare conductive textile. Reproduced with permission.^[147] Copyright 2017, The Royal Society of Chemistry. Screen printing of b. graphene ink on textiles c. Polyurethane (PU) based encapsulation post-treatment to improve washability d. Comparison of the change of electrical resistance of printed textiles with and without encapsulation layer. Reproduced with permission.^[151] Copyright 2022, The Authors.

non-contact printing. Since the substrate is touched by the print master during printing, the first two methods are described as contact printing. Positive contact type resembles the stamping principle, examples include printing presses and woodcuts. Gravure or screen printing are examples of negative contact printing. In the non-contact printing process, the printer does not come in contact with the substrate. The most common example of non-contact printing is inkjet printing where ink is ejected on a substrate from a nozzle.^[157] The available print technologies are briefly introduced in the following section.

3.1. Screen Printing

Screen printing (Figure 5a) generally uses a screen mask which includes a fabric mesh with the patterns of the image. The ink is pressed using a squeegee such that the ink penetrates the substrate through the portion of the mesh not covered with the fabric material, forming a printed pattern.^[158–160] Basically, this is a selective transfer process of ink through the open areas of the unmasked portions of a screen. Masking of the screen is accomplished by the transfer of a photographically produced image from its temporary film base support to the screen.^[161] Low cost and high processing speeds are some potential advantages of screen printing, however, changes in shear force can continually influence ink viscosity, leading to pattern distortion. Here, the printing resolution is limited by the printing speed. Thus, there is a need to optimize the formulation of conductive inks suitable for screen printing while maintaining the good conductivity and fidelity of printed patterns.^[160] One of the biggest advantages

of screen printing is the versatility of the substrates including paper, paperboard, polymer materials, textiles, wood, metal, ceramics, glass, and leather. In addition, the screen printing process enables ink application not just to flat surfaces but to irregular ones too, as long as the thick ink adheres properly to the printed substrate and the screen can adapt to the substrate's shape consistently without distortion.^[162] The wide variety of polymer substrates requires different types of inks. Printing inks must be selected according to the type and surface characteristics of printing substrates. A sharp edge of printed image requires ink with higher viscosity in screen printing than in other printing techniques. Screen printing inks can be categorized by the drying process into the following groups: evaporative (water-based and solvent-based), oxidizing, catalytic, and UV inks. Solvent-based inks are very common in polymer screen printing applications, but there are some other inks that are dried by a slower process of oxidation and polymerization, too. Few inks also use UV energy for curing by polymerization.^[162] Screen printing is by far the most widely used method for wearable e-textile applications. Researchers have attempted screen printing for the fabrication of textile-based strain,^[163] pressure,^[164] temperature,^[165] and humidity sensors.^[166] Several textile-based biosensors such as an electrocardiogram (ECG),^[167,168] electroencephalography (EEG),^[169] electromyography (EMG),^[170] and electro-oculography (EOG)^[170,171] were also reported via screen printing method. In addition to these, several screen-printed textile-based supercapacitors,^[172] heating elements^[144] were also demonstrated. We will discuss in detail about screen-printed wearable e-textiles in the subsequent sections.

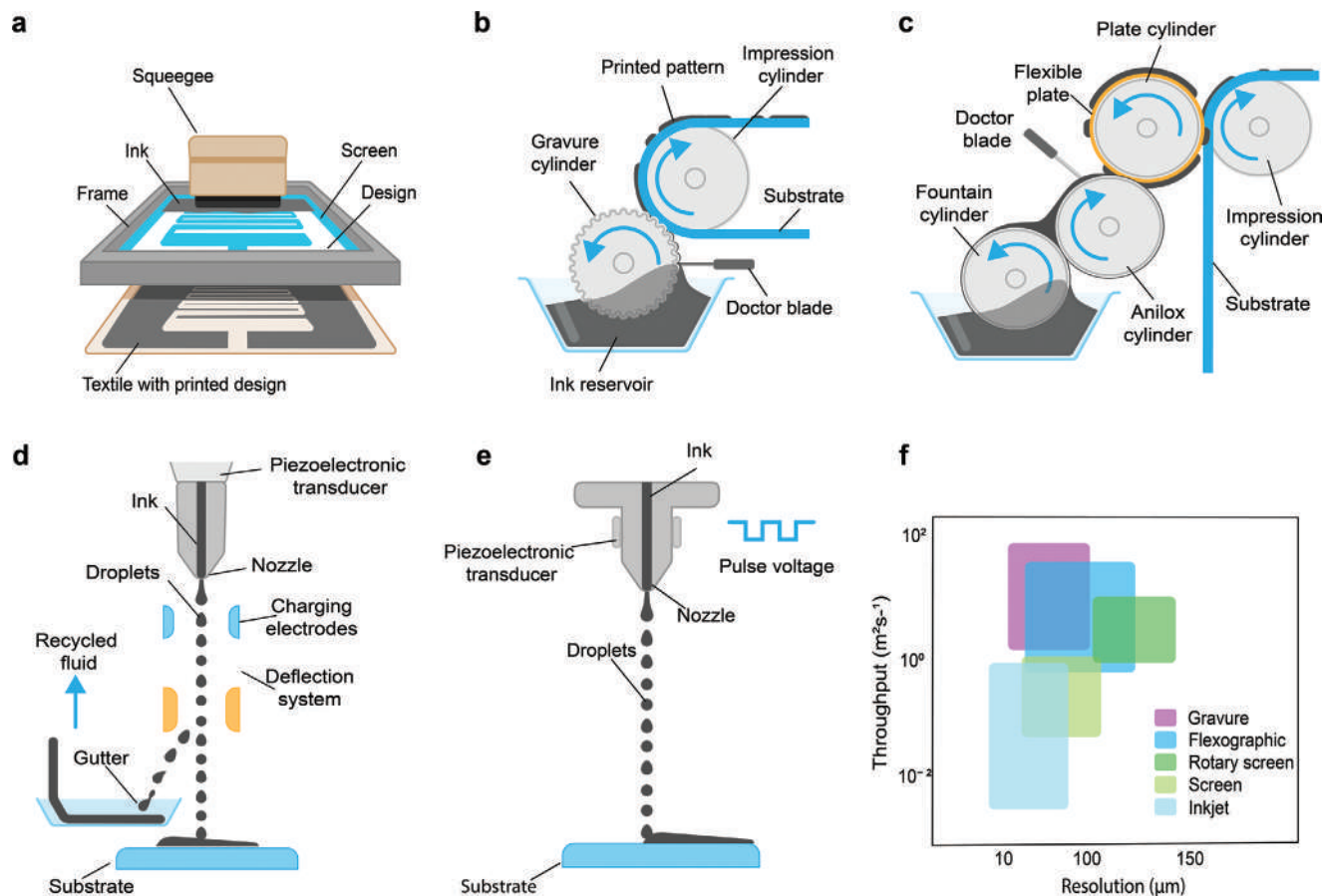


Figure 5. Printing technologies for e-textiles fabrication, a) Screen printing b) Gravure printing c) Flexographic printing d) Continuous inkjet printing, and e) Drop-on-demand inkjet printing f) Comparison of print throughput and best achievable resolution ranges of print technologies. Reproduced with permission.^[173] Copyright 2018, The Royal Society of Chemistry.

3.2. Gravure Printing

Gravure is a widely used roll-to-roll printing method (Figure 5b), characterized by excellent print quality with high speed, often used for large volumes of magazine and catalog printing.^[174,175] An engraved metal roll is used in gravure printing to transfer the ink directly to the substrate. The depression in the engraved surface forms the print pattern. The roll is immersed in the ink bath where the etched portions pick up and hold the ink followed by a blade to remove the excess ink. An impression cylinder pushes the substrate film with the depressed, ink-filled regions of the gravure roll, thus transferring the ink to the film. A dryer after that drives off the solvent creating the final layer of coating.^[176,177] The depressions in the gravure rolls, to hold the ink can be etched chemically, mechanically, or by laser. One of the advantages of gravure printing is that the rolls are hard, and durable, thus is cost-effective for long runs though the initial costs are high. The printing quality depends on the ink viscosity, substrate speeds as well as the pressure of the impression roller. A relatively high print pressure (1–5 MPa) and quite low-viscosity inks (50–200 mPa) perform a good ink transfer. However, comparatively lower viscosity inks (1–10 mPa) have also been applied successfully for the printing

of some biomolecules.^[178] Another advantage is stretchy and unstable fabrics can also be printed by this technique efficiently.^[179] The printing rate in gravure printing may be achieved up to 25–1000 m min⁻¹.^[175] Liquid gravure printing inks are dried by using physical method, i.e., by evaporation of the solvents, and inks of two components by chemical curing. The solvents speed up the drying process, but volatile organic chemicals (VOCs) are emitted, which need to be recovered (typically 87–98%). A small part of the remaining solvents (1–3%) may still penetrate the pores of the paper, causing the characteristic smell of gravure printed products. Recent developments decrease the amount of residual solvents, substitute toluene, and minimize solvent emission. Water-based inks are of increasing interest, due to no VOC emission, especially in the field of packaging materials. But more than threefold to fivefold energy is required in the drying unit than is required with solvent-based inks, and this also involves print quality problems.^[174] Since gravure printing is widely used for large-scale roll-to-roll textile batches, for lab-scale e-textiles it is not a very popular method. However, few researchers reported gravure printing for textile-based humidity sensors.^[180,181] We assume, upon commercialization, that gravure printing might be a high-speed production choice for large-scale e-textile fabrication.

3.3. Flexographic Printing

Like gravure printing, flexographic (shortly named as flexo) printing is another high-speed roll-to-roll printing technique, Figure 5c. The printing process involves transferring ink, from the surface of a flexible plate to the substrate. The pattern is made into plates that are attached to a roll. The printing ink is metered onto the surface of the plate by an “anilox”- an engraved/ etched roller of chrome or ceramic similar to a gravure cylinder but with a uniform distribution of cells (size, shape, and depth). The volume of ink to be transferred to the printing plate depends on this specification of the anilox. The ink is taken into these cells and a doctor blade assembly wipes the excess ink subsequently. The plate transfers the ink film from the anilox to the substrate by impression.^[182] Flexo plates use vulcanized rubber or photopolymer materials that are attached to rotating cylinders.^[183] The difference between flexographic printing the gravure printing is, that instead of relying on impressing the film into the ink containing cavities of the roll, the ink on the flexographic plates relies on the ridges of the pattern.^[176] The relatively inexpensive plates, advanced quality, and productivity of flexographic printing often make a printer difficult to choose between flexographic and gravure printing. Flexography is now dominant process for labeling, leaflets, and cartons markets in packaging.^[182] Flexographic printing allows to achieve increased printing speeds, of $\approx 10 \text{ m}^2 \text{ s}^{-1}$. Resolutions of $\approx 0\text{--}100 \mu\text{m}$ can be achieved. This technique is also suitable for the creation of RF circuits, where very good conductivities are necessary since a thicker ink layer can also be deposited ($5 \mu\text{m}$).^[184] Flexographic inks maybe solvent-based, water-based, or UV-curable inks. To ensure the regular ink flow in the printing unit, low-viscosity printing inks are required in flexographic printing, generally lower than $0.05\text{--}0.5 \text{ Pa s}$ with a flow time equal to $18\text{--}35 \text{ s}$. Concentrates of both solvent- and water-based flexographic have relatively higher viscosity in the range of $0.1\text{--}0.25 \text{ Pa s}$.^[185] High-solvent content and a low level of pigment concentration are required. An exception is for UV-curable inks, which do not include any solvents. The basis for their production is binders, usually acrylates, which under the influence of UV radiation converted into a dried layer. In the case of solvent-based and water-based inks, drying of the ink on a printing base is the result of evaporation of the solvent. The more volatile solvents are in the ink, the quicker the drying occurs.^[186] Similar to gravure printing, flexography is suitable for large-scale production. We assume for large-scale production of commercial-grade e-textiles, flexography could be a suitable choice.

3.4. Inkjet Printing

Inkjet printing (IJP) also known as digital printing of functional materials with specific electrical, chemical, biological, optical, or structural functionalities has gained significant research interest due to its wide range of applications in different processes and purposes, from the batch coding of soft drink cans to smart electronic textiles.^[187,188] IJP allows the deposition of tiny droplets onto the substrate without depending on the high-speed operation of mechanical printing elements. Nozzle sizes for the printers are usually $20\text{--}30 \mu\text{m}$ with ink droplets as small as 1.5 pL with the achievement of high resolution (dots per inch).^[189] Be-

sides 2D print results, in ink jet printing, “structural” fluids can also print layers that harden to form 3D structures. In spite of all these, several considerations such as the printing speed, cost-benefit issues, printed film uniformity and material, and fluids’ jet-ability as ink- are still points of concern for printers.^[190] Two distinct modes of inkjet printing are there, 1) Continuous inkjet (CIJ), suitable for industrial scale and mass production, and 2) Drop-on-demand (DOD), used for small-volume and prototype sample production.

3.5. Continuous Inkjet (CIJ) Printing

Continuous inkjet printing (CIJ) utilizes a pressurized fluid stream and a piezoelectric element at high frequencies ($\approx 20\text{--}80 \text{ kHz}$), to form droplets, Figure 5d. A continuous and consistent stream of fluid droplets of uniform size and spacing can be generated by the careful adjustment of the voltage and frequency of the piezoelectric device. A conductive material placed in the fluid can impart an electric charge on selected drops breaking them off from the fluid stream which are further deflected by means of high voltage deflector plates to form various patterns onto the substrate. Uncharged droplets are captured by a gutter mechanism and re-circulated through the system. A “catcher,” a plate situated below the nozzle to perform patterning, actuates into and out of the path of the droplets, only allowing the droplets to pass when pattern material is required.

For industrial environments, CIJ offers cheaper alternatives and a high print rate by minimizing transient and clogging issues, which is a limitation of DOD.^[191] CIJ printing process possesses high flexibility, precision, and speed allowing it to be used in applications in high-speed graphical applications such as coding, marking, and labeling, as well as textiles and micro-manufacturing industries. The benefits of CIJ over DOD are improved image quality, throw distance, and the ability to deflect droplets independent of gravity.^[192] Since CIJ printing produces large-diameter droplets ($\approx 40 \mu\text{m}$), the print resolution is relatively low. They are able to use volatile solvent-based inks, allowing rapid drying and proper adhesion on many substrates. This also makes the CIJ a messy and environmentally unfriendly technology.^[190] CIJ can be designed as a binary or multiple-deflection system based on the drop-deflection methodology. In a binary deflection system, the drops are either charged or uncharged. The charged drops can fly directly onto the media, while the uncharged drops are deflected into a gutter for recirculation. On the other hand, in a multiple-deflection system, drops are charged and deflected to the media at different levels; the uncharged drops fly straight to a gutter to be recirculated. This approach allows a single nozzle to print a small image swath.^[193]

3.6. Drop-on-Demand (DOD) Inkjet Printing

Drop-on-demand (DOD) printing, today, is the most commonly used printing technique in laboratory and small-volume printers, Figure 5e. Due to the flexibility of the variety of inks used and the simplicity of application, it works very well with the prototype environments. The printer nozzle while passing over the

substrate, an actuator ejects a droplet wherever patterned material is required,^[191] the production of each drop occurs rapidly in response to a trigger signal. Typically DOD print head contains multiple nozzles (100 to 1000, specialist heads may contain only a single), and instead of drop ejection resulting from external fluid pressure as in CIJ printing, the drop's kinetic energy derives from sources located within the print head, very close to each nozzle. In DOD printing, the liquid emerging from the print head in the form of a jet is then detached from the nozzle and collapses under surface tension forces to form one or more droplets.^[194] Typical drop volumes of individual ink drops in DOD are in the range of 1–70 pL and produce print spot sizes in the range of 10–50 μm in diameter. The slower speed (5000–20 000 Hz per second) of making drops is the limitation of DOD.^[195] The high accuracy and small droplet size of DOD inkjet printers are the key advantages for the direct patterning of functional materials. Depending on the way of generating the pressure pulse, the DOD inkjet printers can be further divided into four main types: thermal, piezoelectric, electrostatic, and acoustic. Most of the DOD inkjet printers, on the market, are using either the thermal or piezoelectric principle. Electrostatic and acoustic inkjet methods are yet to be developed for commercial wide-scale application.

The thermal inkjet (often called TIJ) printer head is composed of a chamber that contains the print fluid. On one of the walls of the chamber, there is an electrical resistor designed to heat to high temperatures. Additionally, there is a nozzle to eject the print fluid. When current is applied to the resistor for a short span of time (a few microseconds), it heats the surrounding fluid in its immediate vicinity and causes local boiling (micro-boiling, MB). The rapid pressure rise forces liquid at a distance from the resistor into the nozzle and out of the chamber. The rapid temperature rise and resulting temperature gradients on the resistor shorten its lifetime and therefore the lifetime of the entire head is shorter than other printer heads, such as the piezoelectric head.^[196] Though this is a simple and cheaper technology, there is a limitation of utilizing a range of print liquids (restricted to fluids that will satisfactorily vaporize).

Piezoelectric DOD works in a similar way to TIJ in that droplets are ejected by piezo-ceramic distortion, which occurs when an electric field is applied to it. In a piezo DOD system, the actuator is based on a piezoelectric crystal, which changes shape as a consequence of a current being passed through it. In some print head designs, the piezo component pushes into the ink chamber to create pressure pulses, in others it surrounds the chamber or forms a wall of the chamber. The outer surface of the piezo-ceramic has a conductive coating, that provides an electrical connection to it. The size of the ink droplets is determined by the voltage applied for piezo-ceramic deflection, the pulse duration, and the diameter of the nozzle. Piezoelectric print heads can handle a wider range of liquids than thermal heads and the print heads have longer life. However, the print heads and supplementary hardware are costly.^[197]

In the electrostatic inkjet printing method, the ejecting droplet through the nozzle is induced by electrostatic forces, applied between an electrode and the nozzle attracts the free charges within the ink toward its surface, the charged fluid is separated from the inkjet head as fine droplets. However, it is difficult to make the droplet smaller than the nozzle size in piezoelectric systems. To

overcome this issue, the electrostatic inkjet method was introduced. Besides ejecting fine droplets, electrostatic inkjet printing is also able to print relatively viscous ink, offering higher resolution than that of piezoelectric inkjet printing.

The acoustic inkjet printing technology is a relatively recent development, where droplets are generated by acoustic energy. The ultrasound beam is focused with an acoustic lens onto the surface of fluid that produces an ink droplet. Print head nozzles are safe from clogging in this system with a versatility of ejected droplet sizes (ensured by changing the fluid-to-transducer distance in order to vary the focal spot diameter on the surface of the fluid).^[190]

Inkjet printing delivers a small amount of materials as ink to a specific location of substrate, which opens the door to design versatility.^[190] It does not require stencils; achieving a cost-effective printing choice for a much smaller print run than conventional screen printing.^[198] Being highly adaptive, it can be applied to a wide range of different processes and purposes, from batch to rapid prototyping in product design.^[187] It also provides possibilities for new workflows, short production runs, sustainable printing environments, quick response time, and customization.^[179] Considering all these benefits, inkjet printing is considered to be the future of e-textiles. Therefore, after screen printing, inkjet printing is the most widely used technique to fabricate e-textiles. Researchers have already reported inkjet printing methods to fabricate textile-based strain,^[199] pressure,^[200] temperature,^[201] and humidity sensors.^[202] Several biosensors such as ECG,^[147] EEG,^[203] and EMG^[203] are also reported. Inkjet printing has also been used to fabricate textile supercapacitor electrodes.^[204]

4. Functional Printing Inks

4.1. Formulation of Printable Inks

Conventional printable inks usually contain four components: Dye or pigment, binder, solvent, and additive. The main component colorant may either be a dye or a pigment, which needs to be dispersed properly in a vehicle, consisting of binders, solvents, and additives. All these combinedly provide viscosity and flow properties to the printing ink.^[205] Functional inks, on the other hand, have an electrically functional element instead of or along with the pigment. They usually possess electromagnetic, thermal, chemical, and/or optical properties, and are classified into conductive, semi-conductive, dielectric, and resistive ink categories.^[206] Binder (also called thickener) holds the functional components and contributes to properties such as hardness, gloss, adhesion, and flexibility. They become an integral part of the pigment-binder-substrate system by crosslinking after evaporation (by drying or curing) is carried out of the printing ink. Alkyds, polyamides, polyimides, rubber, ketone, acrylic, epoxide, etc. resins are typical binders used in printing ink formulation. Solvents act as the diluent of the other ink components (i.e., pigments, binders, and additives). The main objective of using a solvent is to prevent the agglomeration of materials along with keeping the ink paste in fluid form, sufficient enough to apply on a substrate. For dissolving polar molecules, polar solvents such as water, alcohol, and esters are widely used. Liquid hydrocarbons are used for nonpolar molecules. Sometimes co-solvents

Table 2. Typical composition of printable inks.^[173]

Composition	Screen	Gravure	Flexographic	Inkjet
Pigment	12–20	12–17	12–17	5–10
Binder	45–65	20–35	40–45	5–20
Solvent	20–30	60–65	25–45	65–95
Modifier and/or additive	1–5	1–2	1–5	1–5

are combined with solvents to cut the cost. An ideal solvent and/or co-solvent dissolves the resin/polymer without dissolving or degrading the pigment; evaporates at a compatible rate with the desired printing process, possesses required viscosity, and should be compatible with the image carrier. Depending on the printing processes, the substrates, the drying conditions, and the final purpose of the prints, water or any of a broad range of organic solvents can be used.^[173] However, the presence of residual toxic solvents in printed electronics still exists which limits the scalable adoption of wearable electronics.^[207] Therefore, for e-textile application a solvent must make a stable solution with the functional ingredients,^[208] should not degrade the textiles themselves, and most importantly need to be non-toxic and safe for physical health for everyday use.^[209] A water-based ink system thus, could be considered to be beneficial to avoid such limitations for the e-textile print ink formulation.^[210] Modifiers and/or additives are added to the print ink to either enhance the printability of the ink or of the cloth. Modifiers may tailor the viscosity or surface tension of the print ink to enhance the printing performance of the print ink. Several types of additives include preservatives (hygroscopic agents), anti-oxidizing agents, fastness enhancers, or functional agents such as anti-flammable agents, antiseptics, and disinfectants.^[211] Additives are incorporated into ink formulations in amounts not exceeding 5%,^[206] **Table 2** presents a typical composition of various print inks.

4.2. Requirements of Conductive Inks

As we discussed in Section 1, the development of electronic textiles hinges on the integration of electro-active materials with textile substrates. The 1D conductive textiles could be typically formed by either spinning inherently conductive polymers or blending electroactive substances into the spinning solution. On the other hand, for 2D conductive fabrics, methods such as padding and coating are commonly employed, ensuring a thorough coverage of electroactive materials. Consequently, these processes involve substantial usage and disposal of conductive materials, often presenting issues with toxicity, environmental impact, and non-biodegradability. However, an alternative approach to address these concerns is through printing, which involves the localized deposition of active materials in the form of printing ink or paste directly onto textiles. This method offers a sustainable solution, significantly reducing material wastage compared to traditional yarn and fabric coating processes. Moreover, printing techniques are known for their simplicity, cost-effectiveness, time efficiency, eco-friendliness, and versatility when applied to various textile substrates. A liquid to be con-

sidered as printing ink or paste must need to possess some attributes.

A liquid has an internal resistance to flow, “viscosity” is a measure of this resistance to flow or shear. It can also be termed as a drag force and is a measure of the frictional properties of the fluid.^[212] According to viscosity, printing inks may be classified as either low-viscosity printing inks or high-viscosity print pastes. Liquid printing inks like flexographic, gravure, and inkjet inks fall under the low-viscosity category.^[185,213] In the case of offset, screen printing, and pad printing inks, the viscosity remains >1 Pa-s, which are categorized as high-viscosity printing inks. The term “rheology”, a key feature to describe the print paste behavior, is “the study of the deformation and flow of matter”.^[214] For a print ink (for lower viscosity formulation, usually used for gravure, flexographic, or inkjet process), density, viscosity, surface tension, drying rate, flow behavior, flow time, etc. are important factors determining the efficient output of the print process. Though the viscosity of a print paste or ink can be modified; it is challenging to keep the same electrical properties with changing the viscosity. Increasing the temperature decreases the viscosity whereas the evaporation of solvent increases the viscosity. Solvent might be used to tune the viscosity of the ink. In addition to this, increasing the dispersant concentration decreases the viscosity of the ink.^[213]

Surface tension of the ink is another important parameter of the print paste or ink, required for the formation of drops, which also affects the interaction between the ink and the substrate, i.e., wettability and printability. Surface tension depends on the composition; solvents such as polar liquids have higher and the non-polar one has lower surface tension. Thus, water (surface tension 73 mN m⁻¹) based inks have higher values, and ethyl alcohol (24 mN m⁻¹) or other nonpolar solvents-based inks have lower values of surface tension.^[215] A proper bonding exists between a liquid and a substrate surface when the surface tension of the liquid is 2–10 mN m⁻¹ lower than the surface energy of the substrates.^[216] An increase in the temperature or an increase in solid content can decrease the surface tension of an ink.^[213]

According to the viscous flow behavior, liquids may either be Newtonian fluids or non-Newtonian fluids. The viscosity of a Newtonian fluid remains constant and they exhibit ideal viscous flow behavior. Any physical or chemical modification to the ideal Newtonian fluid may affect the flow behavior.^[217] Non-Newtonian fluids are two types; Shear-thinning or pseudo-plastic fluids are characterized by an apparent viscosity, which decreases with increasing shear rate.^[218] The usual printing pastes exhibit shear-thinning flow behavior.^[185] In the case of shear thickening (or dilatant) fluids, the apparent viscosity increases reversibly as the shear rate increases.^[219] Shear thickening fluids are not recommended in printing, since the fluid does not distribute properly, particularly with fast-running presses related to the occurrence of the high shearing stresses.

Another characteristic is important for print ink named “thixotropy”. This is a time-dependent phenomenon that means that the viscosity of the fluid depends on time as well as shear rate, i.e., the viscosity of thixotropic fluids decreases with time.^[220] When stirring at a constant shear rate, the gel structures in the ink break, and then a gradual recovery of the structure occurs, when the stress is removed, thus thickening when the ink is kept standing. The highly viscous printing

Table 3. Comparison among various printable ink parameters.^[185,213]

Ink viscosity	Print technology	Viscosity (Pa.s)	Surface tension (mN m ⁻¹)	Layer thickness (μm)	Feature size (μm)	Maximum particle size (nm)	Maximum preferred particle size (nm)	Maximum solid content (%)	Flow Properties
Low-viscosity printing inks	Flexography	0.01–2	28–38	0.04–2.5	80	15 000	3000	40	Newtonian or non-Newtonian shear thinning with a small deviation
	Gravure	0.01–1.1	41–44	0.1–8	70–80	15 000	3000	30	Non-Newtonian
	Inkjet	0.001–0.05	25–50	0.05–20	20–50	1/10th of nozzle diameter	50	20	Non-Newtonian
High-viscosity printing ink (paste inks)	offset	20–100	30–37	0.5–2	10–50	10 000	1000	90	Non-Newtonian, shear thinning, thixotropic
	Screen printing	0.1–1000	30–50	0.015–100	20–100	1/10th of mesh opening	100	90	Thixotropic

inks, in most cases, are thixotropic; therefore, the viscosity of a printed ink is higher than when the ink is in the printing unit rollers.^[185]

Particle size is also an important parameter for functional print ink. Decreasing the particle size increases the surface area and increases the amount of stabilizing agents required. It also results in a high surface-to-volume ratio, lowering the required sintering temperature. Small particle size and uniform size distribution in the ink produce higher viscosity inks and denser printed patterns; therefore, improving the functionality. Moreover, particle morphologies, e.g., nanospheres (NS) and nanowires (NW), also affect both the electrical conductivity and energy needed for sintering. Higher electrical conductivity can also be achieved by using inks with higher solid content. An increase in the solid content also leads to viscosity decrease under shear stress, allowing the ink to flow more smoothly from one surface to another while still preventing excessive spreading of the ink after printing. The rheological behavior of the ink can thus be tailored by changing the solid content of the ink.^[213] **Table 3** provides a typical comparison of various print ink properties.

Printability (i.e., the ability to absorb inks or lacquers or other liquid and paste substances) of any substrate depends on its porosity, surface free energy (SFE), structure and dimension, durability, hydrophilic property, and optical properties. Besides these, the selection of ink with an appropriate level of surface tension is also necessary. It is generally believed that the surface tension of the ink should be lower than the surface free energy of the substrate. Printability of polymer substrates may be improved by increasing in surface free energy of the material (by any means of activation), by the reduction of surface tension of applied inks; and by the maximum reduction of the polar component of substrate SFE.^[215]

Fluid properties such as viscosity and surface tension have an influence on the formation of droplets from an inkjet printer. The spreading behavior of the inks is determined by the hydrodynamic properties namely; the Reynolds number, ($Re = \nu\alpha\rho/\eta$, is the ratio of inertial to viscous forces), and the Weber number, ($We = \nu2\alpha\rho/\eta$, is a balance between inertial and capillary forces).^[221] Both are combined to form the Ohnesorge number (Oh). The inverse of the Ohnesorge number is termed as printability. This is usually expressed by the Z number. The Ohnesorge

number is given as $\sqrt{We/Re}$ or,

$$Oh = \frac{\eta}{\sqrt{(\gamma\rho a)}} \quad (1)$$

where η is dynamic viscosity, γ is surface tension, ρ is density and a is the characteristic length (usually the diameter of the print head's nozzle). The printability,

$$Z = \frac{1}{Oh} = \frac{\sqrt{(\gamma\rho a)}}{\eta} \quad (2)$$

Such a fluid velocity-independent, dimensionless number has advantages as a suitable metric for fluid selection. Fromm suggested that $Z > 2$ for stable drop formation because viscous dissipation prevents drop ejection at lower values. Reis and Derby proposed, on the basis of computational fluid dynamics (CFD) modeling, that Z should be in the range $1 < Z < 10$, with viscous dissipation preventing drop ejection when $Z < 1$, while satellite drops were predicted to form together with the primary drop when $Z > 10$.^[222] It was also found that Z has an influence on droplet volume too. As Z increases there is an increase in volume. Moon and co-workers have said that Z should be between 4 and 14 for an ink to be printable.^[197] Jang et al. observed inks were easily ejected by the applied pressure without significant viscous dissipation when $Z > 14$. The primary droplet fell with a high relative travel velocity so that the separated tail which formed transient satellites could not catch up with the droplet head. The large oscillatory kinetic energy and the high surface tension tend to induce a secondary rupture, which generates a primary droplet and permanent satellites. So fluids with $Z > 14$ are not printable fluids.^[221] Considering the drop generation, drop flight, and drop impact, the optimal value of the physical condition for a robust DOD inkjet printing is typically with surface tension lying in the range of 20–50 mN m⁻¹ and viscosity within the range of 2–20 mPa.s. This range broadly meets the criteria of a suitable ink for DOD inkjet printing to achieve high-resolution print on the desired trajectory, whereas a narrower and specified range would be more applicable for specific print heads.^[49] **Figure 6a** shows the ink properties suitable for inkjet printing. **Figure 6b** displays a drop watcher image showing five nozzles jetting 3

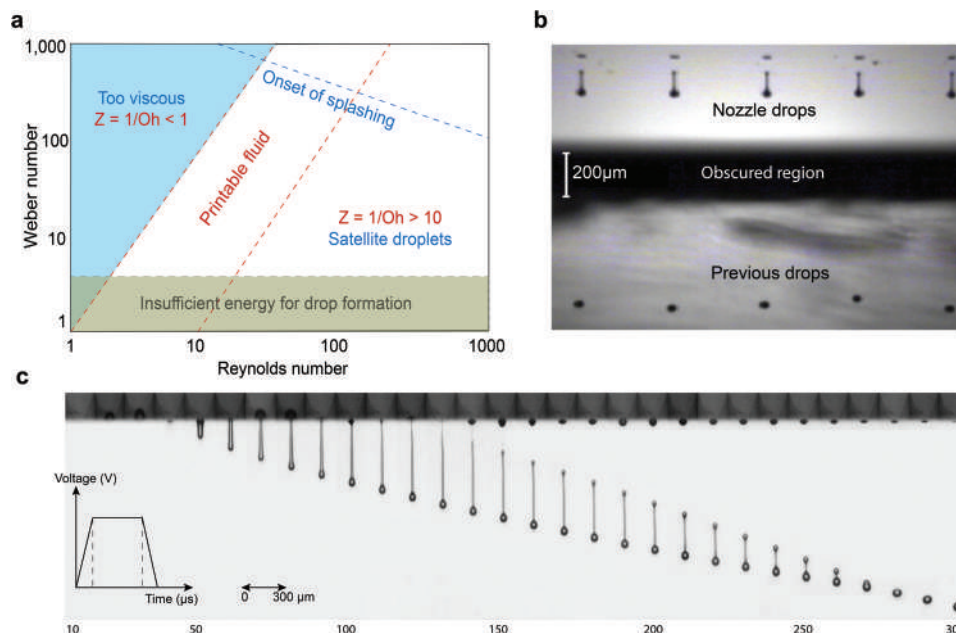


Figure 6. Inkjet Ink property requirement and drop formation. a) Graphical means of assessing ink suitability using nondimensional numbers. Reproduced with permission.^[223] Copyright 2012, Emerald Publishing Limited. b) Example of a drop watcher image on DMP-2831, showing five nozzles jetting 3 wt./wt. % polyDADMAC solution with a 30 μs strobe delay. Reproduced with permission.^[224] Copyright 2020, The Author(s). c) Grayscale images of the ink jetting captured by the drop watcher system with the time sequence of the waveform. Reproduced with permission.^[225] Copyright 2022, The Authors.

wt./wt. % polyDADMAC solution with a 30 μs delay. Figure 6c shows a grayscale image of ink jetting captured by the drop watcher system with the time sequence of the waveform.

5. Applications of Printed E-Textile

5.1. Printed Textile Sensors

Wearable monitoring systems can be used for continuous physiological data monitoring which makes it a promising and effective technology for treatment/care plans for patients or elderly people, assess injury recovery or performance of sports players, etc.^[226] Sensors, with their ability to observe changes in their environment at any event, can provide their corresponding output, based on optical or electrical signals.^[227] Various types of sensors are available for wearable applications, namely motion sensors, biological sensors, and environmental sensors. Wearable motion monitoring systems can be used for navigation, and man-machine interaction, i.e., to detect motion-relevant sensor information, such as posture and position. Gyroscopes, accelerometers, and geomagnetic sensors are a few common motion sensors. Biosensors, a rapidly evolving technology, are composed of biological materials and receptors and act as advanced detectors in biotechnology. They can detect and monitor vital signs and predict early signs of diseases, such as blood pressure sensors, blood glucose sensors, ECG sensors, temperature sensors, etc. Environmental sensors measure relevant indicators in the environment and carry out weather forecasts and health warnings. They also explore the influence of environmental factors on experimental samples in scientific research. This includes temperature and humidity sensors, UV sensors, soil acidity or

alkalinity sensors, light sensors, etc.^[228] Sensors, the core of such wearable monitoring equipment, inevitably contact with the skin but can cause several problems, such as discomfort due to the presence of sensory nerves and sweaty skin. Besides affecting wearer comfort, a conventional rigid sensor may suffer from the signal error of some motion artifacts due to its insufficient flexibility and adaptability. Existing wearable devices are stiff, low precision, and consume high power due to the characteristics of sensing elements and therefore, the development of new flexible sensors is of great significance to meet those challenges.^[229]

Sensors are devices able to detect external stimuli and convert them into standardized signals. Conventional sensors are usually rigid and cannot be deformed readily. Flexible sensors, in contrast, can easily be attached to various surfaces and can be used in wearable and portable electronics. As a result, they enable applications in electronic skin, robot sensing, wearable health monitoring, and so forth. Printed electronics (PE) are a simple but promising aspect in this regard to produce a wide range of electronic circuits and sensor devices on various flexible substrates.^[157,230] Available printing techniques include screen, gravure, inkjet, and even 3D printing technologies have been utilized to produce low cost, light weight, large-area, biocompatible and flexible electronic sensor devices such as electrochemical sensors,^[231–233] enzymatic sensors,^[234,235] pressure sensors,^[236,237] and strain sensors,^[238,239] etc. Among the several printing technologies, screen-printing is a well-established but cheap technique that has been exploited commercially for the fabrication of bio- and chemical sensors.^[240] However, most of the existing flexible and stretchable sensors can detect or monitor only one single stimulus at a time.^[241] To make up for

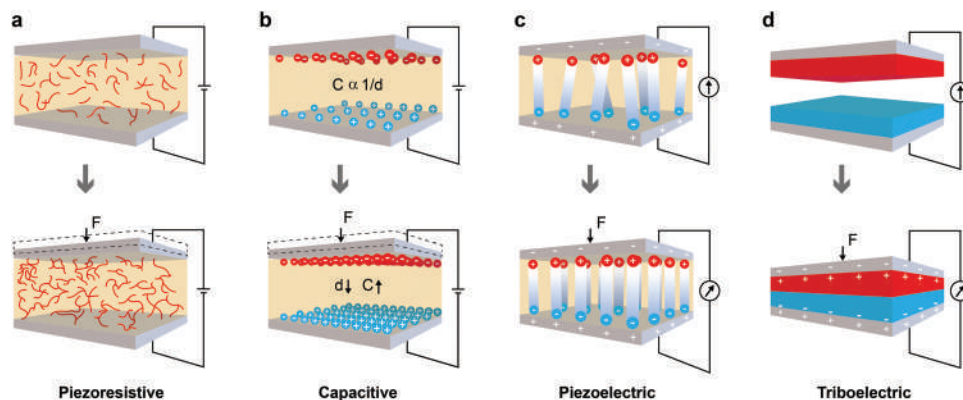


Figure 7. Working principle of printable textile sensors, a) Piezoresistive, b) Capacitive, c) Piezoelectric, and d) Triboelectric sensor.

this drawback and to expand the capacity of sensing applications, recent research has been targeting the development of various multifunctional sensors that can detect multiple stimuli simultaneously or separately.

5.2. Sensor Working Principle

Sensors could be classified as either active or passive sensors. Active sensors can convert the input energy into a measurable difference in potential (V or sometimes I) without any external power supply, however, passive sensors require an external power supply to convert physical stimuli into electrical forms (R, C, L, I). The majority of the textile sensors so far have relied on passive sensing (especially the resistance changes).^[242,243] As per the transduction mechanism, the sensors could again be classified as piezoresistive, capacitive, piezoelectric, triboelectric, inductive, electromagnetic, and photoelectric etc., however, the first four are the most used sensors.^[244,245] **Figure 7.**

The working principle of a piezoresistive sensor is the change of corresponding resistance of the sensor due to the change in the applied pressure from an external source.^[246] The simple structure, working mechanism, ease of fabrication, and excellent performance of such sensor make it popular and thus being studied widely. A resistive sensor is, a conductive network of active materials serving as a resistor under an applied voltage, i.e., the electrical resistance of the conductive network changes as a function of the applied mechanical strain. The variation in the resistance originates from the geometrical changes (i.e., length and cross-sectional area), the intrinsic resistive response of the active materials, the tunneling effect, and/or disconnection mechanism during stretching. While releasing the tensile/compressive strains, the resistance recovers to its initial values in a reversible manner, the deformation state can, therefore, be readily measured by recording the electrical resistance changes.^[247] Conducting fibers, yarns, and/or textiles can be utilized as a resistor when placed in an electronic circuit as well as a sensor device. Sensing functionality can then be achieved in the dynamic mode by measuring changes in the resistance R :

$$R = \rho \frac{L}{A} \quad (3)$$

where ρ , L , and A are the resistivity, length, and average cross-sectional area, respectively. The resistance variation that occurred due to the dimensional change is termed piezo resistivity and is widely studied for its potential application as strain or pressure sensors.

For evaluating the sensing performance and selecting the appropriate piezoresistive physical sensors suitable for specific applications, a few parameters are considered such as sensitivity, stretchability, durability, linearity, selectivity, detection limit, response time, transparency, etc.^[248] Sensitivity (S) is a value to measure the ability of sensors to convert external stimuli into electrical signals.^[249] For strain sensors, gauge factor (GF) is popularly used to evaluate the sensitivity determined by the ratio of normalized resistance change, $\Delta R/R_0$, to the applied strain, ϵ .^[248]

$$GF = \frac{\Delta R/R_0}{\epsilon} \quad (4)$$

For a pressure sensor, if ΔP is the pressure variation, the sensitivity is then defined as:

$$S = \frac{\Delta R/R_0}{\Delta P} \quad (5)$$

Again, for a thermistor, the sensitivity is usually given by the temperature coefficient of resistance, α , which is determined by the ratio of relative resistance change, dR_T/R_T , to the temperature variation, dT .^[248]

$$\alpha = \frac{1}{RT} \frac{dRT/RT}{dT} \quad (6)$$

where R_T is the resistance of the thermistor at a given temperature T .

The stretchability of a sensor is regarded as a measure of the maximum tensile strain that the sensor can sustain with stable sensing performance under repeated loading and unloading. The durability is the capability of the sensor to maintain stable and reliable electrical functionality and mechanical integrity under long-term continuous loading–unloading cycles. Many factors, including microstructural changes, oxidation or corrosion of sensing materials, and environmental influences, can affect the durability of a sensor. The linearity of resistance response

is another important parameter of sensors because nonlinearity makes their calibration complex and difficult. Easy calibration is essential to provide meaningful numerical readings with good repeatability and resolution. The detection limit is a measure of the smallest quantity with a specified precision or reproducibility of a sensor. For example, the detection limit for carbonized silk-based strain sensors and pressure sensors is $\approx 0.01\%$ strain and 0.8 Pa, respectively.^[248] The hysteresis of conventional metal-based sensors is often caused by a combination of mechanical and temperature hysteresis, whereas the viscoelastic nature of polymers and the interactions between the nanomaterials and polymer substrates are the main sources of the hysteresis of stretchable sensors. The response time is defined as the time needed for a measurable response in the steady state.^[248] In addition, optically transparent sensors that are “invisible” and “unfelt” are urgently needed for next-generation wearable sensors because such sensors can be worn on the user’s skin without affecting daily activities. These transparent and elastic sensors can be integrated or combined with other components to design skin-like multifunctional electronic devices.^[248] Piezoresistive pressure sensors can measure statically as well as dynamically with less susceptibility to noise. Their electronics are less complex than those of the sensors. Furthermore, piezoresistive sensors can be produced within a printing process, making them mass-producible, low-cost, and adjustable with regard to spatial resolution.

A capacitive sensor, on the other hand, shows a change in its capacitance when pressure is applied from an external source. Bearing the principle of a parallel-plate capacitor, a dielectric material is sandwiched between plates. With the application of an external force, the distance between plates is altered and a change in capacitance is observed. Capacitive sensors are highly sensitive and very responsive with a wide dynamic detection range.^[250] Capacitive pressure sensors can operate statically as well as dynamically, and their measurements are highly reproducible. They are sensitive to moisture and comparatively cost-intensive to manufacture due to a necessary complex filter system in the electronics to reduce noise. They introduce time-dependence and oscillatory electrical behavior.^[136] If d is the distance between electrodes of area A , ϵ_r is the relative permittivity of the dielectric, and ϵ_0 is the permittivity of vacuum, the capacitance, C for a parallel plate capacitor is determined by):

$$C = \epsilon_r \times \epsilon_0 \frac{A}{d} \quad (7)$$

Piezoelectric sensors are mainly composed of piezoelectric-sensitive materials, able to convert mechanical energy to electric energy and vice versa. When external pressure is applied to deform the material, positive and negative charge separation occurs within the functional material on the two opposite surfaces of the material, forming a potential difference inside. The potential difference is examined to determine the effect of external forces.^[228] Piezoelectric pressure sensors do not need any external power supply and can be measured with high sensitivity. They are less sensitive to temperature influences, but they require complex metrological analysis and are incapable of measuring statically.

The triboelectric sensors convert random mechanical energy into electrical signals without consumption of power while still exhibiting outstanding sensitivity,^[251] by utilizing the coupling

effect of triboelectrification and electrostatic induction.^[252] Triboelectricity is a kind of contact electrification, when the surfaces of two materials with different electron affinities are in contact, they get surface charges of different polarities, electrons transit from a high energy level to a low energy level, converting kinetic energy into electrical energy. As the external kinetic energy causes the two triboelectric materials to produce periodic motion, the induced potential difference between the electrodes also changes periodically. When the load is connected, periodic alternating current is generated, which can then be used as an energy harvester to convert kinetic energy into electrical energy.^[253]

5.2.1. Printed Textile Strain Sensors

Strain sensors can detect deformations or structural changes occurring in infrastructures and are thus used potentially in various applications such as human motion detection, damage detection, characterization of structures, and exhaustion studies of materials in robotic systems, prosthetics, healthcare, and flexible touch panels.^[254] A strain sensor typically consists of a conductive pattern able to reflect a change in the electrical read-out upon geometric deformation.^[173] Several painted (PET),^[255] coated^[256,257] or printed sensors were reported on KAPTON (Inkjet),^[258] plastic (PEN) (screen print),^[259] PI (screen print),^[260] paper (screen print)^[261] or silicon^[254,262] or silicon elastomer (screen print),^[238] (inkjet print).^[263] Textile has also been investigated as a promising substrate for printed sensor fabrication. **Table 4** summarizes the printed textile-based strain sensors.

Rajala et al.^[255] fabricated printed piezoelectric sensors on a flexible PET substrate with solution-processed piezoelectric poly(vinylidene fluoride-co-trifluoroethylene) P(VDF-TrFE) ink as an active layer. Evaporated silver on PET was used as the bottom electrode and the painted Ag glue as the top electrode. The fabricated sensors were characterized in normal and bending mode setups. Normal-mode sensitivities showed values up to 25 pC/N, whereas bending-mode sensitivities showed remarkably high values up to 200 nC/N. Åkerfeldt et al.^[264] also reported a piezoelectric sensor fabricated by using screen printing technology. Melt-spun piezoelectric PVDF fibers with conductive cores were machine embroidered onto a textile glove to function as a sensor element. Electrodes and electrical interconnections were constituted by a screen-printed conductive PEDOT:PSS formulation. A repeated strain of 10% only influenced the resistance of the interconnections initially and to a very limited extent. They also used the sensor data from the glove successfully as input to a microcontroller running a robot gripper, demonstrating its potential applications. In our previous study,^[151] we printed graphene on cotton textiles to form a piezoresistive sensor for monitoring human motion activity at different body parts.

Jang et al.^[265] proposed a printed micro-structured textile strain sensor with high sensitivity and durability. A composite ink, composed of a conductive mixture of elastic microbeads and conducting polymer, was incorporated into the sensor via the inkjet printing process. A microcrack structure on the textile strain sensor, yielding sensitivity with a maximum GF of 57 was developed, **Figure 8a–d**. The printed strain sensor retained high sensing performance with a wide sensing range ($\approx 130\%$), excellent repeatability ($>10\,000$ cycles), and waterproof capabil-

Table 4. Summary of printed textile strain sensors.

Method	Sensing mechanism	Substrate	Composed of	Sensitivity	Stability	Reference
Screen printing	Piezoelectric	Plain warp-knitted, 78% PET, 22% elastane fibers (2015)	PEDOT:PSS printed conductive patch with melt-spun piezoelectric poly(vinylidene fluoride) (PVDF) fibers yarn			[264]
	Piezoresistive	Cotton, Polyester, Cotton/polyester (50/05)-woven, Cotton Knit, Polyester Nonwoven (2018)	Iron oxide, Cobalt, Silver, Single-walled carbon nanotubes, Multi-walled carbon nanotubes			[163]
	Piezoresistive	PU-based stretchable fabric (2021)	Polyurethane (PU) elastomer, CB nanoparticles, poly(3-hexylthiophene-2,5-diyl) (P3HTs), and PDMS microbeads	GF of 57	Wide sensing range ($\approx 130\%$), excellent repeatability ($> 10\,000$ cycles), waterproof capability (contact angle $\approx 112^\circ$)	[265]
	Piezoresistive	Cotton (2022)	Graphene			[151]
Inkjet printing	Capacitive	PET cylindrical fabric (2015)	Silver and Parylene (dielectric layer)	Capacitance change of 0.7% at 1% of strain		[199]
	Piezoresistive	PET (2021)	Graphene-PEDOT: PSS conductive ink	Gauge factor (GF) 165, with linear output signal at strain range 0–0.33%		[266]

ity (contact angle $\approx 112^\circ$). The sensor was further applied to an integrative user-interface device, which monitored the respiration and arm motion signals in real-time under both dry and wet environments. Quintero et al.,^[199] reported inkjet-printed capacitive strain sensors on PET fibers for integration into textiles at a large scale. 10-meter-long functionalized PET fibers were woven with metallic interconnect fibers using a large-scale industrial weaving machine which resulted in a 1 m² smart textile demonstrator. Sensor measurements were performed for strains up to 1% of applications foreseen in predictive maintenance of industrial textiles and in the automotive industry. Kang et al.^[266] reported a flexible strain sensor fabricated by inkjet printing technology of graphene-PEDOT:PSS conductive ink on a PET substrate. A high GF value of ≈ 165 of three high resistive (HR) paths was obtained with a linear output signal at the strain range from 0 to 0.33%.

In addition to conventional screen printing, the latest digital inkjet printing and 3D printing was also employed to fabricate piezoresistive sensor. Alaferdov et al.^[267] proposed a new but simple and scalable method for the fabrication of a piezoresistive wearable strain and bending sensor. The sensor was based on a high aspect ratio (length/thickness $\approx 10^3$) of graphite nanobelt thin films deposited by a modified Langmuir-Blodgett technique onto flexible polymer substrates. High response stability for > 5000 strain-release cycles and a device power consumption as low as 1 nW were achieved. Though not printed, graphene-textile strain sensor was also reported to show tremendous potential for wearable electronic applications. The strain sensor exhibited a distinctive negative resistance variation with increasing strain with high sensitivity, long-term stability, and great comfort. The sensor was demonstrated to detect various human motions such as bending the wrist, while writing English letters, bending a finger at a certain angle, bending the elbow and knee joint at var-

ious angles, during walking and running at different frequencies. Interestingly, the sensor was also able to detect various subtle human motions including signal of finger pulse, signal of a pulse, wrist pulse signal, signals of laughing, crying, during opening and closing of the mouth, and even at different breathing modes, Figure 8e–l. Though not on textiles, 3D printing of PDMS/MWCNT nanocomposite was also reported for realizing strain sensors.^[268]

5.2.2. Printed Textile Pressure Sensors

Flexible electronics have been playing an important role in improving the well-being and quality of life in the form of electronic skin, human-machine interaction interface, physiological signal monitoring, etc.^[249,269] Pressure sensors that can sense and convert pressure input into electrical signals,^[245] are widely applied in various new electronic equipment due to their distinct characteristics with high flexibility, high sensitivity, and light weight.^[228] Intraocular, intracranial, and cardiovascular pressure; cumulatively called physiological pressure, is a key parameter for the assessment of human health providing opportunities for early diagnosis of disease, such as lower limb problems, muscle rehabilitation, and wound monitoring, personalized therapy, and preventive healthcare etc.^[270] Pressure and touch sensors are able to detect physical pressure, physical contact, and even proximity. They represent an interactive technology widely applied in consumer portable devices such as smart phones or touch pads. Pressure sensors can be created via structures where an active sensing layer is “sandwiched” between contacts, or where the active sensing spots are connected to contacts or a combination of both.^[173] Researchers have reported various fabri-

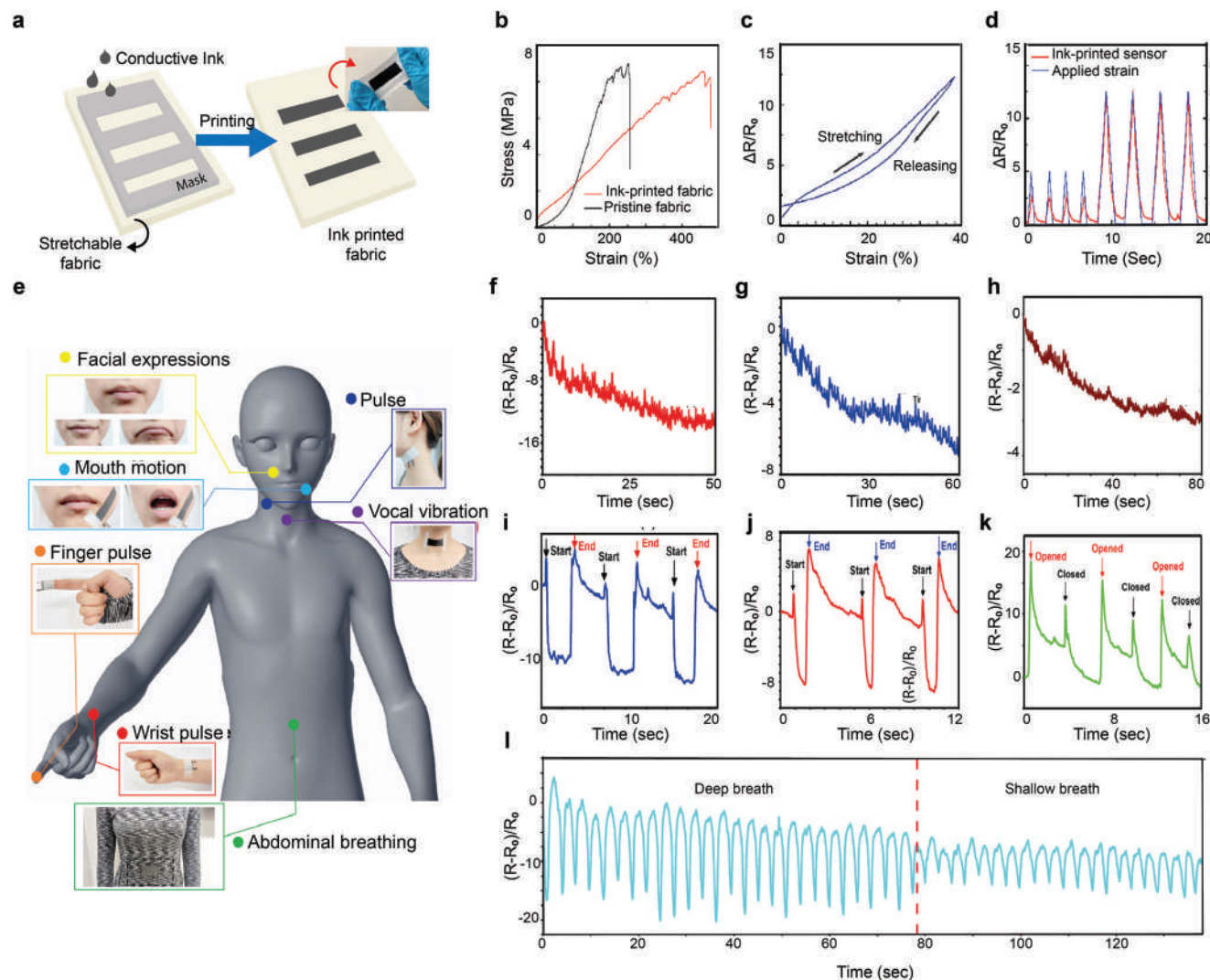


Figure 8. Printed textile strain sensors a) A schematic illustration for the process of inkjet printing bead-blended composite ink onto a stretchable fabric. The inset shows a photograph picture of the ink-printed composite fabric, and b) Stress versus strain curves for tensile deformation on pristine and ink-printed composite fabrics. c) A hysteresis test of the ink-printed textile sensor, d) Time-dependent electrical responses of the ink-printed textile sensor with repeated strains of 20% and 50%. Reproduced with permission.^[265] Copyright 2021, Elsevier Ltd. Applications of the wearable graphene textile strain sensors for detecting various subtle human motions: e) A schematic illustration of the sensor attached to different parts for detecting subtle human motions, f) The signal of finger pulse g) The signal of pulse h) Wrist pulse signal i) The signal of laughing, j) The signal of crying, k) The relative resistance changes during open and close mouth, and l) The detection of respiration rate with different breath modes. Reproduced with permission.^[257] Copyright 2018, American Chemical Society.

cation technologies for realizing textile-based pressure sensors such as conductive Shieldex Nora-Dell woven fabric,^[271] MXene coating of cotton fabric,^[272] dip coating of conductive woven fabric in ZnO solution,^[273] immersion of textiles in conductive GO solution^[257] or painting^[274] or printing on several flexible substrates, i.e., PET^[164] etc. As our review scopes only the printing techniques employed, Table 5 presents a summary of the textile-based printed pressure sensors.

Liu et al.^[276] used CB from diesel soot, an air pollutant produced during incomplete combustion of hydrocarbon fuels, as the active material to fabricate a high-performance flexible all-textile pressure sensor. A dry pristine nonwoven fabric was fumigated at different times over the diesel lamp. PEDOT:PSS and

ethyl alcohol were well-mixed and drop-cast to prepare the conductive fabric. Screen-printing method was adopted to print the commercially conductive silver paste on the pre-cleaned cotton to cover the top CB-coated fabrics to form the sensor, Figure 9a. The pressure sensor exhibited outstanding performances, including high sensitivity (81.61 kPa^{-1} within the range of 0–10 kPa), extra wide workable pressure regime (0–100 kPa), rapid response, and relaxation time (6 and 30 ms, respectively). Zhou et al.^[275] designed a novel all-fabric piezoresistive pressure sensor with a bottom interdigitated textile electrode screen-printed with silver paste and a top bridge of AgNW-coated cotton fabric. Benefiting from the highly porous microstructure, large surface roughness and ultra-low resistance of the conductive fabric, the piezoresis-

Table 5. Summary of printed textile pressure sensors.

Method	Sensing mechanism	Substrate (Reporting year)	Composed of	Sensitivity	Response time	Detection limit	Stability	Reference
Screen printing	Piezoresistive	Cotton (2018)	Ag NWs and Ag paste ink	$2.46 \times 10^4 - 5.65 \times 10^5$ / kPa in a wide pressure range (<30 kPa),	6/16 ms	0.76 Pa	> 41 000 loading–unloading cycles	[275]
	piezoresistive	Cotton (2019)	Carbon black (CB) from diesel soot, Ag paste, PEDOT:PSS	High sensitivity (81.61 kPa ⁻¹ in the range of 0–10 kPa), ultrawide workable pressure regime (0–100 kPa)	Rapid response and relaxation time (6 and 30 ms, respectively)			[276]
Screen and inkjet printing combined	Piezoresistive	Cotton & polyester (2021)	Carbon-PEDOT: PSS nanocomposite solution, Ag nanoparticle ink	1.45/kPa	≈30 ms	150 gm		[200]

textile pressure sensors showed excellent detection performance, including an extra-high sensitivity of 2.46×10^4 kPa⁻¹ to 5.65×10^5 kPa⁻¹ over a wide pressure regime (0–30 kPa), a giant on/off ratio of $\approx 10^6$, a fast response time (6 ms), and a low detection limit (0.76 Pa), Figure 9b–g. In addition, with the ability to detect various tiny signals of the human body, they demonstrated the devices to play the piano and computer games.

Khan et al.^[200] presented a combined screen-inkjet printing fabrication route to develop a pressure-sensing patch by utilizing conductive cotton fabric sandwiched between two parallel electrodes. A conductive nanocomposite solution by mixing carbon-based paste and PEDOT:PSS was used. A nanofibrous stretchable cotton fabric was impregnated in the nanocomposite solution, which was used as the pressure-sensing layer. The metallic plates and interconnect lines were developed by inkjet printing of Ag nanoparticles-based solution on a PET substrate. The sensing blocks were patterned using screen-printing. The thermally sensitive resin on one side of PET substrate enabled the sandwiching of the impregnated fabric through lamination. The produced piezoresistive sensors recorded resistance variation for as small as 1 gm weight. In addition to screen printing and inkjet printing, Li et al.^[277] reported the structural design of 3D flexible wearable pressure sensors using conductive polymer composites, exhibiting excellent piezoresistive performance, such as adjustable GF of 13.70–54.58, exceptional durability, and stability.

5.2.3. Printed Textile Temperature Sensors

Measurement of temperature is a physiological indicator of health pathology.^[278] Continuous body temperature monitoring for patients facilitates healthcare providers to remotely track patients' temperatures, promptly detect fevers, and thus allow timely intervention to prevent critical situations.^[279,280] Flexible temperature sensors are therefore beneficial for real-time temperature monitoring in healthcare, disease diagnosis, and ambient environment detection.^[281] Numerous flexible temperature sensors are already available in the market, however, most of them have not been integrated in a concealed manner and are not feasible for wearable applications due to the inability to bend, drape, or shear.^[282] The utilization of sensors, able to

monitor skin temperature, concealed within everyday textile garments, could therefore greatly benefit patients and healthcare personnel.^[282] Surfaces able to distinguish spatial and temporal changes in temperature are critical for not only flow sensors, microbolometers, or process control but also future applications like electronic skins and soft robotics.^[283] Epidermal temperature sensors, already presented in studies, are mainly fabricated using a traditional photolithography process with several intermediate stages creating a substantial amount of material waste. Printed sensors thus offer great potential due to their flexibility, waste reduction, and low-cost fabrication.^[284]

The microstructure of any conductive network dominates the electrical behavior of the conductive material during the temperature change process. Several conductive materials including carbon nanotubes, graphene, conductive polymers, or metal nanostructures have been utilized to prepare temperature sensors.^[285] Temperature sensors could be resistance temperature detectors (RTDs), thermocouples, or thermistors.^[286] The RTDs use the temperature dependence of the material on electrical resistance to determine the temperature. The increase in temperature causes an increase in resistance due to the electron vibration at a higher temperature preventing the free flow of electrons in conductive materials.^[286] A high degree of accuracy, linearity, and quick response properties of RTDs, make them more preferable than thermocouples.^[286] RTDs are usually constructed with metallic material (such as platinum, nickel, copper, etc.) and thermistors are generally constructed with semiconductor materials. RTD-based temperature sensors can measure big range of temperature changes (–230 °C to 660 °C) whereas thermistor-based temperature sensors have limitations in the temperature range (–100 °C to 300 °C). Thermistors are generally less resistive than RTD-based temperature sensors and can provide fast response, i.e., a small change in temperature can be measured with high accuracy. Due to construction with the semiconductor materials, there are 2 temperature coefficients of thermistor; positive and negative (PTC and NTC respectively). NTC thermistors are widely used as inrush current limiters, and temperature sensors, while PTC thermistors are used as self-resetting overcurrent protectors, and self-regulating heating elements. Most thermistors have NTC, i.e., their resistance value reduces with the increment in temperature. The sensitivity (S) and temperature

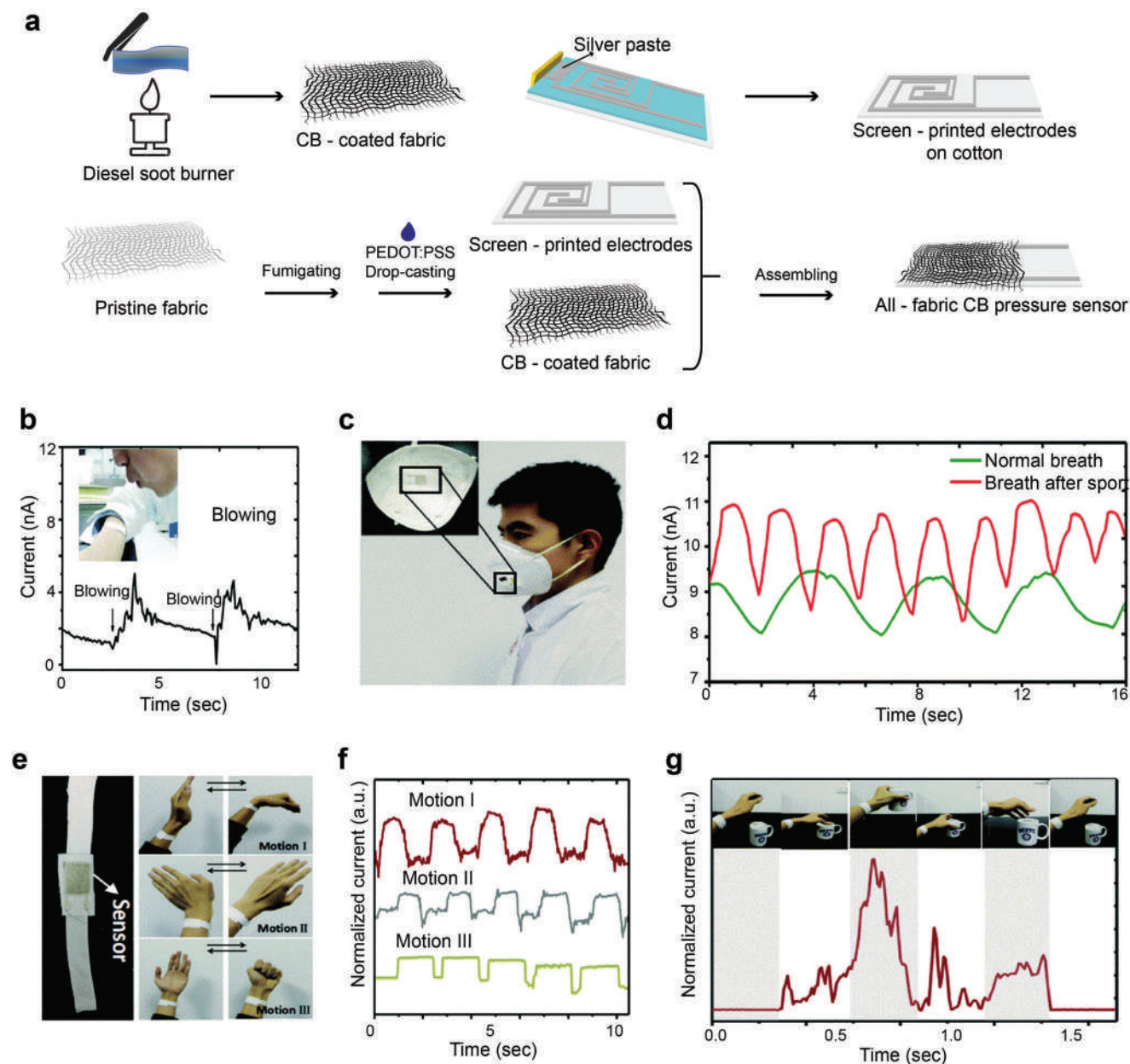


Figure 9. Printed textile pressure sensors a) Schematic illustration of the fabrication of the CB pressure sensor. Reproduced with permission.^[276] Copyright 2019, WILEY-VCH. The real-time current response to different mechanical forces using our textile-based sensor: b) Digital photographs and the current curve for detecting the wind blowing from the mouth, c) The device was directly attached to the air outlet of the mask, d) The current signal responds to respiration under before and after exercise, e) Photographs showing that the flexible detector is fixed on the wrist by an elastic spandex band, and the human motion of bending the wrist (Motion I), waving (Motion II) and holding fist (Motion III), f) Real-time current response corresponding to different human motions, g) The current signal in response to the whole process of lifting and lowering the cup. Reproduced with permission.^[275] Copyright 2018, The Royal Society of Chemistry.

coefficient of resistance (TCR) of the temperature sensors can be calculated by:

$$S = \frac{R_f - R_i}{\Delta T} \quad (8)$$

$$\text{TCR} = \frac{R_f - R_i}{R_f \Delta T} \quad (9)$$

where R_f and R_i denote the resistance value obtained at temperature f °C and i °C respectively, ΔT is the change in temperature. The definition of TCR is the resistance change factor per degree celsius of temperature change. Though other printing techniques such as stencil^[287] and transfer^[288] have been reported, screen printing is most widely used to fabricate temperature sensors on various substrates such as PEN,^[289] PET,^[165,281,289–293] PI,^[283] PI-PET^[294] and PDMS. Table 6. summarizes the reported tempera-

Table 6. Summary of the printed textile temperature sensors.

Method	Substrate (Report year)	Composed of	Temperature Range	Sensitivity	Performance	Reference
Screen printing	PET, paper, textiles (2019)	Flake graphite (FG)/carbon nanotube (CNT)/ polydimethylsiloxane (PDMS) composite films (FG/CNT = 4:1)	40–80 °C	TCR 0.028/K		[165]
Inkjet printing	Taffeta fabric (2021)	Carbon nanotube (CNT) and PEDOT: PSS-based ink	Room temperature to 50 °C	0.15%/°C for CNT, 0.41%/°C for PEDOT:PSS, and 0.31%/°C for CNT/PEDOT:PSS	Bending stability with a resistance change of 0.3% up to 1000 cycles	[295]

ture sensors on various textile substrates.

Wu et al.^[165] reported the fabrication and characterization of a flexible temperature sensor based on flake graphite (FG)/carbon nanotube (CNT)/polydimethylsiloxane (PDMS) composite- screen printed on PET substrate. The sensor shows high-temperature sensitivity and good linearity. It was reported that the TCR value of the FG/CNT/PDMS films can be manipulated by the mass ratio of FG to CNT. At a mass ratio of FG to CNT is 4:1, the TCR was almost reproducible and maintained at the same level of 0.028 K⁻¹ for repeated thermal cycles, indicating its potential for the flexible temperature sensor, **Figure 10a,b**.

Some of the studies also report the exploitation of inkjet printing of conductive materials to produce temperature sensors in various substrates, especially in PEN,^[284] PU,^[296] PI,^[294] PET,^[201] rubber^[263] and paper.^[297–299] Kuzubasoglu et al.^[295] developed a temperature sensor based on carbon nanotube (CNT) and PEDOT: PSS-based ink to inkjet print onto the adhesive polyamide-based taffeta fabric, **Figure 10c–h**. Stable and uniform dispersions of CNT and PEDOT:PSS with Triton X-100 were formulated using three different formulations: CNT-based ink, PEDOT: PSS-based ink, and CNT/PEDOT:PSS composite ink. Produced sensors exhibited NTC behavior and sensitivity of 0.15%/°C for CNT, 0.41%/°C for PEDOT:PSS, and 0.31%/°C for CNT/PEDOT:PSS for temperature varying from room temperature to 50°C. CNT/PEDOT:PSS composite ink printed sensor achieved better-sensing repeatability and demonstrated higher bending stability with a resistance change of 0.3% up to 1000 cycles.^[295] Reported inkjet-printed temperature sensors that can measure a wide range of temperatures are mostly composed of Ag-based ink.^[201,294] However, a unique combination of 3D printing and inkjet printing was also reported to realize a low-cost, fully integrated wireless sensor node for large-area monitoring applications for sensing temperature, humidity, and H₂S levels.^[300]

5.2.4. Printed Textile Humidity Sensor

Similar to temperature, moisture is another critical factor for both the environment and living creatures. Humidity sensing is realized through the interaction between moisture and the sensing materials, such as electrolytes, semiconductor ceramics, polymers, and so forth.^[301] Though there are various fabrication techniques for realizing humidity sensors, printed hu-

midity sensors offer considerably lower costs and increased capabilities for large-scale production.^[302] Various printing technologies have been exploited for the fabrication of humidity sensor on several substrates, e.g. patterning on PI,^[303] screen printing on KAPTON,^[304] glass,^[305] PI,^[306,307] PET,^[308,309] gravure printing on PET^[180,310] and PI,^[311,312] screen and gravure combined on PET,^[181,313] inkjet printing on PET,^[314–317] PI,^[318] paper^[319] and on KAPTON,^[320] photolithography on LiNbO₃,^[321] PI and PES^[322] or piezoelectric^[323] substrate, etc. **Table 7** summarizes the printed textile-based humidity sensors.

Screen printing technology was mostly utilized for the fabrication of humidity sensors. Kutzner et al.^[324] reported screen printing of Ag-paste to fabricate humidity sensors on Polycotton fabric. It was tested between 30%- 90% RH at varying temperatures in the range of 15 °C and 35 °C. The complex sensor signal was measured using a gain/phase analyzer in a frequency range between 10Hz and 100kHz. It indicated a non-linear dependency on humidity for different measurement frequencies. Komazaki et al.^[166] reported capacitive humidity sensor made of screen printing technology. A comb-shaped electrode was printed with conductive silver paste followed by a PDMS passivation layer printed on the back side of the textile, **Figure 11a–c**. The precursor emulsion of the PDMS-CaCl₂ micro composite was then printed on the front side of the textile. The sensor was tested over a humidity range of 30- 95%; the permittivity increased by 10.2% from 30 to 60%RH corresponding to a sensitivity that is 2.7-fold greater than that of a conventional polyimide humidity sensor.

A number of researchers also employed gravure printing technology for the fabrication of humidity sensors.^[180,310–312] Both gravure and screen printing were employed to fabricate the humidity sensors in few studies,^[304,313] however they were not reported on textiles.

A few research groups also reported inkjet printing for humidity sensor fabrication. Weremczuk et al.^[202] presented a humidity sensor inkjet-printed on textile using the ink-jet printing technology, **Figure 11d**. In a controlled environment of 25 °C and 5–95% of RH, the measured impedance modulus versus humidity showed a non-linear distribution over the range from 40 to 95% of RH. Ali et al.^[315] reported an Ag-printed interdigitated electrode on a flexible PET substrate all-printed humidity sensor based on graphene/methyl-red composite with high sensitivity, **Figure 11e–i**. The sensor electrical resistance inversely varies from 11 MΩ to 0.4 MΩ against the RH content from 5% to 95%. The sensor also exhibited 96.36% and 2 869 500% resistive and

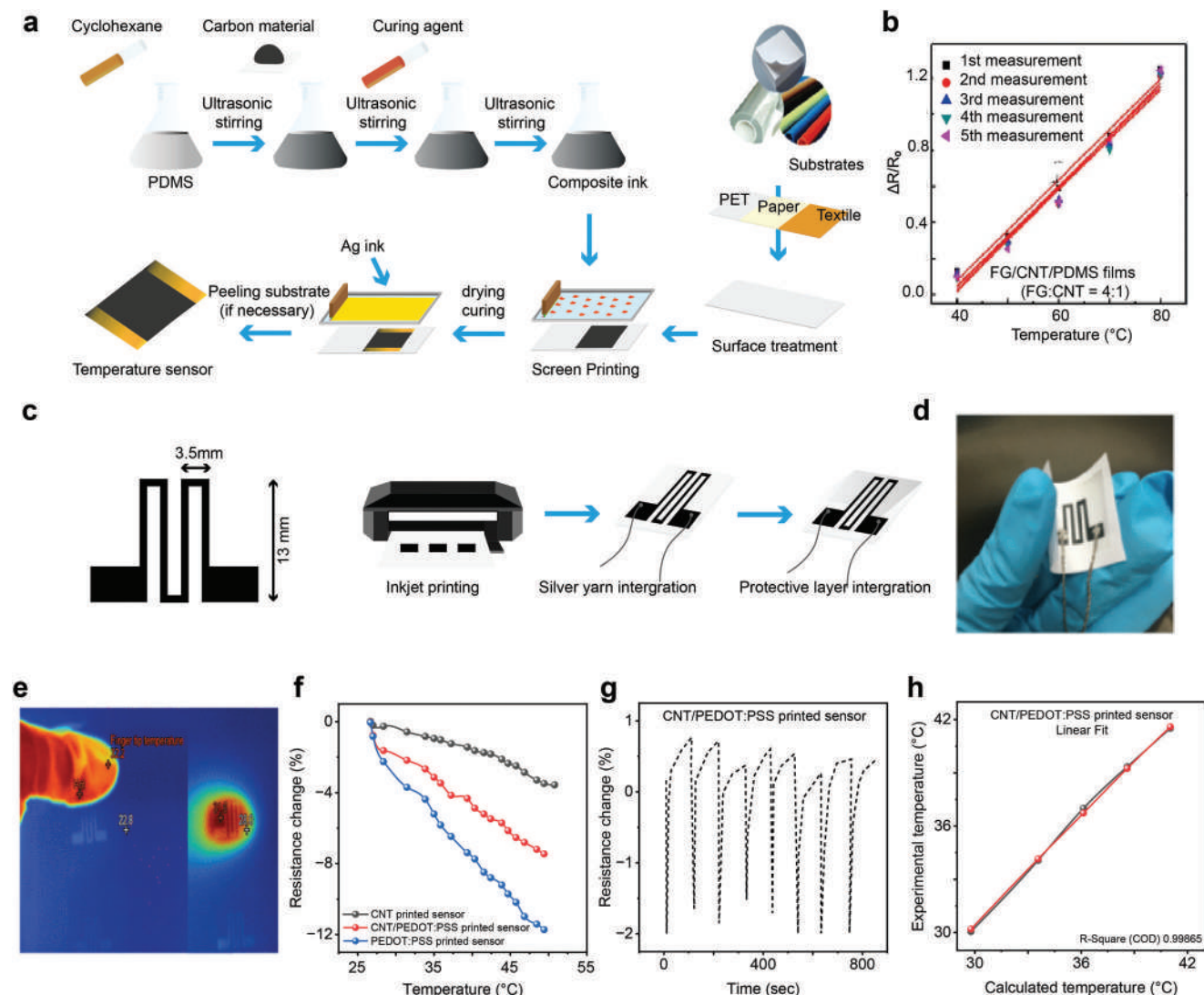


Figure 10. Printed textile temperature sensors a) The preparation process of temperature-sensitive ink and sensor b) Average resistance change of 16 wt.% FG/CNT/PDMS films with FG/CNT = 4:1 as a function of temperature. Reproduced with permission.^[165] Copyright 2019, Springer. c) Layout and printing of the sensor design, d) Digital image of the printed sensor, e) Thermal camera image of experimental configuration, f) Resistance change as a function of temperature for printed temperature sensors. g) Thermal response graphs of the CNT/PEDOT:PSS printed sensors when the finger touches and withdraws from the sensor, and h) Dependence of experimental data of CNT/PEDOT:PSS printed sensors with calculated data from Steinhart–Hart formula. Reproduced with permission.^[295] Copyright 2021, IEEE.

Table 7. Summary of printed textile humidity sensor.

Method	Substrate	Mechanism	Composed of	Humidity range	Sensitivity	Performance	Reference
Screen printing	Poly-cotton (2013)		Ag paste with Nafion (sulfonated tetrafluoroethylene-based fluoropolymer copolymer)	30% – 90% at temperature range of 15 °C – 35 °C			[324]
	Polyester (2019)	Capacitive	Ag paste print followed by a passivation layer of polydimethylsiloxane (PDMS) and CaCl ₂	30- 95%	2.7-fold greater than conventional polyimide sensor		[166]
Inkjet printing	Textile (2012)		Silver nanoparticles (Ag) ink	5–95%			[202]
	Polyester sheet (2013)		PANI	20%–100%			[325]

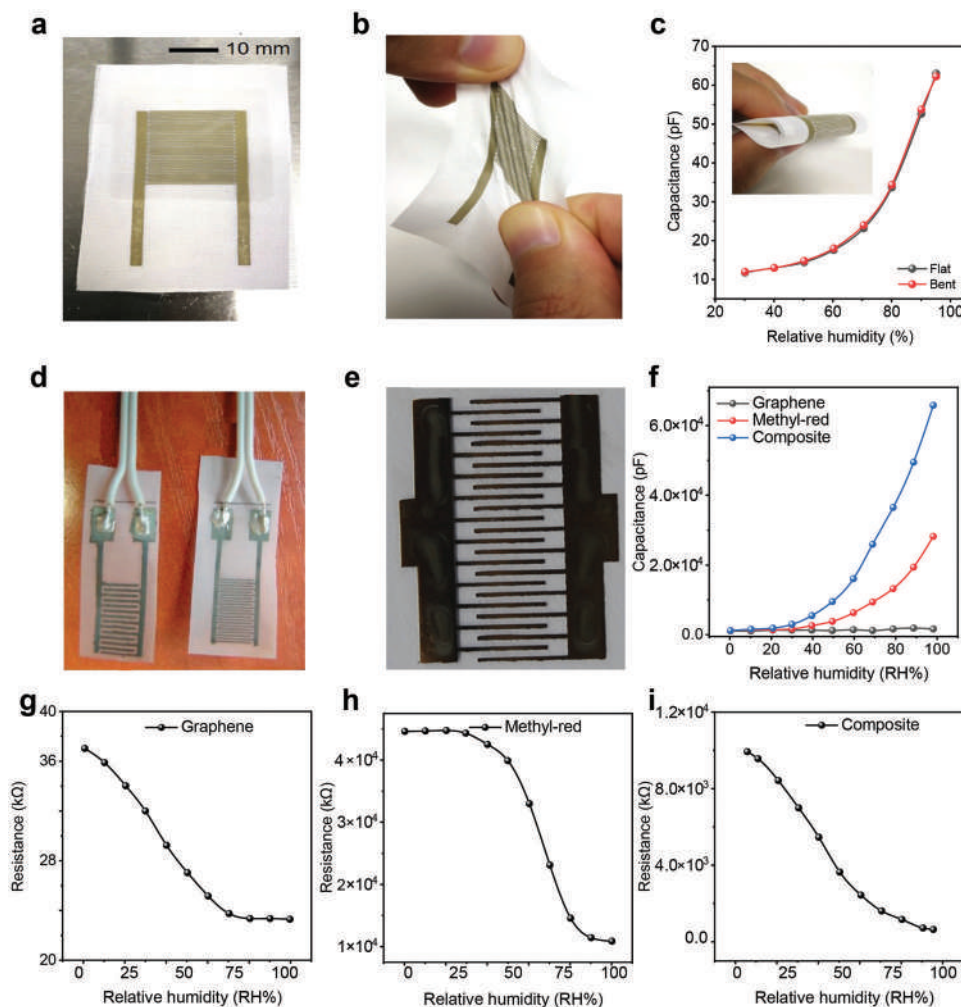


Figure 11. Printed textile humidity sensors a) Photograph of the sensor printed on polyester textiles b) Humidity sensor stretched along the bias c) The output of the sensor in flat and bent (radius: 5 mm) states, the inset presents a photograph of a bent sensor. Reproduced with permission.^[166] Copyright 2019, Elsevier. d) The humidity sensor electrodes printed on textile with Ag nanoparticles ink: sensors of left pattern— $400\mu\text{m} \times 400\mu\text{m}$ and of right pattern— $250\mu\text{m} \times 250\mu\text{m}$. Reproduced with permission.^[202] Copyright 2012, Elsevier. e) The inkjet printed sensor's electrodes with silver ink and zoom image of the area set off by a red solid line with $200\mu\text{m}$ track width of silver electrode, f) Capacitance versus relative humidity (% RH) characteristics curves of the graphene/methyl-red composite, methyle-red only, and graphene only based humidity sensors measured in the humidity chamber at 1 kHz frequency g) Resistance versus relative humidity (% RH) in the graphene film, h) Resistance versus relative humidity (% RH) in the methyle-red film, and i) Composite graphene/methyl-red based humidity sensor. Reproduced with permission.^[315] Copyright 2016, Elsevier.

capacitive sensitivity respectively against humidity. The response and recovery time of the sensor were 0.251 s and 0.35 s, respectively. Kulkarni et al.^[325] synthesized a conducting polyaniline-based ink for printing an interdigitated (IDT) pattern using an inkjet printer on a polyester substrate to prepare a humidity sensor. They reported their sensor response in the humidity atmospheres ranging between 20% and 100% RH.

5.2.5. Printed Textile Electrodes for Electrocardiogram

Biosensors are analytical devices that can convert biological responses into electrical signals. The term “biosensor” was coined by Cammann, and its definition was introduced by IUPAC.^[326] Human activities such as brain activity, heart beating, muscle,

and eye movement, etc. have been widely studied for medical diagnosis^[327] as well as by researchers from diverse fields including neuroscience and engineering.^[328] Cardiovascular disease is one of the leading causes of death all over the world; however, the mortality rate could be significantly reduced simply if an electrocardiogram (ECG) test had been performed regularly on the individuals.^[329] Electrocardiogram is a time-domain representation of body surface potentials, obtained by placing electrodes, originating from the heart. It is a very popular bio-signal not only due to its distinct signals from specific regions of the cardiac system but also because the acquirement of this signal from the patient is completely free of any side effects, unlike other diagnostic methods such as X-rays.^[330] ECG reflects the electric activity of the heart, usually used to determine Heart rate variability (HRV) which is important data for various medical fields.^[331] Therefore,

recently the monitoring of electrocardiogram, and ECG has become an important tool for both clinical diagnosis and home health care, especially for long-term monitoring.^[332] The conventional monitoring of ECG or EEG usually employs standard wet silver/silver chloride (Ag/AgCl) electrode which usually requires conductive gel and prior skin preparation.^[332] Though they have good signal performance in short periods of time and are most commonly used in hospital environments; their short shelf life, skin irritation (i.e., itchiness, reddening, swelling even allergies), and discomfort for patients limit their usage for long-term monitoring. In addition to this, the conductivity of electrolytic gel also decreases gradually since the material gets dried, subsequently degrading the data accuracy.^[333] In comparison to conventional Ag/AgCl rigid metal electrodes, textile electrodes are soft, flexible, and breathable, which allows the wearer comfort more than conventional metal plate electrodes in long-term monitoring. These can also easily be integrated into garments by weaving, knitting, or sewing, which requires no adhesive to be attached to the body, so are skin-friendly (no skin irritation or discomfort) and environmentally friendly (electrodes are reusable). Considering these advantages, many researchers have used textile electrodes in the development of wearable ECG systems.^[334] Though several fabrication technologies have been employed for the fabrication of ECG biosensors, such as knitting of conductive thread,^[334] coating,^[335] embroidery^[246,336] 3D-printing^[337] or MEMS process,^[338] due to the scope of this review limited to printed e-textiles, we will confine our discussion only on printed ECG sensors. **Table 8** summarizes the reported textile-printed electrodes employed as ECG biosensors for electrocardiogram monitoring.

The performance of biosensors is determined in terms of various parameters. The most common parameter is the signal-to-noise (SNR) ratio. This is useful data to measure the quality of recordings, as well as helpful for evaluating a process flow during data analysis, tuning its variable parameters, and diagnosing problematic areas that require additional improvement or refinement. SNR is typically defined as a ratio of signal energy to noise energy.^[360] For any biosensor, A higher signal-to-noise ratio (SNR) leads to a less complicated algorithm in the beat detection step and thus increases in accuracy.^[361]

Sinha et al.^[82] utilized screen-printing of PEDOT:PSS electrodes on a t-shirt to present a platform for monitoring the cardiovascular activity of an athlete both during sedentary conditions and during exercise. PEDOT:PSS is known to be a mixed conductor to functions as both ionic and electronic conductors, in which PEDOT is responsible for electronic conductivity, and PSS contributes to ionic conductivity, both of which are necessary for transduction of the ECG signal. Without using any hydrogel or an adhesive around the electrodes, the ECG signals were recorded in dry skin conditions. The signal amplifies when the skin transpires water vapor or by applying a common lotion on the skin (SNR were 15.42 for dry, and 29.59 in wet condition). The PEDOT:PSS wires connected to PEDOT:PSS electrodes have been shown to record ECG signals comparable to Ag/AgCl connected to copper wires. Ankhili et al.^[83] reported a comparative study of pure cotton and cotton/Lycra knitted fabric to make flexible textile electrodes by screen-printing of PEDOT:PSS conducting polymer. Ag-plated electrodes were also used to compare their performance with developed PEDOT:PSS textile electrodes. The

pure cotton knit textile electrodes exhibited better SNR than the cotton-lycra knit textiles; highest SNR of 33.0505 (before washing) and 7.6069 (after washing) in comparison to 27.7690 (before washing) and 15.6060 (after washing). However, the highest SNR was reported for Ag-plated cotton; 34.7203 (before washing) and 33.1449 (after washing). Ag ink was also used as conductive material for fabricating textile-based ECG electrodes,^[353] **Figure 12a–d**. The ECG signals collected using textile electrodes were comparable to the standard Ag/AgCl electrodes with an SNR of 33.10, 30.17, and 33.52 dB for signals collected from cotton, polyester, and Ag/AgCl electrodes, respectively. Zalar et al.^[354] compared the electrical performance of seven screen-printed dry electrodes (Ag, Ag/PEDOT:PSS, Ag/AgCl, Ag/AgCl/PEDOT:PSS, C, C/AgCl, and PEDOT:PSS) with two commercially available gel electrodes (3M RedDot 50 and Philips NeoLead) on thermoplastic polyurethane substrates. They reported the performance of the electrodes in terms of correlation coefficient. All the screen-printed dry electrodes showed an $r^2 > 0.95$, indicating nearly perfect overlap with the commercial gel electrodes, i.e., the collection of ECG signals with a quality equal to that of gel electrodes.

Inkjet printing is by far the fastest-growing sub-segment in textile printing. Due to providing a number of advantages over traditional printing methods, e.g., screen printing, roller printing, and transfer printing, such as versatility, great resolution, customizing flexibility, reduced downtime and sampling cost, lower waste output, and usage of water and chemicals, it has been growing rapidly.^[362] Therefore, inkjet printing was employed for fabricating ECG electrodes on various substrates including paper,^[363] tattoo paper,^[364] PI substrate,^[365] etc. Bihar et al.,^[358] inkjet printed PEDOT:PSS on a commercial stretchable textile to make electrodes, **Figure 12e–h**. Skin contact was improved by the addition of a cholinium lactate-based inkjet printed ionic liquid gel on the textile. The gel-assisted electrodes made low-impedance contacts with the skin and the accuracy of data was comparable with the commercial wet Ag/AgCl electrodes. However, the common problem associated with inkjet printing of conductive inks on textiles is the difficulty of printing a continuous conductive path on a rough and porous textile surface. To overcome this issue, we reported for the first time the inkjet printing of an organic nanoparticle-based surface pre-treatment onto textiles to enable all inkjet-printed graphene e-textiles.^[147] The functionalized organic nanoparticles presented a hydrophobic breathable coating on textiles followed by an inkjet printing of rGO to form a continuous conductive electrical path. We demonstrated the inkjet-printed e-textile as a biosensor to monitor the heart rate with a high SNR of 22.3.

5.2.6. Printed textile electrodes for Electroencephalography

Electroencephalography (EEG) is a common technique to record the electrical activity of the brain. In sleep studies, it is a compulsory part of polysomnography (PSG) to detect sleep stages and cortical arousals.^[366,367] This is a non-invasive measurement^[368] with negligible health risk and minimal restriction on the users' age. It is regularly monitored along with other neuro imaging techniques such as magnetic resonance imaging (MRI) in the clinic to diagnose neurological disorders such as epilepsy, sleep disorders, and attention deficit hyperactivity disorder (ADHD) as

Table 8. Summary of printed textile ECG electrodes.

Printing method	Substrate (Reporting year)	Composed of	Form/place of operation	Signal-to-noise ratio SNR (dB) / performance	Reference
Brush paint	Woven and knit (2019)	Silver	Cycling suit		[339]
	Knitted Textile (2015)	PEDOT: PSS	Wristband	SNR 16.3	[340]
Screen printing	Polyester/Nylon nonwoven (2008)	Ag/AgCl ink	Chest		[167]
	Fabric (2010)	Ag paste	Band-aid		[168]
	PET foil (2013)	Ag/AgCl-based ink		Stable, very small potential drift (<3 mV/30 min)	[341]
	Escalade (Cotton/polyester / Lycra), 3 × 1 twill woven (2014)	Ag paste/PU paste	Chest band		[170]
	Lagonda (Cotton/polyester/lycra woven (2015)	Ag paste/carbon-loaded rubber	Chest band		[342]
	Polypropylene nonwoven (2015)	Ag/AgCl conductive inks	Chest	SNR 28.68 (dry), 26.70 (wet)	[343]
	Cotton Woven (2016)	PEDOT: PSS			[344]
	Woven (2017)	Ag paste/conductive rubber	Body vest		[345]
	Textile substrate (2017)	PEDOT:PSS conductive organic polymer			[346]
	Knit t-shirt (2017)	PEDOT: PSS	Chest	SNR 15.42 (Dry), 29.59 (Wet)	[82]
	Cotton (2018)	PEDOT: PSS			[347]
	Cotton knit (2018)	PEDOT: PSS	Forearms	Before Washing SNR 24.63, after 11.8333 (7.4 wt.%), 33.0505 and 7.6069 (12.8 wt.%) respectively	[83]
	Cotton/lycra knit (2018)	PEDOT: PSS		Before Washing SNR 17.8022, after 11.5040 (6.3 wt.%), 27.7690 and 15.6060 (11.9 wt.%) respectively	[83]
	Ag-plated cotton	PEDOT:PSS		Before washing 34.7203 and after washing 33.1449	[83]
	Textile (2018)	Ag conductive ink			[348]
PET (2018)	Ag ink print followed by MWCNT/PDMS composite polymer bar coat		correlation coefficient of 0.95	[349]	
Textile (2018)	Silver ink and PEDOT: PSS ink	Chest	SNR 21	[350]	
Cotton (2019)	Graphene ink/ Carboxymethyl Cellulose (CMC)	Wrist		[351]	
Woven PU-coated fabric (2019)	MWCNT with PU binder	Chest		[352]	
Cotton knit fabric (2020)	Silver ink		33.10 (cotton), 33.52 dB (Ag/AgCl electrodes)	[353]	
Polyester knit fabric (2020)	Silver ink		30.17 (polyester), 33.52 dB (Ag/AgCl electrodes)	[353]	
Thermoplastic polyurethane (TPU) (2020)	Ag, Ag/PEDOT:PSS, Ag/AgCl, Ag/AgCl/PEDOT:PSS, C, C/AgCl, and PEDOT:PSS	Anterior wrist on opposite arms	All electrodes show $r^2 > 0.95$, indicating a nearly perfect overlap of the gel and dry electrodes	[354]	
PET (2020)	Laser-induced graphene (LIG), AgCl, carbon inks	Wrist		[355]	
Cotton (2020)	Graphene ink/ Ethyl cellulose (EC)	Wrist		[356]	
Inkjet printing	PET (2015)	Ni particle on activator			[357]
	Hosiery (Pantyhose) (2017)	PEDOT: PSS	Wrist	SNR 12.93 ± 0.80 (dry) and 13.75 ± 0.26 (gel)	[358]
	Cotton (2017)	Reduced graphene oxide (rGO)	Fingertip	SNR 22.3	[147]
	Woven (2019)	Reactive silver	Elbow	SNR 18	[359]

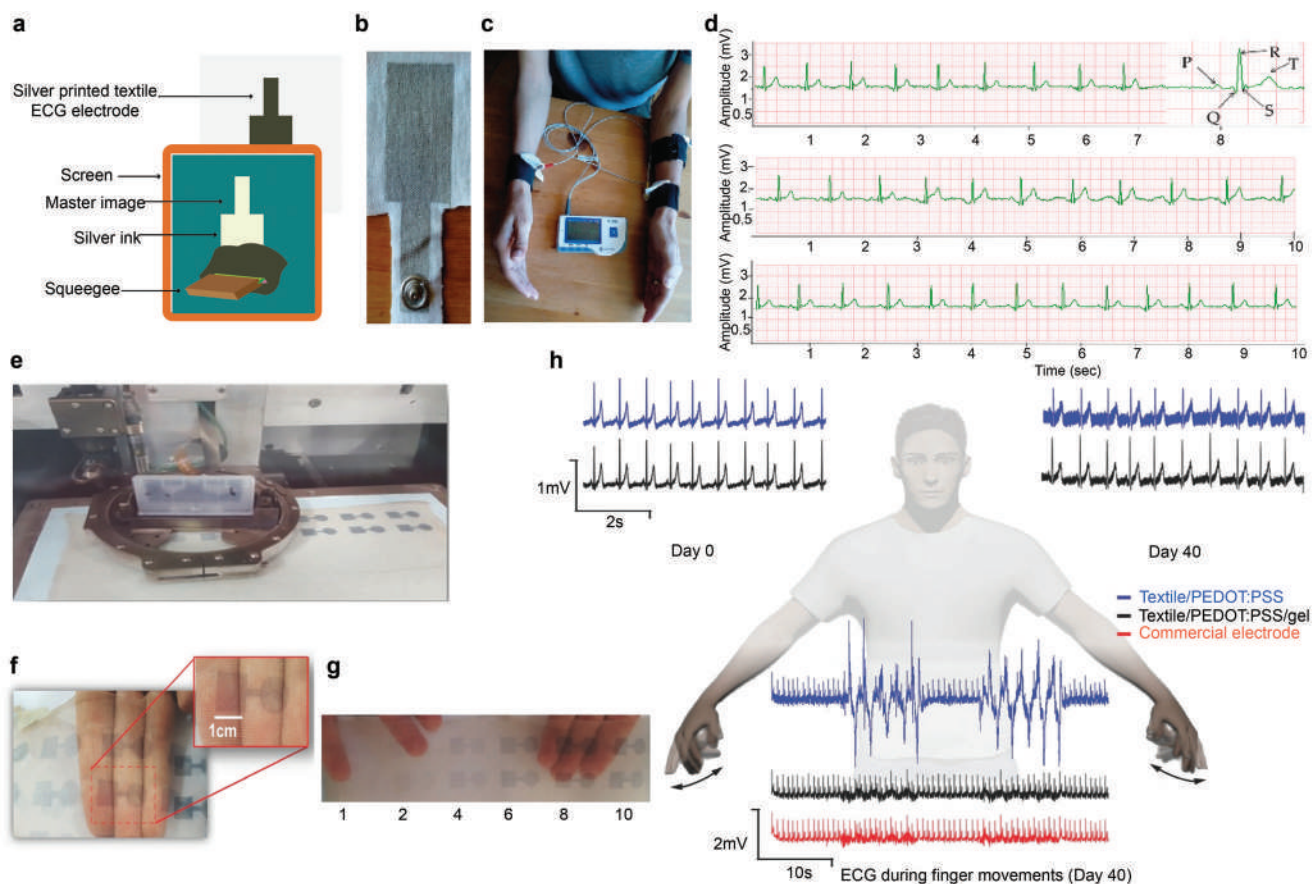


Figure 12. Printed textile electrodes for ECG measurement a) Block diagram for the screen printing process, b) Front view of the developed electrode; c) Component placement setup for ECG measurement, d) ECG signals collected using: (top) silver printed cotton; (middle) silver printed polyester fabric; and (bottom) Ag/AgCl gel electrode. Reproduced with permission.^[353] Copyright 2020, The Authors. e) Photograph of the inkjet printing process, f) Photograph of printed electrodes on a commercial textile with a zoom on an individual electrode, g) Photograph of electrodes with a different number of printed layers (1, 2, 4, 6, 8, 10) h) ECG data acquired under different conditions: static recoding at t_0 in the top left corner, i) Static recording at $t_0 + 40$ d in the top right corner, dynamic recording under repeated hand motion at $t_0 + 40$ d in the bottom center. Reproduced with permission.^[358] Copyright 2017, WILEY-VCH.

well as to evaluate patients with a history of depression and other psychiatric disorders.^[328,369] EEG detects both mind-wandering and mental efforts.^[370,371] Electrode is the most critical component in any device for monitoring biopotentials; where the transduction of potential signals in the tissue to the solid state conductor takes place. Skin surface electrode is especially important in the case of EEG, where the nature of the interface between the recording electrode and the scalp can overwhelmingly influence signal quality and sensitivity. A clinical scalp-EEG setup typically requires a standard 10–20 electrode placement set in which 21-cup electrodes, commonly made of tin, gold, silver, silver-silver chloride, or platinum, are attached to the scalp at precise locations to record the potential differences. However, several factors make the application of conventional electrodes challenging.^[372] It requires a long setup time, and special skills to find correct positions and to create good electrode-skin contact, especially through the hair. Also, conventional EEG electrodes are not usually MRI-compatible. They can cause artifacts in MRI images and the alternating magnetic field can cause tissue heating or electrode (wire) movement. Thirdly, solid metal cup electrodes do not conform properly to the skin, which causes motion artifacts in the EEG

signal.^[373] Development of an effective EEG electrode requires consideration of several factors, including impedance, susceptibility to recording artifacts, long-term stability, safe skin contact, and several practical considerations such as size, weight, simplicity of application, and cost.^[374] Textile-based EEG electrodes were reported by several research groups on different substrates utilizing different conductive materials; pin shaped carbon fiber electrode,^[375] Ag-thread, Ag-plated nylon, spandex, PP knitted textiles,^[376,377] Ni/Cu coated on polyester^[378] or conductive polymer treated fabric,^[379] PANI coated on PU foam,^[380] electroless copper plating on polyester fabrics^[381] or EEG electrodes placed in textile hats,^[382] etc. However, printed textiles have not been widely investigated yet. **Table 9** summarizes the printed textile EEG electrodes for monitoring brain activity.

Wei et al.,^[383] screen-printed Ag-paste with conductive rubber on woven textiles to realize a real-time emotion detection system based on EEG measurement. They used an emotion detection headband coupled with printed signal acquisition electrodes and open source signal processing software (OpenViBE), **Figure 13a,b**. The subject-dependent accuracy, using improved locations, increased to 91.75% from 86.83%. 75% of the partic-

Table 9. Summary of printed textile electrodes for EEG.

Printing method	Substrate (Reporting year)	Composed of	Type	Performance	Reference
Screen print	Textiles (2015)	Ag paste, conductive rubber	Headband	Accuracy of 90 (± 9) %	[169]
	Woven fabric (2017)	Ag paste, conductive rubber	Headband	Accuracy > 90%	[383]
	Cotton Woven (2022)	Graphene	Forehead	Correlation coefficient > 0.998	[151]
Jet printing	Polyurethane nonwoven (2018)	Composite ink of Ag and fluoro-elastomer in methyl ethyl ketone (MEK)	The hairless region behind the ears		[203]

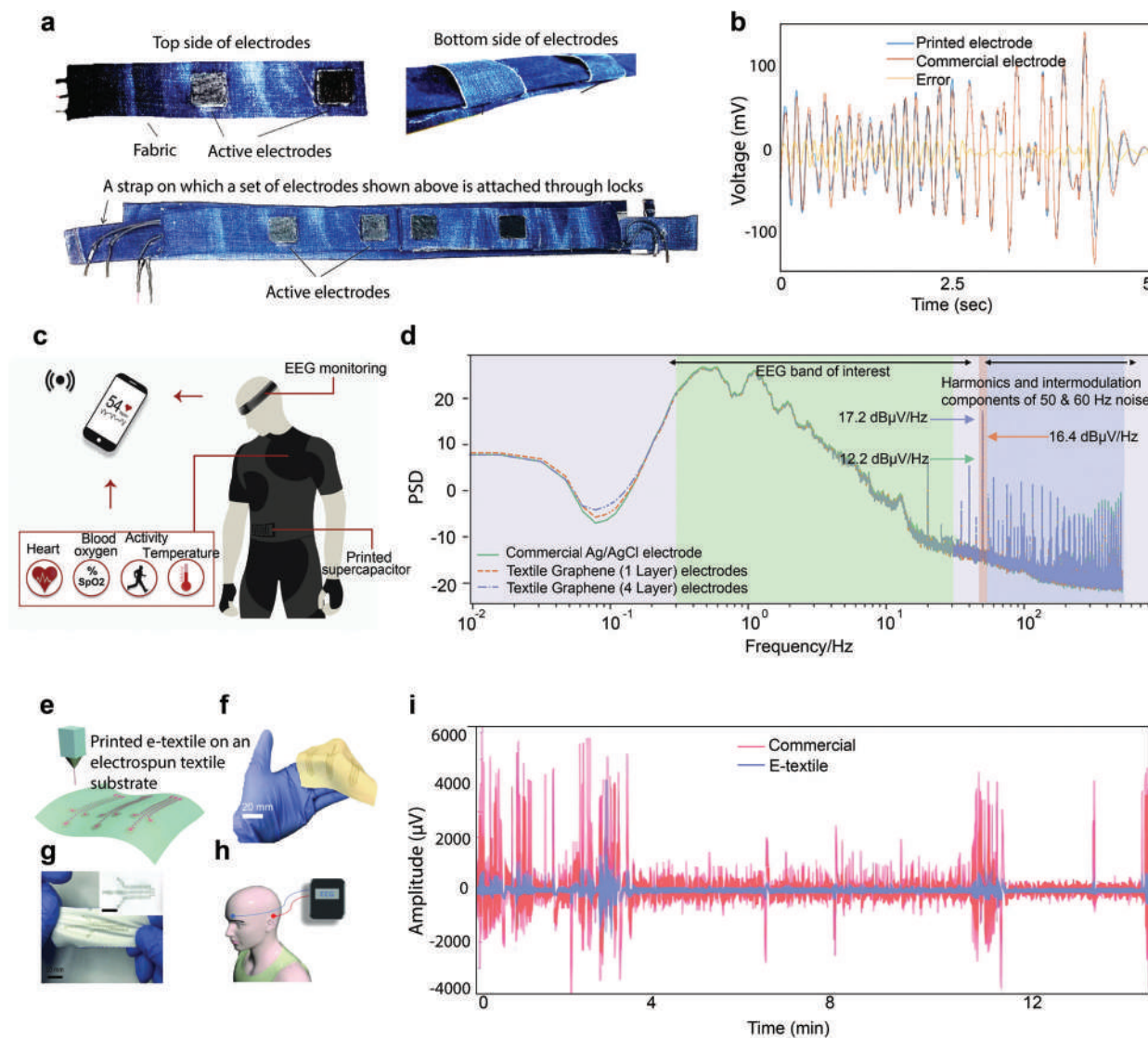


Figure 13. Printed textile electrodes for EEG measurement. a) Top and bottom side of printed electrodes (Top) and the overview of the headband (Bottom) b) EEG electrode comparison results. Reproduced with permission.^[383] Copyright 2017, Elsevier. c) Schematic of placement of EEG headband d) Power spectral density of recorded signal from graphene textiles electrodes against commercial Ag/AgCl electrodes, highlighting the typical frequency band of interest in EEG studies shaded in green. The 50 Hz component and its contribution for each of the electrode types are shaded in red. Also shown are higher frequency harmonics and intermodulation components from 50 to 60 Hz noise shaded in dark blue. Reproduced with permission.^[151] Copyright 2022, The Authors. e) The conceptual drawing of jet-printing nanocomposite inks onto a textile substrate f) A sheet of e-textile with printed conductive serpentine traces. g) Top view photographs of the two-layered e-textile seen from the serpentine traces sides. The main panels and the insets (scale: 10 mm) show stretched and non-stretched states, respectively. h) Schematic illustration of EEG recording from behind the ear i) Raw data collected from a commercial gel EEG electrode behind the left ear, simultaneously with an e-textile electrode behind the right ear (blue). Larger spikes in noise are observed for the commercial sensor due to less mechanical conformation with the skin. Reproduced with permission.^[203] Copyright 2018, WILEY-VCH.

Table 10. Summary of printed textile electrodes for EMG.

Printing method	Substrate	Composed of	Form/place of operation	Signal-to-noise ratio SNR (dB)/Performance	Reference
Stencil printing	Nylon/PU tricot knit (2017)	Flouro-elastomer/silver composite ink	Arm		[410]
Screen printing	Woven Textile (2012)	Conductive ink	Forearm		[411]
	Escalade (Cotton/polyester / Lycra), 3 × 1 twill woven (2014)	Ag paste/PU paste	Armband		[170]
	Woven (2014)	Ag paste, PU paste	Headband		[412]
	Cotton (2019)	PEDOT: PSS	Tibialis anterior muscle		[413]
	PET (2020)	Laser-induced graphene (LIG), AgCl, carbon inks			[355]
	Polyester-cotton fabric (2021)	Ag-polymer ink	Forearm	accuracy of ≈93%	[409]
	Textile and a silver plated lycra fabric (CCSM) (2022)	Ag, PEDOT:PSS			[414]
Jet printing	Polyurethane nonwoven (2018)	Composite of Ag and flouro-elastomer in methyl ethyl ketone (MEK)	Several body part		[203]

ipants achieved a classification accuracy >90%, compared with only 16% of participants before improving the electrode arrangement. In our previous work,^[151] we demonstrated screen-printed graphene-based textile electrodes to record EEG by simulating the EEG part of a PSG using two electrodes and a gelatine head phantom. The correlation coefficient between filtered data collected from graphene-based electrodes over a 20-min record was >0.998, indicating the very similar performance of our electrodes with conventional rigid Ag/AgCl electrodes, Figure 13c,d. La et al.^[203] reported two-layered e-textile patches with high mechanical durability and electrical performance, fabricated by jet-printing. Ag-powder/fluoropolymer-based nanocomposite ink on both sides of the porous textile substrate. They demonstrated their electrode to record true brain signals of the participants while opening and closing their eyes, Figure 13e–i.

5.2.7. Printed Textile Electrode for Electromyography

Electromyography (EMG) is a technique for recording and evaluating electrophysiological signals related to muscle activity (also referred to as the myoelectric signal). This is a fundamental method for understanding the muscle activity of the human body under normal and pathological conditions.^[384] Surface EMG is another non-invasive, painless, and easy technique to assess the myoelectric signal, utilized in various applications including clinical diagnosis of neuromuscular disorders, the study of muscle fatigue, and control of prosthetics, etc.^[385] This is important especially for measuring the electrical activity of muscles without function due to injury or disease as well as active prostheses movement control helping amputees to regain independent and unrestricted life.^[386] EMG is also important to infer motion intention and therefore could be used to control devices such as exoskeletons, biofeedback systems, or assistive tools.^[387]

Textiles were employed as EMG electrodes fabricated through a number of methods. Silver array mechanically attached to fabrics,^[387,388] conductive thread sewn/embroidered into

fabrics,^[389–391] stainless steel/cotton yarn sewn/embroidered into fabrics,^[392] nickel plated copper conductive woven fabric,^[393] PPY coated on nonwoven sheets,^[394–396] PPY coated on woven fabrics and yarns, coated yarn then knit,^[397] PEDOT:PSS selectively coated on knit fabric,^[398] Ag coated on PA yarn to prepare conductive woven,^[399–403] embroidered on woven,^[404] conductive knit fabric,^[405–407] SS and polyester stable fiber yarn conductive knit^[407] multilayer fabric^[408] are among the reported textile EMG electrodes. **Table 10** provides a brief overview of printed textiles for EMG measurement.

Tao et al.^[411] screen printed conductive ink on woven textiles to demonstrate the real-time performance of as-printed electrodes in EMG pattern-recognition-based prosthesis control. Their results tested on seven participants exhibited an accuracy of 91.81% for ten different movements, compared to 96.54% for six basic movements. Pani et al.^[413] demonstrated the performance of polymer-based screen-printed textile electrodes for sEMG signal detection. They deposited PEDOT:PSS onto cotton fabric to form the electrode. While compared with the conventional electrodes, the r^2 value was >97% for all measurement conditions. Court et al.^[409] reported a screen-printing process to deposit four functional layers in turn, on a polyester cotton fabric to realize an EMG electrode, **Figure 14a–d**. An interface layer was printed to smoothen the surface of the fabric and improve printability for the subsequent conductive layer. The conductive layer consists of a silver polymer ink for the conductive tracks, followed by encapsulation using the same ink as the interface layer. The final layer was a stencil-printed conductive carbon rubber paste covering one of the exposed conductor areas, providing a dry electrode contact to the skin. A total of five gestures were uniquely identified with an average accuracy of ≈93% when operating with a switching delay of 150 ms or greater. As described in the previous section the work of La et al.,^[203] reported a jet-printed two-layered e-textile patches of Ag-powder / fluoropolymer-based nanocomposite ink on both sides of the porous textile substrate. They controlled the thickness of the cladded layer which provided a remarkable advantage in designing electrodes for both EMG and EEG applications. A complete wireless EMG system

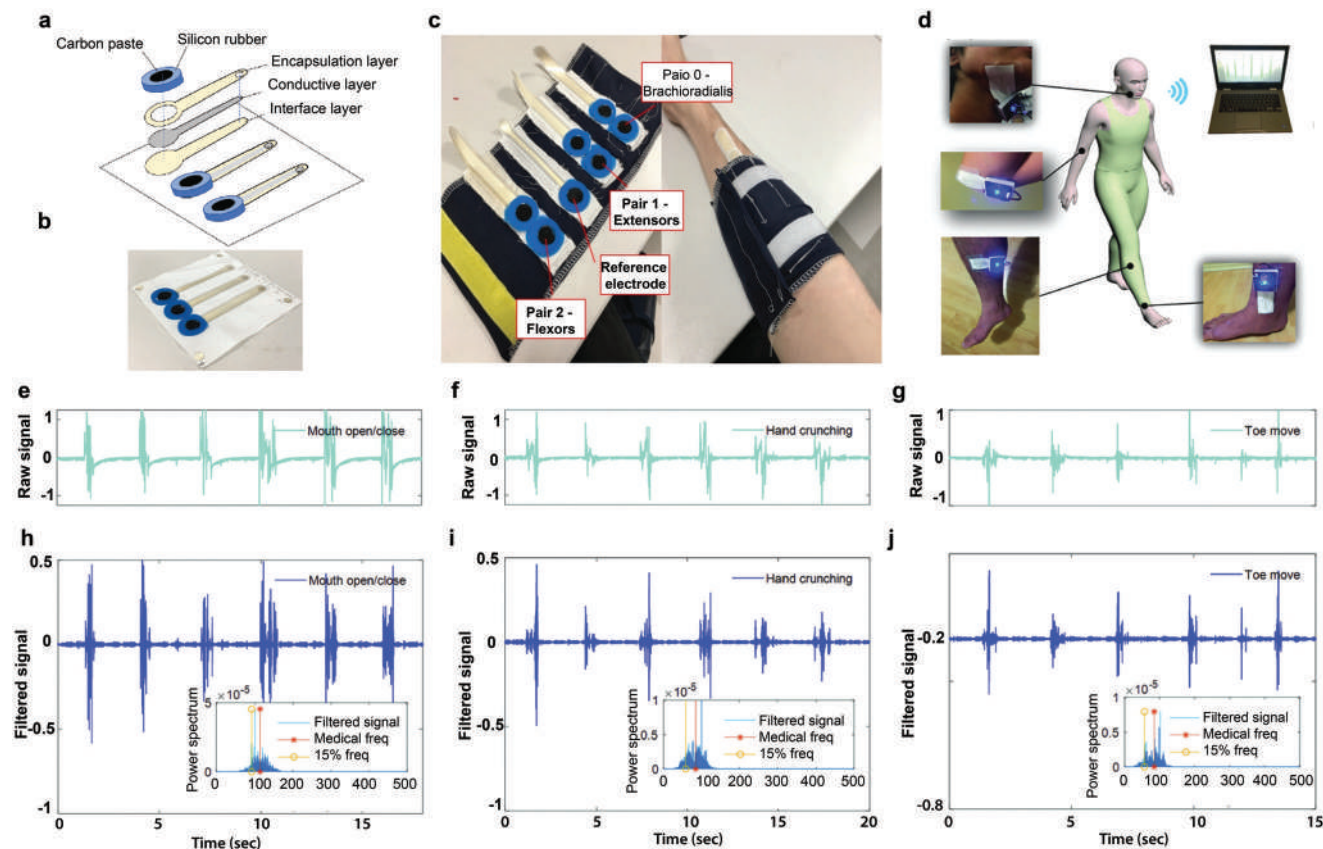


Figure 14. Printed textile electrodes for EMG measurement. a. Exploded view of printed electrodes. b. Complete screen-printed electrode c. Final measurement device. Reproduced with permission.^[409] Copyright 2021, The Authors. d) Schematic illustration of sEMG measurements from various parts of the human body. e) The raw and h) filtered sEMG signals from mouth open/close episodes measured from the submental space. f) The raw and i) filtered sEMG signals from hand crunching episodes measured from the elbow. g) The raw and j) filtered sEMG signals from toe lifting episodes measured from the ankle. Insets are power spectrums obtained by Fourier transforms of each data. Reproduced with permission.^[203] Copyright 2018, WILEY-VCH.

was also demonstrated with their custom-designed data acquisition/transmission electronics, Figure 14e–i.

5.2.8. Printed Textile Electrodes for Electrooculography

Electro-oculography (EOG) is safe, convenient, and efficient thus been the standard eye-movement measurement technique for many decades.^[415] Based on the corneoretinal potential (difference in electrical charge between the cornea and the retina), with the long axis of the eye acting as a dipole, eye movements relative

to the surface electrodes placed around the eye produce an electrical signal that corresponds to eye position.^[416] Graphene-coated textiles were reported as EOG electrodes.^[417] **Table 11** summarizes the printed textiles utilized for the acquisition of EOG.

Myllymaa et al.^[171] utilized screen-printing technology to construct the electrode set consisting of ten electroencephalography (EEG) electrodes, two electrooculography (EOG) electrodes, two ground electrodes, and two reference electrodes. Paul et al.^[170] developed a screen-printed network of electrodes and associated conductive tracks on textiles for medical applications. A polyurethane paste was screen printed on to a woven textile to

Table 11. Summary of printed textile electrodes for EOG.

Printing method	Substrate (Reporting year)	Composed of	Type	Reference
Screen print	Polyester (2013)	Ag ink	Face to face	[171]
	Escalade (Cotton/polyester / Lycra), 3 × 1 twill woven (2014)	Ag paste, PU paste	Headband	[170]
	Woven (2014)	Ag paste, PU paste	Headband	[412]
	PET (2020)	Laser-induced graphene (LIG), AgCl, carbon inks	Forehead	[355]

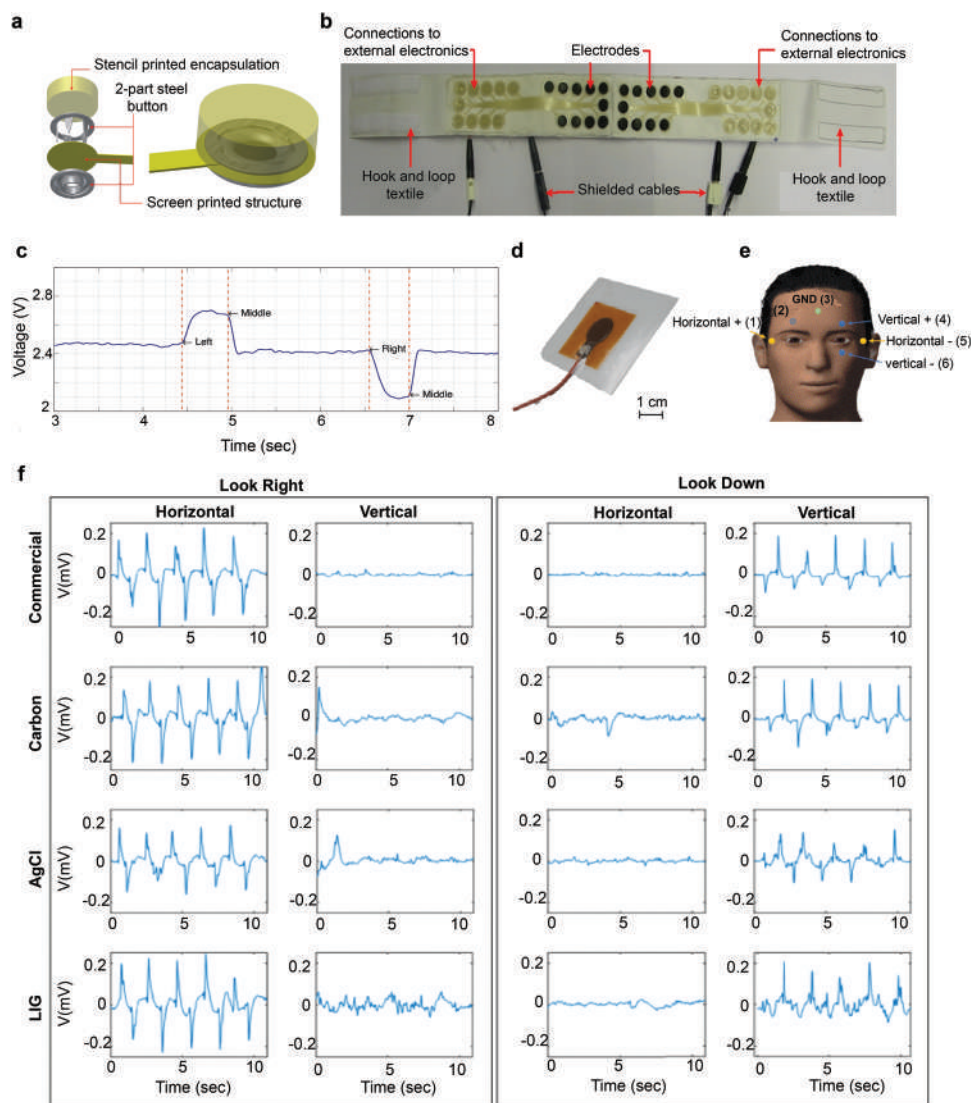


Figure 15. Printed textile electrodes for EOG measurement. a) Fabrication of electrode components, left: individual parts and right: completed electrode. b) Textile headband for EMG and hEOG monitoring. c) hEOG recorded with the textile printed headband. Reproduced with permission.^[170] Copyright 2013, Elsevier. d) Multilayer structure of the developed LIG electrode e) Positions of the electrodes and signal nomenclature. f) EOG signals for different materials and eye movements. Reproduced with permission.^[355] Copyright 2020, The Authors.

create a smooth, high surface energy interface layer. A silver paste was subsequently printed on top of that to provide a conductive track followed by another PU encapsulation layer to protect the silver track from abrasion and creasing. Conductive rubber, with a thickness of 3 mm, was then stencil printed on to the terminations of these conductive tracks to form electrodes. The electrodes, used in contact with the skin, in the form of a headband, were demonstrated and evaluated for the biopotential monitoring applications of ambulatory ECG, EMG, and EOG, **Figure 15a–c**. The same research group further reported^[412] a printed electrode headband, used in a facial EMG and EOG control system. The system was also used to control a mouse cursor or simulate keyboard functions. It was found that 50 Hz noise levels in the printed textile electrodes were similar to commer-

cial disposable electroencephalography electrodes. The effect of a wearable approach on pressure variations and motion artifacts is examined. Toral et al.,^[355] compared three types of electrodes based on (laser-induced graphene) LIG, silver chloride, and carbon inks during the acquisition of biopotentials including ECG, EMG, and EOG. They also developed a completely new framework for the acquisition of EOG based on a printed patch that integrates 6 electrodes for the EOG acquisitions and an ad-hoc signal processing to detect the direction and amplitude of the eye movement, **Figure 15d–f**. Performances of the developed electrodes were compared with commercial ones using the characteristics parameters and showed similar performance with the commercial electrodes with an improvement in the comfort of the user.

Table 12. Summary of Printed Textile Supercapacitors.

Printing Method	Substrate (Reporting year)	Device Configuration	Device capacitance	Energy density	Power density	Capacitance retention	Flexibility	Reference
Screen Printing	Cotton and polyester fabric (2011)	Cotton and polyester screen printed with AC as electrode, polyester separator, and Li_2SO_4 and Na_2SO_4 electrolyte	Electrode 0.43 F cm^{-2} at 5 mA cm^{-2} (Na_2SO_4), $85\text{--}95 \text{ F g}^{-1}$ at $1\text{--}10 \text{ mV s}^{-1}$			92% after 10 000 cycles		[437]
	Carbon fiber knit and woven fabric (2013)	Carbon fabric screen printed with AC with solid polymer electrolyte	88 F g^{-1} , 0.51 F cm^{-2} (Knitted), 66 F g^{-1} , 0.19 F cm^{-2} (Woven)				80% after bending at 90° , 135° , and 180°	[172]
	Cotton, polyester, spandex, 50/50 NycO, Sigma 4 Star, Defender M14 Stretch, Nonwoven 3NP (2016)	Screen printed AC ink with ionic liquid electrolyte (1-ethyl-3-methylimidazolium tetracyanoborate) and graphene foil as current collectors	20 mF cm^{-2} and 4.21 F g^{-1}					[438]
	Silk fabric (2016)	Screen printed current collector and active materials layers [MnO-coated hollow carbon microspheres, acetylene black, and binder in 7:2:1] on commercial silk fabrics and PDMS film, respectively. PDMS-based electrode was pasted with gel electrolyte and transferred on the top of the silk fabric-based electrode	19.23 mF cm^{-2} at 1 mA cm^{-2}			84% after 2000 cycles	98.5% after 100 times bending and 96.8% after 100 times twisting	[439]
	Carbon cloth (2017)	SnO_2 nanoparticles, CNTs, ethyl cellulose, and terpineol composite ink screen-printed onto carbon cloth. Furnace-calcined SnO_2/CNT electrodes sandwiched with PVA- H_2SO_4 gel electrolyte	5.61 mF cm^{-2} (flat) and 5.68 mF cm^{-2} (bent)					[440]
	Cotton Woven (2017)	Screen printing of GO, followed by electrochemical reduction to produce rGO-cotton electrode, with PVA- H_2SO_4 gel electrolyte	2.5 mF cm^{-2} , 257 F g^{-1}			97% after 10 000 cycles	95.6% after folding 180° for 2000 cycles	[441]
	Stretchable textiles (2018)	Fully printed Ag@PPy@ MnO_2 on Ag cathode electrode and activated carbon on Ag anode electrode with PVA- Na_2SO_4 electrolyte	426.3 mF cm^{-2} (cathode), device 95.3 mF cm^{-2}	$0.0337 \text{ mWhcm}^{-2}$ at 0.38 mW cm^{-2}		90.8% after 5000 cycles	86.2% after 40% stretching strain	[442]
	Polyester fabric (2020)	Ag paste printed on PET, MnHCF-MnOx/GO ink overprinted and reduced to form the electrode, PVA-LiCl electrolyte, and paper separator	16.8 mF cm^{-2}	0.5 mWhcm^{-2}	$0.0023 \text{ mW cm}^{-2}$		Stable at bending to angles 60° , 90° , 180° for 100 cycles	[443]
	Cotton fabric (2022)	Graphene ink screen printed on cotton textiles with PVA- H_2SO_4 gel electrolyte	3.2 mF cm^{-2}	0.28 mWhcm^{-2} at 3 mW cm^{-2}		95% after 10 000 cycles		[151]

(Continued)

Table 12. (Continued)

Printing Method	Substrate (Reporting year)	Device Configuration	Device capacitance	Energy density	Power density	Capacitance retention	Flexibility	Reference
Inkjet printing	Polypropylene (PP) fabric (2019)	Reactive inkjet printing of rGO layers on PP fabric as an electrode with PVA-H ₂ SO ₄ gel electrolyte to form flexible solid-state SC	13.3 mF cm ⁻² (79.9 F g ⁻¹) at 0.1 mA cm ⁻²	1.18 mWhcm ⁻²	4.6 mW cm ⁻²	Almost 100% after 5000 cycles		[444]
	carbon cloth (2019)	Nickel cobalt layered double hydroxide-(LDH)/Ag/rGO) as positive and activated carbon as negative electrode with 1 M KOH electrolyte	95 mAh g ⁻¹ at 0.6 A g ⁻¹	76 Whkg ⁻¹	480 W/kg ⁻¹	79.8% after 5000 cycles		[445]
	Bamboo fabric (2020)	MnO ₂ -NiCo ₂ O ₄ printed bamboo fabric as positive electrode, and rGO inkjet printed bamboo fabric as negative electrode with LiCl/PVA gel as solid-state electrolyte	2.12 F cm ⁻² (1766 F g ⁻¹) at 2 mA cm ⁻²	37.8 mW cm ⁻³	2678.4 mW cm ⁻³	92% of after 5000 cycles		[204]
	PP non-woven textile (2021)	Reactive inkjet printing to fabricate PPy layers on textile substrates with direct freezing of inks	72.3 F g ⁻¹ at 0.6 A g ⁻¹ at -12 °C	6.12 Wh kg ⁻¹	139 W kg ⁻¹	55.4% after 2000 cycles		[446]

5.3. Printed Textile Supercapacitors

The continuous development of science and technology increases the demand for energy storage and conversion equipment enormously.^[418] To facilitate the wide growth of wearable electronics technology, it is necessary to provide a constant power supply that is flexible, durable, lightweight, biocompatible, and strong.^[137,204] Currently existing energy storage devices are rigid and bulky and do not demonstrate fabric-like properties such as hand feel, thickness, or drape. Moreover, the integration of multiple components of e-textiles must be systematic to be a part of the garment which also needs to be flexible, light in weight, and highly functional in performance.^[172] Therefore, there is a strong need to develop small, flexible, and high-performance energy storage devices for easy integration with wearable electronics.^[419] Supercapacitors (SCs) or ultracapacitors are promising devices for energy storage having characteristics that lie between dielectric capacitors and conventional batteries.^[420] Electric double-layer capacitors (EDLCs) and pseudo-capacitors are two main types of supercapacitors; EDLCs offer a high power density, good reversibility, and a long cycle life whereas pseudo-capacitors have a much higher energy density and a lower cycle life than EDLCs.^[421] Thin and flexible supercapacitors, due to possessing features such as lightweight, high power density, and their ability to deliver under mechanical deformation conditions are gaining more consideration for wearable electronics. However, the insufficient energy density still limits their use in practical applications.^[204] Enormous efforts have been carried out by researchers to meet these demands for making multifunctional e-textiles and adding value to conventional textiles.^[147] Research regarding the integration of supercapacitors with other flexible textile electronics thus offers the solution of powering wearable e-textiles.^[422] Simple fabrication methods such as photolithography,^[423,424] coating,^[425-427] painting or spraying^[428,429] or laser scribing,^[430,431] sputtering,^[432,433] have been employed for the fabrication of supercapacitors. However, printing technique has also been employed for supercapacitor fabrication in various substrate such as paperboard,^[434] PET film,^[435] PEN, PDMS, etc. Printed electronics represents a paradigm shift in the manufacturing of textile-based supercapacitors in that it provides a whole range of simple, low-cost, time-saving, versatile, and environmentally friendly manufacturing processes.^[436] Table 12 summarizes the printed textiles employed for supercapacitor fabrication.

Just et al.^[437] screen printed porous carbon materials on woven cotton and polyester fabric for fabricating flexible and lightweight electrodes for supercapacitor fabrication. Utilizing a polyester separator and Li₂SO₄ and Na₂SO₄ electrolyte, they reported a high gravimetric capacitance of 85–95 F g⁻¹ and areal capacitance of ≈0.43 F cm⁻² at a scan rate of 1–10 mV s⁻¹. In our previous work,^[441] we printed graphene oxide (GO) ink on cotton woven textiles, followed by electrochemical reduction to produce rGO-cotton electrode, Figure 16a–c. Using a PVA-H₂SO₄ gel electrolyte, our device achieved an areal capacitance of 2.5 mF cm⁻² and a high specific capacitance of 257 Fg⁻¹ which retained its capacitance up to 97% even after 10 000 charge–discharge cycles and up to 95.6% after folding at 180° for 2000 cycles. In our other work,^[151] we utilized the screen printing process to demonstrate a graphene-based multifunctional e-textile platform. Pro-

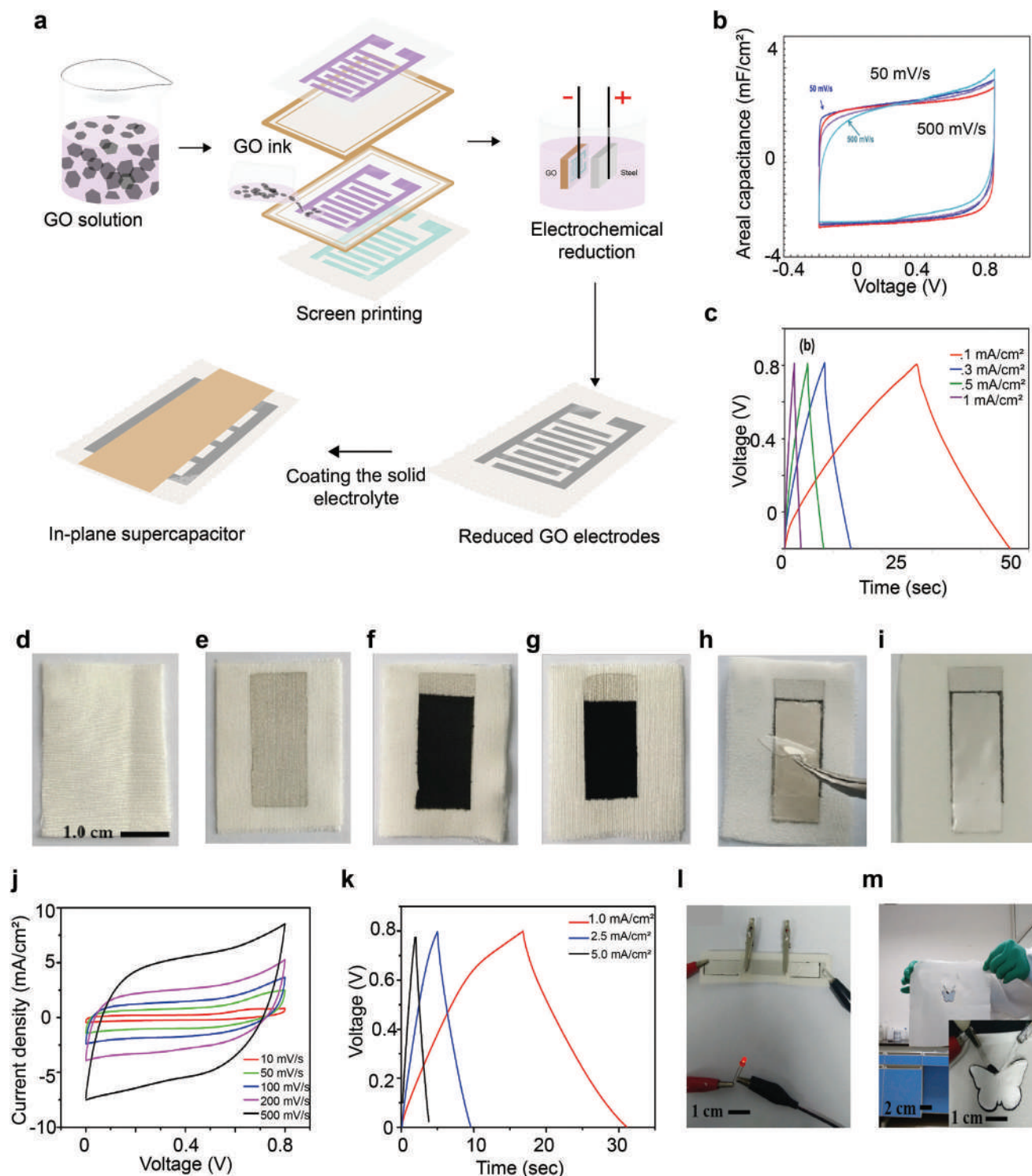


Figure 16. Screen printed textile supercapacitors a) Schematic representation of the printed SC fabrication process. Electrochemical characterization of the printed graphene on textile: b) CV at different scan rates and c) Charge–discharge curves at different current densities. Reproduced with Permission.^[441] Copyright 2017, IOP Publishing Ltd. From a silk fabric to a silk fabric-based fully printed supercapacitor: d) Piece of pristine silk fabric, e) Silk fabric after successively screen printing of silver, f) Carbon, and g) Active materials layers, h) Removal of the PDMS support from the stacked device, i) Single textile-supported supercapacitor. Electrochemical characterization of the supercapacitor: j) CV curves of a supercapacitor at various scan rates. k) Galvanostatic charge–discharge curves over a potential window from 0 to 0.8 V at different current densities, l) Digital photograph of a red LED powered by three supercapacitors connected in series, and m) Digital photograph of a specially designed supercapacitor with a butterfly pattern. Reproduced with permission.^[439] Copyright 2016, American Chemical Society.

duced e-textiles were extremely flexible, conformal, and able to perform as a piezoresistive sensor for activity monitoring. The printed in-plane supercapacitor provided an areal capacitance of $\sim 3.2 \text{ mFcm}^{-2}$ (stability $\approx 10\,000$ cycles). It was also used to record brain activity (EEG) and find comparable to conventional rigid electrodes. One of the high-performing supercapacitors fabricated by screen printing was reported by Liu et al.^[442] Ag current collector, Ag@PPy@MnO₂ composites as a cathode electrode, activated carbon as anode electrode, and gel electrolyte were printed onto a stretchable textile. The cathode electrode exhibited a high areal capacitance (426.3 mFcm^{-2} at 0.5 mAcm^{-2}) and superior cycling ability (98.7% capacitance retention even after 10 000 cycles). The all-printed stretchable asymmetric supercapacitor (ASCs) exhibited an areal capacitance of 95.3 mFcm^{-2} , energy density of $0.0337 \text{ mWh cm}^{-2}$, and 86.2% retention after 40% stretching strain. Zhang et al.^[439] involved both screen printing and transfer printing to construct all-solid-state supercapacitors on a single silk fabric, Figure 16d–m. The system exhibited a high areal capacitance of 19.23 mF cm^{-2} at a current density of 1 mAcm^{-2} and excellent cycling stability with capacitance retention of 84% after 2000 charging/discharging cycles with stable performance and structures after 100 times bending and twisting.

In addition to the rapid development of high-performance active materials for supercapacitor electrode fabrication, attention should also be paid to the eco-friendliness and sustainability of the fabrication processes. The conventional fabrication processes rely on several toxic chemicals or solvents, involving considerable waste of precious functional materials, and/or release of toxic by-products. Inkjet printing, in this regard, is considered as a sustainable technique due to its combination of multiple merits, such as purely additive processing, direct (mask-free) patterning, high resolution, minimized material waste, good scalability, and excellent compatibility with versatility in active materials and substrates selection.^[448] Therefore, inkjet printing has been in increased focus of the e-textile manufacturers, specially for supercapacitors on several substrates such as PET,^[449–455] flexible ITO,^[450] PI,^[456,457] Kapton,^[458,453,454] glass,^[454] paper,^[459] PDMS etc. Giannakou et al.^[447] deposited NiO coplanar electrodes on flexible substrate through the inkjet printing method. The silver nanoparticle ink was inkjet-printed first on a flexible PET substrate in a coplanar interdigitated configuration to form the current collector of the device. Then the NiO nanoparticle ink was printed on top of the interdigitated silver current collector. The structure was annealed to promote nanoparticle sintering of both layers, the electrolyte was drop-cast on top of the active interdigitated region of the device, Figure 17a–c. The highest areal capacitance was reported by Sundriyal et al.^[204] who demonstrated the inkjet-printing of the rGO and metal precursors of MnO₂ and NiCo₂O₄ over the bamboo fabric substrates. Developed MnO₂–NiCo₂O₄/rGO printed asymmetric supercapacitors exhibited a high areal capacitance of 2.12 Fcm^{-2} , excellent energy density of 37.8 mW cm^{-3} , and power density of $2678.4 \text{ mW cm}^{-3}$, good cycle life and high retention. It also indicated no structural failure and capacitance loss under different mechanical deformation conditions, Figure 17d–g. Zhang et al.^[454] reported the highest volumetric capacitance of 562 Fcm^{-3} for inkjet-printed supercapacitors. They demonstrated two types of 2D titanium carbide (Ti₃C₂T_x) MXene inks, in the absence of any additive

or binary-solvent systems high resolution and spatially uniform inkjet printing on AlO_x-coated PET, glass, Kapton substrates.

5.4. Printed E-Textiles for Personalized Thermoregulation

Thermal comfort is a condition of mind, expressing satisfaction with the thermal environment.^[460–465] It represents whether a person feels neither too cold nor too warm. Thermal conditions of the human body are crucial for both physical and psychological health and may become potentially life-threatening if the core body temperature reaches conditions of hyperthermia (above $37.5 \text{ }^\circ\text{C}$ – $38.3 \text{ }^\circ\text{C}$) or hypothermia (below $35 \text{ }^\circ\text{C}$).^[466] Maintaining human body thermal comfort wisely is important for efficient human body energy management, therefore, wearable heaters have recently attracted great interest with the growing demand for wearable and stretchable devices.^[467] The introduction of heating systems made directly from textiles could potentially help humans maintain comfort without using any additional bulky heating arrangement. The main advantage of this improvement is the development of heated materials with built-in flexibility provided by textile structures. With the progressive development of conductive threads, textile-heating systems represent one of the major growing sectors in textiles.^[468] Such heating elements are used in climate control and personal thermal management,^[469] such as protecting us against cold stress both in foul weather outdoor environments and in indoor environments by raising the human body's temperature applied to normal clothes.^[470] A personal heating garment (PHG) is helpful to reduce cold stress and freezing (e.g., frostbite and frostnip) or non-freezing cold injuries (e.g., immersion foot, cracked skin and chilblains caused by chilling of extremities, usually fingers, toes, and ears, etc.).^[471] Heating of smart clothing products based on nontextile electronic components already exists in the market, but these products do not have a big consumer demand yet.^[472] Heating elements can have applications including heated garments, heated molds for industrial use, heated furniture, electrically heated cushions and heated blankets, heating elements for the automotive sector, heating solutions for medicinal purposes, surface heating elements in general, etc. For wearable applications, conducting panels can be used as heating elements. The heating rate is given by the power P that is generated due to Joule heating with current I , running through the conductor with resistance R .^[136]

$$P = RI^2 \quad (10)$$

Several methods have been reported for the fabrication of textile heaters, such as chemical deposition of silver nanoparticles (AgNPs) on widely used cotton fabric,^[150] wrapping of AgNW on yarn,^[473] weaving,^[474] braiding^[475] or knitting^[476] of conductive yarns, etc. However, the coating technique was extensively studied for realizing heating textiles. Textiles coated with several carbonaceous materials,^[477–479] conducting polymers,^[480–482] metals,^[483–485] MXenes,^[486,487] etc were reported by several research groups. Table 13 summarizes the textile-based printed heaters.

Torah et al.^[144] reported for the first time a flexible heater screen-printed directly onto polyester-cotton fabric. They printed

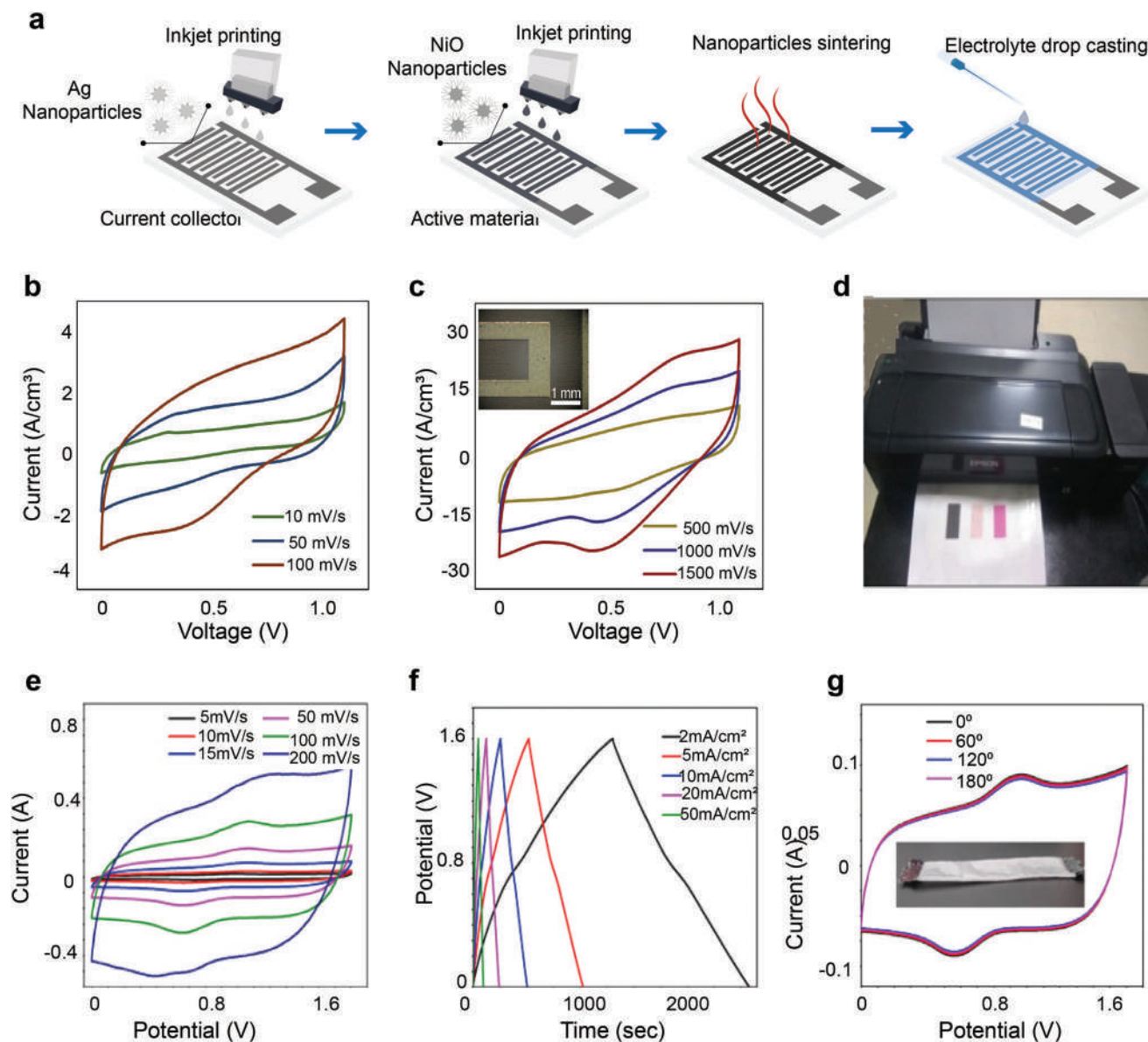


Figure 17. Inkjet printed textile supercapacitors a) Fabrication process of Inkjet Printed NiO supercapacitors. b, c) CV curves of supercapacitors printed on PET with adhesion promoting layer. The devices were scanned at voltage a window from 0 to 1 V at scan rates from 10 to 1500 mV s^{-1} . The interdigitated electrodes and interelectrode gaps of the inset images are 1000 and 500 μm wide respectively. Reproduced with permission.^[447] Copyright 2020, Elsevier Ltd. d) Photograph of the GO ink, Ni-Co precursor ink and KMnO_4 ink on bamboo fabric substrate e) CV curves of $\text{MnO}_2\text{-NiCo}_2\text{O}_4/\text{rGO}$ asymmetric device at different scan rates f) GCD profiles of the $\text{MnO}_2\text{-NiCo}_2\text{O}_4/\text{rGO}$ asymmetric device at various current densities and g) CV curves of the device under different mechanical bending conditions (inset image shows digital photograph of textile supercapacitor. Reproduced with permission.^[204] Copyright 2020, The Author(s).

an initial insulation layer to reduce the roughness of the textile thus improving the surface quality and electrically insulating the subsequently printed heating conductor. A conductive layer was then printed onto the insulation layer to provide the heating element. Finally, another insulation layer was printed on top to provide complete electrical insulation of the conductor layer. The fabric was successfully heated up to 120 °C using a 30V input voltage. Choi et al.,^[489] in 2021 fabricated a high-stretch PTC surface heating textile (PTC-SHT) by screen-printing using a composite paste of PTC powder and multiwall carbon nan-

otubes (MWCNTs) onto a high-stretch textile with embroidered electrodes, **Figure 18a–d**. Overall, the temperature increased to 56.1 °C with a power consumption of 5 W over 7 min. The heat generation characteristics were maintained at 95% after 100 000 cycles of 20% stretch–contraction testing, and the heating temperature remained uniformly distributed within ± 2 °C across the entire heating element.

Tian et al.,^[490] utilized both screen and transfer printing for silver fractal dendrites (Ag FDs) conductive ink on the polystyrene–block–polyisoprene–block–polystyrene (SIS) thin film. The ultra-

Table 13. Summary of printed e-textiles for personalized thermoregulation.

Printing method	Substrate (Reporting year)	Composed of	Maximum Temperature	Performance	Reference
Screen print	Polyester-cotton (2012)	Ag as conductor layer and encapsulation material	120 °C using a 30V input voltage, 35–40 °C using a 12 V battery		[144]
	PET (2019)	PEDOT:PSS, AgNW	99 °C at 12 V and 107 °C at 54 V within 20 s		[488]
	Stretchable textile (2021)	Positive temperature coefficient (PTC) powder and MWCNTs with embroidered electrodes	56.1 °C with a power consumption of 5 W over 7 min	Heat generation maintained 95% after 100 000 cycles of 20% stretch–contraction testing. Heating temperature remained uniformly distributed within ± 2 °C	[489]
Screen and transfer printing	Polystyrene–block–polyisoprene–block–polystyrene (SIS)	Silver fractal dendrites (Ag FDs) conductive ink	52.3 °C at 1 V	Low-voltage driving Joule heating performance	[490]
Electrohydrodynamic printing	Polyethylene terephthalate (PET), paper, glass, polydimethylsiloxane (PDMS) (2018)	AgNW ink	≈ 160 °C at the voltage of 25 V	Maximum heating rate of ≈ 21 °C s ⁻¹ and cooling rate of ≈ 29 °C s ⁻¹ .	[491]
Patternable spray coating	Stretchable fabric (2019)	Ag nanowire/carbon nanotube composites	35 °C–55 °C at 3–5 V		[492]
Scalpel printing	Cotton, polyester woven and nonwoven (2019)	Nano carbon colloidal ink of MWCNT synthesized by globular protein serum bovine albumin (BSA)	Organic NC printed cotton woven fabrics 140 °C at 20 V		[493]
Pattern printing	Stretchable LM@PDMS (2019)	conductive composite of liquid-metal (LM) and polydimethylsiloxane (PDMS)	45.26 and 95.9 °C, at 2.0 and 3.5 V	Suitable as a stretchable wearable electrically driven heater (WEDH) for wearable therapy	[494]

stretchable flexible printed pattern was demonstrated as a low-voltage driving Joule heating performance (heated to 52.3 °C at 1 V). They also reported their heater applications in the bent state, Figure 18e–h. Cui et al.,^[491] reported an electrohydrodynamic printing of Ag-NW ink on several flexible substrates including PET, paper, glass, and PDMS. The printed heater obtained a temperature of up to ≈ 160 °C at the voltage of 25 V with a maximum heating rate of ≈ 21 °C s⁻¹ and a cooling rate of ≈ 29 °C s⁻¹. Arbab et al.,^[493] reported the development of a printable carbon ink of multiwall carbon nanotubes (MWCNT) synthesized by globular protein serum bovine albumin (BSA). The maximum rise in temperature of cotton and polyester, woven, and nonwoven fabrics was reported at 140 °C at 20 V, Figure 18i–m. Though not on textiles, Choi et al.^[495] proposed a transfer printing technique to integrate graphene-based stretchable sensors, actuators, light-emitting diodes, and other electronics in one platform, paving the way toward transparent and wearable multifunctional electronic systems.

5.5. Printed Textile Electrochromics

Electrochromic materials, also called switchable materials, change color in a persistent but reversible manner by an electrochemical reaction, and the phenomenon is called electrochromism. The visible change in transmittance and/or reflectance is associated with an electrochemically induced

oxidation-reduction reaction. It results from the generation of different visible region electronic absorption bands on switching between redox states.^[496] They are usually used in the form of thin film devices such as in electrochromic, or smart windows, architectural glazing, automotive mirrors, rearview mirrors, sunroofs, sunglasses, and other high-end applications.^[497] Electrochromic materials usually include viologens, transition metal oxides (WO₃, MoO₃, V₂O₅, Nb₂O₅), metal hexacyanometallates, conducting polymers, etc. Such materials can also be introduced in textiles to develop color-changing and light-emitting textiles. Upon application of specific stimuli, such textiles can change their optical properties. Some of these textile-based structures have already been used for the development of flexible displays, which can be used for multiple applications, from medical textiles to communicative textiles, as well as for art and fashion.^[498]

Researchers fabricated electrochromic textiles by coating PEDOT:PSS on readymade polyester flex printing fabric,^[499] electrochemical deposition of PANI on metal-plated textiles,^[500] or spray coating of PEDOT:PSS on polyethylene polyethylene terephthalate (PEPES) membranes.^[501] Wei et al.^[502] reported the design, fabrication, and testing of a dispenser-printed electrochromic (EC) display on fabric using PEDOT:PSS. The display was directly printed onto a polyvinyl chloride (PVC)-coated, 100% polyester woven fabric. Each display pixel, consisting of the color-changing and counter electrodes, was separately driven at two voltage direct currents (VDCs). The color change between pale blue and

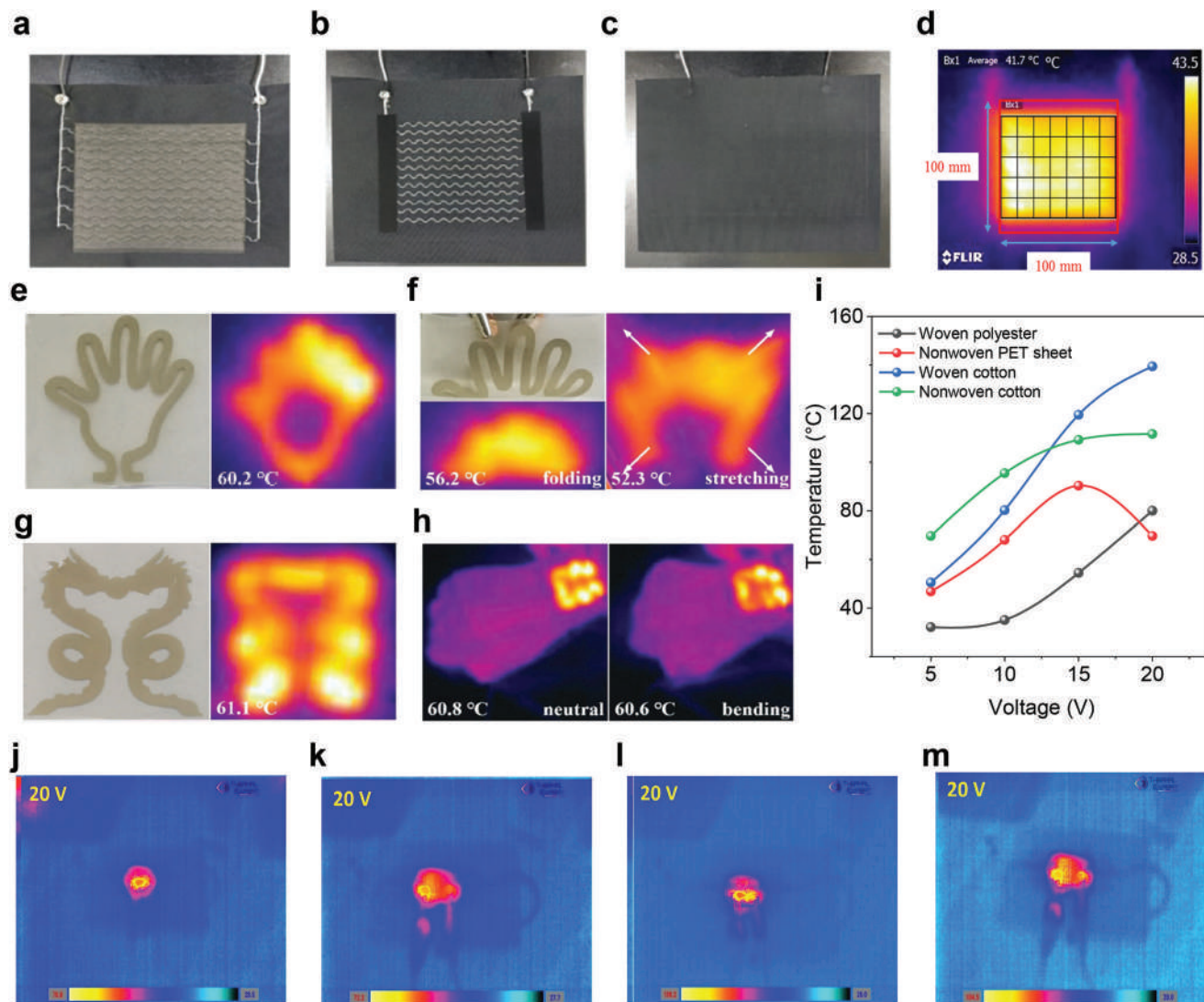


Figure 18. Printed E-textiles for personalized Thermoregulation. Digital photographs of the a) Front b) Back after screen-printing; and c) The finished product. (d) Heating temperature uniformity across the PTC-SHT at an applied voltage of 3 V. Reproduced with permission.^[489] Copyright 2021, The authors. e) The digital photograph and IR image of the multifunctional wearable electronics with palm pattern, and f) Its IR images under folding and stretching at 3 V. g) The digital photograph and IR image of the MWE with double-dragon pattern (top), and h) Its IR images of the pattern attached to the wrist in a natural and bent state (bottom) at 2 V. Reproduced with permission.^[490] Copyright 2019, WILEY-VCH. i) Voltage versus surface Temperature diagram of different types of Organic nanocarbon ink (NC) printed fabrics. Measurement of surface temperature using thermal expert camera for j) Cotton woven k) Polyester woven l) Cotton nonwoven and m) PET sheet at 20V. Reproduced with permission.^[493] Copyright 2018, Elsevier Inc.

dark blue was controlled by switching the polarity using a microcontroller. Two demonstrators, a 3×3 -pixel matrix display and a seven-segment display, were achieved with an average switching speed of 5 s, **Figure 19a–h**. Linderhed et al.^[503] presented a scalable screen printing process to produce stretchable electrochromic displays. Electrochromic PEDOT:PSS inks were screen printed on thermoplastic polyurethane substrate for the manufacturing of stretchable organic electronic devices that retained color contrast with useful switching times at static strains up to 50% and strain cycling up to 30% strain. A double-digit 7-segment ECDs were also produced, which could conform to curved surfaces and be mounted onto stretchable fabrics while remaining fully functional, **Figure 19i–n**.

5.6. Printed Textile Thermoelectrics

Thermoelectric (TE) generators are an excellent candidate for powering wearable electronics and the “Internet of Things,” due to their capability of directly converting heat to electrical energy.^[504,505] Flexible TEs, can directly convert the heat from the human body into useful electricity, providing a promising solution for uninterrupted power to wearables.^[506] Sun et al.^[507] wrapped alternately doped CNT fibers with acrylic fibers and woven into π -type thermoelectric modules. Printing techniques offer a scalable approach to fabricating TE devices on flexible substrates, especially textiles for power generation. For example, Kim et al.^[508] prepared p-type Sb_2Te_3 TE thick films and n-type

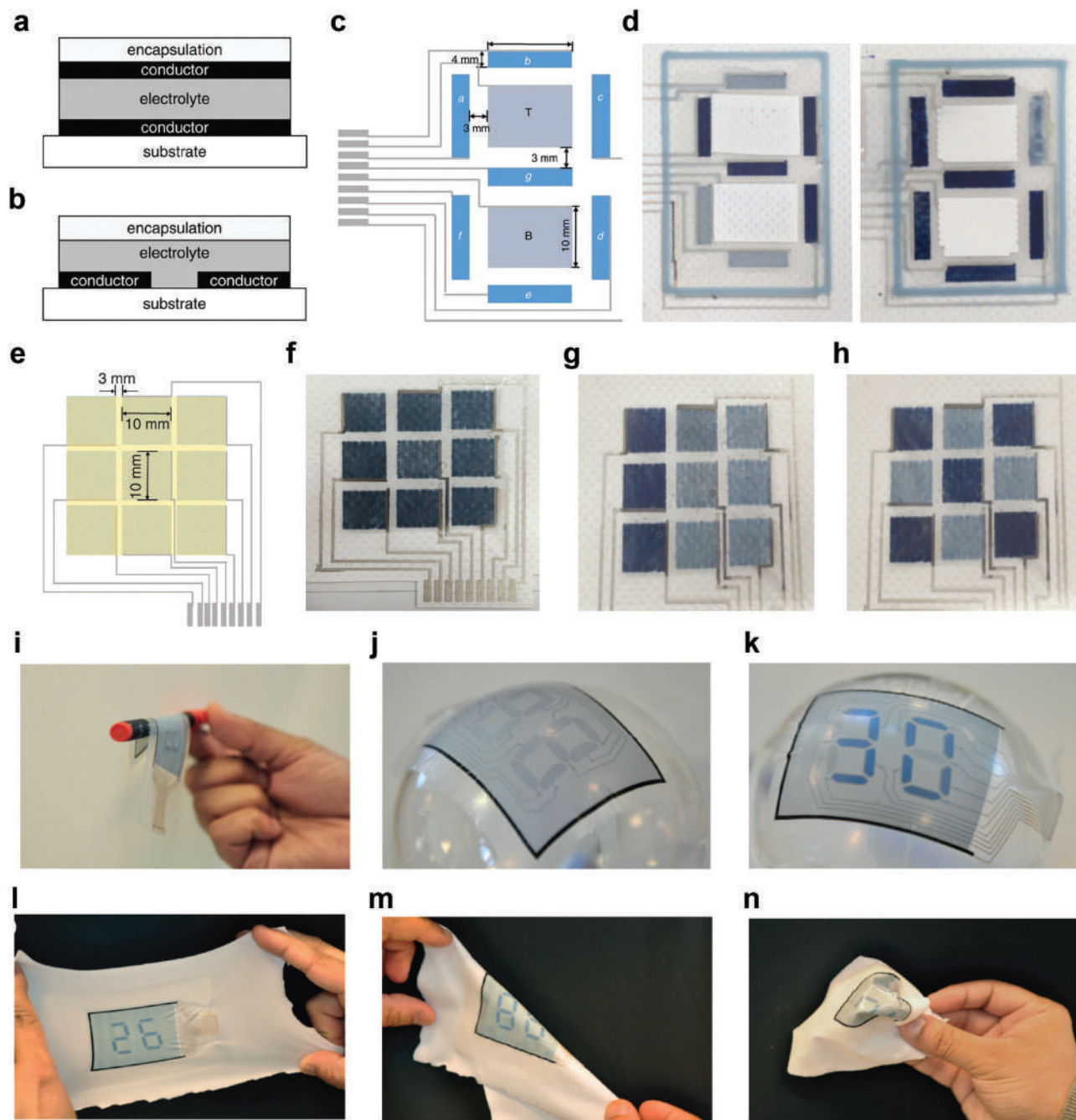


Figure 19. Printed textile electrochromic devices, a) Vertical b) Lateral arrangement. c) Cross-section of seven segment EC display d) Photographs of numbers displayed on EC display- Four and Six, e) Design layout and f) Printed sample of 3×3 matrix display g and h) Examples of EC display with pixels activated Each pixel was able to change between pale blue and dark blue ≈ 5 s. Reproduced with permission.^[502] Copyright 2020, The Institution of Engineering and Technology. Double 7-segment display capable of showing any two-digit number, i) The display has a thin, light, flexible form factor j) A display conforming to a round surface, due to its stretchability, is shown in the off-state, and k) In the on-state as the number '30' l) Functional display attached to elastic textile following the deformation of the fabric upon stretching m) Folding and n) Crumpling. Reproduced with permission.^[503] Copyright 2021, The Author(s).

Bi_2Te_3 TE thick films on glass fiber fabric by screen printing. The thermoelectric conversion factor and ZT values of printed films were ≈ 0.3 at room temperature. Copper foils were printed to interconnect the p-type and n-type TE thick films via a Ni peel-off method to construct the TE generator device. Shin et al.,^[509] also

reported a scalable screen printing of thermoelectric layers on flexible glass fiber fabrics. With high electrical conductivity and low thermal conductivity, the screen-printed TE layers showed high room-temperature ZT values of 0.65 and 0.81 for p-type and n-type, respectively. Assembling thermoelectric modules into the

fabric to harvest energy from body heat could one-day power multitudinous wearable electronics. However, the bottleneck of the printed TE devices still lies in the low performance of the printed TE materials.^[509]

5.7. Printed Textile Optoelectronics

Optoelectronics concerns the study and application of electronic devices that source, detect, and control light. Optoelectronic devices consist of different semiconductor alloys lying on substrates. During the growth of the multi-quantum well of a laser-active region, different layers of semiconductors are sequentially deposited onto the substrate, alternating between well and barrier regions. In well regions, electrons and holes are recombined to provide the laser light, while barrier regions are important for confining the electrons and holes inside the wells.^[510] Incorporating such optoelectronic devices into textiles can increase fabric capabilities and functions, such as fabric-based communications or physiological monitoring.^[511] Most of the reported textile-based optoelectronics are based on embedding multi-material fibers into textiles. The ability to integrate complex electronic and optoelectronic functionalities within soft and thin fibers is one of today's key advanced manufacturing challenges. Multifunctional and connected fiber devices thus will be at the heart of the development of smart textiles and wearable devices.^[512] High-speed fiber LED transmitters and photodetectors present an opportunity for high-bandwidth inter-fiber communication links. Rein et al.,^[511] demonstrated a scalable thermal drawing process of electrically connected diode fibers to construct a macroscopic preform that hosts discrete diodes. Conducting copper or tungsten wires were fed into its inner structure. As the preform is heated and drawn into a fiber, the conducting wires approach the diodes until they make electrical contact, resulting in hundreds of diodes connected in parallel inside a single fiber. They realized two types of in-fiber devices; light-emitting and photodetecting p-i-n diodes. They further embedded these fibers into a fabric. es. Finally, heart-rate measurements with the diodes indicated their potential for implementation in all-fabric physiological-status monitoring systems. However, to the best of our knowledge, printing technology is not yet employed to realize any textile optoelectronics.

6. Conclusion and Perspective

The rapid advancement of the Internet of Things has put people in need of intelligent and controllable multifunctional electronic devices to be utilized in fulfilling different requirements in real life. We expect that textile-based printed flexible and wearable electronics will lead to a revolution in energy and healthcare. In the recent past, they have already gained huge attention due to their softness, breathability, biocompatibility, and durability.^[513,514] Acumen Research and Consulting says the global e-textiles and smart clothing market size is estimated to grow a CAGR above 32.3% over time and reach a market value of \approx US\$15 Bn by 2028.^[515] On the other hand, Printed electronics market was estimated by Transparency Market Research, they reported the global printed electronics market was valued at US\$

12.25 Bn in 2021 and is estimated to advance at a CAGR of 14.2% from 2022 to 2031 to an expected reach of US\$ 45.08 Bn by the end of 2031.^[516] Research and Market estimate the global digital textile printing market of \approx US\$ 2.66 Billion in 2022, with a forecast to grow at a CAGR of 12.1% reaching up to US\$ 6.65 Billion in 2030.^[517] Persistent Market Research expects to attain a value of US\$ 2255.4 Mn for the global market of digital textile printing equipment with growth of a CAGR of 14.9% between 2018 and 2028,^[518] **Figure 20a.**

There are several considerations that need to be addressed before the widescale commercial adoption of wearable electronic textiles. Most of the existing wearable e-textiles can perform only a single functionality, i.e., either as an ECG or temperature or any other sensor; however, a textile that can monitor several health parameters is of special interest for personalized healthcare applications,^[519,520] **Figure 20b.** Future research in textile wearable electronics will be directed to the integration of energy generation, storing and powering the sensors, actuators, electrochromic, shape memory, and even self-repair functionality within the same clothing.^[521] Integration of several electronic components in a multifunctional e-textile is also considered challenging. However, the traditional cut-and-sew method is the simplest method to integrate all the fabric-based electronic devices into final textile products. Adhesive bonding, ultrasonic welding, and laser welding are other joining methods able to eliminate bulky stitched seams and bring less damage to the electronic components within the devices.^[522]

Another consideration of wearable e-textiles is flexibility. The textile substrate is naturally flexible, however, the flexibility of the electrode material to construct the electronic components is the prime concern. Enhancing the electrical performance often requires the deposition of additional conductive material which results in a more rigid platform. Therefore, further exploration in materials or design aspects is still needed, which could possess ultra-flexibility while still keeping ultra-high electrical performances. Washability is often seen as one of the main obstacles to reaching a wider market of e-textile products. Most of the experimental designs lack this criterion hindering the scope of any lab-based device to be used commercially, **Figure 20b.** To assess, improve, and evaluate the extent of e-textiles in terms of washing, repeated test cycles are executed. So far, there are no standardized methods for testing the wash fastness of e-textiles and no protocols to comparably assess the washability of tested products.^[523] Washing e-textiles is challenging; the effect of washing on the performance relies not only on the type of conductive materials or fabrication process but also on the specific textile substrate used (i.e., materials and constructions) along with their interdependency. As such, no global conclusion can be drawn on how a washing program for smart e-textiles should be configured. Considering textile substrates, the applicability and suitability of different textiles depend on the type of conductive track used while looking to achieve the best washability results. On the other hand, if the choice of textile for a smart textile application is fixed due to specific requirements (such as sufficient elasticity for sports clothing, etc.), the type of conductive track used needs to be adapted accordingly for best reliable results.^[149] A fully integrated multifunctional clothing system might be connected with a cloud system which would facilitate the remote monitoring of health parameters for any patient, elderly, or childcare, **Figure 20b.**

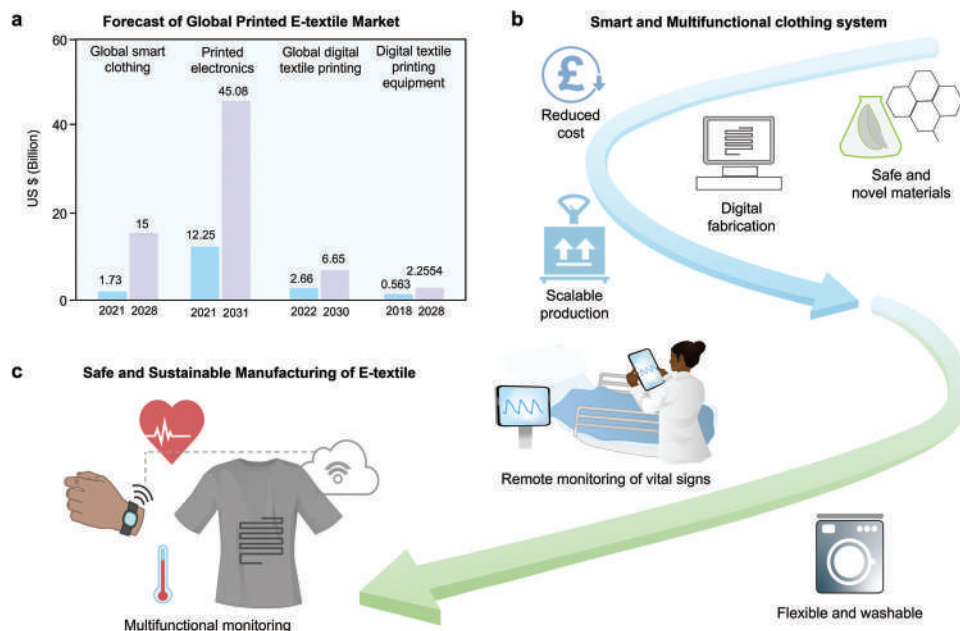


Figure 20. Future prospects and research direction of printed e-textiles. a. Forecast of global printed e-textiles market b. Smart and multifunctional clothing system and c. Safe and sustainable manufacturing of e-textiles.

The most important criterion for the fabrication of textile-based wearable electronics is safety. The primary utilization of such devices is aimed at human health management; therefore, the final device must be safe for the human body as well as for the environment during disposal. Concerns should always be prioritized to find safer and environmentally friendly substitutes than the existing toxic, environmentally unfriendly, and non-bio-compatible materials, Figure 20c.

With the increased attention toward the use of more and more clean energy, the consumer culture around the world has also raised the need for all products to be more sustainable and recyclable to reduce the environmental impact.^[524] This is valid for the wearable electronics industry too.^[525,526] Therefore, the need to explore safe and sustainable manufacturing of electronic devices is an imperative concern of the world today. New eco-friendly, as well as cost-efficient electronic systems, have to be developed, in view of the requirements of emerging ecological concerns and modern society.^[527] Digital fabrication, i.e., inkjet printing is a promising sustainable solution to reduce the material waste and environmental effects of the conventional printing systems, Figure 20c. There are still some limitations in different aspects of inkjet printing including printing speed, cost-benefit issues, printed film uniformity, and fluids' jet-ability as ink—overcoming which would be the future prospect of this leading technology.^[190]

Another very important consideration for the commercial adoption of the wearable electronics industry is the improvement of performance along with the reduction of production costs. For the fabrication of electronic components, replacing an existing material with a new low-cost raw material, such as natural mineral resources could be an attractive option. The combination of low-price raw materials with high-price raw materials without

compromising the performance could be another approach to reduce the overall cost,^[137] Figure 20c.

The textile electrodes to be integrated into the full garment must be scalable for industrial manufacturing. Most of the existing reports on wearable e-textiles are laboratory-based, and addressing all these issues might direct the e-textile industry into large-scale adaptation of e-textiles, Figure 20c. We assume the development of wearable e-textiles will be more rapid and far-reaching with the popularity of new and smart wearable devices.^[528]

Acknowledgements

The authors gratefully acknowledge funding from the UWE partnership PhD award, and UKRI Research England The Expanding Excellence in England (E3) grant. KSN was supported by the Ministry of Education, Singapore, under its Research Centre of Excellence award to the Institute for Functional Intelligent Materials (I-FIM, project No. EDUNC-33-18-279-V12) and by the Royal Society (UK, grant number RSRP\R\190000). J.C. acknowledges the Henry Samueli School of Engineering and Applied Science and the Department of Bioengineering at the University of California, Los Angeles for the startup support. The authors also thank Laura Wescott and Natalie Corner for their professional support with the graphics for this paper.

Conflict of Interest

The authors declare no conflict of interest.

Keywords

E-textiles, printing, wearables, personalized healthcare

Received: June 22, 2023
Revised: September 11, 2023
Published online:

- [1] Y. Niu, H. Liu, R. He, Z. Li, H. Ren, B. Gao, H. Guo, G. M. Genin, F. Xu, *Mater. Today* **2020**, *41*, 219.
- [2] A. Libanori, G. Chen, X. Zhao, Y. Zhou, J. Chen, *Nat. Electron.* **2022**, *5*, 142.
- [3] G. Chen, X. Xiao, X. Zhao, T. Tat, M. Bick, J. Chen, *Chem. Rev.* **2022**, *122*, 3259.
- [4] H. Shen, T. Liu, D. Qin, X. Bo, L. Wang, F. Wang, Q. Yuan, T. Wagberg, G. Hu, M. Zhou, in *Industrial Applications of Carbon Nanotubes* (Eds: H. Peng, Q. Li, T. Chen), Elsevier, Boston **2017**.
- [5] G. Chen, Y. Fang, X. Zhao, T. Tat, J. Chen, *Nat. Electron.* **2021**, *4*, 175.
- [6] F. K. Ko, A. El-Aufy, H. Lam, A. G. Macdiarmid, in *Wearable Electronics and Photonics* (Ed: X. Tao), Woodhead Publishing, Cambridge **2005**.
- [7] D. C. Jones, in *Textile-Led Design for the Active Ageing Population* (Eds: J. McCann, D. Bryson), Woodhead Publishing, xx xx **2015**.
- [8] L. Lu, J. Zhang, Y. Xie, F. Gao, S. Xu, X. Wu, Z. Ye, *JMIR Mhealth. Uhealth.* **2020**, *8*, e18907.
- [9] G. Chen, Y. Li, M. Bick, J. Chen, *Chem. Rev.* **2020**, *120*, 3668.
- [10] Y. Zhang, H. Wang, H. Lu, S. Li, Y. Zhang, *iScience* **2021**, *24*, 102716.
- [11] J. Chen, Y. Huang, N. Zhang, H. Zou, R. Liu, C. Tao, X. Fan, Z. L. Wang, *Nat. Energy* **2016**, *1*, 16138.
- [12] Y. Su, C. Chen, H. Pan, Y. Yang, G. Chen, X. Zhao, W. Li, Q. Gong, G. Xie, Y. Zhou, S. Zhang, H. Tai, Y. Jiang, J. Chen, *Adv. Funct. Mater.* **2021**, *31*, 2010962.
- [13] Z. Zhou, S. Padgett, Z. Cai, G. Conta, Y. Wu, Q. He, S. Zhang, C. Sun, J. Liu, E. Fan, K. Meng, Z. Lin, C. Uy, J. Yang, J. Chen, *Biosens. Bioelectron.* **2020**, *155*, 112064.
- [14] J. C. Yeo, C. T. Lim, in *Wearable Technology in Medicine and Health Care* (Ed: R. K.-Y. Tong), Academic Press, USA **2018**.
- [15] B. Cushman-Roisin, B. T. Cremonini, in *Data, Statistics, and Useful Numbers for Environmental Sustainability* (Eds: B. Cushman-Roisin, B. T. Cremonini), Elsevier, Amsterdam **2021**.
- [16] G. Chen, C. Au, J. Chen, *Trends Biotechnol.* **2021**, *39*, 1078.
- [17] J. Lama, A. Yau, G. Chen, A. Sivakumar, X. Zhao, J. Chen, *J. Mater. Chem. A* **2021**, *9*, 19149.
- [18] S. Shen, X. Xiao, X. Xiao, J. Chen, *Chem. Commun.* **2021**, *57*, 5871.
- [19] S. K. Vashist, J. H. T. Luong, in *Wearable Technology in Medicine and Health Care* (Ed: R. K.-Y. Tong), Academic Press, USA **2018**.
- [20] Y. Gu, T. Zhang, H. Chen, F. Wang, Y. Pu, C. Gao, S. Li, *Nanoscale Res. Lett.* **2019**, *14*, 263.
- [21] Y. Fang, Y. Zou, J. Xu, G. Chen, Y. Zhou, W. Deng, X. Zhao, M. Roustaei, T. K. Hsiai, J. Chen, *Adv. Mater.* **2021**, *33*, 2104178.
- [22] J. Kastner, T. Faury, H. M. Außerhuber, T. Obermüller, H. Leichtfried, M. J. Haslinger, E. Liftinger, J. Innerlohinger, I. Gnatiuk, D. Holzinger, T. Lederer, *Microelectron. Eng.* **2017**, *176*, 84.
- [23] B. A. Kuzubaşoğlu, M. Tekçin, S. K. Bahadır, in *Encyclopedia of Sensors and Biosensors*, 1st Ed. (Ed: R. Narayan), Elsevier, Oxford **2023**.
- [24] Y. E. Elmogahzy, in *Engineering Textiles*, 2nd Ed. (Ed: Y. E. Elmogahzy), Woodhead Publishing, xx xx **2020**.
- [25] F. Cesano, M. J. Uddin, K. Lozano, M. Zanetti, D. Scarano, *Frontiers in Materials* **2020**, *7*.
- [26] T. Lin, Y. Q. Zhang, L. Zhang, F. Klappenberger, in *Encyclopedia of Interfacial Chemistry* (Ed: K. Wandelt), Elsevier, Oxford **2018**.
- [27] A. G. Pandolfo, A. F. Hollenkamp, *J. Power Sources* **2006**, *157*, 11.
- [28] C. Liao, Y. Li, S. C. Tjong, *Int. J. Mol. Sci.* **2018**, *19*.
- [29] S. Mallakpour, S. Rashidmoghadam, in *Composite Nanoabsorbents* (Eds: G. Z. Kyzas, A. C. Mitropoulos), Elsevier, Amsterdam **2019**.
- [30] Z. Lu, R. Raad, F. Safaei, J. Xi, Z. Liu, J. Foroughi, *Frontiers in Materials* **2019**, *6*.
- [31] R. B. Rakhi, in *Nanocarbon and its Composites* (Eds: A. Khan, M. Jawaid, D. Inamuddin, A. M. Asiri), Woodhead Publishing, xx xx **2019**.
- [32] D. Talarico, F. Arduini, A. Constantino, M. Del Carlo, D. Compagnone, D. Moscone, G. Palleschi, *Electrochem. Commun.* **2015**, *60*, 78.
- [33] H. Marsh, F. Rodríguez-Reinoso, in *Activated Carbon* (Eds: H. Marsh, F. Rodríguez-Reinoso), Elsevier Science Ltd, Oxford **2006**.
- [34] J. H. Choi, *Sep. Purif. Technol.* **2010**, *70*, 362.
- [35] W. Gu, G. Yushin, *WIREs Ener. Environ.* **2014**, *3*, 424.
- [36] P. Sinha, S. Banerjee, K. K. Kar, in *Handbook of Nanocomposite Supercapacitor Materials II: Performance* (Ed: K. K. Kar), Springer International Publishing, Cham **2020**.
- [37] M. A. Mutalib, N. M. Rashid, F. Aziz, in *Carbon-Based Polymer Nanocomposites for Environmental and Energy Applications* (Eds: A. F. Ismail, P. S. Goh), Elsevier, Amsterdam **2018**.
- [38] S. Afroj, L. Britnell, T. Hasan, D. V. Andreeva, K. S. Novoselov, N. Karim, *Adv. Funct. Mater.* **2021**, *31*, 2107407.
- [39] S. Bhattacharjee, R. Joshi, A. A. Chughtai, C. R. Macintyre, *Adv. Mater. Interfaces* **2019**, *6*, 1900622.
- [40] N. Karim, S. Afroj, S. Tan, P. He, A. Fernando, C. Carr, K. S. Novoselov, *ACS Nano* **2017**, *11*, 12266.
- [41] M. H. Islam, S. Afroj, M. A. Uddin, D. V. Andreeva, K. S. Novoselov, N. Karim, *Adv. Funct. Mater.* **2022**, *32*, 2205723.
- [42] R. Kumar, S. Sahoo, E. Joanni, R. K. Singh, R. M. Yadav, R. K. Verma, D. P. Singh, W. K. Tan, A. Pérez del Pino, S. A. Moshkalev, A. Matsuda, *Nano Res.* **2019**, *12*, 2655.
- [43] D. G. Papageorgiou, I. A. Kinloch, R. J. Young, *Carbon* **2015**, *95*, 460.
- [44] A. Ciesielski, P. Samorì, *Chem. Soc. Rev.* **2014**, *43*, 381.
- [45] N. Karim, M. Zhang, S. Afroj, V. Koncherry, P. Potluri, K. S. Novoselov, *RSC Adv.* **2018**, *8*, 16815.
- [46] M. Chakraborty, M. S. J. Hashmi, in *Reference Module in Materials Science and Materials Engineering*, Elsevier, Amsterdam, **2018**.
- [47] S. Banerjee, J. H. Lee, T. Kula, N. H. Kim, in *Fillers and Reinforcements for Advanced Nanocomposites* (Eds: Y. Dong, R. Umer, A. K. T. Lau), Woodhead Publishing, Cambridge **2015**.
- [48] S. Bhattacharjee, C. R. Macintyre, P. Bahl, U. Kumar, X. Wen, K. F. Aguey-Zinsou, A. A. Chughtai, R. Joshi, *Adv. Mater. Interfaces* **2020**, *7*, 2000814.
- [49] N. Karim, S. Afroj, D. Leech, A. M. Abdelkader, in *Oxide Electronics* (Ed: A. Ray), John Wiley & Sons, Ltd., Hoboken **2021**.
- [50] S. Afroj, N. Karim, Z. Wang, S. Tan, P. He, M. Holwill, D. Ghazaryan, A. Fernando, K. S. Novoselov, *ACS Nano* **2019**, *13*, 3847.
- [51] M. H. Islam, S. Afroj, N. Karim, *Global Challng.* **2023**, *7*, 2300111.
- [52] F. Sarker, P. Potluri, S. Afroj, V. Koncherry, K. S. Novoselov, N. Karim, *ACS Appl. Mater. Interfaces* **2019**, *11*, 21166.
- [53] R. Kecili, C. M. Hussain, in *Nanomaterials in Chromatography* (Ed: C. M. Hussain), Elsevier, Amsterdam **2018**.
- [54] P. Vandezande, in *Pervaporation, Vapour Permeation, and Membrane Distillation* (Eds: A. Basile, A. Figoli, M. Khayet), Woodhead Publishing, Oxford **2015**.
- [55] F. Sarker, N. Karim, S. Afroj, V. Koncherry, K. S. Novoselov, P. Potluri, *ACS Appl. Mater. Interfaces* **2018**, *10*, 34502.
- [56] M. Inagaki, F. Kang, in *Materials Science and Engineering of Carbon: Fundamentals*, 2nd Ed. (Eds: M. Inagaki, F. Kang), Butterworth-Heinemann, Oxford **2014**.
- [57] R. S. Kalash, V. K. Lakshmanan, C. S. Cho, I. K. Park, in *Biomaterials Nanoarchitectonics* (Ed: M. Ebara), William Andrew Publishing, Cambridge **2016**.
- [58] K. Radhapyari, S. Datta, S. Dutta, N. Jadon, R. Khan, in *Two-Dimensional Nanostructures for Biomedical Technology* (Eds: R. Khan, S. Barua), Elsevier, Amsterdam **2020**.

- [59] V. B. Mohan, R. Brown, K. Jayaraman, D. Bhattacharyya, *Mater. Sci. Eng., B* **2015**, *193*, 49.
- [60] N. Karim, F. Sarker, S. Afroj, M. Zhang, P. Potluri, K. S. Novoselov, *Adv. Sustainable Syst.* **2021**, *5*, 2000228.
- [61] R. Bayan, N. Karak, in *Two-Dimensional Nanostructures for Biomedical Technology* (Eds: R. Khan, S. Barua), Elsevier, Amsterdam **2020**.
- [62] M. H. Islam, M. R. Islam, M. Dulal, S. Afroj, N. Karim, *iScience* **2021**, *25*, 103597.
- [63] J. Phiri, P. Gane, T. C. Maloney, *Mater. Sci. Eng., B* **2017**, *215*, 9.
- [64] L. N. Jin, F. Shao, C. Jin, J. N. Zhang, P. Liu, M. X. Guo, S. W. Bian, *Electrochim. Acta* **2017**, *249*, 387.
- [65] M. Rapisarda, A. Damasco, G. Abbate, M. Meo, A. C. S. Omega **2020**, *5*, 32426.
- [66] I. Shown, A. Ganguly, L. C. Chen, K. H. Chen, *Energy Science & Engineering* **2015**, *3*, 2.
- [67] S. Bhandari, in *Polyaniline Blends, Composites, and Nanocomposites* (Eds: P. M. Visakh, C. D. Pina, E. Falletta), Elsevier, Amsterdam **2018**.
- [68] H. Wang, J. Lin, Z. X. Shen, *J. Sci.: Adv. Mater. Dev.* **2016**, *1*, 225.
- [69] Y. Y. Horng, Y. C. Lu, Y. K. Hsu, C. C. Chen, L. C. Chen, K. H. Chen, *J. Power Sources* **2010**, *195*, 4418.
- [70] Z. Li, L. Gong, *Materials* **2020**, *13*, 548.
- [71] J. Parayangattil Jyothibas, M. Z. Chen, R. H. Lee, *ACS Omega* **2020**, *5*, 6441.
- [72] P. Xue, X. M. Tao, K. W. Y. Kwok, M. Y. Leung, T. X. Yu, *Text. Res. J.* **2004**, *74*, 929.
- [73] A. Harlin, M. Ferenets, in *Intelligent Textiles and Clothing* (Ed: H. R. Mattila), Woodhead Publishing, Cambridge **2006**.
- [74] Y. Huang, H. Li, Z. Wang, M. Zhu, Z. Pei, Q. Xue, Y. Huang, C. Zhi, *Nano Energy* **2016**, *22*, 422.
- [75] Y. He, X. Ning, L. Wan, *Polym. Bull.* **2021**, *79*, 9075.
- [76] S. Nie, Z. Li, Y. Yao, Y. Jin, *Front. in Chem.* **2021**, *9*, 803509.
- [77] V. Koncar, in *Smart Textiles for In Situ Monitoring of Composites* (Ed: V. Koncar), Woodhead Publishing, Cambridge **2019**.
- [78] Z. Zhao, G. F. Richardson, Q. Meng, S. Zhu, H. C. Kuan, J. Ma, *Nanotechnology* **2015**, *27*, 042001.
- [79] B. J. Worfolk, S. C. Andrews, S. Park, J. Reinspach, N. Liu, M. F. Toney, S. C. B. Mannsfeld, Z. Bao, *Proc. Natl. Acad. Sci. USA* **2015**, *112*, 14138.
- [80] L. Manjakkal, A. Pullanchiyodan, N. Yogeswaran, E. S. Hosseini, R. Dahiya, *Adv. Mater.* **2020**, *32*, 1907254.
- [81] Y. Liu, B. Weng, J. M. Razal, Q. Xu, C. Zhao, Y. Hou, S. Seyedin, R. Jalili, G. G. Wallace, J. Chen, *Sci. Rep.* **2015**, *5*, 17045.
- [82] S. K. Sinha, Y. Noh, N. Reljin, G. M. Treich, S. Hajeb-Mohammadalipour, Y. Guo, K. H. Chon, G. A. Sotzing, *ACS Appl. Mater. Interfaces* **2017**, *9*, 37524.
- [83] A. Ankhili, X. Tao, C. Cochrane, V. Koncar, D. Coulon, J. M. Tarlet, *Sensors* **2018**, *18*, 3890.
- [84] G. Liu, X. Chen, J. Liu, C. Liu, J. Xu, Q. Jiang, Y. Jia, F. Jiang, X. Duan, P. Liu, *Electrochim. Acta* **2021**, *365*, 137363.
- [85] S. Khasim, A. Pasha, N. Badi, M. Lakshmi, Y. K. Mishra, *RSC Adv.* **2020**, *10*, 10526.
- [86] A. Boumegnane, A. Nadi, O. Cherkaoui, M. Tahiri, *Mater. Tod.* **2022**, *58*, 1235.
- [87] N. Ibrahim, J. O. Akindoyo, M. Mariatti, *J. Sci. Adv. Mater. Devices* **2022**, *7*, 100395.
- [88] S. C. Sekhar, G. Nagaraju, J. S. Yu, *Nano Energy* **2017**, *36*, 58.
- [89] I. J. Fernandes, A. F. Aroche, A. Schuck, P. Lamberty, C. R. Peter, W. Hasenkamp, T. L. A. C. Rocha, *Sci. Rep.* **2020**, *10*, 8878.
- [90] C. N. Chen, T. Y. Dong, T. C. Chang, M. C. Chen, H. L. Tsai, W. S. Hwang, *J. Mater. Chem. C* **2013**, *1*, 5161.
- [91] J. Olkkonen, J. Leppäniemi, T. Mattila, K. Eiroma, *J. Mater. Chem. C* **2014**, *2*, 3577.
- [92] K. S. Bhat, R. Ahmad, Y. Wang, Y. B. Hahn, *J. Mater. Chem. C* **2016**, *4*, 8522.
- [93] J. Perelaer, B. J. de Gans, U. S. Schubert, *Adv. Mater.* **2006**, *18*, 2101.
- [94] C. K. Kim, G. J. Lee, M. K. Lee, C. K. Rhee, *Powder Technol.* **2014**, *263*, 1.
- [95] X. Xia, C. Xie, S. Cai, Z. Yang, X. Yang, *Corros. Sci.* **2006**, *48*, 3924.
- [96] W. Li, Q. Sun, L. Li, J. Jiu, X. Y. Liu, M. Kanehara, T. Minari, K. Suganuma, *Appl. Mater. Today* **2020**, *18*, 100451.
- [97] H. Lu, M. Lei, C. Zhao, Y. Yao, J. Gou, D. Hui, Y. Q. Fu, *Composites, Part B* **2015**, *80*, 37.
- [98] L. Zhou, C. Li, X. Liu, Y. Zhu, Y. Wu, T. van Ree, in *Metal Oxides in Energy Technologies* (Ed: Y. Wu), Elsevier, Amsterdam **2018**.
- [99] C. Chukwuneke, J. O. Madu, F. V. Adams, O. T. Johnson, in *Nanostructured Metal-Oxide Electrode Materials for Water Purification: Fabrication, Electrochemistry and Applications* (Eds: O. M. Ama, S. S. Ray), Springer International Publishing, Cham **2020**.
- [100] D. Majumdar, T. Maiyalagan, Z. Jiang, *ChemElectroChem* **2019**, *6*, 4343.
- [101] H. Xia, Y. Shirley Meng, G. Yuan, C. Cui, L. Lu, *Electrochem. Solid-State Lett.* **2012**, *15*, A60.
- [102] V. Subramanian, S. C. Hall, P. H. Smith, B. Rambabu, *Solid State Ionics* **2004**, *175*, 511.
- [103] K. Nishio, in *Encyclopedia of Electrochemical Power Sources* (Ed: J. Garche), Elsevier, Amsterdam **2009**.
- [104] D. D. L. Chung, in *Carbon Composites*, 2nd Ed. (Ed: D. D. L. Chung), Butterworth-Heinemann, London **2017**.
- [105] Y. Chen, X. Li, L. Zhou, Y. W. Mai, H. Huang, in *Multifunctionality of Polymer Composites* (Eds: K. Friedrich, U. Breuer), William Andrew Publishing, Oxford **2015**.
- [106] J. Cai, D. Zhang, W. P. Ding, Z. Z. Zhu, G. Z. Wang, J. R. He, H. B. Wang, P. Fei, T. L. Si, *ACS Omega* **2020**, *5*, 29896.
- [107] A. L. Brisse, P. Stevens, G. Toussaint, O. Crosnier, T. Brousse, *Materials* **2018**, *11*, 1178.
- [108] S. K. Meher, G. R. Rao, *J. Phys. Chem. C* **2011**, *115*, 15646.
- [109] C. Guo, M. Yin, C. Wu, J. Li, C. Sun, C. Jia, T. Li, L. Hou, Y. Wei, *Front. Chem.* **2018**, *6*, 636.
- [110] I. Rabani, J. Yoo, H. S. Kim, D. V. Lam, S. Hussain, K. Karuppasamy, Y. S. Seo, *Nanoscale* **2021**, *13*, 355.
- [111] M. Zhang, D. Yang, J. Li, *Vacuum* **2020**, *178*, 109455.
- [112] G. Zhu, Z. He, J. Chen, J. Zhao, X. Feng, Y. Ma, Q. Fan, L. Wang, W. Huang, *Nanoscale* **2014**, *6*, 1079.
- [113] D. Wu, X. Xie, Y. Zhang, D. Zhang, W. Du, X. Zhang, B. Wang, *Front. Mater.* **2020**, *7*.
- [114] L. Xu, M. Jia, Y. Li, X. Jin, F. Zhang, *Sci. Rep.* **2017**, *7*, 12857.
- [115] S. Ramesh, K. Karuppasamy, H. M. Yadav, J. J. Lee, H. S. Kim, H. S. Kim, J. H. Kim, *Sci. Rep.* **2019**, *9*, 6034.
- [116] H. Jiang, C. Li, T. Sun, J. Ma, *Chem. Commun.* **2012**, *48*, 2606.
- [117] Q. Yun, L. Li, Z. Hu, Q. Lu, B. Chen, H. Zhang, *Adv. Mater.* **2020**, *32*, 1903826.
- [118] S. Tanwar, A. Arya, A. Gaur, A. L. Sharma, *J. Phys.: Condens. Matter* **2021**, *33*, 303002.
- [119] N. Joseph, P. M. Shafi, A. C. Bose, *Energy Fuels* **2020**, *34*, 6558.
- [120] A. Schneemann, R. Dong, F. Schwotzer, H. Zhong, I. Senkovska, X. Feng, S. Kaskel, *Chem. Sci.* **2021**, *12*, 1600.
- [121] D. M. Soares, S. Mukherjee, G. Singh, *Chem. Eur. J.* **2020**, *26*, 6320.
- [122] M. Dulal, M. R. Islam, S. Maiti, M. H. Islam, I. Ali, A. M. Abdelkader, K. S. Novoselov, S. Afroj, N. Karim, *Adv. Funct. Mater.* **2023**, *33*, 2305901.
- [123] M. A. Bissett, I. A. Kinloch, R. A. W. Dryfe, *ACS Appl. Mater. Interfaces* **2015**, *7*, 17388.
- [124] M. Acerce, D. Voiry, M. Chhowalla, *Nat. Nanotechnol.* **2015**, *10*, 313.
- [125] J. Bao, K. Jeppson, M. Edwards, Y. Fu, L. Ye, X. Lu, J. Liu, *Electron. Mater. Lett.* **2016**, *12*, 1.
- [126] K. Zhang, Y. Feng, F. Wang, Z. Yang, J. Wang, *J. Mater. Chem. C* **2017**, *5*, 11992.

- [127] J. Pu, K. Zhang, Z. Wang, C. Li, K. Zhu, Y. Yao, G. Hong, *Adv. Funct. Mater.* **2021**, *31*, 2106315.
- [128] B. Anasori, M. R. Lukatskaya, Y. Gogotsi, *Nat. Rev. Mater.* **2017**, *2*, 16098.
- [129] X. Li, Z. Huang, C. Zhi, *Front. Mater.* **2019**, *6*.
- [130] R. Garg, A. Agarwal, M. Agarwal, *Mater. Res. Express* **2020**, *7*, 022001.
- [131] Y. Sun, D. Chen, Z. Liang, *Mater. Tod. Ener.* **2017**, *5*, 22.
- [132] A. Ahmed, M. M. Hossain, B. Adak, S. Mukhopadhyay, *Chem. Mater.* **2020**, *32*, 10296.
- [133] A. Ahmed, S. Sharma, B. Adak, M. M. Hossain, A. M. LaChance, S. Mukhopadhyay, L. Sun, *InfoMat* **2022**, *4*, e12295.
- [134] Z. Zhang, X. Guo, F. Wen, Q. Shi, T. He, B. Dong, C. Lee, in *Reference Module in Biomedical Sciences*, Elsevier, Amsterdam **2021**.
- [135] X. Zhao, Y. Zhou, J. Xu, G. Chen, Y. Fang, T. Tat, X. Xiao, Y. Song, S. Li, J. Chen, *Nat. Commun.* **2021**, *12*, 6755.
- [136] A. Lund, N. M. van der Velden, N. K. Persson, M. M. Hamed, C. Müller, *Mater. Sci. Eng. R Rep.* **2018**, *126*, 1.
- [137] M. R. Islam, S. Afroj, K. S. Novoselov, N. Karim, *Adv. Sci.* **2022**, *9*, 2203856.
- [138] G. Chen, X. Zhao, S. Andalib, J. Xu, Y. Zhou, T. Tat, K. Lin, J. Chen, *Matter* **2021**, *4*, 3725.
- [139] H. Puliylalil, G. Filipič, U. Cvelbar, in *Non-Thermal Plasma Technology for Polymeric Materials* (Eds: S. Thomas, M. Mozetič, U. Cvelbar, P. Špatenka, P. K. M.), Elsevier, xx xx **2019**.
- [140] C. Baquey, M. C. Durrieu, R. G. Guidoin, in *Fluorine and Health* (Ed: A. Tressaud), Elsevier, Amsterdam **2008**.
- [141] B. E. Rapp, in *Microfluidics: Modelling, Mechanics, and Mathematics* (Ed: B. E. Rapp), Elsevier, Oxford **2017**.
- [142] D. Maddipatla, B. B. Narakathu, M. Atashbar, *Biosensors* **2020**, *10*, 199.
- [143] S. P. Sreenilayam, I. U. Ahad, V. Nicolosi, V. Acinas Garzon, D. Brabazon, *Mater. Today* **2020**, *32*, 147.
- [144] R. Torah, K. Yang, S. P. Beeby, M. J. Tudor, in 88th Textile Institute World Conference, IEEE, Shah Alam, Selangor, Malaysia **2012**.
- [145] W. Liu, M. Wang, L. Xu, W. Zhang, Z. Xing, J. Hu, M. Yu, J. Li, G. Wu, in *Radiation Technology for Advanced Materials* (Eds: G. Wu, M. Zhai, M. Wang), Academic Press, USA **2019**.
- [146] R. Salvado, C. Loss, R. Gonçalves, P. Pinho, *Sensors (Basel)* **2012**, *12*, 15841.
- [147] N. Karim, S. Afroj, A. Malandraki, S. Butterworth, C. Beach, M. Rigout, K. S. Novoselov, A. J. Casson, S. G. Yeates, *J. Mater. Chem. C* **2017**, *5*, 11640.
- [148] A. Chauraya, W. G. Whittow, J. C. Vardaxoglou, Y. Li, R. Torah, K. Yang, S. Beeby, J. Tudor, *IET Microwaves Antennas Propag.* **2013**, *7*, 760.
- [149] S. Rotzler, C. Kallmayer, C. Dils, M. von Krshiwoblozki, U. Bauer, M. Schneider-Ramelow, *J. Textile Inst.* **2020**, *111*, 1766.
- [150] B. Niu, S. Yang, T. Hua, X. Tian, M. Koo, *Nano Res.* **2021**, *14*, 1043.
- [151] M. R. Islam, S. Afroj, C. Beach, M. H. Islam, C. Parraman, A. Abdelkader, A. J. Casson, K. S. Novoselov, N. Karim, *iScience* **2022**, *25*, 103945.
- [152] S. Afroj, S. Tan, A. M. Abdelkader, K. S. Novoselov, N. Karim, *Adv. Funct. Mater.* **2020**, *30*.
- [153] S. H. W. Ossevoort, in *Multidisciplinary Know-How for Smart-Textiles Developers* (Ed: T. Kirstein), Woodhead Publishing, Cambridge **2013**.
- [154] L. Windler, M. Height, B. Nowack, *Environ. Int.* **2013**, *53*, 62.
- [155] W. Y. Wang, J. C. Chiou, J. Yip, K. F. Yung, C. W. Kan, *Coatings* **2020**, *10*, 520.
- [156] Y. Gao, R. Cranston, *Text. Res. J.* **2008**, *78*, 60.
- [157] V. Beedasy, P. J. Smith, *Materials* **2020**, *13*.
- [158] B. W. Blunden, J. W. Birkenshaw, in *The Printing Ink Manual* (Eds: R. H. Leach, C. Armstrong, J. F. Brown, M. J. Mackenzie, L. Randall, H. G. Smith), Springer US, Boston, MA **1988**.
- [159] L. W. C. Miles, *Textile Printing*, Society of Dyers and Colourists, Bradford **2003**.
- [160] X. Tang, K. Wu, X. Qi, H.-j. Kwon, R. Wang, Z. Li, H. Ye, J. Hong, H. H. Choi, H. Kong, N. S. Lee, S. Lim, Y. J. Jeong, S. Kim, *ACS Appl. Nano Mater.* **2022**, *5*, 4801.
- [161] H. R. Shemilt, *Circuit World* **1975**, *1*, 7.
- [162] D. Novaković, N. Kašiković, G. Vlačić, M. Pál, in *Printing on Polymers* (Eds: J. Izdebska, S. Thomas), William Andrew Publishing, Norwich, NY **2016**.
- [163] B. Filipowska, B. Wiśniewski, L. Z. Michalak, *Text. Res. J.* **2018**, *88*, 261.
- [164] C. Gerlach, D. Krumm, M. Illing, J. Lange, O. Kanoun, S. Odenwald, A. Hübler, *IEEE Sens. J.* **2015**, *15*, 3647.
- [165] L. Wu, J. Qian, J. Peng, K. Wang, Z. Liu, T. Ma, Y. Zhou, G. Wang, S. Ye, *J. Mater. Sci.: Mater. Electron.* **2019**, *30*, 9593.
- [166] Y. Komazaki, S. Uemura, *Sens. Actuators, B* **2019**, *297*, 126711.
- [167] T. Kang, C. R. Merritt, E. Grant, B. Pourdeyhimi, H. T. Nagle, *IEEE Trans. Biomed. Eng.* **2008**, *55*, 188.
- [168] H. J. Yoo, J. Yoo, L. Yan, *Annu Int Conf IEEE Eng Med Biol Soc* **2010**, *2010*, 5254.
- [169] J. W. Matiko, Y. Wei, R. Torah, N. Grabham, G. Paul, S. Beeby, J. Tudor, *Smart Mater. Struct.* **2015**, *24*, 125028.
- [170] G. Paul, R. Torah, S. Beeby, J. Tudor, *Sens. Actuators, A* **2014**, *206*, 35.
- [171] S. Myllymaa, P. Lepola, T. Hukkanen, A. Oun, E. Mervaala, J. Toyras, R. Lappalainen, K. Myllymaa, *Annu Int Conf IEEE Eng Med Biol Soc* **2013**, *2013*, 6724.
- [172] K. Jost, D. Stenger, C. R. Perez, J. K. McDonough, K. Lian, Y. Gogotsi, G. Dion, *Energy Environ. Sci.* **2013**, *6*, 2698.
- [173] G. Hu, J. Kang, L. W. T. Ng, X. Zhu, R. C. T. Howe, C. G. Jones, M. C. Hersam, T. Hasan, *Chem. Soc. Rev.* **2018**, *47*, 3265.
- [174] R. Szentgyörgyvölgyi, in *Printing on Polymers* (Eds: J. Izdebska, S. Thomas), William Andrew Publishing, Norwich, NY **2016**.
- [175] B. Roth, R. R. Søndergaard, F. C. Krebs, in *Handbook of Flexible Organic Electronics* (Ed: S. Logothetidis), Woodhead Publishing, Oxford **2015**.
- [176] B. A. Morris, in *The Science and Technology of Flexible Packaging* (Ed: B. A. Morris), William Andrew Publishing, Norwich, NY **2017**.
- [177] P. Bajpai, in *Biermann's Handbook of Pulp and Paper (Third Edition)* (Ed: P. Bajpai), Elsevier, Amsterdam **2018**.
- [178] L. Gonzalez-Macia, A. J. Killard, in *Medical Biosensors for Point of Care (POC) Applications* (Ed: R. J. Narayan), Woodhead Publishing, Cambridge **2017**.
- [179] H. Ujiie, in *Textiles and Fashion* (Ed: R. Sinclair), Woodhead Publishing, Cambridge **2015**.
- [180] A. S. G. Reddy, B. B. Narakathu, M. Z. Atashbar, M. Rebros, E. Rebrosova, B. J. Bazuin, M. K. Joyce, P. D. Fleming, A. Pekarovicova, *Sensor Letters* **2011**, *9*, 869.
- [181] V. S. Turkani, B. B. Narakathu, D. Maddipatla, B. J. Bazuin, M. Z. Atashbar, **2018**.
- [182] R. Mumby, in *Packaging Technology* (Eds: A. Emblem, H. Emblem), Woodhead Publishing, Cambridge **2012**.
- [183] T. Dunn, in *Flexible Packaging* (Ed: T. Dunn), William Andrew Publishing, Norwich, NY **2015**.
- [184] A. Vena, E. Perret, S. Tedjini, in *Chipless RFID based on RF Encoding Particle* (Eds: A. Vena, E. Perret, S. Tedjini), Elsevier, Amsterdam **2016**.
- [185] Z. Żółek-Tryznowska, in *Printing on Polymers* (Eds: J. Izdebska, S. Thomas), William Andrew Publishing, Norwich, NY **2016**.
- [186] J. Izdebska, in *Printing on Polymers* (Eds: J. Izdebska, S. Thomas), William Andrew Publishing, Norwich, NY **2016**.
- [187] C. Cie, in *Ink Jet Textile Printing* (Ed: C. Cie), Woodhead Publishing, Oxford **2015**.

- [188] S. H. Ko, in *Micromanufacturing Engineering and Technology*, 2nd Ed. (Ed: Y. Qin), William Andrew Publishing, Boston **2015**.
- [189] A. Manthiram, X. Zhao, W. Li, in *Functional Materials for Sustainable Energy Applications* (Eds: J. A. Kilner, S. J. Skinner, S. J. C. Irvine, P. P. Edwards), Woodhead Publishing, Oxford **2012**.
- [190] A. Soleimani-Gorgani, in *Printing on Polymers* (Eds: J. Izdebska, S. Thomas), William Andrew Publishing, Norwich, NY **2016**.
- [191] B. S. Cook, B. Tehrani, J. R. Cooper, S. Kim, M. M. Tentzeris, in *Handbook of Flexible Organic Electronics* (Ed: S. Logothetidis), Woodhead Publishing, Oxford **2015**.
- [192] J. Mei, M. Lovell, M. Mickle, S. Heston, **2004**, <https://api.semanticscholar.org/CorpusID:52265982>.
- [193] H. P. Le, *J. Imaging Sci. Technol.* **1998**, *42*, 49.
- [194] R. Daly, T. S. Harrington, G. D. Martin, I. M. Hutchings, *Int. J. Pharm.* **2015**, *494*, 554.
- [195] C. Parraman, in *Colour Design*, 2nd Ed. (Ed: J. Best), Woodhead Publishing, Cambridge **2017**.
- [196] E. Bar-Levav, M. Witman, M. Einat, *Micromachines* **2020**, *11*, 499.
- [197] P. J. Smith, A. Morrin, *J. Mater. Chem.* **2012**, *22*, 10965.
- [198] H. Kobayashi, in *Digital Printing of Textiles* (Ed: H. Ujiie), Woodhead Publishing, Cambridge **2006**.
- [199] A. V. Quintero, M. Camara, G. Mattana, W. Gaschler, P. Chabreck, D. Briand, N. F. de Rooij, *Proc. Eng.* **2015**, *120*, 279.
- [200] S. Khan, S. Ali, A. Khan, A. Bermak, *J. Mater. Sci.: Mater. Electron.* **2021**, *33*, 541.
- [201] Q. J. Liew, A. S. A. Aziz, H. W. Lee, M. W. Lee, H. F. Hawari, M. H. Md Khir, *Engineering Proceedings* **2020**, *2*, 3.
- [202] J. Weremczuk, G. Tarapata, R. Jachowicz, *Proc. Eng.* **2012**, *47*, 1366.
- [203] T. G. La, S. Qiu, D. K. Scott, R. Bakhtiari, J. W. P. Kuziek, K. E. Mathewson, J. Rieger, H. J. Chung, *Adv. Healthcare Mater.* **2018**, *7*, 1801033.
- [204] P. Sundriyal, S. Bhattacharya, *Sci. Rep.* **2020**, *10*, 13259.
- [205] V. C. Malshe, in *Reference Module in Chemistry, Molecular Sciences and Chemical Engineering*, Elsevier, xx xx **2019**.
- [206] A. Pekarovicova, V. Husovska, in *Printing on Polymers* (Eds: J. Izdebska, S. Thomas), William Andrew Publishing, Norwich, NY **2016**.
- [207] J. Li, F. Ye, S. Vaziri, M. Muhammed, M. C. Lemme, M. Östling, *Adv. Mater.* **2013**, *25*, 3985.
- [208] F. Torrisi, T. Hasan, W. Wu, Z. Sun, A. Lombardo, T. S. Kulmala, G. W. Hsieh, S. Jung, F. Bonaccorso, P. J. Paul, D. Chu, A. C. Ferrari, *ACS Nano* **2012**, *6*, 2992.
- [209] T. H. Kim, S. G. Kim, *Safet. Heal. Work* **2011**, *2*, 97.
- [210] D. McManus, S. Vranic, F. Withers, V. Sanchez-Romaguera, M. Macucci, H. Yang, R. Sorrentino, G. Parvez, S. K. Son, G. Iannaccone, K. Kostarelos, G. Fiori, C. Casiraghi, *Nat. Nanotechnol.* **2017**, *12*, 343.
- [211] C. Cie, in *Ink Jet Textile Printing* (Ed: C. Cie), Woodhead Publishing, Cambridge **2015**.
- [212] D. S. Viswanath, T. K. Ghosh, D. H. L. Prasad, N. V. K. Dutt, K. Y. Rani, in *Viscosity of Liquids: Theory, Estimation, Experiment, and Data* (Eds: D. S. Viswanath, T. K. Ghosh, D. H. L. Prasad, N. V. K. Dutt, K. Y. Rani), Springer Netherlands, Dordrecht **2007**.
- [213] J. Wiklund, A. Karakoç, T. Palko, H. Yiğitler, K. Ruttik, R. Jäntti, J. Paltakari, *J. Manuf. Mater. Process.* **2021**, *5*, 89.
- [214] in *Rheology Series*, Vol. 3 (Eds: H. A. Barnes, J. F. Hutton, K. Walters), Elsevier, Amsterdam **1989**.
- [215] J. Izdebska, in *Printing on Polymers* (Eds: J. Izdebska, S. Thomas), William Andrew Publishing, Norwich, NY **2016**.
- [216] C. Aydemir, B. N. Altay, M. Akyol, *Color Res. Appl.* **2021**, *46*, 489.
- [217] A. Tabbernor, in *The Printing Ink Manual* (Eds: R. H. Leach, C. Armstrong, J. F. Brown, M. J. Mackenzie, L. Randall, H. G. Smith), Springer US, Boston, MA **1988**.
- [218] L. M. Amoo, R. L. Fagbenle, in *Applications of Heat, Mass and Fluid Boundary Layers* (Eds: R. O. Fagbenle, O. M. Amoo, S. Aliu, A. Falana), Woodhead Publishing, Cambridge **2020**.
- [219] D. B. Braun, M. R. Rosen, in *Rheology Modifiers Handbook* (Eds: D. B. Braun, M. R. Rosen), William Andrew Publishing, Oxford **1999**.
- [220] R. R. Eley (Ed: J. Koleske), ASTM International, West Conshohocken, PA **2012**.
- [221] Z. Yin, Y. Huang, N. Bu, X. Wang, Y. Xiong, *Chin. Sci. Bull.* **2010**, *55*, 3383.
- [222] Y. Liu, B. Derby, *Phys. Fluids* **2019**, *31*, 032004.
- [223] G. Cummins, M. P. Y. Desmulliez, *Circuit World* **2012**, *38*, 193.
- [224] R. Koivunen, R. Bollström, P. Gane, *AIP Adv.* **2020**, *10*, 055309.
- [225] S. Kim, J. H. Choi, D. K. Sohn, H. S. Ko, *Micromachines* **2022**, *13*, 615.
- [226] D. R. Seshadri, R. T. Li, J. E. Voos, J. R. Rowbottom, C. M. Alfes, C. A. Zorman, C. K. Drummond, *npj Digital Medicine* **2019**, *2*, 71.
- [227] S. Sikarwar, S. S. Satyendra, B. C. Yadav, *Photonic Sensors* **2017**, *7*, 294.
- [228] F. Xu, X. Li, Y. Shi, L. Li, W. Wang, L. He, R. Liu, *Micromachines* **2018**, *9*, 580.
- [229] J. Liu, M. Liu, Y. Bai, J. Zhang, H. Liu, W. Zhu, *Sensors* **2020**, *20*.
- [230] N. Karim, S. Afroj, S. Tan, K. S. Novoselov, S. G. Yeates, *Sci. Rep.* **2019**, *9*, 8035.
- [231] E. Sardini, M. Serpelloni, S. Tonello, *Biosensors* **2020**, *10*.
- [232] A. Abdalla, B. A. Patel, *Curr. Opin. Electrochem.* **2020**, *20*, 78.
- [233] A. Moya, G. Gabriel, R. Villa, F. J. Campo, *Current Opinion in Electrochemistry* **2017**, *3*, 29.
- [234] M. E. Payne, A. Zamarayeva, V. I. Pister, N. A. D. Yamamoto, A. C. Arias, *Sci. Rep.* **2019**, *9*, 13720.
- [235] E. Bihar, S. Wustoni, A. M. Pappa, K. N. Salama, D. Baran, S. Inal, *npj Flexible Electronics* **2018**, *2*, 30.
- [236] D. Gräbner, M. Tintelott, G. Dumstorff, W. Lang, *Proceedings* **2017**, *1*.
- [237] B. Andò, S. Baglio, S. Castorina, R. Crispino, V. Marletta, presented at 2019 IEEE Sensors Appl. Symp. (SAS), IEEE, Sophia Antipolis, France **2019**, 2019.
- [238] Y. F. Wang, T. Sekine, Y. Takeda, J. Hong, A. Yoshida, H. Matsui, D. Kumaki, T. Nishikawa, T. Shiba, T. Sunaga, S. Tokito, *ACS Appl. Mater. Interfaces* **2020**, *12*, 35282.
- [239] M. Maiwald, C. Werner, V. Zoellmer, M. Busse, *Sens. Actuators, A* **2010**, *162*, 198.
- [240] K. C. Honeychurch, J. P. Hart, *TrAC Trends Anal. Chem.* **2003**, *22*, 456.
- [241] G. Shen, *Prog. Nat. Sci.: Mater. Int.* **2021**, *31*, 872.
- [242] A. Hatamie, S. Angizi, S. Kumar, C. M. Pandey, A. Simchi, M. Willander, B. D. Malhotra, *J. Electrochem. Soc.* **2020**, *167*, 037546.
- [243] T. Y. Kim, W. Suh, U. Jeong, *Mater. Sci. Eng. R Rep.* **2021**, *146*, 100640.
- [244] J. Zhu, C. Zhou, M. Zhang, *Soft Science* **2021**, *1*, 3.
- [245] J.-w. Zhang, Y. Zhang, Y.-y. Li, P. Wang, *Polymer Rev.* **2021**, *62*.
- [246] S. Tan, M. R. Islam, H. Li, A. Fernando, S. Afroj, N. Karim, *Adv. Sens. Res.* **2022**, *1*.
- [247] H. Souri, H. Banerjee, A. Jusufi, N. Radacsi, A. A. Stokes, I. Park, M. Sitti, M. Amjadi, *Adv. Intell. Syst.* **2020**, *2*, 2000039.
- [248] Q. Zheng, J.-h. Lee, X. Shen, X. Chen, J. K. Kim, *Mater. Today* **2020**, *36*, 158.
- [249] Y. Huang, X. Fan, S. C. Chen, N. Zhao, *Adv. Funct. Mater.* **2019**, *29*, 1808509.
- [250] N. A. Choudhry, L. Arnold, A. Rasheed, I. A. Khan, L. Wang, *Adv. Eng. Mater.*, *23*, 2100469.
- [251] X. Wang, H. Zhang, L. Dong, X. Han, W. Du, J. Zhai, C. Pan, Z. L. Wang, *Adv. Mater.* **2016**, *28*, 2896.
- [252] J. Liu, L. Gu, N. Cui, Q. Xu, Y. Qin, R. Yang, *Research* **2019**, *2019*, 1091632.
- [253] P. Huang, D. L. Wen, Y. Qiu, M. H. Yang, C. Tu, H. S. Zhong, X. S. Zhang, *Micromachines* **2021**, *12*, 158.
- [254] S. Yao, Y. Zhu, *Nanoscale* **2014**, *6*, 2345.
- [255] S. Rajala, M. Schouten, G. Krijnen, S. Tuukkanen, A. C. S. Omega, **2018**, *3*, 8067.

- [256] C. Zhang, G. Zhou, W. Rao, L. Fan, W. Xu, J. Xu, *Cellulose* **2018**, *25*, 4859.
- [257] Z. Yang, Y. Pang, X.-l. Han, Y. Yang, J. Ling, M. Jian, Y. Zhang, Y. Yang, T. L. Ren, *ACS Nano* **2018**, *12*, 9134.
- [258] V. Correia, C. Caparros, C. Casellas, L. Francesch, J. G. Rocha, S. Lanceros-Mendez, *Smart Mater. Struct.* **2013**, *22*, 105028.
- [259] A. Bessonov, M. Kirikova, S. Haque, I. Gartsev, M. J. A. Bailey, *Sens. Actuators, A* **2014**, *206*, 75.
- [260] Y. Xiao, S. Jiang, Y. Li, W. Zhang, *Smart Mater. Struct.* **2020**, *29*, 045023.
- [261] Y. Wei, S. Chen, F. Li, Y. Lin, Y. Zhang, L. Liu, *ACS Appl. Mater. Interfaces* **2015**, *7*, 14182.
- [262] S. J. Woo, J. H. Kong, D. G. Kim, J. M. Kim, *J. Mater. Chem. C* **2014**, *2*, 4415.
- [263] K. Kim, M. Jung, B. Kim, J. Kim, K. Shin, O. S. Kwon, S. Jeon, *Nano Energy* **2017**, *41*, 301.
- [264] M. Åkerfeldt, A. Lund, P. Walkenström, *Text. Res. J.* **2015**, *85*, 1789.
- [265] S. Jang, J. Y. Choi, E. S. Yoo, D. Y. Lim, J. Y. Lee, J. K. Kim, C. Pang, *Compos. Part B Eng.* **2021**, *210*, 108674.
- [266] T. K. Kang, *Coatings* **2021**, *11*, 51.
- [267] A. V. Alaferdov, R. Savu, T. A. Rackauskas, S. Rackauskas, M. A. Canesqui, D. S. de Lara, G. O. Setti, E. Joanni, G. M. de Trindade, U. B. Lima, A. S. de Souza, S. A. Moshkalev, *Nanotechnology* **2016**, *27*, 375501.
- [268] M. Charara, M. Abshirini, M. C. Saha, M. C. Altan, Y. Liu, *J. Intell. Mater. Syst. Struct.* **2019**, *30*, 1216.
- [269] L. Ma, X. Yu, Y. Yang, Y. Hu, X. Zhang, H. Li, X. Ouyang, P. Zhu, R. Sun, C.-p. Wong, *J. Materiom.* **2020**, *6*, 321.
- [270] M. Farooq, T. Iqbal, P. Vazquez, N. Farid, S. Thampi, W. Wijns, A. Shahzad, *Sensors* **2020**, *20*.
- [271] F. Pizarro, P. Villavicencio, D. Yunge, M. Rodríguez, G. Hermosilla, A. Leiva, *Sensors* **2018**, *18*, 1190.
- [272] T. Li, L. Chen, X. Yang, X. Chen, Z. Zhang, T. Zhao, X. Li, J. Zhang, *J. Mater. Chem. C* **2019**, *7*, 1022.
- [273] J. A. Shirley, S. E. Florence, B. S. Sreeja, G. Padmalaya, S. Radha, *J. Mater. Sci.: Mater. Electron.* **2020**, *31*, 16519.
- [274] J. Wang, J. Jiu, M. Nogi, T. Sugahara, S. Nagao, H. Koga, P. He, K. Sukanuma, *Nanoscale* **2015**, *7*, 2926.
- [275] Z. Zhou, Y. Li, J. Cheng, S. Chen, R. Hu, X. Yan, X. Liao, C. Xu, J. Yu, L. Li, *J. Mater. Chem. C* **2018**, *6*, 13120.
- [276] K. Liu, J. Yu, Y. Li, X. Yan, D. Bai, X. Liao, Z. Zhou, Y. Gao, X. Yang, L. Li, *Adv. Mater. Technol.* **2019**, *4*, 1900475.
- [277] Z. Li, B. Li, B. Chen, J. Zhang, Y. Li, *Nanotechnology* **2021**, *32*, 395503.
- [278] T. W. Cheung, T. Liu, M. Y. Yao, Y. Tao, H. Lin, L. Li, *Text. Res. J.* **2022**, *92*, 1682.
- [279] Y. M. Gu, *J. Phys.: Conf. Ser.* **2021**, *1790*, 012021.
- [280] N. Verma, I. Haji-Abolhassani, S. Ganesh, J. Vera-Aguilera, J. Paludo, R. Heitz, S. N. Markovic, K. Kulig, A. Ghoreyshi, *IEEE J Transl Eng Health Med* **2021**, *9*, 2700407.
- [281] Y. Xiao, S. Jiang, Y. Li, W. Zhang, *Smart Mater. Struct.* **2021**, *30*, 025035.
- [282] P. Lugoda, J. C. Costa, C. Oliveira, L. A. Garcia-Garcia, S. D. Wickramasinghe, A. Pouryazdan, D. Roggen, T. Dias, N. Münzenrieder, *Sensors* **2020**, *20*, 73.
- [283] D. Katerinopoulou, P. Zalar, J. Sweelssen, G. Kiriakidis, C. Rentrop, P. Groen, G. H. Gelinck, J. van den Brand, E. C. P. Smits, *Adv. Electron. Mater.* **2019**, *5*, 1800605.
- [284] C. Bali, A. Brandlmaier, A. Ganster, O. Raab, J. Zapf, A. Hübler, *Mater. Today: Proc.* **2016**, *3*, 739.
- [285] S. Li, D. Liu, N. Tian, Y. Liang, C. Gao, S. Wang, Y. Zhang, *Mater. Today Commun.* **2019**, *20*, 100546.
- [286] B. Arman Kuzubasoglu, S. Kursun Bahadir, *Sens. Actuators, A* **2020**, *315*, 112282.
- [287] T. Yokota, Y. Inoue, Y. Terakawa, J. Reeder, M. Kaltenbrunner, T. Ware, K. Yang, K. Mabuchi, T. Murakawa, M. Sekino, W. Voit, T. Sekitani, T. Someya, *Proc Natl Acad Sci U S A* **2015**, *112*, 14533.
- [288] F. Liao, C. Lu, G. Yao, Z. Yan, M. Gao, T. Pan, Y. Zhang, X. Feng, Y. Lin, *IEEE Electron Device Lett.* **2017**, *38*, 1128.
- [289] A. Aliane, V. Fischer, M. Galliani, L. Tournon, R. Gwoziecki, C. Serbutoviez, I. Chartier, R. Coppard, *Microelectron. J.* **2014**, *45*, 1621.
- [290] Y. Yamamoto, S. Harada, D. Yamamoto, W. Honda, T. Arie, S. Akita, K. Takei, *Sci. Adv.* **2016**, *2*, e1601473.
- [291] D. Yamamoto, S. Nakata, K. Kanao, T. Arie, S. Akita, K. Takei, presented at 2017 IEEE 30th Int. Conf. Micro Electro Mech. Syst. (MEMS), Las Vegas, NV, USA, 22–26 Jan. **2017**, p. 2017.
- [292] A. Moschos, T. Syrovoy, L. Syrova, G. Kaltsas, *Meas. Sci. Technol.* **2017**, *28*, 055105.
- [293] G. Liu, Q. Tan, H. Kou, L. Zhang, J. Wang, W. Lv, H. Dong, J. Xiong, *Sensors* **2018**, *18*, 1400.
- [294] S. Ali, A. Hassan, J. Bae, C. H. Lee, J. Kim, *Langmuir* **2016**, *32*, 11432.
- [295] B. A. Kuzubasoglu, E. Sayar, S. K. Bahadir, *IEEE Sens. J.* **2021**, *21*, 13090.
- [296] T. Vuorinen, J. Niittynen, T. Kankkunen, T. M. Kraft, M. Mäntysalo, *Sci. Rep.* **2016**, *6*, 35289.
- [297] J. Courbat, Y. B. Kim, D. Briand, N. F. d. Rooij, presented at 2011 16th Int. Solid-State Sensors, Actuat. Microsys. Conf., Beijing, China, 5–9 Jun **2011**, 2011.
- [298] J. Zikulnig, C. Hirschl, L. Rauter, M. Krivec, H. Lammer, F. Riemelmoser, A. Roshanghias, *Flexible Printed Electron.* **2019**, *4*, 015008.
- [299] D. Barmpakos, C. Tsamis, G. Kaltsas, *Microelectron. Eng.* **2020**, *225*, 111266.
- [300] M. F. Farooqui, M. A. Karimi, K. N. Salama, A. Shamim, *Adv. Mater. Technol.* **2017**, *2*, 1700051.
- [301] X. Zhao, Y. Long, T. Yang, J. Li, H. Zhu, *ACS Appl. Mater. Interfaces* **2017**, *9*, 30171.
- [302] D. Barmpakos, G. Kaltsas, *Sensors* **2021**, *21*.
- [303] D. Zhang, H. Chang, R. Liu, *J. Electron. Mater.* **2016**, *45*, 4275.
- [304] X. Zhang, V. S. Turkani, S. Hajian, A. K. Bose, D. Maddipatla, A. J. Hanson, B. B. Narakathu, M. Z. Atashbar, presented at 2019 IEEE Int. Flex. Print. Sens. Syst. Conf. (FLEPS), 8–10 July **2019**, 2019.
- [305] H. Y. Ahn, J. G. Kim, M. S. Gong, *Macromol. Res.* **2012**, *20*, 174.
- [306] M. J. Kim, M. S. Gong, *Analyst* **2012**, *137*, 1487.
- [307] D. I. Lim, J. R. Cha, M. S. Gong, *Sens. Actuators, B* **2013**, *183*, 574.
- [308] J. R. McGhee, J. S. Sagu, D. J. Southee, P. S. A. Evans, K. G. U. Wijayantha, *ACS Appl. Electron. Mater.* **2020**, *2*, 3593.
- [309] A. Rivadeneyra, J. F. Salmeron, F. Murru, A. Lapresta-Fernández, N. Rodríguez, L. F. Capitan-Vallvey, D. P. Morales, A. Salinas-Castillo, *Nanomaterials* **2020**, *10*.
- [310] A. S. G. Reddy, B. B. Narakathu, M. Z. Atashbar, M. Rebros, E. Rebrosova, M. K. Joyce, *Proc. Eng.* **2011**, *25*, 120.
- [311] H. Jeong, Y. Noh, D. Lee, *Ceram. Int.* **2019**, *45*, 985.
- [312] X. Zhang, D. Maddipatla, A. K. Bose, S. Hajian, B. B. Narakathu, J. D. Williams, M. F. Mitchell, M. Z. Atashbar, *IEEE Sens. J.* **2020**, *20*, 12592.
- [313] V. S. Turkani, D. Maddipatla, B. B. Narakathu, T. S. Saeed, S. O. Obare, B. J. Bazuin, M. Z. Atashbar, *Nanoscale Adv.* **2019**, *1*, 2311.
- [314] U. Altenberend, F. Molina-Lopez, A. Oprea, D. Briand, N. Bärsan, N. F. De Rooij, U. Weimar, *Sens. Actuators, B* **2013**, *187*, 280.
- [315] S. Ali, A. Hassan, G. Hassan, J. Bae, C. H. Lee, *Carbon* **2016**, *105*, 23.
- [316] R. Zhang, B. Peng, Y. Yuan, *Compos. Sci. Technol.* **2018**, *168*, 118.
- [317] M. U. Khan, G. Hassan, M. Awais, J. Bae, *Sens. Actuators, A* **2020**, *311*, 112072.
- [318] A. Rivadeneyra, J. Fernández-Salmerón, J. Banqueri, J. A. López-Villanueva, L. F. Capitan-Vallvey, A. J. Palma, *Sens. Actuators, B* **2014**, *204*, 552.

- [319] C. Gaspar, J. Olkkonen, S. Passoja, M. Smolander, *Sensors* **2017**, 17.
- [320] F. J. Romero, A. Rivadeneyra, A. Salinas-Castillo, A. Ohata, D. P. Morales, M. Becherer, N. Rodriguez, *Sens. Actuators, B* **2019**, 287, 459.
- [321] S. Aziz, D. E. Chang, Y. H. Doh, C. U. Kang, K. H. Choi, *J. Electron. Mater.* **2015**, 44, 3992.
- [322] P. M. Harrey, B. J. Ramsey, P. S. A. Evans, D. J. Harrison, *Sens. Actuators, B* **2002**, 87, 226.
- [323] K. H. Choi, M. Sajid, S. Aziz, B. S. Yang, *Sens. Actuators, A* **2015**, 228, 40.
- [324] C. Kutzner, R. Lucklum, R. Torah, S. Beeby, J. Tudor, presented at 2013 Transduc. Eurosens. XXVII: The 17th Int. Conf. Solid-State Sens., Actuat. Microsyst., Barcelona, Spain, 16–20 Jun **2013**, 2013.
- [325] M. V. Kulkarni, S. K. Apte, S. D. Naik, J. D. Ambekar, B. B. Kale, *Sens. Actuators, B* **2013**, 178, 140.
- [326] P. Mehrotra, *J Oral Biol Craniofac Res* **2016**, 6, 153.
- [327] P. Fayyaz Shahandashti, H. Pourkheyrollah, A. Jahanshahi, H. Ghafoorifard, *Sens. Actuators, A* **2019**, 295, 678.
- [328] P. Sawangjai, S. Hompoonsup, P. Leelaarporn, S. Kongwudhikunakorn, T. Wilaiprasitporn, *IEEE Sens. J.* **2020**, 20, 3996.
- [329] L. Bonek, S. Fenech, N. Sapoznik, A. J. Hanson, S. Masihi, D. Maddipatla, M. Panahi, M. Z. Atashbar, *IEEE Sensors* **2020**, 1.
- [330] M. Chakraborty, S. Das, *Procedia Technol.* **2012**, 4, 830.
- [331] S. W. Weinschenk, R. D. Beise, J. Lorenz, *Eur J Appl Physiol* **2016**, 116, 1527.
- [332] L. F. Wang, J. Q. Liu, H. L. Peng, B. Yang, H. Y. Zhu, C. S. Yang, *Electron. Lett.* **2013**, 49, 739.
- [333] Y. Yang, Z. Yang, Z. Zhu, J. Wang, *Microelectron. J.* **2017**, 69, 86.
- [334] X. An, G. K. Stylios, *Materials* **2018**, 11, 1887.
- [335] A. T. Satti, J. Park, J. Park, H. Kim, S. Cho, *Sensors (Basel)* **2020**, 20.
- [336] S. Tan, S. Afroj, D. Li, M. R. Islam, J. Wu, G. Cai, N. Karim, Z. Zhao, *iScience* **2023**, 26, 106403.
- [337] S. J. Cho, D. Byun, T. S. Nam, S. Y. Choi, B. G. Lee, M. K. Kim, S. Kim, *J. Healthc. Engin.* **2017**, 2017, 9053764.
- [338] H. L. Peng, J. Q. Liu, H. C. Tian, B. Xu, Y. Z. Dong, B. Yang, X. Chen, C. S. Yang, *Sens. Actuators, A* **2015**, 235, 48.
- [339] A. Paiva, D. Vieira, J. Cunha, H. Carvalho, B. Providência, presented at Innovation, Engineering and Entrepreneurship, Cham, Guimarães, Portugal, **2019**.
- [340] S. Takamatsu, T. Lonjaret, D. Crisp, J. M. Badier, G. G. Malliaras, E. Ismailova, *Sci. Rep.* **2015**, 5, 15003.
- [341] L. Rattfält, F. Björefors, D. Nilsson, X. Wang, P. Norberg, P. Ask, *Biomed. Eng. Online* **2013**, 12, 64.
- [342] G. Paul, R. Torah, S. Beeby, J. Tudor, *Sens. Actuators, A* **2015**, 227, 60.
- [343] M. A. Yokus, J. S. Jur, *IEEE Trans. Biomed. Eng.* **2016**, 63, 423.
- [344] D. Pani, A. Achilli, P. P. Bassareo, L. Cugusi, G. Mercuro, B. Fraboni, A. Bonfiglio, *Comput. Cardiol. Conf. (CinC)* **2016**, 373.
- [345] G. Paul, R. Torah, S. Beeby, J. Tudor, *Smart Mater. Struct.* **2017**, 26, 025029.
- [346] A. Achilli, D. Pani, A. Bonfiglio, presented at 2017 Computing in Cardiology (CinC), Rennes, France, 24–27 Sept. **2017**, p. 2017.
- [347] A. Achilli, A. Bonfiglio, D. Pani, *IEEE Sens. J.* **2018**, 18, 4097.
- [348] P. C. Hsu, C. L. Shen, F.-I. Chen, H. Huang, W. C. Wang, T. H. Huang, 2018 Int. Flexible Electron. Technol. Conf. (IFETC), **2018**, p. 1.
- [349] A. A. Chlaihawi, B. B. Narakathu, S. Emamian, B. J. Bazuin, M. Z. Atashbar, *Sens. Bio-Sens. Res.* **2018**, 20, 9.
- [350] J. V. Lidón-Roger, G. Prats-Boluda, Y. Ye-Lin, J. Garcia-Casado, E. Garcia-Breijo, *Sensors* **2018**, 18, 300.
- [351] X. Xu, M. Luo, P. He, X. Guo, J. Yang, *Appl. Phys. A* **2019**, 125, 714.
- [352] F. Seoane, A. Soroudi, K. Lu, D. Nilsson, M. Nilsson, F. Abtahi, M. Skrifvars, *Sensors* **2019**, 19, 4426.
- [353] A. B. Nigusse, B. Malengier, D. A. Mengistie, G. B. Tseghai, L. Van Langenhove, *Sensors* **2020**, 20, 6233.
- [354] P. Zalar, M. Saalmink, D. Raiteri, J. van den Brand, E. C. P. Smits, *Adv. Eng. Mater.* **2020**, 22, 2000714.
- [355] V. Toral, E. Castillo, A. Albretch, F. J. Romero, A. García, N. Rodríguez, P. Lugli, D. P. Morales, A. Rivadeneyra, *IEEE Access* **2020**, 8, 127789.
- [356] X. Xu, M. Luo, P. He, J. Yang, *J. Phys. D: Appl. Phys.* **2020**, 53, 125402.
- [357] F. Haghdoost, V. Mottaghitlab, A. K. Haghi, *Sensor Rev.* **2015**, 35, 20.
- [358] E. Bihar, T. Roberts, E. Ismailova, M. Saadaoui, M. Isik, A. Sanchez-Sanchez, D. Mecerreyes, T. Hervé, J. B. De Graaf, G. G. Malliaras, *Adv. Mater. Technol.* **2017**, 2, 1600251.
- [359] B. M. Li, I. Kim, Y. Zhou, A. C. Mills, T. J. Flewellin, J. S. Jur, *Adv. Mater. Technol.* **2019**, 4, 1900511.
- [360] A. Bakulin, I. Silvestrov, M. Protasov, *Geophys. Prospecting* **2022**, 70, 629.
- [361] P. Phukpattaranont, presented at SIPA Summit Conf. (APSIPA), 2014 Asia-Pacific, 9–12 Dec. **2014**, 2014.
- [362] M. N. Karim, S. Afroj, M. Rigout, S. G. Yeates, C. Carr, *J. Mater. Sci.* **2015**, 50, 4576.
- [363] A. P. Alves, J. Martins, H. P. d. Silva, A. Lourenço, A. Fred, H. Ferreira, *Physiological Computing Systems*, xx xx, Berlin, Heidelberg **2014**.
- [364] J. C. Batchelor, A. J. Casson, presented at 2015 37th Annual International Conference of the IEEE Engineering in Medicine and Biology Society (EMBC), Milan, Italy, 25–29 Aug **2015**, 2015.
- [365] M. M. R. Momota, B. I. Morshed, presented at 2020 IEEE International Conference on Electro Information Technology (EIT), Chicago, IL, USA, 31 Jul-1 Aug **2020**, 2020.
- [366] M. Rusanen, S. Myllymaa, L. Kalevo, K. Myllymaa, J. Töyräs, T. Leppänen, S. Kainulainen, *IEEE Access* **2021**, 9, 132580.
- [367] M. Rusanen, S. Kainulainen, H. Korkalainen, L. Kalevo, K. Myllymaa, T. Leppänen, J. J. Töyräs, E. S. Arnardottir, S. Myllymaa, *IEEE Access* **2021**, 9, 157902.
- [368] V. V. Nikulin, J. Kegeles, G. Curio, *Clinical Neurophysiology* **2010**, 121, 1007.
- [369] P. Lepola, S. Myllymaa, J. Töyräs, T. Hukkanen, E. Mervaala, S. Määttä, R. Lappalainen, K. Myllymaa, *J. Clin. Monit. Comput.* **2015**, 29, 697.
- [370] M. v. Vugt, in *Rethinking Productivity in Software Engineering* (Eds: C. Sadowski, T. Zimmermann), Apress, Berkeley, CA **2019**.
- [371] G. B. Tseghai, B. Malengier, K. A. Fante, L. V. Langenhove, *Autex Res. J.* **2021**, 21, 63.
- [372] N. V. de Camp, G. Kalinka, J. Bergeler, *Sci. Rep.* **2018**, 8, 14041.
- [373] S. Myllymaa, P. Lepola, J. Töyräs, T. Hukkanen, E. Mervaala, R. Lappalainen, K. Myllymaa, *J. Neurosci. Meth.* **2013**, 215, 103.
- [374] N. A. Alba, R. J. Scلابassi, M. Sun, X. T. Cui, *IEEE Trans. Neural Syst. Rehabil. Eng.* **2010**, 18, 415.
- [375] K. P. Gao, H. J. Yang, X. L. Wang, B. Yang, J. Q. Liu, *Sens. Actuators, A* **2018**, 283, 348.
- [376] J. Löfhede, F. Seoane, M. Thordstein, presented at Proceed. of the 10th IEEE ITAB Conf., Corfu, Greece, 3–5 Nov **2010**, 2010.
- [377] J. Löfhede, F. Seoane, M. Thordstein, *Sensors* **2012**, 12, 16907.
- [378] L. Shu, T. Xu, X. Xu, *IEEE Sens. J.* **2019**, 19, 5995.
- [379] C. T. Lin, L. D. Liao, Y. H. Liu, I. J. Wang, B. S. Lin, J. Y. Chang, *IEEE Trans. Biomed. Eng.* **2011**, 58, 1200.
- [380] N. Muthukumar, G. Thilagavathi, T. Kannaian, *J. Textile Inst.* **2016**, 107, 283.
- [381] M. Natarajan, G. T. Govindarajan, *J. Textile. App., Technol. Manag.* **2014**, 8.
- [382] F. Zeng, P. Siriaraya, D. Choi, N. Kuwahara, *Int. J. Adv. Comp. Sci. Appl.* **2020**, 11, 58.
- [383] Y. Wei, Y. Wu, J. Tudor, *Sens. Actuators, A* **2017**, 263, 614.

- [384] L. Guo, L. Sandsjö, M. Ortiz-Catalan, M. Skrifvars, *Text. Res. J.* **2020**, 90, 227.
- [385] A. Prakash, S. Sharma, N. Sharma, *Biomed. Eng. Lett.* **2019**, 9, 467.
- [386] T. Roland, S. Amsüss, M. F. Russold, C. Wolf, W. Baumgartner, *Proc. Eng.* **2016**, 168, 155.
- [387] M. Rojas-Martínez, M. A. Mañanas, J. F. Alonso, *J. NeuroEng. Rehabil.* **2012**, 9, 85.
- [388] M. Gazzoni, N. Celadon, D. Mastrapasqua, M. Paleari, V. Margaria, P. Ariano, *PLoS One* **2014**, 9, e109943.
- [389] A. Shafti, R. B. R. Manero, A. M. Borg, K. Althoefer, M. J. Howard, *IEEE Trans. Neural Syst. Rehabil. Eng.* **2017**, 25, 1472.
- [390] R. B. Ribas Manero, A. Shafti, B. Michael, J. Grewal, J. L. Ribas Fernandez, K. Althoefer, M. J. Howard, *Annu Int Conf IEEE Eng Med Biol Soc* **2016**, 2016, 6062.
- [391] L. Caldani, M. Pacelli, D. Farina, R. Paradiso, presented at 2010 Ann. Int. Conf. IEEE Engin. Med. Biol., 31 Aug-4 Sept. **2010**, 2010.
- [392] I. G. Trindade, J. Lucas, R. Miguel, P. Alpuim, M. Carvalho, N. M. Garcia, presented at the 12th IEEE Int. Conf. E-Health Network, Appl., Serv., Lyon, France, 1-3 July **2010**, 2010.
- [393] G. Li, Y. Geng, D. Tao, P. Zhou, presented at 2011 Annual Int. Conf. IEEE EMBS, 30 Aug-3 Sept. **2011**, 2011.
- [394] Y. Jiang, M. Togane, B. Lu, H. Yokoi, *Front. Neurosci.* **2017**, 11.
- [395] Y. Jiang, S. Sakoda, M. Togane, S. Morishita, B. Lu, H. Yokoi, presented at 2015 IEEE SENSORS, 1-4 Nov 2015, 2015.
- [396] Y.-l. Jiang, S. Sakoda, M. Togane, S. Morishita, H. Yokoi, Singapore, **2017**.
- [397] S. Rodrigues, R. Miguel, J. Lucas, C. Gaiolas, P. Araújo, N. Reis, presented at BIODVICES, **2009**.
- [398] M. Papaioannidou, S. Takamatsu, S. Rezaei-Mazinani, T. Lonjaret, A. Martin, E. Ismailova, *Adv. Healthcare Mater.* **2016**, 5, 2001.
- [399] C. Pylatiuk, M. Muller-Riederer, A. Kargov, S. Schulz, O. Schill, M. Reischl, G. Bretthauer, presented at 2009 IEEE Int. Conf. Rehab. Robot., Kyoto, Japan, 23-26 June **2009**, 2009.
- [400] K. Eguchi, M. Nambu, K. Ueshima, T. Kuroda, *J. Fiber Sci. Technol.* **2017**, 73, 284.
- [401] O. Tikkanen, M. Hu, T. Vilavuo, P. Tolvanen, S. Cheng, T. Finni, *Physiol. Measur.* **2012**, 33, 603.
- [402] T. Finni, M. Hu, P. Kettunen, T. Vilavuo, S. Cheng, *Physiol. Measur.* **2007**, 28, 1405.
- [403] S. L. Colyer, P. M. McGuigan, *J Sports Sci Med* **2018**, 17, 101.
- [404] A. Mangezi, A. Rosendo, M. Howard, R. Stopforth, presented at 2017 Int. Conf. Rehabil. Robotics (ICORR), London, UK, **2017**.
- [405] E. Lendaro, E. Mastinu, B. Håkansson, M. Ortiz-Catalan, *Front. Neurol.* **2017**, 8.
- [406] S. Brown, M. Ortiz-Catalan, J. Petersson, K. Rödbj, F. Seoane, presented at 2016 38th Ann. Int. Conf. IEEE Engin. Med. Biol. Soc. (EMBC), Orlando, FL, USA, 16-20 Aug, **2016**, 2016.
- [407] A. Paiva, H. Carvalho, A. Catarino, O. Postolache, G. Postolache, presented at 2015 9th Int. Conf. Sensing Technol. (ICST), Auckland, New Zealand, 8-10 Dec 2015, 2015.
- [408] B. Sumner, C. Mancuso, R. Paradiso, presented at 2013 35th Ann. Int. Conf. IEEE Engin. Medic. Biol. Society (EMBC), Osaka, Japan, **2013**.
- [409] D. Court, R. Torah, *Proceedings* **2021**, 68, 8.
- [410] H. Jin, N. Matsuhisa, S. Lee, M. Abbas, T. Yokota, T. Someya, *Adv. Mater.* **2017**, 29, 1605848.
- [411] D. Tao, Z. Haoshi, W. Zhenxing, G. Li, presented at Proceed. of 2012 IEEE-EMBS Int. Conf. Biomed. Health Inf., 5-7 Jan **2012**, 2012.
- [412] G. M. Paul, F. Cao, R. Torah, K. Yang, S. Beeby, J. Tudor, *IEEE Sens. J.* **2014**, 14, 393.
- [413] D. Pani, A. Achilli, A. Spanu, A. Bonfiglio, M. Gazzoni, A. Botter, *IEEE Trans. Neural Syst. Rehabil. Eng.* **2019**, 27, 1370.
- [414] K. A. Ohiri, C. O. Pyles, L. H. Hamilton, M. M. Baker, M. T. McGuire, E. Q. Nguyen, L. E. Osborn, K. M. Rossick, E. G. McDowell, L. M. Strohsnitter, L. J. Currano, *Scientific Reports* **2022**, 12, 9650.
- [415] J. M. Furman, F. L. Wuyts, in *Aminoff's Electrodiagnosis in Clinical Neurology*, 6th Ed. (Ed: M. J. Aminoff), W.B. Saunders, London **2012**.
- [416] B. C. Kung, T. O. Willcox, in *Neurology and Clinical Neuroscience* (Eds: A. H. V. Schapira, E. Byrne, S. DiMauro, R. S. J. Frackowiak, R. T. Johnson, Y. Mizuno, M. A. Samuels, S. D. Silberstein, Z. K. Wszolek), Mosby, Philadelphia **2007**.
- [417] A. J. Golparvar, M. K. Yapici, presented at 2017 IEEE SENSORS, 29 Oct.-1 Nov **2017**, 2017.
- [418] R. Zhong, M. Xu, N. Fu, R. Liu, A. A. Zhou, X. Wang, Z. Yang, *Electrochim. Acta* **2020**, 348, 136209.
- [419] J. Kim, R. Kumar, A. J. Bandodkar, J. Wang, *Adv. Electron. Mater.* **2017**, 3, 1600260.
- [420] J. Li, H. Xie, Y. Li, *J. Power Sources* **2013**, 241, 388.
- [421] K. Karthikeyan, S. Amaresh, K. J. Kim, S. H. Kim, K. Y. Chung, B. W. Cho, Y. S. Lee, *Nanoscale* **2013**, 5, 5958.
- [422] A. S. Ghouri, R. Aslam, M. S. Siddiqui, S. K. Sami, *Front. Mater.* **2020**, 7.
- [423] S. Wang, Z. S. Wu, S. Zheng, F. Zhou, C. Sun, H. M. Cheng, X. Bao, *ACS Nano* **2017**, 11, 4283.
- [424] W. Si, C. Yan, Y. Chen, S. Oswald, L. Han, O. G. Schmidt, *Energy Environ. Sci.* **2013**, 6, 3218.
- [425] G. Yu, L. Hu, M. Vosgueritchian, H. Wang, X. Xie, J. R. McDonough, X. Cui, Y. Cui, Z. Bao, *Nano Lett.* **2011**, 11, 2905.
- [426] C. Wei, Q. Xu, Z. Chen, W. Rao, L. Fan, Y. Yuan, Z. Bai, J. Xu, *Carbohydr. Polym.* **2017**, 169, 50.
- [427] M. R. Islam, S. Afroj, N. Karim, *ACS Nano* **2023**, 17, 18481.
- [428] M. G. Say, R. Brooke, J. Edberg, A. Grimoldi, D. Belaineh, I. Engquist, M. Berggren, *npj Flexible Electronics* **2020**, 4, 14.
- [429] S. Tuukkanen, M. Välimäki, S. Lehtimäki, T. Vuorinen, D. Lupo, *Sci. Rep.* **2016**, 6, 22967.
- [430] M. F. El-Kady, R. B. Kaner, *Nat. Commun.* **2013**, 4, 1475.
- [431] J. Gao, C. Shao, S. Shao, F. Wan, C. Gao, Y. Zhao, L. Jiang, L. Qu, *Small* **2018**, 14, 1801809.
- [432] P. Huang, C. Lethien, S. Pinaud, K. Brousse, R. Laloo, V. Turq, M. Respaud, A. Demortière, B. Daffos, P. L. Taberna, B. Chaudret, Y. Gogotsi, P. Simon, *Science* **2016**, 351, 691.
- [433] T. Göhlert, P. F. Siles, T. Päßler, R. Sommer, S. Baunack, S. Oswald, O. G. Schmidt, *Nano Energy* **2017**, 33, 387.
- [434] J. Keskinen, E. Sivonen, S. Jussila, M. Bergelin, M. Johansson, A. Vaari, M. Smolander, *Electrochim. Acta* **2012**, 85, 302.
- [435] Q. Tu, X. Li, Z. Xiong, H. Wang, J. Fu, L. Chen, *J. Energy Storage* **2022**, 53, 105211.
- [436] Y. Z. Zhang, Y. Wang, T. Cheng, L. Q. Yao, X. Li, W. Y. Lai, W. Huang, *Chem. Soc. Rev.* **2019**, 48, 3229.
- [437] K. Jost, C. R. Perez, J. K. McDonough, V. Presser, M. Heon, G. Dion, Y. Gogotsi, *Energy Environ. Sci.* **2011**, 4, 5060.
- [438] S. F. Zopf, M. Manser, *J. Engin. Fib. Fabr.* **2016**, 11, 155892501601100303.
- [439] H. Zhang, Y. Qiao, Z. Lu, *ACS Appl. Mater. Interfaces* **2016**, 8, 32317.
- [440] F. H. Kuok, C. Y. Liao, C. W. Chen, Y. C. Hao, I. S. Yu, J. Z. Chen, *Mater. Res. Express* **2017**, 4, 115501.
- [441] A. M. Abdelkader, N. Karim, C. Vallés, S. Afroj, K. S. Novoselov, S. G. Yeates, *2D Mater.* **2017**, 4.
- [442] L. Liu, Q. Tian, W. Yao, M. Li, Y. Li, W. Wu, *J. Power Sources* **2018**, 397, 59.
- [443] J. Liang, B. Tian, S. Li, C. Jiang, W. Wu, *Adv. Energy Mater.* **2020**, 10, 2000022.
- [444] Z. Stempien, M. Khalid, M. Kozicki, M. Kozanecki, H. Varela, P. Filipczak, R. Pawlak, E. Korzeniewska, E. Słasiadek, *Synth. Met.* **2019**, 256, 116144.

- [445] X. Li, Y. Zhao, J. Yu, Q. Liu, R. Chen, H. Zhang, D. Song, R. Li, J. Liu, J. Wang, *J. Colloid Interface Sci.* **2019**, *557*, 691.
- [446] Z. Stempien, M. Khalid, M. Kozanecki, P. Filipczak, A. Wrzesińska, E. Korzeniewska, E. Szaśiadek, *Materials* **2021**, *14*, 3577.
- [447] P. Giannakou, R. C. T. Slade, M. Shkunov, *Electrochim. Acta* **2020**, *353*, 136539.
- [448] Z. Li, V. Ruiz, V. Mishukova, Q. Wan, H. Liu, H. Xue, Y. Gao, G. Cao, Y. Li, X. Zhuang, J. Weissenrieder, S. Cheng, J. Li, *Adv. Funct. Mater.* **2022**, *32*, 2108773.
- [449] H. Pang, Y. Zhang, W. Y. Lai, Z. Hu, W. Huang, *Nano Energy* **2015**, *15*, 303.
- [450] S. K. Ujjain, R. Bhatia, P. Ahuja, P. Attri, *PLoS One* **2015**, *10*, e0131475.
- [451] Z. Pei, H. Hu, G. Liang, C. Ye, *Nano-Micro Lett.* **2016**, *9*, 19.
- [452] S. K. Ujjain, P. Ahuja, R. Bhatia, P. Attri, *Mater. Res. Bull.* **2016**, *83*, 167.
- [453] P. Giannakou, M. G. Masteghin, R. C. T. Slade, S. J. Hinder, M. Shkunov, *J. Mater. Chem. A* **2019**, *7*, 21496.
- [454] C. Zhang, L. McKeon, M. P. Kremer, S. H. Park, O. Ronan, A. Seral-Ascaso, S. Barwich, C. Ó. Coileáin, N. McEvoy, H. C. Nerl, B. Anasori, J. N. Coleman, Y. Gogotsi, V. Nicolosi, *Nat. Commun.* **2019**, *10*, 1795.
- [455] J. M. Munuera, J. I. Paredes, M. Enterría, S. Villar-Rodil, A. G. Kelly, Y. Nalawade, J. N. Coleman, T. Rojo, N. Ortiz-Vitoriano, A. Martínez-Alonso, J. M. D. Tascón, *ACS Appl. Mater. Interfaces* **2020**, *12*, 494.
- [456] B. Li, N. Hu, Y. Su, Z. Yang, F. Shao, G. Li, C. Zhang, Y. Zhang, *ACS Appl. Mater. Interfaces* **2019**, *11*, 46044.
- [457] L. Li, E. B. Secor, K. S. Chen, J. Zhu, X. Liu, T. Z. Gao, J.-W. T. Seo, Y. Zhao, M. C. Hersam, *Adv. Energy Mater.* **2016**, *6*, 1600909.
- [458] M. H. Ervin, L. T. Le, W. Y. Lee, *Electrochim. Acta* **2014**, *147*, 610.
- [459] K. H. Choi, J. Yoo, C. K. Lee, S. Y. Lee, *Energy Environ. Sci.* **2016**, *9*, 2812.
- [460] Y. Fang, G. Chen, M. Bick, J. Chen, *Chem. Soc. Rev.* **2021**, *50*, 9357.
- [461] Y. Peng, J. Chen, A. Y. Song, P. B. Catrysse, P. C. Hsu, L. Cai, B. Liu, Y. Zhu, G. Zhou, D. S. Wu, H. R. Lee, S. Fan, Y. Cui, *Nat. Sustain.* **2018**, *1*, 105.
- [462] L. Cai, A. Y. Song, W. Li, P. C. Hsu, D. Lin, P. B. Catrysse, Y. Liu, Y. Peng, J. Chen, H. Wang, J. Xu, A. Yang, S. Fan, Y. Cui, *Adv. Mater.* **2018**, *30*, 1802152.
- [463] L. Cai, A. Y. Song, P. Wu, P. C. Hsu, Y. Peng, J. Chen, C. Liu, P. B. Catrysse, Y. Liu, A. Yang, C. Zhou, C. Zhou, S. Fan, Y. Cui, *Nat. Commun.* **2017**, *8*, 496.
- [464] S. Pu, J. Fu, Y. Liao, L. Ge, Y. Zhou, S. Zhang, S. Zhao, X. Liu, X. Hu, K. Liu, J. Chen, *Adv. Mater.* **2020**, *32*, 1907307.
- [465] S. Pu, Y. Liao, K. Chen, J. Fu, S. Zhang, L. Ge, G. Conta, S. Bouzarif, T. Cheng, X. Hu, K. Liu, J. Chen, *Nano Lett.* **2020**, *20*, 3791.
- [466] Y. Peng, Y. Cui, *Joule* **2020**, *4*, 724.
- [467] C. Yeon, G. Kim, J. W. Lim, S. J. Yun, *RSC Adv.* **2017**, *7*, 5888.
- [468] E. Mbise, T. Dias, W. Hurley, in *Electronic Textiles* (Ed: T. Dias), Woodhead Publishing, Oxford **2015**.
- [469] L. Zhang, M. Baima, T. L. Andrew, *ACS Appl. Mater. Interfaces* **2017**, *9*, 32299.
- [470] J. Park, *Polymers* **2020**, *12*, 189.
- [471] F. Wang, C. Gao, K. Kuklane, I. Holmér, *Int J Occup Saf Ergon* **2010**, *16*, 387.
- [472] L. Stygien, S. Varnait-uravliova, A. Abraitien, I. Padleckio, S. Krauledas, *Autex Res. J.* **2020**, *21*.
- [473] M. Zhao, D. Li, J. Huang, D. Wang, A. Mensah, Q. Wei, *J. Mater. Chem. C* **2019**, *7*, 13468.
- [474] L. Hao, Z. Yi, C. Li, X. Li, W. Yuxiu, G. Yan, *Measurement* **2012**, *45*, 1855.
- [475] A. Pragma, H. Singh, B. Kumar, H. Gupta, P. Shankar, *Eng. Res. Expr.* **2020**, *2*, 015003.
- [476] I. Sahta, I. Baltina, N. Truskovska, J. Blums, E. Deksnis, W. I. T. Trans, *Built Environ* **2014**, *137*, 91.
- [477] A. Ahmed, M. A. Jalil, M. M. Hossain, M. Moniruzzaman, B. Adak, M. T. Islam, M. S. Parvez, S. Mukhopadhyay, *J. Mater. Chem. C* **2020**, *8*, 16204.
- [478] D. Wang, D. Li, M. Zhao, Y. Xu, Q. Wei, *Appl. Surf. Sci.* **2018**, *454*, 218.
- [479] H. Kim, S. Lee, *Fibers Polym.* **2018**, *19*, 965.
- [480] S. Maity, A. Chatterjee, B. Singh, A. Pal Singh, *J. Textile Inst.* **2014**, *105*, 887.
- [481] S. Lee, C. H. Park, *RSC Adv.* **2018**, *8*, 31008.
- [482] M. R. Moraes, A. C. Alves, F. Toptan, M. S. Martins, E. M. F. Vieira, A. J. Paleo, A. P. Souto, W. L. F. Santos, M. F. Esteves, A. Zille, *J. Mater. Chem. C* **2017**, *5*, 3807.
- [483] Z. Guo, C. Sun, J. Wang, Z. Cai, F. Ge, *ACS Appl. Mater. Interfaces* **2021**, *13*, 8851.
- [484] Z. Guo, Y. Wang, J. Huang, S. Zhang, R. Zhang, D. Ye, G. Cai, H. Yang, S. Gu, W. Xu, *Cellulose* **2021**, *28*, 7483.
- [485] J. Chen, J. Chen, Y. Li, W. Zhou, X. Feng, Q. Huang, J. G. Zheng, R. Liu, Y. Ma, W. Huang, *Nanoscale* **2015**, *7*, 16874.
- [486] M. Shi, M. Shen, X. Guo, X. Jin, Y. Cao, Y. Yang, W. Wang, J. Wang, *ACS Nano* **2021**, *15*, 11396.
- [487] Q. W. Wang, H. B. Zhang, J. Liu, S. Zhao, X. Xie, L. Liu, R. Yang, N. Koratkar, Z. Z. Yu, *Adv. Funct. Mater.* **2019**, *29*, 1806819.
- [488] X. He, G. Shen, R. Xu, W. Yang, C. Zhang, Z. Liu, B. Chen, J. Liu, M. Song, *Polymers* **2019**, *11*, 468.
- [489] H. N. Choi, S. H. Jee, J. Ko, D. J. Kim, S. H. Kim, *Nanomaterials* **2021**, *11*.
- [490] B. Tian, Q. Liu, C. Luo, Y. Feng, W. Wu, *Adv. Electron. Mater.* **2020**, *6*, 1900922.
- [491] Z. Cui, Y. Han, Q. Huang, J. Dong, Y. Zhu, *Nanoscale* **2018**, *10*, 6806.
- [492] J. Ahn, J. Gu, B. Hwang, H. Kang, S. Hwang, S. Jeon, J. Jeong, I. Park, *Nanotechnology* **2019**, *30*, 455707.
- [493] A. A. Arbab, A. A. Memon, K. C. Sun, J. Y. Choi, N. Mengal, I. A. Sahito, S. H. Jeong, *J. Colloid Interface Sci.* **2019**, *539*, 95.
- [494] Y. Wang, Z. Yu, G. Mao, Y. Liu, G. Liu, J. Shang, S. Qu, Q. Chen, R. W. Li, *Adv. Mater. Technol.* **2019**, *4*, 1800435.
- [495] M. K. Choi, I. Park, D. C. Kim, E. Joh, O. K. Park, J. Kim, M. Kim, C. Choi, J. Yang, K. W. Cho, J. H. Hwang, J. M. Nam, T. Hyeon, J. H. Kim, D. H. Kim, *Adv. Funct. Mater.* **2015**, *25*, 7109.
- [496] P. Talvenmaa, in *Intelligent Textiles and Clothing* (Ed: H. R. Mattila), Woodhead Publishing, Oxford **2006**.
- [497] P. M. Martin, in *Encyclopedia of Modern Optics* (Ed: R. D. Guenther), Elsevier, Oxford **2005**.
- [498] C. Moretti, X. Tao, L. Koehl, V. Koncar, in *Smart Textiles and their Applications* (Ed: V. Koncar), Woodhead Publishing, Oxford **2016**.
- [499] A. Dubey, X. Tao, C. Cochrane, V. Koncar, *I. Access* **2020**, *8*, 182918.
- [500] M. Gicevicius, I. A. Cechanaviciute, A. Ramanavicius, *J. Electrochem. Soc.* **2020**, *167*, 155515.
- [501] C. Graßmann, M. Mann, L. Van Langenhove, A. Schwarz-Pfeiffer, *Sensors* **2020**, *20*, 5691.
- [502] Y. Wei, X. Wang, R. Torah, J. Tudor, *Electron. Lett.* **2017**, *53*, 779.
- [503] U. Linderhed, I. Petsagkourakis, P. A. Ersman, V. Beni, K. Tybrandt, *Flexible Printed Electron.* **2021**, *6*.
- [504] W. Ren, Y. Sun, D. Zhao, A. Aili, S. Zhang, C. Shi, J. Zhang, H. Geng, J. Zhang, L. Zhang, J. Xiao, R. Yang, *Sci. Adv.* **2021**, *7*, eabe0586.
- [505] L. Wang, K. Zhang, *Ener. Environ. Mater.* **2020**, *3*, 67.
- [506] S. Yang, P. Qiu, L. Chen, X. Shi, *Small Sci.* **2021**, *1*, 2100005.
- [507] T. Sun, B. Zhou, Q. Zheng, L. Wang, W. Jiang, G. J. Snyder, *Nat. Commun.* **2020**, *11*, 572.
- [508] S. J. Kim, J. H. We, B. J. Cho, *Energy Environ. Sci.* **2014**, *7*, 1959.
- [509] S. Shin, R. Kumar, J. W. Roh, D. S. Ko, H. S. Kim, S. I. Kim, L. Yin, S. M. Schlossberg, S. Cui, J. M. You, S. Kwon, J. Zheng, J. Wang, R. Chen, *Sci. Rep.* **2017**, *7*, 7317.

- [510] F. Adams, C. Barbante, in *Comprehensive Analytical Chemistry* (Eds: F. Adams, C. Barbante), Elsevier, Amsterdam **2015**.
- [511] M. Rein, V. D. Favrod, C. Hou, T. Khudiyev, A. Stolyarov, J. Cox, C. C. Chung, C. Chhav, M. Ellis, J. Joannopoulos, Y. Fink, *Nature* **2018**, 560, 214.
- [512] W. Yan, A. Page, T. Nguyen-Dang, Y. Qu, F. Sordo, L. Wei, F. Sorin, *Adv. Mater.* **2019**, 31, 1802348.
- [513] Y. Lian, H. Yu, M. Wang, X. Yang, Z. Li, F. Yang, Y. Wang, H. Tai, Y. Liao, J. Wu, X. Wang, Y. Jiang, G. Tao, *J. Mater. Chem. C* **2020**, 8, 8399.
- [514] M. Zhang, M. Zhao, M. Jian, C. Wang, A. Yu, Z. Yin, X. Liang, H. Wang, K. Xia, X. Liang, J. Zhai, Y. Zhang, *Matter* **2019**, 1, 168.
- [515] A. R. a. Consulting, **2021**.
- [516] T. M. Research, Vol. 2022, *Transparency Market Research*, 2022.
- [517] R. a. Market, *Global Digital Textile Printing Market (2022 to 2030) - Size, Share & Trends Analysis Report*, in *Research and Markets*, **2022**.
- [518] P. M. Research, *Persistent Market Research*, **2018**.
- [519] S. Afroj, M. H. Islam, N. Karim, *Proceedings* **2021**, 68, 11.
- [520] S. Yang, C. Li, N. Wen, S. Xu, H. Huang, T. Cong, Y. Zhao, Z. Fan, K. Liu, L. Pan, *J. Mater. Chem. C* **2021**, 9, 13789.
- [521] W. Weng, P. Chen, S. He, X. Sun, H. Peng, *Angew. Chem., Int. Ed.* **2016**, 55, 6140.
- [522] Q. Huang, D. Wang, Z. Zheng, *Adv. Energy Mater.* **2016**, 6, 1600783.
- [523] S. Rotzler, M. Schneider-Ramelow, *Textiles* **2021**, 1, 37.
- [524] S. Maiti, M. R. Islam, M. A. Uddin, S. Afroj, S. J. Eichhorn, N. Karim, *Adv. Sustain. Sys.* **2022**, 6, 2200258.
- [525] N. Karim, S. Afroj, K. Lloyd, L. C. Oaten, D. V. Andreeva, C. Carr, A. D. Farmery, I. D. Kim, K. S. Novoselov, *ACS Nano* **2020**, 14, 12313.
- [526] M. Dulal, S. Afroj, J. Ahn, Y. Cho, C. Carr, I. D. Kim, N. Karim, *ACS Nano* **2022**, 16, 19755.
- [527] S. Verma, S. Arya, V. Gupta, S. Mahajan, H. Furukawa, A. Khosla, *J. Mate. Res. Technol.* **2021**, 11, 564.
- [528] S. Huang, X. Zhu, S. Sarkar, Y. Zhao, *APL Mater.* **2019**, 7, 100901.



Md Rashedul Islam is a PhD candidate under the supervision of Professor Nazmul Karim at the Graphene Application Laboratory of the Centre for Print Research (CFPR), UWE Bristol, UK. He has been investigating Graphene and other 2D materials-based energy storage textiles, aimed at developing and powering next-generation multifunctional wearable electronic textiles for personalized health-care applications. Prior to that, he obtained his BSc and MSc in Textile Engineering, from Bangladesh University of Textiles (BUTEX). He has ≈ 10 years of industry and academic experience related to textile chemical processing, advanced materials, and smart electronic textiles.



Shaila Afroj is a Senior Research Fellow at the Centre for Print Research (CFPR), UWE Bristol (UK), where her research group investigates graphene and other 2D materials-based technologies aimed at developing sustainable wearable electronics textiles and functional clothing for the future. Prior to that, she worked as a Research Associate at the National Graphene Institute (NGI), the University of Manchester after completing her Ph.D. from the same university. She has ≈ 15 years of industry (including multi-national companies like C&A and Intertek) and academic experiences related to sustainable e-textiles, advanced materials, printing, and fashion clothing.



Junyi Yin currently is a graduate student in the Department of Bioengineering at the University of California, Los Angeles under the supervision of Professor Jun Chen. His research focuses on leveraging polymer materials, wearable bioelectronics, and artificial intelligence for personalized healthcare research. Junyi has already published 20 journal articles with 6 of them being the first authors in *Advanced Science*, *Nano Energy*, *Journal of Hazardous Materials*, *Med-X*, and many others.



Kostya S. Novoselov is a condensed matter physicist, specializing in the area of mesoscopic physics and nanotechnology. He is currently Tan Chin Tuan Centennial Professor at the National University of Singapore with broad research interests from mesoscopic transport, ferromagnetism, and superconductivity to electronic and optical properties of graphene and 2D materials. He also has a vast background in nanofabrication and nanotechnology.



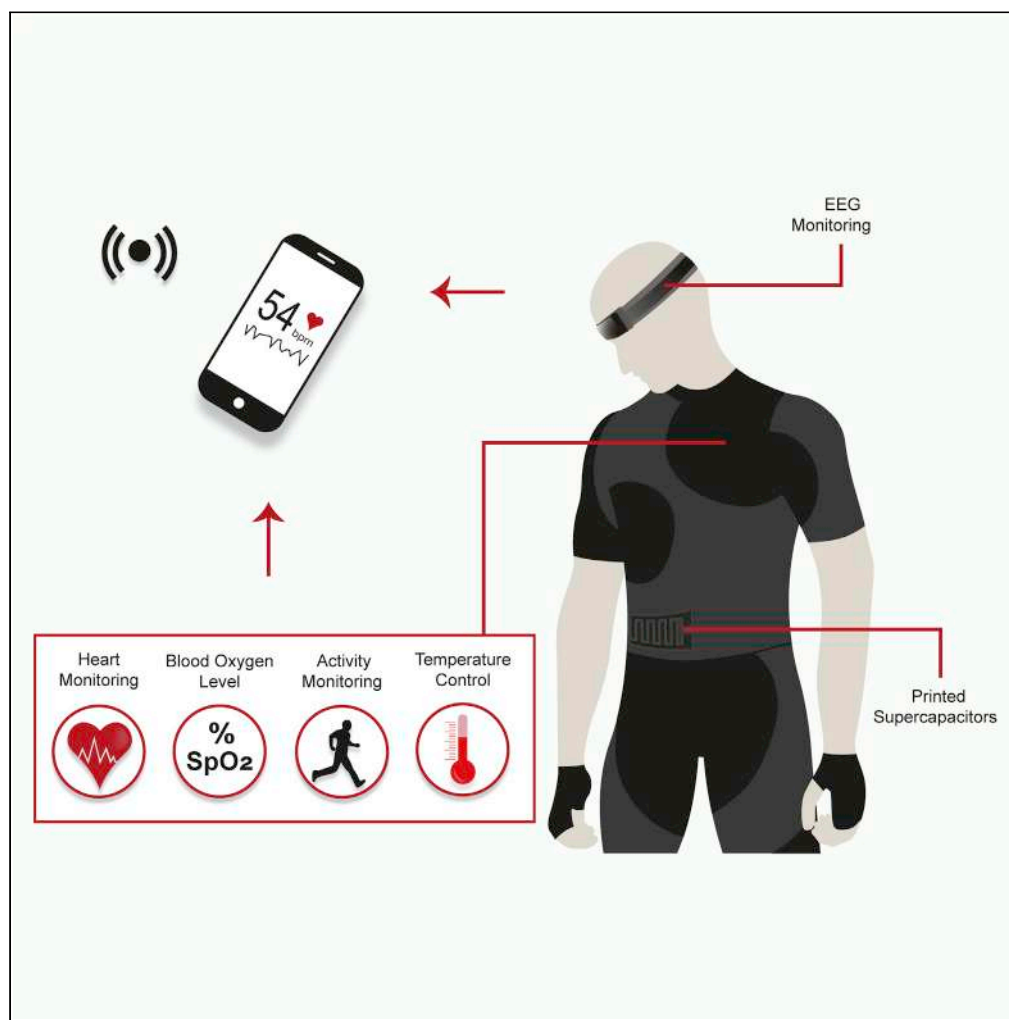
Jun Chen is an Assistant Professor in the UCLA Department of Bioengineering. His research focuses on soft matter innovation for novel bioelectronics. With a current h-index of 102, he was identified to be one of the world's most influential researchers in materials science in Web of Science. He is an associate editor of Biosensors & Bioelectronics, Med-X, VIEW Medicine, FlexMat, and Textiles, Advisory/ Editorial Board Member of Matter, Cell Reports Physical Science, Nano-Micro Letters, Materials Today Energy, etc. Among his many accolades are the V. M. Watanabe Excellence in Research Award, and the ONR Young Investigator Award, among others.



Nazmul Karim is a Professor of Advanced Textiles at the Nottingham Trent University, UK. His research interests lie in the area of new materials and sustainable technologies for developing next-generation wearable e-textiles, sustainable natural fiber-reinforced composites, and high-performance functional clothing. Prior to that, Karim was an Associate Professor at UWE Bristol (UK) and a Knowledge Exchange Fellow (graphene) at the National Graphene Institute of the University of Manchester (UK). He has \approx 15 years of industry and academic experience in new materials and textile-related technologies, and a passion for getting research out of the lab and into real-world applications.

Article

Fully printed and multifunctional graphene-based wearable e-textiles for personalized healthcare applications



Md Rashedul Islam, Shaila Afroj, Christopher Beach, ..., Alexander J. Casson, Kostya S. Novoselov, Nazmul Karim

shaila.afroj@uwe.ac.uk (S.A.)
nazmul.karim@uwe.ac.uk (N.K.)

Highlights

Graphene-based screen-printed conductive, flexible, and machine-washable e-textiles

Able to capture movements demonstrating their potential as activity sensors

In-plane all-solid-state printed textiles supercapacitor showing comparable performance

Perform as EEG bio-signal electrode comparable to current rigid clinical electrodes

Islam et al., iScience 25, 103945
March 18, 2022 © 2022 The Authors.
<https://doi.org/10.1016/j.isci.2022.103945>

Article

Fully printed and multifunctional graphene-based wearable e-textiles for personalized healthcare applications

Md Rashedul Islam,¹ Shaila Afroj,^{1,*} Christopher Beach,² Mohammad Hamidul Islam,¹ Carinna Parraman,¹ Amr Abdelkader,³ Alexander J. Casson,² Kostya S. Novoselov,^{4,5,6} and Nazmul Karim^{1,7,*}

SUMMARY

Wearable e-textiles have gained huge tractions due to their potential for non-invasive health monitoring. However, manufacturing of multifunctional wearable e-textiles remains challenging, due to poor performance, comfortability, scalability, and cost. Here, we report a fully printed, highly conductive, flexible, and machine-washable e-textiles platform that stores energy and monitor physiological conditions including bio-signals. The approach includes highly scalable printing of graphene-based inks on a rough and flexible textile substrate, followed by a fine encapsulation to produce highly conductive machine-washable e-textiles platform. The produced e-textiles are extremely flexible, conformal, and can detect activities of various body parts. The printed in-plane supercapacitor provides an aerial capacitance of $\sim 3.2 \text{ mFcm}^{-2}$ (stability $\sim 10,000$ cycles). We demonstrate such e-textiles to record brain activity (an electroencephalogram, EEG) and find comparable to conventional rigid electrodes. This could potentially lead to a multifunctional garment of graphene-based e-textiles that can act as flexible and wearable sensors powered by the energy stored in graphene-based textile supercapacitors.

INTRODUCTION

Electronic textiles (e-textiles) have emerged as a new class of flexible wearable devices that could interface with the human body, and continuously monitor, collect, and communicate various physiological parameters (Cao et al., 2018; Iqbal et al., 2021; Lin et al., 2020). Unlike existing bulky and rigid wearable devices, e-textiles are lightweight, comfortable and durable, as well as maintain the desirable electrical properties (Komolafe et al., 2019; Vu et al., 2021; Yao et al., 2019). Multifunctional wearables that can detect and distinguish multi-stimuli, and collect a diverse array of signals using a single device, are of great interest for monitoring physiological conditions (Hozumi et al., 2021; Li et al., 2021; Lian et al., 2020). However, the realization of such wearables remains challenging because existing wearable interfaces are limited in terms of performance, scalability, comfortability, and cost (Afroj et al., 2021b; Kim et al., 2019; Wu et al., 2016).

E-textiles that can capture bio-signals, coupled with flexible energy storage devices, constitute a key breakthrough for personalized healthcare applications (Karim et al., 2020; Meng et al., 2020; Zhang et al., 2019). The monitoring of human activities including brain activity (electroencephalogram, EEG), heart (electrocardiogram, ECG), muscle (electromyogram, EMG), and eye movement (electro-oculography, EOG) has widely been used for medical diagnosis (Fayyaz Shahandashti et al., 2019; Sawangjai et al., 2020; Yuce et al., 2008). Such activities can directly be measured using dry or wet electrodes from low-level ion current (i.e. bio-signals) that is already present in human body parts (Fayyaz Shahandashti et al., 2019). Most commonly used electrodes are wet silver chloride (Ag/AgCl) (Chlaihawi et al., 2018). However, such electrodes require time-consuming skin preparation, as well as a gel to maintain low interface impedance, which limits their performance for long-term biopotentials monitoring, due to leaking out and dehydration of the gel, sweat causing short circuits between two adjacent electrodes, and degraded signal quality over an extended time (Wang et al., 2017). Additionally, the gel can create skin irritation and damage, and may even trigger allergic reactions (Peng et al., 2016; Wu et al., 2021). Textiles-based dry electrodes offer attractive alternative (Beach et al., 2018), but are yet to achieve acceptance for medical use (Meziane et al., 2013).

¹Centre for Print Research (CFPR), University of the West of England, Frenchay, Bristol BS16 1QY, UK

²Department of EEE, University of Manchester, Oxford Road, Manchester M13 9PL, UK

³Department of Design and Engineering, Bournemouth University, Dorset, BH12 5BB UK

⁴Department of Materials Science and Engineering, National University of Singapore, Singapore, Singapore

⁵Institute for Functional Intelligent Materials, National University of Singapore, Singapore 117575, Singapore

⁶Chongqing 2D Materials Institute, Liangjiang New Area, Chongqing 400714 China

⁷Lead contact

*Correspondence: shaila.afroj@uwe.ac.uk (S.A.), nazmul.karim@uwe.ac.uk (N.K.)

<https://doi.org/10.1016/j.isci.2022.103945>



The widespread applications for wearable e-textiles have been limited by the lack of lightweight, flexible, and high-performance power supply units (Sundriyal and Bhattacharya, 2020). The existing rigid and bulky energy storage devices hardly resemble a regular fabric in terms of hand feel, thickness, or drape (Jost et al., 2013). To realize next generation multifunctional wearable e-textiles, there remains a need for highly functional but small, flexible and comfortable energy storage devices (Kim et al., 2017; Ren et al., 2021). Flexible textiles supercapacitors (SCs) are promising due to their excellent lifetime, lightweight nature, high power density, and ability to deliver even under mechanically deformed conditions (Huang et al., 2016). However, the challenge to achieving wearable textiles supercapacitors lies within insufficient energy density, complex and time-consuming manufacturing process, and poor performance with electrode materials (Sun et al., 2020).

Graphene-based e-textiles have received significant interests in recent years for wearable electronics applications, due to graphene's extremely high specific surface area, high thermal and electrical conductivity, and excellent mechanical properties (Bhattacharjee et al., 2019, 2020; Islam et al., 2021; Karim et al., 2021b; Wang et al., 2020). Graphene-based textiles could potentially provide a multifunctional platform for manufacturing next generation highly innovative and intelligent e-textile garments that can perform as energy generators and storage devices, sensors, actuators, and electrodes for bio-signal detection, all at the same time (Afroj et al., 2019, 2021a, 2021b; Karim et al., 2021a; Miao et al., 2019). While several scalable techniques were reported to produce graphene-based e-textiles, screen printing in particular is a versatile, highly scalable, and cost-effective technique that has already been exploited commercially for the fabrication of biosensors and chemical sensors (Zhang et al., 2016). Previous studies reported screen printing of graphene-based active materials on textile substrates to fabricate wearable electronics (Abdelkader et al., 2017; Qu et al., 2019; Xu et al., 2019); however, such devices are limited in terms of performance and multifunctionality.

Here, we report a strategy that exploits highly conductive, flexible, and machine-washable graphene-based e-textiles capable of capturing bio-signals and storing energy to develop next-generation multifunctional wearable garments. A simple and scalable screen printing of graphene-based ink on textiles, and subsequent fine encapsulation of conductive track, enables highly conductive and machine-washable e-textiles. Such wearable e-textiles, when bent and compressed in forward and backward directions, demonstrate high flexibility via repeatable response in the electrical resistance change. Additionally, they were able to capture movements of different body parts such as index finger, wrist joint, elbow, and knee joint for demonstrating their potential as such activity sensors. The ink was used to print in-plane electrodes for all-solid-state supercapacitors that showed excellent performance in flexible and non-flexible devices. Finally, the textiles were used to capture EEG bio-signals, offering comparable performance to standard commercial Ag/AgCl electrodes, demonstrating their ability to provide a more comfortable biosensor to current rigid clinical electrodes.

RESULTS AND DISCUSSION

Fully printed and highly conductive graphene-based e-textiles

Figure 1A illustrates the concept of fully printed and multifunctional wearable e-textiles that monitor vital signs including heart rate, temperature, oxygen saturation level and human activities, as well as store energy via flexible textiles supercapacitors. Such e-textiles can be produced via printing highly conductive graphene-based inks using widely used scalable and high-speed screen-printing technique, Figure 1B. The printed patterns on textiles, when placed on several body parts, act as sensors for collecting and monitoring several physiological information. The collected information from various sensors can then be transferred to a remote data management system wirelessly, providing the opportunity for remote monitoring of physiological parameters of adult patients, children, or people who are elderly. Additionally, the flexible supercapacitor offers an attractive alternative to existing rigid and bulky batteries for powering various wearable devices.

An ideal screen-printing ink is pseudoplastic, which demonstrates shear-thinning properties as its viscosity decreases with the increase of shear rate, allowing the ink to flow from the mesh when shear is applied, and a rapid recovery once shear is removed to yield a high-resolution trace during the separation (Hu et al., 2018). Figure 1C shows the change of viscosity from ~ 407.10 cP to ~ 92.02 cP over a shear rate up to 1000 s^{-1} for microfluidized graphene ink used in this study. The shear stress also increases up to ~ 90.49 Pa over the same shear rate, exhibiting the suitability of the graphene-based ink for screen printing. Most favourable technological effects are obtained when the screen-printing inks possess shear thinning

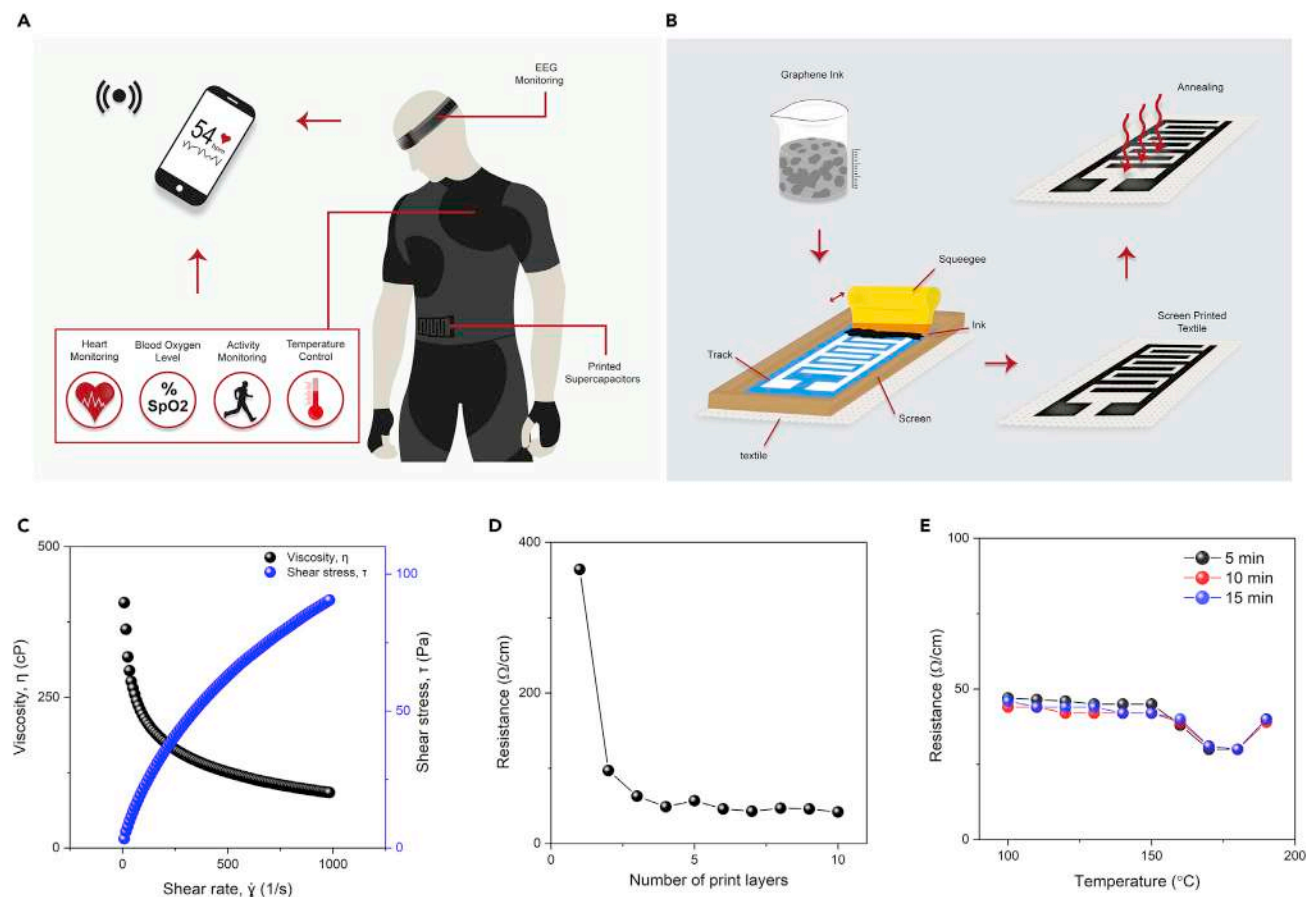


Figure 1. Fully printed and multifunctional wearable e-textiles

(A) Schematic diagram of multifunctional aspect of printed e-textiles.

(B) Schematic diagram of the screen-printing process for preparing graphene-based wearable e-textiles.

(C) Rheological properties of the graphene-based ink, viscosity, and shear stress expressed as a function of shear rate.

(D) The change in electrical resistance with the number of print layers for graphene-based ink-printed cotton fabric.

(E) The change in electrical resistance of graphene-based ink-printed cotton fabric with curing time and temperature.

with slight thixotropy (Izak et al., 2017). In agreement to this, the small, enclosed area of the hysteresis loop (Figure S1) of the print ink also supports the suitability of the graphene-based ink for screen printing.

A simple but highly scalable and most widely used screen-printing technique was used to print graphene-based conductive pattern on textiles to produce highly electrically conductive e-textiles. The number of print layers was optimized. After the first print layer, the electrical resistance of the printed fabric was found to be $\approx 364 \Omega \text{ cm}^{-1}$, Figure 1D. The electrical resistance reduces significantly to $\approx 97 \Omega \text{ cm}^{-1}$ after the second print layer and continues to decrease steadily up to four print layers to $\approx 49 \Omega \text{ cm}^{-1}$ due to the permeation of an increased amount of graphene ink on the textile surface. After four print layers, the resistance reaches a saturation point and becomes steady as observed until ten print layers. Therefore, four print layers were used to prepare graphene-based printed e-textiles for subsequent processes. All the samples were dried at 100°C for 10 min after each print layer during the print-layer optimization process. The curing temperature and time were then optimized for graphene-printed fabrics. Figure 1E shows that the electrical resistance of the graphene-printed fabric decreases with the increase of curing temperature. The phenomenon could be attributed to the increase of contact force between conductive fillers present in the conductive ink and the shrinkage of the organic binder present in the ink, resulting in a reduced electrical resistance of the print pattern (Koshi et al., 2020). It is worth noting that after applying $\sim 180^{\circ}\text{C}$ curing temperature, the cotton fabric turns into a yellow color, as well as the electrical resistance increases, possibly due to the degradation of fiber structures, intra-macromolecular crosslinking, and depolymerization (Afroj et al., 2020). Therefore, we used 170°C for 5 min as curing conditions for all graphene-based printed samples produced for subsequent processes.

We further assessed the effect of curing treatment on fabric properties. The annealed substrate exhibited a change in breaking force of only 2.79% in comparison with the untreated substrate, which is very negligible (Table S1 and Figure S2).

Machine-washable and ultra-flexible graphene-based e-textiles

The poor stability of repeated laundry washings is considered to be one of the major challenges for wide commercial adoption of e-textile products (Rotzler et al., 2020). A good washability is essential for e-textiles to survive intense mechanical deformations and water invasion of washing cycles used during their life cycles (Niu et al., 2021). The washing stability of our graphene-printed e-textiles was assessed following a British Standard (BS EN ISO 105C06 A1S) (ISO, 2010) to evaluate their performance at 10 simulated home-laundry washing cycles. The printed e-textiles patterns (with four print layers) start to lose electrical conductivity just after one washing cycle. The electrical resistance of washed e-textiles was found to be $62.5 \Omega \text{ cm}^{-1}$ (Figure 2A) after the first washing cycle, which is double than that of the unwashed sample. After repeated washing cycles, the electrical conductivity of such e-textiles is reduced drastically, as the resistance increases significantly to $734.0 \Omega \text{ cm}^{-1}$ after 10 washing cycles, which is ~ 10 times higher than the first washing cycle, Figure 2A. A significant variation in the resistance was also observed at various locations of the washed sample's surface. The significant increase in the resistance of non-encapsulated samples could be explained by their more proneness to delamination due to the mechanical forces experienced during washing cycles, resulting in losses of electrical conductivity.

The wash stability of wearable e-textiles can be improved via a number of methods including a textile surface pre-treatment with BSA, or by a post-treatment for instance embedding with polydimethylsiloxane (PDMS), polyurethane (PU) sealing, a screen-printed PU top layer, and transferred mold and hot melt encapsulation to seal conductive track on the textile surface (Afroj et al., 2020). Here, a translucent, thin, and stretchable PU-based encapsulant was used to protect graphene-printed wearable e-textiles. Such encapsulation material adheres with textile materials, keeping the printed graphene layer attached to textiles but covered and protected, Figure 2B. The wash stability performance of graphene-printed textiles after encapsulation was then evaluated, where a slight linear increment in electrical resistance was observed after each washing cycle, Figure 2A. The encapsulated graphene-printed e-textiles show ≈ 1.5 times higher resistance ($35.2 \Omega \text{ cm}^{-1}$) after the first washing cycle in comparison to the unwashed sample. The resistance increases to $118.0 \Omega \text{ cm}^{-1}$ after 10 washing cycles, which is only about 3.5 times higher resistance in comparison to the first wash cycle.

Figure 2C shows smooth and featureless scanning electron microscope (SEM) of un-treated cotton fibers, which was covered with randomly oriented graphene-based flakes after printing highly concentrated graphene inks, Figure 2D. Additionally, unlike graphene oxide (GO), reduced graphene oxide (rGO) or other functionalized graphene derivatives, graphene flakes in microfluidized graphene inks do not create chemical bonding with cellulosic fibers, as they are mainly dominated carbon in their structure without any oxygen-containing functional groups (Afroj et al., 2020). When subjected to mechanical action during washing cycles, such randomly oriented flakes of printed e-textiles are removed, Figure S6C. Therefore, the electrical resistance of graphene-printed e-textiles decreases significantly after each washing cycle. However, the encapsulated printed fabric surface exhibits more resistance to delamination due to the protection of the graphene-printed pattern with thin PU layer, Figure S6D. Thus, the wash stability of graphene-printed e-textiles improved substantially via fine encapsulation with a PU layer without any negative effect on the hand feel as well as flexibility of the conductive e-textiles.

The flexibility of printed, encapsulated, and washed graphene-printed e-textiles was also evaluated, Figures 2F and 2G. Graphene-printed (4layers) and encapsulated cotton fabrics were tested both before and after 10 washing cycles. The change in their electrical resistances per 10 cm length due to bending, compression (both in forward and backward direction) was measured. The cord length, which was measured by the grip distance of the sample ends during the experiment (Figure S7), changed (10–90 mm) when the fabrics were bent and compressed both in forward and backward directions. Figures 2F and 2G exhibit repeatable responses in the change of resistance ($\Delta R/R_0$) during bending and compression in forward direction and backward directions, Figures S8 and S9, respectively. However, the encapsulated samples show excellent repeatability in comparison with the unencapsulated samples for both before and after washing operations. Additionally, the variation of resistances was found almost stable for both unwashed and washed samples subjected to 30 inward (Figure 2H) and outward (Figure S10) folding–releasing operations. It is worth noting that no visible changes in appearance or shape or creasing were observed due to those mechanical actions (bending, compression,

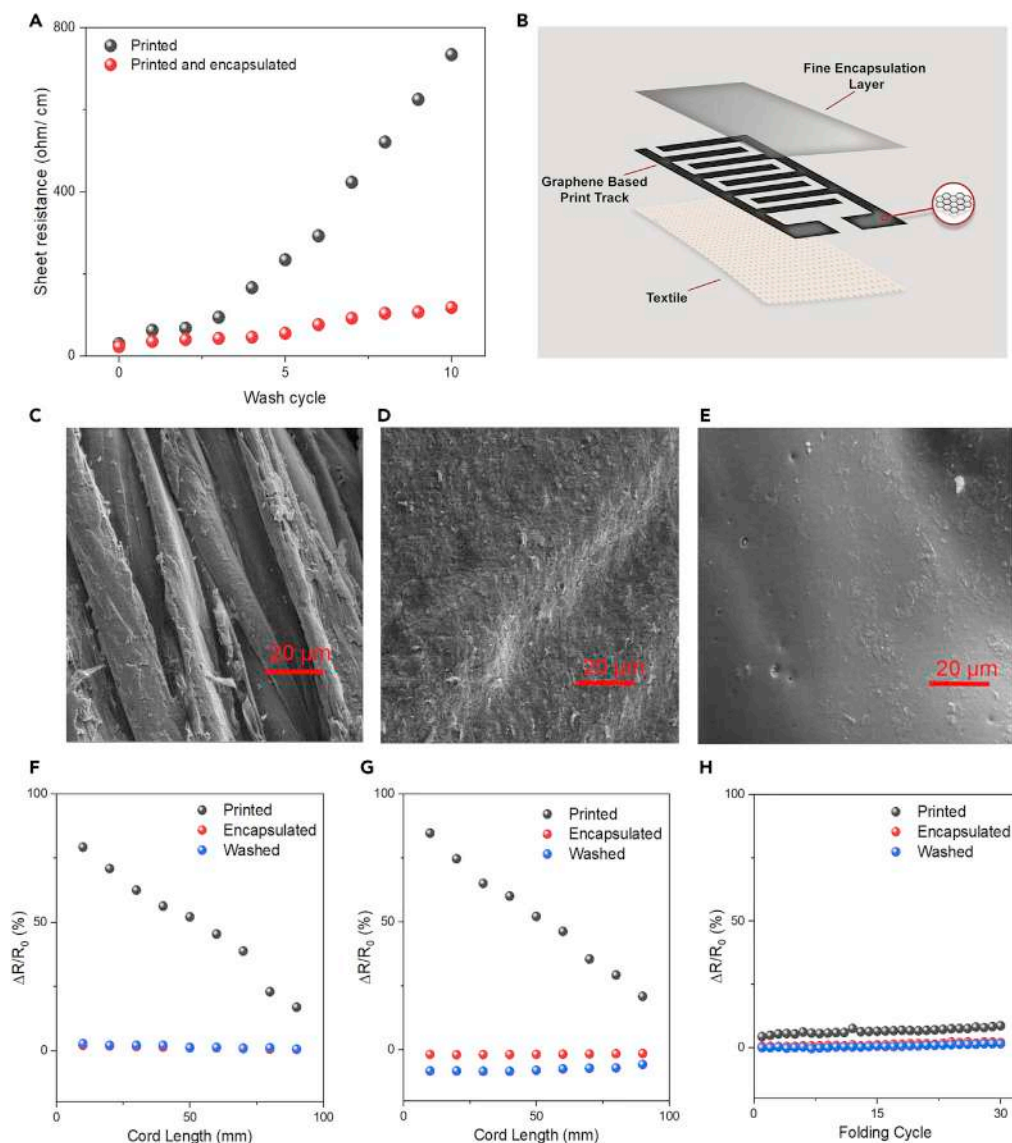


Figure 2. Wash stability and flexibility of printed and encapsulated graphene e-textiles
 (A) The change in electrical resistance with the number of washing cycles of graphene-based ink printed (without encapsulation) and graphene-based ink-printed (with encapsulation) cotton fabric.
 (B) Graphical illustration of graphene-based ink pattern and encapsulation layer on textile substrate.
 (C) Scanning electron microscope (SEM) image of control cotton fiber (X2000).
 (D) SEM image of graphene-based ink-printed (4 layers) cotton fiber (X2000).
 (E) SEM image of graphene-based ink-printed (4 layers) cotton fiber (with encapsulation) after washing (10 washing cycles) (X2000).
 (F) The variation in resistance of the bending sensor in forward direction.
 (G) The variation in resistance of the compression sensor in forward direction.
 (H) The variation in resistance under 30 inward (printed pattern inside) folding–releasing cycles.

and folding cycles), demonstrating excellent flexibility and bendability of encapsulated and washable graphene-based wearable e-textiles.

Activity monitoring wearables of graphene-based e-textiles

Wearable sensors for monitoring individual's as well as patient's health conditions via gathering physiological and movement data have received significant attention now-a-days due to their continuous and non-invasive nature (Karim et al., 2017a; Teymourian et al., 2020; Wang et al., 2019). The strain-type

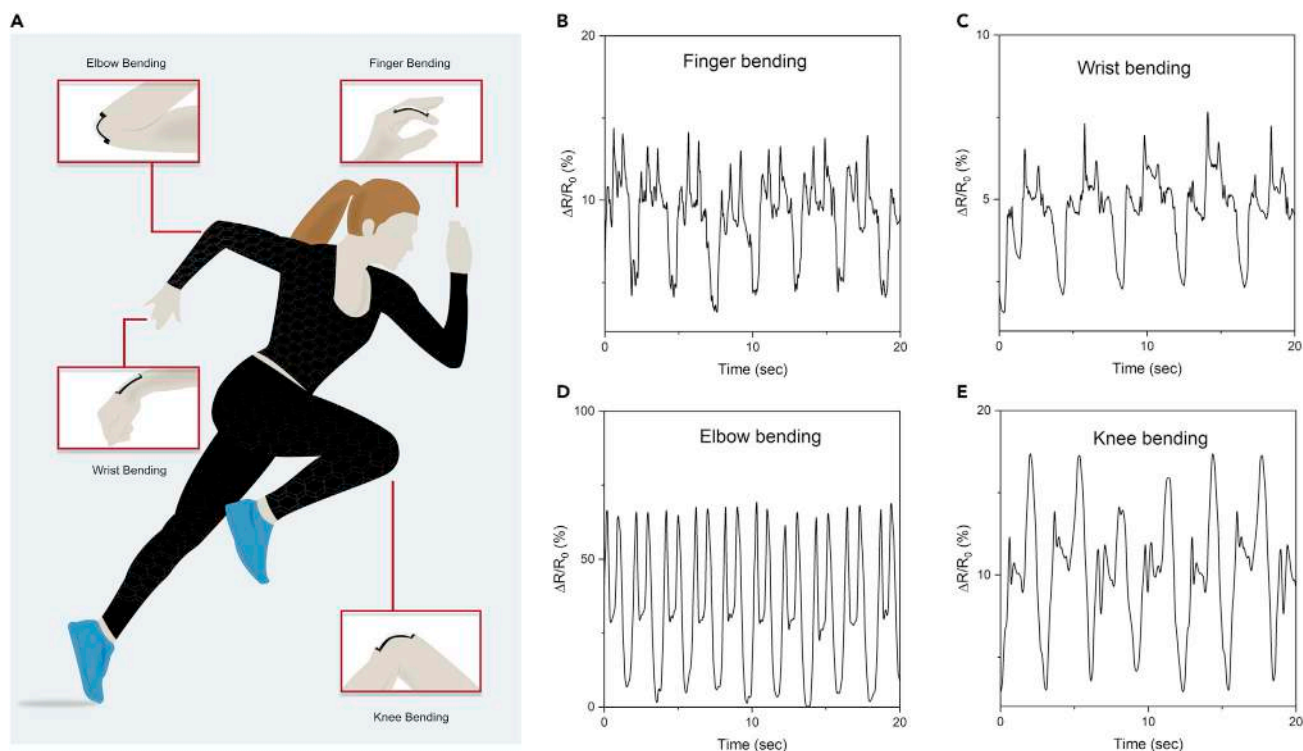


Figure 3. Printed graphene e-textiles as activity monitoring sensors

(A) Schematic diagram showing the application of graphene-based ink-printed textiles as activity monitoring sensors at different body parts. The motion detection represented by the change of resistance as a function of time during (B) finger joint bending (C) wrist joint bending (D) elbow joint bending and (E) knee joint bending by the graphene-based ink-printed textiles.

sensors, composed of conductive network of active materials, serve as resistor under applied voltage, the mechanism of which is known as piezoresistivity. During stretch/compression, the electrical resistance of the conductive track changes as function of the applied mechanical strain that originates from the geometrical changes such as length and/or cross-sectional area, intrinsic resistive response of active materials, tunneling effect, and/or disconnection mechanism. The resistance recovers to its initial values in a reversible manner after releasing from the applied strain. The deformation state, thus, can be readily measured by recording the changes in the electrical resistance of the resistive-type strain sensors (Souri et al., 2020). Graphene-printed conductive, washable, and flexible e-textiles were attached on different body parts such as index finger, wrist joint, elbow, and knee joint to demonstrate their potential as activity sensors, Figure 3A. The change of the resistances with the movement of such body parts were measured (Figures 3B–3E). It is noteworthy here; we utilized the similar printed patterns as piezoresistive sensors at different body parts. Although similar patterns were used, the sensors placed at different body parts such as finger, wrist, elbow, and knee joints were exposed to different stress due to physical movements for different body parts. These produced different strains on the sensors, therefore the resulted repeatable responses were different for different body parts. Repeatable responses of the change of resistances were observed in all the cases over time with outstanding capability of capturing various mechanical actions. This is in agreement with previous study where similar repeatable response and excellent capability of sensitivity measurements were achieved for both unwashed and washed (10 times) skin-mounted strain sensors (Afroj et al., 2020). Such sensors could be used to monitor physical activities such as walking, eating, running, brushing etc of patients or people who are elderly on daily basis and send to their family members or carers to inform about their health status to help them to live independent safely (Al-Khafajiy et al., 2019, Kabiri Ameri et al., 2017). This approach is also effective to study patient’s behavioral changes and recovery processes while still living at their homes.

Printed flexible energy storage e-textiles

We have also printed a solid-state symmetrical supercapacitor device on the textile using the same screen-printing technique. The printed device has five branches on both the cathode and the anode sides; each

Figure 4. Characterization of graphene-based ink-printed textile supercapacitor

(A) CV curves at multiple scan rates, (B) Charge/discharge curves at various current densities, (C) The change of the areal capacitance with the current density, (D) The cyclic stability of the printed supercapacitor measured at 0.1 mA cm^{-2} , (E) CV of the printed supercapacitor at different bending angles, (F) Charge/discharge profile for the supercapacitor with no strain and under strain.

branch is 2 mm in width and 33 mm in length (Figure S14). The distance between each branch on the cathode and the neighbor branch from the anode is 2 mm. The electrochemical performance of the in-plane supercapacitor was assessed by cyclic voltammetry (CV) and galvanostatic charge-discharge. As can be seen in Figure 4A, the CV curves show almost a rectangular shape at all tested scan rates, indicating ideal double-layer capacitance. The lack of any redox peak in the tested electrochemical windows suggests that graphene-based ink is of very good purity, and completely cover the cotton fibers. To calculate the areal capacitance, the charge-discharge profile was recorded at current densities ranging from 0.05 to 0.5 mA cm^{-2} (Figure 4B). In agreement with the CV results, the charge-discharge profiles exhibit an ideal double-layer behavior with a triangular shape and equal time for charge and discharge. Also, there are no visible plateaus or bends in the profiles that might be attributed to a redox reaction. The lack of any IR ($I = \text{current}$ and $R = \text{inner resistance}$) drops at the beginning of the discharge curve suggests good conductivity and low charge barriers at the electrodes. The maximum calculated areal capacitance of the symmetrical printed supercapacitor was 3.2 mF cm^{-2} , which is comparable with many reports existing in literature (Table 1). Even when the current density increased by 10 times to 0.5 mA cm^{-2} , an areal capacitance of 2.6 could be maintained, equivalent to capacitance retention of 81.3% (Figure 4C). The electrochemical stability of the supercapacitor was investigated based on long-term charge-discharge curves at a current density of 0.1 mA cm^{-2} . The devices lost only 5% of their initial capacitance after 10,000 cycles, indicating excellent stability (Figure 4D). Without using any current collector or conductive agents, the printed supercapacitor could deliver a high areal energy density of 0.28 mWh cm^{-2} at the power density of 3 mW cm^{-2} .

For the supercapacitor to be a part of an integrated device/system on a smart textile, it is important to evaluate the performance of the printed device under various loading and strains in multiple directions. We first assessed the performance of the printed supercapacitor using a bending test at various angles. The CV curves were recorded at different bending angles (Figure 4E), which show minor changes of the original unbent curve, suggesting good mechanical stability under bending. Figure 4F shows the charge-discharge curves of the supercapacitors with no strain and under the biaxial strain of 0.1 and 0.2 strains at a constant

Table 1. Comparison of the electrochemical performance of the graphene-ink printed energy storage textile with others reported in the literature

Assembly of energy storage textiles	performance	Energy and power density	Device retention	Flexibility	Application	Ref
Screen-printed rGO on cotton followed by reduction with PVA/H ₂ SO ₄ solid electrolyte	Areal capacitance 2.5 mFcm ⁻²	–	97% after 10,000 cycle	95.6% after folding 180° for 2000 cycles	Supercapacitor	(Abdelkader et al., 2017)
Graphene film with PVA/H ₂ SO ₄ solid electrolyte	2.7 mF cm ⁻²	–	–	–	Supercapacitor	(Chen et al., 2014)
Stretchable textiles fully printed Ag@PPy@MnO ₂ on Ag cathode electrode and activated carbon on Ag anode electrode with PVA/Na ₂ SO ₄ electrolyte	426.3 mF cm ⁻² (cathode)	0.0337 mWh cm ⁻² at 0.38 mWcm ⁻²	90.8% retention after 5000 cycles	86.2% retention after 40% stretching strain	Supercapacitor	(Liu et al., 2018)
PPy electrochemically deposited on rGO-painted SnCl ₂ modified polyester textiles with PVA/H ₂ SO ₄ gel electrolyte	1117 mF cm ⁻² at a current density of 1 mA cm ⁻²	0.0658 mWh cm ⁻² at 1 mA cm ⁻² and 0.5 mW cm ⁻²	100% after 10,000 cycles	98.3% after 1000 bending cycles	Supercapacitor	(Li et al., 2018)
Coating of poly-cotton textiles with graphene ink	Resistance 11.9 Ωsq ⁻¹ , Areal capacitance 2.7 mF cm ⁻²	–	98% after 15,000 cycles	98% after 150 cycles of bending at 180°	Activity monitoring sensor and Supercapacitor	(Aroj et al., 2020)
Kevlar fibers, coated in gold, and then grew ZnO nanowires with PVA/H ₃ PO ₄ solid electrolyte	Areal capacitance 2.4 mF cm ⁻²	2.7 × 10 ⁻⁵ mWhcm ⁻²	–	–	Supercapacitor	(Bae et al., 2011)
CNT on Ti wire with PVA/H ₂ SO ₄ solid electrolyte	Areal capacitance 1.84 mF cm ⁻³	0.16 × 10 ⁻³ mW h cm ⁻³ and 0.01 mW cm ⁻³	80% after 1000 cycles	–	Supercapacitor	(Chen and Dai, 2016)
SnS/S-doped graphene on PET with PVA/H ₂ SO ₄ solid electrolyte	Areal capacitance 2.98 mF cm ⁻²	–	99% after 10,000 cycle	–	Supercapacitor	(Liu et al., 2017)
N-Doped rGO on PET with PVA/H ₃ PO ₄ solid electrolyte	Areal capacitance 3.4 mF cm ⁻²	0.3 mWh cm ⁻³ at 0.2 W cm ⁻³	98% after 2000 cycles	–	Supercapacitor	(Liu et al., 2014)
Graphene ink screen printed on cotton textiles with PVA/H ₂ SO ₄ gel electrolyte	Resistance 30 Ω cm ⁻¹ , Areal capacitance 3.2 mFcm ⁻²	0.28 mWh cm ⁻² at 3 mW cm ⁻²	95% after 10,000 cycles	–	Activity monitoring sensor, EEG electrode, Supercapacitor	This work

current density of 0.1 mA cm^{-2} . Interestingly, the charge-discharge profiles of the supercapacitor under strain exhibit some bending toward the end of the discharge. We expected this bending to occur due to a partial exposure of the substrate cotton fibers to the supercapacitor electrolyte. It is known that the cotton fiber's surface is rich with oxygen functional groups, which might introduce some faradic reaction. Obviously, the contribution of such redox reactions is limited due to the limited exposure of the fiber. There is a noticeable potential IR drop at the beginning of the discharge curve when subjected the electrodes to strain, which increases by increasing the strain. We believe the increase of the electrode resistivity is related to the loss of the graphene flakes under strain, which demonstrates the possibility of using printed graphene electrodes as strain and piezoelectric sensors.

Sleep monitoring via electroencephalography recordings (EEG)

We also demonstrated how our printed graphene-based textile electrodes can be used to record electrophysiological information, specifically the electroencephalogram (EEG). An EEG is a non-invasive method of

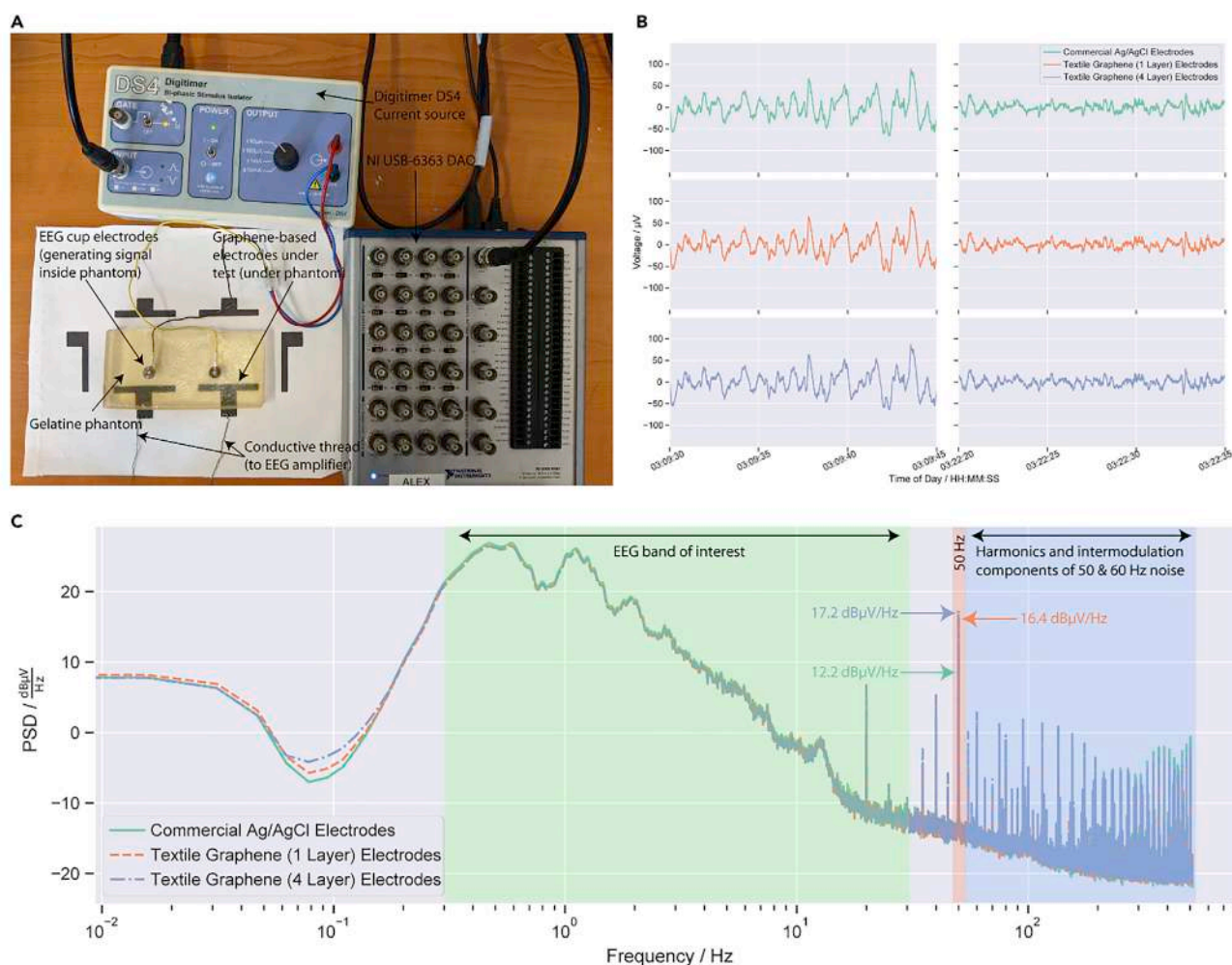


Figure 5. Printed graphene e-textiles for EEG applications

(A) Experimental setup showing signal source (DAQ), current stimulator (Digitimer DS4), gelatine phantom, graphene-based electrodes, and conductive thread connection to EEG Amplifier.

(B) Data collected using the textile graphene-based electrodes against commercial Ag/AgCl electrodes from data from Fpz-Oz data in the SC4001 record from Physionet. (left) A section of the record in deepest stage of sleep (stage 4), indicated by the presence of slow oscillations in the record. (right) A lighter stage of sleep (stage 2), indicated by smaller amplitude higher frequency oscillations.

(C) Power spectral density of recorded signal from graphene textiles electrodes against commercial Ag/AgCl electrodes, highlighting the typical frequency band of interest in EEG studies shaded in green. The 50 Hz component and its contribution for each of the electrode types are shaded in red. Also shown are higher frequency harmonics and intermodulation components from 50 to 60 Hz noise shaded in dark blue.

recording brain activity, undertaken by placing electrodes on the scalp and forehead of a person, and used in a number of areas from sleep studies to epilepsy diagnosis (Biasucci et al., 2019). Here, we demonstrate how these graphene-based e-textiles can be used as electrodes in sleep monitoring, Figure 5A. Sleep studies which take polysomnographic recordings (PSG), consisting principally of EEG recordings and other bio-signals are recordings taken overnight during sleep, Figure 5B. The PSG data is scored into different sleep stages by a trained expert to identify sleep disorders (Sharma et al., 2021; Yildirim et al., 2019). To demonstrate the feasibility of using the e-textiles for EEG recordings, we simulate the EEG part of a PSG using two electrodes and a gelatine head phantom (Owda and Casson, 2021), Figure 5A. This setup simulates one EEG electrode placed on the central forehead (referred to as Fpz in the international 10-20 standard), and a reference electrode placed elsewhere (here, we utilize the Cz location, which is in the center of the scalp). This reference electrode could also be positioned in an alternative hairless location, such as behind the ear, but here we use the Cz location to allow standardization with other datasets.

Prior to any pre-processing or filtering of data, we examine the frequency domain of the EEG recordings by comparing the power spectral density (PSD) of the signals collected from the electrodes. This allows identification of the level of 50 Hz noise picked up by the electrodes, a common source of noise in electrophysiological recordings. This 50-Hz pickup is caused by the electrical mains (which oscillates at 50 Hz in the UK) coupling with the electrodes and measurement equipment. In Figure 5C, the PSD is shown, and we can see that over the frequency band of interest for sleep studies (0.3–30 Hz) (Baker et al., 2012) all electrode types follow each other very closely. At 50 Hz, the commercial Ag/AgCl electrodes have around 12.2 dB μ V/Hz of power contribution, and the graphene-based electrodes have a slightly higher contribution, around 16.4 dB μ V/Hz and 17.2 dB μ V/Hz for the 1-layer and 4-layer electrodes, respectively. We can also see higher frequency noise above 50 Hz in all electrodes, consisting of harmonics and intermodulation components of 50 and 60 Hz noise. These components arise from the 50 Hz noise that is coupled to the electrodes during our experiment and the 60 Hz noise that is present in the original EEG dataset used, (60 Hz is the mains line frequency in the US where the original dataset was collected). In this work, not only are the differences in noise between the graphene-based textiles electrodes and rigid Ag/AgCl electrodes minimal but also this noise does not overlap with the EEG frequency bands of interest, so these power line contributions can be filtered out.

The correlation coefficient between the filtered data collected from both types of graphene-based electrodes over the 20-min record is high at over 0.998, indicating a very strong similarity between the performance of our electrodes and the rigid Ag/AgCl electrodes. Figure 5B shows two 15 s segments of the EEG record data, at two distinct points. In the left figure, data are displayed from the participant when they are in the deepest stage of sleep (stage 4), indicated by the large-amplitude slow-wave oscillations. The right figure shows the data from the participant around 10 min later where they are in a lighter stage of sleep (stage 2), indicated by the higher frequency and smaller amplitude oscillations. Both features can clearly be seen both in the data collected by the graphene-based electrodes and by the rigid Ag/AgCl electrodes indicating similar levels of performance between all electrode types. The results indicate these e-textiles could be utilized for EEG recordings which overcome the limitations of conventional rigid Ag/AgCl electrodes.

Conclusion

A fully printed, highly conductive, flexible, and machine-washable e-textiles platform that can store energy and monitor physiological conditions including bio-signals is reported. The printed conductive textiles show outstanding wash stability even after 10 home laundry washing cycles. The repeatable responses after bending, compression, and folding cycles exhibit the outstanding flexibility of printed e-textiles. Additionally, we demonstrate potential skin-mounted wearable sensors and sleep monitoring applications of such printed e-textiles. Furthermore, an in-plane flexible solid-state supercapacitor device was also fabricated from the printed e-textiles, which was able to provide an aerial capacitance of ~ 3.2 mF cm⁻² and outstanding cyclic stability upto 10,000 cycles. We believe these findings could potentially lead to a truly multifunctional wearable garment for personalized healthcare applications.

STAR★METHODS

Detailed methods are provided in the online version of this paper and include the following:

- KEY RESOURCE TABLE
- RESOURCE AVAILABILITY
 - Lead contact

- Materials availability
- Data and code availability
- **METHOD DETAILS**
 - Materials
 - Screen printing of graphene ink on textiles and encapsulation
 - Characterization of graphene ink and wearable e-textiles
 - Supercapacitor device fabrication and electrochemical characterization
 - Graphene-based wearable EEG

SUPPLEMENTAL INFORMATION

Supplemental information can be found online at <https://doi.org/10.1016/j.isci.2022.103945>.

ACKNOWLEDGMENTS

Authors gratefully acknowledge funding from UWE-Augtex partnership PhD award, and UKRI Research England The Expanding Excellence in England (E3) grant, United Kingdom. Authors also thank Laura Wescott for the professional support with the graphics for this paper. K.S.N. acknowledges support from the Ministry of Education (Singapore) through the Research Centre of Excellence program (grant EDUN C-33-18-279-V12, I-FIM).

AUTHOR CONTRIBUTIONS

N.K. and S.A. planned and designed the experiments. M.R.I. performed most of the experiments, carried out analysis, and prepared draft manuscript under supervision of N.K. and S.A. C.B. performed, analyzed, and wrote EEG section under supervision of A.J.C. A.A. performed, analyzed, and wrote supercapacitor section. The manuscript was prepared with inputs from all authors.

DECLARATION OF INTERESTS

The authors declare no competing interests.

Received: December 14, 2021

Revised: January 19, 2022

Accepted: February 15, 2022

Published: March 18, 2022

REFERENCES

- Abdelkader, A.M., Karim, N., Vallés, C., Afroj, S., Novoselov, K.S., and Yeates, S.G. (2017). Ultraflexible and robust graphene supercapacitors printed on textiles for wearable electronics applications. *2D Mater.* *4*, 035016.
- Afroj, S., Karim, N., Wang, Z., Tan, S., He, P., Holwill, M., Ghazaryan, D., Fernando, A., and Novoselov, K.S. (2019). Engineering graphene flakes for wearable textile sensors via highly scalable and ultrafast yarn dyeing technique. *ACS Nano* *13*, 3847–3857.
- Afroj, S., Tan, S., Abdelkader, A.M., Novoselov, K.S., and Karim, N. (2020). Highly conductive, scalable, and machine washable graphene-based E-textiles for multifunctional wearable electronic applications. *Adv. Funct. Mater.* *30*, 2000293.
- Afroj, S., Britnell, L., Hasan, T., Andreeva, D.V., Novoselov, K.S., and Karim, N. (2021a). Graphene-based technologies for tackling COVID-19 and future pandemics. *Adv. Funct. Mater.* *31*, 2107407.
- Afroj, S., Islam, M.H., and Karim, N. (2021b). Multifunctional Graphene-Based Wearable E-Textiles. *Proceedings* *68*, 11.
- Al-Khafajiy, M., Baker, T., Chalmers, C., Asim, M., Kolivand, H., Fahim, M., and Waraich, A. (2019). Remote health monitoring of elderly through wearable sensors. *Multimedia Tools Appl.* *78*, 24681–24706.
- Bae, J., Song, M.K., Park, Y.J., Kim, J.M., Liu, M., and Wang, Z.L. (2011). Fiber supercapacitors made of nanowire-fiber hybrid structures for wearable/flexible energy storage. *Angew. Chem. - Int. Edition* *50*, 1683–1687.
- Baker, F.C., Turlington, S.R., and Colrain, I. (2012). Developmental changes in the sleep electroencephalogram of adolescent boys and girls. *J. Sleep Res.* *21*, 59–67.
- Beach, C., Karim, N., and Casson, A.J. (2018). Performance of graphene ECG electrodes under varying conditions. In *40th Annual International Conference of the IEEE Engineering in Medicine and Biology Society (EMBC) (IEEE)*, pp. 3813–3816.
- Bhattacharjee, S., Joshi, R., Chughtai, A.A., and Macintyre, C.R. (2019). Graphene modified multifunctional personal protective clothing. *Adv. Mater. Inter.* *6*, 1900622.
- Bhattacharjee, S., Macintyre, C.R., Wen, X., Bahl, P., Kumar, U., Chughtai, A.A., and Joshi, R. (2020). Nanoparticles incorporated graphene-based durable cotton fabrics. *Carbon* *166*, 148–163.
- Biasiucci, A., Franceschiello, B., and Murray, M.M. (2019). Electroencephalography. *Curr. Biol.* *29*, R80–R85.
- Cao, R., Pu, X., Du, X., Yang, W., Wang, J., Guo, H., Zhao, S., Yuan, Z., Zhang, C., Li, C., and Wang, Z.L. (2018). Screen-printed washable electronic textiles as self-powered touch/gesture tribo-sensors for intelligent human-machine interaction. *ACS Nano* *12*, 5190–5196.
- Chen, Q., Li, X., Zang, X., Cao, Y., He, Y., Li, P., Wang, K., Wei, J., Wu, D., and Zhu, H. (2014). Effect of different gel electrolytes on graphene-based solid-state supercapacitors. *RSC Adv.* *4*, 36253–36256.
- Chen, T., and Dai, L. (2016). Flexible and wearable wire-shaped microsupercapacitors based on highly aligned titania and carbon nanotubes. *Energy Storage Mater.* *2*, 21–26.
- Chalhawi, A.A., Narakathu, B.B., Emamian, S., Bazuin, B.J., and Atashbar, M.Z. (2018).

Development of printed and flexible dry ECG electrodes. *Sensing Bio-Sensing Res.* 20, 9–15.

Fayyaz Shahandashti, P., Pourkheyrollah, H., Jahanshahi, A., and Ghafoorifard, H. (2019). Highly conformable stretchable dry electrodes based on inexpensive flex substrate for long-term biopotential (EMG/ECG) monitoring. *Sensors Actuators A: Phys.* 295, 678–686.

Goldberger, A.L., Amaral, L.A., Glass, L., Hausdorff, J.M., Ivanov, P.C., Mark, R.G., Mietus, J.E., Moody, G.B., Peng, C.K., and Stanley, H.E. (2000). PhysioBank, PhysioToolkit, and PhysioNet: components of a new research resource for complex physiologic signals. *Circulation* 101, E215–E220.

Hozumi, S., Honda, S., Arie, T., Akita, S., and Takei, K. (2021). Multimodal wearable sensor sheet for health-related chemical and physical monitoring. *ACS Sensors* 6, 1918–1924.

Hu, G., Kang, J., Ng, L.W.T., Zhu, X., Howe, R.C.T., Jones, C.G., Hersam, M.C., and Hasan, T. (2018). Functional inks and printing of two-dimensional materials. *Chem. Soc. Rev.* 47, 3265–3300.

Huang, Q., Wang, D., and Zheng, Z. (2016). Textile-based electrochemical energy storage devices. *Adv. Energy Mater.* 6, 1–28.

Iqbal, S.M.A., Mahgoub, I., Du, E., Leavitt, M.A., and Asghar, W. (2021). Advances in healthcare wearable devices. *npj Flexible Electronics* 5, 9.

Islam, M.H., Islam, M.R., Dulal, M., Afroj, S., and Karim, N. (2021). The effect of surface treatments and graphene-based modifications on mechanical properties of natural jute fibre reinforced composites: a review. *iScience*, 103597.

ISO, B. (2010). Tests for Colour Fastness Part C06: Colour Fastness to Domestic and Commercial Laundering (British Standards Institution (BSI)).

Izak, P., Mastalska-Poplawska, J., Lis, J., and Stempkowska, A. (2017). Modification of the rheological properties of screen printing ceramic paints containing gold. *J. Phys. Conf. Ser.* 790, 012011.

Jost, K., Stenger, D., Perez, C.R., McDonough, J.K., Lian, K., Gogotsi, Y., and Dion, G. (2013). Knitted and screen printed carbon-fiber supercapacitors for applications in wearable electronics. *Energy Environ. Sci.* 6, 2698–2705.

Kabiri Ameri, S., Ho, R., Jang, H., Tao, L., Wang, Y., Wang, L., Schnyer, D.M., Akinwande, D., and Lu, N. (2017). Graphene electronic tattoo sensors. *ACS Nano* 11, 7634–7641.

Karim, N., Afroj, S., Malandraki, A., Butterworth, S., Beach, C., Rigout, M., Novoselov, K.S., Casson, A.J., and Yeates, S.G. (2017a). All inkjet-printed graphene-based conductive patterns for wearable e-textile applications. *J. Mater. Chem. C* 5, 11640–11648.

Karim, N., Afroj, S., Tan, S., He, P., Fernando, A., Carr, C., and Novoselov, K.S. (2017b). Scalable production of graphene-based wearable E-textiles. *ACS Nano* 11, 12266–12275.

Karim, N., Zhang, M., Afroj, S., Koncherry, V., Potluri, P., and Novoselov, K.S. (2018). Graphene-

based surface heater for de-icing applications. *RSC Adv.* 8, 16815–16823.

Karim, N., Afroj, S., Lloyd, K., Oaten, L.C., Andreeva, D.V., Carr, C., Farmery, A.D., Kim, I.-D., and Novoselov, K.S. (2020). Sustainable personal protective clothing for healthcare applications: a review. *ACS Nano* 14, 12313–12340.

Karim, N., Afroj, S., Leech, D., and Abdelkader, A.M. (2021a). Flexible and wearable graphene-based E-textiles. In *Oxide Electronics*, A. RAY, ed. (John Wiley & Sons, Ltd.).

Karim, N., Sarker, F., Afroj, S., Zhang, M., Potluri, P., and Novoselov, K.S. (2021b). Sustainable and multifunctional composites of graphene-based natural jute fibers. *Adv. Sustainable Syst.* 5, 2000228.

Kemp, B., Zwinderman, A.H., Tuk, B., Kamphuisen, H.a.C., and Oberye, J.J.L. (2000). Analysis of a sleep-dependent neuronal feedback loop: the slow-wave microcontinuity of the EEG. *IEEE Trans. Biomed. Eng.* 47, 1185–1194.

Kim, I., Shahariar, H., Ingram, W.F., Zhou, Y., and Jur, J.S. (2019). Inkjet process for conductive patterning on textiles: maintaining inherent stretchability and breathability in knit structures. *Adv. Funct. Mater.* 29, 1807573.

Kim, J., Kumar, R., Bandothkar, A.J., and Wang, J. (2017). Advanced materials for printed wearable electrochemical devices: a review. *Adv. Electron. Mater.* 3, 1600260.

Komolafe, A., Torah, R., Wei, Y., Nunes-Matos, H., Li, M., Hardy, D., Dias, T., Tudor, M., and Beeby, S. (2019). Integrating flexible filament circuits for E-textile applications. *Adv. Mater. Tech.* 4, 1900176.

Koshi, T., Nomura, K.-I., and Yoshida, M. (2020). Resistance reduction of conductive patterns printed on textile by curing shrinkage of passivation layers. *Micromachines* 11, 539.

Li, X., Liu, R., Xu, C., Bai, Y., Zhou, X., Wang, Y., and Yuan, G. (2018). High-performance polypyrrole/graphene/SnCl₂ modified polyester textile electrodes and yarn electrodes for wearable energy storage. *Adv. Funct. Mater.* 28, 1800064.

Li, Y., Chen, W., and Lu, L. (2021). Wearable and biodegradable sensors for human health monitoring. *ACS Appl. Bio Mater.* 4, 122–139.

Lian, Y., Yu, H., Wang, M., Yang, X., Li, Z., Yang, F., Wang, Y., Tai, H., Liao, Y., Wu, J., et al. (2020). A multifunctional wearable E-textile via integrated nanowire-coated fabrics. *J. Mater. Chem. C* 8, 8399–8409.

Lin, Y., Bariya, M., and Javey, A. (2020). Wearable biosensors for body computing. *Adv. Funct. Mater.* 30, 2008087.

Liu, C., Zhao, S., Lu, Y., Chang, Y., Xu, D., Wang, Q., Dai, Z., Bao, J., and Han, M. (2017). 3D porous nanoarchitectures derived from SnS/S-doped graphene hybrid nanosheets for flexible all-solid-state supercapacitors. *Small* 13, 1603494.

Liu, L., Tian, Q., Yao, W., Li, M., Li, Y., and Wu, W. (2018). All-printed ultraflexible and stretchable asymmetric in-plane solid-state supercapacitors

(ASCs) for wearable electronics. *J. Power Sourc.* 397, 59–67.

Liu, S., Xie, J., Li, H., Wang, Y., Yang, H.Y., Zhu, T., Zhang, S., Cao, G., and Zhao, X. (2014). Nitrogen-doped reduced graphene oxide for high-performance flexible all-solid-state micro-supercapacitors. *J. Mater. Chem. A* 2, 18125–18131.

Meng, K., Zhao, S., Zhou, Y., Wu, Y., Zhang, S., He, Q., Wang, X., Zhou, Z., Fan, W., Tan, X., et al. (2020). A wireless textile-based sensor system for self-powered personalized health care. *Matter* 2, 896–907.

Meziane, N., Webster, J.G., Attari, M., and Nimunkar, A.J. (2013). Dry electrodes for electrocardiography. *Physiol. Meas.* 34, R47–R69.

Miao, P., Wang, J., Zhang, C., Sun, M., Cheng, S., and Liu, H. (2019). Graphene nanostructure-based tactile sensors for electronic skin applications. *Nano-Micro Lett.* 11, 71.

Niu, B., Yang, S., Hua, T., Tian, X., and Koo, M. (2021). Facile fabrication of highly conductive, waterproof, and washable e-textiles for wearable applications. *Nano Res.* 14, 1043–1052.

Owda, A.Y., and Casson, A.J. (2021). Investigating gelatine based head phantoms for electroencephalography compared to electrical and ex vivo porcine skin models. *IEEE Access* 9, 96722–96738.

Peng, H.-L., Jing-Quan, L., Tian, H.-C., Dong, Y.-Z., Yang, B., Chen, X., and Yang, C.-S. (2016). A novel passive electrode based on porous Ti for EEG recording. *Sensors Actuators B: Chem.* 226, 349–356.

Qu, J., He, N., Patil, S.V., Wang, Y., Banerjee, D., and Gao, W. (2019). Screen printing of graphene oxide patterns onto viscose nonwovens with tunable penetration depth and electrical conductivity. *ACS Appl. Mater. Inter.* 11, 14944–14951.

Ren, M., Di, J., and Chen, W. (2021). Recent progress and application challenges of wearable supercapacitors. *Batteries Supercaps* 4, 1–13.

Rotzler, S., Kallmayer, C., Dils, C., Von Krshiwoblozki, M., Bauer, U., and Schneider-Ramelow, M. (2020). Improving the washability of smart textiles: influence of different washing conditions on textile integrated conductor tracks. *J. Textile Inst.* 111, 1766–1777.

Sawangjai, P., Hompoonsup, S., Leelaarporn, P., Kongwudhikunakorn, S., and Wilaiprasitporn, T. (2020). Consumer grade EEG measuring sensors as research tools: a review. *IEEE Sensors J.* 20, 3996–4024.

Sharma, M., Tiwari, J., and Acharya, U.R. (2021). Automatic sleep-stage scoring in healthy and sleep disorder patients using optimal wavelet filter bank technique with EEG signals. *Int. J. Environ. Res. Public Health* 18, 3087.

Souri, H., Banerjee, H., Jusufi, A., Radacs, N., Stokes, A.A., Park, I., Sitti, M., and Amjadi, M. (2020). Wearable and stretchable strain sensors: materials, sensing mechanisms, and applications. *Adv. Intell. Syst.* 2, 2000039.

Sun, T., Shen, L., Jiang, Y., Ma, J., Lv, F., Ma, H., Chen, D., and Zhu, N. (2020). Wearable textile supercapacitors for self-powered enzyme-free smart sensors. *ACS Appl. Mater. Inter.* *12*, 21779–21787.

Sundriyal, P., and Bhattacharya, S. (2020). Textile-based supercapacitors for flexible and wearable electronic applications. *Scientific Rep.* *10*, 13259.

Teymourian, H., Parrilla, M., Sempionatto, J.R., Montiel, N.F., Barfidokht, A., Van Echelpoel, R., De Wael, K., and Wang, J. (2020). Wearable electrochemical sensors for the monitoring and screening of drugs. *ACS Sens* *5*, 2679–2700.

Velcescu, A., Lindley, A., Cursio, C., Krachunov, S., Beach, C., Brown, C.A., Jones, A.K.P., and Casson, A.J. (2019). Flexible 3D-printed EEG electrodes. *Sensors (Basel, Switzerland)* *19*, 1650.

Vu, C.C., Kim, S.J., and Kim, J. (2021). Flexible wearable sensors - an update in view of touch-sensing. *Sci. Technology Adv. Mater.* *22*, 26–36.

Wang, H., Wang, H., Wang, Y., Su, X., Wang, C., Zhang, M., Jian, M., Xia, K., Liang, X., Lu, H., et al. (2020). Laser writing of janus graphene/kevlar

textile for intelligent protective clothing. *ACS Nano* *14*, 3219–3226.

Wang, Q., Ling, S., Liang, X., Wang, H., Lu, H., and Zhang, Y. (2019). Self-healable multifunctional electronic tattoos based on silk and graphene. *Adv. Funct. Mater.* *29*, 1808695.

Wang, R., Jiang, X., Wang, W., and Li, Z. (2017). A microneedle electrode array on flexible substrate for long-term EEG monitoring. *Sensors Actuators B: Chem.* *244*, 750–758.

Wu, C., Kim, T.W., Li, F., and Guo, T. (2016). Wearable electricity generators fabricated utilizing transparent electronic textiles based on polyester/Ag nanowires/graphene core-shell nanocomposites. *ACS Nano* *10*, 6449–6457.

Wu, H., Yang, G., Zhu, K., Liu, S., Guo, W., Jiang, Z., and Li, Z. (2021). Materials, devices, and systems of on-skin electrodes for electrophysiological monitoring and human-machine interfaces. *Adv. Sci.* *8*, 2001938.

Xu, X., Luo, M., He, P., Guo, X., and Yang, J. (2019). Screen printed graphene electrodes on

textile for wearable electrocardiogram monitoring. *Appl. Phys. A* *125*, 714.

Yao, S., Yang, J., Poblete, F.R., Hu, X., and Zhu, Y. (2019). Multifunctional electronic textiles using silver nanowire composites. *ACS Appl. Mater. Inter.* *11*, 31028–31037.

Yildirim, O., Baloglu, U.B., and Acharya, U.R. (2019). A deep learning model for automated sleep stages classification using PSG signals. *Int. J. Environ. Res. Public Health* *16*, 599.

Yuce, M.R., Ng, P.C., and Khan, J.Y. (2008). Monitoring of physiological parameters from multiple patients using wireless sensor network. *J. Med. Syst.* *32*, 433–441.

Zhang, H., Qiao, Y., and Lu, Z. (2016). Fully printed ultraflexible supercapacitor supported by a single-textile substrate. *ACS Appl. Mater. Inter.* *8*, 32317–32323.

Zhang, M., Zhao, M., Jian, M., Wang, C., Yu, A., Yin, Z., Liang, X., Wang, H., Xia, K., Liang, X., et al. (2019). Printable smart pattern for multifunctional energy-management E-textile. *Matter* *1*, 168–179.

STAR★METHODS

KEY RESOURCE TABLE

REAGENT or RESOURCE	SOURCE	IDENTIFIER
Chemicals, peptides, and recombinant proteins		
Screen printing ink	Cambridge Graphene	Graphink 2/CMC
Stretchable encapsulant	DuPont	PE773
PVA	Sigma-Aldrich	341584
H ₂ SO ₄	Sigma-Aldrich	258105

RESOURCE AVAILABILITY

Lead contact

Further information and requests for resources and reagents should be directed to and will be fulfilled by the lead contact, Nazmul Karim (nazmul.karim@uwe.ac.uk)

Materials availability

This study did not generate new unique reagents.

Data and code availability

The published article includes all data generated or analyzed during this study.

METHOD DETAILS

Materials

A water-based graphene dispersion (100 g/L) was prepared using Microfluidized technique (Afroj et al., 2019; Karim et al., 2018). The rheology of graphene-based dispersions was modified using carboxymethylcellulose sodium salt to prepare printable inks, which was supplied by Versarien Limited UK. Microcircuit encapsulant PE773 was purchased from Dupont (USA). 100% cotton fabric (de-sized, scoured, and bleached which are ready-to-dye fabric) was manufactured at Square Fashions Limited (Bangladesh), and donated by 2dtronics Limited (UK).

Screen printing of graphene ink on textiles and encapsulation

A basic hand screen-printing method was used to print graphene-based ink on textiles, and then printed fabric was dried at 100°C for 10 minutes using a small table-top thermo fixation oven (Mini-Thermo, Roaches, UK). Each print cycle consisted of one printing layer (3 passes) followed by drying process. Samples were repeatedly printed and dried to optimize the number of print layers (1–10 layers). Additionally, the curing temperature and time were also optimized using a range of curing temperature (100 °C–190°C with 10°C interval) over a time range (5–15 minutes with 5 minutes interval). For wash stability tests, graphene printed textiles were encapsulated with a fine layer of a microcircuit encapsulant PE773 using the same screen-printing method followed by a drying and curing at 150°C for 1 min.

Characterization of graphene ink and wearable e-textiles

The ink viscosity was characterized using a HAAKE Viscotester iQ Rheometer (ThermoFisher Scientific, UK). Shear stress and viscosity were determined at different shear rates to assess the printing ink's flow properties. The surface topography of the control cotton fabric, graphene-printed fabric, graphene-printed fabric after washing, graphene printed-encapsulated fabric and graphene-printed and encapsulated fabric after washing were analysed using a FEI Quanta 650 field emission scanning electron microscope (SEM).

The electrical resistance of graphene printed textile was measured by a standard multi-meter. The wash stability of graphene printed fabric was carried out according to BS EN ISO 105 C06 A15 method as previously reported (Afroj et al., 2020). During wash stability tests, a conductive track was created with electrically conductive silver paste for measuring the electrical resistance of graphene printed and encapsulated e-textiles, Figure S6B. By following previously reported methods (Afroj et al., 2019; Karim et al., 2017b)

various cord lengths were used to measure the change of resistance of washed and unwashed fabric (10 cm × 1 cm strip) during bending (concave down) and compression (concave upward), [Figure S7](#). A Win Test tensile tester (Testometric, UK) was used to control the cord length both in forward and reverse directions for both bending and compression tests. Printed samples were also subjected to ten repeated folding–release cycles in both inward and outward direction. The change in the resistance of skin mounted graphene-printed fabric sensors on index fingers, wrist, elbow, and knee joint was captured using a Keithley digital multi-meter.

Supercapacitor device fabrication and electrochemical characterization

The supercapacitor device was prepared by following previously reported method ([Abdelkader et al., 2017](#)). The printed graphene textile electrodes were used as the current collector. However, copper sheets were glued to the end of every electrode to ensure good electrical contact with the measuring workstation. The printed electrodes were coated with a hydrogel-polymer electrolyte, poly (vinyl alcohol) (PVA) doped with H₂SO₄. The H₂SO₄ PVA gel electrolyte was prepared as follows: 1 g of H₂SO₄ was added into 10mL of deionized water, and then 1 g of PVA (molecular weight: 89 000–98 000, Sigma-Aldrich) was added. The whole mixture was then heated to 85°C under stirring until the solution became clear. The electrolyte was drop-casted and left to dry overnight under ambient conditions to ensure that the electrolyte completely wetted the electrode and to allow for evaporation of any excess water.

The electrochemical performances of the printed devices were investigated by cyclic voltammetry (CV), and galvanostatic charge/discharge tests. The electrochemical measurements were performed on an Iviumstat Electrochemical Interface. The CV and galvanostatic charge–discharge measures were conducted in the potential range of –0.2 to 0.8 V at different scan rates and current densities. For measuring the CV at different bending angles, the device was attached to a flexible polyethylene terephthalate film.

Graphene-based wearable EEG

To verify the ability of our material to capture EEG information, a phantom head model was created using gelatine in a 1:4 ratio by mass of gelatine to water, creating a replication of the ionic conductors present in the human body, as previously reported ([Velcescu et al., 2019](#)). The phantom consists of two rigid sintered silver/silver chloride (Ag/AgCl) EEG electrodes embedded inside, enabling pre-recorded EEG signals to be played-back; replicating signals present inside the human head and giving a ‘known’ signal to record, allowing verification. We used pre-recorded EEG data from the Physionet Sleep-EDF Database ([Goldberger et al., 2000](#); [Kemp et al., 2000](#)), a dataset consisting of expert-scored PSG sleep study recordings, to generate signals in the phantom. A 20-minute excerpt (03:03:00 – 03:23:00) from participant SC4001 using the Fpz-Oz channel was played back in the phantom using a current source (DS4 Biphasic Stimulus Isolator, Digitimer), set to ±10 μA, in turn connected to a digital-to-analogue voltage source (NI USB-6363, National Instruments, USA). Using silver-loaded conductive thread (Electro Fashion, Kitronik, UK) connections to two of the conductive areas on the textiles were sewn in and in turn connected to an electrophysiological amplifier (Actiwave EEG/ECG 4 channel, CamNtech), sampling at 1024 Hz and 10 bits. The textile electrodes were compared against commercially available gold-standard rigid EEG electrodes (Ag/AgCl disc electrodes and Abralyt HiCl conductive gel) commonly used in EEG studies. Frequency-domain comparisons between electrode types were made by calculating the power spectral density (PSD) using the Welch method with 30 s long windows, 50% overlaps and 2¹⁶ FFT points. Time-domain comparisons were made after filtering with an eight-order zero-phase notch filter with f_L and f_H set to 47.5 Hz and 52.5 Hz respectively, and then filtered with a fourth-order zero-phase low-pass filter with $f_L = 50$ Hz. The 2D correlation coefficient between the filtered data collected from both types of graphene electrodes was calculated against the commercial rigid electrodes.

Scalable Production of 2D Material Heterostructure Textiles for High-Performance Wearable Supercapacitors

Md Rashedul Islam, Shaila Afroj,* and Nazmul Karim*



Cite This: *ACS Nano* 2023, 17, 18481–18493



Read Online

ACCESS |

 Metrics & More

 Article Recommendations

 Supporting Information

ABSTRACT: Wearable electronic textiles (e-textiles) have emerged as a promising platform for seamless integration of electronic devices into everyday life, enabling noninvasive monitoring of human health. However, the development of efficient, flexible, and scalable energy storage solutions remains a significant challenge for powering such devices. Here, we address this challenge by leveraging the distinct properties of two-dimensional (2D) material based heterostructures to enhance the performance of wearable textile supercapacitors. We report a highly scalable and controllable synthesis method for graphene and molybdenum disulfide (MoS_2) through a microfluidization technique. Subsequently, we employ an ultrafast and industry-scale hierarchical deposition approach using a pad-dry method to fabricate 2D heterostructure based textiles with various configurations suitable for wearable e-textiles applications. Comparative analyses reveal the superior performance of wearable textile supercapacitors based on 2D material heterostructures, demonstrating excellent areal capacitance ($\sim 105.08 \text{ mF cm}^{-2}$), high power density ($\sim 1604.274 \mu\text{W cm}^{-2}$) and energy density ($\sim 58.377 \mu\text{Wh cm}^{-2}$), and outstanding capacitive retention ($\sim 100\%$ after 1000 cycles). Our findings highlight the pivotal role of 2D material based heterostructures in addressing the challenges of performance and scalability in wearable energy storage devices, facilitating large-scale production of high-performance wearable supercapacitors.

KEYWORDS: *graphene, 2D materials, heterostructure, wearable electronics, e-textiles, supercapacitors*



Wearable electronics have revolutionized the field of personalized healthcare by enabling noninvasive monitoring of human health during daily life.¹ However, the full-scale deployment of wearable electronic textiles, commonly known as e-textiles, faces significant challenges in terms of powering these devices while maintaining essential textile properties such as flexibility, durability, lightweight, biocompatibility, and strength.² The increasing demand for wearable electronic devices and the need for efficient energy storage systems have spurred significant advancements in the field of textile-based wearable supercapacitors.³ These devices, integrated seamlessly into fabrics, hold immense potential for powering wearable electronics, healthcare monitoring systems, and smart textiles.^{4–7} However, scalable production of high-performance supercapacitors that combine excellent electrochemical properties with the flexibility and comfort of textiles remains a considerable challenge.⁸ To overcome these, there is a pressing need to explore advanced materials and innovative design approaches that can enhance the energy storage performance of wearable textile supercapacitors.

Two-dimensional (2D) material heterostructures offer a compelling solution to enhance energy performance by combining different ingredients into a single ultimate structure.⁹ These heterostructures, formed by stacking 2D materials with complementary properties, exhibit enhanced properties that are not found in the individual materials. By carefully arranging the layers, researchers can manipulate interlayer interactions and band structures, resulting in the creation of diverse tailor-made heterostructures with specific and tailored properties.^{10,11} Electrochemical capacitors store electrical energy either in the electrochemical double layer (EDL) formed by electrolyte ions on the electrode surface or through redox reactions involving the electrode material's

Received: July 6, 2023

Accepted: September 7, 2023

Published: September 11, 2023



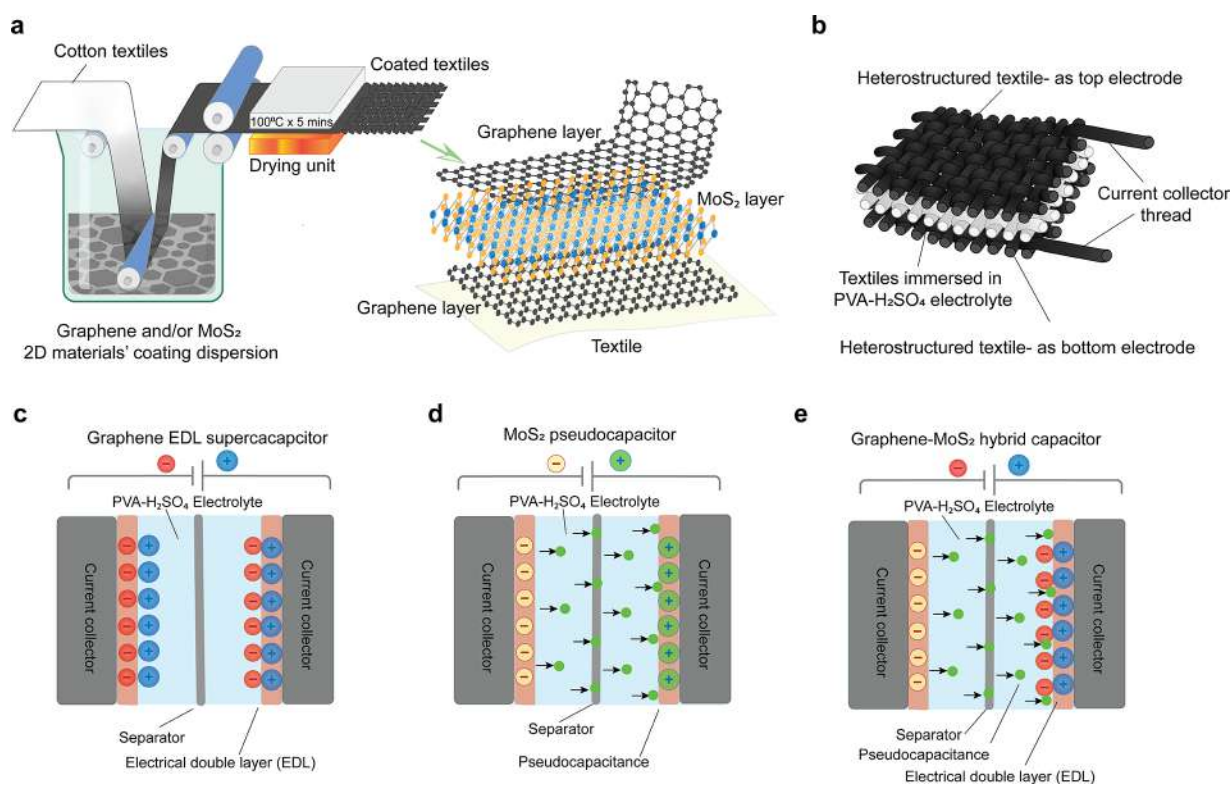


Figure 1. System overview of the 2D material heterostructure textile for supercapacitor applications (a) Scalable pad-dry method for coating of graphene and/or MoS₂ materials for textiles. (b) Schematic of the supercapacitor structure based on heterostructure textiles electrode (c) Graphene based electrical double layer (EDL) supercapacitor. (d) MoS₂-based pseudocapacitor. (e) Graphene-MoS₂-graphene heterostructure based hybrid supercapacitor.

surface regions, known as pseudocapacitance.^{12,13} However, materials that possess both of these properties are rare but crucial for robust and efficient devices.¹⁴ To address this, the fabrication of 2D material based heterostructures combining EDLC and pseudocapacitive materials becomes essential, as it increases the surface area and enhances the active electrochemical sites in the superior heterostructure. This architecture enables energy storage through near-surface ion adsorption and additional contribution from fast reversible Faradaic reactions, leading to high energy and power density.^{15,16} Therefore, 2D material heterostructures offer a versatile approach to enhance energy storage performance through their distinct properties, enabling the development of highly efficient and high-capacity electrochemical capacitors.

The isolation of graphene in 2004¹⁷ unveiled a diverse range of graphene-like 2D materials (2DM) with exceptional mechanical, thermal, and electrical properties.^{18–20} These materials enable the creation of heterostructures with diverse properties. In our previous works, we demonstrated the potential of graphene and its derivatives as functional materials for next-generation wearable electronic textiles.^{21–25} Additionally, we utilized graphene as an efficient supercapacitor electrode material for powering wearable electronic devices.^{26,27} Transition-metal dichalcogenides (TMDs) have attracted significant attention due to their distinct physical properties such as magnetism, charge-density-wave order, superconductivity, and potential applications in high-performance electronic devices.²⁸ TMDs exhibit improved energy storage capabilities compared to traditional electrode materials and other 2D materials like graphene, thanks to their layered structures with sufficient interlayer space.²⁹ Among the various

TMD materials, 2D MoS₂ exhibit good capacitive properties,³⁰ due to the tunable band gap and a large number of active sites with extraordinary physical and chemical properties.³¹ Despite their favorable properties, MoS₂ has limitations, including restacking, unsatisfactory electrical conductivity, inflexibility, and poor interface quality in electronic and electrochemical devices. To overcome these challenges, researchers have explored a wide variety of MoS₂-based heterostructures. Although graphene-MoS₂ heterostructures have been reported for other applications including nonvolatile memory cells,³² superlattice configuration,³³ fiber lasers,³⁴ and supercapacitor electrodes on a nickel³⁵ or graphite³⁶ substrate, their utilization in textile-based wearable supercapacitors remains unexplored.

To fully realize the potential of 2D material based wearable textile supercapacitors, several challenges pertaining to performance and scalable manufacturing must be addressed. These challenges encompass the achievement of high energy storage performance while preserving the desired textile properties of flexibility, durability, light weight, and biocompatibility. Additionally, the development of scalable production methods for synthesizing and integrating 2D materials into textile structures is pivotal for enabling large-scale manufacturing of high-performance wearable supercapacitors. To address these challenges, here we report a scalable microfluidization technique for the production of two prominent 2D materials: graphene and MoS₂. Leveraging the advantages of a microfluidization technique, we successfully exfoliate graphene and MoS₂ dispersions and subsequently hierarchically deposit them in various heterostructure configurations on textiles by using a highly scalable and ultrafast pad-dry method. By harnessing the exceptional properties of 2D

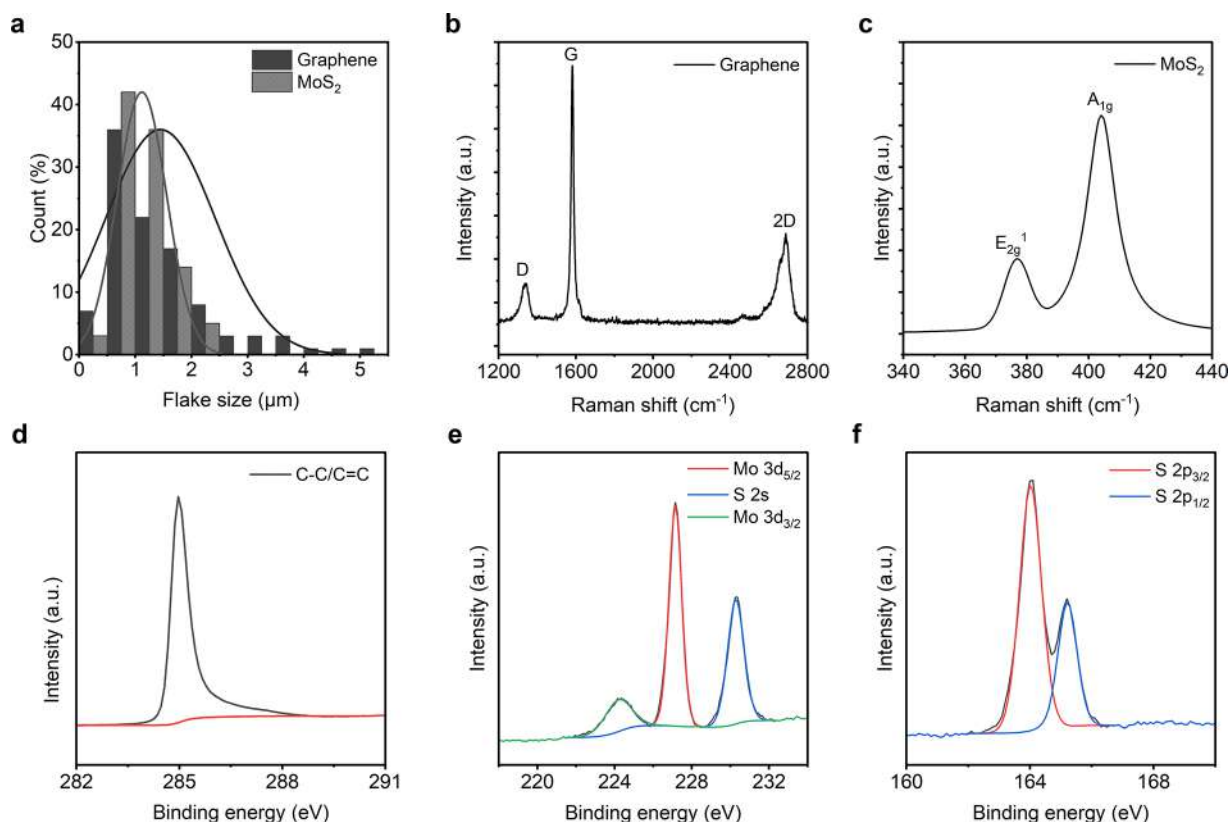


Figure 2. Characterization of microfluidized 2D materials. (a) Size distribution of graphene and MoS₂ flakes. (b) Raman spectrum of graphene flakes. (c) Raman spectrum of MoS₂ flakes. (d) High-resolution XPS spectra of graphene flakes. High-resolution XPS spectra of (e) Mo 3d and S 2s and (f) S 2p of as-prepared MoS₂ flakes.

material based heterostructures, we demonstrate the potential to significantly enhance the energy storage performance of wearable textile supercapacitors while ensuring scalability in manufacturing.

RESULTS AND DISCUSSION

System Overview. 2D material heterostructures offer a platform for tailoring and combining the distinct properties of different 2D materials, enabling the discovery of phenomena and the development of advanced devices and technologies across multiple disciplines.³⁷ In this study, we report graphene and MoS₂ heterostructures, a specific combination of two different 2D materials, stacked together in a layered structure on textile fabrics (Figure 1). The graphene layer can provide higher electrical conductivity, while the MoS₂ layer contributes to the tunable band gap. In such a heterostructure, the band alignment can be modified by changing the stacking configuration or introducing strain. This tunability offers control over the charge transfer, carrier dynamics, and optical properties of the heterostructure, enabling the design of devices with tailored electronic characteristics and efficient charge transport. A highly scalable pad-dry method (Figure 1a) was used to stack graphene and MoS₂ in different configurations on textiles. The heterostructure textiles (Figure 1b) were then utilized as supercapacitor electrodes. While graphene-based supercapacitors work as EDL capacitors (Figure 1c) and MoS₂-based supercapacitors work as pseudocapacitors (Figure 1d), the 2D heterostructure based textile supercapacitors work as hybrid capacitors (Figure 1e). We initially varied the number of graphene coating layers for

graphene based and number of MoS₂ coating layers for MoS₂ based textile supercapacitors. We then attempted to explore supercapacitor performance fabricated from the MoS₂-graphene bilayer coated electrodes and graphene-MoS₂-graphene trilayer coated textile electrodes (Table S1, Section 1 in the Supporting Information).

Scalable Production of 2D Materials via Microfluidization Technique. We use a highly scalable microfluidization technique to exfoliate few-layer two-dimensional (2D) materials (graphene and MoS₂ flakes) from graphite and MoS₂ in water-based dispersions. A microfluidizer generates liquid velocities of 400 ms⁻¹ and several orders of magnitude higher shear rates (>10⁸ s⁻¹) than conventional rotor-based or other homogenizers by passing fluids through microchannels (diameter, *d* < 100 μm) at high pressure (up to 209 MPa).³⁸ Though primarily used for particle size reduction,³⁹ nano-emulsion of immiscible liquids,⁴⁰ disrupting or lysing cells,^{41,42} and deagglomeration and dispersion of carbon nanotubes (CNTs) and graphene nanoplatelets (GNP) into polymers,⁴³ few studies have highlighted the use of the microfluidization technique to produce graphene,^{38,44} graphene quantum dots,³⁷ and two-dimensional (2D) boron nitride nanosheets.⁴⁵ It is also a simple and environmentally friendly technique with 100% exfoliation yield.⁴⁴

Figure 2a shows that the average lateral size of exfoliated graphene flakes is ~1.45 μm and that of the MoS₂ flakes is ~1.25 μm. Figure 2b shows a Raman spectrum of exfoliated graphene flakes after 20 cycles, a typical spectrum for liquid-phase exfoliated graphene, with the characteristic D peak at ~1350 cm⁻¹, G peak at ~1582 cm⁻¹ and an asymmetric 2D band at ~2730 cm⁻¹.^{38,44} Figure 2c shows the Raman

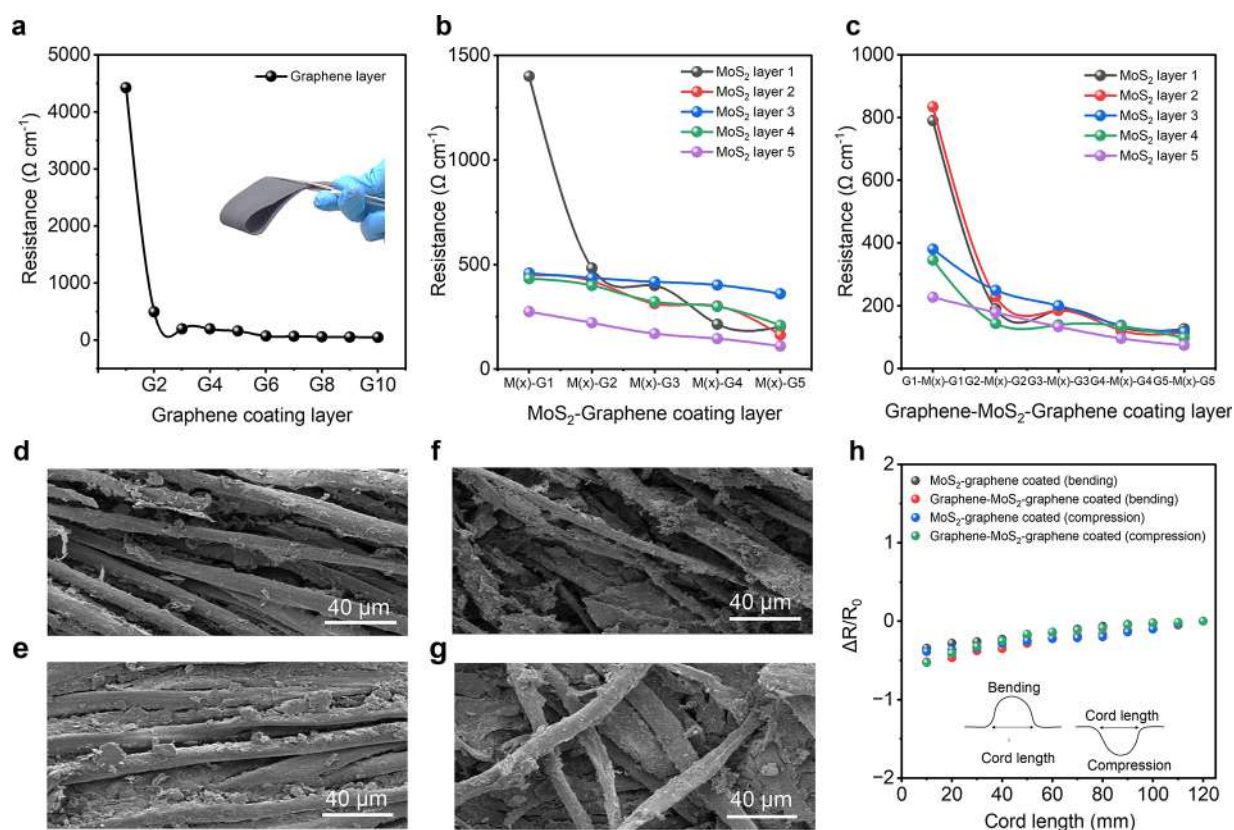


Figure 3. Characterization of the 2DM heterostructure based textiles. The change in the electrical resistance of (a) graphene coated, (b) MoS₂-graphene bilayer coated, and (c) graphene-MoS₂-graphene trilayer coated textiles. Surface morphology of the 2DM coated textiles: scanning electron microscope (SEM) image of the (d) graphene 1 coated textiles, G1 ($\times 1000$), and (e) graphene 10 coated textiles, G10 ($\times 1000$). (f) 4 MoS₂-5 graphene coated textiles, M4G5 ($\times 1000$) and (g) 4 graphene-3 MoS₂-4 graphene coated textiles, G4M3G4 ($\times 1000$). (h) Variation in resistance of MoS₂-graphene bilayer coated and graphene-MoS₂-graphene trilayer coated textiles during bending and compression.

spectrum of exfoliated MoS₂ flakes. Similar to graphene, single-layer and few-layer MoS₂ have distinctive signatures in the Raman spectrum. It contains two prominent peaks: an in-plane (E_{2g}) mode located around $\sim 386\text{ cm}^{-1}$ and an out-of-plane (A_{1g}) mode, which is located at $\sim 404\text{ cm}^{-1}$. The in-plane mode corresponds to the sulfur atoms vibrating in one direction and the molybdenum atom in the other, while the out-of-plane mode is a mode of just the sulfur atoms vibrating out-of-plane. The difference between these two modes ($\sim 18\text{ cm}^{-1}$) can be used as a reliable identification for monolayer MoS₂.

X-ray photoelectron spectroscopy (XPS) measurements were performed to investigate the chemical composition and phase state of the as-prepared graphene and MoS₂ flakes. Figure 2d shows the high-resolution C 1s spectra, which reveals peaks for graphene flakes, dominated by C–C and C=C in aromatic rings ($\sim 284.6\text{ eV}$). The high-resolution XPS spectrum of the exfoliated MoS₂ acquired in the chalcogen binding energy region ($226\text{--}232\text{ eV}$)⁴⁶ exhibits two obvious peaks at ~ 227 and $\sim 230.5\text{ eV}$, corresponding to Mo 3d_{5/2} and Mo 3d_{3/2}, respectively, indicating the characteristic of a Mo⁴⁺ state in MoS₂⁴⁷ (Figure 2e). The peaks of S 2p_{3/2} and S 2p_{1/2} were located at ~ 164.0 and $\sim 165.1\text{ eV}$, respectively, with a spin-orbit splitting of 1.1 eV, revealing the S₂⁻ in MoS₂^{48,49} (Figure 2f).

Scalable Production of Highly Flexible Graphene-MoS₂ Heterostructure-Based E-textiles. In the textile industry, the pad-dry method is widely employed for applying

functional finishes to textiles, such as antimicrobial, water repellency, wrinkle resistance, and moisture management finishes. This method offers a higher production speed, capable of processing $\sim 150\text{ m}$ fabrics with functional finishes in just 1 min. In our study, we utilized a laboratory-scale pad-drying unit designed to mimic the industrial counterpart, demonstrating its potential for large-scale production of e-textiles. To simulate the industrial process, we passed a white cotton control fabric, which had undergone desizing, scouring, and bleaching processes to remove impurities and colors, through a padding bath containing a 10 g L^{-1} graphene dispersion. The mangle's nip rollers were used to remove excessive dispersions from the fabric's surface, ensuring uniform coating. As a result of the black color of the graphene dispersion, the white fabric quickly transformed into black shortly after coating, typically within seconds. Subsequently, the coated fabric was dried at $100\text{ }^\circ\text{C}$ for 5 min in a laboratory dryer to eliminate water/solvent and fix the graphene onto textiles. We repeated this process for up to 10 successive coating layers on graphene-based textiles.

Figure 3a shows the changes in electrical resistance per unit length of the graphene-coated fabric with the number of coating layers. Following the application of a single coating layer with graphene dispersion, the resistance of the fabric was measured to be $\sim 4426.5\text{ }\Omega\text{ cm}^{-1}$. Notably, the resistance underwent a significant reduction of $\sim 89\%$ after the second coating layer, reaching $\sim 493.5\text{ }\Omega\text{ cm}^{-1}$. Furthermore, the resistance continued to decrease with each additional coating

layer, reaching $\sim 71.33 \Omega \text{ cm}^{-1}$ after six layers. We continued the coating process up to ten layers, resulting in a minimum resistance of $\sim 49.62 \Omega \text{ cm}^{-1}$. This observed phenomenon can be attributed to absorption and adsorption mechanisms. Initially, the graphene dispersion is absorbed into the textile fibers, leading to a significant reduction in the resistance during the first few coating cycles. As saturation is reached, the dispersion predominantly adsorbs onto the surface of the textiles, forming a continuous conductive film by establishing improved connections between graphene flakes. As evidenced from the scanning electron microscope (SEM) images, in comparison to the uncoated textiles (Figure S1a, Section 2 in the Supporting Information), a greater amount of graphene flakes deposited on the fiber surface during coating (Figure 3d,e) and their restacking through van der Waals forces exerted by the squeeze rollers consequently reduce the resistance of the fabric. We repeated the same process for the other 2D material, i.e., MoS_2 of the same concentration (10 g L^{-1}). Ten textile samples were coated with MoS_2 from 1 to 10 successive MoS_2 layers. Both the graphene coated and MoS_2 coated textiles were utilized as control electrodes for further studies. The SEM images of the MoS_2 -coated textiles also exhibit similar phenomena (Figure S1b,c, Section 2 in the Supporting Information). It is worth noting that, being a semiconductor, MoS_2 -coated textiles do not show any conductivity at the initial coating layers. After 8–9 coating layers, the textiles exhibited a very high resistance of $\sim 0.8\text{--}0.9 \text{ G}\Omega \text{ cm}^{-1}$, i.e., very poor conductivity.

After preparing graphene and MoS_2 coated textiles, we aimed to produce heterostructures based on these two 2D materials. For bilayered structures, we first coated the textiles with MoS_2 (one to five coating layers), followed by graphene coating (one to five layers). This resulted in 25 configurations (Table S1, Section 1 in the Supporting Information). Figure 3b illustrates the changes in the resistance for the bilayered textiles with varying coating layers in each configuration. The single MoS_2 -single graphene coated textile (M1G1) exhibited a resistance of $\sim 1401 \Omega \text{ cm}^{-1}$. As the number of graphene coatings on top of the MoS_2 layer increased, the sheet resistance continued to decrease. At the second graphene coating (M1G2), the resistance reached $\sim 483.1 \Omega \text{ cm}^{-1}$, which further decreased to $\sim 203.43 \Omega \text{ cm}^{-1}$ after five graphene coatings (M1G5). This phenomenon can be attributed to the increased deposition of conductive material (Figure 3f) on MoS_2 -coated textiles with each additional graphene layer. We also varied the number of MoS_2 base coating layers. It was observed that the sheet resistance decreased by $\sim 80\%$ (from ~ 1401 to $\sim 274.9 \Omega \text{ cm}^{-1}$) between the M1G1 and M5G1 layered textiles. Ultimately, the configuration with the lowest sheet resistance was achieved with M5G5 layered textiles, measuring $\sim 110.75 \Omega \text{ cm}^{-1}$, which was around $\sim 60\%$ lower than that of the M5G1 layered textiles.

To explore the impact of heterostructures on textiles, we investigated trilayered configurations for achieving conductive e-textiles. Initially, we coated the textiles with graphene using a pad-dry method. Subsequently, MoS_2 was applied onto the graphene-coated textiles, followed by an additional graphene layer deposition using the same method. This resulted in another 25 configurations (Table S1, Section 1 in the Supporting Information). Figure 3c illustrates the changes in sheet resistance for the trilayered textiles with varying coating layers in each configuration. The single graphene-single MoS_2 -single graphene (G1M1G1) layered textiles exhibited a

resistance of $\sim 789.8 \Omega \text{ cm}^{-1}$. Increasing the number of MoS_2 and graphene layers contributed to a reduction in the resistance. As the number of MoS_2 layers increased between two single graphene layers (G1-M(*x*)-G1 configuration), the resistance progressively decreased. For the G1M5G1 layer, the resistance measured was approximately $\sim 226.85 \Omega \text{ cm}^{-1}$, which was $\sim 71.27\%$ of that of the initial G1M1G1 layer. Increasing the graphene layers also led to a reduction in the resistance. The G5M1G5 layer exhibited a resistance of $\sim 126 \Omega \text{ cm}^{-1}$, corresponding to an $\sim 84\%$ reduction compared to the initial G1M1G1 layer. Furthermore, increasing all coating layers, including the initial graphene, intermediate MoS_2 , and final graphene layers, significantly reduced the resistance. The configuration with the lowest resistance was achieved with G5M5G5, measuring $\sim 74 \Omega \text{ cm}^{-1}$, representing an $\sim 90.6\%$ reduction compared to the initial G1M1G1 layer. Notably, the trilayered structure demonstrated significantly lower resistance compared to the bilayered structures due to an overall greater deposition of active materials (Figure 3g). The flexibility of the several coated e-textiles was also evaluated. The change in their electrical resistances per 12 cm length during bending, compression, and folding were measured. The cord length, which was measured by the grip distance of the sample ends during the experiment, was changed (10 to 120 mm) when the fabrics were bent and compressed. Similar to the graphene coated textiles (Figure S2a left, Section 3, in the Supporting Information), no significant changes in the resistance ($\Delta R/R_0$) were observed during bending and compression of the heterostructure coated textiles (Figure 3h). Even during folding–releasing operations, the changes in the resistance of the coated textiles were found to be negligible, proving the outstanding flexibility of heterostructure based textiles (Figure S2a right, Section 3, in the Supporting Information). It is worth noting that no visible changes in appearance or shape or creasing were observed due to those mechanical actions (bending, compression, and folding cycles) of the heterostructure-based wearable e-textiles (Figure S2b–e, Section 3, in the Supporting Information).

Electrochemical Characterization of Heterostructure-Based Textile Supercapacitors. Initially, we utilized multiple graphene layer coated textiles as electrodes to fabricate a graphene based symmetric textile supercapacitor. A thorough analysis of the cyclic voltammetry (CV), galvanostatic charge–discharge (GCD), and electrical impedance spectroscopy (EIS) was carried out for the capacitor with the highest capacitance (Section 4 in the Supporting Information). The supercapacitor with a single graphene coating (G1 electrodes) exhibited an areal capacitance of $\sim 7.74 \text{ mF cm}^{-2}$ at a scan rate of 1 mV s^{-1} . The highest areal capacitance of $\sim 80.19 \text{ mF cm}^{-2}$ at a scan rate of 1 mV s^{-1} was achieved with the textile supercapacitor fabricated using 10 graphene coating layers (G10). Similarly, we also fabricated MoS_2 -based symmetric textile supercapacitors (Section 5 in the Supporting Information). Being a semiconductor, the highest areal capacitance with bare MoS_2 was achieved with 10 coating layers (M10) at $\sim 7.1 \text{ mF cm}^{-2}$ and a scan rate of 1 mV s^{-1} . To enhance the capacitance performance of our textile supercapacitors, we explored a combination of heterostructures by depositing both graphene and MoS_2 onto the textile electrodes. We initially coated textiles with MoS_2 at different layer configurations (M*x*, where *x* is the number of coating layers from 1 to 5), followed by graphene coating at different layer configurations (G*x*, where *x* is the number of coating

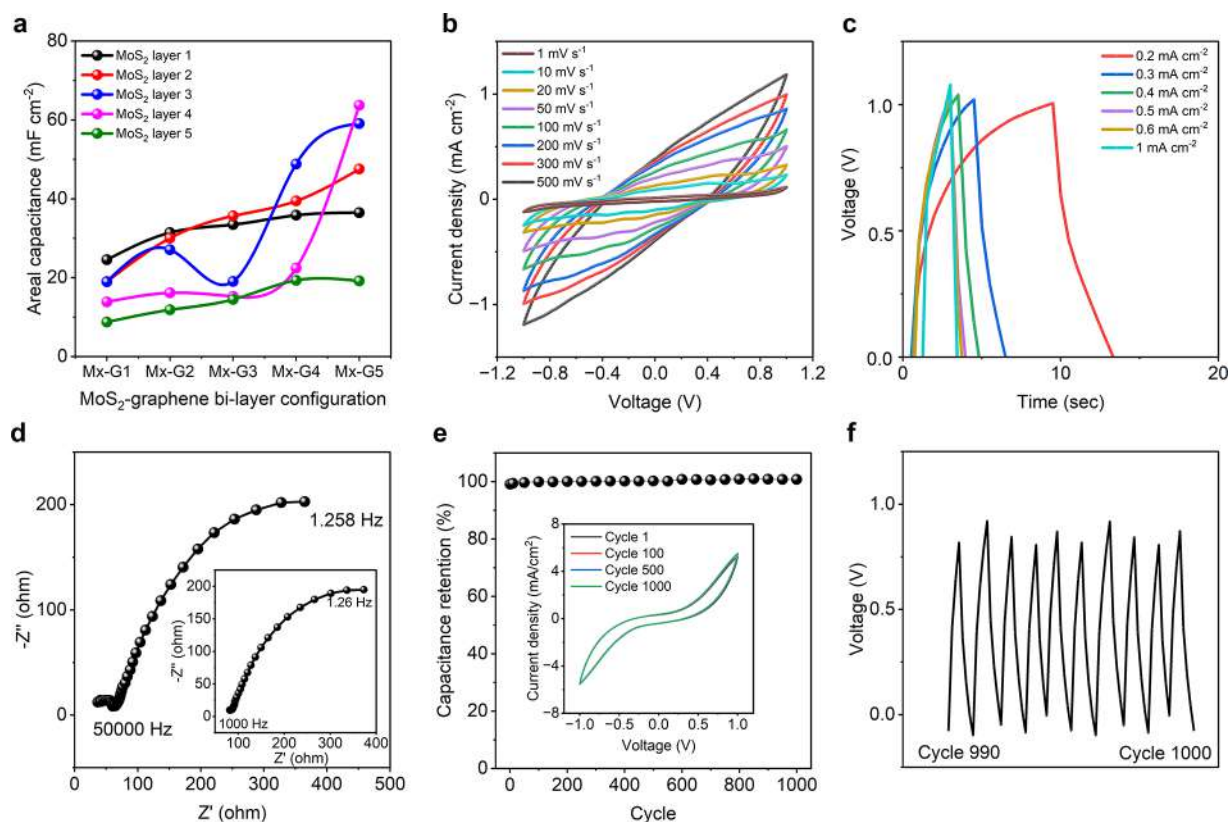


Figure 4. MoS₂-graphene bilayer coated textile supercapacitor. (a) Change of areal capacitance with increase of coating layers. (b) Cyclic voltammetry curves of the GSM4 coated textile supercapacitor at various scan rates. (c) Charge–discharge profile of the GSM4 coated textile supercapacitor at different current densities. (d) Electrical impedance spectroscopy of the device at high frequency. The inset shows the response of the supercapacitor device at low frequency. (e) Capacitance retention of the GSM4 coated textile supercapacitor device up to 1000 cycles. The inset shows the CV curves at the first, 100th, 500th and 1000th cycles. (f) Cyclic test of the supercapacitor (from 990th to 1000th cycles).

layers from 1 to 5). These bilayered configurations of MoS₂ and graphene (Mx-Gx) coated textiles were used as electrodes for the supercapacitors and exhibited the characteristics of a hybrid supercapacitor (ultracapacitor), combining the principles of double-layer capacitance and pseudocapacitance.

A total of 25 samples were fabricated to investigate the effect of bilayered configurations on the areal capacitance of the textile supercapacitors. Figure 4a demonstrates the change of areal capacitance for different layer configurations. The highest areal capacitance of ~ 36.49 mF cm⁻² was achieved when textiles were coated with a single layer of MoS₂ followed by five layers of graphene (M1G5 configuration) at a scan rate of 1 mV s⁻¹. However, increasing the number of MoS₂ layers under a single graphene layer led to a decrease in the areal capacitance. The lowest value of ~ 8.735 mF cm⁻² was obtained when textiles were coated with five layers of MoS₂ under a single graphene layer (M5G1 configuration). Similarly, increasing the number of graphene layers while keeping a single MoS₂ layer also resulted in increased capacitance up to ~ 31.435 mF cm⁻² for the M1G2 configuration. Among the 25 configurations, the highest areal capacitance of ~ 63.73 mF cm⁻² was achieved when textiles were coated with four layers of MoS₂ covered by five layers of graphene (M4G5 configuration). Interestingly, further increasing the number of MoS₂ layers under the graphene layers led to a dramatic reduction in the areal capacitance to ~ 19.16 mF cm⁻². This could be attributed to the excessive amount of graphene interfering with the conductivity of the MoS₂ flakes. There

exists an optimum quantity of both graphene and MoS₂ for achieving ideal hybrid capacitance behavior. We note that the areal capacitance of the MoS₂-graphene bilayered electrode based symmetric textile capacitor was almost similar to that of the graphene electrode based symmetric textile supercapacitor, exhibiting 71.62 mF cm⁻² at 9 coating layers, reaching 80.18 mF cm⁻² after 10th coating layer (Figure S3a, Section 4, in the Supporting Information). However, a textile supercapacitor composed of only MoS₂ electrodes exhibited the highest areal capacitance of only 7.1 mF cm⁻² after 10 coating layers (Figure S4a, section 5, in the Supporting Information).

Several electrochemical tests (CV, GCD, and EIS) were carried out for the best-performing supercapacitor based on M4G5 electrodes. The CV curves exhibited near-rectangular shapes at all tested scan rates, indicating ideal capacitance behavior (Figure 4b). Though for only graphene- and only MoS₂-based supercapacitors, the current density reaches ~ 1.74 mA cm⁻² (Figure S3b, Section 4, in the Supporting Information) and 1.08 mA cm⁻² (Figure S4b) respectively, for the bilayered structure, the current density reaches a maximum of only ~ 1.19 mA cm⁻². The charge–discharge profiles (Figure 4c) showed no plateaus or bends, confirming the absence of redox reactions. The slight potential drop observed at the beginning of the discharge curve was due to the device's ESR, but it did not significantly affect the conductivity or charge barrier of the electrodes. It is to note that, at a current density of 0.2 mA cm⁻², the charge–discharge took ~ 206 s for the graphene-based supercapacitor (Figure

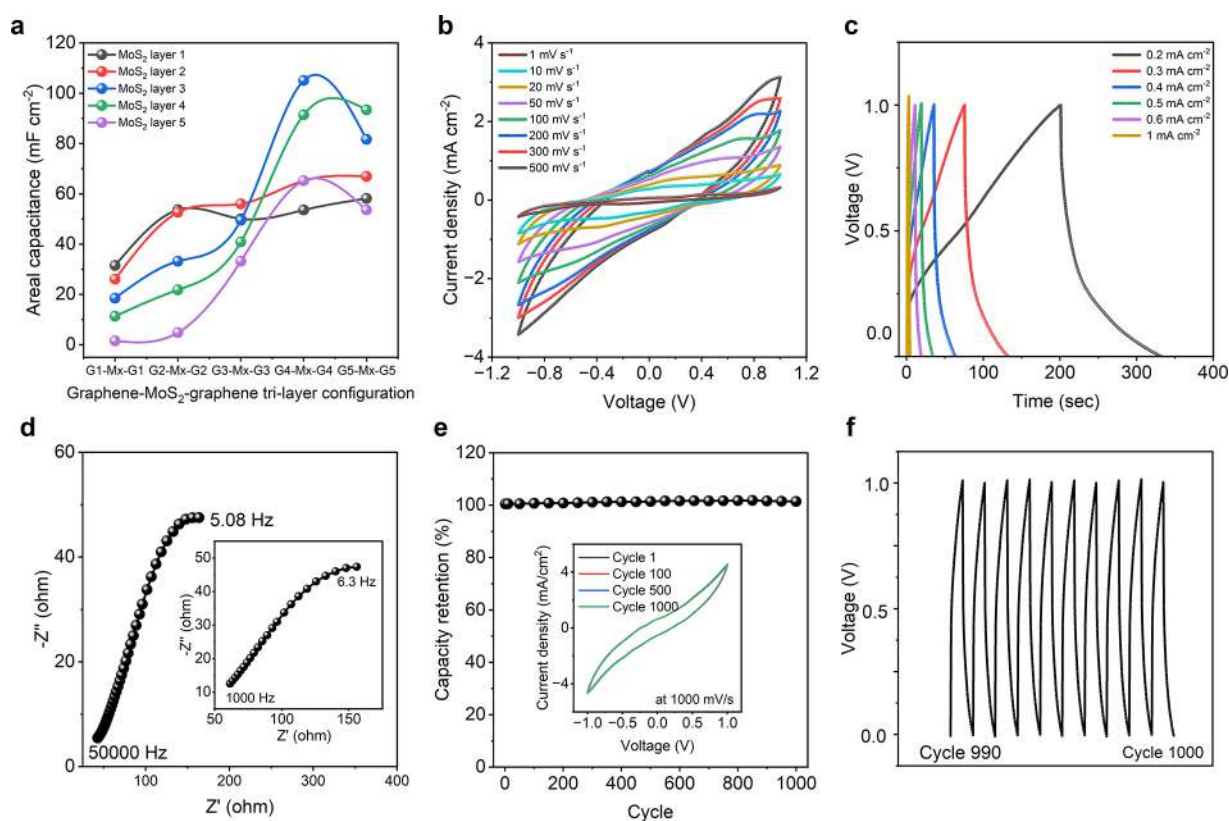


Figure 5. Graphene-MoS₂-graphene trilayer coated textile supercapacitor (a) Change of areal capacitance with increase of coating layers. (b) Cyclic voltammetry curves of the G4M3G4 coated textile supercapacitor at various scan rates. (c) Charge–discharge profile of the G4M3G4 coated textile supercapacitor at different current densities. (d) Electrical impedance spectroscopy of the device at the high frequency range. The inset shows the response of the supercapacitor device at the low frequency range. (e) Capacitance retention of the G4M3G4 coated textile supercapacitor device up to 1000 cycles. The inset shows the CV curves at first, 100th, 500th and 1000th cycles. (f) Cyclic test of the supercapacitor (from 990th to 1000th cycles).

S3c, Section 4, in the Supporting Information) and ~ 8.5 s for the MoS₂-based supercapacitor (Figure S4c, Section 5, in the Supporting Information). In contrast, the MoS₂-graphene bilayered electrode-based textile supercapacitor took ~ 13 s at the same current density. The EIS results (Figure 4d) demonstrated an ESR of ~ 81.63 Ω at a lower frequency range (1 kHz), which decreased to ~ 36.89 Ω at a higher frequency range (50 kHz). The graphene and MoS₂ exhibited ESRs of ~ 37.01 and ~ 29.44 Ω at a lower frequency range (1 kHz) and ~ 26.78 Ω at a higher frequency range (50 kHz) (Figures S3d and S4d in the Supporting Information). The Nyquist plot exhibited a 45° bend at the low-frequency range, indicating the ideal behavior of a capacitor, Figure 4d.

We evaluated the electrochemical stability of the supercapacitor by examining its long-term charge–discharge behavior at a current density of 1 mA cm⁻². The device retained its initial capacitance even after 1000 cycles, demonstrating exceptional stability (Figure 4e). The inset in the figure illustrates the CV profile of the supercapacitor up to 1000 cycles, showing no deviations. To further illustrate this stability, Figure 4f displays the charge–discharge curves specifically from the 990th to the 1000th cycle of the GCD tests. The M4G5 supercapacitor, without the use of any current collector, exhibited an impressive areal energy density of ~ 35.41 $\mu\text{Wh cm}^{-2}$ (~ 44.55 $\mu\text{Wh cm}^{-2}$ for graphene, ~ 3.94 $\mu\text{Wh cm}^{-2}$ for MoS₂) and a power density of 8497.33 $\mu\text{W cm}^{-2}$ (~ 581.05 $\mu\text{W cm}^{-2}$ for graphene and ~ 3550 $\mu\text{W cm}^{-2}$ for MoS₂). Additionally, it achieved a specific energy density of

9.32 Wh kg⁻¹ (~ 12.73 Wh kg⁻¹ for graphene and ~ 1.59 Wh kg⁻¹ for MoS₂) and a power density of $\sim 2,236.14$ W kg⁻¹, (~ 166.01 W kg⁻¹ for graphene and ~ 1420 W kg⁻¹ for MoS₂). The exceptionally high power density shows promise for our textile supercapacitor for next-generation wearable applications.

To achieve higher capacitance performance of our textile supercapacitor, we introduced another initial graphene layer on the previous bilayer configuration, resulting in a trilayered heterostructure component configuration. Initially, we coated textiles with graphene at different layer configurations (G_x, where x is the number of coating layers, 1 to 5). These textiles were then coated with several MoS₂ layers at varying configurations (M_x, where x is the number of coating layers, 1 to 5). Finally, the graphene-MoS₂ coated textiles were further coated with graphene at different layer configurations (G_x, where x is the number of coating layers, 1 to 5). Textiles coated with several trilayered configuration of 2D materials (G_x-M_x-G_x) were then utilized as supercapacitor electrodes. Similar to our bilayered structure, the graphene-MoS₂-graphene trilayered electrodes exhibited a hybrid capacitance behavior when fabricated into a supercapacitor.

Figure 5a demonstrates the change in the areal capacitance of the textile supercapacitors fabricated with graphene-MoS₂-graphene trilayers in various configurations. Like the bilayered structure, we fabricated a total of 25 coated samples to evaluate the effect of trilayered textile electrodes for supercapacitor applications. As observed, supercapacitors fabricated with

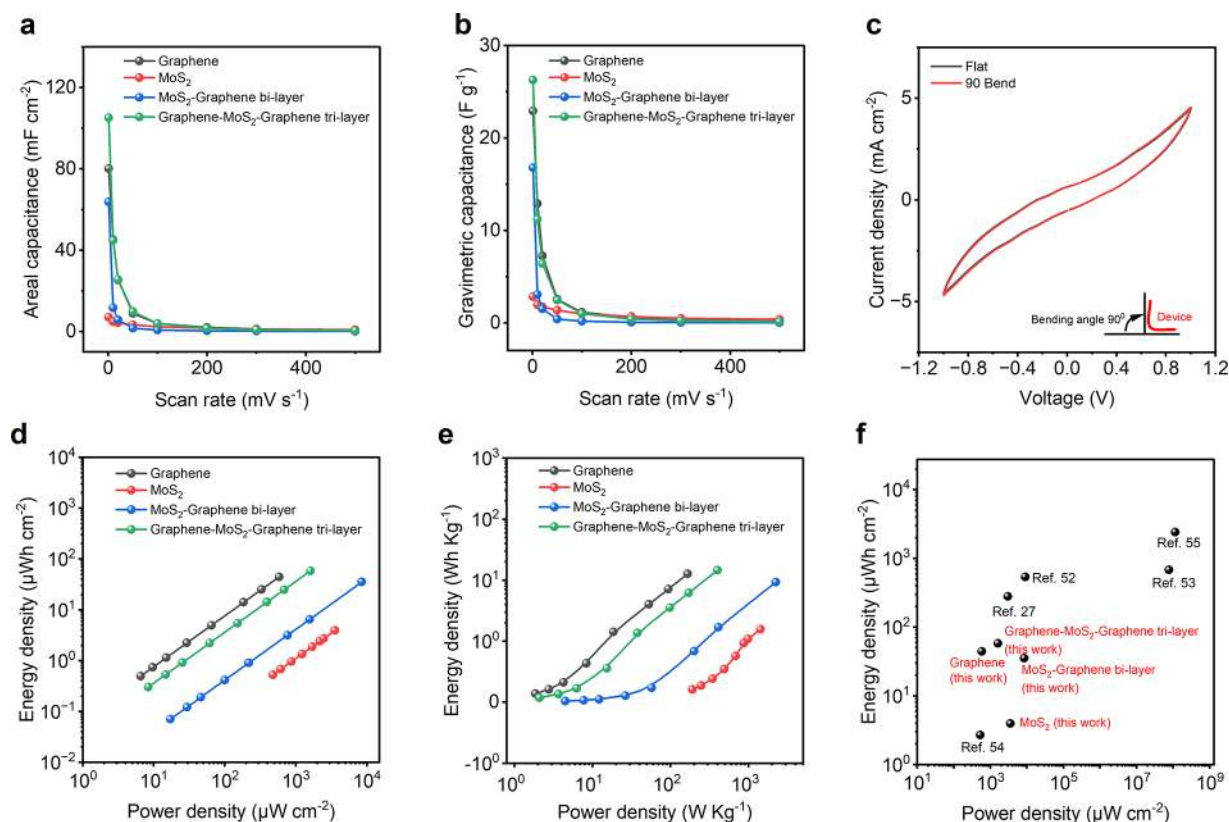


Figure 6. Performance of the 2DM heterostructure based textile supercapacitors. (a) Areal capacitance of 4 as-fabricated textile supercapacitors at different scan rates. (b) Gravimetric capacitance of 4 as-fabricated textile supercapacitors at different scan rates. (c) CV curves of the G4M3G4 supercapacitor in flat and bent (at 90° angle) condition. (d) Ragone plot showing comparison of 4 as-fabricated supercapacitor performances (in terms of areal energy and power density). (e) Ragone plot showing comparison of 4 as-fabricated supercapacitor performances (in terms of specific energy and power density). (f) Ragone plot showing comparison of 4 as-fabricated supercapacitor performances with others in literature.

electrodes containing a single layer of graphene, followed by a single layer of MoS₂ and a final single layer of graphene (i.e., G1M1G1), exhibited an areal capacitance of ~ 31.48 mF cm⁻² at a scan rate of 1 mV s⁻¹. Similar to the bilayered textile SCs, increasing the number of graphene layers enhanced the areal capacitance, reaching values of ~ 53.58 and ~ 58.16 mF cm⁻² at the same scan rate for G4M1G4 and G5M1G5 configurations, respectively. Interestingly, increasing the number of MoS₂ layers between the top and bottom graphene layers further improved the supercapacitor's areal capacitance. With one MoS₂ layer in between top 4-layer and bottom 4-layer graphene the capacitance was ~ 53.58 mF cm⁻², which increased to ~ 65.21 mF cm⁻² with an increase of another layer of MoS₂. The G4M3G4 configuration achieved the highest value of ~ 105.08 mF cm⁻² at a scan rate of 1 mV s⁻¹. However, further increases in the number of MoS₂ layers reduced the capacitance to ~ 91.37 mF cm⁻² (G4M4G4) and ~ 65.21 mF cm⁻² (G4M5G4) at the same scan rate. This phenomenon could be attributed to the fact that the addition of a layer of MoS₂ contributes to fill the voids on the graphene surface, providing additional active sites for charge storage (pseudocapacitance in the case of MoS₂) and improving the overall capacitance. After a certain limit, the excess amount of MoS₂ starts to interfere with the overall charge storage of the structure. Since MoS₂ is a semiconductor material, the presence of excess amount might have obstructed the capacitive behavior of the EDL graphene material as well as the overall heterostructure.

A similar trend was observed for the G5 configuration of trilayered structures. The supercapacitor with a G5M1G5 electrode exhibited an areal capacitance of ~ 58.16 mF cm⁻² at a scan rate of 1 mV s⁻¹, which increased to ~ 93.4 mF cm⁻² at the same scan rate. However, further increases in the number of MoS₂ layers reduced the capacitance to ~ 53.58 mF cm⁻². This phenomenon can be attributed to the amount of active material loaded into each coating layer. For example, the total number of coating layers was 3 for G1M1G1 (~ 31.48 mF cm⁻²), 11 for G5M1G5 (~ 58.16 mF cm⁻²), 11 for G4M3G4 (~ 105.08 mF cm⁻²), and 14 for G5M4G5 (~ 93.4 mF cm⁻²). Textiles can absorb active material up to a certain limit, and beyond saturation, additional coating hinders performance rather than adding functionality. When considering the 11-layered structures (G5M1G5 and G4M3G4), it is evident that despite the reduced amount of highly conductive graphene, the introduction of a semiconductor material within a certain limit increases the capacitance of the fabricated supercapacitor by $\sim 80.69\%$. The effect of MoS₂ presence in the supercapacitor is also evident in electrodes fabricated with G4M1G4 and G4M3G4 structures. The addition of 2 MoS₂ coating layers between the G4-Mx-G4 configuration contributes to an enhancement of $\sim 96.14\%$ in areal capacitance.

We conducted a comprehensive analysis of the electrochemical performance (CV, GCD, and EIS) of our highest-performing supercapacitor configuration (G4M3G4). The CV curves exhibited nearly rectangular shapes at all scan rates (Figure 5b), indicating ideal capacitance behavior. As

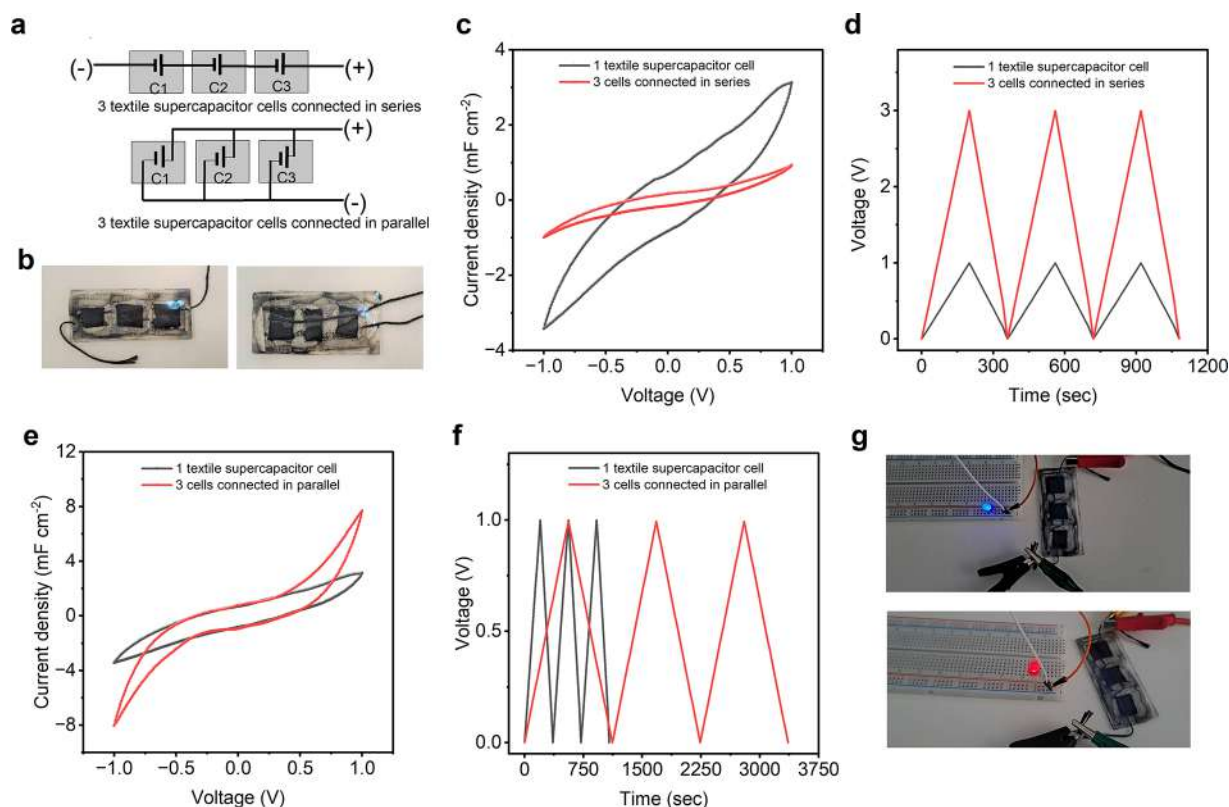


Figure 7. Small-scale integration of 2DM heterostructure based textile supercapacitor. (a) Schematic of 3 supercapacitor cells in series (top) and parallel (bottom) connection. (b) Three as-fabricated textile supercapacitor cells connected in series (left) and parallel (right) connection. (c) CV profile of 1 supercapacitor cell versus 3 supercapacitor cells connected in series (at scan rate 500 mV s^{-1}). (d) GCD curve of 1 supercapacitor cell versus 3 supercapacitor cells connected in series (at current density 0.2 mA cm^{-2}). (e) CV profile of 1 supercapacitor cell versus 3 supercapacitor cells connected in parallel (at scan rate 500 mV s^{-1}). (f) GCD curve of 1 supercapacitor cell versus 3 supercapacitor cells connected in parallel (at current density 0.2 mA cm^{-2}). (g) Three supercapacitor cells connected in series powering LEDs.

previously discussed, in comparison to the other configurations, the current density reaches a maximum of $\sim 3.13 \text{ mA cm}^{-2}$. The absence of redox peaks within the tested electrochemical windows suggests complete coverage of cotton fibers by the graphene-based ink. The charge–discharge profile (Figure 5c) of the G4M3G4 supercapacitor showed no visible plateaus or bends associated with the redox reactions. The minor potential drop observed initially can be attributed to the energy consumption of the device's equivalent series resistance (ESR), which still ensures good conductivity and low charge barrier of the electrodes. It should be noted that the charge–discharge time was extended up to 332 s compared to other heterostructure supercapacitors at the same current density of 0.2 mA cm^{-2} . The EIS analysis revealed a low equivalent series resistance (ESR) of $\sim 61.47 \Omega$ at a lower frequency range (1 kHz) that decreased to $\sim 42.87 \Omega$ at a higher frequency range (50 kHz), as indicated by the Nyquist plot (Figure 5d). The proximity of the vertical lines to the imaginary axis suggests that the supercapacitor behavior closely resembles that of an ideal capacitor. We also investigated the electrochemical stability of the supercapacitor through long-term charge–discharge curves at a current density of 1 mA cm^{-2} . The device maintained its initial capacitance even after 1000 cycles, demonstrating excellent stability (Figure 5e). The inset in Figure 5e depicts the CV profile of the supercapacitor up to 1000 cycles, showing no deviation. Furthermore, Figure 5f presents the charge–discharge curves of the 990th to 1000th

cycle in the GCD tests. The G4M3G4 supercapacitor achieved the highest areal energy density of $\sim 58.37 \mu\text{Wh cm}^{-2}$ ($\sim 35.41 \mu\text{Wh cm}^{-2}$ for M4G5 bilayered supercapacitor, $\sim 44.55 \mu\text{Wh cm}^{-2}$ for graphene, and $\sim 3.94 \mu\text{Wh cm}^{-2}$ for MoS_2 supercapacitor). However, the power density was $1604.27 \text{ mW cm}^{-2}$ (though the highest was for the M4G5 bilayered supercapacitor at $\sim 8497.33 \mu\text{W cm}^{-2}$, with $\sim 581.05 \mu\text{W cm}^{-2}$ for graphene and $\sim 3550 \mu\text{W cm}^{-2}$ for MoS_2 supercapacitor). The specific energy density of $\sim 14.59 \text{ Wh kg}^{-1}$ was achieved, whereas it was $\sim 9.317 \text{ Wh kg}^{-1}$ for M4G5 bilayered, $\sim 12.73 \text{ Wh kg}^{-1}$ for graphene, and 1.59 Wh kg^{-1} for MoS_2 supercapacitor. The power density was reported as $\sim 401.06 \text{ W kg}^{-1}$ ($\sim 2,236.14 \text{ W kg}^{-1}$ for M4G5 bilayer $\sim 166.01 \text{ W kg}^{-1}$ for graphene, and $\sim 1420 \text{ W kg}^{-1}$ for MoS_2 supercapacitor). The exceptionally high energy and power densities show promise for our textile supercapacitor for next-generation wearable applications.

Figure 6 presents a performance analysis of our fabricated supercapacitors. Areal and gravimetric capacitances, as a function of scan rate, are depicted in Figure 6a,b, respectively. It can be observed that higher scan rates result in lower capacitance, possibly due to insufficient time for electrolytes to adsorb and desorb on the electrode surface.⁵⁰ At lower scan rates, electrolyte ion diffusion becomes more efficient, reaching both the external surface and inner active sites of the electrode material.⁵¹ In Figure 6c, the CV curves of the device are shown when it is both flat and bent at a 90° angle, demonstrating the

device's stable electrochemical performance, even under bending conditions. The Ragone plots in Figure 6d,e showcase the energy and power densities of our fabricated supercapacitors. Notably, our graphene-MoS₂-graphene trilayered textiles exhibit impressive energy and power densities of ~58.38 $\mu\text{Wh cm}^{-2}$ and ~1604.27 $\mu\text{W cm}^{-2}$, respectively. These values are either superior or comparable to those reported in previous studies (Figure 6f) on graphene-based wearable supercapacitors.^{27,52–60}

Small-Scale Integration of Textile Supercapacitors. In practical applications, a single supercapacitor often does not provide sufficient voltage and current to power circuits effectively.⁶¹ Therefore, multiple supercapacitors are commonly connected in series and/or in parallel (Figure 7a) to form a "bank" with a specific voltage and capacitance.⁸ Figure 7b shows the small-scale connection of 3 supercapacitors in series (left) and parallel (right). The conductive current collector threads were employed as connection wires for the supercapacitors. Figure 7c shows the CV profiles, and Figure 7d shows the GCD curves of the three series-connected textile supercapacitors. It is evident that the series connection increases the voltage window from 1 to 3 V, with a reduction in capacitance to approximately one-third of a single device. On the other hand, Figure 7e displays the CV profiles, and Figure 7f presents the GCD curves for the three parallel-connected textile supercapacitors. In contrast to the series connection, the parallel connection exhibits nearly 3 times higher capacitance compared to a single device while maintaining the same operating voltage window. Furthermore, the parallelly connected supercapacitors were capable of powering different colored LEDs with varying voltage requirements, as depicted in Figure 7g. This highlights the capability of our textile-based flexible supercapacitors to meet the increasing energy needs of wearable electronics in the future.^{62–64}

CONCLUSIONS

In this work, we report the scalable production of two very promising 2D materials, namely graphene and MoS₂, through a microfluidization technique. Considering the design flexibility of 2D materials for tuning their electronic properties, we report a graphene and MoS₂ heterostructure for wearable e-textiles based supercapacitor fabrication. Supercapacitors were fabricated from graphene-coated textiles, MoS₂-coated textiles, MoS₂-graphene bilayer coated textiles, and graphene-MoS₂-graphene trilayered textiles. The highest areal capacitance was obtained from the supercapacitor fabricated from the graphene-MoS₂-graphene trilayered textile electrodes of ~105.08 mF cm⁻² at a scan rate of 1 mV s⁻¹. The energy and power densities were ~58.38 $\mu\text{Wh cm}^{-2}$ and ~1604.27 $\mu\text{W cm}^{-2}$, respectively. Though the energy density was highest for the trilayered electrode-based supercapacitor, the highest power density was achieved for the MoS₂-graphene bilayered electrode based supercapacitor. The supercapacitors showed an outstanding capacitance retention (~100%) after 1000 cycles. The integration of 3 as-fabricated supercapacitors enable powering up an LED. Overall, these outstanding performances exhibit prospects of 2D material heterostructures to revolutionize the e-textiles, especially the field of energy storage. Industrially the most-known and highly scalable coating method was exploited, which demonstrates the potential of reported fabrication process for the large-scale

production of 2D heterostructure based wearable e-textile supercapacitors.

EXPERIMENTAL METHODS

Materials. A water-based graphene and MoS₂ dispersion (100 g L⁻¹) was prepared using a microfluidization technique. Natural flake graphite (average lateral size ~50 μm) and MoS₂ were purchased from Sigma-Aldrich, UK. Sodium deoxycholate (SDC) powder was purchased from Sigma-Aldrich, UK, and used as received. 100% cotton fabric (desized, scoured, and bleached, which creates a ready-to-dye fabric) was manufactured at Square Fashions Limited (Bangladesh).

Microfluidic Exfoliation of Graphene and MoS₂. Microfluidization is characterized by a homogenization technique; a high pressure (up to 207 MPa)⁶⁵ is applied to a fluid, which forces the liquid to pass through a microchannel (diameter, $d < 100 \mu\text{m}$). This technique offers the advantage of applying high $\dot{\gamma} > 10^6 \text{ s}^{-1}$ to the whole dispersion,⁶⁶ unlike just locally as in the case of sonication and shear-mixing. Previous studies reported a microfluidization technique for a range of purposes such as the production of polymer nanosuspensions,⁶⁵ liposome nanoparticles,⁶⁷ aspirin nanoemulsions,⁶⁸ oil-in-water nanoemulsions,⁴⁰ and deagglomeration and dispersion of carbon nanotubes.⁶⁹ In this study, we used a microfluidization technique to exfoliate graphene and MoS₂ in a scalable quantity following previously reported methods.^{38,44} Briefly, 50 g of graphite powder and 10 g of SDC were placed in a glass bottle and mixed with 500 mL of deionized (DI) water. The mixture was then sonicated for 30 min using an ultrasound bath to allow homogeneous dispersion and placed in an input reservoir of a Microfluidizer (M-110P Microfluidizer, Microfluidics Corp, USA). The dispersion was slowly passed through "Z-type" microfluidic channels of ~200 and ~87 μm diameter with diamond construction at high pressure (~200 MPa). This allows the exfoliation of graphite to few-layer graphene at 100 mL min⁻¹ flow under a high shear rate (~10⁸ s⁻¹) with 100% exfoliation yield. The exfoliated dispersion was then passed through a cooling channel surrounded by cold water (~25 °C) to prevent overheating of the dispersion and collected. This process was repeated 20 times to produce graphene flakes. MoS₂ was also produced following the same method. The obtained dispersion was used as a conductive ink for textile coating.

Scalable Fabrication of Conductive Textiles from 2D Materials Heterostructure. Textile fabrics were padded one dip and one nip through graphene dispersions to a wet pick-up of ~80% on the weight of the fabric (o.w.f.). The wet pick-up % was calculated using the following formula:

$$\text{pick-up \%} = \frac{\text{coated fabric weight} - \text{untreated dry fabric weight}}{\text{untreated dry fabric weight}} \times 100$$

A simple laboratory-scale padder BVHP 2 Bowl (Roaches, UK) was used for coating. The padding roller was set at a speed of 1 m min⁻¹ with a pressure of 0.74 bar. The padded fabrics were subsequently dried at ~100 °C for 5 min in a Mini Thermo Oven, Type 350 Special (Roaches, UK), and studied for e-textile application. Several coated samples were prepared using multiple (1–10) padding passes to establish any improvement in the electrical conductivity of the coated fabrics. We carried out a similar process for MoS₂ as a monomaterial control sample. For the MoS₂-graphene bilayered textiles, we coated the fabrics with MoS₂ first at different configurations (from 1 to 5 layers). The coated fabrics were then again coated with graphene dispersions (from 1 to 5 layers). A total of 25 samples was thus prepared. The resistance of each sample was assessed to check the improvement in the electrical conductivity with the number of coating layers.

For the trilayered structure of graphene and MoS₂, the fabrics were first coated with graphene dispersion (up to 5 layers). The samples were then coated with MoS₂ with the same layer variation (from 1 to 5 layers). The coated samples were further coated with graphene,

keeping the layer variation similar (from 1 to 5 layers). Similar to bilayered structures, a total of 25 samples were produced for obtaining the optimum conductivity of the coated textiles. The total configuration of samples is given in Table S1. The surface topographies of the control cotton fabric, graphene coated fabric, MoS₂ coated, MoS₂-graphene bilayer coated, and graphene-MoS₂-graphene trilayer coated fabric were analyzed using a FEI Quanta 650 field emission scanning electron microscope (SEM).

Supercapacitor Device Fabrication. The 2D material heterostructure coated textiles were used as electrodes, and the conductive textile thread was used as the current collector. The coated electrodes were coated with a hydrogel-polymer electrolyte, poly(vinyl alcohol) (PVA) doped with H₂SO₄. The H₂SO₄-PVA gel electrolyte was prepared as follows: 1 g of H₂SO₄ was added to 10 mL of deionized water, and then 1 g of PVA (molecular weight: 89000–98000) was added. The whole mixture was then heated to 85 °C with stirring until the solution became clear. The electrolyte was drop-cast and left to dry overnight under ambient conditions to ensure that the electrolyte completely wetted the electrode and to allow for evaporation of any excess water. The textile electrodes were then sandwiched with a textile separator to form a textile supercapacitor.

Characterization of Supercapacitors. The electrochemical performances of the printed devices were investigated by cyclic voltammetry (CV), galvanostatic charge/discharge (GCD) tests, and electrochemical impedance spectroscopy (EIS). The electrochemical measurements were performed on an Iviumstat Electrochemical Interface. The CV tests were carried out in the potential range from –1.0 to 1.0 V at different scan rates. Galvanostatic charge–discharge measurements were at different current densities in the potential range of 0–1 V.

The ability to collect and store energy in the form of electrical charge per unit mass, namely, gravimetric capacitance (F g^{–1}), was calculated as per the following formulas:

$$C_m = \frac{A}{2smV}$$

$$C_m = \frac{i\Delta t}{m\Delta V}$$

The charge storage ability per unit area, namely areal capacitance (F cm^{–2}), was calculated as per the following formulas:

$$C_A = \frac{A}{2saV}$$

$$C_A = \frac{i\Delta t}{a\Delta V}$$

The amount of energy able to be delivered, i.e., energy density (Wh kg^{–1}), and how fast the energy can be delivered, namely, power density (W kg^{–1}), were calculated as per the formulas

$$E = \frac{1}{2}CV^2$$

$$P = \frac{E}{t}$$

where I = current density, V = voltage window, i = discharging current, Δv = discharge voltage, Δt = discharge time, A = integrated area of the CV curve, s = scan rate (mV s^{–1}), and m = mass of the electroactive material on both electrodes.

ASSOCIATED CONTENT

Supporting Information

The Supporting Information is available free of charge via the Internet at . The Supporting Information is available free of charge at <https://pubs.acs.org/doi/10.1021/acsnano.3c06181>.

Configurations of different coated samples (graphene, MoS₂, MoS₂-graphene bilayer, and graphene-MoS₂-graphene trilayer), SEM images of uncoated, MoS₂ 1

pass coated, and MoS₂ 10 pass coated, flexibility of the graphene-coated textiles during bending and compression, flexibility of graphene coated, MoS₂-graphene bilayer coated, and graphene-MoS₂-graphene trilayer coated textiles during folding–releasing cycles, graphene-coated textile and fabricated supercapacitor, MoS₂-coated textile and fabricated supercapacitor, MoS₂-graphene bilayer coated textile and fabricated supercapacitor, graphene-MoS₂-graphene trilayer coated textile and fabricated supercapacitor, characterization of graphene-coated textile supercapacitor, characterization of MoS₂-coated textile supercapacitor, and comparison of the capacitance performance of the heterostructure textile based supercapacitor with others in the literature (PDF)

AUTHOR INFORMATION

Corresponding Authors

Shaïla Afroj – Centre for Print Research (CFPR), University of the West of England (UWE), Bristol BS16 1QY, U.K.; National Graphene Institute (NGI), University of Manchester, Manchester M13 9PL, U.K.; orcid.org/0000-0002-0469-261X; Email: shaïla.afroj@uwe.ac.uk

Nazmul Karim – Centre for Print Research (CFPR), University of the West of England (UWE), Bristol BS16 1QY, U.K.; National Graphene Institute (NGI), University of Manchester, Manchester M13 9PL, U.K.; Advanced Textiles Research Group, Nottingham Trent University, Nottingham NG1 4GG, U.K.; orcid.org/0000-0002-4426-8995; Email: nazmul.karim@ntu.ac.uk

Author

Md Rashedul Islam – Centre for Print Research (CFPR), University of the West of England (UWE), Bristol BS16 1QY, U.K.

Complete contact information is available at: <https://pubs.acs.org/10.1021/acsnano.3c06181>

Notes

The authors declare no competing financial interest.

ACKNOWLEDGMENTS

The authors gratefully acknowledge funding from UKRI Research England, an Expanding Excellence in England (E3) grant, and a UWE partnership Ph.D. award.

REFERENCES

- (1) Chen, G.; Xiao, X.; Zhao, X.; Tat, T.; Bick, M.; Chen, J. Electronic Textiles for Wearable Point-of-Care Systems. *Chem. Rev.* **2022**, *122*, 3259–3291.
- (2) Islam, M. R.; Afroj, S.; Novoselov, K. S.; Karim, N. Smart Electronic Textile-Based Wearable Supercapacitors. *Adv. Science* **2022**, *9*, No. 2203856.
- (3) Thekkekara, L. V.; Gu, M. Large-Scale Waterproof and Stretchable Textile-Integrated Laser-Printed Graphene Energy Storages. *Sci. Rep.* **2019**, *9*, 11822.
- (4) Libanori, A.; Chen, G.; Zhao, X.; Zhou, Y.; Chen, J. Smart Textiles for Personalized Healthcare. *Nat. Electron.* **2022**, *5*, 142–156.
- (5) Chen, G.; Fang, Y.; Zhao, X.; Tat, T.; Chen, J. Textiles for Learning Tactile Interactions. *Nat. Electron.* **2021**, *4*, 175–176.
- (6) Yin, J.; Wang, S.; Di Carlo, A.; Chang, A.; Wan, X.; Xu, J.; Xiao, X.; Chen, J. Smart Textiles for Self-Powered Biomonitoring. *Med-X* **2023**, *1*, 3.

- (7) Tat, T.; Chen, G.; Zhao, X.; Zhou, Y.; Xu, J.; Chen, J. Smart Textiles for Healthcare and Sustainability. *ACS Nano* **2022**, *16*, 13301–13313.
- (8) El-Kady, M. F.; Kaner, R. B. Scalable Fabrication of High-Power Graphene Micro-Supercapacitors for Flexible and On-Chip Energy Storage. *Nat. Commun.* **2013**, *4*, 1475.
- (9) Novoselov, K. S.; Mishchenko, A.; Carvalho, A.; Castro Neto, A. H. 2D Materials and Van Der Waals Heterostructures. *Science* **2016**, *353*, 1.
- (10) Guo, H.-W.; Hu, Z.; Liu, Z.-B.; Tian, J.-G. Stacking of 2D Materials. *Adv. Funct. Mater.* **2021**, *31*, No. 2007810.
- (11) Wang, X.; Xia, F. Stacked 2D Materials Shed Light. *Nat. Mater.* **2015**, *14*, 264–265.
- (12) Wu, J. Understanding the Electric Double-Layer Structure, Capacitance, and Charging Dynamics. *Chem. Rev.* **2022**, *122*, 10821–10859.
- (13) Fleischmann, S.; Mitchell, J. B.; Wang, R.; Zhan, C.; Jiang, D.-e.; Presser, V.; Augustyn, V. Pseudocapacitance: From Fundamental Understanding To High Power Energy Storage Materials. *Chem. Rev.* **2020**, *120*, 6738–6782.
- (14) Sheberla, D.; Bachman, J. C.; Elias, J. S.; Sun, C.-J.; Shao-Horn, Y.; Dincă, M. Conductive MOF Electrodes for Stable Supercapacitors With High Areal Capacitance. *Nat. Mater.* **2017**, *16*, 220–224.
- (15) Choi, C.; Ashby, D. S.; Butts, D. M.; DeBlock, R. H.; Wei, Q.; Lau, J.; Dunn, B. Achieving High Energy Density and High Power Density With Pseudocapacitive Materials. *Nat. Rev. Mater.* **2020**, *5*, 5–19.
- (16) Lee, J.-S. M.; Briggs, M. E.; Hu, C.-C.; Cooper, A. I. Controlling Electric Double-Layer Capacitance and Pseudocapacitance In Heteroatom-Doped Carbons Derived From Hypercross-linked Microporous Polymers. *Nano Energy* **2018**, *46*, 277–289.
- (17) Geim, A. K.; Novoselov, K. S. The Rise of Graphene. *Nat. Mater.* **2007**, *6*, 183–191.
- (18) Islam, M. H.; Afroj, S.; Uddin, M. A.; Andreeva, D. V.; Novoselov, K. S.; Karim, N. Graphene and CNT-Based Smart Fiber-Reinforced Composites: A Review. *Adv. Funct. Mater.* **2022**, *32*, No. 2205723.
- (19) Afroj, S.; Britnell, L.; Hasan, T.; Andreeva, D. V.; Novoselov, K. S.; Karim, N. Graphene-Based Technologies for Tackling COVID-19 and Future Pandemics. *Adv. Funct. Mater.* **2021**, *31*, No. 2107407.
- (20) Islam, M. H.; Islam, M. R.; Dulal, M.; Afroj, S.; Karim, N. The Effect of Surface Treatments and Graphene-Based Modifications on Mechanical Properties of Natural Jute Fiber Composites: A Review. *iScience* **2022**, *25*, No. 103597.
- (21) Afroj, S.; Karim, N.; Wang, Z.; Tan, S.; He, P.; Holwill, M.; Ghazaryan, D.; Fernando, A.; Novoselov, K. S. Engineering Graphene Flakes for Wearable Textile Sensors via Highly Scalable and Ultrafast Yarn Dyeing Technique. *ACS Nano* **2019**, *13*, 3847–3857.
- (22) Karim, N.; Afroj, S.; Tan, S.; Novoselov, K. S.; Yeates, S. G. All Inkjet-Printed Graphene-Silver Composite Ink on Textiles for Highly Conductive Wearable Electronics Applications. *Sci. Rep.* **2019**, *9*, 8035.
- (23) Karim, N.; Afroj, S.; Leech, D.; Abdelkader, A. M. Flexible and Wearable Graphene-Based E-Textiles. In *Oxide Electronics*; Ray, A., Ed.; Wiley Online Library: 1998 and 2021; pp 565–566 and 21–49. DOI: 10.1002/9781119529538.ch2.
- (24) Karim, N.; Afroj, S.; Tan, S.; He, P.; Fernando, A.; Carr, C.; Novoselov, K. S. Scalable Production of Graphene-Based Wearable E-Textiles. *ACS Nano* **2017**, *11*, 12266–12275.
- (25) Afroj, S.; Tan, S.; Abdelkader, A. M.; Novoselov, K. S.; Karim, N. Highly Conductive, Scalable, and Machine Washable Graphene-Based E-Textiles for Multifunctional Wearable Electronic Applications. *Adv. Funct. Mater.* **2020**, *30*, No. 2000293.
- (26) Abdelkader, A. M.; Karim, N.; Vallés, C.; Afroj, S.; Novoselov, K. S.; Yeates, S. G. Ultraflexible and Robust Graphene Supercapacitors Printed on Textiles for Wearable Electronics Applications. *2D Mater.* **2017**, *4*, No. 035016.
- (27) Islam, M. R.; Afroj, S.; Beach, C.; Islam, M. H.; Parraman, C.; Abdelkader, A.; Casson, A. J.; Novoselov, K. S.; Karim, N. Fully Printed and Multifunctional Graphene-Based Wearable E-Textiles for Personalized Healthcare Applications. *iScience* **2022**, *25*, No. 103945.
- (28) Zhao, B.; Shen, D.; Zhang, Z.; Lu, P.; Hossain, M.; Li, J.; Li, B.; Duan, X. 2D Metallic Transition-Metal Dichalcogenides: Structures, Synthesis, Properties, and Applications. *Adv. Funct. Mater.* **2021**, *31*, No. 2105132.
- (29) Kumar, P.; Abuhimd, H.; Wahyudi, W.; Li, M.; Ming, J.; Li, L.-J. Review—Two-Dimensional Layered Materials for Energy Storage Applications. *ECS J. Solid State Sci. Technol.* **2016**, *5*, Q3021–Q3025.
- (30) Bello, I. T.; Adio, S. A.; Oladipo, A. O.; Adedokun, O.; Mathevu, L. E.; Dhlamini, M. S. Molybdenum Sulfide-Based Supercapacitors: From Synthetic, Bibliometric, and Qualitative Perspectives. *Int. J. Energy Res.* **2021**, *45*, 12665–12692.
- (31) Lee, C.-S.; Kim, T. H. Large-Scale Preparation of MoS₂/Graphene Composites for Electrochemical Detection of Morin. *ACS Appl. Nano Mater.* **2021**, *4*, 6668–6677.
- (32) Bertolazzi, S.; Krasnozhan, D.; Kis, A. Nonvolatile Memory Cells Based on MoS₂/Graphene Heterostructures. *ACS Nano* **2013**, *7*, 3246–3252.
- (33) Rendón-Patiño, A.; Domenech-Carbó, A.; Primo, A.; García, H. Superior Electrocatalytic Activity of MoS₂-Graphene as Superlattice. *Nanomaterials* **2020**, *10*, 839.
- (34) Liu, H.; Li, Z.; Song, W.; Yu, Y.; Pang, F.; Wang, T. MoS₂/Graphene Heterostructure Incorporated Passively Mode-Locked Fiber Laser: From Anomalous To Normal Average Dispersion. *Opt. Mater. Express* **2020**, *10*, 46–56.
- (35) Vikraman, D.; Rabani, I.; Hussain, S.; Sundaram, K.; Ramesh, S.; Kim, H.-S.; Seo, Y.-S.; Jung, J.; Kim, H.-S. Mixed-Phase MoS₂ Decorated Reduced Graphene Oxide Hybrid Composites For Efficient Symmetric Supercapacitors. *Int. J. Energy Res.* **2021**, *45*, 9193–9209.
- (36) Singh, K.; Kumar, S.; Agarwal, K.; Soni, K.; Ramana Gedela, V.; Ghosh, K. Three-Dimensional Graphene With MoS₂ Nanohybrid As Potential Energy Storage/Transfer Device. *Sci. Rep.* **2017**, *7*, 9458.
- (37) Dulal, M.; Islam, M. R.; Maiti, S.; Islam, M. H.; Ali, I.; Abdelkader, A. M.; Novoselov, K. S.; Afroj, S.; Karim, N. Smart and Multifunctional Fiber-Reinforced Composites of 2D heterostructure-Based Textiles. *Adv. Funct. Mater.* **2023**, No. 2305901.
- (38) Paton, K. R.; Anderson, J.; Pollard, A. J.; Sainsbury, T. Production of Few-Layer Graphene By Microfluidization. *Mater. Res. Express* **2017**, *4*, No. 025604.
- (39) Kotyla, T.; Kuo, F.; Moolchandani, V.; Wilson, T.; Nicolosi, R. Increased Bioavailability of a Transdermal Application of a Nano-Sized Emulsion Preparation. *Int. J. Pharm.* **2008**, *347*, 144–148.
- (40) Jafari, S. M.; He, Y.; Bhandari, B. Production of Sub-Micron Emulsions By Ultrasound and Microfluidization Techniques. *J. Food Eng.* **2007**, *82*, 478–488.
- (41) Tamer, I. M.; Moo-Young, M.; Chisti, Y. Disruption of *Alcaligenes latus* for Recovery of Poly(β -hydroxybutyric acid): Comparison of High-Pressure Homogenization, Bead Milling, and Chemically Induced Lysis. *Ind. Eng. Chem. Res.* **1998**, *37*, 1807–1814.
- (42) Carlson, A.; Signs, M.; Liermann, L.; Boor, R.; Jem, K. J. Mechanical Disruption of *Escherichia Coli* for Plasmid Recovery. *Biotechnol. Bioeng.* **1995**, *48*, 303–315.
- (43) Azoubel, S.; Magdassi, S. The Formation of Carbon Nanotube Dispersions by High Pressure Homogenization and Their Rapid Characterization By Analytical Centrifuge. *Carbon* **2010**, *48*, 3346–3352.
- (44) Karagiannidis, P. G.; Hodge, S. A.; Lombardi, L.; Tomarchio, F.; Decorde, N.; Milana, S.; Goykhman, I.; Su, Y.; Mesite, S. V.; Johnstone, D. N.; et al. Microfluidization of Graphite and Formulation of Graphene-Based Conductive Inks. *ACS Nano* **2017**, *11*, 2742–2755.
- (45) Yurdakul, H.; Göncü, Y.; Durukan, O.; Akay, A.; Seyhan, A. T.; Ay, N.; Turan, S. Nanoscopic characterization of two-dimensional (2D) boron nitride nanosheets (BNNs) produced by microfluidization. *Ceram. Int.* **2012**, *38*, 2187–2193.

- (46) Pace, G.; del Rio Castillo, A. E.; Lamperti, A.; Lauciello, S.; Bonaccorso, F. 2D Materials-Based Electrochemical Triboelectric Nanogenerators. *Adv. Mater.* **2023**, *35*, No. 2211037.
- (47) Li, Y.; Chen, Q.; Zhang, Z.; Li, Q.; Qiao, X. Effects of morphology and crystallinity of MoS₂ nanocrystals on the catalytic reduction of p-nitrophenol. *J. Nanopart. Res.* **2018**, *20*, 327.
- (48) Liu, N.; Kim, P.; Kim, J. H.; Ye, J. H.; Kim, S.; Lee, C. J. Large-Area Atomically Thin MoS₂ Nanosheets Prepared Using Electrochemical Exfoliation. *ACS Nano* **2014**, *8*, 6902–6910.
- (49) Zhou, S.; Gao, J.; Wang, S.; Fan, H.; Huang, J.; Liu, Y. Highly Efficient Removal of Cr(VI) from Water Based on Graphene Oxide Incorporated Flower-Like MoS₂ Nanocomposite Prepared In Situ Hydrothermal Synthesis. *Environ. Sci. Pollut. Res.* **2020**, *27*, 13882–13894.
- (50) Alkhalaf, S.; Ranaweera, C. K.; Kahol, P. K.; Siam, K.; Adhikari, H.; Mishra, S. R.; Perez, F.; Gupta, B. K.; Ramasamy, K.; Gupta, R. K. Electrochemical Energy Storage Performance of Electrospun CoMn₂O₄ Nanofibers. *J. Alloys Compd.* **2017**, *692*, 59–66.
- (51) Xie, Y.; Du, H. Electrochemical Capacitance of a Carbon Quantum Dots–Polypyrrole/Titania Nanotube Hybrid. *RSC Adv.* **2015**, *5*, 89689–89697.
- (52) Hu, Y.; Cheng, H.; Zhao, F.; Chen, N.; Jiang, L.; Feng, Z.; Qu, L. All-In-One Graphene Fiber Supercapacitor. *Nanoscale* **2014**, *6*, 6448–6451.
- (53) Beidaghi, M.; Wang, C. Micro-Supercapacitors Based on Interdigital Electrodes of Reduced Graphene Oxide and Carbon Nanotube Composites with Ultrahigh Power Handling Performance. *Adv. Funct. Mater.* **2012**, *22*, 4501–4510.
- (54) Noh, J.; Yoon, C. M.; Kim, Y. K.; Jang, J. High Performance Asymmetric Supercapacitor Twisted from Carbon Fiber/MnO₂ and Carbon Fiber/MoO₃. *Carbon* **2017**, *116*, 470–478.
- (55) Lin, J.; Zhang, C.; Yan, Z.; Zhu, Y.; Peng, Z.; Hauge, R. H.; Natelson, D.; Tour, J. M. 3-Dimensional Graphene Carbon Nanotube Carpet-Based Microsupercapacitors with High Electrochemical Performance. *Nano Lett.* **2013**, *13*, 72–78.
- (56) Ghasemi, F.; Jalali, M.; Abdollahi, A.; Mohammadi, S.; Sanaee, Z.; Mohajezadeh, S. A High Performance Supercapacitor Based On Decoration of MoS₂/Reduced Graphene Oxide With NiO Nanoparticles. *RSC Adv.* **2017**, *7*, 52772–52781.
- (57) Cai, F.; Tao, C.-a.; Li, Y.; Yin, W.; Wang, X.; Wang, J. Effects of Amount of Graphene Oxide and The Times of Light Scribe On The Performance of All-Solid-State Flexible Graphene-Based Micro-Supercapacitors. *Mater. Res. Express* **2017**, *4*, No. 036304.
- (58) Gao, W.; Singh, N.; Song, L.; Liu, Z.; Reddy, A. L. M.; Ci, L.; Vajtai, R.; Zhang, Q.; Wei, B.; Ajayan, P. M. Direct Laser Writing of Micro-Supercapacitors On Hydrated Graphite Oxide Films. *Nat. Nanotechnol.* **2011**, *6*, 496–500.
- (59) Wang, H.; Lu, Z.; Kong, D.; Sun, J.; Hymel, T. M.; Cui, Y. Electrochemical Tuning of MoS₂ Nanoparticles on Three-Dimensional Substrate for Efficient Hydrogen Evolution. *ACS Nano* **2014**, *8*, 4940–4947.
- (60) Winchester, A.; Ghosh, S.; Feng, S.; Elias, A. L.; Mallouk, T.; Terrones, M.; Talapatra, S. Electrochemical Characterization of Liquid Phase Exfoliated Two-Dimensional Layers of Molybdenum Disulfide. *ACS Appl. Mater. Interfaces* **2014**, *6*, 2125–2130.
- (61) Li, J.; Sollami Delekta, S.; Zhang, P.; Yang, S.; Lohe, M. R.; Zhuang, X.; Feng, X.; Östling, M. Scalable Fabrication and Integration of Graphene Microsupercapacitors Through Full Inkjet Printing. *ACS Nano* **2017**, *11*, 8249–8256.
- (62) Dulal, M.; Afroj, S.; Ahn, J.; Cho, Y.; Carr, C.; Kim, I.-D.; Karim, N. Toward Sustainable Wearable Electronic Textiles. *ACS Nano* **2022**, *16*, 19755–19788.
- (63) Tan, S.; Islam, M. R.; Li, H.; Fernando, A.; Afroj, S.; Karim, N. Highly Scalable, Sensitive and Ultraflexible Graphene-Based Wearable E-Textiles Sensor for Bio-Signal Detection. *Adv. Sensor Res.* **2022**, *1*, No. 2200010.
- (64) Tan, S.; Afroj, S.; Li, D.; Islam, M. R.; Wu, J.; Cai, G.; Karim, N.; Zhao, Z. Highly Sensitive and Extremely Durable Wearable E-textiles of Graphene/Carbon Nanotube Hybrid for Cardiorespiratory Monitoring. *iScience* **2023**, *26*, No. 106403.
- (65) Panagiotou, T.; Mesite, S. V.; Bernard, J. M.; Chomistek, K. J.; Fisher, R. J. *Production of Polymer Nanosuspensions Using Microfluidizer Processor Based Technologies*; NSTI-Nanotech: 2008; Vol. 1, pp 688–691.
- (66) Goldberg, S. Mechanical/Physical Methods of Cell Disruption and Tissue. In *2D PAGE: Sample Preparation and Fractionation*; Posch, A., Ed.; Humana Press: 2008; pp 3–22.
- (67) Lajunen, T.; Hisazumi, K.; Kanazawa, T.; Okada, H.; Seta, Y.; Yliperttula, M.; Urtti, A.; Takashima, Y. Topical Drug Delivery To Retinal Pigment Epithelium With Microfluidizer Produced Small Liposomes. *Eur. J. Pharm. Sci.* **2014**, *62*, 23–32.
- (68) Tang, S. Y.; Shridharan, P.; Sivakumar, M. Impact of Process Parameters In The Generation of Novel Aspirin Nanoemulsions – Comparative Studies Between Ultrasound Cavitation and Microfluidizer. *Ultrason. Sonochem.* **2013**, *20*, 485–497.
- (69) Panagiotou, T.; Bernard, J. M.; Mesite, S. V. *Deagglomeration and Dispersion of Carbon Nanotubes Using Microfluidizer (R) High Shear Fluid Processors*; NSTI-Nanotech: 2008; Vol. 1, pp 39–42.

Highly Scalable, Sensitive and Ultraflexible Graphene-Based Wearable E-Textiles Sensor for Bio-Signal Detection

Sirui Tan, Md Rashedul Islam, Huixuan Li, Anura Fernando, Shaila Afroj, and Nazmul Karim*

Graphene-based wearable electronic textiles (e-textiles) show promise for next-generation personalized healthcare applications due to their non-invasive nature. However, the poor performance, less comfort, and higher material cost limit their wide applications. Here a simple and scalable production method of producing graphene-based electro-conductive yarn that is further embroidered to realize piezoresistive sensors is reported. The multilayer structures improved the conductivity of the piezoresistive sensors, exhibiting good sensitivity with high response and recovery speed. Additionally, the potential applications of such wearable, ultraflexible and machine-washable piezoresistive sensors as pressure and breathing sensors are demonstrated. This will be an important step toward realizing multifunctional applications of wearable e-textiles for next-generation personalized healthcare applications.

1. Introduction

Wearable electronics incorporating physical, chemical, and biological sensors and actuators have rapidly become an inseparable part of our lives for their use in a wide range of applications, especially for personalized health monitoring, wellness-

S. Tan, H. Li, A. Fernando
Department of Materials
The University of Manchester
Oxford Road, Manchester M13 9PL, UK

S. Tan
School of Textile Science and Engineering
Wuhan Textile University
Wuhan 430200, P. R. China

M. R. Islam, S. Afroj, N. Karim
Centre for Print Research (CFPR)
The University of the West of England
Frenchay, Bristol BS16 1QY, UK
E-mail: nazmul.karim@uwe.ac.uk

S. Afroj, N. Karim
The National Graphene Institute
The University of Manchester
Manchester M13 9PL, UK

The ORCID identification number(s) for the author(s) of this article can be found under <https://doi.org/10.1002/adsr.202200010>

© 2022 The Authors. Advanced Sensor Research published by Wiley-VCH GmbH. This is an open access article under the terms of the Creative Commons Attribution License, which permits use, distribution and reproduction in any medium, provided the original work is properly cited.

DOI: 10.1002/adsr.202200010

tracking, and early-warning for COVID-19 and other infectious viruses.^[1–3] Among them, flexible, stretchable, and miniaturized wearable sensors that measure motion, physiological, electrophysiological, and electrochemical signals emanating from the human body present great potential for personalized healthcare applications.^[4–5] Such devices have received considerable attention due to their continuous and non-invasive manner.^[6–7] The miniaturization of electronics, in addition to the wireless revolution, has opened up a new research era of flexible wearable electronics for remote health management of elderly personnel and children.^[8] Featuring

these electronics embedded into textiles, i.e., e-textiles not only presents physical flexibility,^[9–10] but also allows them to interface with the human body and continuously monitor, collect, and communicate various physiological parameters.^[11–12] The continuous monitoring of vital signs of the wearer, including temperature, heart rate, and oxygen saturation level, and any deviation of such vitals from their baseline can alert healthcare professionals at a very early stage and enable them to intervene more quickly.^[13] Textile-based sensors also allow patients to monitor their health at home, such as self-monitoring of medical conditions with connected wearable devices could potentially reduce NHS costs by $\approx 60\%$.^[14] Indeed, such a system provides a solution to the overburdened healthcare system resulting from a rapidly growing ageing society as well as maintaining and encouraging healthy and independent living for all, irrelevant of time and location.^[15] Enormous efforts have been made in industry and academia to incorporate electronic components into textiles to make various forms of e-textiles.^[16]

Based on various transduction mechanisms, flexible sensors could be classified as piezoelectric, capacitive, piezoresistive, and triboelectric sensors.^[17–18] However, the sensitivity of the piezoelectric, triboelectric, and capacitive pressure sensors are limited due to their intrinsic disadvantages.^[19] For example, the piezoelectric sensors suffer from a lack of accuracy originating from the intrinsic hysteresis and creep phenomenon of the piezoelectric materials.^[20] The output signals generated from triboelectric sensors can easily be influenced by environmental conditions, such as temperature and humidity.^[21] In addition to such environmental effects, capacitive sensors also suffer from non-linearity.^[22] In contrast, piezoresistive sensors have widely been

investigated due to their simple structure, excellent sensitivity, and easy signal processing.^[23] Lots of efforts have been made to improve the performance of piezoresistive sensors by developing novel materials and by designing various microstructures.^[24] Nanomaterials, due to possessing high specific surface areas and unique mechanical, electronic, and thermal properties are considered promising for the improvement of sensors.^[25] Among them, graphene, a single atom thick 2D closely packed honeycomb lattice of sp² carbon allotropes, has received much attention from the researcher community, owing to its excellent mechanical, thermal, electrical, and other properties.^[26–28] Since its isolation in 2004, graphene and graphene-like 2D materials have shown great promise as transduction system and supporting substrates for fabricating next generation electronics, especially biosensors. Their extremely high surface area, coupled with a broad range of electrical and optical properties, makes them ideal for biosensing applications.^[29–30] Therefore, graphene-based materials have been explored for various wearable e-textiles applications to monitor heart rate, temperature, or tracking human motion^[31], which were fabricated via coating,^[32] screen printing,^[33] and inkjet printing^[16] techniques. Embroidery is considered to be another promising technique to produce wearable e-textile components because modern embroidery machines are faster and more flexible in terms of pattern generation, also facilitating the integration of high-frequency systems into clothing.^[34–35] Previous studies demonstrated the embroidery process of conductive yarns or wires to work as sensors and data conductors.^[36–39] However, further work is necessary to investigate the potentiality of producing graphene-based yarns in a scalable quantity, and then integrate such electroconductive yarns into fabrics as wearable biosensors via simple embroidery technique.

Herein, we report simple and scalable embroidery of graphene-based conductive yarns to produce highly sensitive and ultraflexible, and machine washable piezoresistive sensor for bio-signal detection. Graphene-based electro-conductive yarns were prepared via highly scalable and ultrafast yarn dyeing technique. Then such yarns were integrated to textiles fabrics via high-speed embroidery technique to produce wearable piezoresistive sensors. The performance of such sensors was compared with the sensors made from commercially available conductive yarns. The effects of sensor structure in terms of sensor shape, design, and multiple layers were then investigated. The potential applications of such wearable e-textiles as pressure and breathing sensors were also demonstrated.

2. Results and Discussion

2.1. Scalable Production of rGO Coated Yarn

The cotton yarn was coated with reduced graphene oxide (rGO) using a laboratory-scale yarn dyeing machine. A modified Hummers method was used to prepare graphene oxide (GO), and then chemically reduced to rGO using ascorbic acid (AA) in the presence of PSS. PSS was used to functionalise the surface of rGO flakes, providing a better dispersibility and preventing agglomeration. The lateral size of GO and rGO dispersions was characterized by field emission gun scanning electron microscopy. **Figure**

1a shows the flake size distribution of the GO and rGO, which was obtained via statistical analysis of 100 flakes. The mean lateral dimension of GO and rGO was found to be $\approx 5.85 \mu\text{m}$ and $\approx 4.86 \mu\text{m}$, respectively. The decreased flake size of GO after reduction may be due to the stresses it was subjected to during pre-mixing and centrifugation steps in post-washing cycles.^[32] Figure 1b shows the flake thickness distribution of GO and rGO, which reveals that the flake thickness of GO and rGO is $\approx 2.07 \text{ nm}$ and 2.2 nm , respectively. Raman spectra of GO and rGO exhibit characteristic peaks at $\approx 1344.78 \text{ cm}^{-1}$ and 1605.95 cm^{-1} , corresponding to D and G bands respectively, Figure 1c. Due to the reduction, the intensity ratio of the D to G band (I_D/I_G) was increased from 0.98 for GO to 1.61 for rGO.

Figure 1d illustrates the changes in the sheet resistance of the rGO coated yarn with the coating time. The sheet resistance was found to decrease significantly with the increase of coating time. The lowest resistance was found $5 \text{ M}\Omega \text{ cm}^{-1}$ after 30 min and was therefore chosen as optimized coating time to investigate the influence of the number of coating cycles on the resistance of the rGO-coated yarns. With each coating cycle, the amount of rGO flakes on the yarn surface increased, and therefore the resistance of conductive yarn decreased. This phenomenon could be explained by the absorption and adsorption phenomena. The absorption of rGO dispersion into the fibres is primarily dominant in the first few coating cycles. Once the saturation point is reached, rGO is then mainly adsorbed on the fibre surface forming a continuous conductive film by creating better connections between flakes. Thus, the sheet resistance of the yarns decreased by accumulating more rGO flakes on the fibre surface (**Figure 2e,f**) and by the restacking of the flakes through the van der Waal forces. It can be seen from Figure 1e, that the resistance of the rGO coated yarn decreased rapidly up to 5 coating cycles and afterwards, the changes in resistance were found very small. This might be caused by the saturation of the cotton yarn with rGO that is absorbing enough graphene flakes during those first 5 cycles. Figure 1f exhibits the effect of curing time and temperature on the conductivity of the rGO-coated yarn. With the increase in curing time and temperature, the residual solvents are volatilized, and the contact between the graphene flakes is increased, resulting in better conductivity of the coated yarn. The resistance was found to as minimum as $0.9 \text{ M}\Omega \text{ cm}^{-1}$. However, at higher temperatures, the strength of the cotton yarn decreases significantly. Therefore, the curing temperature of $150 \text{ }^\circ\text{C}$ for 3 min was chosen as the optimized curing condition for the graphene-coated yarn preparation. Scanning electron microscopy (SEM) images of silver coated thread at different magnification show that silver particles are distributed almost uniformly on the surface, Figure 2a,b. However, there are still some big particles left which might lead to uniform resistance. The silver-coated yarn was cut into small pieces of 1cm each, and then 10 samples were selected to measure the resistance of the thread. The resistance of the silver yarn was found to be $1.98 \pm 0.02 \Omega \text{ cm}^{-1}$. Figure 2c,d show SEM images of Carbon Tenax fibre, and Figure 2e,f show SEM images of graphene sewing thread at different magnifications. Compared to graphene coated yarn, carbon represents much better uniformity and smoother surface due to it being a carbon fibre twisted yarn.

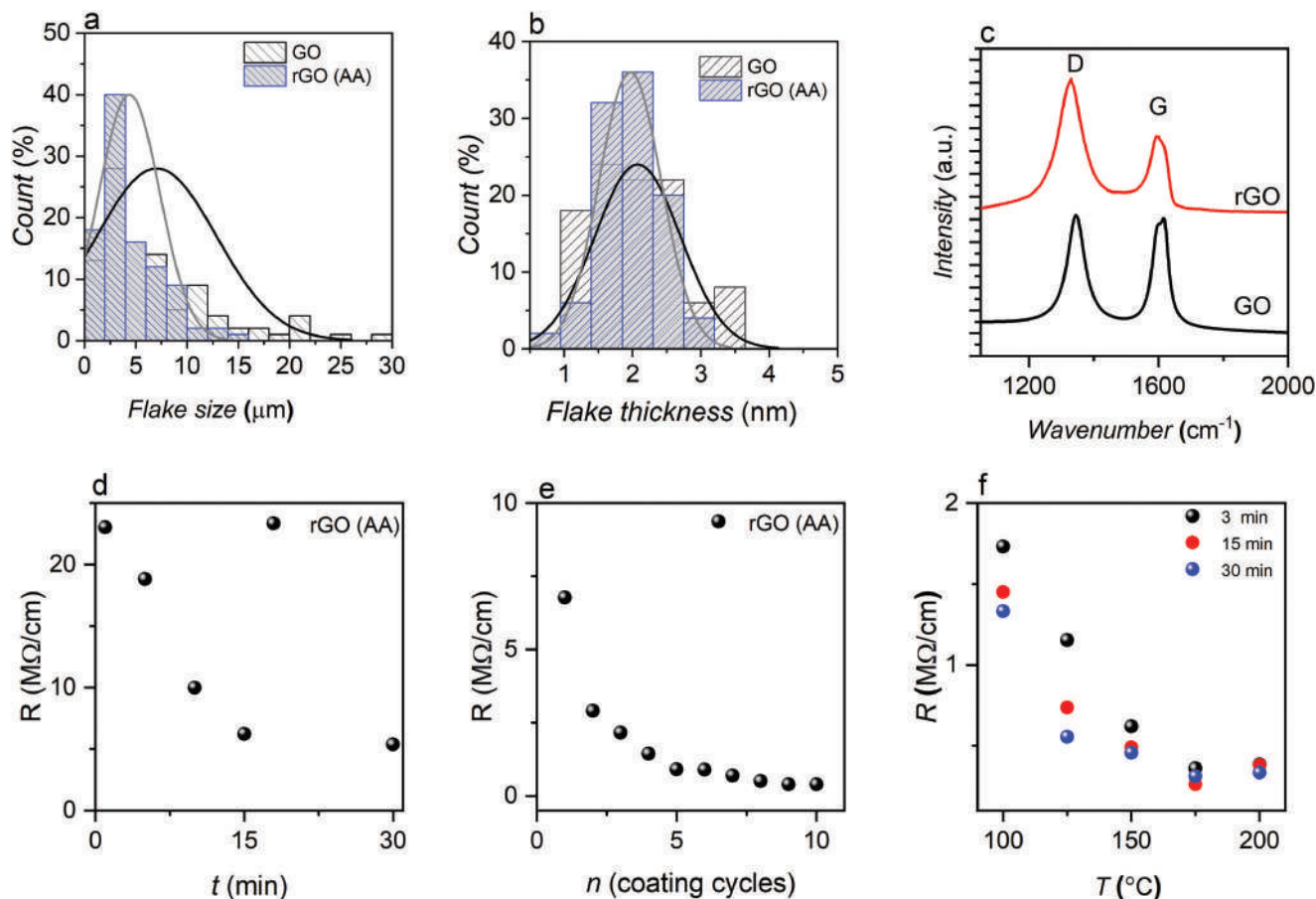


Figure 1. Preparation of rGO and rGO coated conductive yarn. a) Flake size of GO and rGO (AA) b) Flake thickness of GO and rGO (AA) c) Raman spectra of GO and rGO. d) Change of resistance of rGO yarn with coating time. e) Number of coating cycles vs resistance of rGO coated-dried yarn. f) Change of resistance of rGO yarn with curing time and temperature.

2.2. Characterization of the Conductive Sewing Thread

The investigation of three conductive sewing threads shows positive resistance variations during tensile tests and negative resistance variations during compression tests. **Figure 3a** illustrates the mechanical properties of three yarns during tensile tests. **Figure 3a** shows that silver-coated sewing thread provides the best elasticity among the three yarns which can be stretched to $\sim 10\%$ within the elastic limit. The resistance of the thread increases rapidly during the tensile test. Carbon fibre represents a relatively higher strength but lower elasticity, which would not break until the tensile force reaches ≈ 52.4 N. The core of the graphene-coated thread is cotton, so the strength and the elastic limit are both relatively lower than the other synthetic yarns. **Figure 3b–d** represent the electrical properties of each yarn during the tensile test within the elastic limit. It is evident that the change of resistance for graphene coated yarn were $\approx 4.16\%$ (for strain up to 0.5%). The carbon yarn shows the resistance change of $\approx 1.38\%$ (for strain up to 1%) and the silver yarn shows the resistance change of $\approx 65.24\%$ (for strain up to 10%). However, within the same elastic limit (i.e., for the strain of 0.5%), the graphene coated yarn shows the highest change of resistance ($\approx 4.16\%$), compared to both carbon ($\approx 0.86\%$) and silver yarn

($\approx 0.31\%$). Thus, it is evident that the graphene coated yarn shows highest sensitivity among all the yarns, as we are exhibiting linear relationship between the force and resistance. However, **Figure 3e,f** illustrate the compression test results of three yarns up to the breaking point and within the elastic limit. It was found that the graphene-coated thread showed a relatively better performance during the compression test, with a rapid decrease in the resistance. The silver sewing thread used in this paper is the finest yarn among these three yarns, however, their resistance only changed by $0.2 \Omega \text{ cm}^{-1}$ during the compression test from 0 to 40 pa. Compared to silver-coated threads, the carbon fibre twisted yarn shows better results, as their resistance changed by $0.2 \Omega \text{ cm}^{-1}$ during the compression test from 0–18.5 pa.

2.3. Embroidered Piezoresistive Sensor

The fabrication of the embroidered sensor involves the design of the sensor followed by an embroidery process. To investigate the effect of stitch density and stitch size on the sensor performance, for each sewing thread, 5 samples with stitch density $0.5 \text{ stitches mm}^{-2}$ with different stitch sizes (1mm, 3mm, 5mm, 7mm, and 9mm), and 5 samples with stitch density 1 stitch mm^{-2}

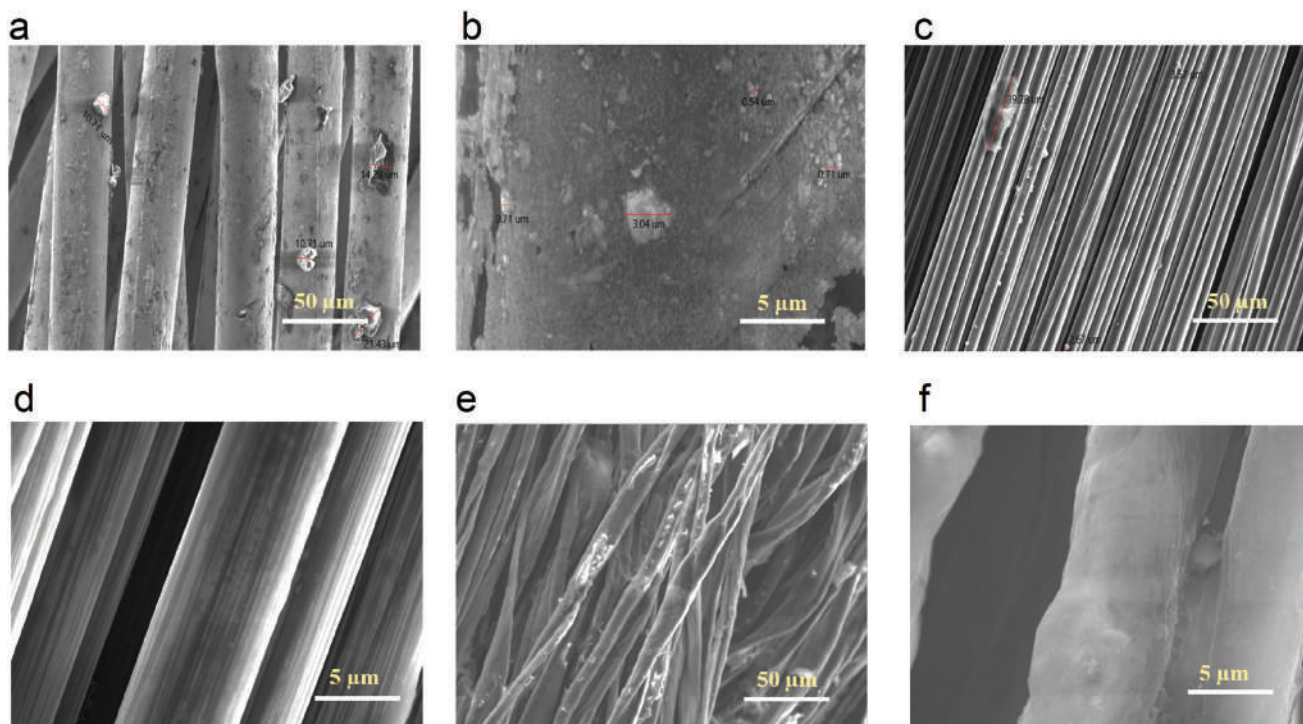


Figure 2. Characterisation of the conductive sewing yarns. SEM image of silver coated thread at a) 500X and b) 5000X magnification. SEM image of carbon Tenax at c) 500X and d) 5000X magnification. SEM image of graphene coated thread at e) 500X and f) 5000X magnification.

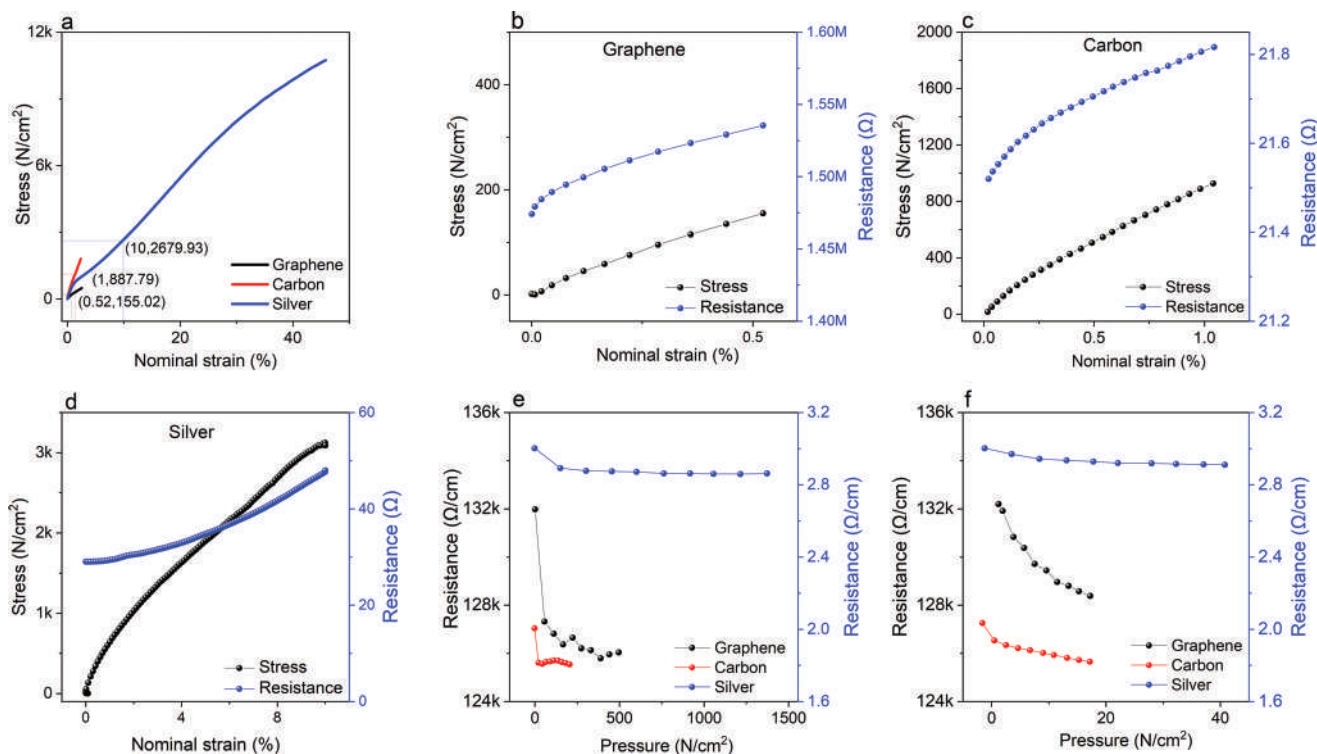


Figure 3. Mechanical properties of graphene, carbon, and silver sewing threads. a) Tensile break tests of graphene, carbon, and silver sewing threads b) Tensile tests within elastic limit of b) graphene, c) Carbon Tenax, and d) silver coated sewing thread. Yarn compression test results. Compression test of e) graphene, carbon, and silver threads up to the break point. f) Graphene, carbon, and silver threads within the elastic limit.

Table 1. The sensitivity ($\Delta R/R_0$) of the sensor with different yarns, stitch size, and stitch density.

Stitch density	Stitch size 1	Stitch size 3	Stitch size 5	Stitch size 7	Stitch size 9
Silver 0.5	-0.547%	-8.881%	-11.586%	-2.306%	-2.141%
Silver 1	-0.1883%	-3.375%	-6.042%	-10.917%	-0.605%
Carbon 0.5	-4.041%	-15.798%	-14.858%	-10.585%	-2.831%
Carbon 1	-2.766%	-10.357%	-11.926%	-9.916%	-4.829%
Graphene 0.5	-8.015%	-13.306%	-16.325%	-12.828%	-5.719%
Graphene 1	-4.580%	-10.102%	-11.687%	-15.059%	-6.103%

with different stitch size (1mm, 3mm, 5mm, 7mm, and 9mm) were prepared. The sensor size was 2 cm × 2 cm. Figure S1a (Supporting Information) is the sketch of the embroidered sensor design and Figure S1b (Supporting Information) is the carbon embroidered sensor sample with a 5 mm stitch size. The sensors were subjected to a compressive cyclic test from 0.1 to 2 N. A pre-load was applied to fix the sensor between a compression board and a wooden cube of the same size as the sensor was used to control the thrust face. The sensors were fixed and connected with the data acquisition card to record the changes in resistance. **Figure 4** represents the cyclic test results for those embroidered piezoresistive sensors.

When the stitch density increased from 0.5 to 1 sewing line per mm, the sensor with a relatively higher stitch size shows better results, especially for those sensors made with relatively thicker sewing thread (Carbon). It is evident from **Table 1**, the embroidered sensors with 5 mm stitch size performed better at 0.5 stitch density, but sensors with 7 mm stitch size performed better while the stitch density is 1. This phenomenon could be attributed to the fact that, when the stitch density increases, the sensor becomes stiffer due to the increase of the number of stitches. The same pressure was applied to the sensor, and the deformation nominal of the stiffer sensor is relatively lower than flexible sensors. As a result, the changes in resistance of the stiffer sensor is not significant as the flexible sensors. However, increasing the stitch size and stitch density at the same time can overcome this problem. Increasing stitch size makes the sensor structure looser and more flexible whereas increasing the stitch density (number of stitches in a certain area) makes the sensor tighter and stiffer. In case of a too loose and flexible sensor, e.g., 0.5 stitch density with 9 mm stitch size, when the compression pressure applied on the sensor, the conductive sewing thread might slip instead of being compressed, which might lead to a relatively lower and unstable performance. On the other hand, in case of a too tight and stiff sensor, e.g., 1 stitch density with 1 mm stitch size, the conductive sewing thread in the structure remain under a relatively higher tension, which leads to a lower deformation and lower changes in resistance during the compression test. Therefore, a series of tests were carried out (Figure 4) to find the most suitable stitch sizes for density 0.5 and 1. Table 1 is the calculated $\Delta R/R_0$ results from Figure 4. Generally, it could be assumed that for all three materials, 2 mm line separation and 5 mm stitch size for embroidered patches provides better relative changes in the electrical resistance. It is worth noting that, though the resistance of the graphene coated thread is relatively higher than carbon or silver threads, their sensitivity, namely the gauge factor is

higher than that of the carbon or silver threads. Also, graphene in its reduced form interacts with the functional groups of the textiles,^[32] therefore becomes an integral part of fibre facilitating a more stable functional fibre/fabric. Instead of using rigid, toxic, nonbiodegradable, expensive, and unstable polymeric or metal substances, graphene thus offers potential for manufacturing conductive textiles for the development of next generation smart wearable e-textiles for personalized health management.

2.4. Effect of Sensor Design and Shape

To further investigate the effect of the design and shape of the embroidered sensor on the performance, five different structures were designed and manufactured (5 mm stitch size), **Figure 5a–e**. Taking into consideration the results of the yarns compression cyclic tests and sensors compression cyclic tests, carbon and graphene coated yarns were used for further experiments. The size of sensors (a) to (c) were 2 × 2 cm² and sensors (d) and (e) were 4 × 4 cm². Sensors labelled (a) to labelled (c) were conductive only single-sided due to using bottom conductive sewing thread, while sensor labelled (d) and sensor labelled (e) were conductive on both sides. The black part of the sensors was embroidered on the front side of the substrate fabric first, turned over and then the red part was embroidered on the back of the substrate. During the compression cyclic, two conductive silver fabrics (2 × 2 cm²) were placed on the sensor (d) and (e)'s two sides to form a sandwich structure. It is evident that sensors with (d) and (e) structures represent relatively higher performance during the cyclic test. Structure (d) and (e) have a relatively higher resistance and larger changes in resistance during the cyclic tests, especially for graphene embroidered sensor. Additionally, the graphene sensor with (e) structure shows higher sensitivity than the carbon sensor. The resistance decreased approximately up to 60% from 0 to 12 500 pa, while for the carbon sensor the resistance decreased up to 45%.

2.5. Effect of Multiple Layer Structure

To compare the effect of multiple layer structure on sensor performance, embroidered sensors labelled (D) and (E) were further manufactured with 3 stitches per mm and 5 mm stitch size (**Figure 6a**) as one layer, two layers, three layers and four layers. Insulation tapes were used to fix the multiple layered structures as well as to protect the sensors. Figure 6b represents the compression test result on the tensile machine with the pressure varying from 0 to 12 500 pa (3 mm min⁻¹). The curves present almost linearity in the pressure region, especially for the sensors with two layers. The sensitivity of the sensor is a critical parameter to evaluate its performance. By increasing the layers from 1 to 4 layers, the sensitivity of the sensors was increased from -0.00278 (one layer) to -0.00505 Pa⁻¹ (two layers), and then decreased to -0.00371 Pa⁻¹ (three layers) and -0.00338 Pa⁻¹ (four layers). It is obvious that sensors with two layers structure have a relatively higher sensitivity and linear relationship between 0 to 12500 Pa pressure. We assume that the electrical conductivity of the two-layered structures increases with the increase of number of layers. Therefore, the deformation due to applied pressure corresponds to more change in the resistance of the sensors, which

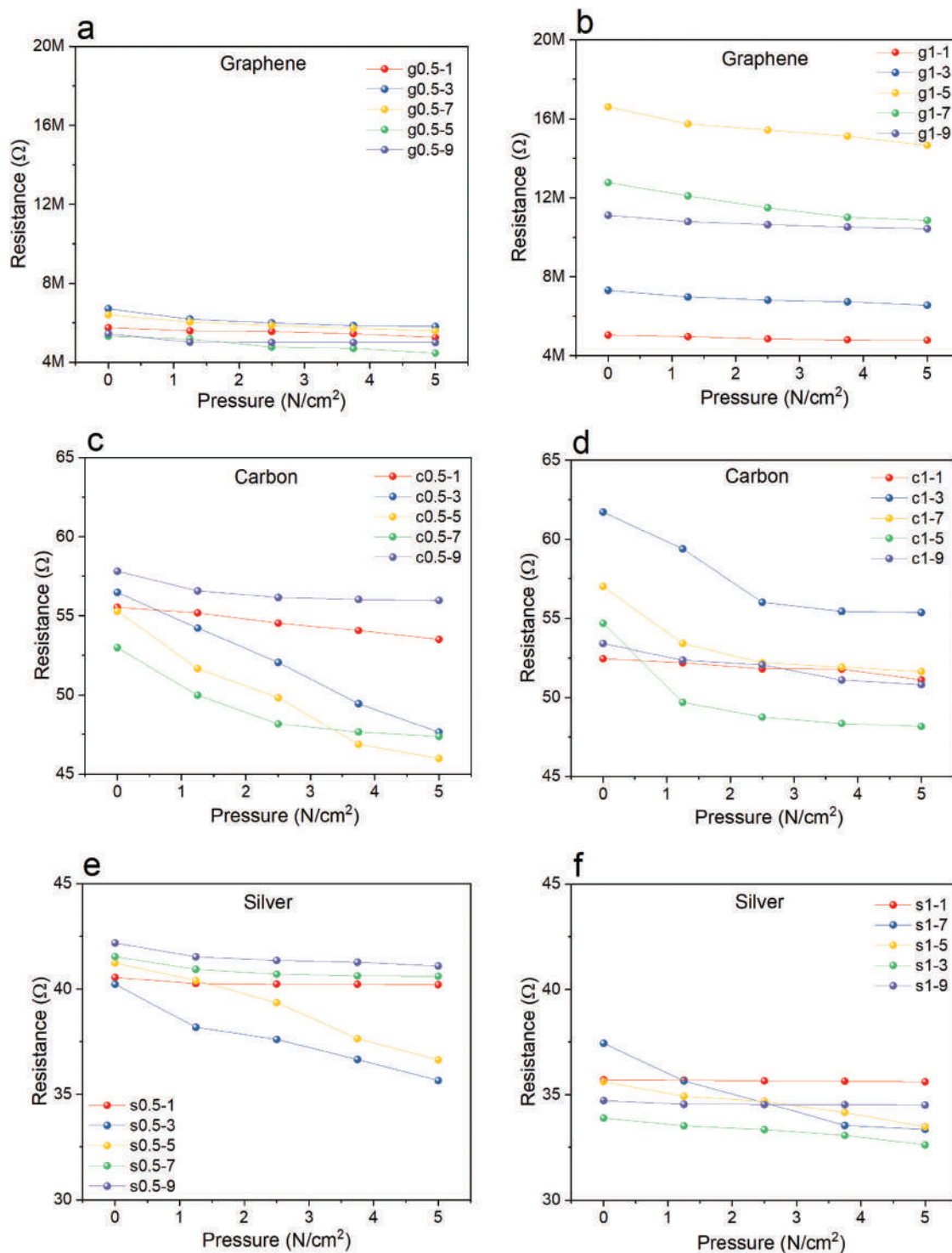
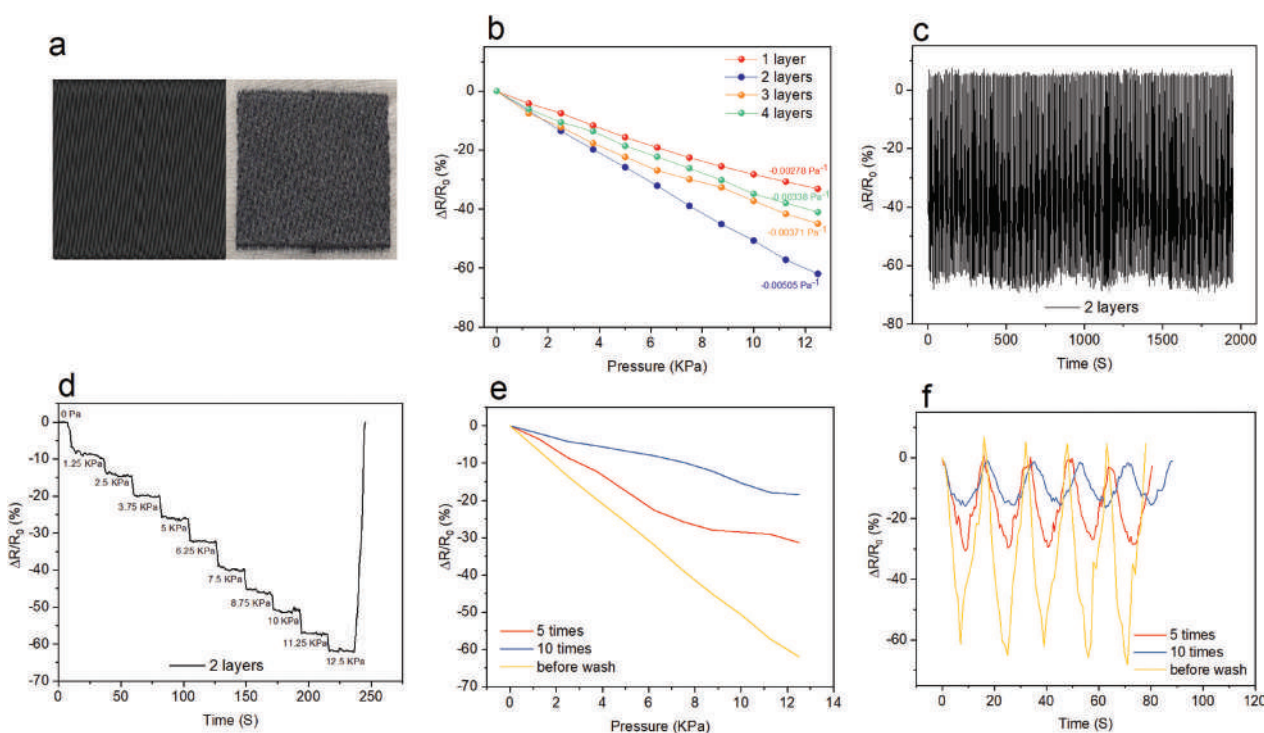
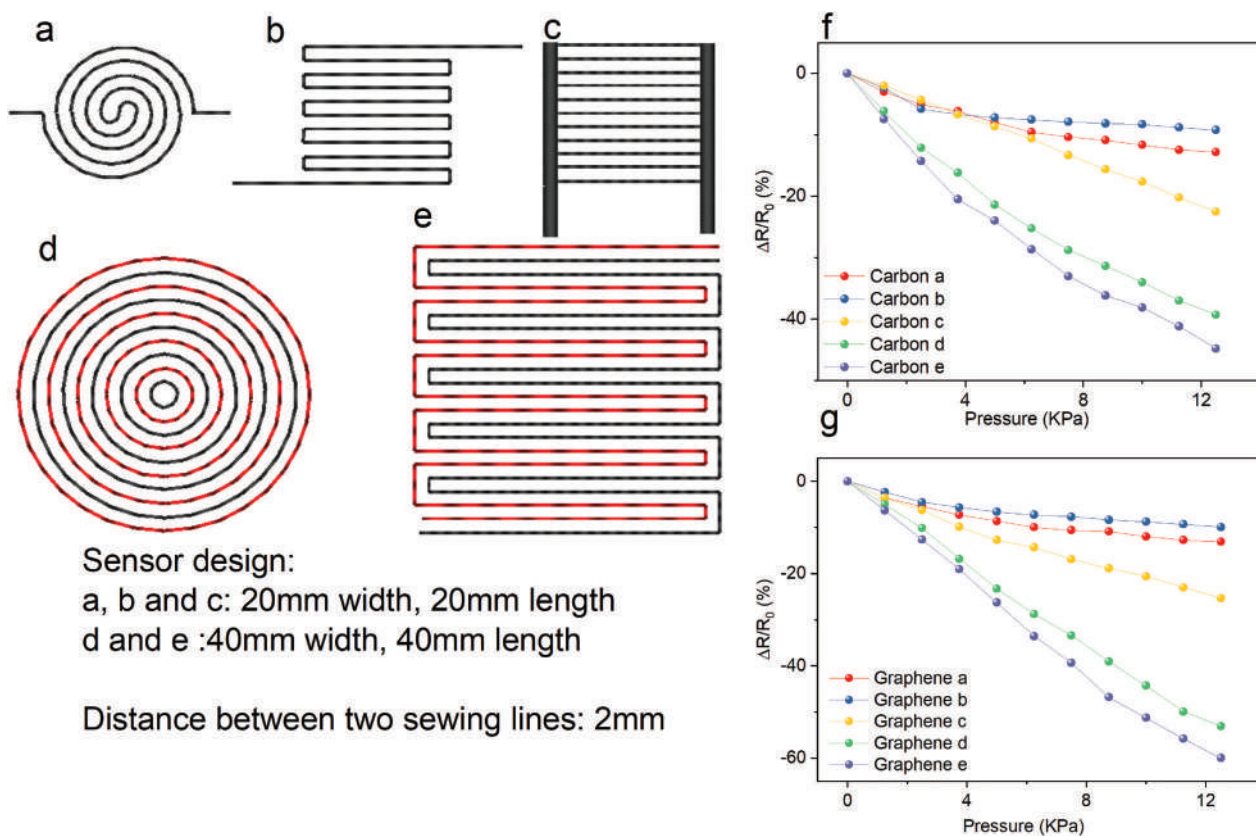


Figure 4. Compression test results of a,b) graphene, c,d) carbon, and e,f) silver piezoresistive sensor.

increased the sensitivity of our piezoresistive sensor. On the other hand, for the three and four-layered sensors, as the thickness increases, the flexibility of the sensors is decreased, and they become more rigid. Thus, the corresponding change in the resistance due to applied pressure is not significant, which reduces

the sensitivity of the sensors. As a result, the sensitivity of the four-layered sensor was found to be less than the three-layered sensor. To test the durability and stability of the best sensitive i.e., two-layered sensor, a 400 cycles cyclic test and a long-term stability test were further employed, Figure 6c,d. During the cyclic



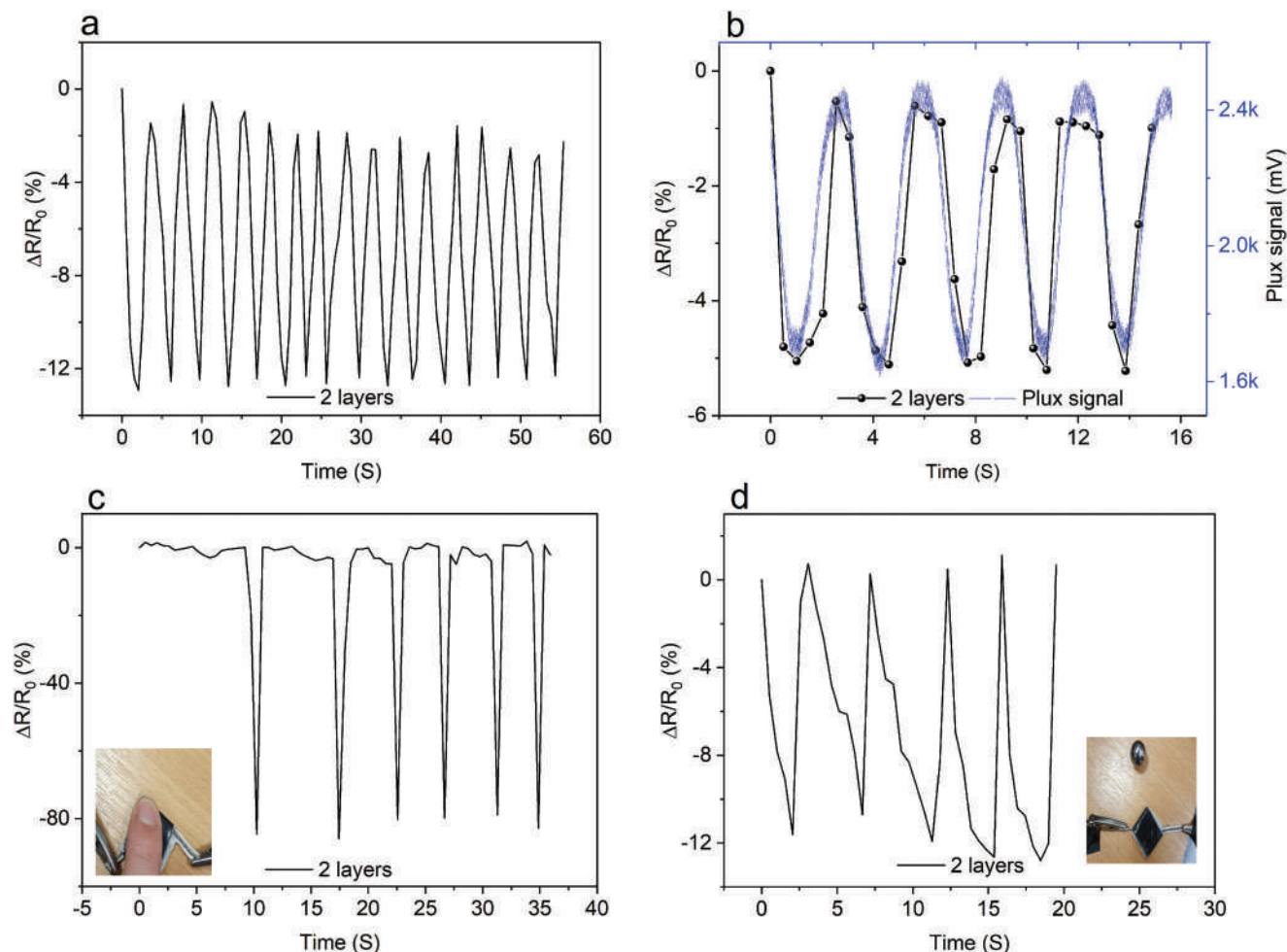


Figure 7. Application of the 2 layered embroidered sensor for a) breath test, b) breath test with the Plux signal system, c) finger touch test, and d) ball hit impact test.

test, the sensor exhibited a good stability and durability, and the resistance of the sensor was not changed significantly after the test. Additionally, the sensor showed good retention and stability since there was no significant variation of the resistance while the applied pressure was stable at different values.

2.6. Bio-Signal Detection of the Piezoresistive Sensor

To investigate the bio-signal sensing performance of our piezoresistive sensors in real-life implications, optimized two-layered sensors were further tested as a breathing sensor, **Figure 7a**. The Plux system was used as the control test, the two-layered sensors were placed under the Plux elastic band around the chest location, Figure S2 (Supporting Information). The NI-9219 card was connected with the sensor to record the changes in the resistance during the breath test. Figure 7b illustrates the performance of the sensors, the curve of the two-layered sensor is almost identical to the Plux sensor, which indicates the prospect of our sensor as a bio signal detection tool. Figure 7c,d exhibits the changes in the relative resistance during the finger touch test and the ball hit impact test, respectively. In both cases, it is seen that these

two-layered piezoresistive sensor has a good response speed and recovery speed making the sensor capable of functioning as a wearable sensor for human movement detection and bio-signal detection.

2.7. Washability of the Embroidered Sensor

Washability is an essential property of wearable sensors. The washability test of our piezoresistive sensors was conducted following the BS EN ISO 105 C06 A1M test method. The resistances of the sensors were measured after 5 and 10 washing cycles. After drying, a single compression test and a 5 cycles cyclic test were carried out, Figure 6e,f. It is evident that washed sensors exhibited relatively poor performance than the unwashed sensors. The total resistance increased by 17.6% after 5 times washing and 42.3% after 10 times washing. During the washing process, the vessel containing the rGO coated cotton yarns was shaken, and the oscillation of the washing bath simulated the stress generated during the standard washing cycles, which might affect the integrity and continuity of the deposited layer, increasing the sheet resistance.^[40] The wash tests have a big influence on the

signal output stability, sensitivity and conductivity of the sensor. However, the wash stability of wearable e-textiles can be improved via several methods,^[41] such as pre- or post-treatment with substances that can act as a molecular glue, polyurethane (PU) sealing, or hot melt encapsulation, etc.^[42] without changing the mechanical and electrical properties of the wearable sensors.

3. Conclusion

In this study, we report a simple and scalable production method for rGO dispersion and the coating of cotton yarns with the rGO dispersion to produce electrically conductive graphene coated yarn. The graphene-based electroconductive yarns thus produced are comparable with the commercially available conductive yarns. The yarns show excellent sensitivity and cyclability when embroidered into a piezoresistive sensor. We also found that multilayer structures could potentially improve the conductivity of the piezoresistive sensors; especially the modified two-layered embroidered sensor show good sensitivity with high response and recovery speed. In addition to working as a pressure sensor, our piezoresistive sensor performed as a breathing sensor, which was comparable with the commercial sensors. Although the washability of the sample is not satisfactory, it could be improved by pre- or post-treatment with encapsulation materials. We believe our simple production method of graphene-based wearable sensors would be an important step toward realizing multifunctional applications of wearable e-textiles for next generation health care devices.

4. Experimental Section

Materials: Flake graphite grade 3061 was kindly supplied by Asbury Graphite Mills, USA. L-ascorbic acid (≈99%), ammonia, and poly (sodium 4-styrene sulfonate) (PSS, Mw ≈70 000, powder) were purchased from Sigma-Aldrich, UK, and used as received. Surface-pre-treated (scoured and bleached) 100% cotton yarn from the University of Manchester textiles laboratory was used. To investigate the performance of graphene-coated yarn with the commercial yarns, metal-coated and non-metallic conductive yarns were chosen as the control yarns. Silver-coated polyamide yarn (Silverpam 250) and carbon yarn (Carbon Tenax) were purchased from TIBTECH innovations, France. The nonconductive polyester sewing thread (ISACORD 40) was purchased from Barnyarns Ripon Ltd, UK. Woven cotton substrate fabric was manufactured internally in the University of Manchester weaving laboratory and water-soluble PVA backing materials were purchased from Abakhan Fabrics, Hobby & Home, Manchester, UK.

Synthesis of Graphene Materials: Graphene oxide (GO) was prepared using a modified Hummers method.^[43] A brown dispersion of GO (1 mg mL⁻¹) was prepared by adding 160 mg of GO to 160 mL of deionized (DI) water and sonicated for 30 min. In order to form a stable dispersion, 1.6 g of PSS was mixed into the GO dispersion by vigorous stirring. The resulting suspension was transferred to a round-bottom flask placed in an oil bath. Ascorbic acid (1.2 g) and NH₃ (required to adjust pH 9–10) were added to the dispersion with vigorous stirring. This mixture was held at 90 °C for 72 h under closed conditions to obtain a black dispersion. Residual ascorbic acid and PSS were removed from the rGO by washing several times with deionized water and finally diluted into distilled water (DI) to adjust the rGO dispersion concentration to 3.2 mg mL⁻¹.

Coating of Textile Yarn with Graphene-Based Ink: A simple dip-coating method was used to coat the cotton textile yarn with the graphene-based ink. Coating and curing conditions such as coating time, the number of coating cycles, curing time, and temperature were optimized. First, a scoured–bleached cotton yarn was coated with the rGO dispersion (≈1.9 mg mL⁻¹) for 1–30 min. Then resistance per cm length of the coated yarn

was measured using a multi-meter (DL9309 Auto Ranging multi-meter, Di-Log, UK). The optimized coating time was used to coat yarn with the same rGO dispersion for a number of coating cycles (up to 10). The changes in the electrical resistance after each cycle were observed and optimized for further studies. The effects of the curing time (5–30 min) and the curing temperature (100–200 °C) on the resistance of the rGO-coated yarn were then observed and optimized. Then a laboratory-scale yarn dyeing machine was used to produce a batch of rGO-coated textiles yarns in scalable quantity.

Characterization of the Conductive Sewing Thread: To investigate the capability of our graphene-coated yarn to manufacture the textile sensors, commercially available silver-coated metallic yarn and non-metallic carbon-conductive yarns were chosen as control samples. Silver was selected due to its high conductivity. The silver sewing thread used in this study is a grafted antibacterial silver-coated thread with a resistance of 198 Ω m⁻¹. The thread also exhibits a stretchability of up to 10% that is an ideal material for sensor construction. However, the oxidation is not avoidable even with an antibacterial layer. Carbon materials are usually strong, stable, and relatively cheaper. Carbon Tenax, used in this study, is a carbon fibre Z twisted sewing thread with a resistivity of 218 Ω m⁻¹. Although the easily broken property of the carbon fibre is unavoidable, their higher conductivity and excellent washability are much better than carbon-coated materials. The surface morphology of three conductive sewing threads was characterized by the Hitachi 3000 scanning electron microscope. Tensile and compression tests were carried out for the characterization of the conductive sewing thread using a Zwick/Roll computerized tensile testing machine (Germany). A National Instrument data acquisition card (NI-9219) was used to record the changes in resistance during the tests.

Embroidered Piezoresistive Sensor: The embroidered sensor consists of conductive lower sewing thread, nonconductive upper sewing thread, substrate fabric, and backing material. To produce embroidered piezoresistive sensors, the sensor pattern was designed on PE-Design software. The stitch density and stitch length were selected through the modelling work, and the yarn tension was adjusted in the embroidered machine to control the ratio between the upper thread and the lower thread. In this study, the sensor stitch size was altered between 1, 3, 5, 7, and 9 mm and the stitch densities were altered from 0.5 or 1 sewing line per mm. The upper thread was usually nonconductive yarn to prevent the conductive particles from the friction between the upper thread and the needle hole. The piezoresistive sensor's sensitivity (S) is an essential parameter for assessing device performance and was characterized using the following equation:

$$S = \frac{\Delta R}{R_0} = \frac{R - R_0}{R_0} \times 100 \quad (1)$$

where ΔR denote the resistance change before and after load applied, R and R_0 denotes the loaded and unloaded samples' resistances, respectively.

The embroidered piezoresistive sensors were subjected to a compressive cyclic test starting from 0.1 to 2 N using a computerised Zwick/Roell tensile tester machine. The ramp and release rates were set at 3 mm min⁻¹. The electrical response was continuously monitored and recorded using a National Instrument-9219 data acquisition card. To test the long-term stability, the piezoresistive sensor was compressed and released for 100 cycles using the tensile tester machine. A plux system was used to measure the BCG signals from a human body without a direct skin contact following appropriate risk assessment, and consent from the participant.

Washability Tests of the Piezoresistive Sensor: The washability of the rGO-coated embroidered sensors was assessed according to BS EN ISO 105 C06 A1M, by treating rGO-coated yarns in a solution containing 4 g L⁻¹ ECE reference detergent B with 10 stainless steel balls at 40 °C for 45 min. A Roaches Washtec-P TOC 3002 was used for the washability test. The steel balls were used to simulate the agitation and abrasion that a garment was subjected to during a standard washing cycle. The sensors were rinsed subsequently in running water at ambient temperature and air-dried at

room temperature prior to further analysis. The sensors were tested after 5 and 10-times washing cycles.

Supporting Information

Supporting Information is available from the Wiley Online Library or from the author.

Acknowledgements

Authors gratefully acknowledge funding from the Government of Bangladesh, UWE-Augstex partnership PhD award, and UKRI Research England The Expanding Excellence in England (E3) grant. This work was submitted as a part of Sirui Tan's PhD thesis at the University of Manchester.

Conflict of Interest

The authors declare no conflict of interest.

Data Availability Statement

The data that support the findings of this study are available from the corresponding author upon reasonable request.

Keywords

bio-signal sensing, e-textiles, graphene, piezoresistive sensors, wearables

Received: July 29, 2022

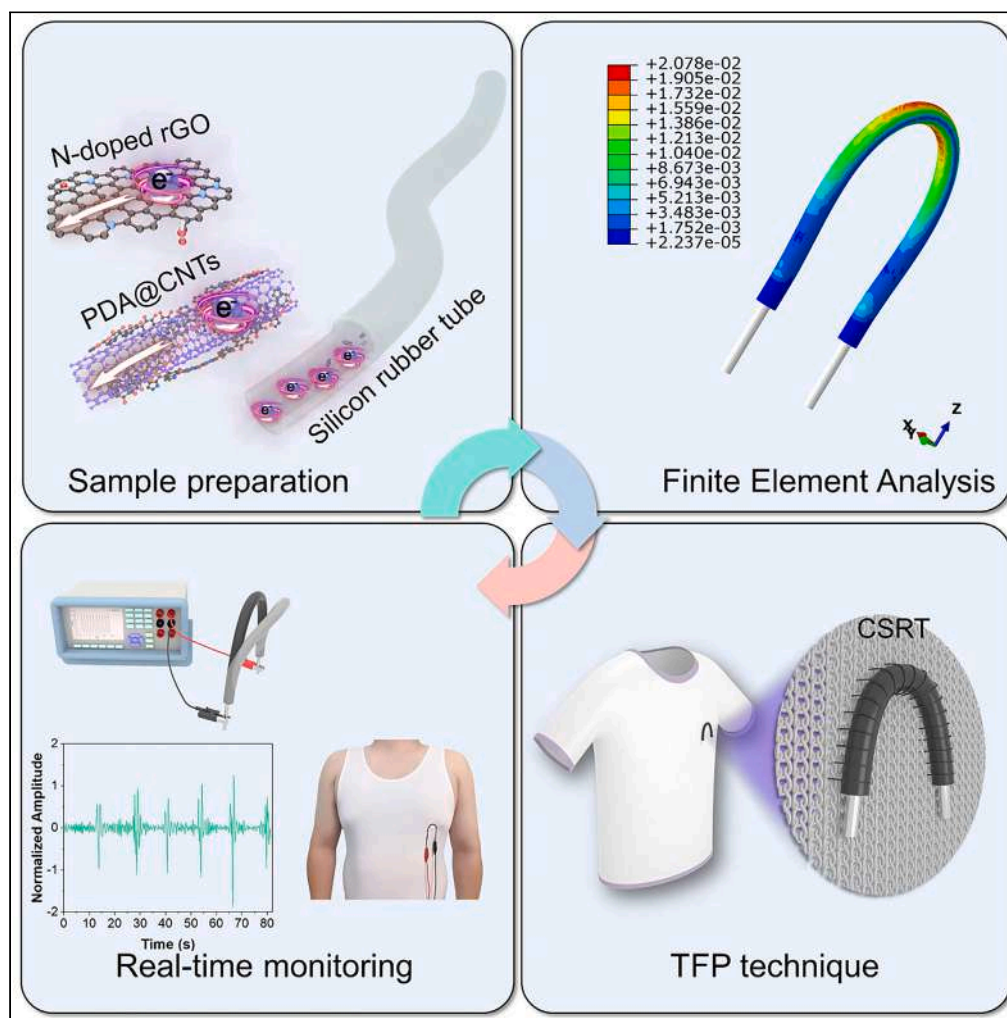
Revised: September 23, 2022

Published online:

- [1] L. Manjakkal, L. Yin, A. Nathan, J. Wang, R. Dahiya, *Adv. Mater.* **2021**, *33*, 2100899.
- [2] M. Lin, Z. Zheng, L. Yang, M. Luo, L. Fu, B. Lin, C. Xu, *Adv. Mater.* **2022**, *34*, 2107309.
- [3] B. Peng, F. Zhao, J. Ping, Y. Ying, *Small* **2020**, *16*, 2002681.
- [4] R. He, H. Liu, Y. Niu, H. Zhang, G. M. Genin, F. Xu, *npj Flexible Electron.* **2022**, *6*, 20.
- [5] Y. Lee, J. Kim, H. Joo, M. S. Raj, R. Ghaffari, D.-H. Kim, *Adv. Mater. Technol.* **2017**, *2*, 1700053.
- [6] D. R. Seshadri, R. T. Li, J. E. Voos, J. R. Rowbottom, C. M. Alfes, C. A. Zorman, C. K. Drummond, *NPJ Digit Med* **2019**, *2*, 72.
- [7] S. Chen, J. Qi, S. Fan, Z. Qiao, J. C. Yeo, C. T. Lim, *Adv. Healthcare Mater.* **2021**, *10*, 2100116.
- [8] S. Lam Po Tang, *Transactions of the Institute of Measurement and Control* **2007**, *29*, 283.
- [9] M. Stoppa, A. Chiolerio, *Sensors (Basel)* **2014**, *14*, 11957.
- [10] M. R. Islam, S. Afroj, K. S. Novoselov, N. Karim, *Adv. Sci.* **2022**, *2203856*.
- [11] S. Afroj, M. H. Islam, N. Karim, *Proceedings* **2021**, *68*, 11.
- [12] M. M. Hasan, M. M. Hossain, *J. Mater. Sci.* **2021**, *56*, 14900.
- [13] Y. Wu, S. S. Mechael, T. B. Carmichael, *Acc. Chem. Res.* **2021**, *54*, 4051.
- [14] N. Karim, S. Afroj, K. Lloyd, L. C. Oaten, D. V. Andreeva, C. Carr, A. D. Farmery, I.-D. Kim, K. S. Novoselov, *ACS Nano* **2020**, *14*, 12313.
- [15] S. Afroj, N. Karim, Z. Wang, S. Tan, P. He, M. Holwill, D. Ghazaryan, A. Fernando, K. S. Novoselov, *ACS Nano* **2019**, *13*, 3847.
- [16] N. Karim, S. Afroj, A. Malandraki, S. Butterworth, C. Beach, M. Rigout, K. S. Novoselov, A. J. Casson, S. G. Yeates, *J. Mater. Chem. C* **2017**, *5*, 11640.
- [17] J. Zhu, C. Zhou, M. Zhang, *Soft Science* **2021**, *1*, 3.
- [18] J.-w. Zhang, Y. Zhang, Y.-y. Li, P. Wang, *Polymer Reviews* **2021**, *62*, 65.
- [19] J. Li, T. Wu, H. Jiang, Y. Chen, Q. Yang, *Advanced Intelligent Systems* **2021**, *3*, 2100070.
- [20] H. Jung, D.-G. Gweon, *Rev. Sci. Instrum.* **2000**, *71*, 1896.
- [21] X. Zeng, H.-T. Deng, D.-L. Wen, Y.-Y. Li, L. Xu, X.-S. Zhang, *Micromachines* **2022**, *13*, 254.
- [22] J. Qin, L.-J. Yin, Y.-N. Hao, S.-L. Zhong, D.-L. Zhang, K. Bi, Y.-X. Zhang, Y. Zhao, Z.-M. Dang, *Adv. Mater.* **2021**, *33*, 2008267.
- [23] J. Li, L. Fang, B. Sun, X. Li, S. H. Kang, *J. Electrochem. Soc.* **2020**, *167*, 037561.
- [24] Q. Du, L. Liu, R. Tang, J. Ai, Z. Wang, Q. Fu, C. Li, Y. Chen, X. Feng, *Adv. Mater. Technol.* **2021**, *6*, 2100122.
- [25] S. Maiti, M. R. Islam, M. A. Uddin, S. Afroj, S. J. Eichhorn, N. Karim, *Adv. Sustainable Syst.* **2022**, 2200258.
- [26] M. H. Islam, M. R. Islam, M. Dulal, S. Afroj, N. Karim, *iScience* **2021**, 103597.
- [27] N. Karim, S. Afroj, S. Tan, K. S. Novoselov, S. G. Yeates, *Sci. Rep.* **2019**, *9*, 1.
- [28] M. H. Islam, S. Afroj, M. A. Uddin, D. V. Andreeva, K. S. Novoselov, N. Karim, *Adv. Funct. Mater.* **2022**, *n/a*, 2205723.
- [29] S. Afroj, L. Britnell, T. Hasan, D. V. Andreeva, K. S. Novoselov, N. Karim, *Adv. Funct. Mater.* **2021**, *31*, 2107407.
- [30] M. Marzana, M. M. A. Khan, A. Ahmed, M. A. Jalil, M. M. Hossain, in *Nanomaterials for Biocatalysis* (Eds: G. R. Castro, A. K. Nadda, T. A. Nguyen, X. Qi, G. Yasin), Elsevier, New York **2022**.
- [31] N. Karim, S. Afroj, D. Leech, A. M. Abdelkader, in *Oxide Electronics* (Ed: A. Ray), John Wiley & Sons, Ltd, Hoboken, New Jersey **2021**, *2*.
- [32] N. Karim, S. Afroj, S. Tan, P. He, A. Fernando, C. Carr, K. S. Novoselov, *ACS Nano* **2017**, *11*, 12266.
- [33] A. M. Abdelkader, N. Karim, C. Vallés, S. Afroj, K. S. Novoselov, S. G. Yeates, *2D Mater.* **2017**, *4*, 035016.
- [34] R. Nolden, K. Zöll, A. Schwarz-Pfeiffer, *Materials (Basel)* **2021**, *14*, 2633.
- [35] R. Seager, S. Zhang, A. Chauraya, W. Whittow, Y. Vardaxoglou, T. Acti, T. Dias, *IET Microwaves, Antennas & Propagation* **2013**, *7*, 1174.
- [36] S. Qureshi, G. M. Stojanović, M. Simić, V. Jeoti, N. Lashari, F. Sher, *Materials (Basel)* **2021**, *14*, 7813.
- [37] M. Martínez-Estrada, B. Moradi, R. Fernández-García, I. Gil, *Sensors (Basel)* **2018**, *18*, 3824.
- [38] M. Martínez-Estrada, B. Moradi, R. Fernández-García, I. Gil, *Sensors (Basel)* **2019**, *19*, 1004.
- [39] D. Bonefačić, J. Bartolić, *Sensors (Basel)* **2021**, *21*, 3988.
- [40] J. Ren, C. Wang, X. Zhang, T. Carey, K. Chen, Y. Yin, F. Torrisi, *Carbon* **2017**, *111*, 622.
- [41] M. R. Islam, S. Afroj, C. Beach, M. H. Islam, C. Parraman, A. Abdelkader, A. J. Casson, K. S. Novoselov, N. Karim, *iScience* **2022**, *25*, 103945.
- [42] S. Afroj, S. Tan, A. M. Abdelkader, K. S. Novoselov, N. Karim, *Adv. Funct. Mater.* **2020**, *30*, 2000293.
- [43] J. P. Rourke, P. A. Pandey, J. J. Moore, M. Bates, I. A. Kinloch, R. J. Young, N. R. Wilson, *Angew. Chem., Int. Ed.* **2011**, *50*, 3173.

Article

Highly sensitive and extremely durable wearable e-textiles of graphene/carbon nanotube hybrid for cardiorespiratory monitoring



Sirui Tan, Shaila Afroj, Daiqi Li, ..., Guangming Cai, Nazmul Karim, Zhong Zhao

shaila.afroj@uwe.ac.uk (S.A.)
nazmul.karim@uwe.ac.uk (N.K.)
zzhao@wtu.edu.cn (Z.Z.)

Highlights

N-doped rGO and polydopamine coated CNT (rGO/CNT) hybrid was prepared

Conductive silicon rubber tube (CSRT) was prepared via vacuum filling of rGO/CNT

CSRT was highly sensitive, flexible, and extremely durable

CSRT was embroidered into a vest to sense wearer heart and breathing rate

Article

Highly sensitive and extremely durable wearable e-textiles of graphene/carbon nanotube hybrid for cardiorespiratory monitoring

Sirui Tan,^{1,2} Shaila Afroj,^{3,*} Daiqi Li,^{1,2} Md Rashedul Islam,³ Jihong Wu,^{1,2} Guangming Cai,^{1,2} Nazmul Karim,^{3,*} and Zhong Zhao^{1,2,4,*}

SUMMARY

Electroconductive textile yarns are of particular interest for their use as flexible and wearable sensors without compromising the properties and comfort of usual textiles. However, the detection of fine actions of the human body is quite challenging since it requires both the relatively higher sensitivity and stability of the sensor. Herein, highly sensitive, ultra-stable, and extremely durable piezoresistive wearable sensors were prepared by loading N-doped rGO and polydopamine-coated carbon nanotubes into silicon rubber tube. The wearable sensors thus produced show an excellent ability to sense subtle movement or stimuli with good sensitivity and repeatability. Furthermore, by bending the straight conductive silicon rubber tube (CSRT) into three different patterns, its sensitivity was then dramatically increased. Finally, the CSRT was found capable of sensing cardiorespiratory signals, indicating that the sensor would be an important step toward realizing bio-signal sensing for next-generation personalized health care applications.

INTRODUCTION

Wearable electronic textiles (e-textiles) are of great interest for personalized healthcare applications^{1–3} as they are flexible, comfortable, and lightweight as well as maintaining the desirable electrical property.^{4,5} In recent years, wearable sensors integrated into clothing have widely been investigated as reliable platforms for monitoring biomedical,⁶ physiological,⁷ and biomimetic⁸ signals. Several e-textile platforms were reported to capture and monitor physiological signals from the human body,⁹ including body temperature,¹⁰ oxygen saturation level,¹¹ heart rate,¹² and human body motion.^{2,13} Both yarn and fabric-based sensors have been employed to produce such wearable e-textile sensors.^{14–17} Despite that the amount and position of conductive materials in the whole configuration vary from one study to another, the performances of e-textile sensors mainly depend on the electrical conductivity of nano-micro materials deposited on textiles, and the flexibility of textile substrates.^{18,19}

Carbonaceous materials such as graphene and carbon nanotubes (CNT) have widely been used as electrically conductive materials for e-textiles applications,²⁰ due to their advantages including excellent electrical conductivity,^{21–23} good mechanical properties^{24–26} and high specific surface area.^{27,28} However, the performances of e-textile sensors based on carbonaceous materials can easily be influenced by external stimuli such as the room temperature,²⁹ oxidation,³⁰ corrosion,³¹ abrasion³² and washing³³ of conductive materials. Researchers have developed various methods to overcome such limitations. For instance, Kim et al. prepared boron-coated multi-walled CNT which maintains superior conductivity even at 1000 °C.³⁴ Joh et al. used PET and PDMS layers to cover conductive materials to prevent the effect of water and oxygen.³⁵ Zhou et al. bridged CNT to PDMS with a silane coupling agent (KH550) to realize the stable adhesion of conductive materials to the substrate.³⁶ However, there remain several challenges that need to be addressed to produce robust and reliable wearable e-textiles. The conductivity and durability of graphene-based materials need further improvements to enable the detection of fine actions of the human body.³⁷ Additionally, the fatigue of the sensor caused by the abrasion during its long-term service is a great concern for such e-textiles.³⁸ Furthermore, the polymer coatings lead to an increase in the thickness, which adversely affects the mechanical properties of the sensor, such as flexibility, elasticity, and recoverability.³⁹

¹State Key Laboratory of New Textile Materials and Advanced Processing Technologies, Wuhan Textile University, Wuhan 430073, China

²School of Textile Science and Engineering, Wuhan Textile University, Wuhan 430200, China

³Centre for Print Research (CFPR), University of the West of England, Frenchay, Bristol BS16 1QY, UK

⁴Lead contact

*Correspondence: shaila.afroj@uwe.ac.uk (S.A.), nazmul.karim@uwe.ac.uk (N.K.), zzhao@wtu.edu.cn (Z.Z.)
<https://doi.org/10.1016/j.isci.2023.106403>



The doping of graphene structure with nitrogen atoms has been proven to be a feasible method to improve its conductivity.⁴⁰ The blending of graphene sheets with CNT is another way to realize improved conductivity, as CNT can bridge graphene sheets to promote electron migrations.⁴¹ However, the poor binding strength between substrate materials and carbon-based materials leads to poor washability, durability, and occurrence of hysteresis.⁴² Filling carbonaceous nanomaterials into the matrices is a feasible way to fabricate continuous fibers or filaments with satisfied conductivity. For instance, carbon-based nanofillers can be integrated into polyethylene matrices via coaxial electrospinning to fabricate thermal conductive nanofibers.⁴³ Besides, rGO and MXene can be injected into polypropylene tubes to shape these nanocarbon materials into fiber-like carbonaceous hybrids for potential wearable supercapacitor applications.⁴⁴ Silicon rubber could be a potential solution as a substrate to mix or cover the conductive materials to form the e-textile due to their good stretchability, flexibility^{45,46} and elastic recovery.⁴⁷ Meanwhile, the hollow tube can act as a mold to model the nanocarbon fillers in a continuous shape. These advantages ensure good mechanical performances of wearable sensors as well as protecting the continuous conductive materials from abrasion, oxidation, and water.⁴⁸ In addition, from the perspective of commercial application, the durability of the sensor can be dramatically improved, thus, the use cost of this sensor can also be lowered. Moreover, using the silicon rubber as the container to cover the conductive powder has more advantages over the mixing method due to the fact that mixing the conductive powder with the silicon rubber directly would have an adverse effect on the mechanical properties of the final e-textile, and the sensitivity of the e-textile can be tailored by adjusting the quantity and compression degree of the conductive powder. Meanwhile, the conductive powder filled inside the matrix can support the outer layer of the matrix and reduce its deformation extent, thus, balancing deformation with recovery and enhancing the reproducibility and stability of the sensor. Compared with liquid-phase and paste-like filling materials, the solid-state conductive powder has higher rigidity. By filling these solid substances into the matrix, the hysteresis effect can be weakened as the extent of deformation can be further reduced.

In this study, N-doped rGO and PDA-coated CNT (PDA@CNT) were separately prepared and then blended together to form a mixed powder with enhanced conductivity. The PDA layer formed on CNTs enhances the adhesion between CNT and graphene sheets and improves the stability of the mixture. The rGO/PDA@CNT hybrid powder was then covered by silicon rubber and mixed with Ecoflex to fabricate flexible e-textile sensors. Doping nitrogen sources can improve the conductivity of hybrid carbon materials-based wearable e-textiles, while the silicon substrates protect them from abrasion, ensuring prolonged service life of the wearable sensors. The as-prepared conductive silicon rubber tube (CSRT) was mounted on the elastic Lycra vest via a tailored fiber placement (TFP) embroidery technique. It provides good firmness and realizes the fixation of filaments at desired positions with variable structures. The sensor was then able to monitor the wearer's signals of respiration and heart rate.

RESULTS AND DISCUSSION

Characterization

CNT has an average radius of approximately 50 nm (Figure 1B). It can be observed from the combined mapping results (Figure 1C) that nitrogen atoms are evenly scattered on the CNT surface after the coating process, indicating successful self-polymerization of dopamine on CNTs. This is consistent with the appearance of a nitrogen peak at ~400 eV in the overall XPS spectrum (Figure 1G) of the mixed powder. By further comparing the obtained and the peaks reported in the literature, the peaks at the binding energy of ~400.4 and ~398.4 eV (Figure 1H) can be assigned to the pyrrolic N and pyridinic N,⁴⁹ respectively. Similarly, the peaks at the 2θ of 26.0° and 42.6° (Figure 1I) can be assigned to (002) and (100) planes of CNTs,^{50,51} respectively. The results from XPS and XRD jointly indicate the existence of PDA coverage on CNTs. However, no obvious trace of N-doped rGO can be observed from the SEM image of the mixed powder (inset in Figure 1I) as the content ratio of N-doped rGO in the filling material is relatively low. This is also reflected by the fact that no prominent diffraction peaks of amorphous graphene were observed in the XRD spectrum of filling materials (Figure 1I).

Sensing capability/electro-mechanical characterization of CSRT and CEF filaments

To assess the sensing capability, CSRT (1.14 S/m) and conductive Ecoflex filament, CEF (0.24 S/m) filaments were subjected to a single compression test (Figures 2A–2F). The changes in the resistance of filaments were measured and recorded via the NI-9219 data acquisition card (National instrument, USA). Linear correlations between the resistance of the CSRT as well as CEF and the compression force applied to the sensors can be clearly observed (Figure 2A and 2D). It is notable that an open circuit occurs for CEF when the

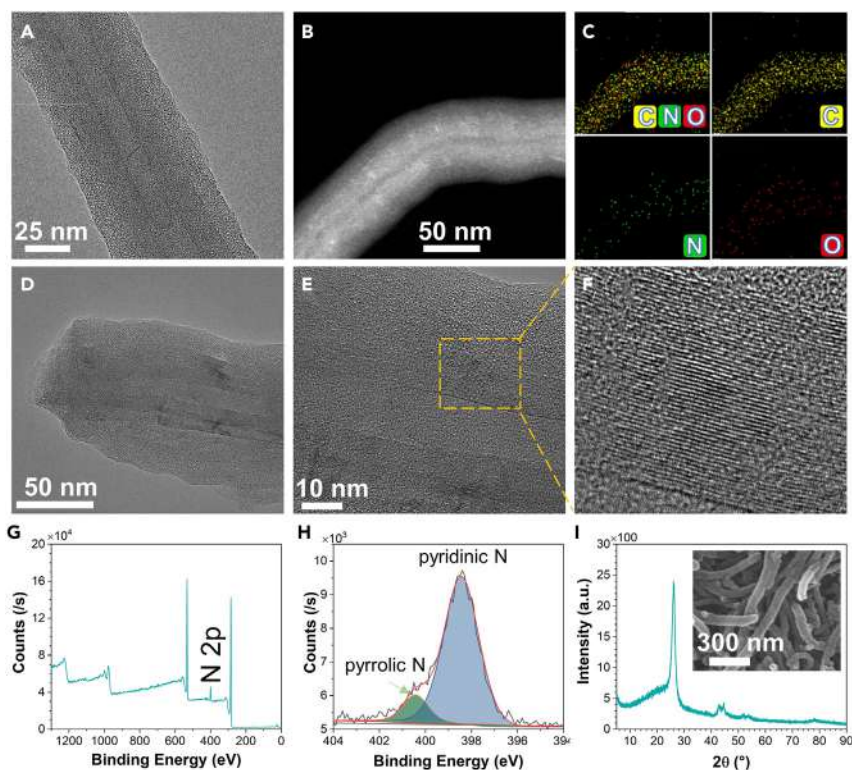


Figure 1. Characterization results of CSRT

- (A) TEM image of the PDA@CNT.
(B) HAADF image of CSRT.
(C) Mapping results of CSRT.
(D) TEM image of CSRT.
(E and F) CNTs in the CSRT.
(G) Wide scan XPS spectrum.
(H) high-resolution spectrum of N1s.
(I) XRD spectrum and SEM (inset) of the mixed powder of PDA@CNT and N-doped rGO.

compression force reaches 38.2 N (Figures 2D and 2E). The open circuit can be attributed to the structural difference between the two filaments (Figure 2D). When the compression force is applied to those two filaments, CEF would become a totally flat two-dimensional structure due to the lower rigidity and softer texture. However, the filling conductive powder inside CSRT will be more tightly compressed while its three-dimensional structure still remains. Specifically, a breakpoint inside the CEF may occur when the force is applied to the filament, leading to the compression of filling materials inside it and sliding of particles against the stress point. Therefore, a clear negative correlation between the resistance of CSRT and the applied compression force can be observed, while the correlation turned positive in the case of CEF.

As presented in Figure S4A, the compression strain curves as the function of force overlap well when the force increased stepwise from 10 to 40 N, indicating stable responsiveness of CSRT to dynamic compression load. However, distinct steps can be observed in the compression strain curves of CEF when the force increased at the intervals of 10 N, suggesting that the CEF deformed and rebounded at different speeds and to different extents when the force changed stepwise. Moreover, wider gaps between the compression and compression back sections can be observed in the compression curves of CEF, reflecting severe hysteresis that CEF exhibited during its compression-recovery cycles. The compressive deformation of CSRT includes the deformation of the silicon rubber tube and the compression of the conductive powder inside. However, as the CEF is made from the Ecoflex blended with the sparsely dispersed conductive nanoparticles which barely affect the strength of the matrix, its deformation and recovery depend mainly on the flexibility of the matrix itself. When the same compression load is applied, the compression strain of CSRT is smaller than CEF as the solid conductive powder inside the CSRT can support the rubber matrix

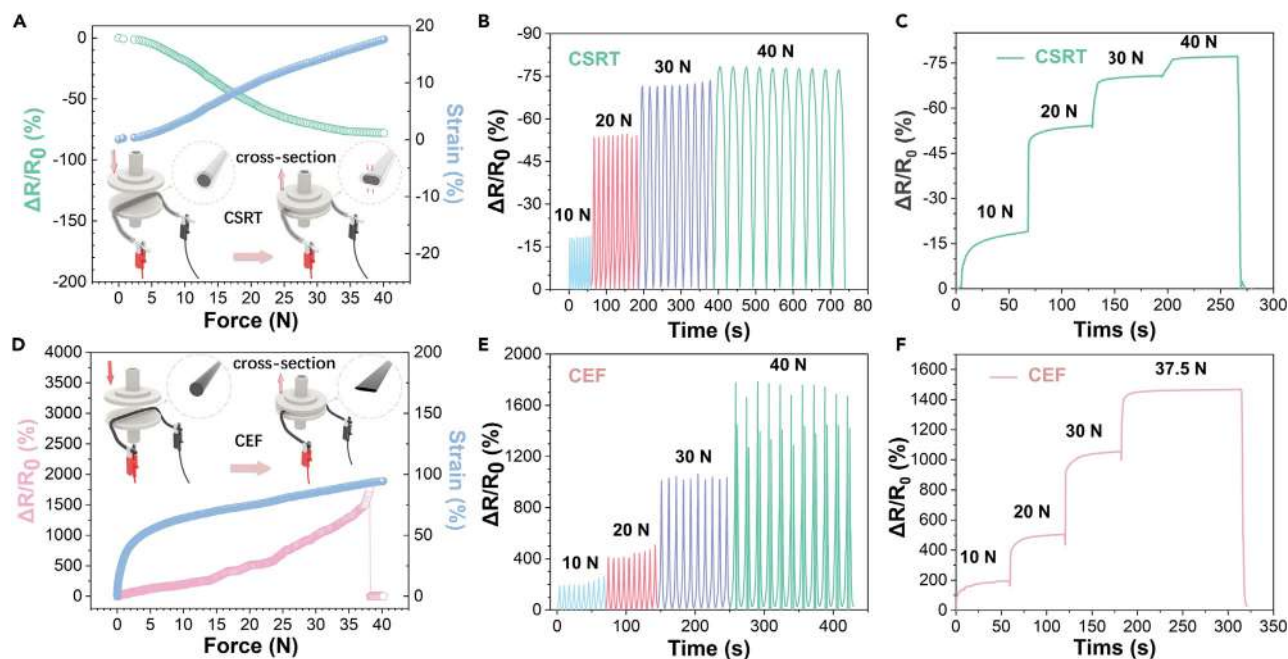


Figure 2. Electro-mechanical test results of CSRT and CEF filaments

- (A) A single compression test result of CSRT filament from 0 to 40 N.
 (B) A stepped compression cyclic test result of CSRT.
 (C) A stepped quasi-static test result of CSRT filament.
 (D) A single compression test result of CEF filament from 0 to 40 N.
 (E) A stepped compression cyclic test result of CEF.
 (F) A stepped quasi-static test result of CEF filament.

against further compression. When the compression load is removed, the CSRT can rapidly recover to its original shape due to its lower compression strain. This narrows the hysteresis caused by the unsynchronized deformation and recovery speed.

Table S1 shows the comparison of the CSRT and CEF with the previous studies. The CSRT and CEF filament present a larger working range than that reported in the previous studies,^{52–59} which is significantly higher than general wearable pressure.⁶⁰ Additionally, they indicate a relatively higher sensitivity as a conductive yarn compared to previous studies.^{52–58,61,62} Moreover, the signal output of the CSRT filament was stable and repeatable, and its flexibility and bendability demonstrate its excellent capability as a wearable filament.

Figures 2B and 2E show the stepped cyclic test results for the CSRT and CEF. The compression force was increased from 10 N to 40 N with the same compression speed employed in the single test. During the cyclic test, CSRT presented excellent durability and stability, and the resistance of CSRT was not changed significantly before and after the test. It can be seen from Figures 2B and 2E that the deformation speed of CEF is faster than that of CSRT. Due to the relatively lower rigidity and recovery speed, the cyclic result of CEF is unstable, especially when the load is around 38.2 N. The changes in resistance of CEF suddenly increased from 1300% to 1600–1800%, and then an open circuit occurred. However, the open circuit happened whenever the compression force reached ~38.2 N during the cyclic test, which means that it can be used as an open circuit alarm.

Figures 2C and 2F exhibit quasi-static test results of those two filaments. The tensile machine will keep the compression load for 1 min at 10 N, 20 N, 30 N, and 40 N for CSRT, and at 10 N, 20 N, 30 N, and 37.5 N for CEF. Both filaments demonstrate good stability during this test, especially when the compression force is over 20 N. However, when the compression is lower than 20 N, it takes more than 10 s for their resistance to become stable.

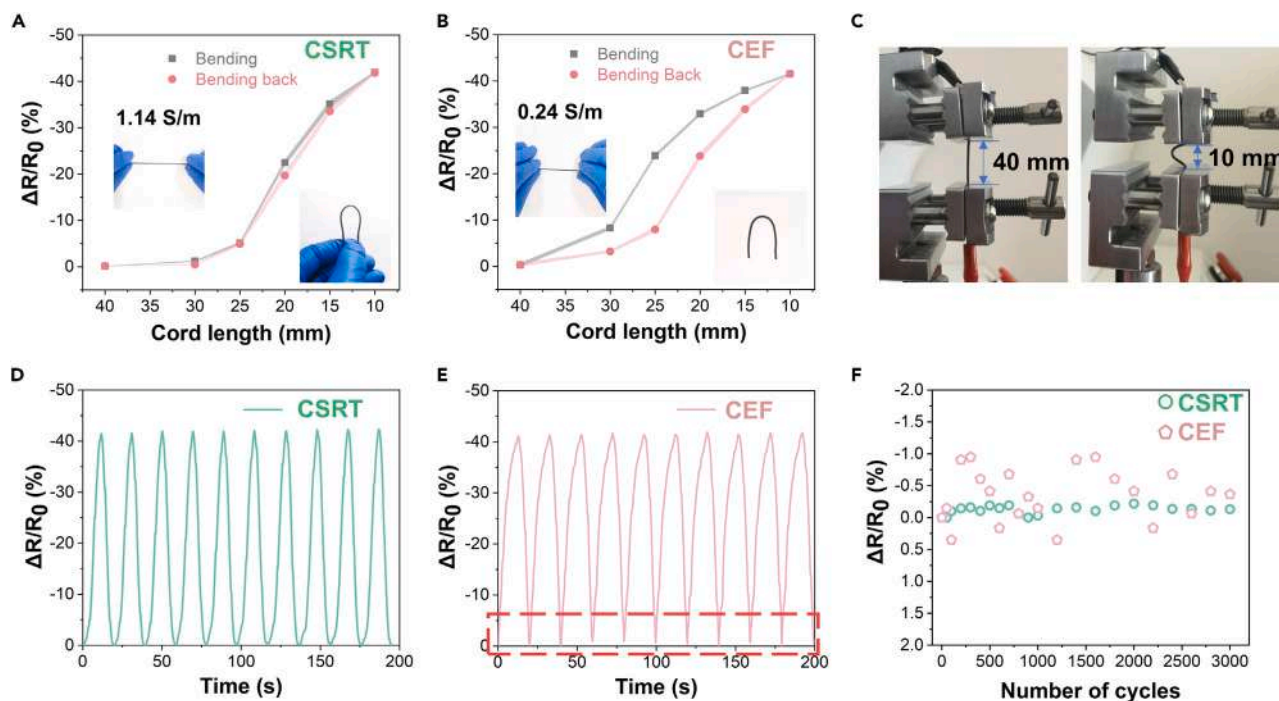


Figure 3. Bending test result of CSRT and CEF filaments

- (A) Bending and bending back result of CSRT filament with error band.
(B) Bending and bending back result of CEF filament with error band.
(C) Optical image of the CSRT filament during the bending test.
(D) Bending cyclic test result of CSRT filament.
(E) Bending cyclic test result of CEF filament.
(F) 3000 times cyclic test result of CEF and CSRT filament.

Performance and flexibility of CSRT and CEF filaments

The flexibility of the as-prepared graphene-CNT-based CSRT and CEF filaments was further investigated. Figures 3A and 3B show the changes in resistances per total length of CSRT and CEF filaments at various bending positions with concave down at various cord lengths (Figure 3C). The cord lengths were controlled with the tensile tester. Here, the cord length is defined as the distance between the tensile tester grips for the filament material under investigation.^{63,64} As seen in Figure 3A, a repeatable response in forward (bending) and reverse (bending back) directions was observed. Similarly, for the CEF, the change in resistance was repeatable in both the forward (bending) and reverse (bending back) directions (Figure 3B).

When Figure 3A and 3B are compared, the error band of the CSRT is relatively smaller than that of CEF, especially at the beginning of the bending process. Moreover, the hysteresis gap between bending and bending back is narrowed when the conductive powder was filled into the silicon rubber tube (Figure 3A). These results indicate that the CSRT has better repeatability and stability. Unlike the compression test, where the change in resistance of CEF increased with the increase of the load, a negative correlation between the resistance of the CEF and its cord length for bending was observed. This may be due to the lower rigidity of the Ecoflex exhibited during the bending test. More specifically, Ecoflex is soft and easy to be bended; hence there is no significant change in the radius of cross-section and volume at the bending point, while the conductive powder inside the CEF was compressed and became closer, facilitating the current flow, which would lead to the decrease in the resistance of the CEF.

After this, 10 cycles and 3000 cycles of bending cyclic tests were carried out for both filaments (Figures 3D–3F). This can be observed in Figures 3A and 3D, the resistance of the CSRT changed slightly at the beginning of the bending process, and the resistance of it decreased significantly from 30 to 10 mm, especially 25–15 mm. It can be also found that compared to CSRT, the CEF's $\Delta R/R_0$ reversed much quickly at the lowest points (also points of 40-mm cord length) as the curves of CEF is non-differentiable at these lowest points of $\Delta R/R_0$ (Figure 3E). From

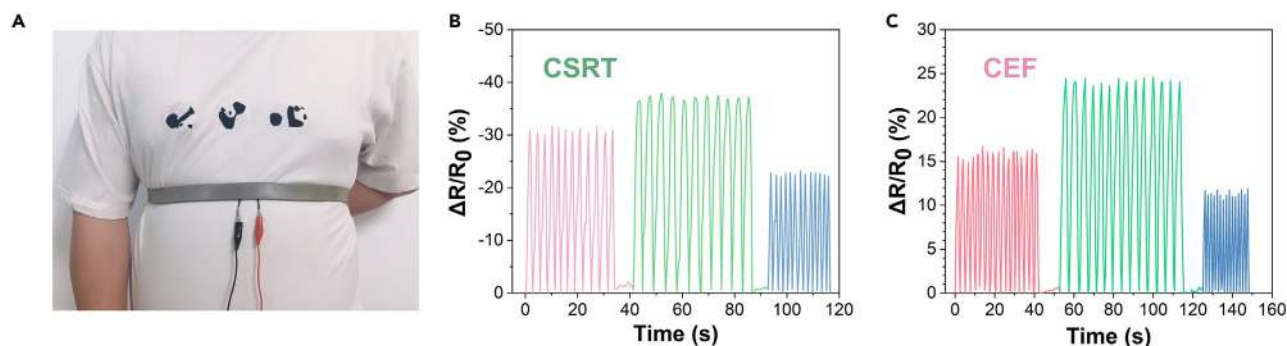


Figure 4. Respiratory signal sensing of the CSRT and CEF sensors

- (A) Image of the subject placed the sensor under the elastic band on the below chest location.
 (B) Resistance of CSRT variation due to respiration.
 (C) Resistance of CEF variation due to respiration.

the perspective of integration, this non-differentiable nature of the CEF's lowest $\Delta R/R_0$ points means that the CEF exhibited higher sensitivity (higher absolute value of $\Delta R/R_0$ compared to CSRT) at the beginning of the bending process. However, it exhibited lower sensitivity at the end of the bending process as the absolute value of CEF's $\Delta R/R_0$ increased at a slightly lower speed than that of CSRT.

Figure 3F is the 3000 cycles bending cyclic test results of the two filaments, the changes in resistance were recorded whenever the cord length reaches 40 mm (straight filament). It can be clearly seen that the resistance of the CSRT is more stable during the long-term cyclic test ($\Delta R/R_0$ is around 0.02% to -0.15%), while that of CEF is scattered ($\Delta R/R_0$ is around 0.34% to -0.94%).

Furthermore, a series of joints activities monitoring tests were carried out to investigate the bendability, reliability, and capability of the CSRT and CEF to monitor human activities. The experimental produces along with corresponding results (presented in Figure S7) and the discussion of the tests are placed in Supporting Information.

Respiration monitoring capability of CSRT and CEF filaments

To investigate the bio-signal sensing performance of those two filaments for real-life implications, they were further tested as breathing sensor. They were placed under an elastic band (Figure 4A) around the chest location. The NI-9219 data acquisition card was connected with filaments to record the changes in the resistance during the breathing test. The breathing test started with normal breath; the subject stopped breathing for a few seconds after 10–12 breathes, and then continued to breathe deeply. After 10–12 deep breathes, the subject started a fast-breathing and the responses of those two filaments to the fast breathing were recorded (as shown in Figures 4B and 4C). During the three-step breathing test, both sensors performed well with excellent stability and outstanding response speed during the fast-breathing test. Although, the changes in resistance fluctuate a little bit during the test, which may be due to not being able to maintain the same breath range by the subject during the test. Nevertheless, such results can still demonstrate that the conductive sensors are capable of bio-signal sensing.

During all the tests above, the CSRT represents a relatively much better performance as a sensor, as it shows relatively more stable signal output, fast recovery speed, and higher sensitivity during the compression and bending test. As for the CEF, it exhibits a good elasticity and relatively greater changes in resistance during the tests, however, the strength and recovery speed of the CEF were significantly weakened due to added PDA@CNT and N-doped graphene powder. Also, the quantity of the conductive powder has a great influence on not only the mechanical properties of CEF but also the electro-mechanical properties. Although it shows a relatively unstable signal output, it presents a stable break circuit when the load arrives at a specific value during the cyclic tests, which exhibits its capability as an open-circuit alarm material.

Comparison of the CSRT structures

It is worth mentioning that we observed lower sensitivity and unstable signal output when the compression load was maintained at lower level. This unstable performance might be caused by gaps in the conductive

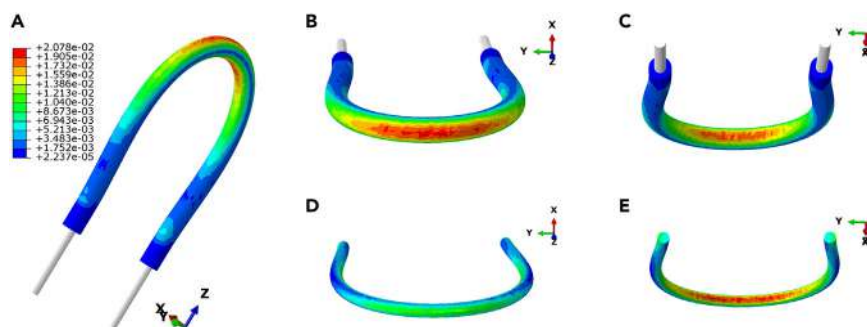


Figure 5. Simulation of the effect of bending on the strain of the CSRT obtained in ABAQUS

(A) Strain distribution of the bended CSRT. Strain distribution on the (B) outer surface and (C) inner surface of the bended CSRT. Strain distribution on the (D) outer surface and (E) inner surface of the conductive powder unit within the bended CSRT.

powder, the CSRT displays an insensitive response to the pressure applied as the conductive powder was first compressed. Once the force applied exceeds this insensitive range, the CSRT exhibits a sharp response to the force as its electrical resistance changes rapidly since the gaps have disappeared. Therefore, to eliminate this insensitive working range in real-life application, the CSRT was bended into three different shapes to fully compress the conductive powder loaded in it.

To reveal the impact of bending force within the CSRT, the process of bending the CSRT into a “U” shape was simulated in ABAQUS. As Figure 5A shows, bending the CSRT into the “U” shape caused the increase of strain within the arch section of the bended CSRT sample. More specifically, the outer and inner surfaces of the bended CSRT underwent obvious stretch (Figure 5B) and compress (Figure 5C), respectively. As the gaps between the tubes and the stainless rods were sealed by Ecoflex, the conductive powder inside the tube cannot overflow alongside the axis direction of the tube. When the CSRT was bended, the inner surface of the conductive powder was densely compressed (Figure 5E) due to the force applied by the tube. It is also notable that the strain of the outer surface of the conductive powder section (Figure 5D) was not dramatically increased to the extent of that observed from the surface of the tube (Figure 5B). The possible reason is that the top area of the conductive powder unit turns relatively sparser when it is shaped into a “U” pattern during the bending of the CSRT. Overall, the simulation results confirm that the bending action provided the pre-load for the CSRT.

However, when more bending arcs are formed, the rigidity of the CSRT will become higher, and the recovery speed will become lower which might lead to an unstable resistance curve during the tests. Therefore, three structures (P1, P2, and P3) were designed and manufactured by TFP (Figure 6A), which were tested under the same condition as the straight CSRT.

Figure 6B illustrates the single compression test results of three structures. Figure 6B shows that all three structures, particularly P3, can improve the sensitivity significantly, when the compression load is under 10N. However, when the force exceeds 10N, the changes in resistance of P3 are not apparent (resistance changes from 60% at 10N to 70% at 40N). It may be due to two arcs push the conductive powders from two sides to the middle area of the structure which can provide higher pre-loads than the other two structures.

Figures 6C–6E indicate the stepped cyclic test results of the three structures, and Figures 6F–6H summarize the stepped long-term stability test results of those three structures. Compared to the straight CSRT, the sensitivity of the three structures from 0 to 5N, increased from 0.01 N^{-1} to 0.052 N^{-1} , 0.09 N^{-1} , and 0.048 N^{-1} . Compared to P2 and P3, P1 shows relatively higher stability and repeatability. There was not a significant drift during both the cyclic test and long-term stability test of structure 1. Moreover, there is a clear difference in the resistance of structure 1 between each load step.

In contrast, the changes in resistance of P2 and P3 fluctuated during the cyclic tests. Although the resistance of P2 did not present an evident drift during the stepped long-term stability tests like P3, the resistance of

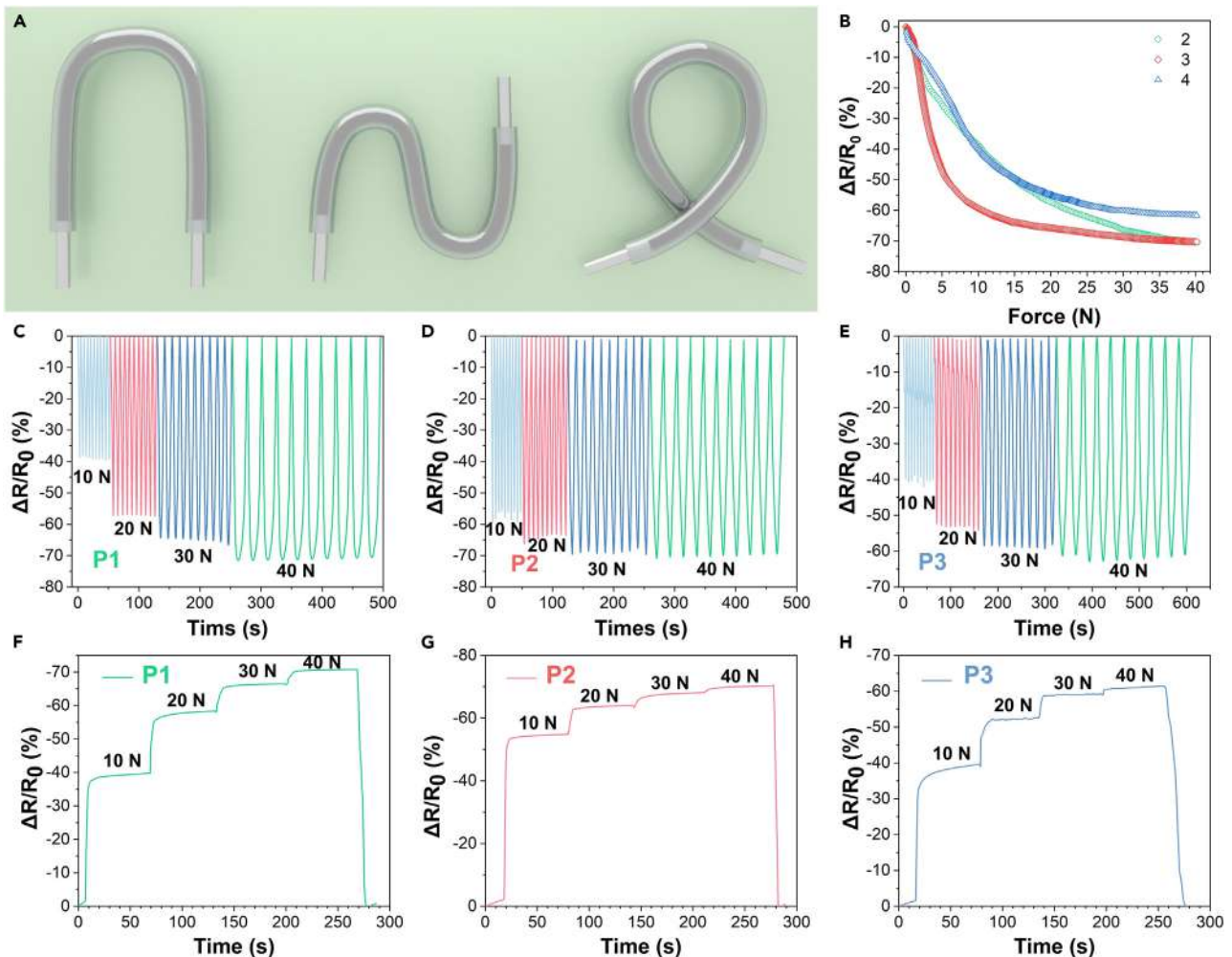


Figure 6. Electro-mechanical test results of the three different structures

(A) CSRT in three different structures.

(B) Single compression test results of the three structures from 0 to 40N.

(C–E) Stepped cyclic test results of the three structures, respectively.

(F–H) Stepped quasi-static test results of the three structures, respectively.

P2 did not describe a clear difference when the compression load reached 30N and 40N. Figure 6D shows that the changes in resistance of P2 at 30N and 40N loads were almost the same, which might have a significant influence on the final applications.

Compared to P2 and P3, P1 exhibits excellent stability of signal output and a more linear resistance-to-force correlation. Moreover, P1 shows a significantly higher sensitivity compared to straight CSRT while the load is under 10 N. Although, P2 presents a relatively most heightened sensitivity at lower compression force, its durability and stability are lower than P1. As discussed above, the resistance of P2 did not exhibit a clear difference when the load reached 30N and 40N.

Respiratory and pulse signal sensing

In order to investigate the bio-sensing capability of the P1 sensor, it was used to detect and measure the pulse and cardiac signals in addition to the breathing test. Figure 7A shows the changes in resistance of P1 during the respiration process. Similar to the straight CSRT, it offers good capability of detecting breathing signals and the collected respiration data was stable without observing any noise.

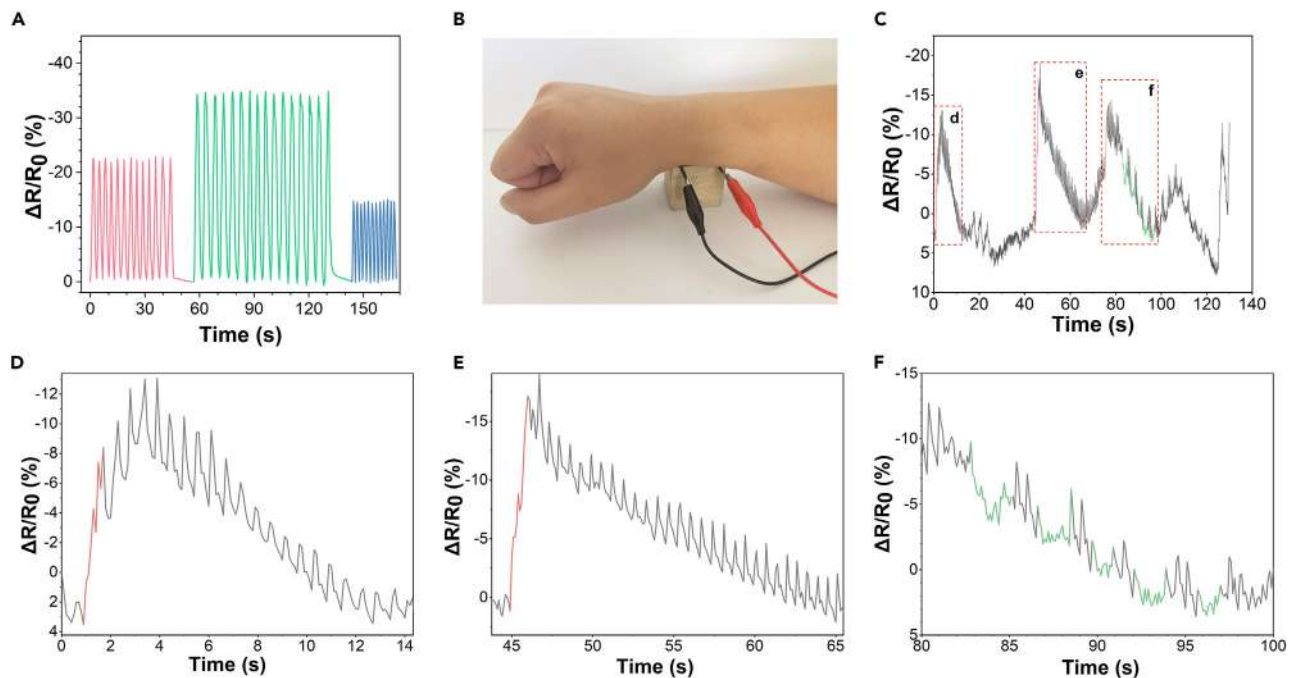


Figure 7. Respiratory and pulse signal captured by P1

- (A) Respiratory signal captured by P1.
(B) Image of the sensor under the wrist during the pulse signal measuring.
(C) Pulse signal captured by P1.
(D) Expanded version of (c) from 0 s to 14 s.
(E) Expanded version of (c) from 45 s to 65 s.
(F) Expanded version of (c) from 80 s to 100 s.

The sensor was then placed between the right part of the wrist and a wooden cube as shown in [Figure 7B](#) ([Video S1](#)). [Figures 7D–7F](#) show the change in resistance due to the wrist pulse for a selected section of total 2 min pulse recorded. During the test, it was found that whenever the subject breathed, the changes in resistance of the sensor increased suddenly (the red line in [Figures 7D–7F](#)), which may be due to the fact that the wrist was placed on the wooden cube. Therefore, every time the subject breathes, the wrist of the subject will apply a slight compression force on the sensor. To verify the data fluctuations were caused by the breath of subject, the subject breath 5 times quickly (the green waves in [Figure 7F](#)). It can clearly be seen that the sensor could capture both respiration signal and pulse signal. In addition, the pulse signals captured during the subject was holding his breath could be clearly observed. Although the trend of the resistance has a sharp drift due to the respiration, it still exhibits the high sensitivity of small bio-signal sensing. In order to eliminate the error caused by wrist movement during respiration, and to assess the sensors' capability of minor simulation/movement detection, the sensor was placed under an elastic band to measure the cardiorespiratory signals.

Cardiorespiratory signal sensing

To capture clean and integral bio-signals and eliminate noise/interferences, the sampling rate of the NI-9219 data acquisition card was set from 10 to 50 Hz. Additionally, a bandpass filter was applied to improve the reliability of the signal output of the sensor. The heartbeat rate varies from person to person, usually 60–100 times per min, namely 1 to 1.67 Hz. Considering the cardiac patients and athletes, the bandpass filter was set from 0.8 to 2 Hz for cardiac signal capturing. The cardiorespiratory test was carried out on two healthy male volunteers. During the cardiorespiratory test, Subject 1 breathed for around 3 min and then held his breath as long as he could ([Video S2](#)) while Subject 2 breathed every 10–15 s.

[Figures 8A](#) and [8B](#) show the cardiorespiratory monitoring results of Subject 1 before and after filter. [Figures 8F](#) and [8G](#) show the cardiorespiratory monitoring results of Subject 2 before and after filter. It

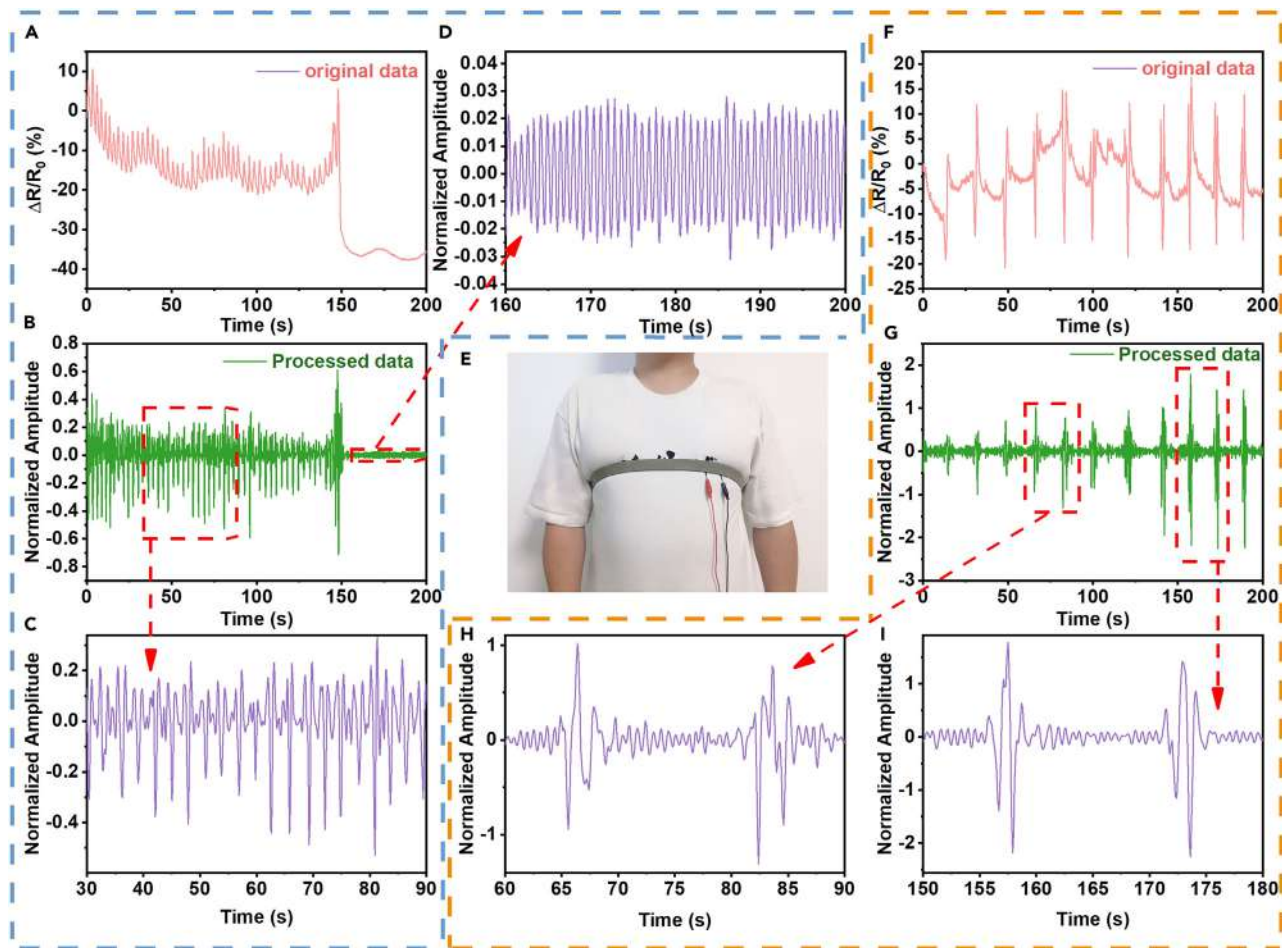


Figure 8. P1 cardiorespiratory signal sensing results

- (A) Subject 1's cardiorespiratory signal captured by P1 without bandpass filter.
- (B) Subject 1's cardiorespiratory signal captured by P1 with bandpass filter.
- (C) Expanded version of (B) from 30 s to 90 s.
- (D) Expanded version of (B) from 160 s to 200 s.
- (E) Image of Subject 2 placed the P1 under the elastic band on the chest location.
- (F) Subject 2's cardiorespiratory signal captured by P1 without bandpass filter.
- (G) Subject 2's cardiorespiratory signal captured by P1 with bandpass filter.
- (H) Expanded version of (G) from 60 s to 90 s.
- (I) Expanded version of (G) from 150 s to 180 s.

shows that the bandpass filter helps to filter noises/interferences and makes both the cardiac signal and respiration signal more visible. Figures 8C and 8D show the change in resistance due to the cardiorespiratory for a selected section of Figure 8B. Figures 8H and 8I show the change in resistance due to the cardiorespiratory for a selected section of Figure 8F. Figure 8D exhibits a highly stable and clear cardiac signal captured by the sensors when the subject held his breath, which demonstrates the high sensitivity of the sensor. Figures 8H and 8I show that sensors can detect both cardiac and respiration signals at the same time. After each breath, the cardiac signals can clearly be monitored by the sensor. Even when the subject breathed normally (as shown in Figure 8C), the sensor is still capable of detecting cardiac signals clearly which shows the superior response speed and high sensitivity of the sensor. It can be clearly observed from Figures 8H and 8I that after each deep breath, the heart rate will decrease and then back to normal. It might be due to respiratory sinus arrhythmia, when the subject inhales and exhales, the heart rate will increase and decrease, respectively. Slight differences can be detected and measured by the sensor, which demonstrates higher accuracy and reliability of the sensor which provides the possibility of monitoring of patient's health at home.

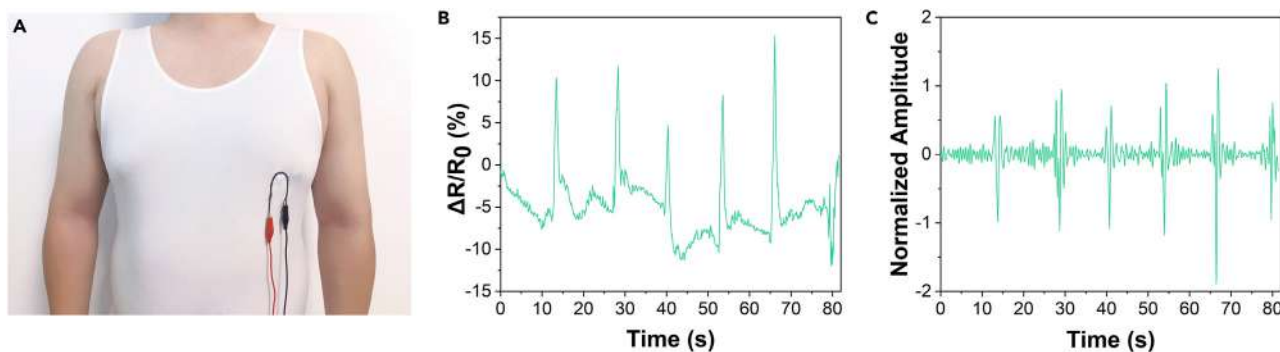


Figure 9. Cardiorespiratory signal captured by P1 on the Lycra vest

(A) Image of Subject 2 wearing the Lycra vest.

(B) Subject 2's cardiorespiratory signal captured by sensor without bandpass filter.

(C) Subject 2's cardiorespiratory signal captured by the sensor with bandpass filter.

Tightly fitting the sensor to the chest of the subject or improving the sensitivity of the sensor can improve the accuracy of cardiorespiratory signal monitoring. Although these two points can be easily realized by utilizing the elastic band, the pressure caused by tight binding may cause inconvenience and discomfort for the wearer.

To consider the capability of the CSRT for daily bio-signal monitoring without the elastic band, the CSRT sensor was sewed onto a vest via the tailored fiber placement (TFP) technique. The main advantage of the TFP is that the upper sewing thread and substrate fabric/cloth can also provide equivalent compression to the CSRT placed in between. Besides, as evidenced by the results of finite element analysis (Figure 5), when the CSRT was sewed onto the substrate in different bended shapes, more pre-loads to it can be generated to improve the sensitivity of the CSRT. Therefore, to investigate the capability of the sensor sensing the cardiac signal without the elastic band, the CSRT was fixed on a Lycra vest at the chest location by the tailored fiber placement technique (Figure 9A).

Same as the above test, the subject worn this Lycra vest and the resistance of the sensor was measured and record by the NI-9219 data acquisition card (Video S3), also the bandpass filter was used to reduce the noise during the cardiac signal-capturing process. Figures 9B and 9C show the test results before and after the filter. It can be clearly seen that, even without the help of the elastic band, the CSRT sensor can still capture the respiratory and cardiac signals. And the same situation can be clearly noticed in Figure 9C that when the subject exhaled, the heart rate decreased.

Figures 8 and 9 exhibit the capability of the CSRT sensor to capture the cardiorespiratory signal with and without the help of the elastic band. The experiments reveal that this CSRT sensor can capture clear cardiac signals while the subject was holding his breath, slow breathing, and normal breathing. Therefore, it is evident that this CSRT sensor has the capability to measure and monitor the cardiorespiratory signal as a wearable sensor. It is worth mentioning that the whole fabrication process of the CSRT took only 30 min for vacuum filling and further 30 min for the evaporation of water from the paste. The total time for the fabrication process can further be shortened with the use of the industrial vacuum instrument. Therefore, by ensuring the supply of adequate conductive paste and silicon rubber tubes, the CSRT can be manufactured continuously for large-scale industrial production. This manufacturing technique also features high reuse rate of the residual paste. The high durability and electro-mechanical performance of the CSRT thus ensures its potential commercial value.

Conclusion

In summary, two different conductive filament sensors were fabricated by using the N-doped rGO and PDA@CNT mixed powders (Figure 10). The CSRT exhibited excellent durability and sensitivity as well as lowered hysteresis during all the tests, while the CEF expressed relatively unstable and lower repeatability during the same tests. Also, the working range (strength) and the recovery speed of the CEF were relatively worse than the CSRT. However, the CEF still shows the ability being an open circuit alarm, the breakpoint would occur every time when the load reach ~ 38.2 N.



Figure 10. Schematic diagram of N-doped rGO and PDA@CNT

To improve the sensitivity of the CSRT to sense slightly force, it was shaped into different structures via the tailored fiber placement technique. The finite element analysis results confirmed that bending curves of the sensor structure could provide a pre-load to the sensor, then improve the ability to sense slight movement or simulate (the sensitivity of the three structures improved 4–9 times than straight filament); especially the one bending curve structure exhibits excellent sensitivity of slight movement/simulate, and the good response speed and repeatability. Moreover, it represents the capability of human bio-signal sensing, especially the cardiorespiratory signal. The sensor was tested under different respiration speeds, under each situation, it could capture and monitor reliable, stable, and precise breathing as well as cardiac signals. Finally, the sensor was fixed on a vest, it still exhibited high sensitivity and accuracy for bio-signal sensing even without the help of any elastic band. The above results demonstrate that the CSRT sensor would be an essential step toward realizing the bio-signal sensing of wearable e-textile for next-generation health care devices. Moreover, once the CSRT is prepared for mass production, the continuous CSRT can be cut into shorter pieces with different lengths as required, thus providing tailor-made choices for potential customers.

Limitations of the study

In this article, we fabricated the conductive silicon rubber tube by filling PDA@CNT and N-doped rGO matrix inside the silicon rubber tube. It shows excellent durability, stability, and sensitivity. In addition, its sensitivity can be adjusted by bending the conductive silicon rubber tube to different angles. Due to the silicon rubber tube chose in this article having a relatively higher rigidity lower extendibility, the conductive silicon rubber tube did not exhibit the sensibility of strain. It is worth noting that choosing an elastic material with higher softness and better ductility as the substrate will result in a decrease in the recoverability of the final sensor as well as the occurrence of deepened hysteresis, which has been observed in the results of CEF. Moreover, the filling conductive materials are dried PDA@CNT and N-doped rGO powders, it might lead to an open-circuit or unstable signal output during the tensile test.

STAR★METHODS

Detailed methods are provided in the online version of this paper and include the following:

- [KEY RESOURCES TABLE](#)
- [RESOURCE AVAILABILITY](#)
 - Lead contact
 - Materials availability
 - Data and code availability

● **METHOD DETAILS**

- Preparation of conductive silicon rubber tube
- Characterization
- Sensing performance of the CSRT and CEF
- Modelling and pre-load analysis in ABAQUS
- Fabrication of the embroidered sensor and bio-signal sensing

SUPPLEMENTAL INFORMATION

Supplemental information can be found online at <https://doi.org/10.1016/j.isci.2023.106403>.

ACKNOWLEDGMENTS

SA and NK are supported by funding from UKRI Research England The Expanding Excellence in England (E3) grant. MRI is supported by the UWE partnership PhD award. This work is also supported by the National Natural Science Foundation of China (Grant Number 52202024).

AUTHOR CONTRIBUTIONS

Sirui Tan: Investigation, Data Curation, Formal analysis, Writing - Original Draft.

Shaila Afroj: Validation, Funding acquisition, Writing - Review & Editing.

Daiqi Li: Validation, Funding acquisition.

Md Rashedul Islam: Writing - Review & Editing.

Jihong Wu: Supervision, Resources.

Guangming Cai: Supervision, Resources.

Nazmul Karim: Project administration, Funding acquisition, Writing - Review & Editing.

Zhong Zhao: Conceptualization, Methodology, Visualization, Writing - Review & Editing.

DECLARATION OF INTERESTS

The authors declare no competing interests.

Received: November 15, 2022

Revised: February 27, 2023

Accepted: March 10, 2023

Published: March 15, 2023

REFERENCES

1. Libanori, A., Chen, G., Zhao, X., Zhou, Y., and Chen, J. (2022). Smart textiles for personalized healthcare. *Nat. Electron.* 5, 142–156. <https://doi.org/10.1038/s41928-022-00723-z>.
2. Islam, M.R., Afroj, S., Beach, C., Islam, M.H., Parraman, C., Abdelkader, A., Casson, A.J., Novoselov, K.S., and Karim, N. (2022). Fully printed and multifunctional graphene-based wearable e-textiles for personalized healthcare applications. *iScience* 25, 103945. <https://doi.org/10.1016/j.isci.2022.103945>.
3. Kong, W.-W., Zhou, C.-G., Dai, K., Jia, L.-C., Yan, D.-X., and Li, Z.-M. (2021). Highly stretchable and durable fibrous strain sensor with growth ring-like spiral structure for wearable electronics. *Compos. B Eng.* 225, 109275. <https://doi.org/10.1016/j.compositesb.2021.109275>.
4. Karim, N., Afroj, S., Tan, S., He, P., Fernando, A., Carr, C., and Novoselov, K.S. (2017). Scalable production of graphene-based wearable E-textiles. *ACS Nano* 11, 12266–12275. <https://doi.org/10.1021/acsnano.7b05921>.
5. Afroj, S., Karim, N., Wang, Z., Tan, S., He, P., Holwill, M., Ghazaryan, D., Fernando, A., and Novoselov, K.S. (2019). Engineering graphene flakes for wearable textile sensors via highly scalable and ultrafast yarn dyeing technique. *ACS Nano* 13, 3847–3857. <https://doi.org/10.1021/acsnano.9b00319>.
6. Eskandarian, L., Lam, E., Rupnow, C., Meghrizi, M.A., and Naguib, H.E. (2020). Robust and multifunctional conductive yarns for biomedical textile computing. *ACS Appl. Electron. Mater.* 2, 1554–1566. <https://doi.org/10.1021/acsaem.0c00171>.
7. Fan, W., He, Q., Meng, K., Tan, X., Zhou, Z., Zhang, G., Yang, J., and Wang, Z.L. (2020). Machine-knitted washable sensor array textile for precise epidermal physiological signal monitoring. *Sci. Adv.* 6, eaay2840.
8. Ke, Y., Jia, K., Zhong, W., Ming, X., Jiang, H., Chen, J., Ding, X., Li, M., Lu, Z., and Wang, D. (2022). Wide-range sensitive all-textile piezoresistive sensors assembled with biomimetic core-shell yarn via facile

- embroidery integration. *Chem. Eng. J.* 435, 135003. <https://doi.org/10.1016/j.cej.2022.135003>.
9. Tan, S., Islam, M.R., Li, H., Fernando, A., Afroj, S., and Karim, N. (2022). Highly scalable, sensitive and ultraflexible graphene-based wearable E-textiles sensor for bio-signal detection. *Advanced Sensor Research* 1, 2200010. <https://doi.org/10.1002/adrs.202200010>.
 10. Rajan, G., Morgan, J.J., Murphy, C., Torres Alonso, E., Wade, J., Ott, A.K., Russo, S., Alves, H., Craciun, M.F., and Neves, A.I.S. (2020). Low operating voltage carbon-graphene hybrid E-textile for temperature sensing. *ACS Appl. Mater. Interfaces* 12, 29861–29867. <https://doi.org/10.1021/acsmi.0c08397>.
 11. Rothmaier, M., Selm, B., Spichtig, S., Haensse, D., and Wolf, M. (2008). Photonic textiles for pulse oximetry. *Opt Express* 16, 12973–12986. <https://doi.org/10.1364/oe.16.012973>.
 12. Tang, J., Wu, Y., Ma, S., Yan, T., and Pan, Z. (2022). Flexible strain sensor based on CNT/TPU composite nanofiber yarn for smart sports bandage. *Compos. B Eng.* 232, 109605. <https://doi.org/10.1016/j.compositesb.2021.109605>.
 13. Afroj, S., Islam, M.H., and Karim, N. (2021). Multifunctional graphene-based wearable E-textiles. *Proceedings* 68, 11. <https://doi.org/10.3390/proceedings2021068011>.
 14. Dulal, M., Afroj, S., Ahn, J., Cho, Y., Carr, C., Kim, I.-D., and Karim, N. (2022). Toward sustainable wearable electronic textiles. *ACS Nano* 16, 19755–19788. <https://doi.org/10.1021/acsnano.2c07723>.
 15. Maity, D., and Kumar, R.T.R. (2018). Polyaniline anchored MWCNTs on fabric for high performance wearable ammonia sensor. *ACS Sens.* 3, 1822–1830. <https://doi.org/10.1021/acssensors.8b00589>.
 16. Chen, S., Peng, S., Sun, W., Gu, G., Zhang, Q., and Guo, X. (2019). Scalable processing ultrathin polymer dielectric films with a generic solution based approach for wearable soft electronics. *Adv. Mater. Technol.* 4, 1800681. <https://doi.org/10.1002/admt.201800681>.
 17. Zahid, M., Zych, A., Dussoni, S., Spallanzani, G., Donno, R., Maggiali, M., and Athanassiou, A. (2021). Wearable and self-healable textile-based strain sensors to monitor human muscular activities. *Compos. B Eng.* 220, 108969. <https://doi.org/10.1016/j.compositesb.2021.108969>.
 18. Pham, V.P., Jang, H.S., Whang, D., and Choi, J.Y. (2017). Direct growth of graphene on rigid and flexible substrates: progress, applications, and challenges. *Chem. Soc. Rev.* 46, 6276–6300. <https://doi.org/10.1039/c7cs00224f>.
 19. Windmiller, J.R., and Wang, J. (2013). Wearable electrochemical sensors and biosensors: a review. *Electroanalysis* 25, 29–46. <https://doi.org/10.1002/elan.201200349>.
 20. Afroj, S., Britnell, L., Hasan, T., Andreeva, D.V., Novoselov, K.S., and Karim, N. (2021). Graphene-based technologies for tackling COVID-19 and future pandemics. *Adv. Funct. Mater.* 31, 2107407. <https://doi.org/10.1002/adfm.202107407>.
 21. Wang, D., Choi, D., Li, J., Yang, Z., Nie, Z., Kou, R., Hu, D., Wang, C., Saraf, L.V., Zhang, J., et al. (2009). Self-Assembled TiO₂-graphene hybrid nanostructures for enhanced Li-ion insertion. *ACS Nano* 3, 907–914.
 22. Islam, M.R., Afroj, S., Novoselov, K.S., and Karim, N. (2022). Smart electronic textile-based wearable supercapacitors. *Adv. Sci.* 9, 2203856. <https://doi.org/10.1002/advs.202203856>.
 23. Maiti, S., Islam, M.R., Uddin, M.A., Afroj, S., Eichhorn, S.J., and Karim, N. (2022). Sustainable fiber-reinforced composites: a review. *Advanced Sustainable Systems* 6, 2200258. <https://doi.org/10.1002/advs.202200258>.
 24. Li, Z., Guo, Q., Li, Z., Fan, G., Xiong, D.B., Su, Y., Zhang, J., and Zhang, D. (2015). Enhanced mechanical properties of graphene reduced graphene oxide/aluminum composites with a bioinspired nanolaminated structure. *Nano Lett.* 15, 8077–8083. <https://doi.org/10.1021/acs.nanolett.5b03492>.
 25. Karim, N., Sarker, F., Afroj, S., Zhang, M., Potluri, P., and Novoselov, K.S. (2021). Sustainable and multifunctional composites of graphene-based natural jute fibers. *Adv. Sustain. Syst.* 5, 2000228. <https://doi.org/10.1002/advs.202000228>.
 26. Islam, M.H., Islam, M.R., Dulal, M., Afroj, S., and Karim, N. (2022). The effect of surface treatments and graphene-based modifications on mechanical properties of natural jute fiber composites: a review. *iScience* 25, 103597. <https://doi.org/10.1016/j.jisci.2021.103597>.
 27. Fan, W., Chu, R., Wang, C., Song, H., Ding, Y., Li, X., Jiang, M., Li, Q., Liu, L., and He, A. (2021). Synthesis and characteristic of the ternary composite electrode material PTCDA/CNT@MPC and its electrochemical performance in sodium ion battery. *Compos. B Eng.* 226, 109329. <https://doi.org/10.1016/j.compositesb.2021.109329>.
 28. Islam, M.H., Afroj, S., Uddin, M.A., Andreeva, D.V., Novoselov, K.S., and Karim, N. (2022). Graphene and CNT-based smart fiber-reinforced composites: a review. *Adv. Funct. Mater.* 32, 2205723. <https://doi.org/10.1002/adfm.202205723>.
 29. Zhou, H., Lai, J., Zheng, B., Jin, X., Zhao, G., Liu, H., Chen, W., Ma, A., Li, X., and Wu, Y. (2021). From glutinous-rice-inspired adhesive organohydrogels to flexible electronic devices toward wearable sensing, power supply, and energy storage. *Adv. Funct. Mater.* 32, 2108423. <https://doi.org/10.1002/adfm.202108423>.
 30. Veeralingam, S., and Badhulika, S. (2021). Bi2S3/PVDF/PPy-Based freestanding, wearable, transient nanomembrane for ultrasensitive pressure, strain, and temperature sensing. *ACS Appl. Bio Mater.* 4, 14–23. <https://doi.org/10.1021/acsbm.0c01399>.
 31. Dai, Z., Ding, S., Lei, M., Li, S., Xu, Y., Zhou, Y., and Zhou, B. (2021). A superhydrophobic and anti-corrosion strain sensor for robust underwater applications. *J. Mater. Chem.* 9, 15282–15293. <https://doi.org/10.1039/d1ta04259a>.
 32. Zeng, Z., Hao, B., Li, D., Cheng, D., Cai, G., and Wang, X. (2021). Large-scale production of weavable, dyeable and durable spandex/CNT/cotton core-sheath yarn for wearable strain sensors. *Compos. Appl. Sci. Manuf.* 149, 106520. <https://doi.org/10.1016/j.compositesa.2021.106520>.
 33. Afroj, S., Tan, S., Abdelkader, A.M., Novoselov, K.S., and Karim, N. (2020). Highly conductive, scalable, and machine washable graphene-based E-textiles for multifunctional wearable electronic applications. *Adv. Funct. Mater.* 30, 2000293. <https://doi.org/10.1002/adfm.202000293>.
 34. Kim, G.M., Choi, W.Y., Park, J.H., Jeong, S.J., Hong, J.-E., Jung, W., and Lee, J.W. (2020). Electrically conductive oxidation-resistant boron-coated carbon nanotubes derived from atmospheric CO₂ for use at high temperature. *ACS Appl. Nano Mater.* 3, 8592–8597. <https://doi.org/10.1021/acsnm.0c01909>.
 35. Joh, H., Lee, S.W., Seong, M., Lee, W.S., and Oh, S.J. (2017). Engineering the charge transport of Ag nanocrystals for highly accurate, wearable temperature sensors through all-solution processes. *Small* 13, 1700247. <https://doi.org/10.1002/sml.201700247>.
 36. Zhou, X., Zhu, L., Fan, L., Deng, H., and Fu, Q. (2018). Fabrication of highly stretchable, washable, wearable, water-repellent strain sensors with multi-stimuli sensing ability. *ACS Appl. Mater. Interfaces* 10, 31655–31663. <https://doi.org/10.1021/acsmi.8b11766>.
 37. Gao, H., Liu, H., Song, C., and Hu, G. (2019). Infusion of graphene in natural rubber matrix to prepare conductive rubber by ultrasound-assisted supercritical CO₂ method. *Chem. Eng. J.* 368, 1013–1021. <https://doi.org/10.1016/j.cej.2019.03.026>.
 38. Cheng, X., Zhang, F., Bo, R., Shen, Z., Pang, W., Jin, T., Song, H., Xue, Z., and Zhang, Y. (2021). An anti-fatigue design strategy for 3D ribbon-shaped flexible electronics. *Adv. Mater.* 33, e2102684. <https://doi.org/10.1002/adma.202102684>.
 39. Zhang, S., Zhao, Y., Du, X., Chu, Y., Zhang, S., and Huang, J. (2019). Gas sensors based on nano/microstructured organic field-effect transistors. *Small* 15, 1805196.
 40. Lin, L., Li, J., Yuan, Q., Li, Q., Zhang, J., Sun, L., Rui, D., Chen, Z., Jia, K., Wang, M., et al. (2019). Nitrogen cluster doping for high-mobility/conductivity graphene films with millimeter-sized domains. *Sci. Adv.* 5, eaaw8337.
 41. Zou, R., Liu, F., Hu, N., Ning, H., Gong, Y., Wang, S., Huang, K., Jiang, X., Xu, C., Fu, S.,

- et al. (2020). Graphene/graphitized polydopamine/carbon nanotube all-carbon ternary composite films with improved mechanical properties and through-plane thermal conductivity. *ACS Appl. Mater. Interfaces* 12, 57391–57400. <https://doi.org/10.1021/acsmami.0c18373>.
42. Davoodi, E., Montazerian, H., Haghniaz, R., Rashidi, A., Ahadian, S., Sheikhi, A., Chen, J., Khademhosseini, A., Milani, A.S., Hoorfar, M., and Toyserkani, E. (2020). 3D-Printed ultra-robust surface-doped porous silicone sensors for wearable biomonitoring. *ACS Nano* 14, 1520–1532. <https://doi.org/10.1021/acsnano.9b06283>.
43. Kalaoglu-Altan, O.I., Kayaoglu, B.K., and Trabzon, L. (2022). Improving thermal conductivities of textile materials by nanohybrid approaches. *iScience* 25, 103825. <https://doi.org/10.1016/j.isci.2022.103825>.
44. Wang, Z., Chen, Y., Yao, M., Dong, J., Zhang, Q., Zhang, L., and Zhao, X. (2020). Facile fabrication of flexible rGO/MXene hybrid fiber-like electrode with high volumetric capacitance. *J. Power Sources* 448, 227398. <https://doi.org/10.1016/j.jpowsour.2019.227398>.
45. Wang, Y., Zhu, L., Mei, D., and Zhu, W. (2019). A highly flexible tactile sensor with an interlocked truncated sawtooth structure based on stretchable graphene/silver/silicone rubber composites. *J. Mater. Chem. C* 7, 8669–8679. <https://doi.org/10.1039/c9tc02356a>.
46. Dong, K., Wang, Y.C., Deng, J., Dai, Y., Zhang, S.L., Zou, H., Gu, B., Sun, B., and Wang, Z.L. (2017). A highly stretchable and washable all-yarn-based self-charging knitting power textile composed of fiber triboelectric nanogenerators and supercapacitors. *ACS Nano* 11, 9490–9499. <https://doi.org/10.1021/acsnano.7b05317>.
47. Hu, Q., Bai, X., Zhang, C., Zeng, X., Huang, Z., Li, J., Li, J., and Zhang, Y. (2022). Oriented BN/Silicone rubber composite thermal interface materials with high out-of-plane thermal conductivity and flexibility. *Compos. Appl. Sci. Manuf.* 152, 106681. <https://doi.org/10.1016/j.compositesa.2021.106681>.
48. Montazerian, H., Rashidi, A., Dalili, A., Najjaran, H., Milani, A.S., and Hoorfar, M. (2019). Graphene-coated spandex sensors embedded into silicone sheath for composites health monitoring and wearable applications. *Small* 15, e1804991. <https://doi.org/10.1002/sml.201804991>.
49. Li, J., Zou, Y., Jin, L., Xu, F., Sun, L., and Xiang, C. (2022). Polydopamine-assisted NiMoO₄ nanorods anchored on graphene as an electrode material for supercapacitor applications. *J. Energy Storage* 50, 104639. <https://doi.org/10.1016/j.est.2022.104639>.
50. Qin, Y., Yuan, J., Li, J., Chen, D., Kong, Y., Chu, F., Tao, Y., and Liu, M. (2015). Crosslinking graphene oxide into robust 3D porous N-doped graphene. *Adv. Mater.* 27, 5171–5175. <https://doi.org/10.1002/adma.201501735>.
51. Zhai, J., Zhang, Y., Cui, C., Li, A., Wang, W., Guo, R., Qin, W., Ren, E., Xiao, H., and Zhou, M. (2021). Flexible waterborne polyurethane/cellulose nanocrystal composite aerogels by integrating graphene and carbon nanotubes for a highly sensitive pressure sensor. *ACS Sustainable Chem. Eng.* 9, 14029–14039. <https://doi.org/10.1021/acssuschemeng.1c03068>.
52. Song, D., Zeng, M.-J., Min, P., Jia, X.-Q., Gao, F.-L., Yu, Z.-Z., and Li, X. (2023). Electrically conductive and highly compressible anisotropic MXene-wood sponges for multifunctional and integrated wearable devices. *J. Mater. Sci. Technol.* 144, 102–110.
53. Cheng, H., Zhang, N., Yin, Y., and Wang, C. (2021). A high-performance flexible piezoresistive pressure sensor features an integrated design of conductive fabric electrode and polyurethane sponge. *Macromol. Mater. Eng.* 306, 2100263.
54. Wei, X., Cao, X., Wang, Y., Zheng, G., Dai, K., Liu, C., and Shen, C. (2017). Conductive herringbone structure carbon nanotube/thermoplastic polyurethane porous foam tuned by epoxy for high performance flexible piezoresistive sensor. *Compos. Sci. Technol.* 149, 166–177.
55. Lv, B., Chen, X., and Liu, C. (2020). A highly sensitive piezoresistive pressure sensor based on graphene oxide/polypyrrole@polyurethane sponge. *Sensors* 20, 1219.
56. Ma, Z., Wei, A., Ma, J., Shao, L., Jiang, H., Dong, D., Ji, Z., Wang, Q., and Kang, S. (2018). Lightweight, compressible and electrically conductive polyurethane sponges coated with synergistic multiwalled carbon nanotubes and graphene for piezoresistive sensors. *Nanoscale* 10, 7116–7126.
57. Mu, Y., Wang, L., Zhang, R., Pashameah, R.A., Alzahrani, E., Li, Z., Alanazi, A.K., Algadi, H., Huang, M., Guo, Z., et al. (2023). Rapid and facile fabrication of hierarchically porous graphene aerogel for oil-water separation and piezoresistive sensing applications. *Appl. Surf. Sci.* 613, 155982.
58. Xu, S., Li, X., Sui, G., Du, R., Zhang, Q., and Fu, Q. (2020). Plasma modification of PU foam for piezoresistive sensor with high sensitivity, mechanical properties and long-term stability. *Chem. Eng. J.* 381, 122666.
59. Iglío, R., Mariani, S., Robbiano, V., Strambini, L., and Barillaro, G. (2018). Flexible polydimethylsiloxane foams decorated with multiwalled carbon nanotubes enable unprecedented detection of ultralow strain and pressure coupled with a large working range. *ACS Appl. Mater. Interfaces* 10, 13877–13885.
60. Zang, Y., Zhang, F., Di, C.-a., and Zhu, D. (2015). Advances of flexible pressure sensors toward artificial intelligence and health care applications. *Mater. Horiz.* 2, 140–156. <https://doi.org/10.1039/c4mh00147h>.
61. Li, X., Li, S., Wu, M., Weng, Z., Ren, Q., Xiao, P., Wang, L., and Zheng, W. (2023). Multifunctional polyether block amides/carbon nanostructures piezoresistive foams with largely linear range, enhanced and humidity-regulated microwave shielding. *Chem. Eng. J.* 455, 140860.
62. Huang, L., Chen, J., Xu, Y., Hu, D., Cui, X., Shi, D., and Zhu, Y. (2021). Three-dimensional light-weight piezoresistive sensors based on conductive polyurethane sponges coated with hybrid CNT/CB nanoparticles. *Appl. Surf. Sci.* 548, 149268.
63. Karim, N., Afroj, S., Leech, D., and Abdelkader, A.M. (2021). Flexible and wearable graphene-based E-textiles. In *Oxide Electronics*, pp. 21–49. <https://doi.org/10.1002/9781119529538.ch2>.
64. Karim, N., Afroj, S., Tan, S., Novoselov, K.S., and Yeates, S.G. (2019). All inkjet-printed graphene-silver composite ink on textiles for highly conductive wearable electronics applications. *Sci. Rep.* 9, 8035. <https://doi.org/10.1038/s41598-019-44420-y>.
65. Yousaf, Z., Sajjad, S., Leghari, S.A.K., Noor, S., Kanwal, A., Bhatti, S.H., Mahmoud, K.H., and El-Bahy, Z.M. (2021). Influence of integrated nitrogen functionalities in nitrogen doped graphene modified WO₃ functional visible photocatalyst. *J. Environ. Chem. Eng.* 9, 106746. <https://doi.org/10.1016/j.jece.2021.106746>.
66. Marechal, L., Bolland, P., Lindenroth, L., Petrou, F., Kontovounisios, C., and Bello, F. (2021). Toward a common framework and database of materials for soft robotics. *Soft Robot.* 8, 284–297.

STAR★METHODS

KEY RESOURCES TABLE

REAGENT or RESOURCE	SOURCE	IDENTIFIER
Chemicals, peptides, and recombinant proteins		
Urea	Sinopharm (Shanghai, China)	Cat#10023218; CAS no. 57-13-6
Carbon nanotubes	Macklin Inc (Shanghai, China)	Cat#C805983; CAS no. 308068-56-6
Tris(hydroxymethyl)aminomethane	Meryer (Shanghai, China)	Cat#M26450; CAS no. 77-86-1
Dopamine hydrochloride	Aladdin (Shanghai, China)	Cat#D103111; CAS no. 62-31-7
Graphene oxide suspension	Macklin Inc (Shanghai, China)	Cat#S926159; CAS no. 7782-42-5
Ecoflex 00–20	Smooth-On Inc (Macungie, USA)	SDS No. 823A

RESOURCE AVAILABILITY

Lead contact

Further information and requests for resources and reagents should be directed to and will be fulfilled by the lead contact, Zhong Zhao (zzhao@wtu.edu.cn).

Materials availability

This study did not generate new unique reagents.

Data and code availability

The published article includes all data generated or analyzed during this study.

METHOD DETAILS

Preparation of conductive silicon rubber tube

Urea was employed as the nitrogen source to dope rGO following a modified process reported by Yousef et al.⁶⁵ As demonstrated in [Figure 10](#), 3 g urea was dissolved in 50 mL graphene oxide (GO) suspension (2 mg/mL) under sonification for 30 min. Nitrogen doping of GO was carried out by transferring the suspension into an autoclave and subjecting it to hydrothermal reaction at 180 °C for 5 h. After the hydrothermal reaction, the N-doped GO in the suspension was collected via centrifugation and then thoroughly rinsed with deionized water. Finally, N-doped GO was dispersed in L-ascorbic acid solution and reduced to N-doped rGO by heating the dispersion at 85 °C for 2 h.

2 g dopamine hydrochloride was dissolved in 1 L deionized water. The pH of the dopamine solution was then buffered to ~8.5 by dissolving 1.2 g Tris(hydroxymethyl) aminomethane in it. 1 g CNTs was subsequently dispersed into the dopamine solution. Dopamine formed a polydopamine (PDA) layer on the CNTs by dispersing CNTs into the dopamine hydrochloride solution under sonication for 30 min. The PDA coated CNTs (PDA@CNT) were collected via vacuum filtration. Finally, the collected solid was rinsed with deionized water to remove the excess chemicals and dried in dark at room temperature.

0.2 g N-doped rGO and 1 g PDA@CNT were added into 20 mL ethanol. The mixture was then subjected to vigorous sonication to form a suspension of the two materials. Finally, a paste was obtained by reducing the volume of the suspension to 10 mL through the evaporation of ethanol, which was realized by heating the suspension at 60 °C for 10 min in an oven. The paste was employed as the filling material and loaded into the pore of the silicon rubber tube via vacuum filling. When this vacuum filling process was duplicated in the industrial level, the conductive paste can be loaded into longer silicon rubber tube to manufacture continuous CSRT efficiently. A relatively large inner diameter of the tube will result in the adhesion of the powder only onto the inner wall, while a relatively small inner diameter will cause the insufficient loading amount of the powder. Therefore, to ensure sufficient amount of powder loaded into the tube and balance the flexibility of the tube, a silicon rubber tube with the outer and inner diameters of 2 and 1 mm were used as the container. Two stainless-steel rods with the diameter of 1.5 mm and the conductivity of 2.83 S/m were

inserted 5 mm into the two ends of CSRT. The seams between the silicon rubber tube and the stainless-steel rods were sealed with Ecoflex to avoid the leakage of the conductive powder.

To reveal the influence of the structure of the silicon rubber tube on the performance of the sensor, a similar filament with the matrix of Ecoflex was set as control and tested along with the CSRT filament during the compression, bending and respiratory tests. Specifically, 1 g mixed powder comprised of the N-doped rGO and PDA@CNT (w/w = 1: 5) was dispersed into 10 mL A and B components of Ecoflex, respectively. The two dispersions were then mixed together *via* manual stirring and loaded into a syringe which was then pre-heated to 70 °C. The Ecoflex elastomer was then extruded from the syringe and immersed into a hot water bath (70 °C) for curing. A piece of CEF featuring a diameter of 2 mm and even distribution of the mixed powder in it was obtained after retrieving the cured Ecoflex sample from the water bath and drying it at 50 °C. The prominent flexibility of CSRT (Figure 3A) ensures the wearable characteristic of the tube-shaped composite while doping rGO with nitrogen is beneficial for the further improvement of its conductivity (Figure S5), making CSRT the candidate for the sensor with subtle action sensing ability.

Characterization

The PDA@CNT was scanned by a Talos F200x TEM (FEI, USA) to examine the coverage of PDA on the CNTs. To further reveal the composition of PDA@CNT, mapping of the elements was conducted using a Super-X EDS analyzer equipped with the TEM. The morphology of the filling material was characterized *via* a GeminiSEM 300 SEM (ZEISS, Germany), while its composition was analyzed by a ESCALAB Xi+ XPS analyzer (Thermo Fisher Scientific, USA) and a D8 Advance X-ray diffractor (Bruker, Germany).

Sensing performance of the CSRT and CEF

The electro-mechanical properties of the prepared two sensors were carried out using a 507A computerized tensile testing machine (DongRi instrument Co., Ltd., China). Specifically, the CSRT or CEF were tightly compressed by the two compression boards of a 507A computerized tensile testing machine. The sensor was then compressed by keeping the lower board stationary and moving the upper board downwards at a speed of 2 mm/min (Figure S8). 0–40 N compression force was applied on the sensors for the single and stepped cyclic tests.

The sensitivity (S) of a piezoresistive sensor is an essential parameter for the assessment of the device performance and was characterized using the following equation:

$$S = \frac{\Delta R}{R_0} \times 100\% = \frac{R - R_0}{R_0} \times 100\%$$

where ΔR denote the resistance change before and after load applied, R and R_0 denotes the loaded and unloaded samples' resistances, respectively. Various cord lengths were used during the bending test to measure the changes in resistance of CSRT and CEF sensors (40 mm). The cord length of the sensor was controlled by adjusting the distance between the two holders of the tensile machine. A certain length of the CSRT and CEF sensor (40 mm) were placed under an elastic band on the lower chest location of two participants for the respiratory and heart beat signal capturing. The changes in the resistance of the sensor during the mechanical tests on the tensile machine, bending tests on the machine, heart beat and respiration monitoring were measured and recorded *via* a half-bridge circuit built in a NI-9219 data acquisition card (National instrument, USA). Approval of the publication of cardiorespiratory data has been granted by both the two participants.

Modelling and pre-load analysis in ABAQUS

A cylinder model (Figure S6) featuring a tube and a finer cylinder whose diameter fits exactly the inner diameter of the tube was established in ABAQUS. The finer cylinder was mounted in the center of the tube to simulate the core-sheath structure of the silicon rubber tube filled with conductive powder. The finer cylinder was shorter than the tube while their difference in length was compensated by two shorter rods whose one end was in close contact with the end faces of the finer cylinder. The two rods stick out from each end of the tube and act as the electrodes of the sensor. To simulate the intrinsic mechanical properties of silicon rubber, powder and stainless steel, the materials of the tube, the finer cylinder and the rods were set as isotropic hyper-elastic solid with the C10 value of 0.02264 and the D1 value of 0,⁶⁶ isotropic elastic solid with the Young's modulus of 0.05 and Poisson's ratio of 0.4, and uniform solid with the mass density of 7.8×10^{-9} , respectively. The linear model was then bended into a "U" shape and the strain inside the

tube and the equivalent conductive powder unit was calculated using ABAQUS/Explicit. The damping approximation quasi-static analysis was employed to eliminate the vibration during the bending process.

Fabrication of the embroidered sensor and bio-signal sensing

The CSRT was fixed on the cotton woven fabric as different structures by using the creative 1.5 Cherry computerized embroidery machine (PFAFF, Germany). Tailored fiber placement (TFP) presser foot was used to place the CSRT yarn on the substrate fabric. The TFP structures were subjected to compression tests under the same conditions specified in (Figure 2). The structure with relatively better performance was selected and used to capture bio-signals. Sensor was mounted on the below chest and chest location to measure the breath and heartbeat signals respectively, and it was placed under the wrist to detect the pulse signals. Finally, the sensor was fixed on a Lycra vest on the chest location to measure the cardiorespiratory signals without the elastic band. The changes in resistance of the embroidered sensor during the mechanical tests and the bio-signal sensing on the human body were measured and recorded via the half-bridge circuit provided by the NI-9219 data acquisition card.

Review

The effect of surface treatments and graphene-based modifications on mechanical properties of natural jute fiber composites: A review

Mohammad Hamidul Islam,¹ Md Rashedul Islam,¹ Marzia Dulal,¹ Shaila Afroj,¹ and Nazmul Karim^{1,*}

SUMMARY

Natural fiber reinforced composites (FRC) are of great interests, because of their biodegradability, recyclability, and environmental benefits over synthetic FRC. Natural jute FRC could provide an environmentally sustainable, light weight, and cost-effective alternative to synthetic FRC. However, the application of natural jute FRC is limited because of their poor mechanical and interfacial properties. Graphene and its derivatives could potentially be applied to modify jute fiber surface for manufacturing natural FRC with excellent mechanical properties, and lower environmental impacts. Here, we review the physical and chemical treatments, and graphene-based modifications of jute fibers, and their effect on mechanical properties of jute FRC. We introduce jute fiber structure, chemical compositions, and their potential applications first. We then provide an overview of various surface treatments used to improve mechanical properties of jute FRC. We discuss and compare various graphene derivative-based surface modifications of jute fibers, and their impact on the performance of FRC. Finally, we provide our future perspective on graphene-based jute fibers research to enable next generation strong and sustainable FRC for high performance engineering applications without conferring environmental problems.

INTRODUCTION

Sustainable and biodegradable natural fiber reinforced composites (FRC) have received significant interests in recent years, because of their lower environmental impacts (Mohanty et al., 2018; Zheng and Suh, 2019; Karim et al., 2015), including less carbon emission and fossil fuel consumption, lower cost and density, and ease of fabrication. The use of such fibers could offer an unprecedented combination of stiffness, strength, and toughness at low density (Wegst et al., 2015; Karim et al., 2021b). Therefore, natural FRC could potentially be used as lightweight and environmentally sustainable composites to replace glass, carbon, or other synthetic FRCs in numerous applications such as automotive, construction, and household. The commonly used natural fibers to manufacture the composite are flax, jute, hemp, banana, ramie, and kenaf. Among them, the jute fibers have attracted significant interest, as jute is the second most produced (mainly in Bangladesh, India, and China) natural fiber after cotton, and is at least 50% cheaper than flax and other natural fibers (Koronis et al., 2013). However, jute fibers suffer from lower mechanical properties and poor adhesion when reinforced with a matrix, because of the presence of large amounts (20 wt.%–50 wt.%) of noncellulosic materials such as hemicellulose and lignin (Sarker et al., 2018). The presence of noncellulosic materials provides lower crystallinity and hydrophilicity of fibers (Gassan and Bledzki, 1999b), and is responsible for poor mechanical properties of composites. Nevertheless, the strong interfacial bond between fiber and matrix could potentially provide higher mechanical and interfacial properties of the composites. The surface modification of the jute fiber is considered to be essential to improve their adhesion with a polymer matrix.

There are various physical and chemical treatments that have been carried out to remove the noncellulosic materials and improve the mechanical properties of the jute fiber and their composites. Among them, the alkali treatment is the most popular surface treatment which removes noncellulosic materials and impurities from the interfibrillar region of jute fiber. Thus such treatment makes the fibrils more

¹Centre for Print Research (CFPR), The University of West of England, Frenchay, Bristol BS16 1QY, UK

*Correspondence: nazmul.karim@uwe.ac.uk
<https://doi.org/10.1016/j.isci.2021.103597>



capable of rearranging themselves along the direction of tensile deformation and provides a better load sharing capability between themselves to contribute to higher stress development during the tensile test (Bledzki and Gassan, 1999). The surface treatment of jute fiber at lower alkali concentration for a prolonged period of time can enhance the mechanical properties of jute fiber (Roy et al., 2012; Sarker et al., 2018). In addition, various other combined surface treatments including alkali-silane (Dilfi et al., 2018), alkali-plasma (Gibeop et al., 2013), alkali-beaching (Rajesh and Prasad, 2014), and alkali-acetylation (Mwaikambo and Ansell, 1999) have been investigated. However, the improvement of mechanical properties with such treatments is limited and some of the treatments are expensive (such as plasma treatment).

Recently, graphene and its derivatives including graphene flakes (G), graphene oxide (GO), and reduced graphene oxide (rGO) have attracted tremendous attention for high-performance composite applications because of their incredible mechanical properties. Graphene derivatives (GO and rGO) could be produced in a huge quantity in their stable dispersions. In addition, such materials provide good chemical reactivity and handling characteristics because of their intrinsic functional groups (Afroj et al., 2019). Furthermore, graphene-based and electrically conductive flakes can be produced in a scalable quantity via microfluidization technique, and used for smart composites applications (Karim et al., 2018; Afroj et al., 2020). Previous studies (Da Luz et al., 2020, Karim et al., 2021b; Sarker et al., 2018; Sarker et al., 2019) demonstrate significant improvement in mechanical properties and performances of graphene-modified jute fibers and their composites via forming either bonding (GO) or mechanical interlocking (G) between fibers and graphene-based flakes. In addition, graphene-based jute FRC have been developed for high-performance composites multifunctional smart composites applications, as demonstrated by effective electro-magnetic interference shielding (Karim et al., 2021b) and de-icing applications (Karim et al., 2018). Such developments may lead to manufacturing of smart and sustainable natural fiber composites for next generation high performance engineering applications without conferring environmental problems.

Although there have been many previous reviews focusing on jute fibers and their composites (Chandekar et al., 2020; Gupta et al., 2015; Singh et al., 2018; Shah et al., 2021), there remains a lack of a review about the physical and chemical treatments of jute fiber, its modification with graphene-based materials, and their effect on the mechanical and multi-functional properties of the composites. In this review, we introduce jute fibers, their key constituents determining the mechanical properties and potential applications. We provide an overview of various surface treatments of jute fibers and their effect on mechanical properties of jute fiber reinforced composites. We then discuss graphene-based surface modifications of jute fibers, and their effect on interfacial, tensile, and multifunctional properties of fiber reinforced composites. Finally, we present our views on future research directions, and recommendations for developing next generation smart, strong, and sustainable natural fiber reinforced composites.

INTRODUCTION TO JUTE

Jute plant

Jute is a type of bast fiber, extracted from the plant, Figure 1A. Jute belongs to the Tiliaceae family with nearly 30 to 40 capsularis species (Singh et al., 2018). There are mainly two types of jute having the scientific name *Corchorus capsularis* (white jute) and *Corchorus olitorius* (Tossa jute) (Islam, 2013). For successful cultivation, jute plants need plain alluvial soil and tropical rainfall (~125–150 mm per month), warm weather (~20°C–40°C), and high humidity (~70%–80%) (Rahman, 2010). The jute plant grows up from seeds to a height of 3 to 4 m, and then fibers are extracted after harvesting, which is about 4 to 5 months from the cultivation. The typical yield is ~34 tonnes per hectare of green plants, which provides ~2 tonnes per hectare of dry retted fiber. The current annual worldwide production of jute fiber is ~3.2 million tonnes (Aly-Hassan, 2015). Jute is one of the world's most important natural fibers second only to cotton in terms of production. Bangladesh, India, China, Nepal, Myanmar, Thailand, and Vietnam are the major jute producing countries.

Jute fiber

Jute fiber is extracted from the bast of the plant. The jute fiber extraction process involves retting, stripping, washing, drying, and packing. The retting process is carried out either via a biological method or a chemical method with the help of chemicals including ammonium oxalate, sodium sulphite, etc. However,

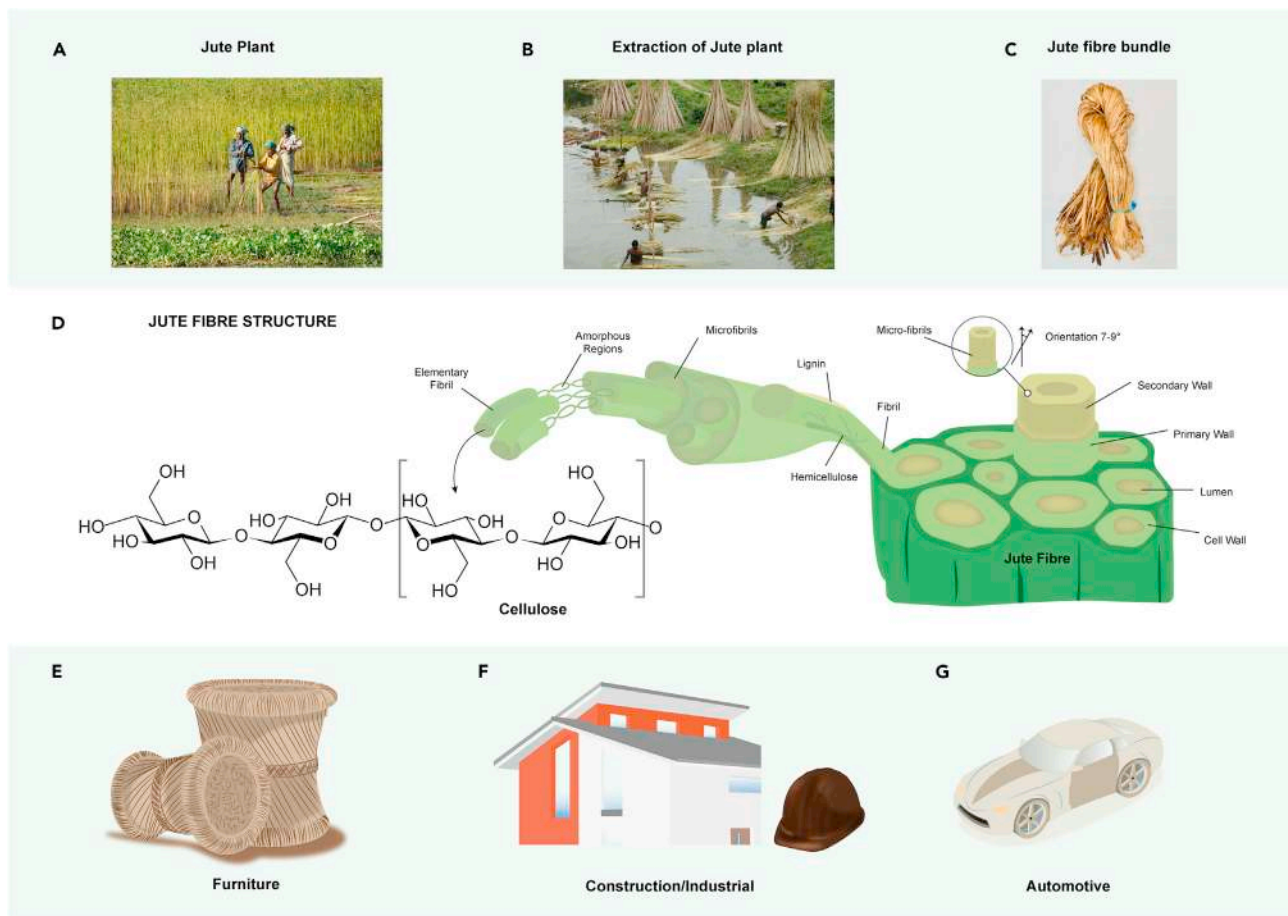


Figure 1. Introduction to Jute

(A) Jute plant (B) the extraction of jute fibers from the plant (C) jute fibers bundle and (D) the structure of jute fiber. Applications of jute fiber and its composites: (E) furniture, (F) constructions, and (G) automobile.

the chemical retting process is expensive (Rahman, 2010). In the biological retting process, the jute stems are tied into a bundle, and then immersed into slow running water for ~20 days. After the retting process, the non-fibrous materials are scraped off from the jute stem (Figure 1B) by the stripping process. After the fibers are separated, they are ready for further processing and various applications, Figure 1C. The structure of the jute fiber is illustrated Figure 1D.

The chemical composition and the configuration of the jute fiber depend on the climate conditions and degradation processes. In addition, the chemical constituents vary in different jute grades. The main chemical constituents of jute fibers are cellulose, hemicelluloses, lignin, pectin, wax, and moisture which are shown in Table 1.

Table 1. Chemical constituents of jute fiber

Cellulose (%)	Hemicellulose (%)	Lignin (%)	Pectin (%)	Wax (%)	Moisture (%)	References
61.2	13.2	13.7	–	0.5	–	(Mukherjee et al., 1993)
61–71	13.6–20.4	12–13	0.2	0.5	12.6	(Rowell, 2000)
61–71.5	12–13	13.6–20.4	0.2	0.5	12.6	(Goda and Cao, 2007)
71	14	13	–	–	–	(Khalil et al., 2012)
58–63	21–24	12–14	–	–	–	(Masoodi and Pillai, 2012)

Table 2. Mechanical parameters of jute fiber

Tensile strength (MPa)	Young's modulus (GPa)	Elongation at break (%)	Density (g/cm ³)	Reference
393–773	26.5	1.5–1.8	1.3	(Faruk et al., 2012)
400–800	10–30	1.5–1.8	1.46	(Saravana Bavan and Mohan Kumar, 2010)
393–773	13–26.5	1.16–1.5	1.3–1.45	(Chandrasekar et al., 2017)
393–773	19.0–26.5	1.16–1.8	1.5	(Ganesan et al., 2021)

The mechanical properties of jute fiber mainly depend on the nature of the plant, the cultivation environment, the locality in which it is grown, the age, and the extraction methods used (Khan et al., 2015). The tensile properties of the jute fiber are different at different positions of raw jute fiber, which become uniform throughout fibers after chemical treatments (Varma et al., 1989). The important mechanical parameters of jute fiber are presented in Table 2.

Jute fiber applications

Traditionally, jute has been used to manufacture packaging materials including hessian, sacking, ropes, twines, and backing cloth for carpets. Depending on fiber properties, a wide range of diversified jute products (Figure 1E) have been produced via various chemical modifications and finishing processes (Islam and Xiaoying, 2016). Jute fibers have also been used as reinforcing materials for thermoplastic and thermoset composites (Shahinur et al., 2021; Mahesh et al., 2021b; Luz et al., 2015). Such fibers are sustainable, biodegradable, and available in abundance, which has drawn significant research interests over the years for fiber reinforced composites applications, because of their lower environmental impacts than synthetic fiber reinforced composites (Pougnnet et al.). Therefore, the application of jute fiber composites has been increasing progressively in a wide range of areas such as aerospace, automobile, marine, sporting goods, construction, and other industries (Figures 1F and 1G). Jute fiber composites are being mostly used in the interior with very limited applications in exterior components. The hybrid jute fiber composites also have been widely used in various structural and engineering applications (Nurazzi et al., 2021). Table 3 shows the potential and in use application of jute fiber composites.

Table 3. Potential and in use application of jute fiber composites

Composites	Surface modification	Manufacturing technique	Main properties	Potential and in use application	Ref
Jute/epoxy	H + A + rGO (0.5%)	VARI	TS-513 (MPa) YM-55 (GPa)	High-performance engineered application and EMI shielding device.	(Karim et al., 2021b)
Jute/epoxy	H + A + GO (0.75%) H + A + GnP (0.75%)	VARI	TS-379 (MPa) YM-45 (GPa) TS-294 (MPa) YM-38 (GPa)	Stiffness driven structural applications.	(Sarker et al., 2019)
Jute/PP	Silane + GONP (0.05g/L)	Compounding	TS-43.8 (MPa) FS-63 (MPa)	Automotive industry, household products and so on.	(Chen et al., 2020)
Jute/epoxy	GO (0.75%) FG (0.75%)	Compression molding	TS-58 (MPa) FS-18 (MPa) TS-59 (MPa) FS-18.8 (MPa)	Indoor applications, it can be a good substitute for wood.	(Sadangi et al., 2021)
Jute/rubber/- jute/rubber/jute		Compression molding	EA- 38.7 (J) BL- 88 (m/s)	Secondary sacrificial structural applications such as claddings.	(Mahesh et al., 2021a)
Jute/polymer	Graft copolymerisation	Radiation method		Automobile industry, footwear industry, construction, home/garden furniture, and the toy sectors	(Khan et al., 2015)

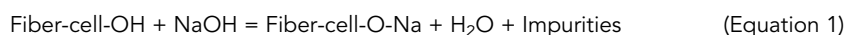
H = hot water treatment, A = alkali treatment, GO = Graphene oxide coated, GnP = graphene flake coated and rGO = reduced graphene oxide coated, GF = Functionalized graphene, TS: Tensile strength, YM: Young's modulus, FS: Flexural strength, EA: Energy absorption and BL: Ballistic Limit.

SURFACE MODIFICATIONS

The limitations of using jute fibers as reinforcements for composites are the poor mechanical properties because of the hydrophilic nature of fiber, weak fiber-matrix interfacial bonding, and poor wettability. Therefore, the surface modification of jute fibers is required. The fiber matrix interfacial bonding and moisture resistance could be enhanced by the removal of the impurities like wax, hemicellulose, lignin, and also adding other chemicals onto the fiber's surface (Thyavihalli Girijappa et al., 2019; Chandrasekar et al., 2017). There are several jute fiber surface modification techniques which have already been used such as physical methods (Militký and Jabbar, 2015), chemical treatments (Gassan and Bledzki, 1999a), and nanomaterials modifications (Sarker et al., 2019; Karim et al., 2021b). Physical methods include stretching, calendaring, combing, cold plasma treatment, and electric discharge (Sinha and Panigrahi, 2009; Chandrasekar et al., 2017; Sever et al., 2011). Physical methods do not change the chemical composition of the fibers; however, they change the surface and structural properties of the fibers. Various chemical treatments have been used including alkalization (Brodowsky and Mäder, 2012; Gassan and Bledzki, 1999a; Roy et al., 2012; Saha et al., 2010), bleaching (Khondker et al., 2005; Alves et al., 2011), silane treatment (Wang et al., 2010; Hong et al., 2008; Dilfi et al., 2018), acetylation (Rana et al., 1997), and hot water treatment (Sarker et al., 2018). The chemical treatment of the jute fibers changes the chemical composition, as well as surface properties of the fiber.

Alkaline treatment

Alkaline treatment is the most commonly used chemical modification technique for jute fibers. Sodium hydroxide (NaOH) is extensively used for the alkali treatment of jute fiber. The alkali treatment of jute fiber removes noncellulosic materials such as hemicellulose, lignin, wax, and oils that surround the external surface of the jute fiber. Alkali treatment of the jute fibers eliminates the moisture-related hydroxyl groups which decrease the hydrophilic nature of the fiber. When NaOH reacts with jute fiber, it produces water molecules, and Na-O- combines with the cell wall of the fiber to produce fiber-cell-O-Na groups referring to Equation 1.



The alkali treatment directly affects the jute fiber properties which removes noncellulosic materials and makes the fiber more capable of rearranging themselves along the fiber direction and as well as improving the fiber matrix adhesion. This permits a better load shearing capability, which results in higher tensile strength in the composites (Wang et al., 2019b).

The NaOH treatment of the jute fiber is performed by dipping the fiber in a NaOH solution for a certain time and temperature. The efficiency of NaOH treatment of jute fiber depends on the NaOH concentration, treatment time, temperature, and material liquor ratio. A previous study (Saha et al., 2010) investigated physio-chemical properties of jute fibers treated with different concentrations (0.5%–18%) of NaOH, temperature, and time. The study showed that a 30 min dipping of the fibers in 0.5% NaOH solution followed by 30 min NaOH-stream treatment increased the tensile strength of the fiber up to ~65%. Another study (Roy et al., 2012) suggested that a lower-concentration (~0.5 wt% alkali treatment for a prolonged time enhanced tensile strength and elongation at break of jute fibers by ~82% and ~45%, respectively, and reduced the hydrophilicity by ~50.5%.

Mechanical properties of the alkali-treated jute fiber reinforced thermoplastic and thermoset composites have been studied extensively, Table 4 (Ray et al., 2001; Gassan and Bledzki, 1999b; Sinha and Rout, 2009; Mohanty et al., 2000; Kapatel, 2021). The studies report improved tensile strength, Young's modulus, interfacial shear strength (IFSS), flexural properties, and impact strength of the composites. The effects of hot-alkali treatments with different concentrations (2%, 4%, 6%, 8%, and 10%) on the mechanical properties of the jute/epoxy composites have been investigated (Wang et al., 2019b). Composites with 6% NaOH-treated jute fabric showed the best improvement. The tensile strength, flexural strength, tensile modulus, and flexural modulus of 6% NaOH-treated fabrics reinforced composites were enhanced by 37.5%, 72.3%, 23.2%, and 72.2%, respectively, as compared with those of untreated fabrics reinforced composites. The schematic illustration of the fine structure of cellulose and other polysaccharides of hot-alkali treated jute fibers at different alkali concentrations are shown in

Table 4. Mechanical properties of untreated and alkali-treated jute fiber reinforced composites

Composites	Treatment type and time	Tensile strength (MPa)	Change (%)	Flexural strength (MPa)	Change (%)	Impact strength (J)	Change (%)	Ref.
Jute/epoxy	Untreated	46.7		62.4				(Boopalan et al., 2012)
	20% NaOH 2 h	97.5	108.7	80.1	28.4			
Jute/epoxy	Untreated	25		41		2.2		(Mahesh et al., 2021b)
	5% NaOH 24 h	34	36	47	14.6	3.4	54.5	
	10% NaOH 24 h	17	-32	22	-46.3	2.55	15.9	
	15% NaOH 24 h	15	-40	18	-56.1	2.4	9.1	
Jute/epoxy	5% NaOH 24 h	12.46	-	39.08	-	2.63	-	(Gopinath et al., 2014)
	10% NaOH 24 h	10.5	-	32.5	-	2.0	-	
Jute/polyester	5% NaOH 24 h	9.24	-	44.71	-	3.25	-	
	10% NaOH 24 h	7.92	-	40.5	-	2.75	-	
Jute/epoxy	Untreated	95		98		6.35		(Kapatel, 2021)
	5% NaOH 6 h	136	43.2	140	42.9	9.1	43.3	
	10% NaOH 6 h	147	54.7	155	58.2	11.67	83.8	
	15% NaOH 6 h	156	64.2	162	65.3	15.42	142.8	
	20% NaOH 6 h	145	52.6	159	62.2	13.02	105.0	

Figures 2A–2C and SEM images of untreated alkali-treated jute fibers are also shown in Figures 2D–2F (Wang et al., 2019b). The surface morphologies of untreated jute fibers are smoothly covered with pectin, wax, and impurities, which may reduce the contact area between jute fibers and resin. The alkali treatment removes pectin, wax, and impurities, and creates many wrinkles, gaps and micro-voids. Jute fiber becomes clean and rough after alkali treatment. The crystalline structures of cellulose are improved, the spacing of adjacent cellulose chains is shortened, hydrogen bonds are formed to connect the adjacent cellulose chains, and the strength of the fiber is improved as a result of alkali treatment.

In other work, flexural properties of the 5% alkali-treated jute fiber/unsaturated-polyester resin composites for different treatment times (2 h, 4 h, and 6 h) were investigated (Sinha and Rout, 2009). Flexural strength of the composite prepared with 2 h and 4 h alkali-treated fibers were found to increase by $\sim 3.16\%$ and $\sim 9.5\%$, respectively, compared to untreated jute fiber composites. Another study found that the tensile strength and flexural strength of 20% alkali-treated jute/epoxy composites improved by $\sim 108\%$ and $\sim 28\%$, respectively, when compared to untreated jute/epoxy composites (Boopalan et al., 2012). Mahesh et al. studied the influence of NaOH concentrations on the treatment of jute fabric, and its effect on the mechanical properties of the jute/epoxy composites (Mahesh et al., 2021b). The jute fabric was treated with three different concentrations of NaOH (5%, 10%, and 15%) for 24 h at room temperature, and composites were manufactured using the compression molding technique. The study found that the tensile strength of the 5% NaOH treated jute/epoxy composites was enhanced by $\sim 36\%$ compared to untreated jute/epoxy composite. However, the tensile strength of the 10% and 15% NaOH treated jute/epoxy composites reduces by $\sim 47\%$ and $\sim 66.66\%$, respectively, compared to untreated jute/epoxy composites.

Silane and alkali-silane treatment

The silane molecules have different functional groups at both ends. One such functional group reacts with hydrophilic groups of the jute fiber and the other with hydrophobic groups in the polymer matrix to form a bridge between them (Xie et al., 2010; Pickering et al., 2016). For this reason, silane treatment improves the interfacial adhesion between jute fiber and polymer matrix. The most commonly used silanes are amino, methacryl, glycidoxo, vinyl, azido, and alkylsilanes. During the silane treatment of natural fiber (Figure 3), the hydrolysis of alkoxy groups on silane takes place to form silanol (Si-OH) groups, which can then react with hydroxyl groups on the fiber surface (Pickering et al., 2016).

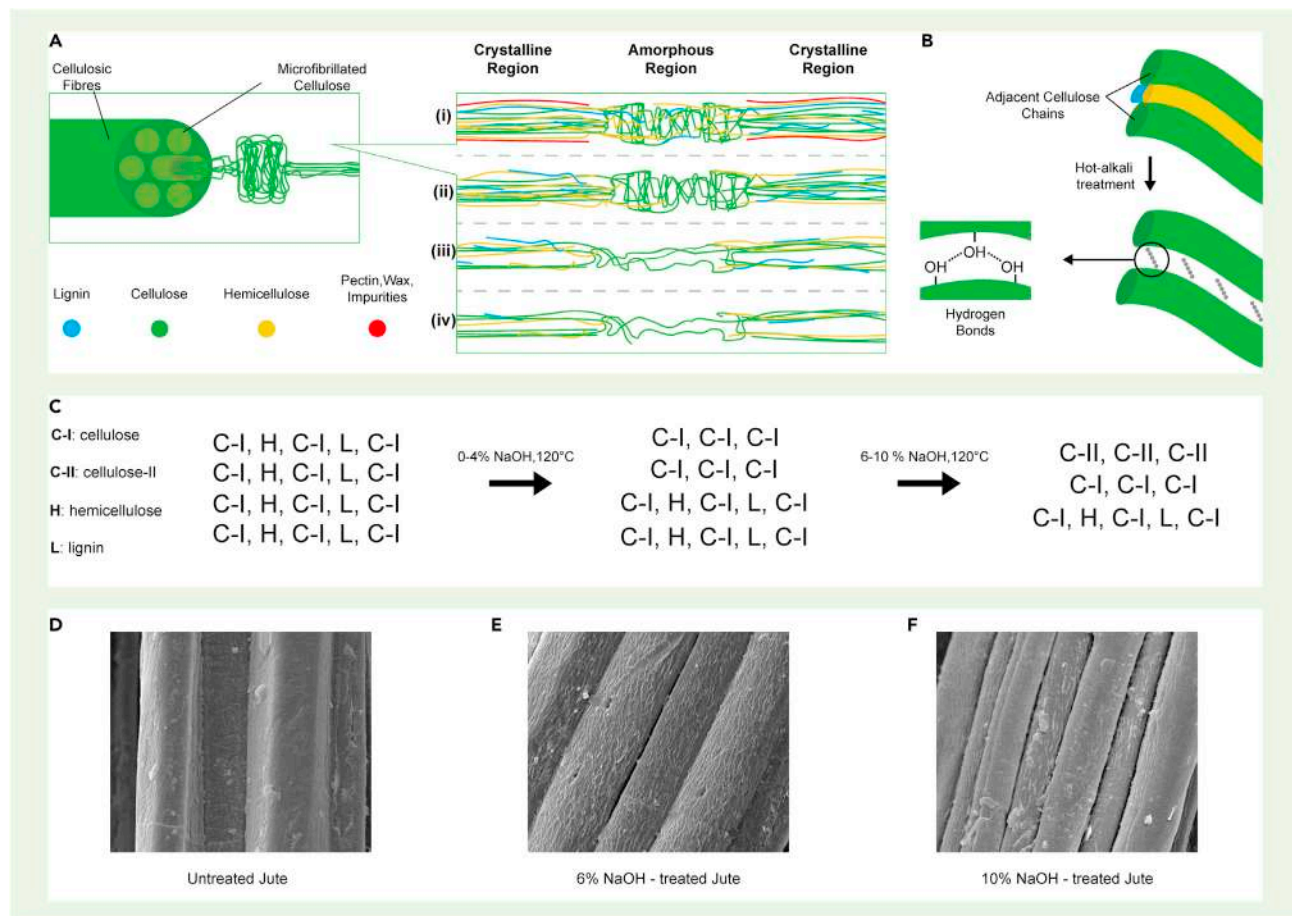


Figure 2. The alkali treatment of jute fiber

(A) The schematic of the fine structure of cellulose and other polysaccharides of hot-alkali-treated jute fibers (i) untreated, (ii) 2% NaOH-treated, (iii) 4% NaOH-treated, (iv) 6%–10% NaOH-treated, (B) the adjacent cellulose chains, (C) the changes of cellulose, hemicellulose, and lignin contents. SEM images of jute fibers surface: (D) Untreated, (E) 6% NaOH-treated, and (F) 10% NaOH-treated. Reproduced with permission (Wang et al., 2019b).

In one study (Seki, 2009), the effect of oligomeric siloxane treatment of jute fabrics on mechanical properties of jute/epoxy and jute/polyester composites was studied. At first, the jute fabrics were treated with 5% (w/w) NaOH solution for 2 h, and then the alkali-treated jute fabrics were treated with 1% siloxane. The jute/epoxy and jute/polyester composites were manufactured by the hand lay-up method. The mechanical

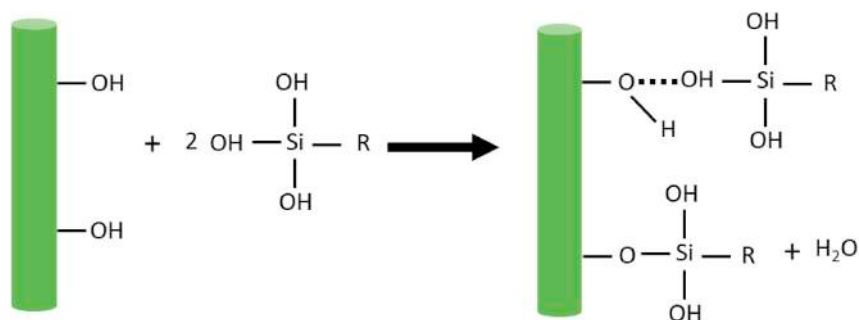


Figure 3. Reaction of silane with natural fiber (R representing organic group, ... representing hydrogen bonding)

Table 5. Mechanical properties of alkali and silane treated jute fiber reinforced composites

Composites	Treatments	Tensile strength (MPa)	Change (%)	Tensile modulus (GPa)	Change (%)	Flexural strength (MPa)	Change (%)	ILSS (MPa)	Change (%)	Ref.
Jute/epoxy	untreated	61.41		5.46		82.94		11.46		(Seki, 2009)
	5% NaOH	66.49	8.3	6.39	17	91.19	9.9	14.18	23.7	
	5% NaOH +1% siloxane	80.93	31.8	6.93	26.9	101.37	22.2	23.96	109	
Jute/polyester	untreated	45.77		3.99		59.44		8.35		
	5% NaOH	48.31	5.5	5.91	48.1	68.14	14.6	10.10	21	
	5% NaOH +1% siloxane	59.92	30.9	6.47	62.2	81.81	37.6	16.92	102.6	
Jute/epoxy	untreated					87.0		8.1		(Dilfi et al., 2018)
	1% NaOH					101.1	16.2	8.5	4.9	
	1% silane					107.8	23.9	8.9	9.9	
	1% NaOH +1% silane					128.5	47.7	9.3	14.8	
Jute/epoxy	Woven raw	56.7		7.01				51.3		(Pinto et al., 2014)
	Woven +5% NaOH+ 1% silane	55.5	-2.1	9.54	36.1			37.8	-26.3	
	UD raw	76.6		11.9				41.7		
	UD + 5% NaOH+ 1% silane	74.3	-3	13.40	12.6			38.7	-7.2	

UD = Unidirectional.

properties such as tensile, flexure, and interlaminar shear strengths of the siloxane treated composites were increased by ~32%, ~22%, and ~109% for jute/epoxy composite and ~31%, ~37%, and ~103% for jute/polyester composite compared to untreated jute fiber composites. It is worth mentioning that the obtained results from that study (Seki, 2009) were normalized with a 35% fiber volume fraction and presented in Table 5. In addition, the effect of amino-silane treatment on the performance of jute/polycarbonate thermoplastic composites was investigated in another study (Khan and Hassan, 2006). It was found that the tensile strength, bending strength, bending modulus, and tensile modulus of silane treated jute/polycarbonate composite were enhanced by ~28%, ~35%, ~62%, and ~70%, respectively, when compared to the untreated jute/polycarbonate composite.

Plasma and alkali-plasma treatment

Many researchers investigated the plasma treatment of jute fibers to manufacture the jute FRC with improved mechanical properties (Sever et al., 2011; Sinha and Panigrahi, 2009; Kafi et al., 2009). Plasma treatment introduces polar or excited groups to the fibre surface, or grafts a new polymer layer on the fiber surface that enables formation of strong covalent bonds between fiber and polymer matrix. In addition, such treatment roughens the fiber surface to enhance mechanical interlocking between fibers and polymer matrix, and improve the fiber-matrix adhesion (Yuan et al., 2002; Seki et al., 2010). The effect of plasma treatment on mechanical properties of jute fiber and jute/PLA FRC was investigated and compared with alkali-treated (AT) jute FRC (Gibeop et al., 2013). The plasma treatment of jute fibers was carried out at plasma power of 3 kV and 20 kHz for various exposure times (30s, 60s, 90s, and 120s) using helium and acrylic acid as carrier gas and monomer, respectively. The alkali treatment of jute fibers was carried out using various concentrations (3%, 5%, and 7% w/w%) of NaOH. The composites were manufactured by injection molding method using 20/80 (w/w%) jute/PLA composition. The plasma-treated jute/PLA composites provided better mechanical properties compared to untreated and alkali-treated jute/PLA composites. Tensile strength, young's modulus, and flexural strength were increased by ~28%, ~17%, and ~20%, respectively, for plasma-treated jute/PLA composite, compared to untreated jute/PLA composite.

In another study (Seki et al., 2010), the effect of the low-frequency (LF) and radio-frequency (RF) oxygen plasma treatment of jute fibers on mechanical properties of jute/polyester composites was investigated.

The alkali-treated jute fibers were plasma treated with LF and RF at different plasma power (30 W, 60 W, and 90 W) for 15 min. The mechanical properties of the composites were enhanced with the increase in plasma power for both LF and RF systems. The tensile strength, flexural strength, and ILSS were enhanced by ~40%, ~36%, and ~72%, respectively, for LF plasma-treated jute fibers at 90 W, and by ~63%, ~77%, and ~129%, respectively, for RF plasma-treated fibres at 90 W, when compared to those of untreated jute fibres.

Alkali-bleaching

Alkali treatment followed by hydrogen peroxide (H₂O₂) bleaching was carried out to modify short jute fibers, and the effect of such treatment on composites' tensile properties was investigated (Rajesh and Prasad, 2014). The jute fibers were treated with various concentrations of NaOH (5%, 10%, and 15%) followed by H₂O₂ (10 mL/L) treatment. The composites were manufactured with different weight% (5%, 10%, 15%, 20%, and 25%) of treated and untreated jute fiber content with PLA matrix via an injection molding technique. Jute/PLA composites with 10% NaOH treated fibers followed by H₂O₂ bleaching at 20% fiber loading provided ~7.5% and ~40% higher tensile strength and modulus, respectively, than those of untreated jute fiber/PLA composites.

GRAPHENE-BASED HIGH-PERFORMANCE JUTE FIBER COMPOSITES

Graphene-based surface modifications for jute fiber composites can be carried out either via treating reinforcing materials (e.g., fibers) with graphene and its derivatives (Sarker et al., 2019) or mixing such materials with a suitable polymer matrix (Sadangi et al., 2021; Costa et al., 2020). A wide range of coating processes has been used to deposit graphene-based materials on the fiber or fabric surface. Among them, dip-coating (Sarker et al., 2019; Dilfi et al., 2019) and spray coating (Wang et al., 2019a) are the most popular techniques for coating natural fiber or fabric. Dip coating is the easiest and effective method where the fibre is immersed into the dispersion of graphene and its derivatives. In the spray coating process, simple spraying of graphene-based materials can be carried out directly on the fiber surface to obtain a homogenous surface covering of deposited materials. In the matrix modification process, the graphene-based materials are mixed with a suitable resin and then infused them the fiber reinforced materials using existing resin impregnation system.

Graphene-based materials

The isolation of graphene, a one-atom-thick two-dimensional layer of sp²-bonded carbon (Georgakilas et al., 2015; Karim et al., 2019), has unveiled a wide range of novel two-dimensional materials with outstanding physicochemical properties (Novoselov et al., 2012; Park and Park, 2021) and is therefore highly admired by the researcher community for both blue sky and application-based research (Afroj et al., 2021a, 2021b; Pereira et al., 2020b). A possible route of harnessing these properties for applications might be the incorporation of graphene into composite materials (Pereira et al., 2020a; Ahmed et al., 2021). The fundamental requirements for such applications include high scalability, reliability, and cost-effective production process. The final properties of the graphene-based material depend on the number of graphene layers, average lateral dimension, atomic carbon/oxygen ratio, surface chemistry, surface area, and material purity (Wick et al., 2014; Da Luz et al., 2020). The poor solubility of graphene limits its wide-scale industrial applications (Johnson et al., 2015). Among the two oxidative derivatives of graphene, graphene oxide (GO) exhibits less electrical conductivity and high solubility in water (Karim et al., 2021a), and reduced graphene oxide (rGO) exhibiting properties between graphene and GO (Mohan et al., 2015), is sparingly dispersible in water or other solvents and offers admirable electrical conductivity (Yusuf et al., 2019).

There are various synthetic approaches for the preparation of graphene and its derivatives, which could be categorized under two groups-namely bottom-up and top-down techniques; all producing graphene with different morphologies, different flake diameter and thickness, corrugation and surface chemistry (Lee et al., 2019; Madurani et al., 2020). The bottom-up technique, usually employed for small scale production, includes methods such as micromechanical peeling of graphite, chemical vapor deposition (CVD), plasma enhanced CVD, and epitaxial growth of graphene on SiC substrate. In these techniques, graphene flakes are deposited on a suitable substrate from carbon sources and allow the production of contamination-free graphene with control over initiation and growth of graphene by correct choice of substrate (Liu et al., 2020). However, bottom-up methods are not very popular for application-based research work and

large-scale production due to their low yield, complex processing and associated higher cost (Yang and Wang, 2016). On the other hand, for larger scale production of graphene, several top-down techniques are followed where graphene is mainly exfoliated from bulk (Luo et al., 2012). Benefits of such processes include solution based processability, ease of implementation, and higher yield compared to bottom-up processes (Yang and Wang, 2016). Liquid phase exfoliation, electrochemical exfoliation using ionic intercalation, chemical oxidation of graphite to make GO and sometimes followed by the reduction to make rGO, have been employed as popular top-down techniques (Narayan and Kim, 2015).

Among several exfoliation methods, the liquid phase exfoliation (LPE) is a versatile, scalable, sustainable, and cost-effective method to produce single-layer graphene, and therefore used widely (Ren et al., 2018; Bonaccorso et al., 2016). Basically, in liquid phase exfoliation (LPE) processes, ultrasonic or shear energy are applied to break inter-sheet forces of carbon in presence of a stabilizing liquid (Hernandez et al., 2008), either in a non-aqueous solution (Hernandez et al., 2008; Hassoun et al., 2014; Khan et al., 2010) or an aqueous solution with surfactant (Hernandez et al., 2008). Possibly because of this in-plane fracture during the exfoliation and purification process to separate unexfoliated flakes, the flake size of graphene produced by LPE is mostly below $1 \mu\text{m}^2$ (Lotya et al., 2009; Hernandez et al., 2008; Khan et al., 2010; Maragó et al., 2010). Among other LPE processes, microfluidization produces graphene with 100% yield by weight (Y_w) and a higher concentration compared to other LPE processes as the force acts over the whole volume of the liquid, whereas, bath sonication, tip sonication, and shear exfoliation generally produce graphene of lower concentration as well as lower yield (up to 2%) by weight (Y_w). Electrochemical expansion process offers much better yield by weight ($Y_w > 70\%$). To enjoy the distinctive properties of graphene it is important to produce and maintain graphene as individual sheets. However, graphene sheets tend to agglomerate and even restack to form graphite through van der Waals interactions (Li et al., 2008). Therefore, the other viable way to produce solution-processable graphene on a large scale is through reduction of graphene oxide with added functionality (Liu et al., 2012b; Lonkar et al., 2015). Various types of chemical reduction (via ascorbic acid, sodium hydrosulphite, hydrazine hydrate, hydriodic acid with acetic acid, etc), thermal reduction and electrochemical reduction can be used to achieve different properties in rGO depending on various final applications (Karim et al., 2017, 2021a; Afroj et al., 2021a, 2021b). However, the disadvantage of this route is that none of these reduction processes can completely reduce and eliminate the many structural defects introduced by the oxidation process (Zhang et al., 2010; Kang et al., 2009; Yang et al., 2009). The proper fine tuning of the synthesis protocols still remains a challenge (Li et al., 2020) for obtaining quality graphene-based materials for their wide range of applications (Yusuf et al., 2019; Ren et al., 2018).

Lower crystallinity, hydrophilicity, and inherent electrical insulation properties of jute fiber results in lower mechanical, poor interfacial, and electrical properties of jute fiber reinforced composites that limits their application as multifunctional composites (Gassan and Bledzki, 1999b; Karim et al., 2021b). Few carbon based materials were reported to enhance properties of jute fiber composites earlier (Zhuang et al., 2011; Islam et al., 2020; Saiteja et al., 2020; Tzounis et al., 2014); however, a recent study reported for the first time the incorporation of graphene and its derivatives to design high-performance natural fiber composites (Sarker et al., 2018). In this study alkali-treated jute fibers were coated with graphene flakes and GO which enhanced interfacial shear strength by $\sim 236\%$ and tensile strength by $\sim 96\%$. Considering the improved characteristics of rGO making it an ideal material for composite, Karim et al. incorporated rGO with jute fiber which significantly improved the tensile strength by $\approx 183\%$ along with the Young's modulus of the composites by $\approx 450\%$ (Karim et al., 2021b).

Graphene-based jute: Single fiber properties

The surface modification of jute fibers with graphene oxide (GO) (Sarker et al., 2018), reduced graphene oxide (rGO) (Karim et al., 2021b), and graphene flakes (G) (Sarker et al., 2018, 2019) have been carried out. Jute fibers were chemically treated with hot water and 0.5% NaOH to remove noncellulosic materials. The chemically treated jute fibers were then coated with graphene derivatives via simple dip-coating method, Figure 4A. The jute fibers were immersed in GO, rGO, and G dispersions for 30 min and subsequently dried at 80°C for 30 min. The surface characteristics and mechanical properties of untreated and treated jute fibers were investigated.

The wide-scan X-ray photoelectron spectroscopy (XPS) spectra in Figure 4B show that the C/O ratio of jute fibers decreased from ~ 5.5 to ~ 3.8 after coating with GO, because of the presence of

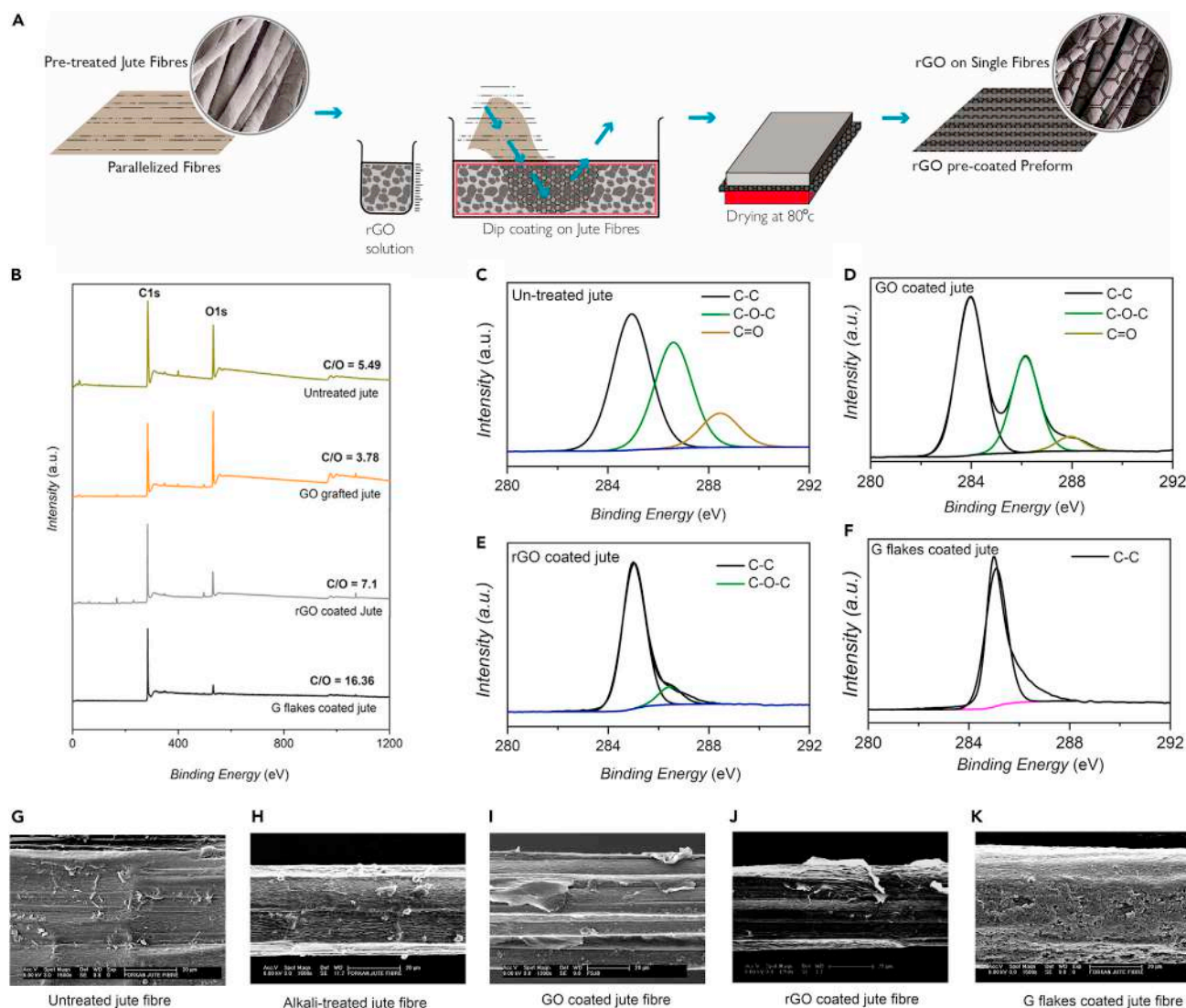


Figure 4. Graphene-based jute fibers: Coating, surface functionalities, and morphologies

(A) Schematic diagram showing 2D material coating process on jute fibers and the preparation of 2d material-coated jute fiber preforms, (B) wide scan XPS spectrum of untreated, GO, rGO, and G flakes coated jute fiber (C) high resolution C(1s) XPS spectrum of untreated jute fiber, (D) high resolution C(1s) XPS spectrum of GO-coated jute fiber, (E) high resolution C(1s) XPS spectrum of rGO-coated jute fiber, (F) high resolution C(1s) XPS spectrum of G flake-coated jute fiber. SEM image of (G) untreated jute fiber (X1500); (H) HA0.5 treated jute fiber (X1500); (I) GO treated jute fiber (X1200); (J) rGO treated jute fiber (X1250); and (K) G flakes treated jute fiber (X1500). Reproduced with permission (Sarker et al., 2018, Karim et al., 2021b).

oxygen-containing functional groups in GO (Abdelkader et al., 2017). The C/O ratio of rGO coated jute fiber increased to ~ 7.1 because of the partial restoration of graphene structures. The maximum C/O ratio of ~ 16.4 was obtained for jute fibers coated with G flakes, which may be because of the absence of oxygen-containing functional groups in their structures (Afroj et al., 2020). The high resolution C1s XPS spectra of untreated and GO coated jute fibers are similar, and show the presence of three main components: C-C bond (≈ 284.5 eV) in cellulosic structure, C-O-C groups (hydroxyl and epoxy, ≈ 286.5 eV), and C=O groups (carbonyl, ≈ 288.3 eV), Figures 4C and D. The peaks associated with the oxygen functional groups significantly diminished after coating with rGO, with small amounts of residual oxygen functional groups left as evident from the peak around 287.5 eV, Figure 4E. The C1s spectrum of G-coated jute fibers is similar to graphene or graphite, mainly dominated by C-C/C=C, Figure 4F. Therefore, G-flakes are loosely attached to cellulosic jute fibers, because of the absence of oxygen-containing functional groups (Sarker et al., 2018).

Scanning electron microscope (SEM) images show smooth untreated jute fiber surface (Figure 4G), because of the presence of wax, fat, lignin, and hemicellulose, which becomes rough after alkali treatment (Figure 4H) because of the removal of the noncellulosic materials. It was found that the GO and rGO uniformly coated the jute fiber surface (Figures 4I and 4J) (Sarker et al., 2018; Karim et al., 2021b), because of the chemical interaction between the hydroxyl group of the jute fiber and the oxygen functional group of the GO and rGO. However, the G-flakes provided a uniform coating with plenty of unfixed graphene flakes on the fiber surface (Figure 4K) (Sarker et al., 2018).

Tensile properties and interfacial shear strength (ILSS) of the untreated, alkali-treated, GO, rGO, and G-coated jute fibers were also investigated (Sarker et al., 2018; Karim et al., 2021b). A single fiber microbond pull-out test was used to measure ILSS. Optical and SEM images of microdroplets of epoxy on jute fiber before and after microbond test are shown in Figures 5B and 5C and IFSS results are shown in Figure 5A. The ILSS of GO (1%), rGO (0.5%), and GnP (10%) coated single jute fiber composites was increased by ~236%, ~97%, and ~164%, respectively compared to untreated jute fiber epoxy composites. Such a significant improvement of IFSS with GO is associated with the presence of a huge amount of oxygen functional group such as hydroxyl (-OH), epoxide (C-O-C), carbonyl (C=O), and carboxyl (O-C=O) in GO. Such functional groups interact with the groups of epoxy resin and form a strong mechanical interlocking at the fiber/matrix interface via suitable bonding. Similarly, there was a large increment in IFSS of G-flakes coated jute fibers (Sarker et al., 2018), which may be related to the strong mechanical interlocking of G-flakes onto the rough and porous jute fiber surface. However, IFSS of rGO coated jute fibers increased slightly. Nevertheless, the effect of rGO coating on improving IFSS value is better than other natural and synthetic fibers modified by traditional alkali and nanomaterials (Karim et al., 2021b).

The single fiber tensile test of untreated and treated jute fibers was carried out via mounting the fiber on the paper frame. The single fiber tensile test shows the increase of tensile strength from 295 MPa to 575, 814, and 474 MPa, and Young's modulus from 30 GPa to 48, 78, and 52 GPa for 1% GO, 0.5% rGO, and 10% G flakes coated jute fibers (Karim et al., 2021b; Sarker et al., 2018), Figures 5D and 5E and Table 6. Such significant improvement in tensile properties is attributed to the strong bonds between the functional groups of graphene derivatives and those of chemically treated jute fibers. In addition, the coating with G flakes provides increased stiffness of jute fiber, which enables the removal of stress concentrations on the fiber surface during tensile loading, resulting in the enhancement of the tensile properties. The SEM images of the fractured specimen after the tensile test show uneven microfibrils fracture for untreated jute fibers because of stress concentration between the cellulosic microfibrils in the fiber, Figures 5F1 and 5G1. However, a linear breakage of microfibrils was observed with graphene derivatives coated jute fiber (Figures 5F2, 5F3, and 5G2) which is responsible for more loading capacity along with the tensile deformation. The rGO coating on jute fibers provides the highest tensile properties obtained so far with alkali treatment and nanosurface engineering of jute fibers (Karim et al., 2021b; Sarker et al., 2018).

Ultrahigh performance of graphene-based jute fiber composites

Although mechanical properties of individual fibers have been increased significantly via treating jute fibers with graphene-based materials, the main challenge is how such excellent properties can be translated to jute FRC for real world applications. In our previous study (Sarker et al., 2019), we addressed this challenge via a novel strategy of combining physical and chemical modifications of jute fiber preforms to manufacture next generation jute FRC. Before graphene coating, the jute fiber mats were prepared by physical and chemical treatment of the jute fibers. Unidirectional (UD) jute/epoxy composites were prepared with alkali-treated and graphene materials-coated jute fibers via vacuum-assisted resin infusion (VARI) method. The longitudinal tensile strength, Young's modulus, and strain% of jute/epoxy composite were increased with the increase of concentration of GO up to 0.75mg/mL because of the nano-engineering effect of graphene materials on jute fibre but after this concentration of GO deteriorate the tensile properties of composites because of the agglomeration of GO flakes, Figures 6A and 6B and Table 7. In addition, mechanical properties of rGO-based natural jute fibres UD composites were investigated (Karim et al., 2021b). The Young's modulus, tensile strength, and tensile strain of the rGO-based jute FRC increased with the increase in rGO concentrations, and the maximum improvement was achieved with 0.5% rGO coated jute epoxy composites, Figures 6A and 6B. The combination of all physical and chemical treatments together with rGO coating resulted in ~450% and ~183% improvement in Young's modulus and the tensile strength of the composites, which is the highest improvement in the tensile properties of any kind of natural fiber

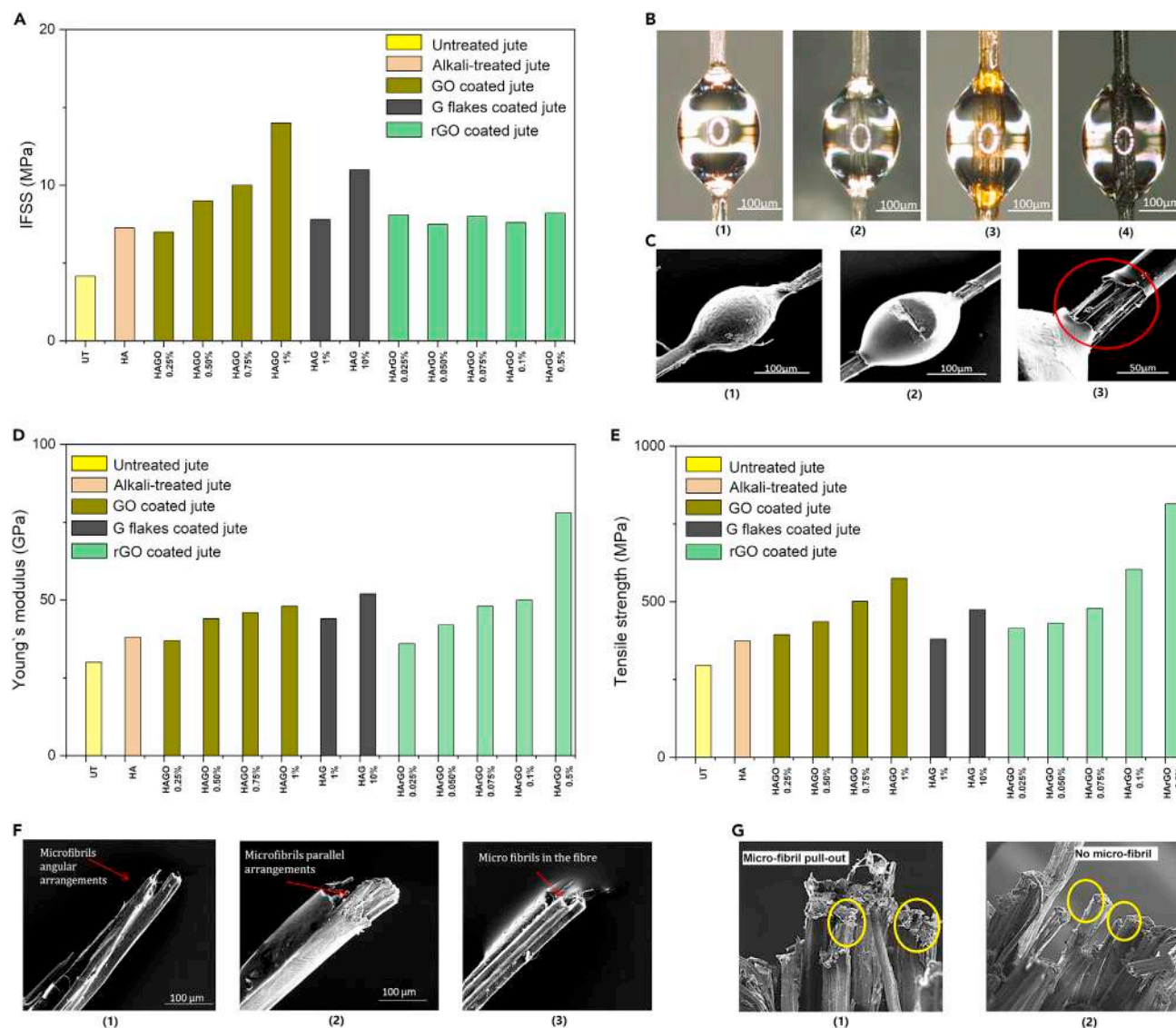


Figure 5. High performance graphene-based jute fibers

(A) Interfacial shear strength (IFSS) of untreated, alkali-treated, GO, rGO, and G flake-coated jute fibers, (B) Optical microscopic images of the microdroplet of epoxy on (1) untreated; (2) alkali-treated; (3) GO-coated; and (4) G flake-coated jute fibers (X200) before microbond test, (C) SEM image of microdroplets of epoxy on jute fiber (1) before microbond test; (2) after microbond test; and (3) de-bonded area (red circle line) after microbond test (X250), (D) Young's modulus and (E) tensile strength of untreated, alkali-treated, GO, rGO, and G flake-coated jute fibers, (F) SEM images of the fracture specimen after single fiber tensile test (1) untreated; (2) GO-coated; and (3) G flake-coated jute fiber (X250) and (G) SEM images of the fracture specimen after single fiber tensile test (1) untreated and (2) rGO-coated jute fiber (X250). Reproduced with permission (Sarker et al., 2018, Karim et al., 2021b).

composites reported in the literature. SEM images of the fracture surfaces of the graphene material-based jute/epoxy composites are shown in Figures 6C–6F.

In another study, mechanical and thermal properties of the graphene oxide nanoplatelets (GONPs) modified jute/polypropylene composites were investigated and compared with untreated jute/PP composites (Chen et al., 2020). Firstly, the jute fiber surface was treated with a silane coupling agent and then the jute fiber was coated with GONPs. Three different types of silane coupling agents 3-aminopropyltriethoxysilane (KH550), 3-Glycidoxypropyltrimethoxysilane (KH560) and 3-Methacryloxypropyltrimethoxysilane (KH 570) were used. Among them, KH 570 provided the best performance. The GONPs effectively improved the fiber matrix interfacial adhesion. The study revealed that the tensile and flexural strength of the silane and GONPs modified jute/PP composites increased by 16.2% and 12.4%, respectively, compared to untreated

Table 6. Tensile properties of untreated, alkali-treated, GO, rGO, and G flakes coated jute fibers

Fiber	Treatment	Tensile strength (MPa)	Change %	Young's modulus (GPa)	Change %	Ref
Jute	Untreated	295		30		(Sarker et al., 2018)
	H	293	-1	29	-3	
	H + A	374	27	38	27	
	H + A + GO 0.25%	394	34	37	23	
	H + A + GO 0.50%	436	48	44	47	
	H + A + GO 0.75%	501	70	46	53	
	H + A + GO 1%	575	95	48	60	
	H + A + G 1%	380	29	44	47	
	H + A + G 10%	474	61	52	73	
	H + A + rGO 0.025%	414	40	36	20	(Karim et al., 2021b)
	H + A + rGO 0.050%	431	46	42	40	
	H + A + rGO 0.075%	478	62	48	60	
	H + A + rGO 0.1%	604	105	50	67	
	H + A + rGO 0.5%	814	176	78	160	

H = Hot water treatment, A = Alkali treatment, GO = Graphene oxide coated, G = Graphene flake coated and rGO = Reduced graphene oxide coated.

jute/PP composites. The crystallization temperature of silane and GONPs modified jute fiber PP composites also increased by $\sim 3^{\circ}\text{C}$.

The mechanical behavior of rGO filled jute/epoxy composites was investigated at different temperatures to quantify the effect of temperature and rGO filler on the mechanical properties of the composites (Pa and M, 2019). The tensile strength, compressive strength, flexural strength, energy absorption, and ILSS were analyzed at various temperature conditions with 2% rGO-based jute/epoxy composites and compared with unfilled jute epoxy composites. The rGO filled jute/epoxy composite exhibited better mechanical properties at all temperatures compared to the unfilled jute/epoxy composites Figures 6G and 6H and Table 7. The hybrid composites tested for strength at sub-zero temperatures showed enhanced mechanical properties compared to room temperature conditions.

The influence of GONPs and silica-decorated graphene oxide (SiO_2 @GONPs) at different loadings (0, 0.1, 0.3, and 0.5 wt.-% with respect to the matrix) on the flexural and high-velocity impact properties of jute fiber/epoxy composites was also investigated (Amirabadi-Zadeh et al., 2021). The multiscale composites (jute/epoxy, GONPs/jute/epoxy, and SiO_2 @GONPs/jute/epoxy) were prepared using the static pressing assisted hand layup method. The most promising results were obtained with 0.3 wt.-% of SiO_2 @GONPs modified jute/epoxy composites. The study found that the flexural strength, energy absorption capability, and impact limit velocity of the 0.3 wt.-% SiO_2 @GONPs modified jute/epoxy composite improved by $\sim 40\%$, $\sim 61\%$, and $\sim 28\%$, respectively, from those of the neat jute/epoxy composites. In other study, the effect of two different nanofillers such as graphene oxide (GO) and functionalized graphene (FG) on the mechanical properties of the Jute/epoxy composites have been investigated at different nanofiller contents (0.5, 0.75, and 1 wt.-%) (Sadangi et al., 2021). It was found that jute/epoxy composites with nano fillers have better mechanical properties such as tensile and flexural strength compared to composite without any nanofiller, and composites with 0.75 wt.-% nanofiller exhibited best results. Jute/epoxy composites with FG exhibited better mechanical properties than the jute/epoxy composites with GO, Figures 6I and 6J.

Drilling and milling processes are widely used during the assembly of composite parts with other components (Liu et al., 2012a). The surface finish attained after drilling and milling operation is an issue of concern as a rough surface may lead to crack initiation and finally failure of components. The milling and drilling performance of graphene-modified jute/basalt hybrid composites have been investigated and compared with pure jute and pure basalt fiber composites (Kishore et al., 2021). The addition of graphene (0.2 wt.-%, 0.4 wt.-% and 0.6 wt.-%) to hybrid composites improved lubrication and led to reduced surface roughness.

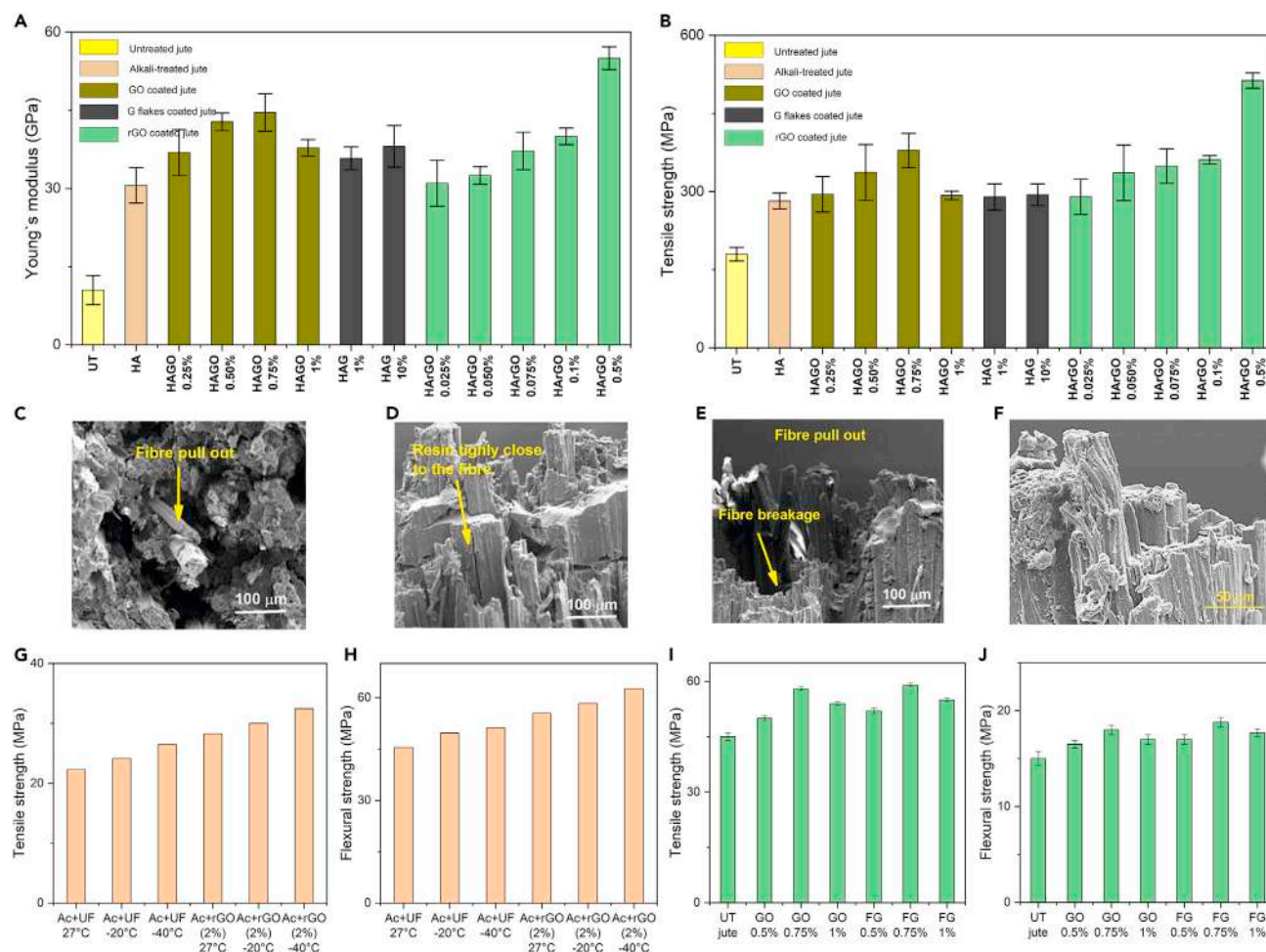


Figure 6. Ultrahigh performance of graphene-based jute fiber composites

Longitudinal (A) Young's modulus, (B) tensile strength of untreated, alkali-treated and graphene materials treated jute fiber/epoxy composites. SEM images of the fracture surfaces of (C) untreated, (D) GO coated, (E) graphene-coated, and (F) rGO coated jute/epoxy composites after the longitudinal tensile test. Reproduced with permission (Sarker et al., 2018, Karim et al., 2021b). (G) Tensile strength (H) flexural strength of acetone treated unfilled and rGO filled jute/epoxy composites at different temperatures. Reproduced with permission (Pa and M, 2019). (I) Tensile strength and (J) flexural strength of untreated, GO and FG based jute/epoxy composite. Reproduced with permission (Sadangi et al., 2021).

CONCLUSION AND OUTLOOK

With growing environmental concerns with petrochemical-based synthetic fibers (Uddin et al., 2021; Karim et al., 2020), researchers have turned their attention to biodegradable fibers from renewable sources. However, such materials suffer from poor performance properties and thermal stability (Karim et al., 2014). Therefore, key challenge is to produce sustainable, biodegradable, and lightweight composites which provide combinations of excellent strength, stiffness, toughness, and multi-functionalities. An overview of jute surface modifications using the physical and chemical methods and further modification with graphene and its derivatives is provided. In addition, the effect of such surface treatments and graphene-based modifications on mechanical and multifunctional properties of jute FRC is extensively reviewed. A great effort has been paid to improve the mechanical and functional properties of jute FRC via physical and chemical treatments of jute fibers, and also incorporating graphene-based 2D materials. A wide range of studies has been carried out to improve the interfacial adhesion between jute fibers and polymer matrix such as physical (plasma), chemical (alkali, bleaching, silane), or combined physical and chemical (alkali-plasma) or different chemical (alkali-bleaching, alkali-silane) treatments. Such treatments have improved the mechanical and interfacial properties of the composites. However, this improvement is not sufficient to use developed composites as an alternative to synthetic FRC. A combined physical and chemical treatment using graphene-based materials modified jute fiber/epoxy composites showed a significant increase in the

Table 7. Mechanical properties of untreated, hot water, alkali, graphene flakes, graphene oxides, and reduced graphene oxide treated jute fibre/ epoxy composites

Composites	Treatment/ modification	V_f	Tensile strength (MPa)	Young's modulus (GPa)	Strain to failure (%)	Flexural strength (MPa)	ILSS (MPa)	Ref
Jute/epoxy	Untreated	0.24	180 ± 13	10.5 ± 2.8	0.80 ± 0.05			(Sarker et al., 2019)
	H	0.50	230 ± 19.7	26.5 ± 3.45	0.85 ± 0.09			
	HA (0.5%)	0.54	282 ± 15.4	30.6 ± 3.4	0.86 ± 0.09			
	HA + GO (0.25%)	0.54	295 ± 33.9	36.9 ± 4.4	0.84 ± 0.07			
	HA + GO (0.50%)	0.54	337 ± 53.3	42.8 ± 1.7	0.94 ± 0.10			
	HA + GO (0.75%)	0.56	379 ± 33	44.6 ± 3.6	0.93 ± 0.05			
	HA + GO (1%)	0.56	292.7 ± 8.4	37.8 ± 1.6	0.78 ± 0.01			
	HA + GnP(1%)	0.55	290 ± 25	35.8 ± 2.2	0.84 ± 0.08			
HA + GnP(10%)	0.55	294 ± 21	38.1 ± 4.0	0.80 ± 0.07				
Jute/epoxy	HA + rGO (0.025%)	0.54	290 ± 33.9	31 ± 4.4	0.84 ± 0.07			(Karim et al., 2021b)
	HA + rGO (0.050%)	0.54	336 ± 53.3	32.5 ± 1.7	0.86 ± 0.10			
	HA + rGO (0.075%)	0.56	349 ± 33	37.2 ± 3.6	0.93 ± 0.05			
	HA + rGO (0.1%)	0.56	361 ± 8.4	40 ± 1.6	0.99 ± 0.01			
	HA + rGO (0.5%)	0.60	513 ± 15	55 ± 2.2	1.13 ± 0.08			
Jute/Epoxy	UF 27°C	0.39	22.26			45.45	2.22	(Pa and M, 2019)
	UF -20°C		24.12			49.65	4.11	
	UF -40°C		26.46			51.21	5.40	
	Ac + rGO (2%) 27°C		28.26			55.41	2.43	
	Ac + rGO (2%) -20°C		30.01			58.31	4.34	
	Ac + rGO (2%) -40°C		32.44			62.64	5.70	
Jute/Epoxy	Pure jute	60%	45 ± 1.06			15 ± 0.75		(Sadangi et al., 2021)
	GO (0.5%)		50 ± 0.75			16.5 ± 0.4		
	GO (0.75%)		58 ± 0.50			18 ± 0.50		
	GO (1%)		54 ± 0.50			17 ± 0.50		
	FG (0.5%)		52 ± 0.75			17 ± 0.50		
	FG (0.75%)		59 ± 0.50			18.8 ± 0.50		
	FG (1%)		55 ± 0.50			17.7 ± 0.40		

(UF = Unfilled, Ac = Acetone treated, FG = Functionalized graphene).

tensile and interfacial properties and comparable specific properties to those of glass fibers with added multifunctionalities. There has been very limited research that used graphene-based materials to modify jute fiber and manufacture FRC. Therefore, more research is needed for better understanding of the interactions among graphene-based materials, reinforcing fibers and matrix materials to promote this novel class of composites materials for industrial applications.

There is a growing interest in sustainable, biodegradable, and lightweight smart materials for structural composites applications, that would offer unprecedented combinations of stiffness, strength, toughness and multifunctionality. Most of these researches have used petrochemical-based or nonbiodegradable polymer matrices to manufacture jute FRC that are not fully green (100% bio-based) composites. The application of these bio-based nonbiodegradable composites has been increasing in the automotive and other manufacturing industries. Some green composites are manufactured using bio-based and biodegradable resin but the application of such materials is limited in the automotive and other structural applications, because of their poor mechanical properties. Efforts should be put into developing suitable bio-based and biodegradable resin for manufacturing green and environmentally sustainable high-performance natural FRCs. Such composites could potentially help reducing non-degradable plastic waste and improve the overall carbon footprints associated with composites industries. Based on the articles discussed in this review, the researchers should pay attention toward the development of the next generation

of high-performance green composites by incorporating the graphene and other 2D materials in the jute fiber reinforced composite.

ACKNOWLEDGMENTS

The authors acknowledge Expanding Excellence in England (E3) funding from Research England, United Kingdom, and also graphic support from Laura Wescott.

REFERENCES

- Abdelkader, A.M., Karim, N., Vallés, C., Afroj, S., Novoselov, K.S., and Yeates, S.G. (2017). Ultraflexible and robust graphene supercapacitors printed on textiles for wearable electronics applications. *2D Mater* 4, 035016.
- Afroj, S., Britnell, L., Hasan, T., Andreeva, D.V., Novoselov, K.S., and Karim, N. (2021a). Graphene-based technologies for tackling COVID-19 and future pandemics. *Adv. Funct. Mater.* 2107407.
- Afroj, S., Islam, M.H., and Karim, N. (2021b). Multifunctional graphene-based wearable E-textiles. *Proceedings* 68, 11.
- Afroj, S., Karim, N., Wang, Z., Tan, S., He, P., Holwill, M., Ghazaryan, D., Fernando, A., and Novoselov, K.S. (2019). Engineering graphene flakes for wearable textile sensors via highly scalable and ultrafast yarn dyeing technique. *ACS Nano* 13, 3847–3857.
- Afroj, S., Tan, S., Abdelkader, A.M., Novoselov, K.S., and Karim, N. (2020). Highly conductive, scalable, and machine washable graphene-based E-textiles for multifunctional wearable electronic applications. *Adv. Funct. Mater.* 30, 2000293.
- Ahmed, A., Adak, B., Faruk, M.O., and Mukhopadhyay, S. (2021). Nanocellulose coupled 2D graphene nanostructures: Emerging paradigm for sustainable functional applications. *Ind. Eng. Chem. Res.* 60, 10882–10916.
- Alves, C., Dias, A., Diogo, A., Ferrão, P., Luz, S., Silva, A., Reis, L., and Freitas, M. (2011). Eco-composite: the effects of the jute fiber treatments on the mechanical and environmental performance of the composite materials. *J. Compos. Mater.* 45, 573–589.
- Aly-Hassan, M.S. (2015). Chapter 2 - A new perspective in multifunctional composite materials. In *Multifunctionality of Polymer Composites*, K. Friedrich and U. Breuer, eds. (William Andrew Publishing), pp. 42–65.
- Amirabadi-Zadeh, M., Khosravi, H., and Tohidlou, E. (2021). Preparation of silica-decorated graphene oxide nanohybrid system as a highly efficient reinforcement for woven jute fabric reinforced epoxy composites. *J. Appl. Polym. Sci.* 138, 49653.
- Bledzki, A., and Gassan, J. (1999). Composites reinforced with cellulose based fibres. *Prog. Polym. Sci.* 24, 221–274.
- Bonaccorso, F., Bartolotta, A., Coleman, J.N., and Backes, C. (2016). 2D-crystal-based functional inks. *Adv. Mater.* 28, 6136–6166.
- Boopalan, M., Umapathy, M., and Jenyfer, P. (2012). A comparative study on the mechanical properties of jute and sisal fiber reinforced polymer composites. *Silicon* 4, 145–149.
- Brodowsky, H., and Mäder, E. (2012). Jute fibre/epoxy composites: Surface properties and interfacial adhesion. *Composites Sci. Technol.* 72, 1160–1166.
- Chandekar, H., Chaudhari, V., and Waigaonkar, S. (2020). A review of jute fiber reinforced polymer composites. *Mater. Today Proc.* 26, 2079–2082.
- Chandrasekar, M., Ishak, M., Sapuan, S., Leman, Z., and Jawaid, M. (2017). A review on the characterisation of natural fibres and their composites after alkali treatment and water absorption. *Plast. Rubber Compos.* 46, 119–136.
- Chen, Y., Chen, W., Liang, W., Wang, Q., Zhang, Y., Wang, J., and Chen, C. (2020). Graphene oxide nanoplatelets grafted jute fibers reinforced PP composites. *Fibers Polym.* 21, 2896–2906.
- Costa, U.O., Nascimento, L.F.C., Garcia, J.M., Bezerra, W.B.A., Da Luz, F.S., Pinheiro, W.A., and Monteiro, S.N. (2020). Mechanical properties of composites with graphene oxide functionalization of either epoxy matrix or curaua fiber reinforcement. *J. Mater. Res. Technol.* 9, 13390–13401.
- Da Luz, F.S., Garcia Filho, F.D., Del-Río, M.T., Nascimento, L.F., Pinheiro, W.A., and Monteiro, S.N. (2020). Graphene-incorporated natural fiber polymer composites: A first overview. *Polymers* 12, 1601.
- Dilfi, K.F.A., Che, Z., and Xian, G. (2019). Grafting ramie fiber with carbon nanotube and its effect on the mechanical and interfacial properties of ramie/epoxy composites. *J. Nat. Fibers* 16, 388–403.
- Dilfi, K.F.A., Balan, A., Bin, H., Xian, G., and Thomas, S. (2018). Effect of surface modification of jute fiber on the mechanical properties and durability of jute fiber-reinforced epoxy composites. *Polym. Composites* 39, E2519–E2528.
- Faruk, O., Bledzki, A.K., Fink, H.-P., and Sain, M. (2012). Biocomposites reinforced with natural fibers: 2000–2010. *Prog. Polym. Sci.* 37, 1552–1596.
- Ganesan, K., Kailasanathan, C., Rajini, N., Ismail, S.O., Ayirilmis, N., Mohammad, F., Al-Lohedan, H.A., Tawfeek, A.M., Issa, Z.A., and Aldhayan, D.M. (2021). Assessment on hybrid jute/coir fibers reinforced polyester composite with hybrid fillers under different environmental conditions. *Constr. Build. Mater.* 301, 124117.
- Gassan, J., and Bledzki, A.K. (1999a). Alkali treatment of jute fibers: Relationship between structure and mechanical properties. *J. Appl. Polym. Sci.* 71, 623–629.
- Gassan, J., and Bledzki, A.K. (1999b). Possibilities for improving the mechanical properties of jute/epoxy composites by alkali treatment of fibres. *Compos. Sci. Technol.* 59, 1303–1309.
- Georgakilas, V., Perman, J.A., Tucek, J., and Zboril, R. (2015). Broad family of carbon nanoallotropes: Classification, chemistry, and applications of fullerenes, carbon dots, nanotubes, graphene, nanodiamonds, and combined superstructures. *Chem. Rev.* 115, 4744–4822.
- Gibeop, N., Lee, D., Prasad, C.V., Toru, F., Kim, B.S., and Song, J.I. (2013). Effect of plasma treatment on mechanical properties of jute fiber/poly (lactic acid) biodegradable composites. *Adv. Compos. Mater.* 22, 389–399.
- Goda, K., and Cao, Y. (2007). Research and development of fully green composites reinforced with natural fibers. *J. Solid Mech. Mater. Eng.* 1, 1073–1084.
- Gopinath, A., Kumar, M.S., and Elayaperumal, A. (2014). Experimental investigations on mechanical properties of jute fiber reinforced composites with polyester and epoxy resin matrices. *Proced. Eng.* 97, 2052–2063.
- Gupta, M., Srivastava, R., and Bisaria, H. (2015). Potential of jute fibre reinforced polymer composites: A review. *Int. J. Fiber Textile Res.* 5, 30–38.
- Hassoun, J., Bonaccorso, F., Agostini, M., Angelucci, M., Betti, M.G., Cingolani, R., Gemmi, M., Mariani, C., Panero, S., Pellegrini, V., and Scrosati, B. (2014). An advanced lithium-ion battery based on a graphene anode and a lithium iron phosphate cathode. *Nano Lett.* 14, 4901–4906.
- Hernandez, Y., Nicolosi, V., Lotya, M., Blighe, F.M., Sun, Z., De, S., McGovern, I.T., Holland, B., Byrne, M., Gun'ko, Y.K., et al. (2008). High-yield production of graphene by liquid-phase exfoliation of graphite. *Nat. Nanotechnol.* 3, 563–568.
- Hong, C., Hwang, I., Kim, N., Park, D., Hwang, B., and Nah, C. (2008). Mechanical properties of silanized jute-polypropylene composites. *J. Ind. Eng. Chem.* 14, 71–76.
- Islam, M.J., Rahman, M.J., and Mieno, T. (2020). Safely functionalized carbon nanotube-coated jute fibers for advanced technology. *Adv. Compos. Hybrid Mater.* 3, 285–293.
- Islam, M.M. (2013). Biochemistry, medicinal and food values of jute (*Corchorus capsularis* L. and C.

- olitorius L.) leaf: A review. *Int. J. Enhanc Res. Sci. Technol. Eng.* **2**, 135–144.
- Islam, M.M., and Xiaoying, J. (2016). Customer's perception towards buying eco-friendly diversified jute products: An empirical investigation in Dhaka city, Bangladesh. *J. Marketing Consumer Res.* **24**, 34–39.
- Johnson, D.W., Dobson, B.P., and Coleman, K.S. (2015). A manufacturing perspective on graphene dispersions. *Curr. Opin. Colloid Interfaces Sci.* **20**, 367–382.
- Kafi, A.A., Hurren, C.J., Huson, M.G., and Fox, B.L. (2009). Analysis of the effects of atmospheric helium plasma treatment on the surface structure of jute fibres and resulting composite properties. *J. Adhes. Sci. Technol.* **23**, 2109–2120.
- Kang, H., Kulkarni, A., Stankovich, S., Ruoff, R.S., and Baik, S. (2009). Restoring electrical conductivity of dielectrophoretically assembled graphite oxide sheets by thermal and chemical reduction techniques. *Carbon* **47**, 1520–1525.
- Kapatel, P.M. (2021). Investigation of green composite: Preparation and characterization of alkali-treated jute fabric-reinforced polymer matrix composites. *J. Nat. Fibers* **18**, 510–519.
- Karim, N., Afroj, S., Malandraki, A., Butterworth, S., Beach, C., Rigout, M., Novoselov, K.S., Casson, A.J., and Yeates, S.G. (2017). All inkjet-printed graphene-based conductive patterns for wearable e-textile applications. *J. Mater. Chem. C* **5**, 11640–11648.
- Karim, M.N., Afroj, S., Rigout, M., Yeates, S.G., and Carr, C. (2015). Towards UV-curable inkjet printing of biodegradable poly (lactic acid) fabrics. *J. Mater. Sci.* **50**, 4576–4585.
- Karim, M.N., Rigout, M., Yeates, S.G., and Carr, C. (2014). Surface chemical analysis of the effect of curing conditions on the properties of thermally-cured pigment printed poly (lactic acid) fabrics. *Dyes Pigm.* **103**, 168–174.
- Karim, N., Afroj, S., Leech, D., and Abdelkader, A.M. (2021a). Flexible and wearable graphene-based E-textiles. In *Oxide Electronics*, A. RAY, ed. (Wiley).
- Karim, N., Sarker, F., Afroj, S., Zhang, M., Potluri, P., and Novoselov, K.S. (2021b). Sustainable and multifunctional composites of graphene-based natural jute fibers. *Adv. Sustain. Syst.* **5**, 2000228.
- Karim, N., Afroj, S., Lloyd, K., Oaten, L.C., Andreeva, D.V., Carr, C., Farmery, A.D., Kim, I.-D., and Novoselov, K.S. (2020). Sustainable Personal Protective clothing for healthcare applications: A review. *ACS Nano* **14**, 12313–12340.
- Karim, N., Afroj, S., Tan, S., Novoselov, K.S., and Yeates, S.G. (2019). All inkjet-printed graphene-silver composite ink on textiles for highly conductive wearable electronics applications. *Sci. Rep.* **9**, 8035.
- Karim, N., Zhang, M., Afroj, S., Koncherry, V., Potluri, P., and Novoselov, K.S. (2018). Graphene-based surface heater for de-icing applications. *RSC Adv.* **8**, 16815–16823.
- Khalil, H.A., Bhat, A., and Yusra, A.I. (2012). Green composites from sustainable cellulose nanofibrils: A review. *Carbohydr. Polym.* **87**, 963–979.
- Khan, M.A., and Hassan, M.M. (2006). Effect of γ -aminopropyl trimethoxy silane on the performance of jute–polycarbonate composites. *J. Appl. Polym. Sci.* **100**, 4142–4154.
- Khan, M.A., Rahaman, M.S., Al-Jubayer, A., and Islam, J. (2015). Modification of jute fibers by radiation-induced graft copolymerization and their applications. In *Cellulose-Based Graft Copolymers: Structure and Chemistry*, V.K. Thakur, ed. (CRC Press), pp. 209–235.
- Khan, U., O'Neill, A., Lotya, M., De, S., and Coleman, J.N. (2010). High-concentration solvent exfoliation of graphene. *Small* **6**, 864–871.
- Khondker, O., Ishiaku, U., Nakai, A., and Hamada, H. (2005). Tensile, flexural and impact properties of jute fibre-based thermosetting composites. *Plast. Rubber Compos.* **34**, 450–462.
- Kishore, M., Amrita, M., and Kamesh, B. (2021). Experimental investigation of milling on basalt-jute hybrid composites with graphene as nanofiller. *Mater. Today Proc.* **43**, 726–730.
- Koronis, G., Silva, A., and Fontul, M. (2013). Green composites: A review of adequate materials for automotive applications. *Compos. B Eng.* **44**, 120–127.
- Lee, X.J., Hiew, B.Y.Z., Lai, K.C., Lee, L.Y., Gan, S., Thangalazhy-Gopakumar, S., and Rigby, S. (2019). Review on graphene and its derivatives: Synthesis methods and potential industrial implementation. *J. Taiwan Inst. Chem. Eng.* **98**, 163–180.
- Li, D., Müller, M.B., Gilje, S., Kaner, R.B., and Wallace, G.G. (2008). Processable aqueous dispersions of graphene nanosheets. *Nat. Nanotechnol.* **3**, 101–105.
- Li, D., Zou, W., Song, S., Ye, Y., Jiang, W., Qin, Q.H., Xiao, Y., Ye, Z., Chen, L., and Zuo, D. (2020). Selective coupling reaction inhibits graphene defects: Regulating the orderly precipitation of carbon atoms. *Appl. Nanoscience* **10**, 587–595.
- Liu, D., Tang, Y., and Cong, W.L. (2012a). A review of mechanical drilling for composite laminates. *Compos. Struct.* **94**, 1265–1279.
- Liu, J., Tang, J., and Gooding, J.J. (2012b). Strategies for chemical modification of graphene and applications of chemically modified graphene. *J. Mater. Chem.* **22**, 12435–12452.
- Liu, Z., Chen, Z., Wang, C., Wang, H.I., Wuttke, M., Wang, X.-Y., Bonn, M., Chi, L., Narita, A., and Müllen, K. (2020). Bottom-up, on-surface-synthesized armchair graphene nanoribbons for ultra-high-power micro-supercapacitors. *J. Am. Chem. Soc.* **142**, 17881–17886.
- Lonkar, S.P., Deshmukh, Y.S., and Abdala, A.A. (2015). Recent advances in chemical modifications of graphene. *Nano Res.* **8**, 1039–1074.
- Lotya, M., Hernandez, Y., King, P.J., Smith, R.J., Nicolosi, V., Karlsson, L.S., Blighe, F.M., De, S., Wang, Z., McGovern, I.T., et al. (2009). Liquid phase production of graphene by exfoliation of graphite in surfactant/water solutions. *J. Am. Chem. Soc.* **131**, 3611–3620.
- Luo, B., Liu, S., and Zhi, L. (2012). Chemical approaches toward graphene-based nanomaterials and their applications in energy-related areas. *Small* **8**, 630–646.
- Luz, F.S.D., Lima, E.P., Louro, L.H.L., and Monteiro, S.N. (2015). Ballistic test of multilayered armor with intermediate epoxy composite reinforced with jute fabric. *Mater. Res.* **18**, 170–177.
- Madurani, K.A., Suprpto, S., Machrita, N.I., Bahar, S.L., Illiya, W., and Kurniawan, F. (2020). Progress in graphene synthesis and its application: History, challenge and the future outlook for research and industry. *ECS J. Solid State Sci. Technol.* **9**, 093013.
- Mahesh, V., Joladarashi, S., and Kulkarni, S.M. (2021a). Damage mechanics and energy absorption capabilities of natural fiber reinforced elastomeric based bio composite for sacrificial structural applications. *Def. Technol.* **17**, 161–176.
- Mahesh, V., Mahesh, V., and Harursampath, D. (2021b). Influence of alkali treatment on physio-mechanical properties of jute–epoxy composite. *Adv. Mater. Process. Tech.* **1–12**.
- Maragó, O.M., Bonaccorso, F., Saija, R., Privitera, G., Gucciardi, P.G., Iati, M.A., Calogero, G., Jones, P.H., Borghese, F., Denti, P., et al. (2010). Brownian motion of graphene. *ACS Nano* **4**, 7515–7523.
- Masoodi, R., and Pillai, K.M. (2012). A study on moisture absorption and swelling in bio-based jute-epoxy composites. *J. Reinf. Plast. Comp.* **31**, 285–294.
- Militký, J., and Jabbar, A. (2015). Comparative evaluation of fiber treatments on the creep behavior of jute/green epoxy composites. *Compos. B: Eng.* **80**, 361–368.
- Mohan, V.B., Brown, R., Jayaraman, K., and Bhattacharyya, D. (2015). Characterisation of reduced graphene oxide: Effects of reduction variables on electrical conductivity. *Mater. Sci. Eng. B* **193**, 49–60.
- Mohanty, A.K., Khan, M.A., and Hinrichsen, G. (2000). Influence of chemical surface modification on the properties of biodegradable jute fabrics—polyester amide composites. *Compos. A: Appl. Sci. Manuf.* **31**, 143–150.
- Mohanty, A.K., Vivekanandan, S., Pin, J.-M., and Misra, M. (2018). Composites from renewable and sustainable resources: Challenges and innovations. *Science* **362**, 536–542.
- Mukherjee, A., Ganguly, P., and Sur, D. (1993). Structural mechanics of jute: The effects of hemicellulose or lignin removal. *J. Textile Inst.* **84**, 348–353.
- Mwaikambo, L.Y., and Ansell, M.P. (1999). The effect of chemical treatment on the properties of hemp, sisal, jute and kapok for composite reinforcement. *Angew. Makromolek. Chem.* **272**, 108–116.
- Narayan, R., and Kim, S.O. (2015). Surfactant mediated liquid phase exfoliation of graphene. *Nano Converg.* **2**, 20.

- Novoselov, K.S., Fal, V., Colombo, L., Gellert, P., Schwab, M., and Kim, K. (2012). A roadmap for graphene. *Nature* 490, 192–200.
- Nurazzi, N., Asyraf, M., Fatimah Athiyah, S., Shazleen, S., Rafiqah, S., Harussani, M., Kamarudin, S., Razman, M., Rahmah, M., and Zainudin, E. (2021). A review on mechanical performance of hybrid natural fiber polymer composites for structural applications. *Polymers* 13, 2170.
- Pa, P., and M, S. (2019). Viscoelastic and mechanical behaviour of reduced graphene oxide and zirconium dioxide filled jute/epoxy composites at different temperature conditions. *Mater. Today Commun.* 19, 252–261.
- Park, B.J., and Park, H.S. (2021). Enhanced electrical conductivity of doped graphene fiber via vacuum deposition. *Carbon Lett.* 31, 613–618.
- Pereira, A.C., Lima, A.M., Demosthenes, L.C., Oliveira, M.S., Costa, U.O., Bezerra, W.B., Monteiro, S.N., Rodriguez, R.J., Deus, J.F., and Anacleto Pinheiro, W. (2020a). Ballistic performance of ramie fabric reinforcing graphene oxide-incorporated epoxy matrix composite. *Polymers* 12, 2711.
- Pereira, P., Ferreira, D.P., Araújo, J.C., Ferreira, A., and Fangueiro, R. (2020b). The potential of graphene nanoplatelets in the development of smart and multifunctional ecomposites. *Polymers* 12, 2189.
- Pickering, K.L., Efendy, M.A., and Le, T.M. (2016). A review of recent developments in natural fibre composites and their mechanical performance. *Compos. A: Appl. Sci. Manuf.* 83, 98–112.
- Pinto, M.A., Chalivendra, V.B., Kim, Y.K., and Lewis, A.F. (2014). Evaluation of surface treatment and fabrication methods for jute fiber/epoxy laminar composites. *Polym. Compos.* 35, 310–317.
- Pougnnet, H., Lepp, E., Ead, A.S. & Carey, J. The application of bio-Based composites in wind turbine blades.
- Rahman, M.S. (2010). Jute—a versatile natural fibre. Cultivation, extraction and processing. In *Industrial Applications of Natural Fibres: Structure, Properties and Technical Applications* (John Wiley & Sons), pp. 135–161.
- Rajesh, G., and Prasad, A.V.R. (2014). Tensile properties of successive alkali treated short jute fiber reinforced PLA composites. *Proced. Mater. Sci.* 5, 2188–2196.
- Rana, A., Basak, R., Mitra, B., Lawther, M., and Banerjee, A. (1997). Studies of acetylation of jute using simplified procedure and its characterization. *J. Appl. Polym. Sci.* 64, 1517–1523.
- Ray, D., Sarkar, B.K., Rana, A., and Bose, N.R. (2001). Effect of alkali treated jute fibres on composite properties. *Bull. Mater. Sci.* 24, 129–135.
- Ren, S., Rong, P., and Yu, Q. (2018). Preparations, properties and applications of graphene in functional devices: A concise review. *Ceramics Int.* 44, 11940–11955.
- Rowell, R.M. (2000). Characterization and factors effecting fiber properties. *Natural Polymers and Agrofibers Based Composites.*
- Roy, A., Chakraborty, S., Kundu, S.P., Basak, R.K., Majumder, S.B., and Adhikari, B. (2012). Improvement in mechanical properties of jute fibres through mild alkali treatment as demonstrated by utilisation of the Weibull distribution model. *Bioresour. Technol.* 107, 222–228.
- Sadangi, A., Panda, K.K., Kumari, K., Srivatsava, M., and Dalai, N. (2021). Comparison study of various properties of jute reinforced composites with different nanofillers. *Mater. Today Proc.* 16, 1239–1243.
- Saha, P., Manna, S., Chowdhury, S.R., Sen, R., Roy, D., and Adhikari, B. (2010). Enhancement of tensile strength of lignocellulosic jute fibers by alkali-steam treatment. *Bioresour. Technol.* 101, 3182–3187.
- Saiteja, J., Jayakumar, V., and Bharathiraja, G. (2020). Evaluation of mechanical properties of jute fiber/carbon nano tube filler reinforced hybrid polymer composite. *Mater. Today Proc.* 22, 756–758.
- Saravana Bavan, D., and Mohan Kumar, G. (2010). Potential use of natural fiber composite materials in India. *J. Reinf. Plast. Compos.* 29, 3600–3613.
- Sarker, F., Karim, N., Afroj, S., Koncherry, V.S., Novoselov, K., and Potluri, P. (2018). High-performance graphene-based natural fiber composites. *ACS Appl. Mater. Interfaces* 10, 34502–34512.
- Sarker, F., Potluri, P., Afroj, S., Koncherry, V.S., Novoselov, K., and Karim, N. (2019). Ultrahigh performance of nanoengineered graphene-based natural jute fiber composites. *ACS Appl. Mater. Interfaces* 11, 21166–21176.
- Seki, Y. (2009). Innovative multifunctional siloxane treatment of jute fiber surface and its effect on the mechanical properties of jute/thermoset composites. *Mater. Sci. Eng. A* 508, 247–252.
- Seki, Y., Sarikanat, M., Sever, K., Erden, S., and Gulec, H.A. (2010). Effect of the low and radio frequency oxygen plasma treatment of jute fiber on mechanical properties of jute fiber/polyester composite. *Fibers Polym.* 11, 1159–1164.
- Sever, K., Erden, S., Gülec, H., Seki, Y., and Sarikanat, M. (2011). Oxygen plasma treatments of jute fibers in improving the mechanical properties of jute/HDPE composites. *Mater. Chem. Phys.* 129, 275–280.
- Shah, S.S., Shaikh, M.N., Khan, M.Y., Alfasane, M.A., Rahman, M.M., and Aziz, M.A. (2021). Present status and future prospects of jute in nanotechnology: A review. *Chem. Record* 21, 1631–1665.
- Shahinur, S., Hasan, M., Ahsan, Q., Sultana, N., Ahmed, Z., and Haider, J. (2021). Effect of rot-, fire-, and water-retardant treatments on jute fiber and their associated thermoplastic composites: A study by FTIR. *Polymers* 13, 2571.
- Sinha, H., Singh, J.I.P., Singh, S., Dhawan, V., and Tiwari, S.K. (2018). A brief review of jute fibre and its composites. *Mater. Today Proc.* 5, 28427–28437.
- Sinha, E., and Panigrahi, S. (2009). Effect of plasma treatment on structure, wettability of jute fiber and flexural strength of its composite. *J. Compos. Mater.* 43, 1791–1802.
- Sinha, E., and Rout, S. (2009). Influence of fibre-surface treatment on structural, thermal and mechanical properties of jute fibre and its composite. *Bull. Mater. Sci.* 32, 65.
- Thyaviahalli Girijappa, Y.G., Mavinkere Rangappa, S., Parameswaranpillai, J., and Siengchin, S. (2019). Natural fibers as sustainable and renewable resource for development of eco-Friendly composites: A comprehensive review. *Front. Mater.* 6, 226.
- Tzounis, L., Debnath, S., Rooj, S., Fischer, D., Mäder, E., Das, A., Stamm, M., and Heinrich, G. (2014). High performance natural rubber composites with a hierarchical reinforcement structure of carbon nanotube modified natural fibers. *Mater. Des.* 58, 1–11.
- Uddin, M.A., Afroj, S., Hasan, T., Carr, C., Novoselov, K.S., and Karim, N. (2021). Environmental impacts of personal protective clothing used to combat COVID- 19. *Adv. Sustain. Syst.* 2100176.
- Varma, I., Krishnan, S.A., and Krishnamoorthy, S. (1989). Effect of chemical treatment on density and crystallinity of jute fibers. *Textile Res. J.* 59, 368–370.
- Wang, W., Xian, G., and Li, H. (2019a). Surface modification of ramie fibers with silanized CNTs through a simple spray-coating method. *Cellulose* 26, 8165–8178.
- Wang, X., Chang, L., Shi, X., and Wang, L. (2019b). Effect of hot-alkali treatment on the structure composition of jute fabrics and mechanical properties of laminated composites. *Materials* 12, 1386.
- Wang, X., Cui, Y., Xu, Q., Xie, B., and Li, W. (2010). Effects of alkali and silane treatment on the mechanical properties of jute-fiber-reinforced recycled polypropylene composites. *J. Vinyl Additive Technol.* 16, 183–188.
- Wegst, U.G., Bai, H., Saiz, E., Tomsia, A.P., and Ritchie, R.O. (2015). Bioinspired structural materials. *Nat. Mater.* 14, 23–36.
- Wick, P., Louw-Gaume, A.E., Kucki, M., Krug, H.F., Kostarelos, K., Fadeel, B., Dawson, K.A., Salvati, A., Vázquez, E., Ballerini, L., et al. (2014). Classification framework for graphene-based materials. *Angew. Chem. Int. Ed.* 53, 7714–7718.
- Xie, Y., Hill, C.A.S., Xiao, Z., Militz, H., and Mai, C. (2010). Silane coupling agents used for natural fiber/polymer composites: A review. *Compos. A: Appl. Sci. Manuf.* 41, 806–819.
- Yang, D., Velamakanni, A., Bozkolcu, G., Park, S., Stoller, M., Piner, R.D., Stankovich, S., Jung, I., Field, D.A., Ventrice, C.A., and Ruoff, R.S. (2009). Chemical analysis of graphene oxide films after heat and chemical treatments by X-ray photoelectron and micro-Raman spectroscopy. *Carbon* 47, 145–152.
- Yang, W., and Wang, C. (2016). Graphene and the related conductive inks for flexible electronics. *J. Mater. Chem. C* 4, 7193–7207.

Yuan, X., Jayaraman, K., and Bhattacharyya, D. (2002). Plasma treatment of sisal fibres and its effects on tensile strength and interfacial bonding. *J. Adhes. Sci. Technol.* *16*, 703–727.

Yusuf, M., Kumar, M., Khan, M.A., Sillanpää, M., and Arafat, H. (2019). A review on exfoliation, characterization, environmental and energy

applications of graphene and graphene-based composites. *Adv. Colloid Interfaces Sci.* *273*, 102036.

Zhang, J., Yang, H., Shen, G., Cheng, P., Zhang, J., and Guo, S. (2010). Reduction of graphene oxide via ascorbic acid. *Chem. Commun.* *46*, 1112–1114.

Zheng, J., and Suh, S. (2019). Strategies to reduce the global carbon footprint of plastics. *Nat. Clim. Change* *9*, 374–378.

Zhuang, R.-C., Doan, T.T.L., Liu, J.-W., Zhang, J., Gao, S.-L., and Mäder, E. (2011). Multi-functional multi-walled carbon nanotube-jute fibres and composites. *Carbon* *49*, 2683–2692.

Sustainable Fiber-Reinforced Composites: A Review

Saptarshi Maiti, Md Rashedul Islam, Mohammad Abbas Uddin, Shaila Afroj, Stephen J. Eichhorn, and Nazmul Karim*

Sustainable fiber reinforced polymer (FRP) composites from renewable and biodegradable fibrous materials and polymer matrices are of great interest, as they can potentially reduce environmental impacts. However, the overall properties of such composites are still far from the high-performance conventional glass or carbon FRP composites. Therefore, a balance between composite performance and biodegradability is required with approaches to what one might call an eco-friendly composite. This review provides an overview of sustainable FRP composites, their manufacturing techniques, and sustainability in general at materials, manufacturing, and end-of-life levels. Sustainable plant-based natural fibers and polymer matrices are also summarized, followed by an overview of their modification techniques to obtain high-performance, multifunctional, and sustainable FRP composites. Current state-of-the-art mechanical and functional properties of such composites are then surveyed and provide an overview of their potential applications in various industries, including automobile, aerospace, construction, medical, sports, and electronics. Finally, future market trends, current challenges, and the future perspective on sustainable natural FRP composites are discussed.

1. Introduction

Fiber-reinforced polymer (FRP) composites, comprised of a polymer matrix reinforced with fibers, have drawn significant interest in the last two decades as an alternative to traditional monolithic materials due to their higher specific strength and modulus, lightweight, adjustable deformation behavior, and good corrosion resistance. Consequently, they have been used in many applications, for example, in aerospace, automotive, medical, energy, and sports industries.^[1–3] To manufacture FRP composites, synthetic fibers (e.g., carbon, glass, aramid) are the most popular choice as reinforcement materials due to their superior physical and mechanical properties compared to other fiber types. Additionally, synthetic polymers have widely been used as polymer matrices because of their higher adhesive properties, chemical resistance, moisture resistance, excellent mechanical properties, good fatigue

resistance, low shrinkage, and strong durability at low and high temperatures and high electrical resistance. However, the environmental impacts of synthetic fibers and polymers are widespread and substantial, as they are non-biodegradable and can stay in the environment for hundreds of years.^[4,5] Additionally, the production of such materials from fossil fuels releases a significant amount of excess greenhouse gases (GHG), contributing to global warming. Furthermore, fossil fuel depletion, increasing awareness of the environmental crisis, and sustainability, in general, have forced researchers and innovators to shift towards manufacturing sustainable, biodegradable, and recyclable FRP composites.^[6] Indeed, the use of renewable and biodegradable fibrous materials and polymer matrices to manufacture FRP composites could considerably reduce the environmental impacts of such composites.

As sustainability is rapidly becoming a global priority across many industries, composite industries are also driving towards manufacturing sustainable composites. The development of such composites with lightweight and high performance at a lower cost is mainly dominated by the utilization of biodegradable and sustainable materials. Composites containing at least one of these components (matrix or reinforcement) obtained from natural resources are categorized as partially bio-degradable composites, and composites with all constituents from natural resources are called fully bio-degradable green composites.^[7] Natural fibers, in this context, are proven

S. Maiti
 Department of Fibres and Textile Processing Technology
 Institute of Chemical Technology
 Matunga (E), Mumbai 400019, India
 M. R. Islam, S. Afroj, N. Karim
 Centre for Print Research (CFPR)
 The University of the West of England
 Bristol BS16 1QY, UK
 E-mail: nazmul.karim@uwe.ac.uk
 M. A. Uddin
 Department of Dyes and Chemicals Engineering
 Bangladesh University of Textiles (BUTex)
 Tejgaon, Dhaka 1208, Bangladesh
 S. J. Eichhorn
 Bristol Composites Institute
 School of Civil
 Aerospace
 and Mechanical Engineering
 The University of Bristol
 University Walk, Bristol BS8 1TR, UK

 The ORCID identification number(s) for the author(s) of this article can be found under <https://doi.org/10.1002/adsu.202200258>.

© 2022 The Authors. Advanced Sustainable Systems published by Wiley-VCH GmbH. This is an open access article under the terms of the Creative Commons Attribution License, which permits use, distribution and reproduction in any medium, provided the original work is properly cited.

DOI: 10.1002/adsu.202200258

to be proficient materials for producing sustainable composites due to their abundance, lightweight properties, and low cost along with good mechanical properties, high specific strength, non-abrasive nature, eco-friendliness, and biodegradable features.^[8,9] Additionally, the environmental impacts of such fibers are significantly lower than that of synthetic fibers.^[10] Furthermore, the lower abrasive characteristics of natural fibers compared to glass fibers make their processing easier. Therefore, natural fibers (e.g., jute, flax, kenaf, hemp, and sisal) are becoming increasingly attractive to composite manufacturers^[11,12] as a replacement for glass and mineral fillers^[13] for producing sustainable composites.

An approach to an environmentally friendly composite could be manufactured via using natural fibers reinforced with biodegradable polymers as a matrix that can be composted at the end of their life cycle. Also, the addition of nanomaterials with either natural fibers or the matrix material or with both the components increases the strength of the composites significantly.^[14]

However, the overall properties of such composites are still far from the high-performance conventional glass-fiber reinforced composites. Therefore, a balance between composite performance and biodegradability is required with approaches to what one might call an eco-friendly composite.^[15] Many

research are currently in progress to improve the durability and strength of bio-composite for effective dynamic applications.^[16] Additionally, the composites industry is forecasted to grow significantly with the development of new fibers and polymer matrices. The industry will need to shift towards biodegradable and/or recycled fiber and polymers, with a lowering of the environmental impact to contribute towards global net-zero targets to obtain zero or no excess GHG emissions by 2050 for the sustainable composite industry.

While several reviews have focused on natural fiber reinforced composites,^[17–20] there remains a lack of a comprehensive review on the recent progress of sustainable fibers and polymer matrices to produce eco-friendly FRP. This review provides a brief overview of sustainable FRP composites (**Figure 1**) and their manufacturing techniques. We then review materials sustainability for FRP composites, followed by sustainable fibers and polymer matrices for sustainable FRP composites. The mechanical, physical, and thermal properties of sustainable FRP composites and its potential applications are then discussed. Finally, we present our recommendations and perspectives on future research directions. We believe, the review will be helpful to enhance scientific research and upgrade the technological capabilities of composite industries and facilitate reliable and

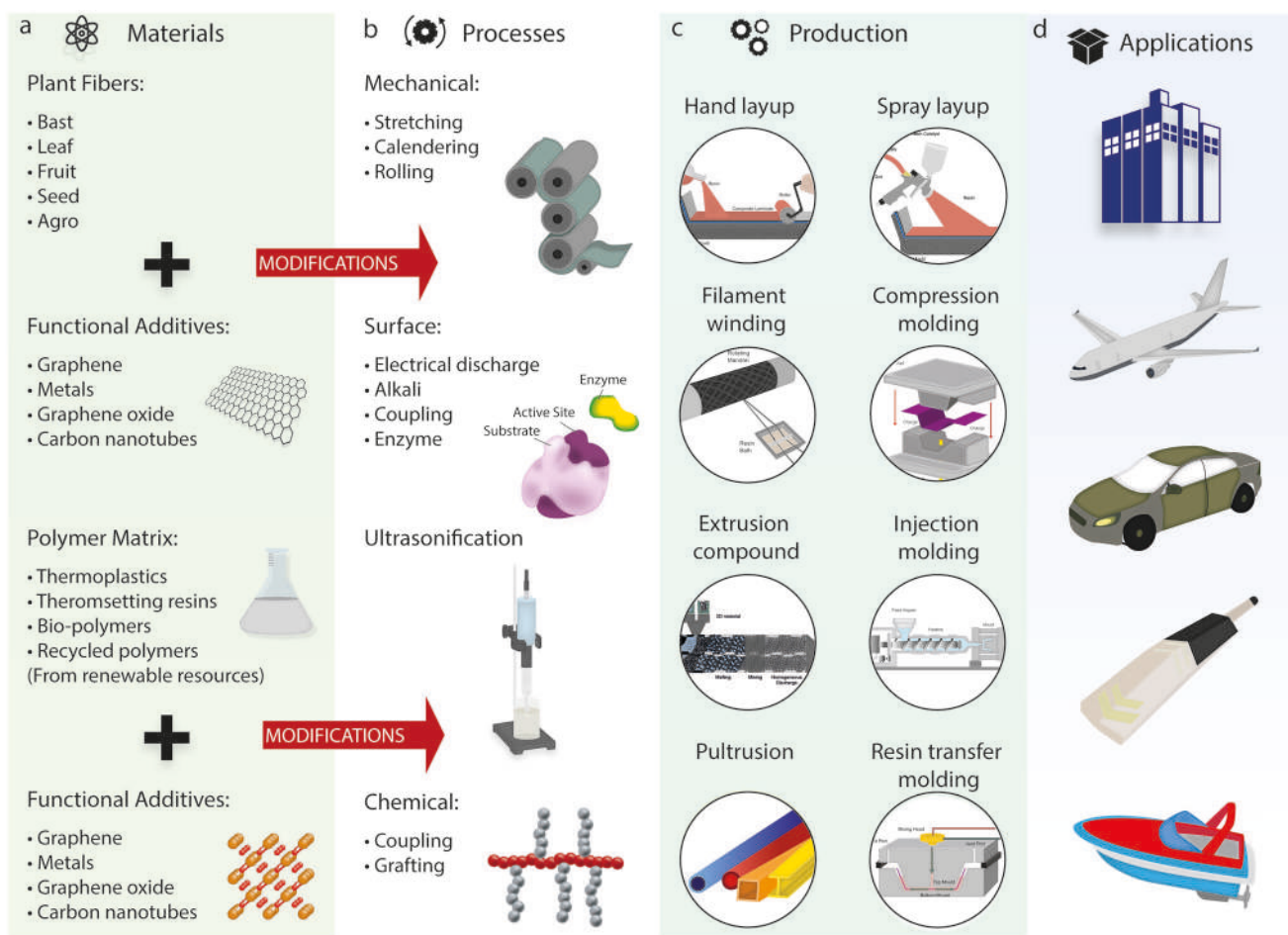


Figure 1. Sustainable FRP composites: a) materials, b) modification processes, c) composite manufacturing methods, and d) applications of fiber reinforced composites.

sustainable infrastructure development (United Nation Sustainable Development Goals (SDG) 9). It will also encourage the efficient use of natural resources, reduce synthetic waste generation and encourage the composite industries to adopt sustainable practices (SDG 12).

2. Fiber Reinforced Polymer (FRP) Composites and Manufacturing Techniques

2.1. Introduction to Composites

Composites are bi-phase or multi-phase materials, composed of two or more different materials, offering significantly improved bulk properties than their constituent materials. These enhanced properties include a high strength to weight ratio, high toughness, excellent dimensional stability, high durability and stiffness, flexural strength, and resistance to corrosion, wear impact, and fire.^[21–23] The evidence of combining different materials in buildings and construction works was found in ancient times. The earliest examples of composites in construction were found in 3400 B.C. when the Mesopotamians created plywood by gluing wood strips at different angles.^[24,25] The advances in material science have accelerated the development of synthetic materials, as an alternative to natural materials

for composites manufacturing. During this phase of development, the invention of polymer resins and glass fibers around the 1930s, and the development of carbon fibers in the 1960s laid the groundwork for the manufacture of modern FRP composites. Additionally, the industry has developed expertise since then in specialized molding processes, allowing manufacturers to tailor several unique properties of composites. **Figure 2** summarizes the chronological development of composites materials and their applications in several industries including infrastructure, transport, and communication from 3400 B.C. to the present day.^[24,25]

Composite materials can be classified according to their constituents, that is, base material and reinforcement material. The base material, also termed as a matrix or a binder material, binds or holds the reinforcement materials in composite structures. Depending on the matrix materials, composites may be classified as: organic matrix composites, metal matrix composites, and ceramic matrix composites. Organic matrix composites could further be classified as carbon matrix composites and polymer matrix composites. The reinforcing materials may be present in the form of fibers, particles, platelets, or whiskers of natural or synthetic materials. Based on these reinforcement materials, composites can be classified broadly either as fiber reinforced composites, particle reinforced composites, and laminar or sheet-molded composites.^[22,26,27] In this review,

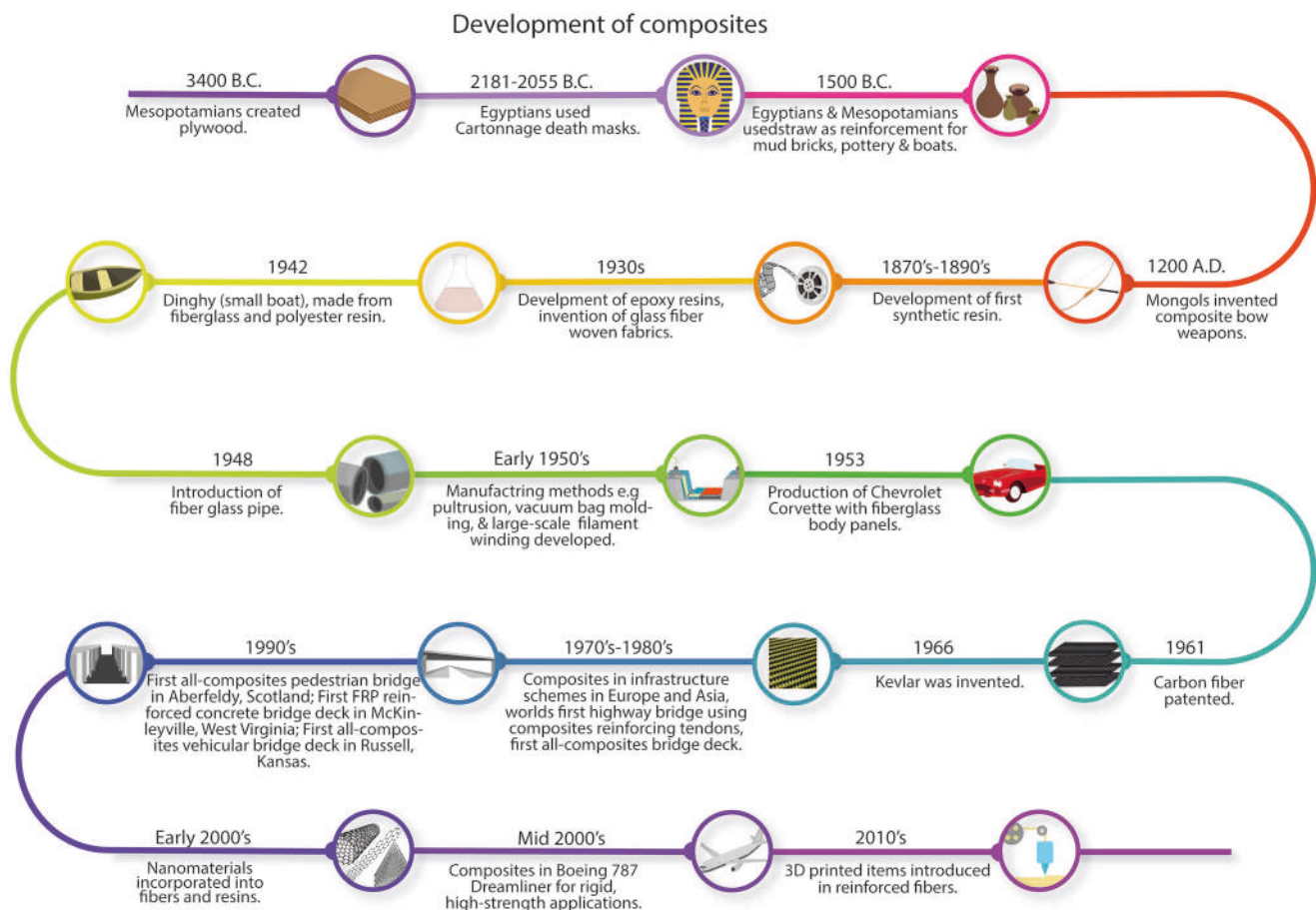


Figure 2. Chronological development of composites manufacturing for several industries.

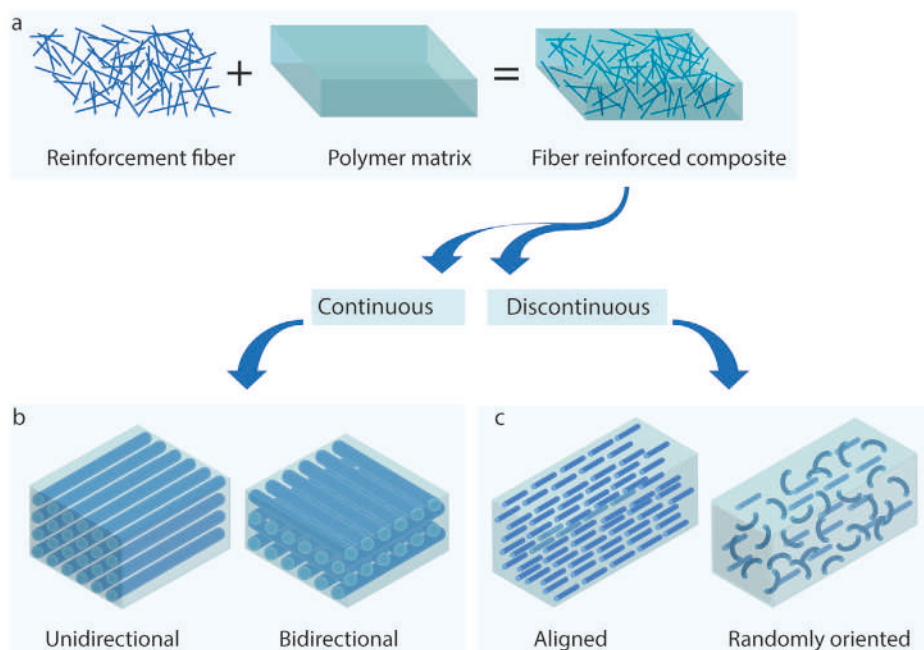


Figure 3. The general structural assembly of FRP composites and their classification: a) Basic constituents of FRP composites, b) continuous FRP composites: unidirectional and bi-directional, and c) discontinuous FRP composites: aligned and randomly oriented composites. Reproduced with permission.^[35] Copyright 2022, Wiley-VCH.

we mainly focus on sustainable FRP composites, due to their intriguing properties.

2.2. Fiber Reinforced Polymer Composites

FRP composites comprise a polymer matrix reinforced with fibers (Figure 3a).^[28] The fibers may either be natural or synthetic, and the most common polymer matrices used are thermosetting plastics (e.g., epoxy, vinyl ester, polyester) and phenol formaldehyde resins. FRP composites are used for lightweight structural applications because of their superior mechanical properties and lightweight nature.^[29] These composites exhibit superior material properties, which in most cases the traditional engineering materials (e.g., metals) cannot provide at low weight. These can be manufactured to any geometry to obtain maximum efficiency in terms of the utilization of material strength.^[30] Since lightweight design is important in various industries, including aerospace, wind energy, and automotive applications, FRP composites are attracting significant interest for such weight-sensitive applications due to their excellent stiffness and strength combined with a low density.^[31] Additionally, FRP composites offer several other advantages, including that they are typically electrochemically non-corrosive and have tunable properties for specific applications.^[32] Natural/plant fiber composites, another significant branch of FRP composites, have experienced a rapid expansion over the last few decades due to the advantages offered by plant fibers. These advantages include abundance, environmental friendliness, biodegradability, nontoxicity, low cost and density, flexibility during processing, and high tensile and flexural modulus.^[33]

Furthermore, they provide better flexural and impact strength, higher moisture resistance, less shrinkage, and improved weatherability.^[34] Therefore such composites offer greater efficiency based on their life cycle assessment (LCA) compared to traditional engineering materials, and represent a promising alternative for future sustainable industries.^[30]

FRP composites can be classified according to the length of the constituent fibers.^[35] Composites with long fiber reinforcements are termed as continuous FRP composites (Figure 3b), while composites with short fiber reinforcements are termed as discontinuous FRP composites (Figure 3c). The placement of fibers can be unidirectional or bidirectional in the case of continuous (Figure 3b), and aligned or random for discontinuous (Figure 3c) FRP composites. When more than one fiber is used as reinforcement in a single polymer matrix, it is then termed as hybrid FRP composite. The type, length, arrangements, and orientation of fibers define the properties and structural behavior of the final composites.^[35]

2.3. Manufacturing of FRP Composites

For manufacturing FRP composites, a fiber preform is prepared first by weaving, knitting, braiding, or stitching fibers in long sheets or matt structures, followed by reinforcement with a polymer matrix. Prepregs, composed of fiber materials pre-impregnated with a thermoplastic or thermoset polymer matrix, are sometimes used, which need a certain temperature to get cured and formed into a desired composites shape. Depending on the curing conditions, the composite manufacturing techniques can be categorized either as open or closed

molding. In open molding, reinforcement materials and resins are exposed to air as they cure or harden. The most common open molding processes for manufacturing FRP composites are hand lay-up,^[36] spray-up,^[37] and filament winding.^[38] In closed-molding, raw materials, that is, reinforcement materials and resins get cured inside a two-sided mold or within a vacuum bag. The closed molding process requires special equipment and is mainly used in large plants that produce large volumes of materials. Compression molding,^[39,40] extrusion compounding,^[41] injection molding,^[42] pultrusion,^[43] resin transfer molding (RTM),^[44] and vacuum assisted resin transfer molding (VARTM)^[45] are closed molding processes used for the manufacture of FRP composites.

Hand layup is the most widely used technique for manufacturing open mold composites. It involves manually laying down the individual layers of reinforcement materials and pouring the liquid resin over them. A roller is usually used to force down the resin to consolidate the laminate, thoroughly wetting various reinforcement layers and removing the entrapped air (Figure 4a). The relatively low start-up cost allows the manufacturing of a wide range of products with various geometries, new parts, and designs. However, there are several disadvantages of this method, including lower production rate and lower reinforcement volume fraction, nonuniform distribution of reinforcement materials and matrices due to lack of precision in human hand, which make the process inappropriate for large-scale manufacturing of high-quality composites.^[46–49]

Spray layup is another open molding technique where a handgun is used to spray the resin instead of pouring it over the laid-up fibers. The use of a roller can assist simultaneously by fusing the fibers into the matrix material and enabling the removal of bubbles and voids before curing (Figure 4b). The operator controls thickness and consistency, therefore such a process is more dependent on the operator than the hand lay-up itself. The fiber orientation and the fiber constraints determine the mechanical properties of the final product.^[47,50] Filament winding is another open molding technique that is useful when manufacturing axisymmetric components such as pipes, tubes, tanks, vessels, driveshaft, missiles, and pressure vessels. This technique offers certain advantages over other manufacturing approaches, such as producing components with higher fiber volume fractions (60–80%) and higher specific strengths.^[51] In this technique, resin-impregnated continuous fiber is wound on a rotating mandrel with a certain winding angle, controlled by the mandrel speed and that of the carriage guide. After winding, the resin is solidified via curing for thermosetting resins, followed by removal of the mandrel,^[52] (Figure 4c).

Compression molding is a very popular manufacturing technique among closed molding techniques, due to the precise and rapid production of quality composite parts at a high volume.^[53] In such a technique, prepregs are placed into an open heated mold cavity, then closed with a top plug, and compressed with a large hydraulic press to ensure the uniform distribution of materials all over the mold^[54] (Figure 4d). The combination

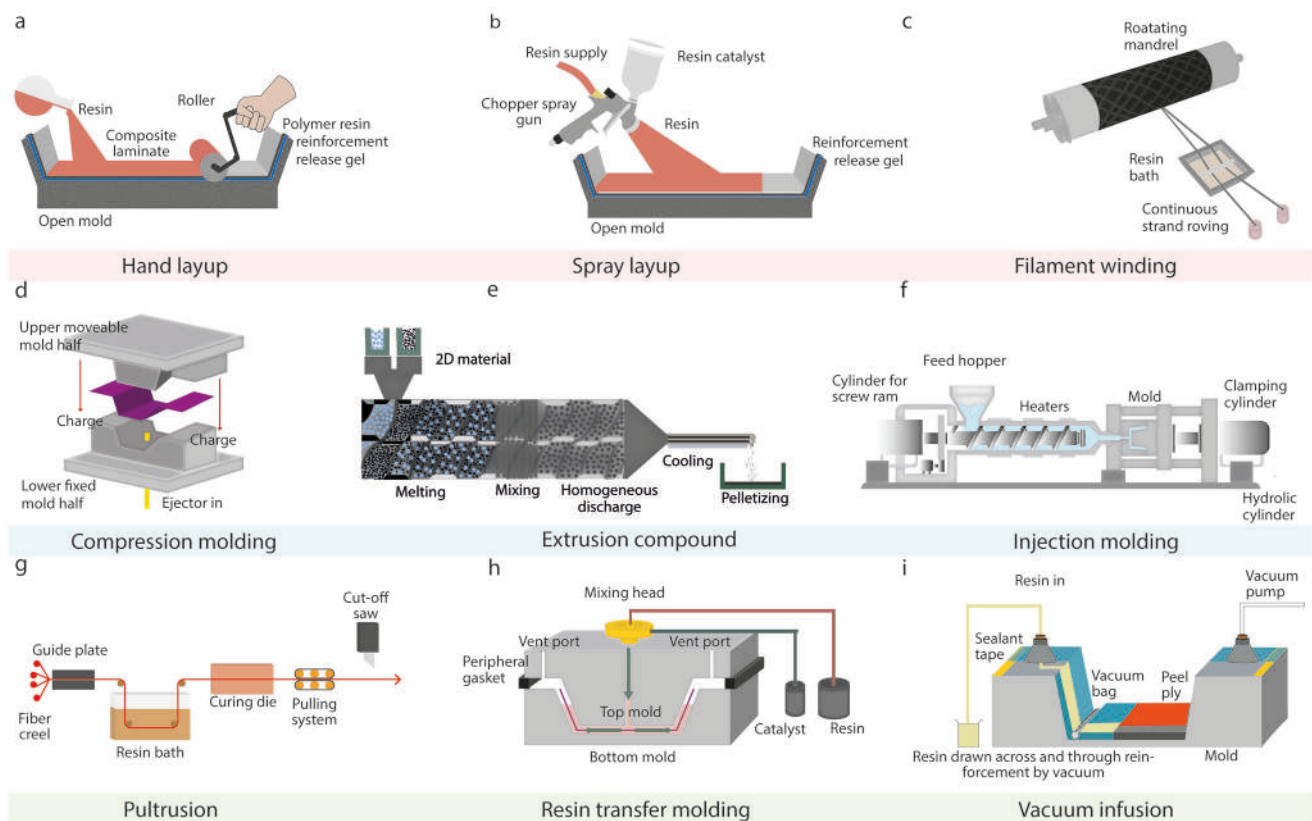


Figure 4. Schematics of common composite manufacturing techniques, a) hand layup, b) spray layup, c) filament winding, d) compression molding, e) extrusion compound, f) injection molding, g) pultrusion, h) RTM, and i) vacuum infusion or vacuum assisted resin transfer.

of two manufacturing techniques has also been reported: for example, the use of hand lay-up followed by a compression molding technique.^[55]

Extrusion compounding, another closed molding technique, is a continuous process of manufacturing composites with constant cross-sections including rods, sheets, pipes, and films, and produced by forcing softened polymer through a 2D die opening. Fiber and polymer matrix mixtures are fed into the extruder through a hopper, conveyed forward by a feeding screw, and forced through a die, converting them to a fiber-reinforced polymer product (Figure 4e). Heating elements placed over the barrel soften and melt the polymer. Both stiff and soft materials can be formed into any shape with a smooth surface finish. With a similar principle, in injection molding, after metering the required amount of material into the barrel, the screw injects the material into the mold through a nozzle where the material gets cooled and achieves its final shape^[56] (Figure 4f). Injection molding can fabricate complex 2D composite parts of various shapes and sizes with high precision at a very low cycle time.^[47,57]

Pultrusion is another continuous process of manufacturing FRP composites with constant cross-sections. The term pultrusion comes from combining the words, “extrusion” and “pull”. Unlike extrusion, where profiles are manufactured by pushing material through a die, the material is pulled instead. Layers of fibrous materials are impregnated with resin, followed by drawing through a stationary, temperature-controlled die that polymerizes the resin. A continuous profile is pulled from the production line using a pull-off unit (Figure 4g) and cut off at the required length.^[58,59] Pultrusion offers manufacturing of very lightweight but high-strength composites with great uniformity and extremely low manufacturing defects in products. **Figure 5** represents a comparative schematic of the tensile strength versus fiber volume fraction for several composite manufacturing methods.^[60]

RTM is another closed-mold process, which can manufacture high-performance composite components in medium

volumes (1000s to 10 000s of parts). The basic principle involves the laying of dry reinforcement materials inside a closed mold cavity, adjusting the mold to a predetermined cavity height followed by the injection of a low viscosity resin (typically 0.1 to 1 Pas⁻¹) through a channel to the laid reinforcement material under moderate pressure (usually 3.5–7 bar; Figure 4h). High pressure is avoided due to the risk of displacement and disorientation of the reinforcement material inside the mold cavity.^[61,62] Vacuum infusion or VARTM is an improved version of the RTM process. The preform reinforcement materials are sealed in a vacuum bag and a perforated tube is placed between the vacuum bag and the resin container. The vacuum force draws the resin through the perforated tubes over the reinforcement materials leaving no room for excess air, thereby consolidating the laminate structure (Figure 4i). The high-quality products obtained due to the reduction in void content make the VARTM process popular for large objects.^[47,63,64]

Several automated techniques are emerging to manufacture composites that can replace the human operator; they are advanced in process control and repeatable with reduced manufacturing times. For example, robotic filament winding (RFW) technology, uses an industrial robot to place fibers impregnated with resin along the required direction.^[65] Automated tape lay-up (ATL) is an automated process for laying up prepreg tapes, which can save more than 70–85% of the time and cost spent on manual lay-up. This process is used in the manufacturing of carbon–epoxy prepreg components for both military and commercial aircraft, such as the wing skins of F-22 Raptor, tilt-rotor wing skins of V-22 Osprey, and the skins of wing and stabilizer of the B-1 Lancer and B-2 Spirit bombers, empennage parts (e.g., spars, ribs, I-beam stiffeners) for the B777, A340-500/600, A380 airliners, etc. Automated fiber placement (AFP) is another automated production method for large aircraft structures from prepreg.^[66] Such automated processes can produce composites with comparable strength to traditional techniques, making the processes beneficial in speeding up the production and cutting labor costs. However, their use is limited due to the cost of specialized machinery and constraints in the fabrication of complex parts.^[67]

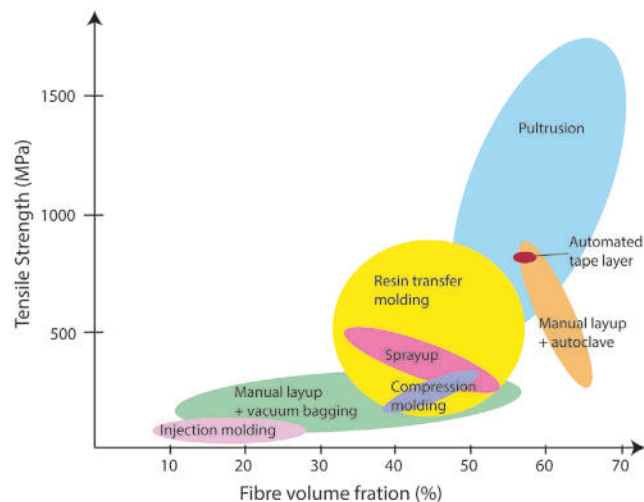


Figure 5. A comparison of tensile strength versus fiber volume fraction for several composite manufacturing techniques. Reproduced with permission.^[60] Copyright 2018, Wiley-VCH.

2.4. Outlook on Manufacturing

The manufacturing of composites has always been an issue in terms of large-scale production. A common realization within the composites industry is that a true breakthrough in the use of composite materials will not be realized solely via a reduction in raw material costs but, more importantly, by reduced manufacturing costs.^[68] However, the present trend for reducing the manufacturing cost is focusing on more automation during FRP composites manufacturing. It is also worth noting that, challenges not only exist with the technical aspect but also the lack of knowledge and expertise about novel and sustainable composites manufacturing among the designer and manufacturers of FRP composites. Additionally, developing countries are aiming for fast industrialization, improved exports, self-reliability, and lessening

the import for a better economy. Therefore, there remains a need to exploit locally available resources, and invest in local research and development for composites manufacturing in the future.

3. Sustainability and Sustainability Index for FRP Composites

3.1. Sustainability

Sustainability, and more precisely “sustainable development”, has developed an increased focus in the last four decades, which arose from the environmental movement in the late 1960s and 1970s. It became a focal point in 1987 with the landmark report entitled “Our Common Future”, where it was defined as “Sustainable development is the development that meets the needs of the present without compromising the ability of future generations to meet their own needs”.^[69] This Brundtland definition created a global explosion of academic debate and policy issues, leading to the United Nations Conference on Environment and Development (UNCED) in Rio in 1992.^[70] The concept of sustainability expanded to a balance between economic, social, and environmental factors to meet future demands of resources.^[71] As such, the sustainability parameters for the environment include the use of water, energy, and chemicals, emission of GHGs, and generation of wastewater, waste materials, and chemicals throughout the supply chain. Nowadays, sustainability is measured using LCA in various forms such as cradle to cradle, cradle to grave, and cradle to gate, which have helped to understand environmental impacts more holistically.^[72,73]

3.2. Sustainability for FRP Composites

There are more than 40 000 industrial composite products in various sectors such as energy, transportation, medical, construction, etc.^[73,74] The use of composites is increasing every day, particularly for industrial applications.^[75–77] For example, in airplanes, approximately 38% of the major components are now made from composite materials.^[78] As a result, the environmental impact of the composites has become a reality along with the other sectors, where increasing environmental awareness, growing waste management issues, and rising crude oil prices have created great concerns from both legislative and consumer perspectives.^[79,80] For FRP composites, natural plant fibers have been used as bio-composites in automotive, interiors, construction, transport, insulation material, etc., in combination with other synthetic fibers.^[80–82] The carbon footprint of such fibers is in the range 0.3 to 0.5 tons CO₂eq, which is significantly lower in comparison to that of glass fibers (≈1.7 to 2.5 tons CO₂eq) during the fiber production stage. However, the footprint is higher for natural fibers than for glass during composite manufacturing, which somewhat offsets the advantages.^[83] The comparison of LCA of bio-composites and glass FRP composites can be reviewed in this context (Figure 6),^[80] which reveals— a) natural fiber composites have a lower environmental impact than glass-based materials; b) an increase of natural fibers could reduce the base fiber content; c) the final product could have lighter weight adding fuel efficiency; d) recycling could be extended for biobased parts in other applications. Environmental sustainability in the composites sector can therefore be divided into three categories: a) materials used, b) manufacturing process of composites, c) end-of-life and recycling.^[81]

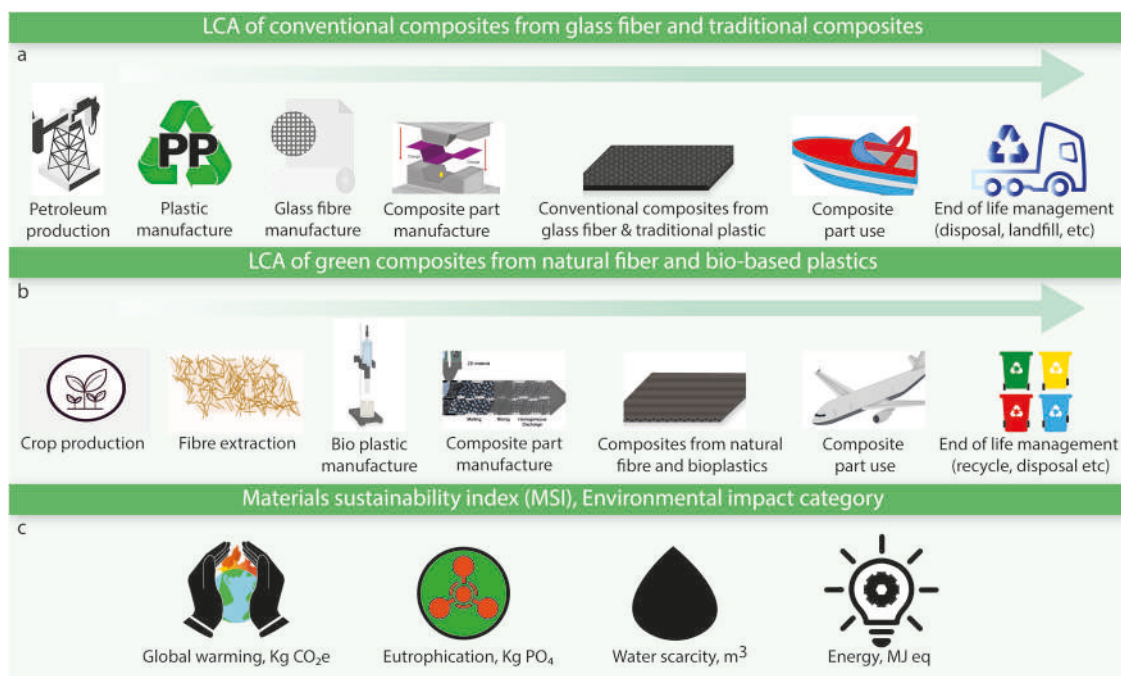


Figure 6. Simplified LCA study approach for a) conventional composites from glass fibers and traditional plastics, b) green composites from natural fibers and bio-based plastics, and c) environmental impact category for materials sustainability index (MSI).

Table 1. Carbon footprints of FRP composite components: Natural and synthetic fibers and Conventional epoxy resin polymer.

Composite components	Energy intensity [MJ kg ⁻¹]	Ref	CO ₂ emission [kg CO _{2eq} /Kg of fiber]	Ref
Glass fiber	13–32	[93,94]	1.4–2.95	[91,92,95]
Carbon fiber	183–286	[96]	29.4	[84,97]
Recycled carbon fiber	<250	[97]	4.65	[98]
Jute fiber	9.6	[84]	0.97	[84]
Flax fiber	6.5	[99]	0.90	[83]
Epoxy resin	76–80	[96]	6.70	[100]

3.2.1. Material Used

Glass and carbon fibers dominate composite applications due to the demand for high-performance and lightweight materials.^[84,85] Natural fiber-based composites are limited in use as their mechanical, thermal, electrical, and chemical properties for particular applications are often less than glass and carbon fibers.^[86] However, the biodegradability of plastics and synthetic fibers is of great concern nowadays. As a result, the demand for natural fiber-based composites is rising.^[84] Different polymers, mostly synthetic, are used to produce composites for various applications, and are typically non-degradable such as epoxy, unsaturated polyester, vinyl ester. Epoxy, the most widely used matrix material, has many other uses, including as adhesives, coatings, and casting materials. These resins are derived from petroleum-based sources.^[86] To improve their performance, several modifiers such as rubbers and elastomers are also used. It is possible to use bio-resins such as tannin, lignin, furan, rosin, and bio-modifiers in a ratio to the synthetic resin to reduce their environmental impacts.^[87,88]

Since sustainability of any composite material depends on the input resources and biodegradability, a comparative index, known as Higg material sustainable index (MSI), was developed by the Sustainable Apparel Coalition (SAC). It is based on a cradle-to-gate material impact assessment, which assists in identifying and comparing materials and processes with the highest/lowest impact.^[89] MSI assesses five environmental impacts: global warming potential (GWP), nutrient pollution in water (eutrophication), water scarcity, fossil fuel depletion, and chemistry, and features 80+ example materials, including natural and synthetic fibers, leather, and metals. In addition, material traceability is also getting more focus as it can improve the value during the end-of-life stages.^[90]

Jute and flax are increasingly used in technical applications; their environmental impact is extensively studied compared to synthetic counterparts. Jute and flax production are usually water-intensive, mainly required during land preparation, plant growth, and the retting process compared to the corresponding glass and carbon fiber.^[84] In addition, the production of natural fiber also requires fertilizers and pesticides to some extent—the impact of this can be countered by using organic fertilizers such as meat slurry. However, the carbon footprint of these natural fibers is much lower than that of glass and carbon fibers, **Table 1**. The production of 1 kg of glass fiber emits between

1.4 to 2.95 kg of CO_{2eq},^[91,92] whereas their natural fiber counterpart has a carbon footprint of ≈ 0.9 CO_{2eq}.

3.2.2. Manufacturing Process of Composites

The environmental impacts in the processing stages are dominated by the use of energy, along with GHG emissions.^[73] The European Composites Industry Association (EuCIA) has created an online tool, “Eco Impact Calculator for composites”, to measure the impact of the production of composites, which allows companies to quantify the manufacturing part of the life cycle.^[101] Although the composite manufacturing process adds carbon emissions in the production of natural fiber-based composite; it is still 50% lower than glass fiber-based composites. Even virgin carbon fibers release a significant amount of GHG during production, with a total value of 29.45 kg CO_{2eq}, which is approximately 60 000 times higher than natural fibers. A recycled carbon fiber-based composite has significantly low GHG emission during production which is five times higher than jute and flax fiber,^[98] and up to half that of hemp-based biocomposites.^[102] In addition, natural fiber can act as a carbon sink during its growth, although, the embedded carbon will be released back into the atmosphere at the end of life.^[83] Water use is a concern for jute and flax; these biodegradable fibers can enhance soil quality at the end of their life. Therefore, replacing synthetic fibers with natural plant-based biocomposites could pave the way for sustainable composite applications. On the other hand, epoxy resin, which is very popular for composites applications, has several disadvantages in terms of GWP and biodegradability as this resin is very difficult to recycle.^[103,104] Different alternatives have been researched, such as epoxidized sucrose soyate resin (ESS) (0.287 kg CO_{2eq}/kg of ESS),^[105] vegetable oil-based resin (5.7 kg CO_{2eq}/kg of resin),^[106] supersap bioresin (5.7 kg CO_{2eq}/kg of resin),^[107] or bio-based ECH (epichlorohydrin) resins with ≈61% reduction of the GWP.^[108]

3.2.3. End-of-Life and Recycling

Sustainability is becoming a focal point in the material selection process, particularly in the use phase.^[73] Additionally, there are other specific concerns for particular types



Figure 7. Criteria for sustainable fibers.

of applications; for example, fluoride emissions during the manufacturing of traditional glass-composite materials are significantly hazardous to the environment.^[77] Waste disposal and waste management are key aspects of the sustainability of composites. FRP composites have different end life compared to traditional textiles. First, because the composites are made of different parts, which means the end-of-life for the product does not mean the end-of-life for the parts.^[73] Second, there are limited options for the reuse and recycling of composites due to the poor performance properties of reused or recycled material. As a result, only 15% of the composites produced in the UK are reused or recycled each year at their end-of-life.^[109] Moreover, recycling is not commercially viable in some cases, particularly for glass fiber composites in wind-turbine applications.^[110] Innovation would be key in the area of recycling and end-of-life management for better material circularity.^[110]

4. Sustainable Fibers

There have been several efforts across the world to grow fibers that are sustainable, biodegradable, and lightweight

for structural composite applications, and could be manufactured at high volume and low cost. Sustainable fibers, commonly known as “Eco-friendly” fibers, have an insignificant impact on the environment during their production processes, and meet at least half of the criteria as illustrated in **Figure 7** including low water and energy consumption, being made from waste materials and used renewable resources, have control on chemical consumption, and soil erosion. Such fibers are biodegradable, and many of them often originate from bio-based resources. The growing interest towards the use of sustainable fibers from renewable and biodegradable sources to produce bio-based and high-potential green products have driven many researchers to investigate the possible use of natural fibers as reinforcement materials for green and potentially sustainable bio-composites.^[111]

Natural fibers are categorized mainly based on their origin from plants, animals, or minerals. Some natural fibers are produced from the different sections of plants and trees. Plant-based cellulosic fibers can be classified primarily into seed fibers (cotton, coir, and kapok), bast fibers (jute, flax, ramie, hemp, and kenaf), and leaf fibers (sisal, pineapple, banana, abaca), **Figure 8**. Natural plant fibers are entirely derived from vegetable sources, therefore completely biodegradable and sustainable. The major chemical components of natural plant fibers are cellulose, hemi-cellulose, lignin, pectin, and wax.^[112–115] The presence of predominantly hydrophilic cellulose affects the interfacial bonding between the fibers and a polymer matrix because, typically, these matrices are hydrophobic. Therefore, chemical treatment of such fibers is one of the ways to optimize the bonding between the fibers and polymer matrix. Such treatments modify –OH functional groups present on the surface of the fibers, and increase the surface roughness, thereby enhancing the interfacial interaction between the fibers and a matrix.^[116–120]

The properties of composites significantly depend on the properties of reinforcement materials, that is, the natural fibers,^[121–124] **Table 2**. Therefore, the selection of such materials during the design and manufacturing of sustainable composites plays a crucial role in determining their performance. Various natural fibers have been used or have the potential to be used

a Bast fibers			
Fiber	Cellulose, %	Lignin, %	Y Modulus, GPa
Flax	~70	~2.2	25-80
Jute	60-70	12-14	10-30
Ramie	68-75	0.6-0.7	44-128

b Fruit fibers			
Fiber	Cellulose, %	Lignin, %	Y Modulus, GPa
Coir	32-43	40-45	4-6
Kapok	~43	13-15	~4
Palm	~65	~29	~1.7

c Leaf fibers			
Fiber	Cellulose, %	Lignin, %	Y Modulus, GPa
Sisal	~65	~10	9.38
Pineapple	~80	~12.7	~82
Banana	~61.5	~15	3.5-32

d Agro wastes			
Fiber	Cellulose, %	Lignin, %	Y Modulus, GPa
Bagasse	25-45	15-25	20-27
Corn	35-40	7-18.5	2.38-4.5
Rice	41-57	8-20	~2.5

Figure 8. Chemical compositions of several sustainable natural fibers: a) bast fibers, b) fruit fibers, c) leaf fibers, and d) agro waste fibers.^[126]

Table 2. Mechanical properties of different natural fibers compared to conventional reinforcing fibers.^[19,27,121,125,136–139]

Fiber		Density [g cm ⁻³]	Tensile Strength [MPa]	Young's Modulus [GPa]	Elongation at break [%]	Equilibrium moisture content [%]
Eco-friendly sustainable natural fibers	Cotton	1.5–1.6	287–597	5.5–12.6	7–8	–
	Jute	1.44	393–773	10–30	1.5–1.8	12
	Flax	1.54	345–2000	27–85	1–4	7
	Hemp	1.47	368–800	17–70	1.6	9
	Kenaf	1.2	240–930	14–53	1.6	–
	Ramie	1.5–1.56	400–1000	27–128	1–4	9
	Coir	1.25	220	6	15–25	10
	Abaca	1.5	980	–	–	15
	Oil palm (empty fruit bunch)	0.7–1.55	248	3.2	2.5	–
	Sugar palm	1.5	421.4	10.4	9.8	–
	Baggase	1.2	20–290	19.7–27.1	1.1	8.8
	Sisal	1.33	600–700	38	2–3	11
	Pineapple	1.5	170–1627	82	1–3	13
	Banana	1.35	355	33.8	5.3	–
	Bamboo	0.6–1.1	140–230	11–17	–	8.9
	Henequen	1.4	500	13.2	4.8	–
Nettle	1.51	650	38	1.7	–	
Conventional fibers	E-glass	2.5	2000–3500	70–77	4.5–4.9	–
	S-glass	2.5	4570	86–90	4.5–4.9	–
	Carbon	1.8–1.9	3400–5400	230–440	1.4–1.8	–
	Aramid	1.45	3400–4000	130–185	2.5	–

for sustainable FRP composites, which have been discussed here.

4.1. Bast Fibers

Bast fibers are potential sustainable fibers produced from the outer layers of plant stems. They are mainly composed of cellulose, hemi-cellulose, and various proportions of lignin. The most valuable fiber crops that have attracted interest as reinforcements for composites are jute, flax, ramie, hemp, and kenaf.^[125]

4.1.1. Jute (*Corchorus Capsularis/Olitorius*)

Popularly known as “Golden Fiber”, Jute is extracted from the bark of the white jute plant (*Corchorus capsularis*), and is a 100% biodegradable, recyclable, and environmentally friendly natural fiber. After cotton, jute is the second most produced natural fiber globally, mainly in developing countries including Bangladesh, India, and China. Jute is a lignocellulosic fiber and is at least ≈50% cheaper than flax and other similar natural fibers. Jute plants can grow up to 15–20 cm in four months, and the fibers are extracted post-harvesting. Such fibers are characterized by high aspect ratio (i.e., length to diameter ratio, l/d), high strength to weight ratio, and have good insulation properties.^[127] Jute

has widely been used in the manufacturing of flexible packaging materials, carpet backing, geo-textiles, and green composites.

4.1.2. Flax (*Linum Usitatissimum*)

The cloth made from flax fibers is popularly known as “Linen” in the textile industry. Flax fibers are also cellulosic fibers but have higher crystallinity than jute fibers. The technical fibers extracted from the plant can be very long (up to 90 cm) with a diameter of 12–16 μm. France, Belgium, and Netherlands are the leading manufacturers of flax fibers.^[125] They have higher specific tensile properties than glass fibers in addition to low density, higher strength, and stiffness. The higher strength makes them attractive for composite applications. There have been extensive studies investigating flax as reinforcing materials in the form of non-woven mats and combined with a natural resin to develop sustainable composites for the future.^[125,128,129]

4.1.3. Ramie (*Boehmeria Nivea*)

Ramie is a strong, lustrous, soft, and fine bast fiber, extracted from the inner bark of the ramie plant. It is one of the oldest vegetable fibers, and was used to wrap mummies in Egypt.^[130] China is the pioneer of ramie fiber production. The challenge

with this fiber processing is removing its gum content which is about 30% of the total fiber weight, making it very difficult to be spun. This extracted gum can sometimes be used as a natural resin to develop a green particle board or other biocomposites. Ramie is often used in the manufacturing of fishing nets, ropes, tents, household furnishings, and composites.^[131]

4.1.4. Hemp (*Cannabis Sativa*)

Hemp, most widely grown in Asia and Europe, can grow up to ≈1.2–4.5 m with plant stems of ≈2 cm in diameter.^[132,133] A core usually covers the inner girth, and the outer layer is the bast fiber attached to the inner layer via a glue-like substance called pectin. The fibers have excellent mechanical strength and Young's modulus as well as good insulation properties.^[134] Such fibers are generally used in ropes and mulching, and have found applications as reinforcement for composites.^[135]

4.1.5. Kenaf (*Hibiscus Cannabinus*)

Kenaf is a strong, stiff, and tough bast fiber, with high resistance to insects. It is mainly extracted from the flowers of the plant with an outer fiber and an inner core. The outer fiber is known as the bast, which makes 40% dry weight of the stalks, and the inner core covers the remainder. Kenaf fibers have low density and high specific mechanical properties^[127] and are completely biodegradable. It has traditionally been used for making cords, ropes, and storage bags. Nevertheless, it has found recent applications as composites reinforcements for automobiles, construction, furniture, and packaging applications.^[140,141]

4.2. Leaf Fibers

Using lignocellulosic leaf fibers (sisal, pineapple, and banana) as reinforcements in thermoplastic and thermosetting resins to develop low-cost and lightweight composites is an emerging field of research. Such fibers have several advantages: low density, low cost, non-abrasive nature, low energy consumption, high specific properties, and biodegradability.^[125]

4.2.1. Sisal (*Agave Sisalana*)

Sisal, originating from Mexico, is one of the most widely used leaf fibers and consists of the rosette of leaves with a height of up to 1.5–2 m. Sisal fiber is easily cultivated with short renewal times. The fiber has high tenacity and tensile intensity, abrasion, saltwater, acid, and alkali resistance.^[127] It was originally used to make ropes and twines. Recently, it has seen applications as a reinforcement for composite materials, and furniture.^[142,143]

4.2.2. Pineapple Leaf Fiber (PALF-*Ananas Comosus*)

Pineapple leaf fiber is a crop waste after fruit cultivation and is white, creamy, and lustrous like silk, and ten times coarser than

cotton fiber. It is a multi-cellular lignocellulosic fiber. It shows excellent mechanical, physical, and thermal properties.^[144] Some of the major applications for such fibers are in automobiles, mats, construction, and advanced composite materials.^[145]

4.2.3. Banana Fiber (*Musa Acuminata*)

Banana fiber, also known as “Musa fiber” is one of the world's strongest natural fibers.^[146] It is biodegradable and extracted from the pseudostem of the banana tree, which is incredibly durable. It consists of thick-walled cell tissue bonded together by natural gums and is primarily composed of cellulose, hemicellulose, and lignin. It is often assumed that banana fibers have similar properties to natural bamboo fiber; however their fineness, spin ability, and tensile strength are much better than that of bamboo fibers.^[147] Banana fibers can produce a few different types of textiles with various thicknesses and weights depending on what part of the banana stem the fiber has been extracted from. Banana fibers can be used to make ropes, mats, and woven fabrics as well as handmade papers. These fibers have been used as reinforcement materials for manufacturing green composites.^[131]

4.2.4. Bamboo Fiber (*Bambusoideae*)

Bamboo fibers are also known as natural glass fibers due to their fiber alignment in the longitudinal direction.^[148,149] Such fibers are extracted from natural bamboo trees via different physical and mechanical methods. Bamboo fibers have received interest due to their high aspect ratios as well as high strength-to-weight ratios.^[150] Additionally, the surface of such fibers are round and smooth. They are lighter, stiffer, and stronger than glass fibers, which make them attractive reinforcement materials for making advanced composite materials for various industries.^[151–153]

4.3. Fruit Fibers

The fruits and seeds of plants are often attached to hairs or fibers or encased in a husk that may be fibrous. Such fibers are an attractive combination of cellulose and lignin. They are widely known for their durability and thermal insulation properties and possess high potential as reinforcements for composite applications.^[115]

4.3.1. Coir (*Cocos Nucifera*)

Coir is a short and coarse fiber extracted from the outer shell of coconuts. The thickness of coir fiber is very high as compared to that of other natural fibers and shows very good chemical resistance. The slow decomposition rate of coir fibers makes them suitable for making durable geo-textiles. There are two types of coir: coarser brown coir and finer white coir.^[154] More commonly used coir is brown coir obtained from mature coconuts. Coir fibers are mostly used for making rugs, mattresses,

doormats, building boards, insulation boards, cement boards, building panels, and composites.^[125]

4.3.2. Kapok (*Ceiba Pentandra*)

Kapok fibers are obtained from the seed hairs of kapok trees. They are cotton-like fibers with colors varying from yellowish to light brown. They are extremely lightweight and hydrophobic.^[155] Conventionally, kapok fibers are used as buoyancy materials, oil absorbents, biofuels, insulation materials for heat and sound, and reinforcement materials for composites.^[156–158]

4.3.3. Palm (*Phoenix Dactylifera*)

Palm fibers are usually obtained from the fruits, rachis, and leaves of the date palm trees. Such fibers can potentially be used as sources of cellulose and lignin. They can be used as reinforcements for thermoplastic and thermosetting polymer-based composites in the automotive sector.^[159]

4.4. Agro Waste Fibers

The primary fiber wastes produced from agricultural activities are a rich source of cellulose. They have potential as reinforcing materials due to their wide availability and benefits of being renewable, degradable, and economical. Such biomass wastes provide several excellent specific properties especially mechanical, thermal, and biodegradability, making them suitable as reinforcements for FRP composite applications.^[160]

4.4.1. Sugarcane Fiber (*Bagasse*)

Sugarcane bagasse is a fibrous material obtained as a residue from sugarcane after crushing to extract the juice. It is mainly composed of two components, that is, the outer rind and inner pith. The rind consists of a strong fibrous structure, which protects the inner components of a soft spongy structure. It contains long, fine fibers that are randomly arranged throughout the stem and bonded together via hemi-cellulose and lignin.^[161] The inner component contains smaller fibers, mainly composed of cellulose. Sugarcane bagasse approximately comprises of 50% cellulose, 25% hemicellulose, and 25% lignin. It has widely been used as a composite reinforcement due to its high cellulose content which exhibits a highly crystalline structure.^[162] Cement composites, false ceilings, particle boards, and lightweight structures are some of the applications using bagasse as one of the reinforcement materials.^[163]

4.4.2. Corn Stalk

Corn stalks are composed of a pith and rind. The pith of corn stalks is rich in hemicellulose, fat, protein, and sugar.^[164] However, the primary components of corn stalk rind are cellulose and lignin, thereby resulting in high strength and toughness.

Because of the weakly bonded pith, corn stalks can exhibit poor strength. So the pith needs to be removed when preparing corn stalk fibers. The rind of corn stalk has been used for manufacturing corn stalk fiber-based composite materials.^[165]

4.4.3. Rice Straw

Rice straws (RS) belong to the family of non-wood bio-fibers. It is a residue obtained from the agricultural production of rice. Rice is the major crop in Vietnam, India, and Bangladesh, therefore a huge quantity of rice residues are available after rice husking.^[166] Such residues are either used as animal feed or disposed of as waste by burning them in the field, associated with carbon emissions. However, embedding of such residues in polymer composites as reinforcement materials could reduce environmental pollution and find potential applications in the reinforcement of composites.^[160]

4.5. Outlook on Sustainable Fibers

The application of natural fibers in FRP composites results in various limitations because of their reduced durability, high moisture absorption, and moderate mechanical properties. One of the major challenges identified with natural fibers when used as reinforcements for FRP composites is the incompatibility between hydrophilic natural fibers and hydrophobic matrices during mixing, leading to undesirable properties of the final composites.^[167] The weaker adhesive nature of the polymer matrices introduces lower strength to the composite. Additionally, degradation due to the presence of water is another major challenge due to the higher hydrophilicity of the fibers. The presence of hemi-cellulose increases the swelling capacity of the natural FRP composites which makes them unsuitable for outdoor applications.^[167] The variability in natural fiber properties like length and diameter is also a very challenging aspect during composite manufacturing. Therefore, to develop high-performance sustainable FRP composites, the current challenges with sustainable fibers such as poor interfacial properties, water absorption, materials inconsistency, and swelling need to be addressed.

5. Polymer Matrix

An FRP composite is a physical mixture of at least two components with different physical and chemical properties: reinforcement materials which are usually fibers, and a matrix which is usually a polymer. Polymer matrices are an essential part of a FRP composite, which can protect the fiber surface from mechanical abrasion, as well as hold and protect the reinforcing material from adverse environmental effects without disturbing its orientation and position within the composite (**Figure 9a**). Additionally, it acts as a stress transfer medium by distributing the applied load equally within the composite. Furthermore, it helps with the isolation of fibers, so that the individual fibers can act separately to stop or slow down crack propagation.^[168,169] In this review, based on the sources, polymer matrices have

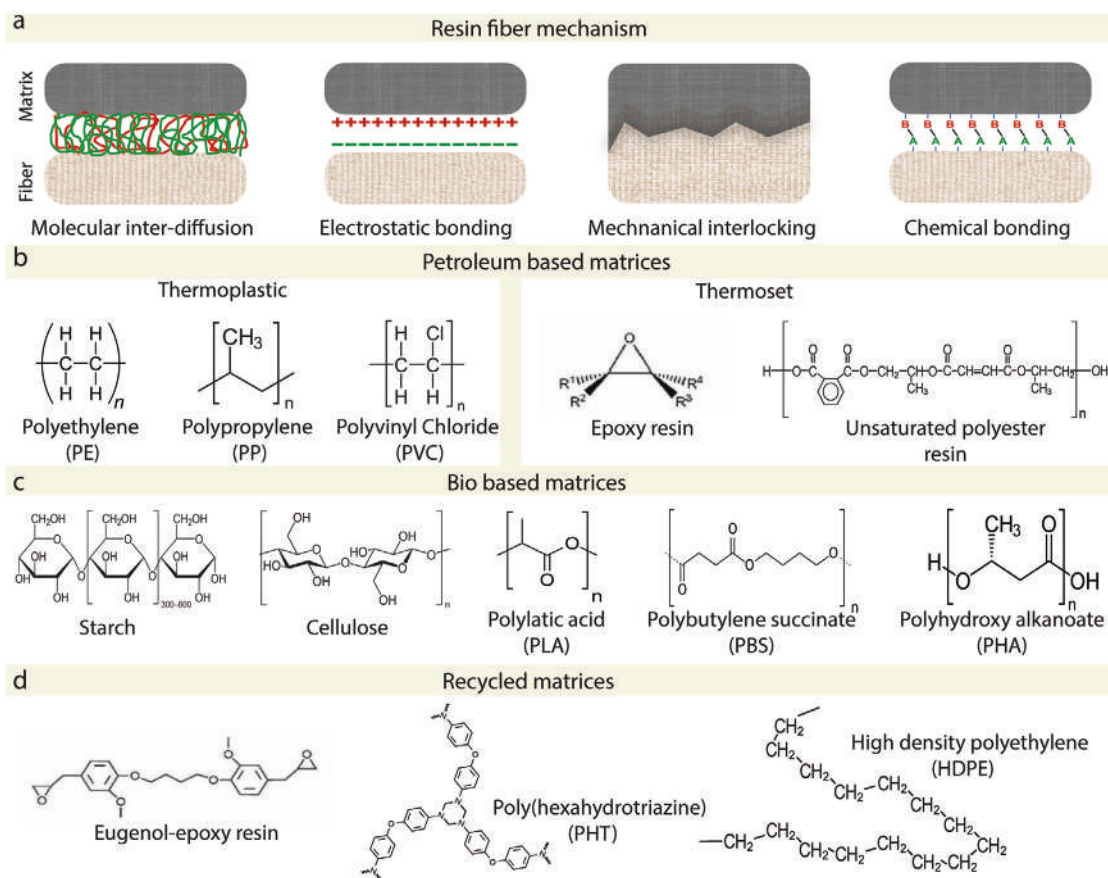


Figure 9. a) Resin-fiber mechanism for FRP composites. Examples of several polymer matrices used for manufacturing of fiber reinforced composites: b) Petroleum-based, c) bio-based, and d) recycled matrices). Reprinted with permission.^[170] Copyright 2019, SAGE Publications.

been categorized into three major classes: synthetic, bio-based, and recycled. Major types of polymer matrix are shown with some examples (Figure 9b–d) and some of their key properties are illustrated in Table 3.

5.1. Synthetic Matrices

Synthetic or petroleum-based polymers, produced from abundant petroleum-based resources, are the most commonly used matrices for FRP composites. The common synthetic polymers are usually thermoplastics and thermosets (Figure 9b).

5.1.1. Thermoplastic Polymers

These are melt-processable plastics that can be easily heated and softened for shaping or molding. Thermoplastic polymers are generally high molecular weight compounds. The polymer chains in thermoplastics are associated with each other through intermolecular entanglements. When they are subjected to a raised temperature, such intermolecular entanglements weaken easily, resulting in a viscous liquid. In this state, thermoplastic polymers can be easily reshaped and are typically used in composites by various polymer processing techniques such as injection molding, compression molding, calendaring,

and extrusion. Such polymers have approximately ten times more resistance to impact, greater tolerance to damage, higher re-formability, as well as higher processing temperature and pressures as compared to thermosets.^[182] Most commonly used thermoplastic polymers for fiber-reinforced composites are: polypropylene (PP), polyvinyl chloride (PVC), and polyethylene (PE). Among them, PP is perhaps the most widely used because of its moderate to good mechanical properties. Additionally, PP provides moderate dimensional stability, higher resistance to thermal deformation, and higher flame resistance.^[171] Therefore, PP has become an obvious choice as a matrix for manufacturing natural fiber-reinforced composites. PVC is another thermoplastic polymer that is popular for building structures and construction sectors due to its compatibility with natural fibers, economical, durability, flame, and chemical resistance.^[171]

5.1.2. Thermoset Polymers

These polymers undergo an irreversible chemical reaction during molding (often known as curing/cross-linking) to change from a liquid or rubbery state to the final solid state. Once they are fully cured, the shape of such materials cannot be changed significantly via heating. Thermoset polymers contain small, unlinked molecules, which usually require the addition

Table 3. Summary of some key properties of polymer matrices.

Matrices	Resin	Density [g cc ⁻¹]	Tensile strength [MPa]	Elongation at break [%]	Young's modulus [GPa]	Compression strength [MPa]	Properties	Reference
Thermoplastic	Polyethylene (PE)	0.91–0.95	25–45	150	0.3–0.5	–	Low cost, good solidity, chemical resistance, ageing resistant	[171,172]
	Polypropylene (PP)	0.90–0.91	20–40	80	1.1–1.6	–	Low cost, good solidity, chemical resistance	[171,173]
	Polyvinyl chloride (PVC)	1.3–1.5	52–90	50–80	3.0–4.0	–	Low cost, weather resistant, non-inflammable, good haptics	[171,172]
	Polystyrene (PS)	1.04–1.05	35–60	1.6	2.5–3.5	–	Lightweight, water resistant, excellent shock absorption, anti-bacterial	[115,171]
Thermoset	Unsaturated polyester (UPE)	1.2–1.5	40–90	2	2.0–4.5	90–250	Poor linear shrinkage, excellent wettability of fibers, room temperature curable by addition of hardener	[171,174]
	Epoxy (EP)	1.1–1.4	28–100	1–6	3.0–6.0	100–200	Low cost and low toxicity, high strength, low shrinkage, excellent adhesion to fibers, chemical, and solvent resistant	[175,176]
	Phenolic (PH)	1.3	35–62	1–2	2.8–4.8	210–360	Good strength and dimensional stability, heat, solvents, acids, and water resistant	[176,177]
	Vinyl ester (VE)	1.2–1.4	69–86	4–7	3.1–3.8	86	Good strength and mechanical properties	[171,178]
Bio-based	Poly(lactic acid) (PLA)	1.2–1.3	57–185	2.1–30.7	5.1–19.5	–	High strength, high modulus, good appearance, highly biodegradable, less green-house gases emission	[115,179]
	Polybutylene succinate (PBS)	1.26	39–55	5–12	3.6–7.4	–	Inherent biocompatibility and biodegradability	[115,180]
	Poly(hydroxy alkanooate) (PHA)	1.2–1.3	10–39	2–1200	0.3–3.8	–	Biodegradable with lack of toxicity, reduction of fossil usage	[115,179]
Recycled	High-density polyethylene (HDPE)	0.9–1.0	32.0–38.2	150	1.3	–	Stiff, durable, high-temperature stability, UV resistant, easily recycled	[115,181]
	Polyethylene terephthalate (PET)	1.5–1.6	55–159	300	2.3–9.0	–	Highly rigid, good tensile strength, good barrier effect, easily recycled	[115,181]

of another material (curing agent/cross-linker/catalyst) and/or heat to initiate the chemical reaction. During such reactions, the molecules cross-link, and form significantly longer molecular chains and a cross-linked network, which results in a solidified material. Thermoset matrices provide better resistance to creep, higher modulus, good stability to thermal variations, and higher chemical resistance than thermoplastic matrices.^[183] However, such matrices are fragile and provide very low fracture toughness at room temperature. Most commonly used thermoset polymer's matrices for FRP composites are unsaturated polyesters, phenolics, epoxy, and vinyl esters.^[184]

Epoxy Resin: Epoxy resins show excellent mechanical and chemical properties, corrosion resistance, good dimensional, and thermal stability, and are widely used as matrices for FRP composites.^[185] Such polymer matrices have been an obvious choice owing to their good stiffness, dimensional stability, and chemical resistance.^[186]

Unsaturated Polyester Resin: Unsaturated polyester, commonly known as polyester resin, is another popular and versatile synthetic co-polymer that is often used as the matrix for composites manufacturing. It is a linear chained polymer having an ester bond formed by polycondensation of unsaturated dibasic

acids with diols or by saturated dibasic acids with unsaturated diols.^[174] It is primarily used in compression molding, injection molding, RTM, hand lay-up, filament winding, and pultrusion processes.^[187] Such resin is used in the manufacturing of about 85% FRP that is used in cars, boats, and aircrafts.^[188]

5.2. Bio-Based Polymers

The sustainable approach to reducing the environmental impacts of synthetic polymer-based composites is to replace them with bio-based or biodegradable polymers. Such bio-based materials not only help in reducing carbon emissions by substituting fossil carbon but also impart added advantages including biodegradability, biocompatibility, carbon dioxide sequestration, and the reduction of global warming.^[189] Bio-based polymers are biodegradable in nature as they can undergo deterioration upon exposure to aerobic, anaerobic, or microbial processes. Bio-based polymers are usually produced via three most common methods: 1) The direct use of natural bio-based polymers (starch and cellulose) with partial modifications; 2) The production of polymers from organic waste residues such as polylactic acid (PLA) and polybutylene succinate (PBS); and 3) The direct synthesis via microorganisms such as polyhydroxyalkanoate (PHA).^[190]

5.2.1. Polylactic Acid (PLA)

Among various bio-based matrices, PLA is the most commercially popular polymer, which is also a feasible alternative to petroleum-based polymers. In terms of its biodegradability, PLA is a flexible polymer that can be optimized to degrade either over a very short period or a long period of time via varying their composition during synthesis.^[191] It is well-known for good structural stability with high transparency, and is mainly used for making composites for packaging in the food industry.^[192]

5.2.2. Polyhydroxy Alkanoate (PHA)

PHA polymers are aliphatic polyesters that can biologically be produced as cytoplasmic aggregations in various bacteria with specific nutrients and growing conditions, like abundant amount of carbon and deficiency of one or more important nutrients such as sulfur, phosphorus, nitrogen, oxygen, and other trace elements like iron, calcium, magnesium.^[190] They possess high thermal stability, and are completely biodegradable and biocompatible polymeric systems which are perfectly suitable for an extensive range of composite applications.^[193]

5.3. Recycled Polymers

Currently, polymers are either burned or end up in landfill at the end of their lifecycle, which is not environmentally friendly. In recent years, there has been a focus on alternative matrix materials that can be recycled and reused easily after the end

of their life.^[194] Commercial companies like Connora Technologies and Adesso Advanced Materials Co. Ltd. have developed acid-degradable and amine-based hardeners which allow thermoset epoxy to be broken apart upon the addition of a suitable acid.^[195–197] A similar strategy has been developed using anhydride hardener that can easily be broken down by an acidic solution in the presence of a zinc chloride catalyst.^[198]

Another approach includes the rebuilding of matrix materials entirely, developing new kinds of polymers that can be recycled or reused in a simple way. A eugenol-derived epoxy vitrimer has been developed, in which cross-links can be broken down at elevated temperature, allowing remolding.^[199] In addition, several recyclable polymer materials have been developed in which monomers are reversibly linked through a boroxine ring.^[200] Such polymers behave like classical thermosets, showing a good solvent resistance and mechanical properties but can be broken down in boiling water, reshaped, and reformed. Perhaps the most appealing fact from an environmental point of view is the idea of developing a polymer matrix that can be easily recycled back to its monomeric units for making into new polymer matrix.^[201] Various approaches have been made for such polymers, like poly(hexahydrotriazine) (PHT) and self-immolative polymers.^[202]

5.4. Outlook on Polymer Matrices

Recently, extensive research has been taking place in the field of composites to find suitable polymer matrices. The incorporation of these polymers in the composites shows several advantages like low cost, low density, and reduced abrasiveness.^[171] However, further research is required to explore the scope and limitations of such polymeric materials. The research direction must focus on the development of materials that maintain a balance between the composite structure and properties, as well as the capability to be manufactured at scale and lower cost. As most of the polymer matrices used for manufacturing FRP composites are non-biodegradable, the first step towards sustainable FRP composites could be the use of bio-based polymer resins and/or partially degradable composites.

6. Modifications for Sustainable FRP Composites

6.1. Surface Functionalization of Natural Fibers

Jute, flax, hemp, and sisal are the four main dominating bast fibers, used as reinforcing materials for natural fiber reinforced composites. Among them, jute has gained significant attention due to its prospect to replace partially or fully conventional glass fibers owing to lower specific gravity and higher specific modulus. It's also the second-most produced natural fiber after cotton, found mainly in Bangladesh, India, and China, and is at least 50% cheaper than flax and other natural fibers.^[13,84]

Natural fibers could offer an attractive alternative to synthetic fibers, due to their lower production cost, lower density, and long individual fiber length. However, natural fiber reinforced composites still suffer from poor mechanical properties in comparison to conventional synthetic fibers.^[13] The mechanical

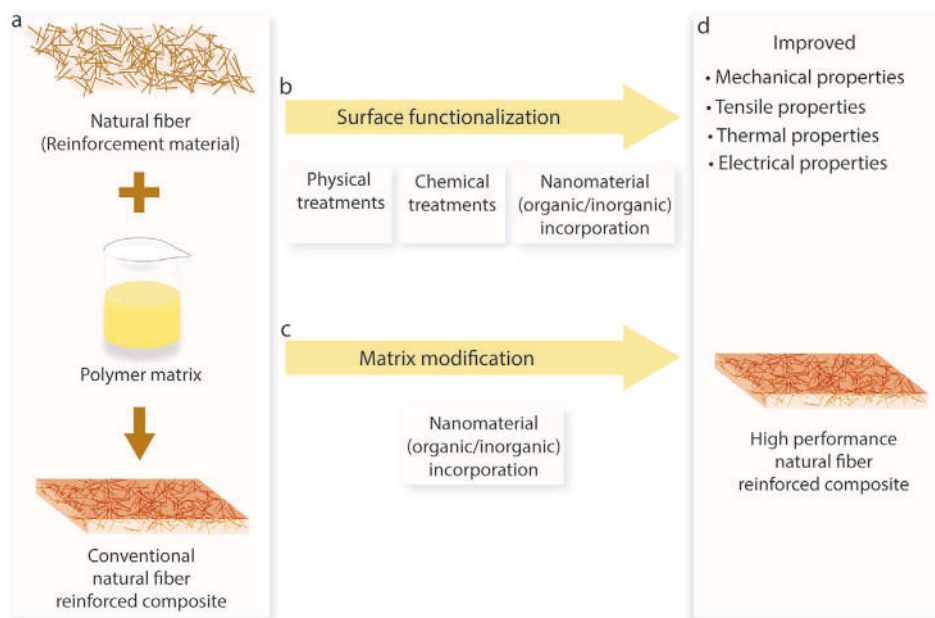


Figure 10. Improvement of a) conventional natural FRP composite properties by b) surface functionalization of fibers and/or c) matrix modification to produce d) high performance natural FRP composites.

properties of FRP composites depend on the proportion and properties of the constituent fibers and matrix materials, the orientation of fibers through the matrix, and the manufacturing methods.^[17] However, being the main load-bearing constituent, the properties of reinforcement materials, that is, the fiber in the case of fiber reinforced composites, are dominant among all. **Figure 10** illustrates the scope for altering the properties of fiber-reinforced composites.

Several physical and chemical treatments have been reported to enhance the mechanical performance of natural fibers and their composites. Physical treatments do not change the chemical composition of fibers. They only modify the surface and structural properties of fibers. Some physical treatments include stretching, calendaring, combing, cold plasma treatment, and electric discharge.^[203–205] In contrast, chemical modifications of natural fibers permanently alter the nature of fiber cell walls either by grafting polymers on the fiber surface, bulking or cross-linking within the fiber cell wall. Such treatments provide more dimensional stability, reduce water absorption capacity and give resistance to the fibers against fungal decay.^[206] Alkali treatment is the most popular chemical treatment,^[207] which removes impurities including wax, hemicellulose, and lignin from the fiber surface, separating elementary fibers from technical fibers to improve the fiber packing in composites, resulting in a strong fiber-matrix interface and improving the load bearing capacity of the reinforcement materials. It was evident that the treatment with a lower alkali concentration (≈ 0.5 wt.%) for a prolonged period of time is an effective technique to enhance the mechanical properties of jute fiber, though micro-voids can still produce a weak fiber/matrix interface. Attempts to overcome such flaws, either by nanomaterial grafting or other surface modifications including silane treatment, acetylation, etherification, peroxide and plasma treatment to enhance the composite's performance

have been reported.^[33,206] Additionally, several combined surface treatments have also been investigated^[33] including alkali-silane,^[208] alkali-plasma,^[209] alkali-bleaching,^[210] alkali-acetylation,^[211] etc. Unfortunately, many such treatments are expensive and time-consuming but provides a minor improvement in composite performances.^[12] Therefore, the field of research to investigate newer surface treatments to enhance composite performances still remains attractive.

Nanomaterials, due to their higher specific surface areas of up to $1000 \text{ m}^2 \text{ g}^{-1}$, and for their unique mechanical, electronic, and thermal properties are presently considered high-potential filler materials for the improvement of mechanical and physical properties of multifunctional polymer material.^[212] Several carbonaceous materials were reported to be utilized for the modification of natural fiber reinforced composites, in particular carbon nanotubes (CNTs).^[35] Shen et al.^[213] treated ramie fibers/epoxy composites with different CNT contents ranging from 0 to 0.6 wt.% and the investigation showed that, interlaminar shear strength (ILSS), flexural strength, and flexural modulus were improved by about 38%, 34%, and 37% respectively. Islam et al.,^[214] increased the mechanical strength of jute fibers composites by dip-drying jute fibers with CNTs. They also demonstrated enhanced thermal stability, flame retardancy, electrical conductivity and showed potential to be applied in different electrical and electronic devices as well as in polymer composites as conductive fillers. Zhuang et al.,^[215] dip coated hydrophilic jute fibers/fabrics in interconnected multi-walled carbon nanotube (MWCNT) networks to obtain electrically semiconducting jute fiber surfaces which were further used as temperature, relative humidity, and stress/strain sensors. Saiteja et al.,^[216] also demonstrated an enhancement of mechanical properties for jute fiber reinforced composites by treating with a dispersion of MWCNT.

Graphene, since its isolation in 2004, has received huge interests from researchers attention due to its outstanding mechanical, thermal, electrical, and other properties.^[217,221] Such incredible properties of graphene and its derivatives^[222–224] were utilized for designing high-performance natural fiber composites.^[35] Ganapathy et al.^[225] used graphene as a filler for banyan aerial root fibers reinforced epoxy composites at various compositions. They reported that hybrid composites containing 4% of graphene achieved the highest tensile (40.6 MPa) and flexural strength (163.23 MPa). Alkali-treated jute fibers were coated with graphene flakes and graphene oxide (GO) by Sarker et al.^[13] to enhance interfacial shear strength up to $\approx 236\%$ and tensile strength up to $\approx 96\%$. Karim et al.^[84] introduced reduced GO into jute fiber to improve the tensile strength and Young's modulus of the composites significantly by up to $\approx 183\%$ and up to $\approx 450\%$, respectively. Additionally, organic materials, inorganic nanofillers such as alumina, magnesia, silica, zinc oxide, titanium dioxide, and calcium carbonate have also been used for fiber surface modification.^[226]

6.2. Polymer Matrix Modification with Nanomaterials

Like fiber modification, many research groups have reported matrix modifications to improve the performance of FRP composites. Gojny et al.,^[227] applied a standard shear-mixing technique to disperse double-wall nanotubes in an epoxy resin. They demonstrated that, in comparison to a carbon black filled epoxy, the addition of only 0.1 wt.% of CNT with epoxy resin leads composites to an increased tensile strength and Young's modulus while also retaining ductility. In another study,^[212] they significantly improved the matrix-dominated properties (e.g., ILSS), by treating the glass FRPs with CNT/epoxy matrix although tensile properties were not affected. Costa et al.,^[228] exhibited that, compared to control curaua fibers (CF) reinforced composites, CF reinforced composites having polymer matrix functionalized with GO offer superior tensile performance, higher yield strength (64%), tensile strength (40%), Young's modulus (60%) and toughness (28%). As found for the reinforcement modification, inorganic nanoparticles are also used for matrix modification of fiber reinforced composites.^[229,230] Prasad et al.^[231] introduced titanium dioxide (TiO₂) nanoparticles for the epoxy matrix reinforcement. Adding only 6% TiO₂ nanoparticle in flax fiber reinforced epoxy composites improved the tensile strength up to 12% and Young's modulus up to 23%. In another study, TiO₂ filled (4 wt.%) jute epoxy composite showed an increase in tensile and compressive strength by 31% and 34% compared to an unfilled composite.^[232]

6.3. Hybridization with Synthetic Fibers

The inherent limitations of natural fibers such as having inferior mechanical properties along with a higher water absorption limit their use in comparison with commonly used glass and carbon fiber-based composites. Hybrid composites consisting of two or more fibers in one matrix are therefore seen as a solution to enhance the properties of natural fiber-reinforced polymer composites.^[233] Such composites have already achieved

mechanical properties equal to or sometimes even greater than conventional fiber-reinforced polymer matrix composites. Synthetic fibers are introduced along with natural fibers by an optimal stacking sequence, which imparts advantages of both fibers to the resultant composites.^[234] Glass fiber is the most used fiber for hybridizing purposes due to its low cost, great availability, and ease of manufacturing.^[8] However, several research groups have reported the hybridization of various natural fibers with different synthetic fibers. Examples include natural sugar palm fiber hybridized with glass fiber,^[235] kenaf fiber hybridized with glass,^[236] or Kevlar fiber,^[237] oil palm empty fruit bunches fiber with glass fiber,^[238] pineapple leaf fibers with glass fibers,^[239] bamboo fiber with glass fiber,^[240] jute fiber with glass,^[241] or carbon,^[242] hemp fiber with carbon fiber,^[243] flax with glass fiber,^[244] ramie fiber with glass fiber,^[245] and sisal with glass,^[246] carbon,^[247] or aramid fiber.^[248] Synthetic fiber films are also reported as hybridization materials. For example, Shamsuyeva et al.^[249] investigated the effect of the epoxy-based coating of flax textiles on their tensile properties and corresponding PA6 biocomposites after thermo-oxidative aging.^[250] They demonstrated, that the treated flax fiber reinforced composites demonstrate increased tensile strength and modulus for all test conditions. A combined treatment of silanization and partially bio-based epoxy resin coated flax fiber composites with PA6 film was also investigated.

6.4. Outlook on Modifications

From the above review, it is evident that the surface modification of natural fibers in composites is justified for engineering applications owing to their mechanical properties. However, there are a lot of challenges involved in controlling and improving the mechanical properties of natural FRP composites. Further exploration is also required from the research forum to support and motivate the utilization of natural fibers as well as novel modification techniques in advancements of natural FRP composites.^[251] With the significant progress in materials science, it can be assumed that in near future these advancements will lead us towards the enhanced properties of natural FRP composites, particularly for novel applications. Future research is required to overcome the impediments like moisture absorption for long-term stability in outdoor applications, interfacial compatibility, swelling, etc.

7. Properties of Fiber Reinforced Composites

7.1. Mechanical Properties

Mechanical properties of sustainable FRP composites are the most important factors, determining their potential applications in various sectors including automobiles, aerospace, household, and sports. **Figure 11** illustrates important parameters, that generally influence the mechanical properties of FRP composites. They can be grouped into three categories a) reinforcing fibers; b) polymer matrices; and c) composites manufacturing processes. As fibers are used as reinforcement materials for FRP composites, the first thing to look out for is the

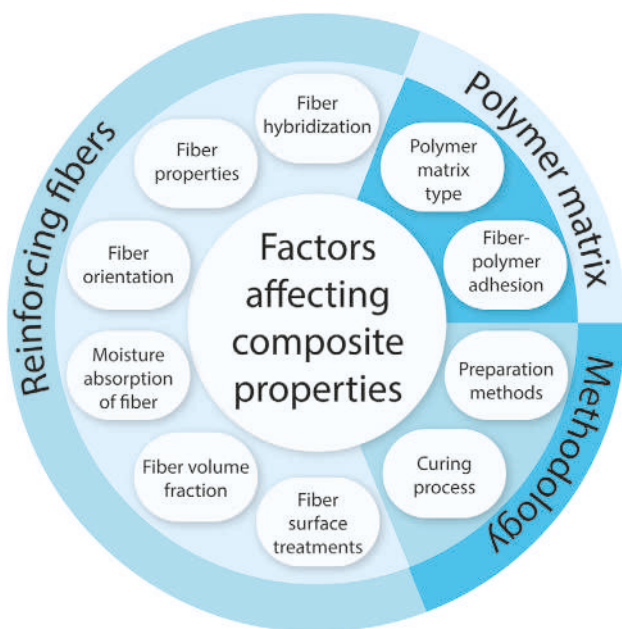


Figure 11. Influencing factors for mechanical properties of FRP composites.

fiber properties, including their orientations, moisture absorption, surface treatment, and hybridization.^[252–254]

Enhanced mechanical properties of composites are achieved when the fibers are aligned in a direction parallel to the applied load. However, it is very challenging to obtain such alignment with natural fibers, as they tend to orient themselves randomly. The tensile strength and Young modulus of FRP reduces significantly with an increase in fiber orientation angle relative to the test direction.^[254] Natural fibers are often carded and placed in sheets prior to matrix impregnation, in order to obtain a high degree of fiber alignment.^[255]

It is often observed that the presence of moisture in the fiber hinders the ultimate strength of composites. Natural fibers are usually hygroscopic in nature, which has an effect on the mechanical properties of their composites. Fiber dispersion and volume fraction are the other two important factors that influence the properties of short natural fiber reinforced composites, which commonly have hydrophilic fibers and hydrophobic matrices. Longer fibers can increase their tendency to agglomerate. The good fiber dispersion promotes good interfacial bonding, thereby reducing voids by ensuring that the fibers are surrounded by the matrix.^[256] Fibers can also undergo certain surface treatments or modifications in order to impart specific functionalities and enhance mechanical properties.

The polymer matrix plays a major role in fiber-reinforcement in a composite. They protect fiber surfaces from mechanical damage, act as a barrier against adverse environments, and transfer loads to the fibers. The most commonly used matrices in natural FRP composites are thermoset or thermoplastic polymers, as they are lightweight and can be processed at lower temperatures.^[257] Fiber-matrix adhesion plays a significant role in determining the mechanical properties of composites.^[258] As the stress is transferred between the fiber and the matrix, a good interface bonding between them is required to achieve

optimum reinforcement and enable crack propagation. However, natural FRP composites have a limited interaction between the hydrophilic fibers and hydrophobic matrices, leading to poor interfacial bonding and mechanical performance. Such interfacial bonding can be improved via surface modifications or functionalization.^[9,12,13,33,84]

As already mentioned, the common methods used for the manufacture of FRP composites are vacuum infusion, extrusion, compression molding, and injection molding. The speed, pressure, and temperature of such processes are key factors that influence the mechanical properties of FRP composites. It is possible for the fibers to degrade when they are subjected to high temperature, which limits the use of thermoplastic matrices as degradation can occur around the melting point of the polymer. In an extrusion process, thermoplastic polymers are usually in the form of pellets or beads, which are softened and mixed with the fiber by means of a single or two co-rotating screws, compressed and forced out at a steady rate through a die. High screw speeds result in fiber breakage, air entrapment, and excessive melt temperatures.^[259,260] Whereas low screw speeds lead to poor mixing and insufficient wetting of the fibers. Better fiber dispersion and mechanical performance are achieved through the twin screw system rather than a single screw extruder.^[261]

Recently, the mechanical properties of natural FRP composites have been enhanced substantially via better raw materials extraction and selection, interfacial engineering, and improved composite manufacturing processes.^[262] In a previous study,^[263] both untreated and treated banana fibers have been considered to develop hybrid composite material. The untreated banana fiber was treated with caustic soda in order to increase the wettability, and then used as a reinforcement material. It was found that after alkali treatment, there was an improvement in the mechanical properties including tensile, flexural, and impact strength of the hybrid composites. In another study,^[264] natural bamboo fiber reinforced composite was used, investigating its tensile and flexural strengths, and surface hardness. The effect of fiber loading on mechanical properties of the composite was studied. It was found that maximum values of tensile & flexural, and surface hardness of the composite were achieved at a 25% wt.% loading. Hybridization of sisal fiber with coconut spathe and ridge gourd was reported by Girisha et al.,^[265] which resulted in a significant enhancement in tensile properties when compared to the individual components. The tensile strength was found to be increased by $\approx 65\%$.

7.2. Tensile Properties

Tensile properties of natural FRP composites are primarily affected by the fiber-matrix interfacial adhesion.^[182] They can also be improved via physical and chemical modifications of fibers and polymer matrices. It is largely dependent on the volume fraction of the fiber in matrix. Generally, when there is an increase in the fiber volume fraction up to an optimum level, there is more distribution of load among the fibers, and the applied force can be carried even after the fibers fracture which can lead to a higher tensile strength.^[266] However, with

further increases in the fiber volume fraction beyond the optimum level, the composite will become brittle, and the matrix is unable to withstand the additional load from the fibers, thereby resulting in a lower tensile strength.^[267] Additionally, irregular trends for the tensile properties are also sometimes observed because of several factors that include fiber degradation, non-compatibility between the fibers and the matrix, and an inappropriate selection of manufacturing processes.^[266]

7.3. Flexural Properties

Flexural stiffness is one of the important properties to measure the resistance of a composite against bending deformation. It mainly depends on two parameters: the moment of inertia and the modulus of the composite. It has been found that the flexural strength of natural FRP composites increases with the increase in fiber content up to an their optimum level.^[268] However, further increases in the fiber content beyond the optimum level reduces the flexural strength, due to defects in the wetting of fibers that can create stress concentrations in the composites.^[268] The fracture toughness of composites, which means a composite's resistance to crack propagation, is primarily affected by the fiber-matrix interfacial bonding strength, fiber volume fraction, and the intrinsic properties of the matrix.^[183]

7.4. Compressive Properties

The compressive behavior of natural fiber reinforced composites mainly depends on fiber volume fraction and the reinforcement architectures.^[183,269] The compressive strength of composites is found to be higher at a higher fiber volume fraction within its threshold point, due to a reduction in void.^[183] Furthermore, high compressive strength can be attributed to a high fiber-matrix compaction and good homogeneity of composites. However, as the fiber volume fraction crosses the optimum level, the compressive strength decreases. Generally, when the fiber volume fraction crosses 1.5%, a reduction of compressive strength of nearly 8.5% occurs for every 0.5% increase in fiber volume.^[270,271] However, it has been observed that the compressive strength of natural FRP composites gradually decreases when there is an increase in the fiber volume fraction.^[271,272]

7.5. Impact Strength

The impact behavior of natural FRP composites primarily depends on the fiber-matrix bonding level, which is another important parameter for assessing the mechanical properties of composites. The impact properties of composites can be enhanced by various modification methods. The impact loading may be the result of debris, falling objects, crashes, and impacts. Some of the parameters that influence the impact strength of composites are energy absorption, fiber pull-out, favorable bonding, and the level of adhesion.^[183]

7.6. Inter-Laminar Properties

In a study on interface modification and characterization of natural FRP composites, it has been observed that the quality of the fiber-matrix interface is required to identify the application of natural fibers as composite reinforcement.^[273] Some researchers have also concluded that, because the fibers and matrices are chemically different in nature, strong adhesion at fiber-matrix interfaces is necessary for the successful transfer and distribution of stress. Fiber-matrix interfacial characteristics affect the behavior of various natural FRP composites, such as jute, flax, yarn, and woven fibers reinforced with PP, polyester, epoxy resins.^[274] It has been noted that such natural FRP composites possess a high critical load for damage initiation, strong fiber-matrix adhesion, and high fiber strength and modulus. The alkali treatment of natural fibers like jute, kapok, hemp, and woven fibers can change their structure, which can increase fiber-resin adhesion as well as interfacial energy.^[275]

7.7. Hardness

Lundquist et al.^[276] investigated that a pulp fiber reinforced thermoplastic composite results in a strength increase by a factor of 2.3 and stiffness increase by a factor of 5.2 relative to the virgin polymer. Kenaf-maleated PP composites have a higher strength and specific modulus, at a lower cost than those reinforced with coir, sisal thereby making them good alternatives to the existing materials.^[277] Ramanaiah et al.^[278] in 2012, developed a new natural borassus seed shoot fiber reinforced composite with varying fiber volume content ranging from around 12–31%. The hardness of the composites decreased with an increase in the fiber content. Sreekala et al.^[279] in 2002, investigated the mechanical behavior of hybrid phenol-formaldehyde-based composites reinforced with oil palm fibers and glass. Hybridizing oil palm fibers with glass fibers demonstrated improved properties, such as tensile strength, modulus, and flexural strength but poor hardness properties.

7.8. Tribological Properties

Wear and friction are the two vital tribological phenomena that occur due to the relative motion of solid surfaces, deteriorating materials, and dissipating energy.^[280] Such properties of sisal fiber reinforced composites were studied at high temperatures. After studying the effect of different fiber volume fractions on the friction coefficient and the wear rate of such composites, it was found that the friction coefficient showed multiple trends at different temperatures whereas the wear rate significantly increased at higher temperatures. Generally, at higher fiber volume fractions, defects are found in the composites due to the poor dispersion of fibers in the matrix.^[281]

The coefficient of friction (COF) is a quantitative number defining the frictional behavior of a material. In wear tests, a friction value is either the number determined at the end of the test or an average of values collected during the test. Wear is a progressive loss of material from the surfaces during chemical

and/or mechanical processes.^[282] The worn-out surfaces of kenaf fiber reinforced epoxy (KFRE) composite have been observed at different operating parameters. It is found that high thermo-mechanical activity is responsible for the debonding and formation of micro-cracks thereby deteriorating the fiber-matrix interfacial bond and increasing the wear on the application of high load.^[283]

The tribological properties of brake pads were significantly enhanced by the addition of RS and rice husk dust into the composites.^[284] In another study, the friction coefficient and wear rate of chopped sugar cane fiber reinforced polyester (CSCRFP) were compared with those of chopped glass fiber reinforced polyester (C-GRP) composites at different lengths of fiber. For 1 mm of fiber it was found that the wear rate of CSCRFP composites was nearly 10 times higher than C-GRP composites.^[285]

7.9. Flame Retardancy

The potential applications of natural fibers have been limited by their poor flammability. Numerous research has been carried out to improve the flame retardancy of natural FRP composites.^[286,287] Natural polymers and fibers are organic materials that are highly sensitive to fire. In the presence of a flame, the burning of a composite material occurs in five consecutive steps: heating, ignition, combustion, decomposition, and propagation.^[288] The burning of composites mainly results in two forms of products with a high cellulose content and high lignin content. High cellulose content gives rise to higher flammability, whereas higher lignin content means that there is a greater chance of char formation.^[289]

The flame retardancy of composites can be achieved by undertaking different procedures like the introduction of fire barriers, such as coatings and additives used as intumescent. However, another method of reducing combustion is by increasing the stability and char formation in the composite, resulting in reduced flammability, decreased visible smoke, as well as restricting the volume of products produced because of combustion.^[290] Flame retardant coatings are another method that helps in the improvement of flame retardant properties of composites. Flame retardants like magnesium hydroxide ($Mg(OH)_2$), ammonium polyphosphate (APP), and a mixture of these two were incorporated into sisal fiber reinforced composites for the enhancement of flame retardancy.^[291] Natural fiber PP composites containing $Mg(OH)_2$ were analyzed by Sain et al.,^[288] where the flame retardant properties with boric acid were studied. It was found that 25% $Mg(OH)_2$ could reduce the flammability effectively almost by $\approx 50\%$. In another study involving kenaf/PP fiber reinforced composites,^[292] APP was used as a flame retardant with three different compositions. The results showed that the flame retardant property of kenaf/PP composites was improved with an increase in concentration of APP irrespective of the types used.

Flame retardancy is mainly evaluated in terms of Limiting Oxygen Index (LOI), that is, the minimum amount of oxygen (vol%) required to sustain a stable combustion of any material. The higher the LOI value indicates better flame retardant properties of a material as illustrated in Table 4.

Table 4. Classification based on LOI values.^[293]

LOI	Remark
< 21	Flammable
= 21	Marginally stable
21–28	Slow burning
28–100	Self-extinguishing
> 100	Intrinsically non-flammable

Another most important standard assessment method of flame retardancy is a UL 94 classification (Table 5). UL 94 is a plastic flammability standard released by the Underwriters Laboratories (USA).^[294] It classifies plastics according to the manner in which they burn in various orientations and part thicknesses from the lowest to the highest flame retardancy in six different ratings.

Thermo-mechanical studies of bio-based composites derived from lactic and thermoset resins and flax and flax/basalt fiber reinforced composites were carried out, where mechanical and thermal properties of such composites were found to be better than the pure flax FRP composite.^[295] Srinivasan et al.^[296] found that a hybrid composite of banana, flax, and glass fibers has better thermal stability and flame resistance than the flax and banana fiber reinforced composites. In another study,^[297] it was demonstrated that the thermal treatment of ramie fiber was efficient in modifying the inner structures and surface of the fibers.

7.10. Thermal Conductivity

The use of heat-insulating materials is a well-known approach to reducing energy costs and improving manufacturing efficiency in various sectors like packaging, construction, automobile, and aerospace. Natural fibers contain lumens which are an air-filled hollow portion, therefore the thermal conductivity of their composites decreases with an increase in fiber content. With an increase in fiber volume fraction, the amount of air contained in the composite also increases, thereby resulting in heat insulation.^[298] Pujari et al.^[299] investigated the thermal

Table 5. Classification based on UL 94 rating.^[294]

UL 94 Rating	Remark
HB	Slow burning on a horizontal part
V-2	Burning stops within 30 s on a part allowing for drops of vertical flammable plastic
V-1	Burning stops within 30 s on a vertical part allowing for drops of plastic that are not in flames
V-0	Burning stops within 10 s on a vertical part allowing for drops of plastic that are not in flames
5VB	Burning stops within 60 s on a vertical part allowing for drops of plastic that are not in flames; plaque specimens may develop a hole
5VA	Burning stops within 60 s on a vertical part allowing for drops of plastic that are not in flames; plaque specimens may not develop a hole

conductivity of randomly-oriented banana and jute fiber-based epoxy composites and reported it to be very low at the maximum fiber volume fraction. Li et al.^[300] found that the thermal conductivity of flax fiber/HDPE composite reduced with the increase of fiber volume fraction. Agrawal et al.^[301] studied the influence of fiber treatment on the thermal conductivity of an oil palm fiber/phenolic composite and found that silane and alkali treatments increased the thermal conductivity of the composite more than an acetylation treatment, signifying that the latter was more appropriate than the former treatments for enhancing the heat-insulating characteristics of a natural fiber composite.

7.11. Acoustic Properties

Sometimes vibration is a desirable physical phenomenon. However, continuous vibration in structural materials often leads to problems like noise pollution and the formation of fatigue cracks.^[302] Noise pollution is a very concerning problem in urban life. It causes not only sleep disturbance and annoyance, but also leads to severe health issues such as heart attacks and hearing loss.^[303] Therefore, the development of materials with enhanced vibration damping properties is becoming increasingly important now-a-days. Presently, in many buildings, automobiles, and movie theatres, sound absorbing materials are used to mitigate the noise and vibration through the absorption of acoustic waves, as noise in the form of sound waves propagates through the sound absorber and gets absorbed.^[304] Natural fibers are known to have ease in handling and good acoustic insulation properties owing to their viscoelastic behavior as compared to inorganic fibers like glass and carbon.^[305] Because of such phenomena, natural fiber reinforced composites show better vibration damping properties. Researchers have studied the free vibration characteristics of banana/sisal fiber reinforced composite beams and found that the chemical treatment enhances the free vibration and mechanical properties due to the improvement of the interfacial bond of fiber-matrix system.^[306] In other research it was found that the damping properties of flax fiber composites increased with the twist and crimp because of the enhanced intra-yarn and inter-yarn friction.^[307]

7.12. Electrical Properties

Natural fiber reinforced composites can be used for electrical applications for shielding the cables, or as an insulator for wires.^[308] The demand for natural fiber reinforced composites as dielectrics is increasing, because of their electrical insulating properties. The dielectric constant of any material depends on its polarizability and it increases with the increase in the polarizability of a material. However, the dielectric loss factor decreases with the increase in frequency at a constant temperature.^[309] Joseph & Thomas^[310] investigated electrical properties of banana fiber reinforced composites. Treatments with caustic, silanes, acetyl, and latex under heat, decreased the dielectric constant. It was also observed that the dielectric constant increased with a rise in temperature and decreased

with a rise in frequency. After the removal of water, the value of the dielectric constant was decreased. To make wires, flexibility is also one of the vital criteria. The whole length of the wire can be easily accommodated in a small space by using flexible polymers. In the case of natural FRP composite manufacturing processes, hardeners are often used. When hardeners are used composites become brittle in nature. But when the same brittle composites show good electrical properties along with mechanical properties, they can be used for the fabrication of switchboards and other electrical panels.^[20]

7.13. Water Absorption

One of the major problems with natural FRP is their high moisture regain.^[311] Mechanical properties of FRP have a strong dependency on the fiber-matrix interface adhesion.^[312] It is well known that the fibers are rich sources of cellulose, hemicelluloses, lignin, and pectins, all of which are having hydroxyl groups. Therefore, they are strongly polar while most polymers show considerable hydrophobicity. Water absorption of a fiber reinforced composite will depend on the absorption characteristics of both the reinforcing material, that is, the fiber as well as the polymer matrix. Generally, the high water intake by composite materials results in the development of pressure on nearby structures, swelling, increments in their deflection, a conceivable decline in their strength, and increased weight of wet profiles. Excessive water absorption of a composite will also create a suitable platform for microbial attack on the composites.^[313]

7.14. Biodegradability

An important and characteristic functionality of sustainable fiber reinforced composites is their biodegradability, which originates mostly from microbial action.^[124] Biodegradability is an indispensable and effective function for the waste treatment of green composites after completing their service life. However, the introduction of biodegradability in composites effectively brings about lower durability. Thus, there must be a control over the biodegradability behavior. Synthetic fibers like carbon, glass, and aramid reinforced composites are causing problems to the environment as they are not as easily degradable as natural fibers. The development of natural fiber reinforced composites promotes the use of environmentally friendly materials due to their biodegradability. Biodegradable materials, which are also bio-based in nature, are ideal for the development of a sustainable world. They have the potential to be used as recyclable products, as they can be collected, processed, and reused or left in the environment for natural degradation.^[314] Rwawiire et al.^[315] analyzed polymer matrices derived from natural resources like polyhydroxyalkanoates (PHAs), cellulose, thermoplastic starch (TPS), and PLA. They found that biodegradable composites have comparable properties to synthetic-based materials. Wang and Shih,^[316] analyzed bamboo fiber structure and extraction methods. They reinforced the fiber with polymers and analyzed their mechanical properties, cost, and energy of extraction, CO₂ absorption, renewability, recyclability,

and biodegradability. They found that bamboo fiber-based composites are comparable with glass composite in terms of their performance properties due to their low cost, lightweightness, and most importantly biodegradability.

There are mainly five types of biodegradable bio-based polymers commercially available: protein-based polymers, bacterial PHA-based polymers, cellulose ester-based polymers, PLA-based polymers, and starch-based polymers. In a study involving starch-based biodegradable reinforced composites with date palm and flax fibers, it was found that TPS composites are hydrophilic and biodegradable. The rate of biodegradation and water uptake was reported to be inversely proportional to the fiber fraction.^[317]

8. Applications of FRP Composites

Natural FRP composites have become popular in automotive, aerospace, aircraft, biomedical industries, electrical parts, packaging, and construction sectors (Table 6), owing to their good mechanical performance, economical production, vibration damping, lightweight, sound attenuation, eco-friendliness, and biodegradability.^[138,318] Natural FRP composites have widely been applied in the automobile industry for a long time. Henry Ford, and George Washington Carver, made the first attempt to use natural fibers in the automobile industry using hemp and flax fibers in 1941.^[319] Similarly, Audi launched the A2 midrange car in 2002, where door trim panels were made of flax/sisal reinforced polyurethane composites.^[320] In the past decades, legislation from North American and European governments have encouraged the application of natural FRP composites in the automotive sector. Biocomposites obtained from natural fibers are extensively applied in automobile parts, such as interior parts, dashboards, trays, headliners, seat backs, and door panels by various manufacturers and suppliers all over the world. Almost all major car manufacturers such as Toyota, Mercedes-Benz, General Motors, Ford, Chrysler, Daimler, BMW, and Audi are using bio-based composites in multitudinous applications.^[321]

Usually, natural FRP composites are predominantly applied for interior automotive parts due to their relatively low mechanical properties and intrinsic moisture sensitivity. Various automobile interior parts including storage bins, package shelves, floor mats, seat backs/fillers/liners, dashboard, and indoor panels are typically made of natural fibers.^[322] Examples of natural FRP composites used for automobile exterior components include flax/polyester composites in the engine and transmission enclosures for sound insulation, abaca-reinforced composites for the spare tire well covers, fender components, spoilers, bumpers, seat frame, and load floors.^[323] Owing to a low environmental impact, low thermal conductivity, and the light weight of renewable materials, natural FRP composites have advanced their applications in architecture, building construction, furniture, soil blending, and masonry.^[138]

8.1. Automobile

Traditionally composites used in the automotive sector are mostly made up of synthetic fibers such as carbon and glass as

reinforcing materials. However, renewable and bio-based reinforcing materials are becoming increasingly attractive as alternatives to reduce environmental impacts.^[358,359] Several natural fibers such as jute, hemp, flax, kenaf, sisal, and coir have been investigated to produce bio-composites for automobile applications, Table 7. Such biocomposites are popular for automobile applications, as they provide lightweight, improved fuel efficiency, and low production costs. They are used to manufacture various automobiles components such as seat pads, armrests, headrests, trunk covers, cup holders, door panels, and bumpers.^[360] Additionally, biocomposites are effective in reducing noise and vibrations through damping.^[361] For example, Ford uses bio-based cushions, seats made of soy foam, and hemp fiber composites in the front grills.^[362] Similarly, interior panels of Mercedes-Benz use jute-based biocomposites, flax reinforced composites for trunk covers and shelves, and rear panel shelves are made up of sisal fiber composites.^[363] Toyota uses kenaf fibers in their covers for tires, soy foams for seats, and PLA/PP-based biocomposites inside package trays, toolbox areas, and trims. Volkswagen also uses biocomposites for the construction of package trays, door inserts, panels, and flap linings.^[322]

8.2. Aerospace

Almost half of the components of an aircraft are made of composites. The potential benefits of those composite components are they are lightweight and only require a simple assembly. Natural FRP composites have found use on a large scale for the development of aircrafts for civil transport and military fighters, helicopters, and the launching of satellites and missiles. Some of the aircraft components are made of conventional composites such as propellers, turbine engine fan blades, main wings, wing ribs, rear bulkhead, keel beam, engine cowlings, doors, elevators, airbrakes, spoilers, and the rudder.^[364,365]

8.3. Construction

In the construction industry, biocomposites are often used to manufacture roof tiles, floor matting, ceilings, doors, windows, and window frames. Load-bearing applications include the manufacturing of tanks, pipes, beams, and floor slabs.^[366] Furthermore, biocomposites are employed in the rehabilitation and repairing of various structural components. Due to better acoustic and thermal properties, natural FRP composites are used as soundproofing and insulating materials.^[367] Hemp-lime-concrete composites have shown better sound absorption ability than any other binders.^[368] LCA, ecological aspects, and durability properties are taken into consideration for the selection of any biocomposites for the construction sector. Lightweight and good mechanical properties are very important for such applications.^[321,369]

8.4. Medical

Composites are often used in medical devices where they are progressively replacing glass and metals. Over the years, the

Table 6. Potential applications of natural FRP composites.

Sector	Fibers	Applications	Ref.
Civil construction	Banana	Compressed earth block	[324]
	Jute, sisal, ramie, pineapple	Cementitious materials	[325,326]
	Flax, jute, sisal, hemp, coir, palm	Masonry	[327]
	Jute	Deck panel	[328]
	Kenaf	Ceiling	[329]
	Wheat straw, corn husk	Thermal insulation materials	[330]
	Wood cellulose, cork	Thermal insulation materials	[331]
Furniture and architecture	Lignocellulose, straw	Lounge furniture	[332]
	Hemp	Chair furniture	
	Hemp, flax	Ignot bio- and Polycal acoustic panel	
	Lignocellulose	BioMat research pavilion	
Sports and clothes	Hemp, jute, bamboo, sugarcane bagasse, coconut, banana	Footwear	[333]
	Flax, hemp	Racing bicycle	[334]
	Flax	Bicycle frame	[335]
	Jute	Winter overcoat	[336]
	Jute, sisal, coconut, areca, banana	Helmet shell	[337]
	Kenaf	Ballistic armor materials, mobile phone casing	[334,338,339]
	Kenaf, pineapple	Recurve bow	[340]
Aerospace	Palm	Sports utility	[341]
	Hemp	Electronics racks for helicopter	[342]
	Ramie	Aircraft wing boxes	[343]
Biomedical and pharmaceutical	Kenaf	Aircraft materials	
	Sugarcane	Drugs, antimicrobial, antibiotics	[344]
	Flax, ramie	Bone grafting, orthopedic implants	[345]
	Hemp, sisal, coir	Orthoses materials	[346]
	Jute	Enzyme	[344]
Others	Jute, sugarcane, flax, bamboo	Biomedical nanoparticles, antibiotics	
	Sisal	Drug delivery	
	Bamboo	Packaging	[347]
	Banana, bamboo, flax, jute, kenaf, palm, sisal	Dielectric materials	[348,349]
	Flax	Electrodes	[350]
	Flax, jute, coir, sisal	Wind turbine blades	[351]
	Flax, seagrass	Marine materials	[352,353]
	Jute	Solar parabolic trough collector	[354]
	Jute, flax, kenaf, hemp	EMI shielding	[355,356]
	Wood cellulose	Battery	[357]

advancement in natural materials, sterilization techniques, and surgical methods have allowed the use of composite materials in many ways. At present, medical practice utilizes a large number of medical implants and devices. Composites in the form of artificial hearts, pacemakers, heart valves, bio-sensors, dental implants, intraocular lenses, vascular grafts, joint and bone replacements, and sutures are widely used to restore and/or replace the function of degenerated/disturbed organs or tissues, to help in healing, to enhance function, and to rectify abnormalities, thereby enhance the quality of patient's life.^[370]

8.5. Sports

Composites are used for sports equipment because they are lightweight, strong, highly resistant to wear and tear, are fatigue and friction resistant, are easily transportable, thermally stable, highly durable, and have good shock absorption properties.^[341] They also provide flexibility in design and fabrication, therefore can be processed and shaped very easily. There are multitudinous goods made of natural FRP composites materials that include bows and arrows, hockey sticks, softball bats, tennis and badminton rackets, sailing and planning boats, and sailboards.^[371,372]

Table 7. Natural FRP composites in automotive.^[320]

Automobile	Fibers	Applications
Audi	Sisal, flax	Seat back, side, and back door panel, boot liners, hat rack, spare tire liners
BMW	Sisal, flax	Door panels, headliner panels, boot liners, seat backs, noise insulation panels, molded foot well liners, bumpers, fender liners, shields
Chevrolet	Flax	Trim panels
Citroen	Vegetable, wood	Interior door paneling, parcel shelves, boot liners, mudguards
Daimler	Sisal, hemp, flax, coir	Door panels, engine and transmission covers, pillar cover panels, windshields, dashboards, business tables
Fiat	Bamboo	Door panels
Ford	Wheat straw, Tomato, rice husks, hemp, kenaf	Floor trays, door panels, B-pillars, boot liners, wiring brackets, storage, front grills
General Motors	Kenaf, hemp, flax	Seat backs, inner door panels, cargo area floors
Lotus	Kenaf, sisal, hemp	Body panels, spoilers, seats, interior carpets
Mercedes-Benz	Banana, flax, sisal, hemp	Inner door panels, door panels, rear panel shelves, engine encapsulation, trunk covers
	Wood, sisal, flax, abaca	Door panels, engine encapsulation, spare wheel pan covers, door liners, seat backrests, parcel shelves, trunk covers
Toyota	Sweet potato, Sugarcane, kenaf	Door panels, seat backs, floor mats, spare tire covers, and package shelves
	Kenaf	Spare tire covers
Volkswagen	Sisal, Flax	Door panels, seat backs, boot-lid finish panels, boot liners
Volvo	Wood, rapeseed, jute, hemp	Seat padding, natural foams, cargo floor trays, dashboards, ceilings

8.6. Electrical and Electronics

Natural FRP composite materials are characterized by high strength and modulus, low thermal expansion, good electrical and thermal conductivity, and a low dielectric constant. The application of composites in electrical and electronics include inter-connections in housings, heat sinks, connectors, electrical contacts, thermal interface materials, light emitting diodes (LEDs) interlayer dielectrics, and printed circuit boards.^[373–375]

8.7. Others

Natural fiber reinforced composites are extensively used in storage tanks, columns, reactors for acidic and alkaline environments, structural supports, pumps and blowers, exhaust stacks, piping, ducting, scrubbers, industrial gratings, composite vessels, casings, stacks, ducts, fan blades, and drive shafts.^[376]

9. Outlook

The application of sustainable and natural FRP composites is increasing rapidly owing to their numerous advantages including their eco-friendly nature, biodegradability, and low cost, with relatively good mechanical properties. Thus, the natural FRP composites market is estimated to reach nearly 3.7 million tons in 2022, and is expected to register a compound annual growth rate (CAGR) of more than 9% during the forecast period (2022–2027).^[20] Globally, the primary

manufacturers of natural FRP composites include Trex Company, Inc., The AZEK Company, and Fiberon LLC. Among them, Trex Company, Inc. has the largest market share of over 10%. Asia-Pacific is the largest market that holds a share of production of over 30%. It is anticipated that the biggest market for natural FRP composites will be the building and construction sector followed by the automobile sector. Natural fibers are becoming an integral part of replacing synthetic fibers as the reinforcing materials for composites due to their great contributions towards a less polluted environment through eco-friendly materials consumption in different sectors.

Synthetic fibers have traditionally been an integral part of composite materials. However, the global scenario and outlook has completely turned into approaches leading toward biodegradability, recyclability, and sustainability. New environmental challenges and concerns have triggered the search for novel and sustainable products and processes. Engineering natural fibers with functional nanomaterials improves the mechanical properties of the composites. Instead of conventional petroleum-based polymers, using bio-based polymer matrices potentially reduces environmental hazards as well as enhancing biodegradability. Newer fibers have been developed which have opened up new market opportunities, since there has been a growing awareness about the importance of biodegradability and sustainability among the general population. It is an interesting fact that natural FRP composites are emerging as a realistic alternative to glass and carbon fiber reinforced composites (Figure 12a). Additionally, researchers have been investigating continuously to improve the manufacturing strategies to optimize material wastage, manufacturing time, and overall composite costs.



Figure 12. Future research direction of natural FRP composites.

Biocomposites could potentially replace petroleum-based composite materials for smart and multi-functional applications.^[377] If we investigate the applications of biocomposites, it has demonstrated potential for the automotive and construction sectors in a major proportion, which is currently the leading market for these materials. However, the challenge remains in replacing conventional synthetic FRP composites with those that exhibit comparable functional and structural stability upon use, storage, and environmental degradation on disposal.^[378] In addition to an improvement in the functional performance, research attention is also needed to overcome current barriers to using natural fibers. One of the barriers could be the compatibility of natural fibers in comparison to conventional glass or carbon fibers in terms of processing, functionalization, etc. Also, the low annual availability, as well as seasonality hinders the expanded use of natural fibers as reinforcing materials for composite manufacturing. Since, “sustainability” has become a key talking point for the industry in very recent years, researchers and composite manufacturers have been trying to find a balance between the performance of composites and sustainability. However, the relative advantages of natural fiber composites in comparison with conventional materials must be emphasized when developing new products, especially keeping in consideration the growth of the synthetic composites industry and their corresponding environmental effects. Though benefits such as reduced carbon footprint, biodegradability, and renewability are important, they are not easily recognized and appreciated by potential users, which significantly limits the spread and adoption of natural FRP composites. However, the market and commercialization

of biocomposites are expected to expand in the near future owing to the identification of novel applications and the development of efficient manufacturing technologies. Research is being carried out on bio-based materials to overcome some hindrances such as high moisture absorption, inadequate toughness, and reduced long-term stability that are required mainly for outdoor applications. It is reported that one of the major hurdles for commercialization of sustainable FRP composites until recently is the inadequacy in the recognition of research and development in developing nations, where such fibers are abundantly available. At the same time, it is noteworthy that such a hurdle has been overcome by many industrialized nations, especially in UK and Europe who are taking the lead in the development of sustainable FRP composites in recent years.^[379] New generations of biocomposites are eventually expected to be used in a wide range of applications majorly in mass-produced consumer products for short-term as well as long-term indoor applications^[380,381] (Figure 12b).

Biocomposites are sustainable and can be totally recyclable (Figure 12c), but at the same time can be more expensive. Because of their recyclability, such composites are getting extensively popular in the packaging sector. Upon the selection of a proper matrix, biocomposites can also be totally biodegradable, but their biodegradation will be difficult to control. Biocomposites possess good specific properties, but there is a high variation in their properties. However, such problems can be overcome by suitable modifications and advanced processing of natural fiber and their composites. Recent advancements in genetic engineering, the development of natural fiber, and composite science and technology will offer valuable opportunities for enhanced value-added

materials from renewable resources with improved support for global sustainability campaigns. Natural fibers are mainly biodegradable, but renewable resource-based biopolymers can be generated to be either biodegradable or non-biodegradable as per the specific demands for a particular application. Such a unique balance of properties can generate novel applications and at the same time can open up new market development opportunities for biocomposites in the 21st-century green materials world.

Acknowledgements

S.M. and M.R.I. contributed equally to this work. The authors acknowledge UKRI Expanding Excellence in England (E3) funding from Research England, and also graphic supports from Laura Wescott.

Conflict of Interest

The authors declare no conflict of interest.

Keywords

fiber reinforced polymer composites, natural fibers, recycled polymers, sustainable composites

Received: June 6, 2022
Revised: August 1, 2022
Published online:

- [1] M. Domm, in *Structure and Properties of Additive Manufactured Polymer Components* (Eds: K. Friedrich, R. Walter, C. Soutis, S. G. Advani, I. H. B. Fiedler), Woodhead Publishing, UK **2020**.
- [2] A. Scribante, P. K. Vallittu, M. Özcan, *Biomed. Res. Int.* **2018**, *2018*, 4734986.
- [3] N. Karim, M. Zhang, S. Afroj, V. Koncherry, P. Potluri, K. S. Novoselov, *RSC Adv.* **2018**, *8*, 16815.
- [4] A. A. M. Thiruchitrambalam, A. Athijayamani, N. Venkateshwaran, P. A. Elaya, *Mater. Phys. Mech.* **2009**, *8*, 165.
- [5] N. Karim, S. Afroj, K. Lloyd, L. C. Oaten, D. V. Andreeva, C. Carr, A. D. Farmery, I.-D. Kim, K. S. Novoselov, *ACS Nano* **2020**, *14*, 12313.
- [6] M. A. Uddin, S. Afroj, T. Hasan, C. Carr, K. S. Novoselov, N. Karim, *Adv. Sustainable Syst.* **2022**, *6*, 2100176.
- [7] W. T. Y. Tze, D. J. Gardner, C. P. Tripp, S. C. O'Neill, *J. Adhes. Sci. Technol.* **2006**, *20*, 1649.
- [8] G. R. Arpitha, M. R. Sanjay, P. Senthamaraiannan, C. Barile, B. Yogesha, *Exp. Tech.* **2017**, *41*, 577.
- [9] M. Ashadujjaman, A. Saifullah, D. U. Shah, M. Zhang, M. Akonda, N. Karim, F. Sarker, *Mater. Res. Express* **2021**, *8*, 055503.
- [10] F. M. Al-Oqla, M. S. Salit, in *Materials Selection for Natural Fiber Composites* (Eds: F. M. Al-Oqla, M. S. Salit), Woodhead Publishing, UK **2017**.
- [11] R. B. Baloyi, S. Ncube, M. Moyo, L. Nkiwane, P. Dzingai, *Sci. Rep.* **2021**, *11*, 361.
- [12] F. Sarker, P. Potluri, S. Afroj, V. Koncherry, K. S. Novoselov, N. Karim, *ACS Appl. Mater. Interfaces* **2019**, *11*, 21166.
- [13] F. Sarker, N. Karim, S. Afroj, V. Koncherry, K. S. Novoselov, P. Potluri, *ACS Appl. Mater. Interfaces* **2018**, *10*, 34502.
- [14] M. Ramesh, C. Deepa, L. R. Kumar, M. Sanjay, S. Siengchin, *J. Ind. Text.* **2022**, *51*, 55185.
- [15] A. K. Bledzki, J. Gassan, *Prog. Polym. Sci.* **1999**, *24*, 221.
- [16] A. Vinod, M. R. Sanjay, S. Suchart, P. Jyotishkumar, *J. Cleaner Prod.* **2020**, *258*, 120978.
- [17] I. Shakir Abbood, S. a. Odaa, K. F. Hasan, M. A. Jasim, *Mater. Today: Proc.* **2021**, *43*, 1003.
- [18] O. Adekomaya, T. Jamiru, R. Sadiku, Z. Huan, *J. Reinf. Plast. Compos.* **2016**, *35*, 3.
- [19] H. A. Aisyah, M. T. Paridah, S. M. Sapuan, R. A. Ilyas, A. Khalina, N. M. Nurazzi, S. H. Lee, C. H. Lee, *Polymers* **2021**, *13*, 471.
- [20] M. Y. Khalid, A. Al Rashid, Z. U. Arif, W. Ahmed, H. Arshad, A. A. Zaidi, *Results Eng.* **2021**, *11*, 100263.
- [21] H. M. Saleh, in *Characterizations of Some Composite Materials* (Ed: M. Koller), IntechOpen, UK **2018**.
- [22] P. Priyanka, A. Dixit, H. S. Mali, *Mech. Compos. Mater.* **2017**, *53*, 685.
- [23] M. T. Isa, A. S. Ahmed, B. O. Aderemi, R. M. Taib, I. A. Mohammed-Dabo, *Composites, Part B* **2013**, *52*, 217.
- [24] Vol. 2022, American Composites Manufacturers Association, **2016**.
- [25] <https://www.mar-bal.com/language/en/applications/history-of-composites/>.
- [26] I. D. Ibrahim, T. Jamiru, R. E. Sadiku, W. K. Kupolati, S. C. Agwuncha, G. Ekundayo, *J. Reinf. Plast. Compos.* **2015**, *34*, 1347.
- [27] A. Atmakuri, A. Palevicius, A. Vilkauskas, G. Janusas, *Polymers* **2020**, *12*, 2088.
- [28] N. Boddeti, Y. Tang, K. Maute, D. W. Rosen, M. L. Dunn, *Sci. Rep.* **2020**, *10*, 16507.
- [29] M. Mehdikhani, L. Gorbatikh, I. Verpoest, S. V. Lomov, *J. Compos. Mater.* **2019**, *53*, 1579.
- [30] A. Belarbi, M. Dawood, B. Acun, in *Sustainability of Construction Materials*, 2nd ed. (Ed: J. M. Khatib), Woodhead Publishing, UK **2016**.
- [31] Y. Swolfs, L. Gorbatikh, I. Verpoest, *Composites, Part A* **2014**, *67*, 181.
- [32] L. S. Lee, R. Jain, *Clean Technol. Environ. Policy* **2009**, *11*, 247.
- [33] M. H. Islam, M. R. Islam, M. Dulal, S. Afroj, N. Karim, *iScience* **2021**, *25*, 103597.
- [34] Y. Zhou, M. Fan, L. Chen, *Composites, Part B* **2016**, *101*, 31.
- [35] M. H. Islam, S. Afroj, M. A. Uddin, D. V. Andreeva, K. S. Novoselov, N. Karim, *Adv. Funct. Mater.* **2022**, <https://doi.org/10.1002/adfm.202205723>.
- [36] V. Prasad, M. A. Joseph, K. Sekar, M. Ali, *Mater. Today: Proc.* **2018**, *5*, 24862.
- [37] B. Xiao, Y. Yang, X. Wu, M. Liao, R. Nishida, H. Hamada, *Fibers Polym.* **2015**, *16*, 1759.
- [38] S. Misri, M. R. Ishak, S. M. Sapuan, Z. Leman, in *Manufacturing of Natural Fiber Reinforced Polymer Composites* (Eds: M. S. Salit, M. Jawaid, N. B. Yusoff, M. E. Hoque), Springer International Publishing, Cham **2015**.
- [39] R. Luchoo, L. T. Harper, M. D. Bond, N. A. Warrior, A. Dodworth, *Plast., Rubber Compos.* **2010**, *39*, 216.
- [40] D. M. Corbridge, L. T. Harper, D. S. A. De Focatiis, N. A. Warrior, *Composites, Part A* **2017**, *95*, 87.
- [41] K. Oksman, M. Skrifvars, J. F. Selin, *Compos. Sci. Technol.* **2003**, *63*, 1317.
- [42] J. L. Thomason, *Composites, Part A* **2002**, *33*, 1283.
- [43] K. Van de Velde, P. Kiekens, *Compos. Struct.* **2001**, *54*, 355.
- [44] Z. Sun, J. Xiao, L. Tao, Y. Wei, S. Wang, H. Zhang, S. Zhu, M. Yu, *Materials* **2018**, *12*, 13.
- [45] M. Agwa, S. M. Youssef, S. S. Ali-Eldin, M. Megahed, *J. Ind. Text.* **2020**, *51*, 13.
- [46] M. Elkington, D. Bloom, C. Ward, A. Chatzimichali, K. Potter, *Adv. Manuf.: Polym. Compos. Sci.* **2015**, *1*, 138.

- [47] D. K. Rajak, D. D. Pagar, P. L. Menezes, E. Linul, *Polymers* **2019**, *11*, 1667.
- [48] A. Gunge, P. G. Koppad, M. Nagamathu, S. B. Kivade, K. V. S. Murthy, *Compos. Commun.* **2019**, *13*, 47.
- [49] R. R. P. Kuppusamy, S. Rout, K. Kumar, in *Modern Manufacturing Processes* (Eds: K. Kumar, J. P. Davim), Woodhead Publishing, UK **2020**.
- [50] K. Balasubramanian, M. T. H. Sultan, N. Rajeswari, in *Sustainable Composites for Aerospace Applications* (Eds: M. Jawaid, M. Thariq), Woodhead Publishing, UK **2018**.
- [51] R. Gonzalez Henriquez, P. Mertiny, in *Comprehensive Composite Materials II* (Eds: P. W. R. Beaumont, C. H. Zweben), Elsevier, Oxford **2018**.
- [52] G. D. Shrigandhi, B. S. Kothavale, *Mater. Today: Proc.* **2021**, *42*, 2762.
- [53] C. H. Park, W. I. Lee, in *Manufacturing Techniques for Polymer Matrix Composites (PMCs)* (Eds: S. G. Advani, K.-T. Hsiao), Woodhead Publishing, UK **2012**.
- [54] V. P. Matveenko, N. A. Kosheleva, I. N. Shardakov, A. A. Voronkov, *Int. J. Smart Nano Mater.* **2018**, *9*, 99.
- [55] J. I. P. Singh, S. Singh, V. Dhawan, *J. Nat. Fibers* **2018**, *15*, 687.
- [56] Y. W. Leong, S. Thithanasarn, K. Yamada, H. Hamada, in *Natural Fiber Composites* (Eds: A. Hodzic, R. Shanks), Woodhead Publishing, UK **2014**.
- [57] H. Fu, H. Xu, Y. Liu, Z. Yang, S. Kormakov, D. Wu, J. Sun, *ES Mater. Manuf.* **2020**, *8*, 3.
- [58] P. A. Arrabiyeh, D. May, M. Eckrich, A. M. Dlugaj, *Polym. Compos.* **2021**, *42*, 5630.
- [59] S. M. Moschiar, M. M. Reboredo, H. Larrondo, A. Vazquez, *Polym. Compos.* **1996**, *17*, 850.
- [60] G. D. Goh, Y. L. Yap, S. Agarwala, W. Y. Yeong, *Adv. Mater. Technol.* **2019**, *4*, 1800271.
- [61] N. S. Karaduman, Y. Karaduman, in *Fiber Reinforced Composites* (Eds: K. Joseph, K. Oksman, G. George, R. Wilson, S. Appukuttan), Woodhead Publishing, UK **2021**.
- [62] S. Erden, K. Ho, in *Fiber Technology for Fiber-Reinforced Composites* (Eds: M. Ö. Seydibeyoğlu, A. K. Mohanty, M. Misra), Woodhead Publishing, UK **2017**.
- [63] B. I. Ahmad Nawaz, M. Sadiq Khattak, L. Ali, U. Saleem, A. Ullah, M. Zafar Ijaz, W. Mao, in *Polyester – Production, Characterization and Innovative Applications* (Ed: N. O. Camlibel), IntechOpen, UK **2017**.
- [64] M. Akif Yalcinkaya, G. E. Guloglu, M. Pishvar, M. Amirhosravi, E. Murat Sozer, M. Cengiz Altan, *J. Manuf. Sci. Eng.* **2019**, *141*, 011007.
- [65] L. Sorrentino, E. Anamateros, C. Bellini, L. Carrino, G. Corcione, A. Leone, G. Paris, *Compos. Struct.* **2019**, *220*, 699.
- [66] A. P. Mouritz, in *Introduction to Aerospace Materials*, Woodhead Publishing, UK **2012**.
- [67] J. Frketic, T. Dickens, S. Ramakrishnan, *Addit. Manuf.* **2017**, *14*, 69.
- [68] M. Bannister, *Composites, Part A* **2001**, *32*, 901.
- [69] J. Butlin, *J. Int. Dev.* **1989**, *1*, 284.
- [70] I. Scoones, *Dev. Pract.* **2007**, *17*, 589.
- [71] H. Hanson, *Mater. Technol.* **2001**, *16*, 81.
- [72] C. Cao, in *Advanced High Strength Natural Fiber Composites in Construction* (Eds: M. Fan, F. Fu), Woodhead Publishing, UK **2017**.
- [73] EuCIA, *Composites and Sustainability – the Big Picture*, EuCIA, **2017**.
- [74] SMI COMPOSITES, *Green and Sustainable: Eco-Friendly Composite Materials*.
- [75] K. Friedrich, *Adv. Ind. Eng. Polym. Res.* **2018**, *1*, 3.
- [76] M. Šmelko, M. Spodniak, K. Semrád, P. Tulipán, P. Lipovský, V. Moucha, 2018 XIII Int. Scientific Conf. – New Trends in Aviation Development (NTAD), Curran Associates, Inc., Slovakia **2018**, p. 128.
- [77] O. C. Frank O'Brien-Bernini, *Composites and Sustainability - When Green Becomes Golden* **2011**.
- [78] I. Vajdová, E. Jenčová, S. Szabo Jr., L. Melníková, J. Galanda, M. Dobrowolska, J. Ploch, *Int. J. Environ. Res. Public Health* **2019**, *16*, 4008.
- [79] A. M. Mhatre, A. S. M. Raja, S. Saxena, P. G. Patil, in *Green Composites: Sustainable Raw Materials* (Ed: S. S. Muthu), Springer Singapore, Singapore **2019**.
- [80] M. M. Amar, K. Mohanty, L. T. Drzal, S. E. Selke, B. R. Harte, G. Hinrichsen, in *Natural Fibers, Biopolymers, and Biocomposites* (Eds: M. M. Amar, K. Mohanty, L. T. Drzal), CRC Press, Boca Raton **2005**.
- [81] S. M. Alexander Bismarck, T. Lampke, in *Natural Fibers, Biopolymers, and Biocomposites* (Eds: M. M. Amar, K. Mohanty, L. T. Drzal), CRC Press, Boca Raton **2005**.
- [82] M. Fan, F. Fu, in *Advanced High Strength Natural Fiber Composites in Construction* (Eds: M. Fan, F. Fu), Woodhead Publishing, **2017**.
- [83] M. C. Niels de Beus, M. Barth, M. Carus, **2019**, <http://hempinc.com/wp-content/uploads/2016/01/15-04-Carbon-Footprint-of-Natural-Fibres-nova1.pdf>.
- [84] N. Karim, F. Sarker, S. Afroj, M. Zhang, P. Potluri, K. S. Novoselov, *Adv. Sustainable Syst.* **2021**, *5*, 2000228.
- [85] V. T. Rathod, J. S. Kumar, A. Jain, *Appl. Nanosci.* **2017**, *7*, 519.
- [86] A. C. Jadhav, P. Pandit, T. N. Gayatri, P. P. Chavan, N. C. Jadhav, in *Green Composites: Sustainable Raw Materials* (Ed: S. S. Muthu), Springer Singapore, Singapore **2019**.
- [87] S. K. Sahoo, V. Khandelwal, G. Manik, in *Green Composites: Processing, Characterisation and Applications for Textiles* (Ed: S. S. Muthu), Springer Singapore, Singapore **2019**.
- [88] R. Auvergne, S. Caillol, G. David, B. Boutevin, J.-P. Pascault, *Chem. Rev.* **2014**, *114*, 1082.
- [89] Sustainable Apparel Coalition, Higg Product Tools.
- [90] S. J. Steven Brown, *A Vision and Roadmap for Sustainable Composites* **2019**.
- [91] *Life cycle assessment of CFGF - Continuous Filament Glass Fibre Products*, GlassFibreEurope, Rue Belliard 199, B-1040 Brussels, 2016.
- [92] G. Wernet, C. Bauer, B. Steubing, J. Reinhard, E. Moreno-Ruiz, B. Weidema, *Int. J. Life Cycle Assess.* **2016**, *21*, 1218.
- [93] H. Stiller, *Material Intensity of Advanced Composite Materials: Results of Asudy for the Verbundwerkstofflabor Bremen e.V.* **1999**.
- [94] J. L. Pellegrino, in *Office of Industrial Technologies* (Eds: M. Greenman, M. Gridley, C. P. Ross, D. Wishnick, J. Shell, D. J. McCracken), Energy Efficiency and Renewable Energy, U.S. Department of Energy, Golden, Colorado **2002**.
- [95] A. D. L. Rosa, G. Cozzo, A. Latteri, G. Mancini, A. Recca, G. Cicala, *Chem. Eng. Trans.* **2013**, *32*, 1723.
- [96] T. Suzuki, J. Takahashi, in *The Ninth Japan Int. SAMPE Symp.*, **2005**.
- [97] *Composite Recycling & LCA*, Stuttgart, Germany **2017**.
- [98] G. M. Wood, C. Nelson, E. Poulin, Institute for Advanced Composites Manufacturing Innovation, Knoxville, TN (United States) Composites Recycling Technology Center, Port Angeles, WA (USA), **2020**.
- [99] J. Diener, U. Siehler, *Macromol. Mater. Eng.* **1999**, *272*, 1.
- [100] G. Venkatesh, J. Hammervold, H. Brattebø, *J. Ind. Ecol.* **2009**, *13*, 532.
- [101] EuCIA. ECO IMPACT CALCULATOR for composites.
- [102] J. Haufe, M. Carus, The European Industrial Hemp Association (EiHA).
- [103] S. J. Pickering, *Composites, Part A* **2006**, *37*, 1206.
- [104] V. Kočí, E. Picková, *Pol. J. Environ. Stud.* **2020**, *29*, 653.
- [105] S. Ghasemi, M. P. Sibi, C. A. Ulven, D. C. Webster, G. Pourhashem, *Molecules* **2020**, *25*, 2797.

- [106] J. M. Chard, L. Basson, G. Creech, D. A. Jesson, P. A. Smith, *Sustainability* **2019**, *11*, 1001.
- [107] A. D. La Rosa, G. Recca, J. Summerscales, A. Latteri, G. Cozzo, G. Cicala, *J. Cleaner Prod.* **2014**, *74*, 135.
- [108] Sustainable Epoxy Resin Features bio-based ECH.
- [109] Sustainable Composites- A partnership between the NCC and CPI, Vol. **2022**, National Composite Centre.
- [110] NCCUK, Sustainable Composites.
- [111] S. Luhar, T. Suntharalingam, S. Navaratnam, I. Luhar, J. Thamboo, K. Poologanathan, P. Gatheeshgar, *Sustainability* **2020**, *12*, 10485.
- [112] Y. Sun, J. Cheng, *Bioresour. Technol.* **2002**, *83*, 1.
- [113] A. Thygesen, J. Oddershede, H. Lilholt, A. B. Thomsen, K. Ståhl, *Cellulose* **2005**, *12*, 563.
- [114] A. Thygesen, B. Madsen, A. B. Bjerre, H. Lilholt, *J. Nat. Fibers* **2011**, *8*, 161.
- [115] T.-D. Ngo, in *Natural and Artificial Fiber-Reinforced Composites as Renewable Sources* (Ed: E. Günay), InTechOpen, UK **2017**.
- [116] D. Athith, M. Sanjay, T. Yashas Gowda, P. Madhu, G. Arpitha, B. Yogesha, M. A. Omri, *J. Ind. Text.* **2018**, *48*, 713.
- [117] W. Liu, A. K. Mohanty, L. T. Drzal, M. Misra, *Ind. Eng. Chem. Res.* **2005**, *44*, 7105.
- [118] R. Mahjoub, J. M. Yatim, A. R. Mohd Sam, S. H. Hashemi, *Constr. Build. Mater.* **2014**, *55*, 103.
- [119] P. Manimaran, P. Sentharamaikannan, M. R. Sanjay, M. K. Marichelvam, M. Jawaid, *Carbohydr. Polym.* **2018**, *181*, 650.
- [120] M. R. Sanjay, G. R. Arpitha, P. Sentharamaikannan, M. Kathiresan, M. A. Saibalaji, B. Yogesha, *J. Nat. Fibers* **2019**, *16*, 600.
- [121] M. Jawaid, H. P. S. Abdul Khalil, *Carbohydr. Polym.* **2011**, *86*, 1.
- [122] X. Li, L. G. Tabil, S. Panigrahi, *J. Polym. Environ.* **2007**, *15*, 25.
- [123] A. K. Mohanty, M. Misra, G. Hinrichsen, *Macromol. Mater. Eng.* **2000**, *276*, 1.
- [124] D. N. Saheb, J. P. Jog, *Adv. Polym. Technol.* **1999**, *18*, 351.
- [125] Y. G. Thyavihalli Girijappa, S. Mavinkere Rangappa, J. Parameswaranpillai, S. Siengchin, *Front. Mater.* **2019**, *6*, 226.
- [126] M. Ramesh, K. Palanikumar, K. H. Reddy, *Renewable Sustainable Energy Rev.* **2017**, *79*, 558.
- [127] K. Rohit, S. Dixit, *Polym. Renewable Resour.* **2016**, *7*, 43.
- [128] A. P. More, *Adv. Compos. Hybrid Mater.* **2022**, *5*, 1.
- [129] L. Yan, N. Chouw, K. Jayaraman, *Composites, Part B* **2014**, *56*, 296.
- [130] R. Kochhar, *Ramie: The Ancient Fabric that could Transform Indian Dressing*, **2018**.
- [131] S. Debnath, in *Sustainable Fibers and Textiles* (Ed: S. S. Muthu), Woodhead Publishing, UK **2017**.
- [132] R. Bhoopathi, M. Ramesh, C. Deepa, *Proc. Eng.* **2014**, *97*, 2032.
- [133] S. Réquillé, A. L. Duigou, A. Bourmaud, C. Baley, *Ind. Crops Prod.* **2018**, *123*, 573.
- [134] M. Carus, *The European Hemp Industry: Cultivation, Processing and Applications for Fibres, Shivs, Seeds and Flowers* **2017**.
- [135] J. Müssig, S. Amaducci, A. Bourmaud, J. Beaugrand, D. U. Shah, *Composites, Part C* **2020**, *2*, 100010.
- [136] M. L. Sanyang, S. M. Sapuan, M. Jawaid, M. R. Ishak, J. Sahari, *Renewable Sustainable Energy Rev.* **2016**, *54*, 533.
- [137] J. Summerscales, N. P. J. Dissanayake, A. S. Virk, W. Hall, *Composites, Part A* **2010**, *41*, 1329.
- [138] L. Mohammed, M. N. M. Ansari, G. Pua, M. Jawaid, M. S. Islam, *Int. J. Polym. Sci.* **2015**, *2015*, 243947.
- [139] S. Z. Rogovina, E. V. Prut, A. A. Berlin, *Polym. Sci., Ser. A* **2019**, *61*, 417.
- [140] B. B. Mansingh, J. S. Binoj, N. Manikandan, N. P. Sai, S. Siengchin, S. Mavinkere Rangappa, K. N. Bharath, S. Indran, in *Plant Fibers, their Composites, and Applications* (Eds: S. Mavinkere Rangappa, J. Parameswaranpillai, S. Siengchin, T. Ozbakkaloglu, H. Wang), Woodhead Publishing, UK **2022**.
- [141] S. Gnanasekaran, S. Ayyappan, *Asian J. Eng. Appl. Technol.* **2018**, *7*, 110.
- [142] P. Sahu, M. K. Gupta, *J. Reinf. Plast. Compos.* **2017**, *36*, 1759.
- [143] K. Senthilkumar, N. Saba, N. Rajini, M. Chandrasekar, M. Jawaid, S. Siengchin, O. Y. Alotman, *Constr. Build. Mater.* **2018**, *174*, 713.
- [144] S. H. S. M. Fadzullah, M. Zaleha, in *Green Approaches to Bio-composite Materials Science and Engineering* (Eds: V. Deepak, J. Siddharth, Z. Xiaolei, G. Prakash Chandra), IGI Global, Hershey, PA, USA **2016**.
- [145] M. Asim, K. Abdan, M. Jawaid, M. Nasir, Z. Dashtizadeh, M. R. Ishak, M. E. Hoque, *Int. J. Polym. Sci.* **2015**, *2015*, 950567.
- [146] A. Kaur, Banana Fibre: A revolution in textiles, fibre2fashio.com, **2015**.
- [147] V. Hendriksz, Sustainable Textile Innovations: Banana Fibres, Fashion United, **2017**.
- [148] P. Zakikhani, R. Zahari, M. T. H. Sultan, D. L. Majid, *Mater. Des.* **2014**, *63*, 820.
- [149] G. Wang, F. Chen, in *Advanced High Strength Natural Fiber Composites in Construction* (Eds: M. Fan, F. Fu), Woodhead Publishing, **2017**.
- [150] D. U. Shah, B. Sharma, M. H. Ramage, *Int. J. Adhes. Adhes.* **2018**, *85*, 15.
- [151] S. A. H. Roslan, Z. A. Rasid, M. Z. Hassan, *IOP Conf. Ser.: Mater. Sci. Eng.* **2018**, *344*, 012008.
- [152] P. Lokes, T. S. A. Surya Kumari, R. Gopi, G. Babu Loganathan, *Mater. Today: Proc.* **2020**, *22*, 897.
- [153] S. R. Mousavi, M. H. Zamani, S. Estaji, M. I. Tayouri, M. Arjmand, S. H. Jafari, S. Nouranian, H. A. Khonakdar, *J. Mater. Sci.* **2022**, *57*, 3143.
- [154] D. R. A. Jain, B. Chanana, *Int. J. Appl. Home Sci.* **2016**, *2*, 313.
- [155] J. Prachayawarakorn, S. Chaiwatyothin, S. Mueangta, A. Hanchana, *Mater. Des.* **2013**, *47*, 309.
- [156] A. N. Oumer, O. Mamat, *Asian J. Sci. Res.* **2013**, *6*, 401.
- [157] G. K. Mani, J. B. B. Rayappan, D. K. Bisoyi, *J. Appl. Sci.* **2012**, *12*, 1661.
- [158] R. H. Sangalang, *Orient. J. Chem.* **2021**, *37*, 513.
- [159] A. Alawar, A. M. Hamed, K. Al-Kaabi, *Composites, Part B* **2009**, *40*, 601.
- [160] M. Bassyouni, S. Waheed Ul Hasan, in *Biofiber Reinforcements in Composite Materials* (Eds: O. Faruk, M. Sain), Woodhead Publishing, UK **2015**.
- [161] T. C. Mokhena, M. J. Mochane, T. E. Motaung, L. Z. Linganisio, O. M. Thekisoe, S. P. Songca, in *Sugarcane – Technology and Research* (Ed: A. B. d. Oliveira), IntechOpen, UK **2017**.
- [162] M. A. Mahmud, F. R. Anannya, *Heliyon* **2021**, *7*, e07771.
- [163] D. G. Devadiga, K. S. Bhat, G. T. Mahesha, *Cogent Eng.* **2020**, *7*, 1823159.
- [164] Z. Chen, Z. Chen, J. Yi, D. Feng, *Sustainability* **2019**, *11*, 4050.
- [165] T. X. Liu DeJun, G. LianXing, *J. Shenyang Agric. Univ.* **2009**, *40*, 740.
- [166] N. F. S. Mission, *A Status Note on Rice in India*, Ministry of Agriculture & Farmers Welfare, Government of India, **2016**.
- [167] P. Jagadeesh, M. Puttegowda, P. Boonyasopon, S. M. Rangappa, A. Khan, S. Siengchin, *Polym. Compos.* **2022**, *43*, 2545.
- [168] S. K. Mazumdar, *Composites Manufacturing Materials, Product, and Process Engineering*, CRC Press, USA **2001**.
- [169] W. D. Callister Jr., D. G. Rethwisch, *Fundamentals of Materials Science and Engineering: An Integrated Approach*, Wiley, USA **2018**.
- [170] R. Latif, S. Wakeel, N. Zaman Khan, A. Noor Siddiquee, S. Lal Verma, Z. Akhtar Khan, *J. Reinf. Plast. Compos.* **2019**, *38*, 15.
- [171] T. G. Yashas Gowda, M. R. Sanjay, K. Subrahmanya Bhat, P. Madhu, P. Sentharamaikannan, B. Yogesha, *Cogent Eng.* **2018**, *5*, 1446667.
- [172] M.-Y. Lyu, T. G. Choi, *Int. J. Precis. Eng. Manuf.* **2015**, *16*, 213.
- [173] M. R. Rahman, N.-A. A. B. Taib, M. K. B. Bakri, S. N. L. Taib, in *Advances in Sustainable Polymer Composites* (Ed: M. R. Rahman), Woodhead Publishing, UK **2021**.

- [174] Y. Gao, P. romero, H. Zhang, M. Huang, F. Lai, *Constr. Build. Mater.* **2019**, 228, 116709.
- [175] F. I. Chowdhury, in *Advances in Sustainable Polymer Composites* (Ed: M. R. Rahman), Woodhead Publishing, UK **2021**.
- [176] H. P. S. AK, C. K. Saurabh, M. Asniza, Y. Y. Tye, M. R. Nurul Fazita, M. I. Syakir, H. M. Fizree, A. F. I. Yusra, M. K. M. Haafiz, M. A. Kassim, N. L. M. Suraya, in *Cellulose-Reinforced Nanofibre Composites* (Eds: M. Jawaid, S. Boufi, H.P.S AK), Woodhead Publishing, UK **2017**.
- [177] S.-H. Lee, Y. Teramoto, N. Shiraiishi, *J. Appl. Polym. Sci.* **2002**, 84, 468.
- [178] N. Gupta, R. Ye, M. Porfiri, *Composites, Part B* **2010**, 41, 236.
- [179] J. Ryzd, W. Sikorska, M. Kyulavska, D. Christova, *Int. J. Mol. Sci.* **2014**, 16, 564.
- [180] K. Amulya, R. Katakajwala, S. Ramakrishna, S. Venkata Mohan, *Composites, Part C* **2021**, 4, 100111.
- [181] V. Mahesh, S. Joladarashi, S. M. Kulkarni, *Def. Technol.* **2021**, 17, 257.
- [182] R. D. S. G. Campilho, *Natural Fiber Composites*, 1st ed., CRC Press, USA **2016**.
- [183] O. Faruk, A. K. Bledzki, H.-P. Fink, M. Sain, *Prog. Polym. Sci.* **2012**, 37, 1552.
- [184] D. Ratna, in *Recent Advances and Applications of Thermoset Resins*, 2nd ed. (Ed: D. Ratna), Elsevier, Netherlands **2022**.
- [185] V. Fiore, A. Valenza, in *Advanced Fiber-Reinforced Polymer (FRP) Composites for Structural Applications* (Ed: J. Bai), Woodhead Publishing, UK **2013**.
- [186] H. Ren, J. Sun, Q. Zhao, Q. Zhou, Q. Ling, *Polymer* **2008**, 49, 5249.
- [187] J. L. Vilas, J. M. Laza, M. T. Garay, M. Rodríguez, L. M. León, *J. Polym. Sci., Part B: Polym. Phys.* **2001**, 39, 146.
- [188] L. U. Devi, S. S. Bhagawan, S. Thomas, *J. Appl. Polym. Sci.* **1997**, 64, 1739.
- [189] L. Henke, N. Zarrinbakhsh, H.-J. Endres, M. Misra, A. K. Mohanty, *J. Polym. Environ.* **2017**, 25, 499.
- [190] M. Cunha, M.-A. Berthet, R. Pereira, J. A. Covas, A. A. Vicente, L. Hilliou, *Polym. Compos.* **2015**, 36, 1859.
- [191] I. Kellersztein, E. Amir, A. Dotan, *Polym. Adv. Technol.* **2016**, 27, 657.
- [192] X. Zhang, M. Fevre, G. O. Jones, R. M. Waymouth, *Chem. Rev.* **2018**, 118, 839.
- [193] M. Venkateswar Reddy, S. Venkata Mohan, *Bioresour. Technol.* **2012**, 114, 573.
- [194] V. Srebrnkoska, G. Bogojeva-Gaceva, D. Dimeski, *Qual. Life* **2017**, <https://doi.org/10.7251/QOL1002139S>.
- [195] J. P. Stefan, L. Bo, Q. Bing, *Novel Agents for Reworkable Epoxy Resins*, **2011**.
- [196] Q. Bing, L. Xin, L. Bo, *Novel Curing Agents and Degradable Polymers and Composites based Thereon*, **2014**.
- [197] *PlasticsNet*, **2014**.
- [198] T. Liu, X. Guo, W. Liu, C. Hao, L. Wang, W. C. Hiscox, C. Liu, C. Jin, J. Xin, J. Zhang, *Green Chem.* **2017**, 19, 4364.
- [199] T. Liu, C. Hao, L. Wang, Y. Li, W. Liu, J. Xin, J. Zhang, *Macromolecules* **2017**, 50, 8588.
- [200] W. A. Ogden, Z. Guan, *J. Am. Chem. Soc.* **2018**, 140, 6217.
- [201] D. J. Fortman, J. P. Brutman, G. X. De Hoe, R. L. Snyder, W. R. Dichtel, M. A. Hillmyer, *ACS Sustainable Chem. Eng.* **2018**, 6, 11145.
- [202] R. Kaminker, E. B. Callaway, N. D. Dolinski, S. M. Barbon, M. Shibata, H. Wang, J. Hu, C. J. Hawker, *Chem. Mater.* **2018**, 30, 8352.
- [203] E. Sinha, S. Panigrahi, *J. Compos. Mater.* **2009**, 43, 1791.
- [204] M. Chandrasekar, M. R. Ishak, S. M. Sapuan, Z. Leman, M. Jawaid, *Plast., Rubber Compos.* **2017**, 46, 119.
- [205] K. Sever, S. Erden, H. A. Gülec, Y. Seki, M. Sarikanat, *Mater. Chem. Phys.* **2011**, 129, 275.
- [206] M. Sood, G. Dwivedi, *Egypt. J. Pet.* **2018**, 27, 775.
- [207] V. K. Shrivasthabelagola Nagaraja Setty, G. Goud, S. Peramanahalli Chikkegowda, S. Mavinkere Rangappa, S. Siengchin, *J. Nat. Fibers* **2020**.
- [208] K. F. Anna Dilfi, A. Balan, H. Bin, G. Xian, S. Thomas, *Polym. Compos.* **2018**, 39, E2519.
- [209] N. Gibeop, D. W. Lee, C. V. Prasad, F. Toru, B. S. Kim, J. I. Song, *Adv. Compos. Mater.* **2013**, 22, 389.
- [210] G. Rajesh, A. V. R. Prasad, *Procedia Mater. Sci.* **2014**, 5, 2188.
- [211] L. Y. Mwaikambo, M. P. Ansell, *Macromol. Mater. Eng.* **1999**, 272, 108.
- [212] F. H. Gojny, M. H. G. Wichmann, B. Fiedler, W. Bauhofer, K. Schulte, *Composites, Part A* **2005**, 36, 1525.
- [213] X. Shen, J. Jia, C. Chen, Y. Li, J.-K. Kim, *J. Mater. Sci.* **2014**, 49, 3225.
- [214] M. J. Islam, M. J. Rahman, T. Mieno, *Adv. Compos. Hybrid Mater.* **2020**, 3, 285.
- [215] R.-C. Zhuang, T. T. L. Doan, J.-W. Liu, J. Zhang, S.-L. Gao, E. Mäder, *Carbon* **2011**, 49, 2683.
- [216] J. Saiteja, V. Jayakumar, G. Bharathiraja, *Mater. Today: Proc.* **2020**, 22, 756.
- [217] S. Afroj, L. Britnell, T. Hasan, D. V. Andreeva, K. S. Novoselov, N. Karim, *Adv. Funct. Mater.* **2021**, 31, 2107407.
- [218] N. Karim, S. Afroj, S. Tan, P. He, A. Fernando, C. Carr, K. S. Novoselov, *ACS Nano* **2017**, 11, 12266.
- [219] S. Afroj, N. Karim, Z. Wang, S. Tan, P. He, M. Holwill, D. Ghazaryan, A. Fernando, K. S. Novoselov, *ACS Nano* **2019**, 13, 3847.
- [220] S. Afroj, M. H. Islam, N. Karim, *Proceedings* **2021**, 68, 11.
- [221] M. R. Islam, S. Afroj, C. Beach, M. H. Islam, C. Parraman, A. Abdelkader, A. J. Casson, K. S. Novoselov, N. Karim, *iScience* **2022**, 25, 103945.
- [222] S. Afroj, S. Tan, A. M. Abdelkader, K. S. Novoselov, N. Karim, *Adv. Funct. Mater.* **2020**, 30, 2000293.
- [223] S. Bhattacharjee, C. R. Macintyre, P. Bahl, U. Kumar, X. Wen, K.-F. Aguey-Zinsou, A. A. Chughtai, R. Joshi, *Adv. Mater. Interfaces* **2020**, 7, 2000814.
- [224] N. Karim, S. Afroj, D. Leech, A. M. Abdelkader, in *Oxide Electronics* (Ed: A. Ray), John Wiley & Sons, Ltd, USA **2021**, p. 2.
- [225] T. Ganapathy, R. Sathiskumar, M. R. Sanjay, P. Senthamarikannan, S. S. Saravanakumar, J. Parameswaranpillai, S. Siengchin, *J. Nat. Fibers* **2021**, 18, 1029.
- [226] A. Amjad, A. Anjang Ab Rahman, H. Awais, M. S. Zainol Abidin, J. Khan, *J. Ind. Text.* **2021**, 51, 65S.
- [227] F. H. Gojny, M. H. G. Wichmann, U. Köpke, B. Fiedler, K. Schulte, *Compos. Sci. Technol.* **2004**, 64, 2363.
- [228] U. O. Costa, L. F. C. Nascimento, J. M. Garcia, W. B. A. Bezerra, G. F. Fabio da Costa, F. S. da Luz, W. A. Pinheiro, S. N. Monteiro, *J. Mater. Res. Technol.* **2020**, 9, 13390.
- [229] M. Hemath, S. Mavinkere Rangappa, V. Kushvaha, H. N. Dhakal, S. Siengchin, *Polym. Compos.* **2020**, 41, 3940.
- [230] S. S. Vinay, M. R. Sanjay, S. Siengchin, C. V. Venkatesh, *Polym. Compos.* **2021**, 42, 1727.
- [231] V. Prasad, D. Suresh, M. A. Joseph, K. Sekar, M. Ali, *Mater. Today: Proc.* **2018**, 5, 11569.
- [232] P. A. Prasob, M. Sasikumar, *Polym. Test.* **2018**, 69, 52.
- [233] M. J. Suriani, R. A. Ilyas, M. Y. M. Zuhri, A. Khalina, M. T. H. Sultan, S. M. Sapuan, C. M. Ruzaidi, F. N. Wan, F. Zulkifli, M. M. Harussani, M. A. Azman, F. S. M. Radzi, S. Sharma, *Polymers* **2021**, 13, 3514.
- [234] S. Y. Nayak, S. Shenoy, M. T. Hameed Sultan, C. R. Kini, A. Seth, S. Prabhu, S. N. A. Safri, *Front. Mater.* **2021**, 7, 609010.
- [235] A. Afzaluddin, M. Jawaid, M. S. Salit, M. R. Ishak, *J. Mater. Res. Technol.* **2019**, 8, 950.
- [236] A. Atiqah, M. A. Maleque, M. Jawaid, M. Iqbal, *Composites, Part B* **2014**, 56, 68.

- [237] R. Yahaya, S. M. Sapuan, M. Jawaid, Z. Leman, E. S. Zainudin, *Adv. Compos. Lett.* **2016**, 25, 096369351602500.
- [238] H. P. S. A. Khalil, S. Hanida, C. W. Kang, N. A. N. Fuaad, *J. Reinf. Plast. Compos.* **2007**, 26, 203.
- [239] P. Venkata Deepthi, K. Sita Rama Raju, M. I. Reddy, *Mater. Today: Proc.* **2019**, 18, 2114.
- [240] M. M. Thwe, K. Liao, *J. Mater. Sci.* **2003**, 38, 363.
- [241] V. Chaudhary, P. K. Bajpai, S. Maheshwari, *J. Nat. Fibers* **2018**, 15, 80.
- [242] M. V. Ramana, S. Ramprasad, *Mater. Today: Proc.* **2017**, 4, 8654.
- [243] M. Ramesh, C. Deepa, G. R. Arpitha, V. Gopinath, *World J. Eng.* **2019**, 16, 248.
- [244] A. Paturel, H. N. Dhakal, *Molecules* **2020**, 25, 278.
- [245] R. Giridharan, *Composites, Part B* **2019**, 167, 342.
- [246] M. Aslan, M. Tufan, T. Küçükömeroğlu, *Composites, Part B* **2018**, 140, 241.
- [247] P. Noorunnisa Khanam, H. P. S. Abdul Khalil, M. Jawaid, G. Ramachandra Reddy, C. Surya Narayana, S. Venkata Naidu, *J. Polym. Environ.* **2010**, 18, 727.
- [248] L. X. Zhong, S. Y. Fu, X. S. Zhou, H. Y. Zhan, *Composites, Part A* **2011**, 42, 244.
- [249] N. Vellguth, M. Shamsuyeva, H.-J. Endres, F. Renz, *Composites, Part C* **2021**, 6, 100198.
- [250] M. Shamsuyeva, B. P. Chang, N. Vellguth, M. Misra, A. Mohanty, H.-J. Endres, *J. Compos. Sci.* **2020**, 4, 64.
- [251] A. K. Mohanty, M. Misra, L. T. Drzal, *Compos. Interfaces* **2001**, 8, 313.
- [252] Ankit, M. Rinawa, P. Chauhan, D. Suresh, S. Kumar, R. Santhosh Kumar, *Mater. Today: Proc.* **2021**.
- [253] C. Elanchezhian, B. V. Ramnath, G. Ramakrishnan, M. Rajendrakumar, V. Naveenkumar, M. K. Saravanakumar, *Mater. Today: Proc.* **2018**, 5, 1785.
- [254] K. P. Ashik, R. S. Sharma, *J. Miner. Mater. Charact. Eng.* **2015**, 3, 420.
- [255] P. V. Joseph, K. Joseph, S. Thomas, *Compos. Sci. Technol.* **1999**, 59, 1625.
- [256] H. Peltola, B. Madsen, R. Joffe, K. Nättinen, *J. Mater. Sci. Eng. A* **2011**, 1, 190.
- [257] J. Holbery, D. Houston, *JOM* **2006**, 58, 80.
- [258] C. H. Lee, A. Khalina, S. H. Lee, *Polymers* **2021**, 13, 438.
- [259] K. L. Pickering, M. G. A. Efendy, T. M. Le, *Composites, Part A* **2016**, 83, 98.
- [260] M. Feldmann, H. P. Heim, J. C. Zarges, *Composites, Part A* **2016**, 83, 113.
- [261] R. Malkapuram, V. Kumar, Y. S. Negi, *J. Reinf. Plast. Compos.* **2009**, 28, 1169.
- [262] N. Srinivasababu, K. M. M. Rao, J. Suresh kumar, *Int. J. Eng.* **2009**, 3, 403.
- [263] J. Santhosh, N. Balanarasimman, R. Chandrasekar, S. Raja, *Int. J. Res. Eng. Technol.* **2014**, 3, 144.
- [264] D. Kumar, *Int. J. Adv. Mech. Eng.* **2014**, 4, 551.
- [265] S. G. C. G. Rangasrinivas, *Int. J. Mod. Eng. Res.* **2012**, 2, 471.
- [266] H. Ku, H. Wang, N. Pattarachaiyakoop, M. Trada, *Composites, Part B* **2011**, 42, 856.
- [267] C. R. Bowen, A. C. E. Dent, R. Stevens, M. G. Cain, M. Stewart, *Multi-Mater. Micro Manuf.* **2005**.
- [268] M. Z. Khan, S. K. Srivastava, M. Gupta, *J. Reinf. Plast. Compos.* **2018**, 37, 1435.
- [269] B. T. Węclawski, M. Fan, D. Hui, *Composites, Part B* **2014**, 67, 183.
- [270] V. Afroughsabet, T. Ozbakkaloglu, *Constr. Build. Mater.* **2015**, 94, 73.
- [271] M. Ismail, *AL Rafdain Eng. J.* **2007**, 15, 42.
- [272] N. G. Ozerkan, B. Ahsan, S. Mansour, S. R. Iyengar, *Int. J. Sustainable Built Environ.* **2013**, 2, 131.
- [273] J. George, M. S. Sreekala, S. Thomas, *Polym. Eng. Sci.* **2001**, 41, 1471.
- [274] J. Gassan, *Composites, Part A* **2002**, 33, 369.
- [275] L. Y. Mwaikambo, M. P. Ansell, *J. Appl. Polym. Sci.* **2002**, 84, 2222.
- [276] L. Lundquist, B. Marque, P. O. Hagstrand, Y. Leterrier, J. A. E. Månson, *Compos. Sci. Technol.* **2003**, 63, 137.
- [277] M. Zampaloni, F. Pourboghrat, S. A. Yankovich, B. N. Rodgers, J. Moore, L. T. Drzal, A. K. Mohanty, M. Misra, *Composites, Part A* **2007**, 38, 1569.
- [278] K. V. Ramanaiah, K. Hema, C. Reddy, *J. Mater. Environ. Sci.* **2012**.
- [279] M. S. Sreekala, J. George, M. G. Kumaran, S. Thomas, *Compos. Sci. Technol.* **2002**, 62, 339.
- [280] E. Omrani, P. L. Menezes, P. K. Rohatgi, *Eng., Sci. Technol., Int. J.* **2016**, 19, 717.
- [281] C. Wei, M. Zeng, X. Xiong, H. Liu, K. Luo, T. Liu, *Polym. Compos.* **2015**, 36, 433.
- [282] P. L. Menezes, C. J. Reeves, M. R. Lovell, in *Tribology for Scientists and Engineers: From Basics to Advanced Concepts* (Eds: P. L. Menezes, M. Nosonovsky, S. P. Ingole, S. V. Kailas, M. R. Lovell), Springer New York, New York, NY **2013**.
- [283] C. W. Chin, B. F. Yousif, *Wear* **2009**, 267, 1550.
- [284] I. Mutlu, *J. Appl. Sci.* **2009**, 9, 377.
- [285] N. S. M. El-Tayeb, *Wear* **2008**, 265, 223.
- [286] A. U. R. Shah, M. N. Prabhakar, J.-I. Song, *Int. J. Precis. Eng. Manuf.-Green Technol.* **2017**, 4, 247.
- [287] R. Sonnier, A. Taguet, L. Ferry, J.-M. Lopez-Cuesta, in *Towards Bio-based Flame Retardant Polymers* (Eds: R. Sonnier, A. Taguet, L. Ferry, J.-M. Lopez-Cuesta), Springer International Publishing, Cham **2018**.
- [288] M. Sain, S. H. Park, F. Suhara, S. Law, *Polym. Degrad. Stab.* **2004**, 83, 363.
- [289] A. Alhuthali, I. M. Low, C. Dong, *Composites, Part B* **2012**, 43, 2772.
- [290] Z. N. Azwa, B. F. Yousif, A. C. Manalo, W. Karunasena, *Mater. Des.* **2013**, 47, 424.
- [291] R. Jeencham, N. Suppakarn, K. Jarukumjorn, *Composites, Part B* **2014**, 56, 249.
- [292] A. Subasinghe, D. Bhattacharyya, *Composites, Part A* **2014**, 65, 91.
- [293] A. A. Younis, *Egypt. J. Pet.* **2016**, 25, 161.
- [294] Protolabs, UL 94 Classification and Flame-Retardant Thermoplastics, Vol. 2022, Protolabs, **2019**.
- [295] F. O. Bakare, S. K. Ramamoorthy, D. Åkesson, M. Skrifvars, *Composites, Part A* **2016**, 83, 176.
- [296] V. S. Srinivasan, S. Rajendra Boopathy, D. Sangeetha, B. Vijaya Ramnath, *Mater. Des.* **2014**, 60, 620.
- [297] J.-M. Yuan, Y.-R. Feng, L.-P. He, *Polym. Degrad. Stab.* **2016**, 133, 303.
- [298] J. Yang, H. Wu, S. He, M. Wang, *J. Porous Media* **2015**, 18, 971.
- [299] S. Pujari, A. Ramakrishna, K. T. Balaram Padal, *J. Inst. Eng. (India): Ser. D* **2017**, 98, 79.
- [300] X. Li, L. G. Tabil, I. N. Oguocha, S. Panigrahi, *Compos. Sci. Technol.* **2008**, 68, 1753.
- [301] R. Agrawal, N. S. Saxena, M. S. Sreekala, S. Thomas, *J. Polym. Sci., Part B: Polym. Phys.* **2000**, 38, 916.
- [302] V. G. Geethamma, R. Asaetha, N. Kalarikkal, S. Thomas, *Resonance* **2014**, 19, 821.
- [303] D. Halperin, *Sleep Sci.* **2014**, 7, 209.
- [304] I. M. De Rosa, C. Santulli, F. Sarasini, *Composites, Part A* **2009**, 40, 1456.
- [305] S. H. Hanipah, M. A. P. Mohammed, A. S. Baharuddin, *Compos. Interfaces* **2016**, 23, 37.
- [306] M. Rajesh, J. Pitchaimani, N. Rajini, *Proc. Eng.* **2016**, 144, 1055.
- [307] F. Duc, P. E. Bourban, J. A. E. Månson, *Compos. Sci. Technol.* **2014**, 102, 94.
- [308] N. Chand, A. Nigrawal, D. Jain, *J. Nat. Fibers* **2008**, 5, 270.
- [309] D. S. D. Pathania, *Int. J. Theor. Appl. Sci.* **2009**, 1, 34.

- [310] S. Joseph, S. Thomas, *J. Appl. Polym. Sci.* **2008**, *109*, 256.
- [311] M. S. Sreekala, S. Thomas, *Compos. Sci. Technol.* **2003**, *63*, 861.
- [312] M. J. John, S. Thomas, *Carbohydr. Polym.* **2008**, *71*, 343.
- [313] M. H. Ab Ghani, S. Ahmad, *Adv. Mater. Sci. Eng.* **2011**, *2011*, 406284.
- [314] Y. Cao, S. Shibata, I. Fukumoto, *Composites, Part A* **2006**, *37*, 423.
- [315] S. Rwaiire, B. Tomkova, J. Militky, L. Hes, B. M. Kale, *Appl. Acoust.* **2017**, *116*, 177.
- [316] Y.-Y. Wang, Y.-F. Shih, *J. Taiwan Inst. Chem. Eng.* **2016**, *65*, 452.
- [317] M. Duhovic, S. Peterson, K. Jayaraman, in *Properties and Performance of Natural-Fibre Composites* (Ed: K. L. Pickering), Woodhead Publishing, UK **2008**.
- [318] A. Gholampour, T. Ozbakkaloglu, *J. Mater. Sci.* **2020**, *55*, 829.
- [319] *Natural Fibers, Biopolymers, and Biocomposites* (Eds: M. M. Amar, K. Mohanty, L. T. Drzal), CRC Press, Boca Raton **2005**.
- [320] M. Li, Y. Pu, V. M. Thomas, C. G. Yoo, S. Ozcan, Y. Deng, K. Nelson, A. J. Ragauskas, *Composites, Part B* **2020**, *200*, 108254.
- [321] S. Syath Abuthakeer, R. Vasudaa, A. Nizamudeen, *App. Mech. Mater.* **2017**, *854*, 59.
- [322] R. Dunne, D. Desai, R. Sadiku, J. Jayaramudu, *J. Reinf. Plast. Compos.* **2016**, *35*, 1041.
- [323] M. K. Huda, I. Widiastuti, *J. Phys.: Conf. Ser.* **2021**, *1808*, 012015.
- [324] M. Mostafa, N. Uddin, *Case Stud. Constr. Mater.* **2016**, *5*, 53.
- [325] S. R. Ferreira, M. Pepe, E. Martinelli, F. de Andrade Silva, R. D. Toledo Filho, *Composites, Part B* **2018**, *140*, 183.
- [326] K. Zhao, S. Xue, P. Zhang, Y. Tian, P. Li, *Materials* **2019**, *12*, 3498.
- [327] O. A. Cevallos, R. S. Olivito, R. Codispoti, L. Ombres, *Composites, Part B* **2015**, *71*, 82.
- [328] R. Gopinath, R. Poopathi, S. S. Saravanakumar, *Adv. Compos. Hybrid Mater.* **2019**, *2*, 115.
- [329] E. U. Akubueze, C. S. Ezeanyanoso, S. O. Muniru, C. C. Igwe, G. O. Nwauzor, U. Ugoh, I. O. Nwaze, O. Mafe, F. C. Nwaeche, *Curr. J. Appl. Sci. Technol.* **2019**, *36*, 1.
- [330] C. Rojas, M. Cea, A. Iriarte, G. Valdés, R. Navia, J. P. Cárdenas-R, *Sustainable Mater. Technol.* **2019**, *20*, e00102.
- [331] D. Bottino-Leone, M. Larcher, D. Herrera-Avellanosa, F. Haas, A. Troi, *Energy* **2019**, *181*, 521.
- [332] H. Dahy, *Sensors* **2019**, *19*, 738.
- [333] L. Kohan, C. R. Martins, L. Oliveira Duarte, L. Pinheiro, J. Baruaque-Ramos, *SN Appl. Sci.* **2019**, *1*, 895.
- [334] M. Carus, L. Dammer, K. Iffland, S. Piotrowski, L. Sarmento, R. Chinthapalli, A. Raschka, *Current situation and trends of the bio-based industries in Europe with a focus on bio-based materials: pilot study for BBI JU*, Nova-Institute, Hürth, Germany **2017**.
- [335] A. Amiri, T. Krosbakken, W. Schoen, D. Theisen, C. A. Ulven, *Proc. Inst. Mech. Eng., Part P* **2018**, *232*, 28.
- [336] G. M. Zakriya, G. Ramakrishnan GR, D. Abinaya, S. Brundha Devi, A. Senthil Kumar, S. Theyva Kumar, *J. Ind. Text.* **2016**, *47*, 781.
- [337] B. Bharath, G. C. Kumar, G. Shivanna, S. S. Hussain, B. Chandrashekar, B. A. S. Raj, S. A. Kumar, C. Girisha, *Mater. Today: Proc.* **2018**, *5*, 2716.
- [338] S. Jambari, M. Y. Yahya, M. R. Abdullah, M. Jawaid, *Fibers Polym.* **2017**, *18*, 563.
- [339] R. Yahaya, S. M. Sapuan, M. Jawaid, Z. Leman, E. S. Zainudin, *Measurement* **2016**, *77*, 335.
- [340] A. FauziF, Z. Ghazalli, J. P. Siregar, T. Zahari, K. Kadirgama, J. N. Hadi, *Adv. Environ. Biol.* **2015**.
- [341] E. M. Yusup, S. Mahzan, M. A. H. Kamaruddin, *IOP Conf. Ser.: Mater. Sci. Eng.* **2019**, *494*, 012040.
- [342] C. Scarponi, M. Messano, *Composites, Part B* **2015**, *69*, 542.
- [343] D. K. Rajak, D. D. Pagar, P. L. Menezes, E. Linul, *Polymers* **2019**, *11*, 1667.
- [344] T. D. Tavares, J. C. Antunes, F. Ferreira, H. P. Felgueiras, *Biomolecules* **2020**, *10*, 148.
- [345] S. Kumar, D. Zindani, S. Bhowmik, *J. Mater. Eng. Perform.* **2020**, *29*, 3161.
- [346] F. Sarasini, J. Tirillò, D. Puglia, J. M. Kenny, F. Dominici, C. Santulli, M. Tofani, R. De Santis, *RSC Adv.* **2015**, *5*, 23798.
- [347] M. R. Nurul Fazita, K. Jayaraman, D. Bhattacharyya, M. K. Mohamad Haafiz, C. K. Saurabh, M. H. Hussin, H. P. S. Abdul Khalil, *Materials* **2016**, *9*, 435.
- [348] H. B. Bhuvanewari, D. L. Vinayaka, M. Ilangovan, N. Reddy, *J. Mater. Sci.: Mater. Electron.* **2017**, *28*, 12383.
- [349] H. B. Bhuvanewari, N. Reddy, *Adv. Compos. Hybrid Mater.* **2018**, *1*, 635.
- [350] Y. Zhang, T. Mao, H. Wu, L. Cheng, L. Zheng, *Adv. Mater. Interfaces* **2017**, *4*, 1601123.
- [351] G. R. Kalagi, R. Patil, N. Nayak, *Mater. Today: Proc.* **2018**, *5*, 2588.
- [352] L. Calabrese, V. Fiore, T. Scalici, A. Valenza, *J. Appl. Polym. Sci.* **2019**, *136*, 47203.
- [353] M. Seggiani, P. Cinelli, N. Mallegni, E. Balestri, M. Puccini, S. Vitolo, C. Lardicci, A. Lazzeri, *Materials* **2017**, *10*, 326.
- [354] K. S. Reddy, H. Singla, *IOP Conf. Ser.: Mater. Sci. Eng.* **2017**, *222*, 012016.
- [355] C. Xia, H. Ren, S. Q. Shi, H. Zhang, J. Cheng, L. Cai, K. Chen, H.-S. Tan, *Appl. Surf. Sci.* **2016**, *362*, 335.
- [356] C. Xia, J. Yu, S. Q. Shi, Y. Qiu, L. Cai, H. F. Wu, H. Ren, X. Nie, H. Zhang, *Composites, Part B* **2017**, *114*, 121.
- [357] H. Yuan, F. Wang, S. Li, Z. Lin, J. Huang, *New J. Chem.* **2020**, *44*, 1846.
- [358] B. P. Mooney, *Biochem. J.* **2009**, *418*, 219.
- [359] R. Ryntz, S. Kozora, in *Green Chemistry in Government and Industry* (Eds: B. M. Anthony, P. Heinz), De Gruyter, Germany **2020**.
- [360] P. Peças, H. Carvalho, H. Salman, M. Leite, *J. Compos. Sci.* **2018**, *2*, 66.
- [361] O. Akampumuza, P. M. Wambua, A. Ahmed, W. Li, X.-H. Qin, *Polym. Compos.* **2017**, *38*, 2553.
- [362] C. Andresen, C. Demuth, A. Lange, P. Stoick, R. Pruszko, *Biobased Automobile Parts Investigation*, Iowa State University, USA **2012**.
- [363] F. P. La Mantia, M. Morreale, *Composites, Part A* **2011**, *42*, 579.
- [364] J. Hinrichsen, *Airbus A380: Requirements for the Selection of Materials and Manufacturing Technologies* **2001**.
- [365] J. Hinrichsen, in *Around Glare: A New Aircraft Material in Context* (Ed: C. Vermeeren), Springer Netherlands, Dordrecht **2002**.
- [366] A.-A. Nahiyani, F. M. A. Muhammad, K. M. S. Mohd, *J. Mater. Sci. Chem. Eng.* **2021**, *9*, 1.
- [367] A. S. Mosallam, A. Bayraktar, M. Elmikawi, S. Pul, S. Adanur, *SOJ Mater. Sci. Eng.* **2014**, *2*, 25.
- [368] O. Kinnane, A. Reilly, J. Grimes, S. Pavia, R. Walker, *Constr. Build. Mater.* **2016**, *122*, 674.
- [369] M. Fan, in *Management, Recycling and Reuse of Waste Composites* (Ed: V. Goodship), Woodhead Publishing, UK **2010**.
- [370] S. Ramakrishna, J. Mayer, E. Wintermantel, K. W. Leong, *Compos. Sci. Technol.* **2001**, *61*, 1189.
- [371] J. L. Wang, *App. Mech. Mater.* **2012**, *155–156*, 903.
- [372] F. H. Froes, *JOM* **1997**, *49*, 15.
- [373] B. C. Suddell, in *Proc. of the Symp. on Natural Fibres*, UK **2008**.
- [374] T. Y. Kam, J. H. Jiang, H. H. Yang, R. R. Chang, F. M. Lai, Y. C. Tseng, in *Int. Conf. on Energy and Sustainable Development: Issues and Strategies*, Asian Institute of Technology, Klong Luang, Thailand **2010**.
- [375] G. A. Georgiou, M. A. Drewry, *Insight* **2007**, *49*, 137.
- [376] G. Gupta, A. Kumar, R. Tyagi, S. Kumar, *Int. J. Innov. Res. Sci., Eng. Technol.* **2016**, *5*, 6907.
- [377] L. T. Drzal, A. K. Mohanty, M. Misra, **2001**.
- [378] K. G. Satyanarayana, G. G. C. Arizaga, F. Wypych, *Prog. Polym. Sci.* **2009**, *34*, 982.
- [379] T. Gurunathan, S. Mohanty, S. K. Nayak, *Composites, Part A* **2015**, *77*, 1.
- [380] P. Lodha, A. N. Netravali, *Ind. Crops Prod.* **2005**, *21*, 49.
- [381] A. K. Mohanty, M. Misra, L. T. Drzal, *J. Polym. Environ.* **2002**, *10*, 19.



Saptarshi Maiti is presently a Post-Doctoral Fellow at the Institute of Chemical Technology (ICT), Mumbai, India. He holds a Ph.D. (Tech.) and MTech in Textile Chemistry from Department of Fibers and Textile Processing Technology, ICT-Mumbai. He has worked as a Visiting Research Fellow at the School of Materials, at The University of Manchester, UK, funded by the UAA-ICT Dhirubhai Ambani Lifetime Achievement Award. His research areas of interest are Graphene, Dendritic polymers, Protein extraction from waste resources, Natural dyeing and Green processing of Textiles. He is a Life member of The Indian Natural Fiber Society (INFS).



Md Rashedul Islam is a Ph.D. student under the supervision of Dr. Nazmul Karim at the Graphene Application Laboratory of the Centre for Print Research, UWE, Bristol, UK. He has been investigating Graphene and other 2D materials-based energy storage textiles, aiming to develop and power next-generation multifunctional wearable electronic textiles for personalized healthcare. Prior to that, he obtained his BSc and MSc in Textile Engineering, from Bangladesh University of Textiles (BUTex) Bangladesh. He has about 9 years of industry and academic experience related to textile chemical processing, advanced materials, and smart electronic textiles.



Mohammad Abbas Uddin is an Assistant Professor at Bangladesh University of Textiles. He is also working on future skills development of textile graduates in collaboration with a2i, and as Assistant Director in skill development project funded by ADB. Dr. Abbas is one of the authors for producing “National Chemical Management Guideline for Textile industry” 2021. He has over 18 years of experience, specializing in Textile wet processing, value chain, and environmental sustainability. He holds a Ph.D. from the University of Manchester, MBA from IBA, University of Dhaka, and Masters from Curtin University.



Shaila Afroj is Senior Research Fellow at the Centre for Print Research (CFPR), UWE Bristol, where she investigates graphene and other 2D materials-based technologies aimed at developing next-generation wearable electronics textiles and sustainable functional clothing. Prior to that, she worked as a Research Associate at National Graphene Institute, the University of Manchester after completing her Ph.D. from the same university. She has about 14 years of industry (including multi-nationals companies like C&A and Intertek) and academic experiences related to smart textiles, advanced materials, wearable electronics, and fashion textiles.



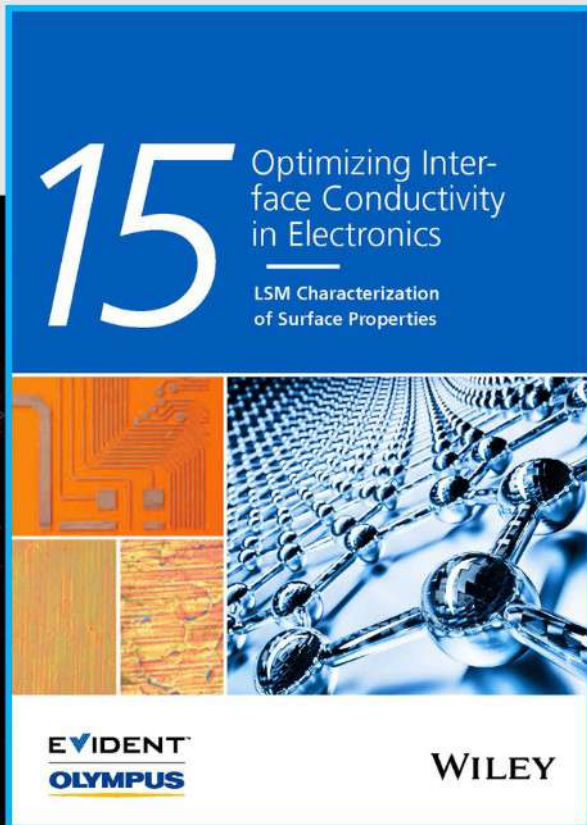
Stephen Eichhorn is a Professor of Materials Science and Engineering at the School of Civil, Aerospace, and Mechanical Engineering, University of Bristol. He is a world-leading expert in cellulosic materials conducting research into fiber-based composites, textile fibers spun from solution, supercapacitors, and batteries. Publishing over 150 peer-reviewed papers he is currently a Fellow of the Royal Society of Chemistry, Institute of Materials, Minerals, and Mining (IOMMM), and the Institute of Physics. He was awarded the Rosenhain Medal and Prize (IOMMM, in 2012), the Hayashi Jisuke Prize from the Japanese Cellulose Society in 2017, and the Swinburne Medal (IOMMM, in 2020).



Nazmul Karim is Associate Professor at the Centre for Print Research (CFPR), UWE Bristol. He is currently leading a research team to investigate graphene and other 2D materials-based technologies for developing next-generation wearable electronic textiles, environmentally sustainable functional clothing, and fiber-reinforced composites. Prior to that, Dr. Karim was a Knowledge Exchange Fellow (graphene) at the National Graphene Institute of University of Manchester. He has about 14 years of industry and academic experience in new materials and textile-related technologies, and a passion for getting research out of the lab and into real-world applications.



Optimizing Interface Conductivity in Electronics



The latest eBook from
Advanced Optical Metrology.
Download for free.

Surface roughness is a key parameter for judging the performance of a given material's surface quality for its electronic application. A powerful tool to measure surface roughness is 3D laser scanning confocal microscopy (LSM), which will allow you to assess roughness and compare production and finishing methods, and improve these methods based on mathematical models.

Focus on creating high-conductivity electronic devices with minimal power loss using laser scanning microscopy is an effective tool to discern a variety of roughness parameters.

EVIDENT
OLYMPUS

WILEY

Smart and Multifunctional Fiber-Reinforced Composites of 2D Heterostructure-Based Textiles

Marzia Dulal, Md Rashedul Islam, Saptarshi Maiti, Mohammad Hamidul Islam, Iftikhar Ali, Amr M. Abdelkader, Kostya S. Novoselov, Shaila Afroj,* and Nazmul Karim*

Smart and multifunctional fiber reinforced polymer (FRP) composites with energy storage, sensing, and heating capabilities have gained significant interest for automotive, civil, and aerospace applications. However, achieving smart and multifunctional capabilities in an FRP composite while maintaining desired mechanical properties remains challenging. Here, a novel approach for layer-by-layer (LBL) deposition of 2D material (graphene and molybdenum disulfide, MoS₂)-based heterostructure onto glass fiber fabric using a highly scalable manufacturing technique at a remarkable speed of $\approx 150 \text{ m min}^{-1}$ is reported. This process enables the creation of smart textiles with integrated energy storage, sensing, and heating functionalities. This methodology combines gel-based electrolyte with a vacuum resin infusion technique, resulting in an efficient and stable smart FRP composite with an areal capacitance of up to $\approx 182 \mu\text{F cm}^{-2}$ at 10 mV s^{-1} . The composite exhibits exceptional cyclic stability, maintaining $\approx 90\%$ capacitance after 1000 cycles. Moreover, the smart composite demonstrates joule heating, reaching from ≈ 24 to $\approx 27 \text{ }^\circ\text{C}$ within 120 s at 25 V. Additionally, the smart composite displays strain sensitivity by altering electrical resistance with longitudinal strain, enabling structural health monitoring. These findings highlight the potential of smart composites for multifunctional applications and provide an important step toward realizing their actual real-world applications.

response to environmental stimuli, such as mechanical, chemical, electrical, light, temperature, and moisture.^[1] Such composites, composed of a polymer matrix reinforced with fibers and functional materials, have diverse applications in fields such as chemical and strain sensing, energy harvesting and storage, actuators, switches, robots, artificial muscles, and controlled drug delivery.^[2] With the increasing demand for multifunctional materials in various industries,^[3] there has been a growing interest in developing smart composites^[4,5] that can perform multiple functions within a single structure. However, the development of smart composites presents several challenges, including achieving a balanced trade-off between the mechanical, electrical, and thermal properties of the composite material, and ensuring the compatibility of the individual components. Additionally, scalability and cost-effectiveness are important considerations in the development of smart composites.^[6] Furthermore, metals, polymers, and carbon-based nanomaterials have traditionally been used to create smart composites.^[7-9] However,

such materials are prone to oxidation, often have poor mechanical properties, and require complicated and expensive synthesis processes.^[10,11] Among the various materials being explored for smart composite applications, two-dimensional (2D)

1. Introduction

Smart fiber-reinforced polymer (FRP) composites are a class of materials that exhibit reversible changes in their properties in

M. Dulal, M. R. Islam, M. H. Islam, I. Ali, S. Afroj, N. Karim
Centre for Print Research
The University of the West of England
Bristol BS16 1QY, UK
E-mail: shaila.afroj@uwe.ac.uk; nazmul.karim@uwe.ac.uk

S. Maiti
Department of Fibres and Textile Processing Technology
Institute of Chemical Technology
Matunga (E), Mumbai 400019, India

 The ORCID identification number(s) for the author(s) of this article can be found under <https://doi.org/10.1002/adfm.202305901>

© 2023 The Authors. Advanced Functional Materials published by Wiley-VCH GmbH. This is an open access article under the terms of the Creative Commons Attribution License, which permits use, distribution and reproduction in any medium, provided the original work is properly cited.

DOI: 10.1002/adfm.202305901

A. M. Abdelkader
Department of Design and Engineering
Bournemouth University
Talbot Campus, Poole BH12 5BB, UK

K. S. Novoselov
Institute for Functional Intelligent Materials
Department of Materials Science and Engineering
National University of Singapore
Singapore 117575, Singapore

K. S. Novoselov, S. Afroj, N. Karim
National Graphene Institute (NGI)
The University of Manchester
Oxford Road, Manchester M13 9PL, UK

materials have shown promise due to their excellent mechanical, electrical, and thermal properties. In addition, such materials can be stacked together in LBL fashion to create heterostructures-based multifunctional composites with pre-designed properties and functionalities.

The concept of creating on-demand, designer materials is a fascinating idea, though it remains challenging to implement. It is difficult to achieve the optimal combination of various ingredients to create the ultimate material. Since the isolation of graphene in 2004, 2D materials have opened exciting opportunities to create heterostructures with diverse and tunable properties.^[12] Such one-atom-thick crystals, including graphene, metals like niobium diselenide (NbSe₂), semiconductors such as MoS₂, and insulators like hexagonal boron nitride (hBN), have a broad range of stable properties.^[13] By stacking different 2D crystals held together via van der Waals forces, we can create heterostructures with a far greater range of combinations than traditional growth methods. Nonetheless, there remains a need for a comprehensive strategy to address the challenge of blending crystals with distinct properties and generating highly scalable combinations with predetermined attributes and functionalities.

Graphene is by far the most extensively investigated 2D material due to its excellent mechanical, chemical, and electronic properties.^[14–24] Graphene's distinctive physicochemical properties make it a promising candidate^[25] material for supercapacitors,^[22,26] electrochemical biosensors,^[27,28] and physical sensors.^[14,29,30] Additionally, other 2D materials (e.g., MoS₂, hBN) received huge attention not only because of their 2D structure, but also due to their unique chemical and physical properties.^[31–33] Depending on its crystalline phase, MoS₂'s electronic properties can range from semiconductor to metallic. MoS₂ has a large bandgap that ranges from 1.2 (bulk material) to 1.8 eV (monolayer), making it a promising candidate material in nanoelectronics for high-performance and low-power device applications.^[34] As graphene and MoS₂ have complementary properties^[35] such as optical absorption, thermal conductivity, electronic band, and mechanical properties, it was reported that the combination of graphene and MoS₂ in specific ways to develop 2D heterostructures could potentially offer unique properties for various applications.^[36–40] 2D heterostructures must be efficiently built in addition to having the necessary stability, reliability, pattern ability, and interface properties for the manufacture of smart devices.^[41,42] Applications in graphene/MoS₂ heterostructures are severely hindered by the challenges of manufacturing van der Waals stacks of atomically thin materials on a large scale,^[43] limited detectivity, ultra-weak light absorption.^[44,45] Since graphene/MoS₂ devices are primarily created through mechanical exfoliation, their performance is severely constrained, limiting applications, and making them highly challenging to deploy in practical use. Therefore, there remains a need for ultrafast, low cost, and mass production of 2D heterostructure-based smart FRP for real-life multifunctional applications.

Here, our approach is to introduce the integration of 2D materials into composites and opens up new avenues for the development of high-performance smart materials for various applications. We report the ultrafast fabrication of smart FRP composites using a 2D heterostructure-based device as a functional material. We demonstrate the successful integration of a

graphene/MoS₂ heterostructure on the glass fabrics, and then infused such fabrics into a polymer matrix, resulting in a smart FRP composite with excellent mechanical properties and multifunctionalities. We then demonstrate potential multimodal uses of developed smart FRP composites for structural energy storage, joule surface heating, and health monitoring applications.

2. Results and Discussion

2.1. Design Approach

Multifunctional smart composite by design is an appealing concept that is extremely challenging to implement in reality. We currently lack a universal solution for the challenge of combining the best qualities of various components into one ideal structure. Here, we attempt to create and research a structure that can perform multiple functions (**Figure 1**). Our multifunctional smart composite includes the functionalities of structural energy storage, joule heating, and strain sensitivity. Initially, we investigated the functionality of 2D heterostructure-based glass fiber fabric as supercapacitor electrodes, heating textiles, and strain sensor. To replicate all these functionalities in a single composite structure, we integrated the 2D heterostructure-based glass fiber fabric in a composite structure as reinforcement materials, utilizing bio-epoxy resin as matrix and electrolyte coated glass fiber fabric as separator. We incorporated 2D heterostructures made of graphene/MoS₂ as their building blocks in glass fiber fabric because they have intriguing electronic properties at their nanoscale interfacial regions. This gives them the ability to control the confinement and transport of charge carriers, excitons, photons, phonons, and other particles in order to produce a wide range of exceptional physical, chemical, thermal, and/or mechanical properties. The electrochemical properties for advanced energy storage devices and electrocatalysis can be well controlled to meet some functionalities by logical design and synthesis of this heterostructures in our composite.^[13,46] Additionally, a piezoresistive sensor network formation can perform continuous load monitoring^[47] as a result of the integration of 2D heterostructure into FRP composite materials, which represents a smart structural solution. We then successfully demonstrated the functionality of our manufactured composite as structural energy storage device, heating element, and strain sensor, for the potential applications of structural battery, de-icing, and structural health monitoring (SHM) from a single structure, respectively (**Figure 1a,b**).

2.2. Scalable Production of Graphene/MoS₂ Heterostructure on Glass Fiber Fabrics

Here, we report a highly scalable method^[48,49] for the LBL deposition of graphene/MoS₂ heterostructures onto glass fiber fabric. To the best of our knowledge, this is the first time such a technique has been applied to the manufacturing of next-generation smart composites for structural energy storage, surface joule heating, and SHM applications. We have used a laboratory-scale pad-dry-cure machine for the LBL deposition of 2D materials (graphene and MoS₂) onto glass fabrics, enabling the creation of 2D heterostructures for smart FRP composites applications.

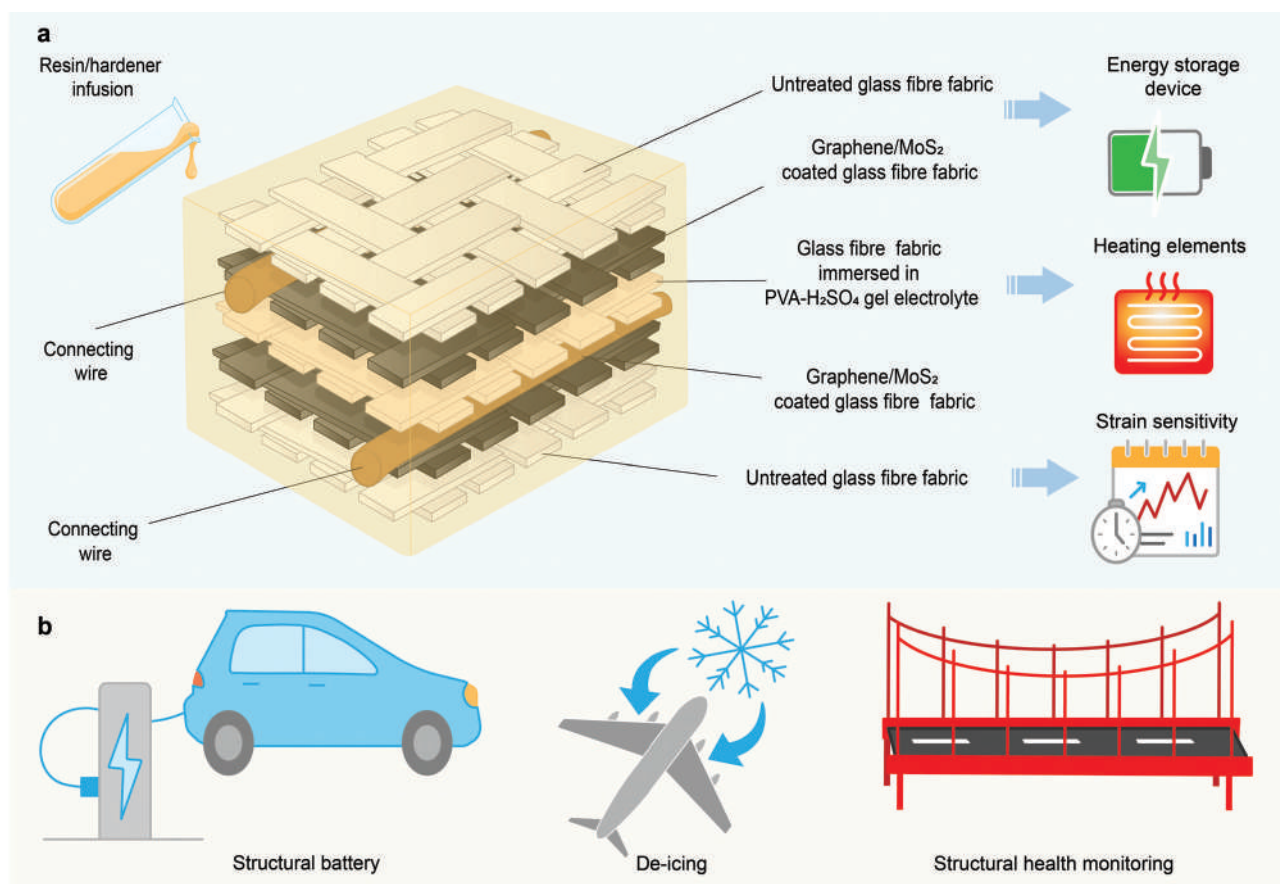


Figure 1. a) Design approach for 2D heterostructure-based smart and multifunctional composite and b) their potential applications.

Pad-dry-cure is a popular method for applying functional finishes (e.g., softening effect, antimicrobial, and water repellent) to textiles, and it is also an ultrafast continuous production method that can potentially coat up to ≈ 150 m of textiles in just 1 min. The schematic diagram for the pad-dry-cure method is shown in **Figure 2a**, where graphene and MoS_2 are deposited onto control glass fiber fabric. **Figure 2b** displays the resulting sample after pad-dry-cure process. The presence of graphene flakes on the glass fiber is further demonstrated by scanning electron microscope (SEM) images. Untreated glass fiber can be seen as smooth fiber (**Figure 2c**). Significant flake deposition on individual fiber surfaces was seen after coating with graphene ink in graphene/ MoS_2 heterostructure (G3M1G3). A continuous conductive fabric is created by wrapping the individual fiber with flakes, as shown in **Figure 2d**, allowing current to flow through the structure.

The results presented in **Figure 2e** demonstrate a clear correlation between the number of graphene layers and the resistance of the 2D heterostructure. As the number of graphene layers increases, the resistance decreases, with an average resistance of $\approx 0.48 \text{ k}\Omega \text{ cm}^{-1}$ for up to six graphene layers. Additionally, we observed that the add-on% increases rapidly until the third layer of graphene deposition but then increases slowly until the sixth layer, with the add-on% moving averages remaining relatively constant after that point. Interestingly, the add-on% of the resultant G3M1G3 structure (three layers of graphene, one layer of

MoS_2 , three layers of graphene) was $\approx 26.56\%$ when we added another layer of MoS_2 in the middle of the six graphene layers, meaning three graphene layers, one MoS_2 layer, and again three graphene layers were deposited in this sequence. This is $\approx 42\%$ better than the resultant G6 add-on%, which as we had previously observed, was $\approx 18.68\%$. Later analysis and experiments, however, showed that the add-on% does not change that much ($\approx 26\%$) even when the number of MoS_2 layer deposition was increased from one to three in the graphene/ MoS_2 heterostructure. Instead, we found that the resistance increased with the increase MoS_2 layer deposition in the middle from one to three in graphene/ MoS_2 heterostructure because when interlayer distance increases, the interlayer connection weakens and the charge transfer from the graphene layer to the MoS_2 layer is less,^[50] which led us to choose a single deposited MoS_2 layer in the resulting graphene/ MoS_2 heterostructure (G3M1G3) for further testing and characterization.

2.3. Graphene/ MoS_2 Heterostructure-Based Energy Storage Device

Graphene/ MoS_2 hybrid-coated textiles have the potential to serve as ideal candidate electrodes for energy storage devices due to their high conductivity and mechanical flexibility within the interlayer distance of graphene/ MoS_2 .^[50,51] The combination of

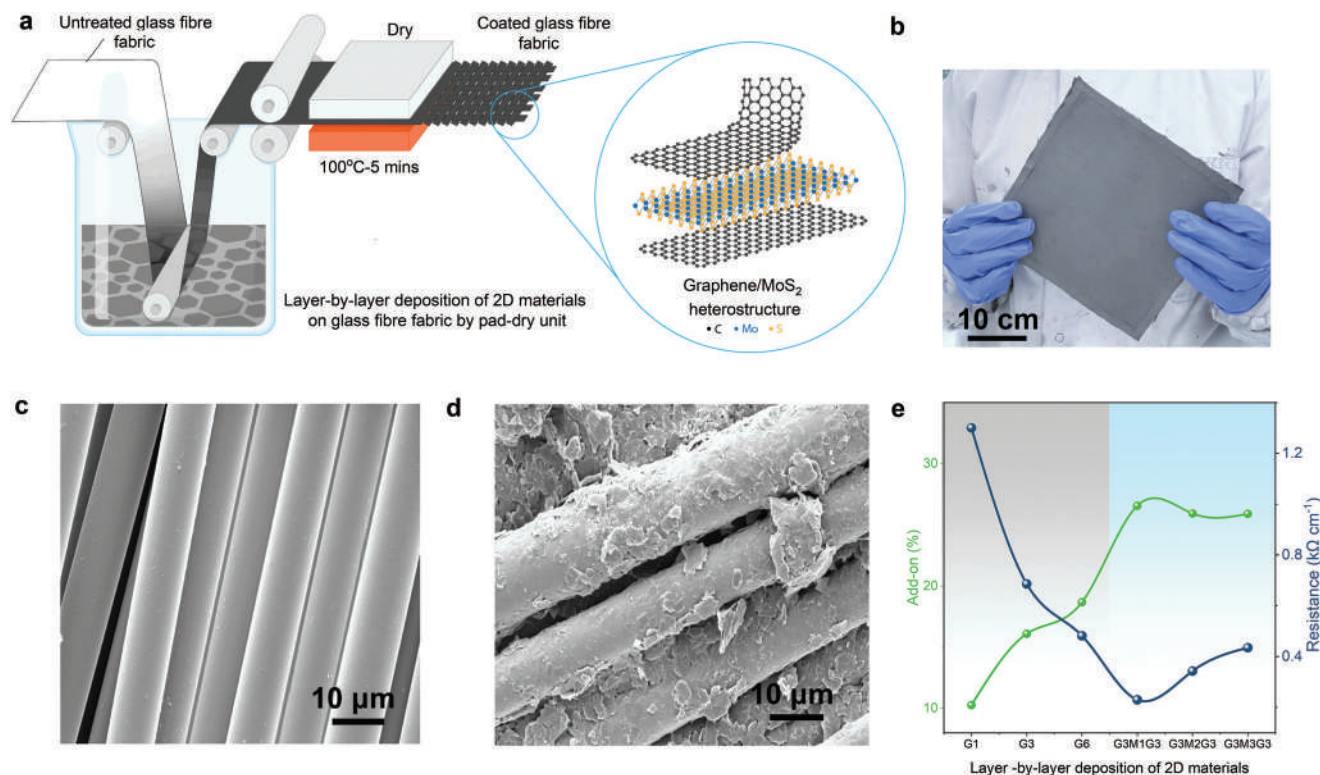


Figure 2. a) LBL deposition of graphene and MoS_2 for the creation of 2D heterostructure on glass fiber fabrics via highly scalable pad-dry-cure process; b) 2D heterostructure coated glass fiber fabric; c) SEM image of smooth and featureless control glass fiber fabric ($\times 3000$); d) SEM image of 2D heterostructure-based glass fiber fabrics (G3M1G3) ($\times 3000$); e) The effect of LBL deposition of 2D materials on the add-on.% and resistance ($\text{k}\Omega \text{cm}^{-1}$) of 2D heterostructure-based glass fiber fabrics.

graphene and MoS_2 flakes on the textiles creates a porous film with nano- and micro-channels, resulting from the wide range in size and thickness.^[52,53] Such unique structure facilitates the interaction between the electrolyte and the graphene/ MoS_2 hybrid coating, improving its wettability. The electrolyte's wettability is a critical factor in the development of high-performance energy storage devices since uneven wetting can lead to an unstable solid electrolyte interface film and an uneven distribution of current density.^[54] Energy storage devices use a range of mechanisms, such as electrical double-layer and pseudocapacitance, to achieve high specific capacitance. To create a high-performance energy storage device such as a supercapacitor, two methods can be employed.^[55] The first method involves increasing the surface area to boost the capacitance of the double layer (Figure 3a), while the second method aims to raise the likelihood of reversible faradic redox reactions to increase the capacitance of the pseudocapacitor (Figure 3b). To improve the capacitive properties of the energy storage device, we intend to construct a heterostructure by combining two types of 2D materials, graphene and MoS_2 , which exhibit double-layer-type and pseudocapacitor-type capacitance, respectively.

To demonstrate the feasibility of using LBL-based electrodes in energy storage devices, we constructed each device with two identical coated electrodes and a poly(vinyl alcohol) (PVA)- H_2SO_4 gel electrolyte, as shown in Figure 3c. Copper wires were used as current collectors and were connected directly to the potentiostat terminals. Cyclic voltammetry (CV) and galvanostatic

charge-discharge (GCD) were used to evaluate the electrochemical performance of the sandwich-shaped symmetric energy storage device. Our results indicate that increasing the number of graphene layers in the electrode improves the areal capacitance performance up to six layers (G6), as shown in Figure 3d. However, the addition of one layer of MoS_2 to configure a three graphene, one MoS_2 , and three graphene layers (i.e., G3M1G3) results in the highest areal capacitance. However, further increase in the number of MoS_2 layers in this graphene heterostructure by more than one-layer leads to a decrease in areal capacitance, as shown in Figure 3d. Initially, the inclusion of a single coating layer of MoS_2 serves to fill defects and voids on the graphene surface, thereby creating additional active sites for charge transfer and enhancing the overall conductivity of the fabric. Consequently, this leads to an increase in the areal capacitance. However, as the number of MoS_2 layers is further increased, it begins to impede conductivity, as indicated by resistance changes shown in Figure 2e. This can be attributed to the insulating nature of MoS_2 , which, with a higher number of layers, hinders the material's charge transfer pathways. The influence of this effect is evident in Figure 3d, where the hybrid G3M1G3 sample demonstrates an areal capacitance of $\approx 18.76 \text{ mF cm}^{-2}$ at a scan rate of 10 mV s^{-1} , while the G6-based supercapacitor exhibits a slightly lower capacitance of around 14.90 mF cm^{-2} .

It has been reported that increasing the scan rate can cause a decrease in capacitance due to ion transport limitations near the electrodes.^[57,58] Figure 3e depicts CV curves for the

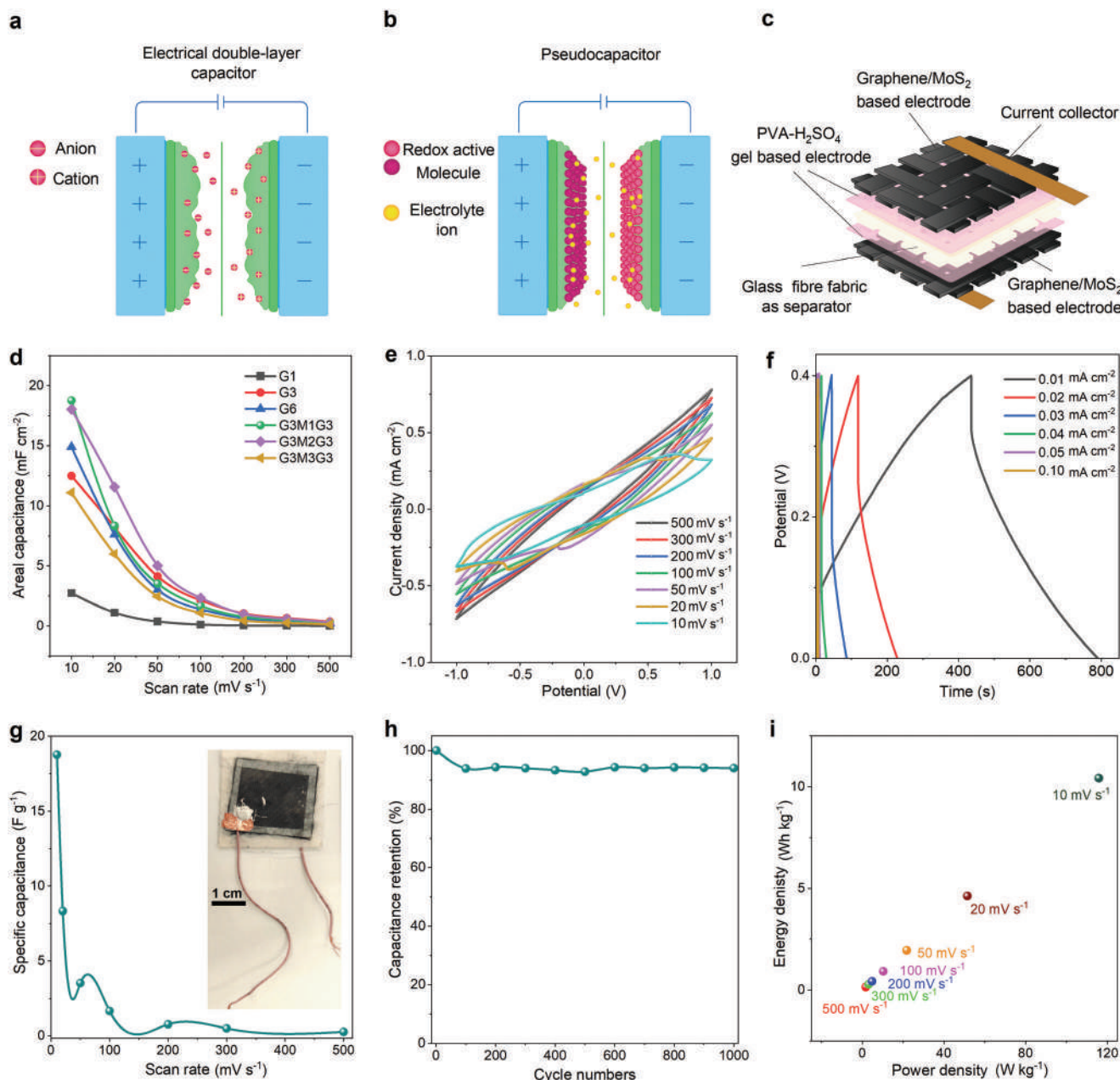


Figure 3. The schematic diagram of a) an EDLC and b) a redox type of pseudocapacitor;^[56] c) Schematic diagram of graphene/MoS₂ heterostructure-based energy storage device; d) Areal capacitance of G1, G3, G6, G3M1G3, G3M2G3, and G3M3G3-based energy storage devices at different scan rates; e) CV graph of G3M1G3 based energy storage device at different scan rates; f) GCD graph of G3M1G3 based energy storage device at different current density; g) Specific Capacitance of G3M1G3 based energy storage device at different scan rates; h) Changes of capacitance retention (%) of the G3M1G3 based energy storage device at different cycles; i) Changes of energy density with the change of power density due to different scan rates.

supercapacitor device made of G3M1G3 coated electrodes at various scan rates. CV measurements were performed in a potential window (V) between -1.0 and 1.0 V. The curves possess a large, enveloped area even at high scan rates, resulting from the excellent double layer capacitance of graphene and high pseudocapacitance of MoS₂. Moreover, in order to fully grasp the differences, we additionally assess various CV graphs of G1, G3, G6, G3M2G3, and G3M3G3 coated glass fiber fabric electrodes for energy storage devices to compare with G3M1G3, which is

shown in Figure S1a, Supporting Information. For the galvanostatic charging/discharging test of the as-prepared supercapacitor, a current density of 0.01 to 0.1 mA cm⁻² was used, as shown in Figure 3f. The G3M1G3-based energy storage device has the longest discharging time (t) at a current density of 0.01 mA cm⁻², which is ≈ 354.5 s (0.09 h) in the potential range of 0 to 0.4 V. It is worth noting that the maximum current that can be applied in a GCD experiment is limited by the ability of the system to maintain the triangular shape without causing a significant voltage

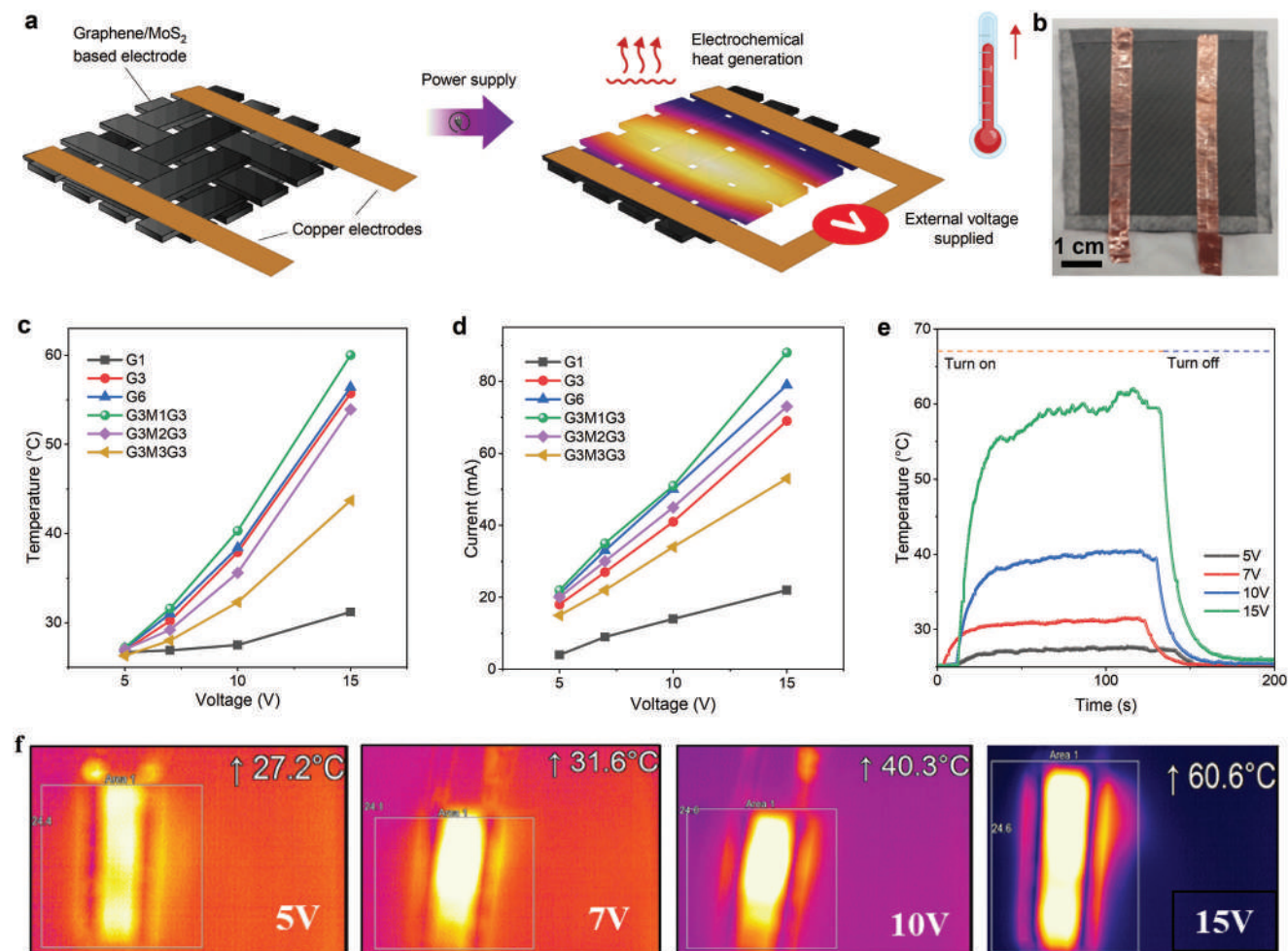


Figure 4. a) Schematic diagram of heating elements; b) Original sample of heating elements; c) Temperature change of G1, G3, G6, G3M1G3, G3M2G3, and G3M3G3-based heating elements with the change of supplied voltage 5, 7, 10, and 15 V; d) I - V graphs of G1, G3, G6, G3M1G3, G3M2G3, and G3M3G3-based heating elements with the change of supplied voltage 5, 7, 10, and 15 V; e) Time-Temperature graphs of G3M1G3-based heating element at different supplied voltages with the influence of heat turns on and turn-off; f) Surface temperature's thermal images of G3M1G3-based heating element at different supplied voltages.

drop when the current polarity is switched. Similarly, the maximum voltage that can be applied to GCD analysis is one that keeps both the charging and discharging branches of the GCD linear.

In order to improve the performance of similar devices, researchers have investigated heterostructures of 2D materials, including derivatives of graphene and MoS_2 , to enhance the performance of supercapacitors.^[59–65] However, such studies have not been conducted with the goal of developing energy storage devices for textiles and their composites. Our work focuses on demonstrating the energy storage capability of textiles. Despite being a relatively new field, our textile-based energy storage device, which utilizes LBL deposition of graphene/ MoS_2 and a PVA- H_2SO_4 gel electrolyte, represents a promising starting point. We have shown that this device has a specific capacitance of $\approx 18.7 \text{ F g}^{-1}$ (Figure 3g) and a capacitance retention of $\approx 94\%$ even after 1000 cycles (Figure 3h). In addition, such supercapacitor is capable of delivering an energy density of $\approx 10.42 \text{ Wh kg}^{-1}$ at a power density of $\approx 115.82 \text{ W kg}^{-1}$ (Figure 3i).

2.4. Graphene/ MoS_2 Heterostructure-Based Fabric for Joule Heating

Joule heating is a physical phenomenon that occurs when a current flows through an electrical conductor, resulting in the production of thermal energy.^[66] This thermal energy causes an increase in the temperature of the conductor material, leading to the term “heating.” Joule heating is essentially a conversion of “electrical energy” into “thermal energy,” in accordance with the principle of energy conservation. The application of joule heating to fibers, textiles, and woven fabrics made of conductive materials has gained popularity in the fields of heating elements for composites and therapeutic purposes. When conductive fibers and textiles are connected to external electrodes, illustrated in Figure 4a, electrical currents and resistance cause joule heating. This heating effect can be utilized to provide stable, controlled thermal regulation to textiles, often requiring lower power sources.^[67,68] To practically implement active heating textiles, the surface of the textile material is coated LBL with

2D materials. The morphology, electrical conductivities, and thermal conductivities of epoxy-based composites,^[69] as well as the surface heater,^[70] are linked to joule heating performance. In our study, we explored the use of various configurations of graphene and MoS₂ heterostructure layers to create conductive heating textiles. Figure 4b shows an image of the glass fiber fabric coated with such 2D materials. Joule heating also provides a direct path for inside-out crystallization of the conformal MoS₂ layer, enabling excellent interfacial interaction between the MoS₂ and the underlying carbon-based material (e.g., 2D graphene).^[71] Due to extremely quick heating, simple processing, and ability to integrate with textiles^[70] and other components,^[72] in our study we investigated various configurations of graphene and MoS₂ heterostructure layers to create conductive heating textiles where glass fiber fabric was coated with these 2D materials (Figure 4b).

We conducted electro-thermal characterization using six different samples of coated glass fiber fabric, with five specimens for each category, all of the same area (4 cm × 4 cm). We applied various voltages (5, 7, 10, and 15 V) across the entire sample, and measured the change in temperature of the coated fabric (due to joule heating) (Figure 4c) and the current–voltage characteristics (Figure 4d). For instance, applying 15 V to the glass fiber fabric coated with six layers of graphene (G6) resulted in a current of ≈0.08 A and the temperature reaching up to ≈56.4 °C within 120 s. Figure 4c,d illustrates that the currents and temperatures exhibit an upward trend with an increasing number of graphene layers in the glass fiber fabric, aligning with Ohm's law, which establishes a direct relationship between current and applied voltage in a conductor. Graphene, known for its unique composition and characteristics, serves as an exceptional electrical conductor. Consequently, the fabric's overall conductivity improves as more graphene layers are integrated into its structure. Upon the application of a voltage, this enhanced conductivity facilitates a higher flow of electrical current, resulting in increased current values. As the current passes through the conductive fabric, it encounters resistance, leading to the generation of heat. By employing layers of G3M1G3-coated glass fiber fabric, the temperature of the structure reaches ≈60 °C within the same duration (120 s) and at the same voltage (15 V), with the current reaching 0.09A. This clearly demonstrates the superior performance compared to utilizing only G6 layers. Therefore, it becomes evident that an optimized MoS₂ layer can enhance joule heating in graphene-coated glass fiber fabric by filling the voids on the graphene surface, thereby promoting greater charge transfer mobility and improved overall conductivity. However, when the number of MoS₂ layers exceeds one, a decline in temperature and current is observed. This suggests that an increased number of insulating MoS₂ layers may introduce higher resistance, impede current flow, and result in reduced heat generation. The time-temperature curves of a glass fiber fabric with conductive G3M1G3 networks for an integrated joule heater for various voltages and temperature stability are shown in Figure 4e (Figure S1b, Supporting Information, compares G3M1G3 with the same time-temperature graph for G1, G3, G6, G3M2G3, and G3M3G3 coated glass fiber electrodes for heating elements). This textile framework can thus be considered for the use in surface heating applications. Thermal images (Figure 4f) show that heat is distributed uniformly across the area of the conductive coated glass fiber fabric.

2.5. Graphene/MoS₂ Heterostructure-Based Fabric for Strain Sensitivity

Strain sensors have greatly evolved in recent years and are now used in a wide variety of applications. However, despite the remarkable advancement in the development of nanomaterials, creating strain sensors in a scalable approach that enables high sensitivity and stability over a long period of time remains a challenge for potential applications in wearable electronics, soft robotics, and healthcare monitoring. In this study, we developed a strain sensor based on graphene/MoS₂ heterostructure by utilizing the high mobility of graphene and the structural rigidity of MoS₂. To demonstrate the strain sensitivity, we used woven glass fiber with graphene/MoS₂ coatings, and at least five samples of each strain sensor were tested to investigate changes in relative resistance ($\Delta R/R_0$). Piezoresistivity-based sensors typically rely on translating changes in resistance (Figure 5a), which typically follow a linear relationship, into external mechanical loading.^[73] The gauge factor (GF) is the first metric used to measure the performance of such piezoresistive sensors, and it is defined as the relative resistance changes versus tensile strain.^[74] A low GF or a nonlinear response can result in poor repeatability for strain/release cycles.^[75] To analyze our G3M1G3 coated (Figure 5b) strain sensor's performance we calculated the GF using the expression

$$GF = \frac{\Delta R/R_0}{\epsilon} \quad (1)$$

where $\Delta R = R_\epsilon - R_0$; R_0 and R_ϵ are the initial resistance and resistance at a specific strain ϵ , respectively.

The load elongation graph in Figure 5c shows that treating the sample with G3M1G3 improves the load by around 8.62% while changing the strain by about 5%, compared to the untreated sample (Figure S1c, Supporting Information, compares G3M1G3 with the same load-elongation curve for G1, G3, G6, G3M2G3, and G3M3G3-based glass fiber fabric electrodes). Figure 5d demonstrates that $\Delta R/R_0$ increases linearly with the strain under tensile load. Our graphene/MoS₂ heterostructure-based strain sensor exhibits a moderate gauge factor (GF) on glass fiber fabric, reaching ≈26.86 at a maximum strain of 5% (with $\Delta R/R_0$ of ≈134.30%) (Figure 5d). This result aligns with the principle of strain sensor performance, wherein a high gauge factor signifies greater resistance change and increased sensitivity.^[76,77] The load versus elongation curve for five cycles of cyclic tensile testing at 1% and 2% strains is depicted in Figure 5e. As strain% increases, the load and elongation also rise. Cyclic tensile testing was conducted for five cycles at 1% and 2% strain levels at the same speed. The graph shows that at 2% strain, the sample rises to an average load of ≈385 N before returning, whereas at 1% strain, the sample reaches an average load of 185 N before returning, and the load decreases slightly with each subsequent cycle.

Figure 5f indicates that during cyclic testing, $\Delta R/R_0$ changes irreversibly under a given strain at the beginning, but after straining gets on the reversible path. We performed five cycles of 2% and 1% strain at various speeds (1 and 2 mm min⁻¹) and ran 100 cycles at 1 mm min⁻¹ and 1% strain to observe the cyclic stability. Figure 5g illustrates that the relative $\Delta R/R_0$ changes gradually with no radical shift after 6000s (30 cycles). The sensor can

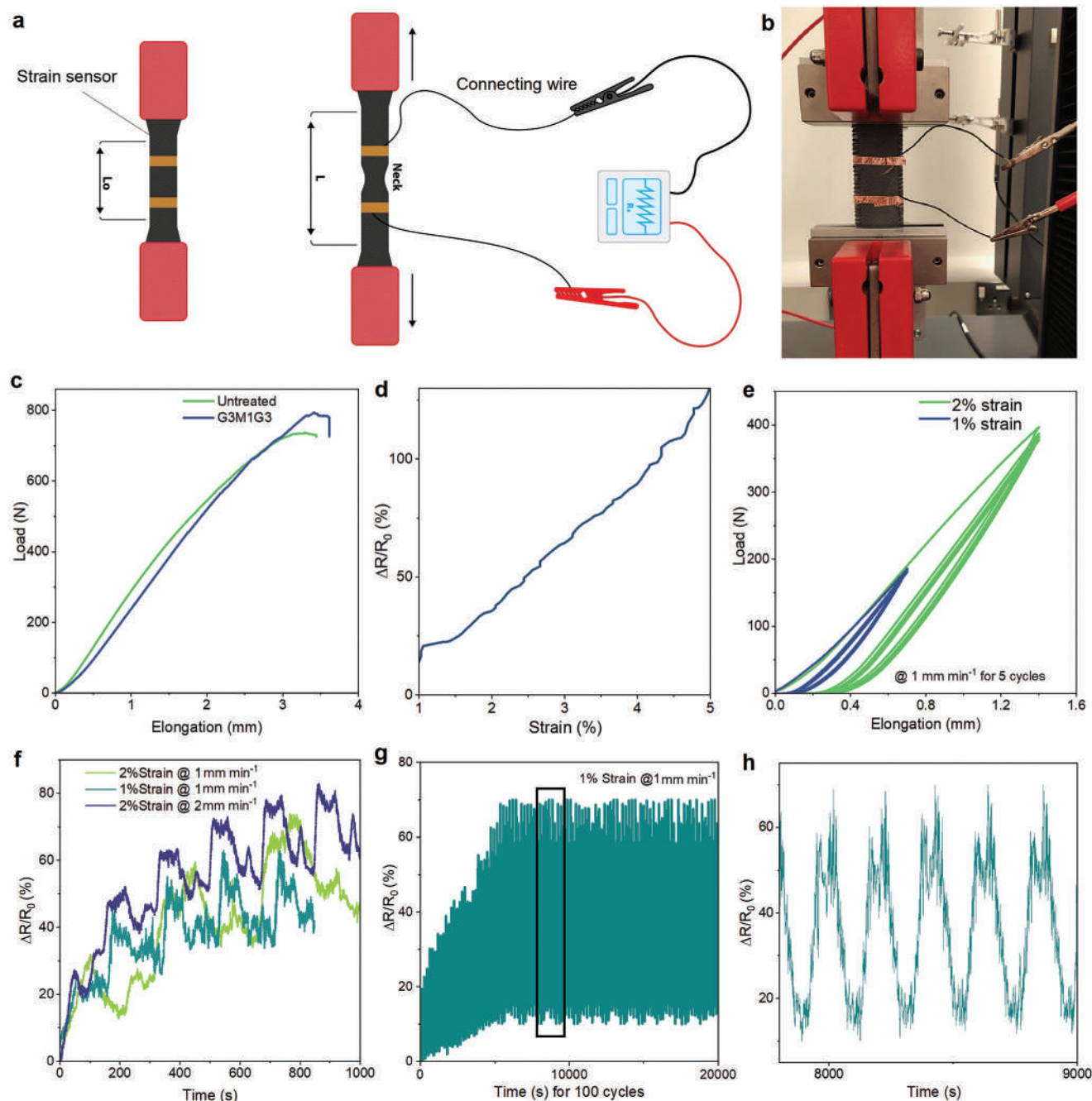


Figure 5. a) Schematic diagram of strain sensitivity measurement; b) Original sample testing image; c) Load–elongation graph of tensile testing of untreated and graphene/MoS₂ heterostructure treated glass fiber fabric (G3M1G3); d) $\Delta R/R_0$ changes with the strain; e) Load–elongation graph of cyclic tensile testing at 1 mm min⁻¹ speed up to 1% and 2% strain for five cycles; f) $\Delta R/R_0$ change of cyclic tensile test for five cycles with time at different strain and same speed; g) $\Delta R/R_0$ change of cyclic tensile test for 100 cycles with time up to 1% strain at 1 mm min⁻¹; h) Selective area $\Delta R/R_0$ change at wide angle for cyclic stability with time.

operate for at least 20 000 s (100 cycles) under a strain of 1%. Even after numerous stretching–releasing cycles, the sensor resistance can return to its initial state, with an average relative resistance change of 70%. Figure 5h provides a close-up of the curve between ≈ 8000 and ≈ 9000 s in Figure 5g, which presents the relative resistance changes–time curves of the G3M1G3 sensor.

2.6. Concurrent Characterization of Smart Composite Structure

In previous sections, we demonstrated that the deposition of 2D material-based heterostructures onto glass fiber fabric using the LBL technique resulted in multifunctional textiles with promising applications in energy storage, joule heating, and strain sensing. Our aim is to develop a smart and multifunctional FRP

composite by incorporating all these functions into a single composite and that can perform these functions concurrently when needed with potential applications in the automotive, civil, and aerospace industries. **Figure 6a** illustrates the manufacturing flow of the proposed smart composite, while **Figure 6b** shows the representation of the original sample. To develop smart composites for energy storage, we formed graphene/MoS₂ heterostructure-based composites using a vacuum assisted resin infusion process (VARI) technique and an acid-based electrolyte. These composites have relatively lower tensile properties but can be used for various applications in energy storage, joule heating, and strain sensing.

The electrochemical performance of the structural energy storage composite is presented in **Figure 6c**, where typical CV profiles are displayed at various scan rates. **Figure 6d** shows the areal capacitance of this composite at different scan rates, with the highest capacitance achieved being 0.18 mF cm⁻² (182 μF cm⁻²) at a scan rate of 10 mV s⁻¹. Furthermore, we tested the cyclic stability of the structural energy storage device, as shown in **Figure 6e**, where our device exhibits excellent stability of 90% even after 1000 cycles.

We also investigated the joule heating characteristics of the developed multifunctional composite structure. **Figure 6f** shows the current–voltage (*I*–*V*) curve of the graphene/MoS₂ heterostructure-based (G3M1G3) composite, as well as the temperature rise. Although the temperature does not increase significantly as the voltage increases from 15 to 25 V, the current gradually changes from 8 to 12 mA linearly. It is evident from the time temperature graph (**Figure 6g**) that with an increase in applied voltage of up to 25 V, the temperature rose from ≈24 to ≈27 °C in just 120 s. However, the heat dissipated quickly when turned off, taking less than 100 s for the temperature to drop. **Figure 6h** displays the actual thermal images for the composite's surface temperature changes at 15, 20, and 25 V.

The stress–strain graph in **Figure 6i** shows that the untreated composite breaks (**Figures S2 and S3**, Supporting Information) when the stress reaches ≈391.09 MPa at strain ≈2.84%, but the G3M1G3 composite breaks before that threshold, which is ≈297.36 MPa at strain ≈3.25%. The interfacial bond between the fibers and the matrix, as well as the existence of void somehow may result in a reduction in stress. Despite a decrease in mechanical properties, the smart sensing capabilities of our developed composite can be highly beneficial for the creation of smart structures that can monitor their own stress levels. This is made possible by variations in the degree of fiber alignment, which causes the electrical resistance of the composite to change reversibly with longitudinal strain. Our smart composite structure (G3M1G3) also demonstrated excellent strain sensitivity, making it an effective strain sensing device. The composite's resistance changed in response to applied strains, and we measured the electrical conductivity and resistance three times to determine the average values. As shown in **Figure 6j**, as strain increases up to 0.5%, the Δ*R*/*R*₀ reaches ≈16%, and GF becomes ≈32.

From the cyclic test results shown in **Figure 6k**, we observed that the Δ*R*/*R*₀ value increased with each successive five cycles. This behavior is attributed to the fiber arrangement becoming less neat at the end of the first cycle, which causes a disturbance. The likelihood of adjacent fiber layers touching one another increases with a less orderly fiber arrangement. Previ-

ous studies have shown that multifunctional composites with an average tensile strength can yield better energy densities, and although our smart multifunctional composite shows lower strength compared to untreated composite, it still has better mechanical strength than some other composites.^[80–83] Additionally, our composite demonstrates better sensitivity and a slight increase in capacitance, as well as improvements in heating elements using gel-based electrolytes in the graphene/MoS₂ heterostructure. Overall, these findings represent an initial proof of concept for our multifunctional composite material.

3. Conclusion

We have demonstrated the successful creation of smart FRP composites based on a graphene/MoS₂ heterostructure for multifunctional applications. These composites exhibit remarkable mechanical and electrochemical properties, including an areal capacitance of ≈182 μF cm⁻² and an elastic modulus of ≈8 GPa when used to create structural battery composite materials. The strain sensitivity of such composites, with a Δ*R*/*R*₀ rise of up to ≈16% when strain is up to ≈0.5% with slight surface heating upon increasing the applied voltage by up to 25 V, the temperature rose from ≈24 to ≈27 °C in ≈120 s, surpasses any previous structural battery materials reported in the literature (**Table S1**, Supporting Information). Overall, our findings provide important insights into the complementary, and occasionally antagonistic, mechanical, and electrochemical functions of graphene/MoS₂ heterostructures. Our results demonstrate the potential of using 2D material-based heterostructures to mitigate the negative mechanical properties of each constituent and create smart composites with improved mechanical and electrochemical properties. We hope that our work will inspire further research in this area and lead to the development of novel and high-performance smart composites for a variety of applications.

4. Experimental Section

Materials: The microfluidized graphene (≈7 nm thick, <2 μm lateral size, <30% wt%) and molybdenum disulfide (MoS₂) (few layer <2 μm lateral size, 100 g L⁻¹) dispersions were purchased from Cambridge Graphene Ltd (UK). PVA (molecular weight: 31 000–50 000, 98–99% hydrolyzed) and sulfuric acid (H₂SO₄) (puriss, 95–97%) were purchased from Merck, UK. ONE high biobased epoxy laminating resin (30% bio-content) and ONS high biobased slow laminating hardener (mixed bio-content 21%), based on Super Sap formulation were purchased from Entropy Resins, UK, and 200 GSM (grams per square meter) twill woven glass fabrics were purchased from Easy Composites, UK.

LBL Deposition of 2D Materials into Glass fiber Fabric: A simple laboratory scale pad–dry–cure method was used to coat glass fiber fabric with varying numbers of layers of graphene and MoS₂ using a BVHP PADDER—vertical and horizontal (350) 2 Bowl (Roaches, UK). The coated fabrics were then batch dried with a Mini Thermo Oven Type 350 Special (Roaches, UK) at 100 °C for 5 min. The padding roller pressure and speed were adjusted and the fabrics (25 cm × 25 cm) were periodically padded with 2D material dispersions in different layer configuration. Each padding cycle included one padding and one drying pass. Samples were repeatedly pad-dried as following which denoted the number of padding (coating) cycles. The curing time and temperature of the pad-dried samples were kept for 5 min at 100 °C in the oven as reported previously.^[52]

- 1) One pass coating of glass fiber fabric with graphene ink—G 1

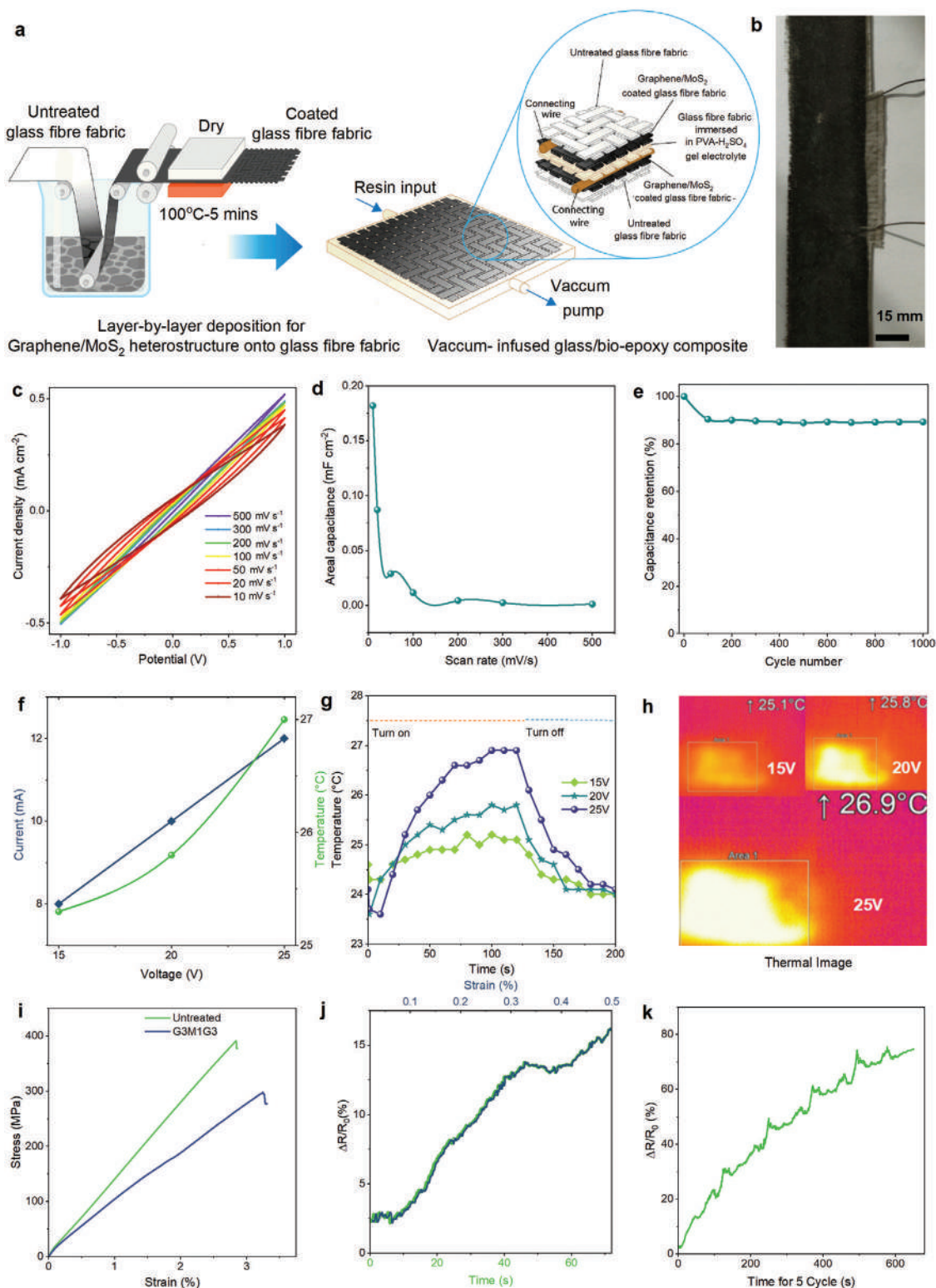


Figure 6. a) Schematic of smart composite manufacturing process^[78–79] from untreated fabric pad-dry to vacuum infusion; b) Original sample of Smart composite; Structural energy storage device performance: c) CV graph, d) areal capacitance at different scan rates of smart composite, and e) capacitance retention (%) at different cycles; Joule heating performance: f) Current and temperature changes with the change of supplied voltages, g) time–temperature graph at different voltages with the influence of heat turn on and turn off, and h) thermal images of samples at different voltages; Strain sensitivity performance: i) Stress–strain Graph of untreated and G3M1G3-based composites, j) $\Delta R/R_0$ change in comparison with time and strain, k) and $\Delta R/R_0$ change with time for five cycles.

- 2) Three pass coating of glass fiber fabric with graphene ink—G3
- 3) Six pass coating of glass fiber fabric with graphene ink—G6
- 4) Three graphene—one MoS₂—three graphene pass coating of glass fiber fabric —G3M1G3
- 5) Three graphene—two MoS₂—three graphene pass coating of glass fiber fabric —G3M2G3
- 6) Three graphene—three MoS₂—three graphene pass coating of glass fiber fabric —G3M3G3

The graphene and MoS₂ add-on (%) were calculated using following equation.

$$\text{Add-on (\%)} = \frac{m_n - m_0}{m_0} \times 100 \quad (2)$$

where m_0 is the mass of the uncoated fabric specimen and m_n is the mass of “ n ”-time graphene/MoS₂-coated fabric specimen.

Fabrication of Energy Storage Device: The energy storage device was developed in the form of a sandwich, with the coated samples acting as electrode materials on the top and bottom layers and the middle separator, which was made of a piece of glass fiber fabric immersed in a hydrogel-polymer electrolyte PVA doped with H₂SO₄ (Figure 3c).^[84,85] Current was collected by connecting copper wires to the fabric surface using silver electronic paste DM-SIP-3067S (DYCOTEC Materials, UK). To ensure good electrical contact with the measuring workstation, copper wire was, however, permanently adhered to the ends of each electrode. The PVA-H₂SO₄ gel electrolyte was made as following: After adding 1 g of PVA to 10 mL of deionized water, 1 g of H₂SO₄ was added. Afterward, the entire mixture was heated to ≈85 °C while being stirred up until the solution was clear. The electrolyte was drop-casted onto the separator fabric and maintained in the aforementioned sandwiched form. It was then left to dry overnight under ambient conditions to ensure complete wetting of the electrode by the electrolyte and allow for the evaporation of any excess water.^[18]

The electrochemical performances of the as-fabricated textile energy storage device were investigated by cyclic voltammetry (CV), and GCD tests. The electrochemical measurements were performed on an Iviumstat electrochemical interface. The CV and GCD measures were conducted in the potential range −1.0 to 1.0 V at different scan rates and current densities to calculate the following key metrics^[86] for the characterization of an energy storage device.

Charge storage ability per unit mass: Gravimetric capacitance [F g^{−1}],

$$C_m = \frac{A}{2smV} \quad (3)$$

Charge storage ability per unit area: Areal capacitance [F cm^{−2}],

$$C_A = \frac{A}{2saV} \quad (4)$$

Amount of energy able to deliver: Energy density [Wh kg^{−1}],

$$E = \frac{1}{2} CV^2 \quad (5)$$

How faster is the energy to deliver: Power density [W kg^{−1}],

$$P = \frac{E}{t} \quad (6)$$

where, C = capacitance, V = voltage window, t = discharge time, A = integrated area of the CV curve, s = scan rate (mV s^{−1}), m = mass of the electroactive material on both electrodes, and a = area of the electrode.

Heating Properties of the Coated Fabric: The electro-thermal behavior of coated glass fiber fabric was measured using a thermal camera (TIM640, Micro-Epsilon, Germany) and a power supply unit (Stabilized Power Supply L 30D, Farnell Instruments LTD, UK) which supplies different voltages ranging from 5, 7, 10, and 15 V and the current was noted

from the power supply unit. The coated glass fiber fabrics were placed over the device plate. The thermal camera was installed on a tripod and connected to the computer. The thermal images obtained by the camera were extracted on the computer through the device software (TIM Connect). The changes in temperature of the coated glass fabric and achieved current were observed and recorded at various supplied voltages.

Strain Sensitivity of the Coated Glass Fiber Fabric: 2D materials coated glass fiber fabrics were also tested for strain sensitivity. The samples were held between the caliper’s external jaws by two large metal clips (Testometric Tensile Tester, load cell 100 kgf) hooked up to a multimeter. The multimeter monitored the relative change in the electrical resistance while stretching the fabric sensor. The voltmeter’s voltage was set to 1.0 V. Stretch and recovery tests of the fabrics were performed using five specimens (70mm × 25mm) of each set of untreated and graphene/MoS₂ coated fabrics. The fabric stretch ratio or strain (%) denoted as ϵ was calculated using the following formula.

$$\text{Strain (\%)}, \epsilon = \frac{L - L_0}{L_0} \times 100 \quad (7)$$

where L_0 is the initial gauge length of testing specimen while L is the length of testing specimen under loading.

Manufacturing of Multifunctional Smart Composite Structure: Multifunctional smart composite was manufactured using a VARI.^[11] The process employed room temperature-curable biobased laminating epoxy resin and biobased laminating hardener.^[87] The slow-curing bio-hardener and bio-epoxy resin were mixed at a ratio of 100:43. 10 g of PVA-H₂SO₄ gel electrolyte was then mixed with an amount of 200 g of epoxy-hardener mixture to achieve the best balance of electrochemical and mechanical performance. Then, with a weight-to-epoxy-hardener ratio of 5%, a piece of glass fiber fabric was immersed in PVA-H₂SO₄ gel electrolyte. Untreated glass fiber fabric was positioned against a backplate made of a smooth metal sheet; electrolyte-coated glass fiber fabric was sandwiched between the graphene/MoS₂ coated fabrics to act as separators and electrodes, respectively. Over the top electrode, a second absorbent layer of untreated glass fiber fabric was subjected. The surface of each electrode contains a connecting wire attached to it. Prior to that, untreated and treated glass fabrics were then dried in an oven at 50 °C for 15 min to ensure there was no moisture left in the fibers. To de-mold the resin-infused composite from the metal base plate, a peel ply was used. A mesh fabric was additionally used to guarantee an even flow of resin during the infusion procedure. Finally, a nylon plastic bag was used to completely seal the arrangement, ensuring a negative atmospheric pressure inside the bag by switching on the vacuum pump. To avoid the presence of any air bubbles, the resin was de-gassed twice; for 30 min before and for 10 min after mixing with the hardener and electrolyte as the pot life was only 43 min. By marking the resin level in the resin reservoir and continually monitoring the change in level over time, the resin was then infused into the bag using an inlet pipe while keeping a consistent flow. To ensure that composites were fully cured, infused preforms were kept at room temperature for 24 h inside the bag.

Supporting Information

Supporting Information is available from the Wiley Online Library or from the author.

Acknowledgements

The authors gratefully acknowledge funding from the Commonwealth Scholarship Commission (CSC) UK for a Ph.D. scholarship for M.D., and UKRI Research England the Expanding Excellence in England (E3) grant. The authors also acknowledge scientific illustration support from Natalie Corner. KSN acknowledges support from the Ministry of Education, Singapore (Research Centre of Excellence award to the Institute for Functional

Intelligent Materials, I-FIM, project No. EDUNC-33-18-279-V12) and from the Royal Society (UK, grant number RSR/R\190000).

Conflict of Interest

The authors declare no conflict of interest.

Data Availability Statement

The data that support the findings of this study are available from the corresponding author upon reasonable request.

Keywords

2D materials, energy storage devices, fiber reinforced composites, heating elements, heterostructures, multifunctional smart composites, structural health monitoring

Received: May 30, 2023

Revised: July 13, 2023

Published online:

- [1] M. H. Islam, S. Afroj, M. A. Uddin, D. V. Andreeva, K. S. Novoselov, N. Karim, *Adv. Funct. Mater.* **2022**, *32*, 2205723.
- [2] X. Yu, H. Cheng, M. Zhang, Y. Zhao, L. Qu, G. Shi, *Nat. Rev. Mater.* **2017**, *2*, 17046.
- [3] R. F. Gibson, *Compos. Struct.* **2010**, *92*, 2793.
- [4] N. Yamamoto, R. G. de Villoria, B. L. Wardle, *Compos. Sci. Technol.* **2012**, *72*, 2009.
- [5] A. Mirabedini, A. Ang, M. Nikzad, B. Fox, K.-T. Lau, N. Hameed, *Adv. Sci.* **2020**, *7*, 1903501.
- [6] E. García-Macías, A. D'Alessandro, R. Castro-Triguero, D. Pérez-Mira, F. Ubertini, *Compos. Struct.* **2017**, *163*, 195.
- [7] H. Asanuma, *JOM* **2000**, *52*, 21.
- [8] K. Chu, S.-C. Lee, S. Lee, D. Kim, C. Moon, S.-H. Park, *Nanoscale* **2015**, *7*, 471.
- [9] S. Araby, Q. Meng, L. Zhang, I. Zaman, P. Majewski, J. Ma, *Nanotechnology* **2015**, *26*, 112001.
- [10] C. Liao, Y. Li, S. C. Tjong, *Int. J. Mol. Sci.* **2018**, *19*, 3564.
- [11] N. Karim, F. Sarker, S. Afroj, M. Zhang, P. Potluri, K. S. Novoselov, *Adv. Sustainable Syst.* **2021**, *5*, 2000228.
- [12] Y. Lei, T. Zhang, Y.-C. Lin, T. Granzier-Nakajima, G. Bepete, D. A. Kowalczyk, Z. Lin, D. Zhou, T. F. Schranghamer, A. Dodda, A. Sebastian, Y. Chen, Y. Liu, G. Pourtois, T. J. Kempa, B. Schuler, M. T. Edmonds, S. Y. Quek, U. Wurstbauer, S. M. Wu, N. R. Glavin, S. Das, S. P. Dash, J. M. Redwing, J. A. Robinson, M. Terrones, *ACS Nanosci. Au* **2022**, *2*, 450.
- [13] K. S. Novoselov, A. Mishchenko, A. Carvalho, A. H. C. Neto, *Science* **2016**, *353*, aac9439.
- [14] J. J. Park, W. J. Hyun, S. C. Mun, Y. T. Park, O. O. Park, *ACS Appl. Mater. Interfaces* **2015**, *7*, 6317.
- [15] S. Afroj, L. Britnell, T. Hasan, D. V. Andreeva, K. S. Novoselov, N. Karim, *Adv. Funct. Mater.* **2021**, *31*, 2107407.
- [16] Y. Wang, Y. Wang, Y. Yang, *Adv. Energy Mater.* **2018**, *8*, 1800961.
- [17] C. Yan, J. Wang, W. Kang, M. Cui, X. Wang, C. Y. Foo, K. J. Chee, P. S. Lee, *Adv. Mater.* **2014**, *26*, 2022.
- [18] M. R. Islam, S. Afroj, C. Beach, M. Islam, C. Parraman, A. Abdelkader, A. Casson, K. Novoselov, N. Karim, *iScience* **2022**, *25*, 103945.
- [19] M. Dulal, S. Afroj, J. Ahn, Y. Cho, C. Carr, I.-D. Kim, N. Karim, *ACS Nano* **2022**, *16*, 19755.
- [20] F. Sarker, P. Potluri, S. Afroj, V. Koncherry, K. S. Novoselov, N. Karim, *ACS Appl. Mater. Interfaces* **2019**, *11*, 21166.
- [21] S. Tan, S. Afroj, D. Li, M. R. Islam, J. Wu, G. Cai, N. Karim, Z. Zhao, *iScience* **2023**, *26*, 106403.
- [22] N. Karim, S. Afroj, A. Malandraki, S. Butterworth, C. Beach, M. Rigout, K. Novoselov, A. Casson, S. Yeates, *J. Mater. Chem. C* **2017**, *5*, 11640.
- [23] M. A. Uddin, S. Afroj, T. Hasan, C. Carr, K. S. Novoselov, N. Karim, *Adv. Sustainable Syst.* **2022**, *6*, 2100176.
- [24] S. Maiti, M. R. Islam, M. A. Uddin, S. Afroj, S. J. Eichhorn, N. Karim, *Adv. Sustainable Syst.* **2022**, *6*, 2200258.
- [25] N. Karim, S. Afroj, K. Lloyd, L. C. Oaten, D. V. Andreeva, C. Carr, A. D. Farmery, I.-D. Kim, K. S. Novoselov, *ACS Nano* **2020**, *14*, 12313.
- [26] M. F. El-Kady, V. Strong, S. Dubin, R. B. Kaner, *Science* **2012**, *335*, 1326.
- [27] S. Lin, W. Feng, X. Miao, X. Zhang, S. Chen, Y. Chen, W. Wang, Y. Zhang, *Biosens. Bioelectron.* **2018**, *110*, 89.
- [28] S. Tan, M. R. Islam, H. Li, A. Fernando, S. Afroj, N. Karim, *Adv. Sens. Res.* **2022**, *1*, 2200010.
- [29] R. Rahimi, M. Ochoa, W. Yu, B. Ziaie, *ACS Appl. Mater. Interfaces* **2015**, *7*, 4463.
- [30] L.-Q. Tao, H. Tian, Y. Liu, Z.-Y. Ju, Y. Pang, Y.-Q. Chen, D.-Y. Wang, X.-G. Tian, J.-C. Yan, N.-Q. Deng, Y. Yang, T.-L. Ren, *Nat. Commun.* **2017**, *8*, 14579.
- [31] M. Saraf, K. Natarajan, S. M. Mobin, *ACS Appl. Mater. Interfaces* **2018**, *10*, 16588.
- [32] F. Clerici, M. Fontana, S. Bianco, M. Serrapede, F. Perrucci, S. Ferrero, E. Tresso, A. Lamberti, *ACS Appl. Mater. Interfaces* **2016**, *8*, 10459.
- [33] K. Chang, W. Chen, *ACS Nano* **2011**, *5*, 4720.
- [34] S. Bertolazzi, J. Brivio, A. Kis, *ACS Nano* **2011**, *5*, 9703.
- [35] J.-W. Jiang, *Front. Phys.* **2015**, *10*, 287.
- [36] L. Britnell, R. M. Ribeiro, A. Eckmann, R. Jalil, B. D. Belle, A. Mishchenko, Y.-J. Kim, R. V. Gorbachev, T. Georgiou, S. V. Morozov, A. N. Grigorenko, A. K. Geim, C. Casiraghi, A. H. C. Neto, K. S. Novoselov, *Science* **2013**, *340*, 1311.
- [37] R. Zan, Q. M. Ramasse, R. Jalil, T. Georgiou, U. Bangert, K. S. Novoselov, *ACS Nano* **2013**, *7*, 10167.
- [38] K. Roy, M. Padmanabhan, S. Goswami, T. P. Sai, S. Kaushal, A. Ghosh, *Solid State Commun.* **2013**, *175–176*, 35.
- [39] G. Algara-Siller, S. Kurasch, M. Sedighi, O. Lehtinen, U. Kaiser, *Appl. Phys. Lett.* **2013**, *103*, 203107.
- [40] N. Myoung, K. Seo, S. J. Lee, G. Ihm, *ACS Nano* **2013**, *7*, 7021.
- [41] S. K. Chakraborty, B. Kundu, B. Nayak, S. P. Dash, P. K. Sahoo, *iScience* **2022**, *25*, 103942.
- [42] O. A. Moses, L. Gao, H. Zhao, Z. Wang, M. L. Adam, Z. Sun, K. Liu, J. Wang, Y. Lu, Z. Yin, X. Yu, *Mater. Today* **2021**, *50*, 116.
- [43] Y. Xue, Y. Zhang, Y. Liu, H. Liu, J. Song, J. Sophia, J. Liu, Z. Xu, Q. Xu, Z. Wang, *ACS Nano* **2016**, *10*, 573.
- [44] W. Deng, Y. Chen, C. You, B. Liu, Y. Yang, G. Shen, S. Li, L. Sun, Y. Zhang, H. Yan, *Adv. Electron. Mater.* **2018**, *4*, 1800069.
- [45] U. Sundararaju, M. A. S. M. Haniff, P. J. Ker, P. S. Menon, *Materials* **2021**, *14*, 1672.
- [46] J. Mei, T. Liao, Z. Sun, *Energy Environ. Mater.* **2021**, *5*, 115.
- [47] R. Janeliukstis, D. Mironovs, *Mech. Compos. Mater.* **2021**, *57*, 131.
- [48] S. Afroj, N. Karim, Z. Wang, S. Tan, P. He, M. Holwill, D. Ghazaryan, A. Fernando, K. S. Novoselov, *ACS Nano* **2019**, *13*, 3847.
- [49] N. Karim, S. Afroj, S. Tan, P. He, A. Fernando, C. Carr, K. S. Novoselov, *ACS Nano* **2017**, *11*, 12266.
- [50] Q. Fang, M. Li, X. Zhao, L. Yuan, B. Wang, C. Xia, F. Ma, *Mater. Adv.* **2022**, *3*, 624.
- [51] C. Lee, X. Wei, J. W. Kysar, J. Hone, *Science* **2008**, *321*, 385.
- [52] S. Afroj, S. Tan, A. M. Abdelkader, K. S. Novoselov, N. Karim, *Adv. Funct. Mater.* **2020**, *30*, 2000293.

- [53] L. Song, T. Wang, W. Jing, X. Xie, P. Du, J. Xiong, *Mater. Res. Bull.* **2019**, *118*, 110522.
- [54] D. H. Jeon, *Energy Storage Mater.* **2019**, *18*, 139.
- [55] J. Wang, Z. Wu, K. Hu, X. Chen, H. Yin, *J. Alloys Compd.* **2015**, *619*, 38.
- [56] X. Chen, R. Paul, L. Dai, *Natl. Sci. Rev.* **2017**, *4*, 453.
- [57] A. Shameem, P. Devendran, V. Siva, R. Packiaraj, N. Nallamuthu, S. A. Bahadur, *J. Mater. Sci.: Mater. Electron.* **2019**, *30*, 3305.
- [58] T. Kim, W. Choi, H.-C. Shin, J.-Y. Choi, J. M. Kim, M.-S. Park, W.-S. Yoon, *J. Electrochem. Sci. Technol.* **2020**, *11*, 14.
- [59] W. Xiao, W. Zhou, T. Feng, Y. Zhang, H. Liu, L. Tian, *Materials* **2016**, *9*, 783.
- [60] K.-J. Huang, L. Wang, Y.-J. Liu, Y.-M. Liu, H.-B. Wang, T. Gan, L.-L. Wang, *Int. J. Hydrogen Energy* **2013**, *38*, 14027.
- [61] S. Patil, A. Harle, S. Sathaye, K. Patil, *CrystEngComm* **2014**, *16*, 10845.
- [62] D. Vikraman, K. Karuppasamy, S. Hussain, A. Kathalingam, A. Sanmugam, J. Jung, H.-S. Kim, *Composites, Part B* **2019**, *161*, 555.
- [63] R. Zhou, C.-j. Han, X.-m. Wang, *J. Power Sources* **2017**, *352*, 99.
- [64] N. H. A. Rosli, K. S. Lau, T. Winie, S. X. Chin, S. Zakaria, C. H. Chia, *J. Energy Storage* **2022**, *52*, 104991.
- [65] M. Fu, Z. Zhu, W. Chen, H. Yu, Q. Liu, *J. Mater. Sci.* **2020**, *55*, 16385.
- [66] A. Hussain, M. Malik, T. Salahuddin, S. Bilal, M. Awais, *J. Mol. Liq.* **2017**, *231*, 341.
- [67] J. Tabor, K. Chatterjee, T. K. Ghosh, *Adv. Mater. Technol.* **2020**, *5*, 1901155.
- [68] M. H. Islam, M. R. Islam, M. Dulal, S. Afroj, N. Karim, *iScience* **2022**, *25*, 103597.
- [69] P. Yang, S. Ghosh, T. Xia, J. Wang, M. A. Bissett, I. A. Kinloch, S. Barg, *Compos. Sci. Technol.* **2022**, *218*, 109199.
- [70] N. Karim, M. Zhang, S. Afroj, V. Koncherry, P. Potluri, K. S. Novoselov, *RSC Adv.* **2018**, *8*, 16815.
- [71] S. Upama, A. Mikhalchan, L. Arévalo, M. Rana, A. Pendashteh, M. J. Green, J. J. Vilatela, *ACS Appl. Mater. Interfaces* **2023**, *15*, 5590.
- [72] M. O. Faruk, A. Ahmed, M. A. Jalil, M. T. Islam, A. M. Shamim, B. Adak, M. M. Hossain, S. Mukhopadhyay, *Appl. Mater. Today* **2021**, *23*, 101025.
- [73] Y. Ma, N. Liu, L. Li, X. Hu, Z. Zou, J. Wang, S. Luo, Y. Gao, *Nat. Commun.* **2017**, *8*, 1207.
- [74] H. Zhang, D. Liu, J.-H. Lee, H. Chen, E. Kim, X. Shen, Q. Zheng, J. Yang, J.-K. Kim, *Nano-Micro Lett.* **2021**, *13*, 122.
- [75] A. Chhetry, M. Sharifuzzaman, H. Yoon, S. Sharma, X. Xuan, J. Y. Park, *ACS Appl. Mater. Interfaces* **2019**, *11*, 22531.
- [76] W. Zhang, S. Piao, L. Lin, Y. Yin, J. Guo, Z. Jiang, Y. Cho, R. Li, J. Gao, H. Pang, Y. Piao, *Chem. Eng. J.* **2022**, *435*, 135068.
- [77] F. S. Irani, A. H. Shafaghi, M. C. Tasdelen, T. Delipinar, C. E. Kaya, G. G. Yapici, M. K. Yapici, *Micromachines* **2022**, *13*, 119.
- [78] H. Qian, A. R. Kucernak, E. S. Greenhalgh, A. Bismarck, M. S. P. Shaffer, *ACS Appl. Mater. Interfaces* **2013**, *5*, 6113.
- [79] E. Senokos, Y. Ou, J. J. Torres, F. Sket, C. González, R. Marcilla, J. J. Vilatela, *Sci. Rep.* **2018**, *8*, 3407.
- [80] C. Meng, N. Muralidharan, E. Teblum, K. E. Moyer, G. D. Nessim, C. L. Pint, *Nano Lett.* **2018**, *18*, 7761.
- [81] A. Thakur, X. Dong, *Manuf. Lett.* **2020**, *24*, 1.
- [82] K. Moyer, C. Meng, B. Marshall, O. Assal, J. Eaves, D. Perez, R. Karkkainen, L. Roberson, C. L. Pint, *Energy Storage Mater.* **2020**, *24*, 676.
- [83] P. Liu, E. Sherman, A. Jacobsen, *J. Power Sources* **2009**, *189*, 646.
- [84] X. Peng, L. Peng, C. Wu, Y. Xie, *Chem. Soc. Rev.* **2014**, *43*, 3303.
- [85] A. M. Abdelkader, N. Karim, C. Vallés, S. Afroj, K. S. Novoselov, S. G. Yeates, *2D Mater.* **2017**, *4*, 035016.
- [86] M. R. Islam, S. Afroj, K. S. Novoselov, N. Karim, *Adv. Sci.* **2022**, *9*, 2203856.
- [87] M. Islam, S. Afroj, N. Karim, *ChemRxiv* **2023**.